Industrial Crystallization

Fundamentals and Applications

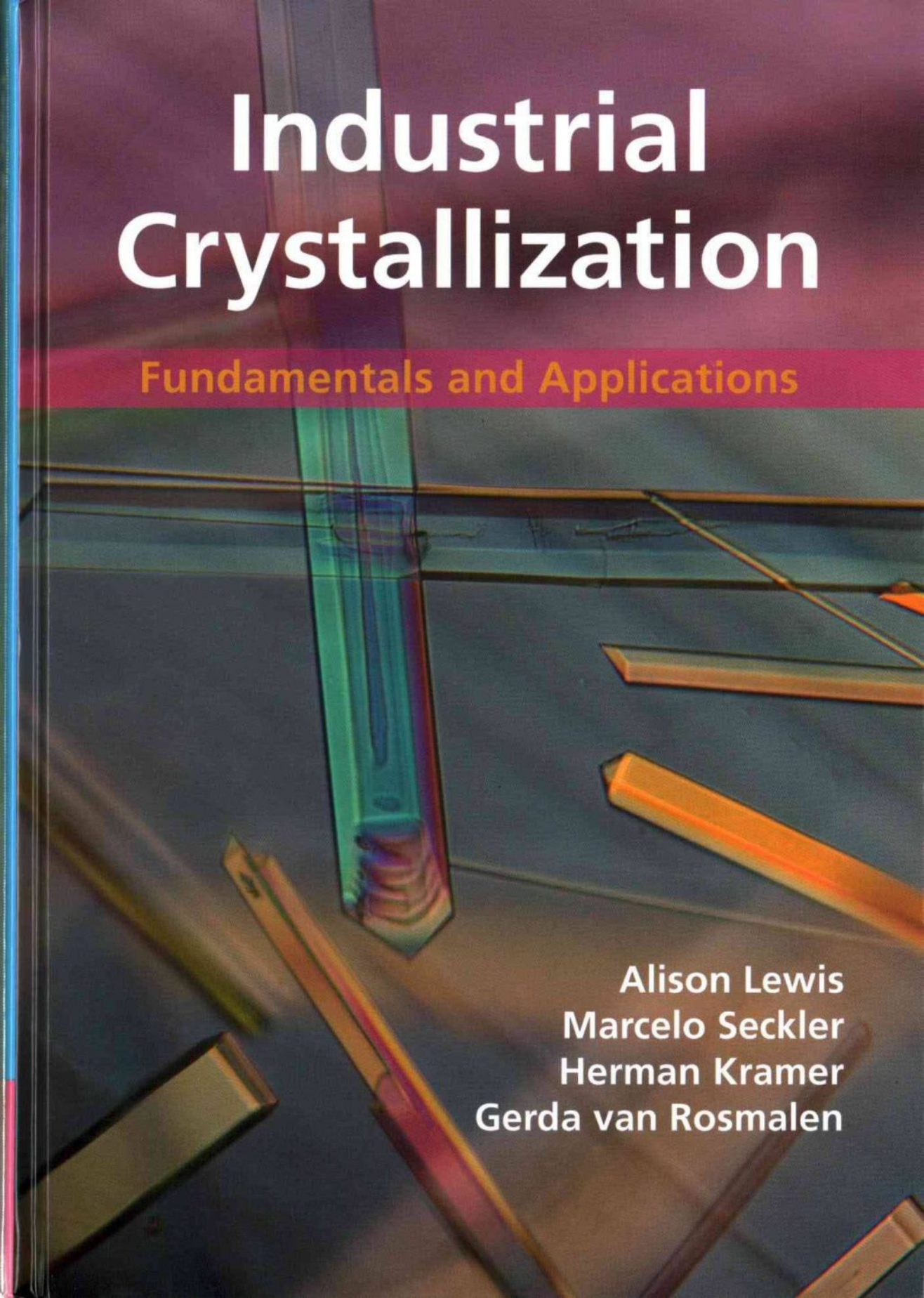

Alison Lewis
Marcelo Seckler
Herman Kramer
Gerda van Rosmalen

Industrial Crystallization

Bridging the gap between theory and practice, this text provides the reader with a comprehensive overview of industrial crystallization.

Newcomers will learn all of the most important topics in industrial crystallization, from key concepts and basic theory, to industrial practices. Topics covered include the characterization of a crystalline product and the basic process design for continuous evaporative and cooling crystallization, as well as batch crystallization. Also included are measurement techniques, and details on precipitation, melt crystallization, and polymorphism, as well as the impact of additives and impurities on process and product features.

Each chapter begins with an introduction explaining the importance of the topic, and is supported by homework problems and worked examples. Real-world case studies are also provided, as well as new industry-relevant information, making this an ideal resource for industry practitioners, students, and researchers in the fields of industrial crystallization, separation processes, particle synthesis, and particle technology.

Alison Lewis is a Professor at the University of Cape Town where she founded the Crystallization and Precipitation Research Unit. She is also a registered professional engineer, a Fellow of the South African Academy of Engineering (FSAAE), the South African Institute of Chemical Engineers (FSAIChE), and the South African Institute of Mining and Metallurgy (FSAIMM).

Marcelo Seckler is an Associate Professor at the University of São Paulo. He has previously been the CEO of the Brazilian Association for Chemical Engineers and the President of the Higher Council. He is now a member of the Higher Council. He also has a fellowship in productivity in technology from Brazil's National Council for Scientific and Technological Development.

Herman Kramer is an Associate Professor in the Department of Process and Energy at Delft University of Technology, and he is also a board member of the European Working Party on Industrial Crystallization and organizer of a number of international conferences.

Gerda van Rosmalen spent twenty years as Professor of Industrial Crystallization and Clean Technology at the Laboratory for Process Equipment at Delft University of Technology, and her distinguished positions include being a board member of the Working Party on Industrial Crystallization of the European Federation of Chemical Engineers.

Industrial Crystallization

Fundamentals and Applications

ALISON EMSLIE LEWIS
University of Cape Town

MARCELO MARTINS SECKLER
University of São Paulo

HERMAN KRAMER
Delft University of Technology

GERDA VAN ROSMALEN
Delft University of Technology

CAMBRIDGE
UNIVERSITY PRESS

CAMBRIDGE
UNIVERSITY PRESS

University Printing House, Cambridge CB2 8BS, United Kingdom

Cambridge University Press is part of the University of Cambridge.

It furthers the University's mission by disseminating knowledge in the pursuit of education, learning and research at the highest international levels of excellence.

www.cambridge.org
Information on this title: www.cambridge.org/9781107052154

First published 2015

Printed in the United Kingdom by TJ International Ltd. Padstow Cornwall

A catalogue record for this publication is available from the British Library

Library of Congress Cataloguing in Publication data
Lewis, Alison E., 1963–
Industrial crystallization : fundamentals and applications / Alison Lewis, University of Cape Town, Marcelo Seckler, University of São Paulo, Herman Kramer, Delft University of Technology, Gerda van Rosmalen, Delft University of Technology.
pages cm
Includes bibliographical references and index.
ISBN 978-1-107-05215-4 (alk. paper)
1. Crystallization – Industrial applications. 2. Crystal growth. 3. Chemistry, Technical. 4. Chemical engineering. I. Seckler, Marcelo, 1961– II. Kramer, Herman J. M. III. Rosmalen, Gerda van, 1936– IV. Title.
TP156.C7L49 2015
548′.5 – dc23 2015003495

ISBN 978-1-107-05215-4 Hardback

Additional resources for this publication at www.cambridge.org/9781107052154

Cover photo credit – Marcos Rodriguez-Pascual

Contents

Nomenclature

Main

Variable	Description	Unit	Chapter
a	activity	M	1
a	surface area of a solute entity in the cluster surface	m^2	4
A	crystal or particle surface area	m^2	2
A	Rate parameter of primary nucleation rate expression	$m^{-3}\ s^{-1}$	4
A_1, A_2	parameters for stress energy of a crystal, see eq. 5.45		5
A_{AZ}	cross sectional area of the annular zone of a DTB crystallizer	m^2	3
A_{hex}	circulation heat exchanger area	m^2	3
A_T	total crystal surface area per unit crystallizer volume	$m^2\ m^{-3}$	2
b, i, j, h, k	parameters in secondary nucleation rate expressions eq. 4.33 and eq. 4.34	–	4
B, B_0	secondary nucleation rate	$\#\ sm^{-3}$	4, 5, 7, 8
$B(L, t), B(v, t)$	particle birth rate for nuclei of size L or volume v	$\#\ m^{-3}\ m^{-1}\ s^{-1}$	7, 8
$b(\varepsilon,v)$	breakage function	m^{-1}	7
B	Burgers vector	m	5
C	attrition constant defined in eq. 4.46		4
C	empirical kernel of agglomeration		6
c	molar concentration	$kmol\ m^{-3}$	4
c	massic concentration	$kg\ m^{-3}$	5
c_b	impurity concentration in the bulk	$kmol\ m^{-3}$	2, 12
c_c	impurity concentration in the crystal	$kmol\ m^{-3}$	2, 12
$c_{c,G}$	impurity concentration in the crystal growing at a growth rate G	$kmol\ m^{-3}$	12
c_i	impurity concentration at the interface	$kmol\ m^{-3}$	12
$C(n)$	concentration of clusters of size n in solution	$\#\ molecules\ m^{-3}$	4
C_o	concentration of nucleation sites in solution	$\#\ molecules\ m^{-3}$	4, 5
$\overline{C_{A0}}$	initial reactant concentration	$kmol\ m^{-3}$	11

(*cont.*)

(*cont.*)

Variable	Description	Unit	Chapter
c_{eq}, $c_{eq,real}$	solubility; solubility of secondary nuclei with stress in the crystal lattice	kmol m^{-3}	4
c_p	specific heat	kJ $kg^{-1}°C^{-1}$	3
C_s, C_s^*	seed loading ratio defined in eq. 8.5, critical seed loading ratio	–	8
C_v	parameter for eq. 3.8	m s^{-1}	3
CV	coefficient of variation of the CSD	–	2
d, D	tee branch and tee run diameters in T-mixer	m	11
D	molecular diffusivity	m^2 s^{-1}	4, 5
$D(L, t)$, $D(v, t)$	particle death rate	# m^{-3} m^{-1} s^{-1}, # m^{-3} m^{-3} s^{-1}	7, 8
$D_{crystallizer}$	crystallizer diameter	m	3
$D_{DTB\_crystallizer}$	DTB crystallizer diameter	m	3
D_i	turbulent diffusivity	m^2 s^{-1}	11
D_{imp}	impeller diameter	m	3, 4, 11
d_m	molecular diameter	m	4
D_{lin}	linear crystal dissolution rate	m s^{-1}	5
$D_{vapor-head}$	crystallizer diameter that avoids liquid entrainment in the vaporhead	m	3
D_τ	crystallizer diameter that provides the residence time τ	m	3
E_D, E_R	Arrhenius activation energy for the crystal growth rate parameter, defined in eq. 5.37 and eq. 5.38		5
F	force	J mol^{-1}	1
f	flux of growth units towards a crystal surface	# m^{-2} s^{-1}	5
$f(n)$	frequency of attachment of entities to a cluster of size n	# s^{-1}	4
$f_o(n^*)$	equilibrium frequency of attachment	# s^{-1}	4
$f_o(n_{2D}^*)$	frequency of attachment of growth units at the edge of a critical nucleus with a surface area of $2\pi\ r_{2D}^* h$	s^{-1}	5
g	acceleration due to gravity	m s^{-2}	11
g	flux of growth units leaving a crystal surface	# m^{-2} s^{-1}	5
G	Gibbs free energy	J mol^{-1}	1
G	overall crystal growth rate	m s^{-1}	3, 4, 5
$g(n)$	frequency of detachment of entities to a cluster of size n	# s^{-1}	4
$G(L)$	size-dependent component of the overall crystal growth rate in eq. 5.45	–	5
$G(t)$	time-dependent component of the overall crystal growth rate with rate dispersion	m s^{-1}	5
$G(L, t)$, $G(\eta, L, t)$	overall crystal growth rate	m s^{-1}	5
G_{eff}, G_{kin}, G_{att}	effective, kinetic and attrition crystal growth rate, see eq. 4.37.	m s^{-1}	4
G_L	size-dependent overall crystal growth rate	m s^{-1}	5, 7, 8

(*cont.*)

Variable	Description	Unit	Chapter
G_v	volumetric growth rate	$m^3\ s^{-1}$	5
h	step height of a growing crystal	m	5
H	enthalpy	$J\ mol^{-1}$	1
H	Vickers hardness		4
H	enthalpy of crystallizer contents	J	3
$h(L)$	classification function	–	7
$H(L)$	secondary nuclei size distribution function, eq. 4.41	–	4
J	nucleation rate	$\#\ m^3\ s^{-1}$	4, 7, 8
J_{2D}	nucleation rate on a crystal surface	$\#\ m^{-2}\ s^{-1}$	5
K	Newton number for impeller, eq. 4.36	–	4
k	Boltzmann constant, 1.3806503×10^{-3}	JK^{-1}	4, 6
k_2	rate constant for two-step nucleation eq. 4.32		4
k_a	particle surface shape factor	–	2,4
K_{att}	parameter for eq. 4.39		4
k_d	mass transfer coefficient of solute in a solution adjacent to a growing or a dissolving crystal, defined in eq. 5.28 and eq. 5.47	$m\ s^{-1}$	5
K_D	massic crystal growth rate coefficient considering diffusion and rough surface disintegration, defined in eq. 5.48	$m\ s^{-1}$	5
k_{d0}	parameter defined in eq. 5.38	$m\ s^{-1}$	5
$k_{distr,i}$	effective distribution coefficient for incorporation of impurity i in a particle, molar or massic base	–	2, 3, 12
K_E, $K_{c\text{-}c}$, $K_{c\text{-}i}$	parameters for eq. 4.36		4
k_g	linear growth rate-based crystal growth rate coefficient defined in eq. 5.35 and eq. 5.36	$m\ s^{-1}$	5
K_G	mass-based crystal growth rate coefficient considering diffusion and surface integration, defined in eq. 5.31	$m\ s^{-1}$	5
$k_{m\&h}$	mass-based crystal growth rate coefficient considering diffusion and heat transfer, defined in eq. 5.40	$m\ s^{-1}$	5
k_n	reaction rate constant	$m^3\ kg^{-1}\ s^{-1}$ for first-order reaction	11
k_N, $k_N{}^1$	secondary nucleation rate constant, defined in eqs. 4.33 and 4.34		4
k_r	parabolic growth rate constant (eq. 5.10), linear growth rate constant (eqs. 5.11 and 5.21), exponential growth rate constant (eqs. 5.16 and 5.17) or overall surface integration controlled growth rate constant (eq. 5.29)	$[m\ s^{-1}]$, $[m\ s^{-1}]$, $[m\ s^{-1}]$ or $[kg^{-1}\ m^4\ s^{-1}]$	5

(*cont.*)

(*cont.*)

Variable	Description	Unit	Chapter
k_{r0}	parameter defined in eq. 5.37	–	5
$k_{r,d}$	massic dissolution rate by rough surface disintegration	m s^{-1}	5
K_{sp}	solubility product	kmol m^{-3}	
k_v	particle volume shape factor	–	2, 4, 7
L	crystal size, particle size	m	2, 4, 5, 6
$L_{1,0}$	number weighted mean of the CSD	m	2
$L_{2,1}$	length weighted mean of the CSD	m	2
$L_{4,3}$	volume weighted mean of the CSD	m	2, 3
$L_{c\text{-}c}$, $L_{c\text{-}i}$	parameters for eq. 4.36	–	4
L_D	mode of the CSD	m	2
L_F	cut size for fines removal in an MSMPR crystallizer	m	7
L_g	parameter for size dependent growth rate expression, eq. 5.43	–	5
L_i, L_j	sizes of particles of size classes i, j	–	6
$\overline{L_k}$	average of upper and lower bound of the k size interval	m	6
L_M, L_{50}	median size of the CSD	m	2, 10
L_P	cut size for classified product removal in an MSMPR crystallizer	m	7
L_T	total crystal length per unit crystallizer volume	m m^{-3}	2
M	mass	kg	5, 8
m, n	number of streams entering and leaving a crystallizer	–	7
m	molecular mass	kg $kmol^{-1}$	4
$M_{stream,comp}$	mass of a component in a stream. See subscripts for the list of streams and components	kg	4
$m(L)$, $m(L, t)$	mass density distribution	kg m^{-3} m^{-1}	2, 7
$M(L)$	cumulative oversize mass distribution	kg m^{-3}	2
$m+$, $m-$	concentration of the cations, anions	mol L^{-1}	
$M_{B,y}$	yield in melt crystallization	(mol solids) (mol feed)$^{-1}$	12
m_j	jth moment of the crystal size distribution with length as internal coordinate	m^j m^{-3}	4, 6, 7
m_j	jth moment of the crystal size distribution with volume as internal coordinate	m^j m^{-3j}	7
M_T	crystal mass per unit suspension volume	kg m^{-3}susp	2, 3, 4
n	reaction order	–	11
n	parameter for size dependent growth rate expression, eq. 5.43	–	5
N	number of supercritical clusters	–	4
N	stirrer speed	s^{-1}	3,11
$n(L)$, $n(v)$	number density distribution based on	# m^{-3} m^{-1}	2, 5, 6, 7,
$n(L, t)$, $n(v, t)$	particle size, on particle volume		8
$N(L)$	cumulative oversize number distribution	# m^{-3}	2

(*cont.*)

Variable	Description	Unit	Chapter
n^*	number of entities in a critical radius cluster	–	4
n_0	number density of nuclei	# m^{-3}	4, 5
N_A	Avogadro's number, 6.023×10^{26}	# k mol^{-1}	4
N_i	number of particles in size class i	# m^{-3}	6, 8
N_p	power number of an impeller, also called Newton number, defined by eq. 11.6	–	11
N_q	flow number of an impeller	–	11
N_T	total crystal number per unit crystallizer volume	# m^{-3}	2
N_c, N_0	number of crystals and droplets	–	4
Nu	Nusselt number, $Nu = \alpha\ L/\lambda$	–	5
P	pressure	bar	1
P	probability of nucleation	–	4
P	production rate of a crystallizer	(kg crystals) s^{-1}, (kg crystals) $batch^{-1}$	3
P_0	power input of stirrer	W or W (kg suspension)$^{-1}$	4, 7, 11
P_{susp}	minimum power needed to suspend particles in a mixed vessel	W(kg suspension)$^{-1}$	3
q_c	pumping capacity of an impeller	$m^3\ s^{-1}$	11
q_L	number density of secondary nuclei	$m^{-3}\ m^{-1}$	
Q_{heat}	heat duty to a crystallizer	J s^{-1}	3
r	ratio between upper and lower bounds of a size interval	–	
r, r^*, r^*_{2D}	cluster radius, critical radius, 2D critical nucleus radius	m	4
r, s	parameters for disruption rate given in eq. 6.17	–	6
R	ideal gas constant	J mol^{-1} K^{-1}	1
$R - 1$	fines-to-product flow ratio in an MSMPR crystallizer	–	7
$r(L_1, L_2)$	rate of collisions or rate of agglomeration	# $m^{-3}\ s^{-1}$	6, 7
$r(v_1, v_2)$	rate of collisions or rate of agglomeration	# $m^{-3}\ s^{-1}$	6, 7
r_0	radius of the molecule	m	
r_{agg}	agglomeration rate	# $m^{-3}\ s^{-1}$	6
R_A	mass-based crystal growth rate	kg $m^{-2}\ s^{-1}$	5
R_{HD}	crystallizer height-to-diameter ratio	–	3
$r_{i,j}$	collision rate between particles from interval i and j	# $m^{-3}\ s^{-1}$	6
R_{lin}	average linear crystal growth rate	m s^{-1}	5
r_c	length scale below which linear elasticity theory breaks down	[m]	5
S	entropy	J mol^{-1} K^{-1}	1
S	supersaturation ratio	–	4, 6
$S(v)$	selection function for particle breakage	s^{-1}	7
Sh	Sherwood number, $Sh = k_d L D^{-1}$	–	

(*cont.*)

(*cont.*)

Variable	Description	Unit	Chapter
T	temperature	°C or K	1, 5, 6
$T - T_{eq}$	undercooling	K	1, 4, 9, 12
T_R	roughening temperature	K	5
t, t_i	time or residence time, induction time	s	3, 4, 5
u	fluid velocity	m s^{-1}	11
v, V	side stream and main stream velocity of a T-mixer	m s^{-1}	
V	particle volume	m^3	2
V, $V(t)$	suspension volume	m^3	4, 7, 8, 11
$v(L)$	volume density distribution	m^3 m^{-3} m^{-1}	7
V_A, V_R, V_{TOT}	interaction potential between particles: attractive, repulsive and total	J	6
$\dot{V}_{att}$, $V_{att,ij}$	volumetric attrition of all crystals and of crystals of size i with impeller section j	m^3 m^{-3} s^{-1}	4
$v_{coll,ij}$	collision velocity of a crystal with an impeller	m s^{-1}	4
V_{cryst}	crystallizer volume, eq. 4.43	m^3	4
V_M	molecular volume	m^3 $molecule^{-1}$	4, 5
V_{macr}	detectable macroscopic volume	m^3	4
v_{max}	allowable vapor velocity in crystallizer head	m s^{-1}	3
v_{ss}	settling velocity of a particle in a suspension	m s^{-1}	3
v_{step}	step velocity of a growing crystal	m s^{-1}	5
v_{sup}	superficial velocity of a fluid in a pipe	m s^{-1}	3
V_T	crystal volume per unit suspension volume	m^3 m^{-3}	2, 7
v_{tip}	tip speed of stirrer	m s^{-1}	3
w	solute mass fraction	kg (kg solution)$^{-1}$	1
W^*	nucleation work	J	4
w_{eq}	solubility in mass fraction	kg (kg solution)$^{-1}$	2, 3
W_i	stress energy of one crystal	J	5
$W_{p,ij} W_{p,min}$	energy of the impact of a crystal with an impeller, eq. 4.44. minimum impact energy, eq. 4.47	J	4
$w_{phase,comp}$	mass fraction of component in a given phase of the crystallizer product stream	(kg i) (kg solid)$^{-1}$	3
W_{stir}, W_{pump}	electrical energy costs for stirring and recirculating in a continuous crystallizer	W	3
$w_{stream,phase,comp}$	mass fraction of component in a given phase of a stream. The stream is usually a suspension	(kg component) (kg phase)$^{-1}$	3
$w_{stream,comp}$	mass fraction of component or solvent in the liquid phase of the stream	(kg solvent) (kg solution)$^{-1}$	3
x	impurity mol fraction in liquid phase	(mol impurity) (mol solution)$^{-1}$	12
y	impurity mol fraction in crystalline phase	(mol impurity) (mol crystal)$^{-1}$	12

(*cont.*)

Variable	Description	Unit	Chapter
z	Zeldovitch factor	–	4, 5
z-1	ratio between the volumetric flow rate of the classifier recycle to the classifier product	–	7
$Z(n, t)$	number concentration of clusters with n solute entities	–	4
$Z_{i,j}$	number of crystals of size class i that collide with the impeller segment j	# m^{-3} s^{-1}	4

Greek letters

Variable	Description	Unit	Chapter
α	recycle ratio, liquid recycle flow per unit liquid flow out of the crystallizer	–	3
α	heat transfer coefficient	W m^{-2} K^{-1}	5
β	parameter in correlation for interfacial tension in eq. 4.10. Value 0.414	–	4
β	collision frequency kernel for agglomeration	m^3 $\#^{-1}$ s^{-1}	6
β_0	Size independent part of agglomeration kernel	–	6
β_1	Size dependent part of agglomeration kernel	m^3 $\#^{-1}$ s^{-1}	6
β_{agg}	agglomeration rate constant or agglomeration kernel	m^3 s^{-1}	6, 7
β_{disr}	disruption kernel	m^3 s^{-1}	6
δ, δ_h	boundary layer thickness for mass transfer and for heat transfer around a growing crystal	M	5
γ	activity coefficient	–	1
γ	particle surface energy	J m^{-2}	2
γ, γ_{eff}	interfacial free energy for homogeneous and heterogeneous primary nucleation	J m^{-2}	4
γ_{edge}	edge free energy of a growing crystal	J	4
λ	thermal conductivity	W m^{-1} K^{-1}	5
λ_0	step distance of a growing crystal	M	5
Λ	macroscale of turbulence	M	11
Γ	shear rate	s^{-1}	6
Γ / K_r	fracture resistance	–	4
ΔG	Gibb's free energy of phase change	J $molecule^{-1}$	2, 4
ΔG^*, $\Delta G_2{}^*$	energy barrier for nucleation from solution and for nucleation inside a cluster	J $molecule^{-1}$	4
ΔH_{evap}	enthalpy of evaporation	kJ kg^{-1}	3
ΔH_{cr}	enthalpy of crystallization	kJ kg^{-1}	5

(*cont.*)

(*cont.*)

Variable	Description	Unit	Chapter
Δm	mass of crystals formed in a batch	kg	8
ΔP	pressure drop around the circulation pump of a continuous crystallizer	Pa	3
$\Delta T_{hex,max}$	allowable temperature elevation of the suspension as it passes through the circulation heater of a crystallizer	°C	3
$\Delta\mu$	supersaturation	J mol^{-1} or J molecule^{-1}	4, 5, 9
ε	specific power input from impeller, energy dissipation rate	Wkg^{-1}	4, 6, 11
ε	volume fraction of liquid in a suspension	(m^3 liquid) (m^3 suspension)$^{-1}$	3, 7
η	mosaic spread associated with distortion of the crystal lattice	rad	5
η	Kolmogorov microscale of turbulence, defined by eq. 6.15	m	6
$\eta_{survival}$	secondary nuclei survival efficiency, eq. 4.42	–	4
$\eta_{geometric,\,j}$, $\eta_{target,ij}$	geometric and target efficiency parameters for eq. 4.42	–	4
$\eta(C_1, T)$	viscosity inside the clusters in two-step nucleation	–	4
θ	contact angle between a nucleus and a foreign substrate	°	4
μ	chemical potential	J mol^{-1}	1, 4, 9
μ	dynamic viscosity	Pa.s	3, 6
μ	shear modulus		4, 5
ν	kinematic viscosity	m^2 s^{-1}	6, 11
v_0	volume occupied by a molecule in the cluster	m^3	
ρ	density	kg m^{-3}	2, 3, 4, 5, 11
$\rho_{feed,liquid}$	liquid density in the feed stream	(kg liquid) (m^3 liquid)$^{-1}$	3
$\rho_{crystal}$, ρ_{liquid}	density of the crystalline and the liquid phase respectively	kg m^{-3}	3, 5
σ	standard deviation		2
σ	relative supersaturation	–	3
τ	residence time	s	3, 5, 7
τ_P, τ_L	residence time of product crystals and liquid in an MSMPR crystallizer	s	7
τ_{macro}, τ_{meso}, τ_{micro}	macromixing, mesomixing and micromixing time	s	11
τ_c, τ_d	circulation time, time for turbulent dispersion	s	11
τ_e, τ_R	time constant for engulfment and for chemical reaction	s	11
υ	Poisson ratio	–	5

(*cont.*)

Variable	Description	Unit	Chapter
$\varphi_{crystal}$	volume fraction of crystals	–	4
φ_2	cluster volume fraction	–	4
$\varphi_{H,stream}$	enthalpy of a stream	J s^{-1}	3
$\varphi_{v,prod}$	volumetric production rate of a crystallizer	m^3 suspension s^{-1}	3
$\varphi_{v,stream}$	volumetric flow rate of a stream	m^3 s^{-1}	3
$\varphi_{hex,max}$	allowable heat flux in circulation heat exchanger of evaporative crystallizer	J m^{-2}	3
Ψ	overall agglomeration efficiency of collisions between particles	–	6
ψ_{profit}	profit of a crystallization unit	€ $year^{-1}$	3
$\psi_{capital}$	capital costs	€ $year^{-1}$	3
ψ_{mb}	economic material balance costs and operation costs	€ $year^{-1}$	3
ψ_{oper}	economic material balance		
ξ	particle volume in population balance for agglomeration	m^3	7

Subscripts

0,e	start and end of a batch	3
b	bulk	2
circ	circulation stream between crystallizer body and heater in an evaporative crystallizer	3
cla	clear liquor advance stream in an MSMPR	7
crystal	crystal phase	2, 3, 7
eq	equilibrium	1, 2
feed	feed stream to a crystallizer	3
final	final condition in a batch	3, 8
hetero	heterogenenous primary nucleation	4
homo	homogeneous primary nucleation	4
i	interface	5
i	a component	3, 7
in	inflow stream	7
init	initial condition in a batch	3, 8
liquid	liquid phase	3
out	outflow stream	7
product	product stream	3
solvent	a component	3
seed	seeds to batch crystallizer	8
solid	solid phase (for multi-component crystals)	7
susp	suspension (slurry)	1, 3
tank	mixing vessel	6
vapor	vapor stream leaving a crystallizer	3

Streams: crystallizer feed, crystallizer product flow. Phases: liquid and crystal. Components: *i*, solvent.

Abbreviations

CFD	computational fluid dynamics
CSD	crystal size distribution
DT	draft tube crystallizer
DTB	draft tube baffle crystallizer
FC	forced circulation crystallizer
MSMPR	mixed suspension mixed product removal
ODE	ordinary differential equation
PF	plug flow reactor
PSD	particle size distribution

Industrial crystallization in practice

From process to product

Scope of the book

Crystallization refers to the phase transformation of a compound from a fluid or an amorphous solid state to a crystalline solid state. However, a crystallization process is not just a separation process; it is also a production process and a purification technique, as well as a branch of particle technology. It thus encompasses key areas of chemical and process engineering (Davey and Garside, 2000).

Crystallization is an extremely old unit operation, but is still used to produce highly specified speciality chemicals, and pharmaceuticals. In fact, there are few branches of the chemical and process industries that do not, at some stage, employ crystallization or precipitation for production or separation purposes (Mullin, 2003). Crystalline products include bulk chemicals such as sodium chloride and sucrose, fertilizer chemicals such as ammonium nitrate, potassium chloride, ammonium phosphates and urea; valuable products such as pharmaceuticals, platinum group metal salts and organic fine chemicals; products from the new and rapidly expanding field of engineered nanoparticles and crystals for the electronics industry, as well as biotechnology products such as protein crystals.

Although crystallization is an increasingly important industrial process, one that is governed by thermodynamics of phase separation, mass and heat transfer, fluid flow and reaction kinetics, it is not usually explicitly covered in any of the existing core chemical engineering material.

A large percentage of final or intermediate industrial products consist of a product of a crystallization process, i.e. tiny crystals or particles that have to conform to product specifications with respect to crystal size and shape, crystal size distribution, degree of agglomeration and uptake of either liquid or solid impurities. These product properties relate to the selected type of crystallization process as well as to the specific crystallization mode and type of hardware used for production. Crystallization is therefore much more than just a simple separation process. Unfortunately, the technology to design, operate and optimize crystallization processes is usually covered only very briefly as part of a broader overview on separations or particle technology, such as the chapter on Crystallization and Precipitation by Mullin in *Ullmann's Encyclopaedia of Industrial Chemistry* (Mullin, 2003) or other, similar, volumes (Richardson *et al.*, 2002 and Ruthven, 1997). The few textbooks that do focus on

industrial crystallization are mostly more than nine years old (Hurle, 1993, Jones, 2002, Mersmann, 2001, Mullin, 2001, Myerson, 2001, Nývlt, 1992, Söhnel and Garside, 1992, Ulrich and Glade, 2003) and do not cover the latest developments in what has recently been a rapidly changing field. A recent contribution to the field is the volume edited by Beckmann (2013).

In a crystallization process, many factors inter-relate, and thus it is not easy to operate the process unless there is an awareness of how all of these factors are connected. So the choices that are made have many interactive consequences. For example, the stirring in a crystallizer affects the interaction among particles in the suspension, and growth, agglomeration and attrition. In organic crystallization, for example, the solvent choice can have a significant influence on the nucleation of a certain polymorph, but also on the growth kinetics. In addition, there are many examples of how early choices in the design of a process or crystallizer can have a negative impact on the process. This is crucial and typical for crystallization – unlike other fields, like distillation. The interaction between the different aspects of the crystallization process and the crystallizer equipment is also why this book cannot be read as a collection of single separate chapters, and also why all the chapters refer to each other.

This book covers the field of crystallization as both a separation and a particle synthesis process. The main focus is on crystallization as a production process and how the product specifications introduce complexities into crystallization process and equipment. It is an attempt to collect the most relevant information from the currently scattered and disparate material in order to learn how to develop, operate and optimize industrial crystallization processes and their equipment. In addition, this book intends to provide new and industrially relevant information that has not been published before.[1]

It is aimed at undergraduate and postgraduate students, as well as industrial practitioners, and therefore, there is a balance between theoretical underpinnings (equations) and conceptual approaches to the various aspects of crystallization processes.

The book has three main objectives:

- to update the current information on industrial crystallization in line with recent advances in the field;
- to provide a core teaching text for undergraduate and postgraduate students studying separation processes, particle synthesis, particle technology and industrial crystallization at university level;
- to provide a text that is accessible to industrial practitioners – engineers and chemists involved in the development, operation and optimization of industrial crystallization processes in the pharmaceutical, fine chemicals, metallurgical, food, bioprocessing, pigments and dye production industries.

[1] "Industrial" in this case means that the text deals only with a suspension of small crystals or particles (mass crystallization) and not with large single crystals for electronic devices. Books about single large crystals are mostly called crystal growth.

Summary of the chapters

Chapter 1: Thermodynamics, crystallization methods and supersaturation

The choice of which crystallization method to use depends on the solubility of the final product. This chapter covers how the thermodynamics of crystallization, in the form of either phase diagrams or mathematical solubility models, provides the information required to select a crystallization method. Thermodynamics also defines the maximum yield and the energy consumption associated with the process. The supersaturation, the driving force for the crystallization process, is also defined and it is discussed how this can be expressed in terms of concentrations, undercooling or activities. For precipitation and anti-solvent crystallization, the supersaturation is generally high. It is also necessary to take into account the speciation of the different components in the system.

Chapter 2: Characterization of a crystalline product

Particulate products have to meet increasingly stringent demands on quality. The product specifications are generally related to properties such as the crystal size distribution of the product, the shape of the crystals, the mother liquor inclusions in the crystals, the uptake of impurities in the crystal lattice, the degree of agglomeration and the surface roughness of the crystals. This chapter deals with each of these features, outlining the characteristics of each, as well as how they are characterized through measurement.

Chapter 3: Basic process design for crystallization

This chapter discusses the basic design of industrial crystallizers. The major design tasks are the selection of the crystallization method, the crystallizer equipment and the mode of operation, the calculation of the flow sheet of the process and of the dimensions of the equipment, the area for heat transfer and evaporation, and the power requirement for the circulation devices. With the help of a costing model, the basic design also yields a first cost estimate of the process, in terms of both capital and operational costs.

The method described in this chapter has been developed and tested for evaporative and cooling crystallization processes, but can be adapted relatively easily for melt crystallization processes from suspensions. Examples are given for evaporative and cooling processes, for a DTB evaporative crystallizer, including mother liquor recycling, and for an Oslo evaporative crystallizer.

Chapter 4: Nucleation

Crystallization starts with the formation of a new crystalline phase. This nucleation of crystals is only possible if the liquid is supersaturated or undercooled. There are two mechanisms by which nucleation occurs: primary and secondary nucleation. This chapter deals with classical approaches to primary and secondary nucleation, but also covers new research on the latest thinking around two-step nucleation processes.

Chapter 5: Crystal growth

Whilst nucleation concerns the formation of the smallest possible sized particles that do not redissolve under the given conditions, the next step is crystal growth. This chapter covers the basic concepts of crystal growth and the different growth mechanisms, as well as equations to model the growth rate. The influence of the growth mechanism on surface roughness and crystal shape is also addressed.

Chapter 6: Agglomeration

Agglomeration is the process by which particles collide and adhere, and are eventually cemented together with crystalline material to form a stable particle or agglomerate. Particle agglomeration plays an important (but not always desirable) role in the formation of larger particles in precipitation and crystallization processes. This chapter discusses the physicochemical steps that lead to the formation of these agglomerates. In addition, mathematical models are discussed that are capable of describing the agglomeration process. Some basic modelling approaches are also included.

Chapter 7: The population balance equation

In crystallization processes, the size distribution of the produced crystals is essential because it determines not only the efficiency of the subsequent solid–liquid separation and drying steps, but also the final quality of the crystalline product. In this chapter, the concept of the population balance is introduced in order to describe the evolution of the crystal size distribution (CSD) in the crystallizer. This population balance describes the evolution of the number of crystals as a function of the crystal size, as a result of the crystallization kinetics and convection (mixing and in- and output flows). Modeling this CSD also requires the mass and enthalpy balances, as they describe the process conditions for the crystallization processes in the crystallizer. In addition, equations for the kinetic phenomena in the crystallizer, like nucleation, growth and agglomeration, are needed to connect the mass and energy balances to the population balance.

Solution methods for PBE-based crystallizer models are discussed, and it is shown how this information can be used in the design phase to select the appropriate crystallizer equipment, including specific features to manipulate the CSD. Multi-compartment models that describe the effects of profiles in the process conditions on the performance of an industrial crystallizer are also introduced. Profiles in conditions are unavoidable for crystallizers with large volumes or complex geometries. Multi-compartment models are therefore important to predict the CSD in scaling up.

Chapter 8: Batch crystallization

Although crystallization during batch operation is dictated by the same kinetic phenomena as the continuous crystallization process, and thus, in principle, can be described by the same models, there are a number of aspects of a batch-operated crystallization process that require special attention and are discussed in this chapter. These include the dynamic nature of the batch process, the changing suspension volume, the dominating

influence of the start-up phase (i.e. the initial population of crystals) on the product quality and the additional degree of freedom that the batch mode offers in the operation of the process. In batch crystallization, seeding is preferred over unseeded operation for better control of the product quality. However, the addition of seeds brings its own complications. This chapter covers these and other aspects of batch crystallization, such as the impact of supersaturation control during batch operation.

Chapter 9: Measurement techniques

The major process variables in a crystallization process are the level of supersaturation of the solute in the solution, the crystal size distribution and their distribution over the crystallizer. These variables determine the processes of nucleation, growth and agglomeration, which dominate the crystallization process. This chapter reviews and explains the latest available techniques for measuring these process variables.

Chapter 10: Industrial crystallizers

This chapter focuses on two aspects: firstly, the selection of an appropriate crystallizer and secondly, the optimization of an existing crystallizer to achieve the desired outcome. Several different types of industrial crystallizers are discussed, with a view to highlighting their distinguishing features, as well as how to optimize their operation in an industrial environment.

Chapter 11: Precipitation and anti-solvent crystallization

Although there is not a well-defined distinction between crystallization and precipitation, its definition is often based on the speed of the process, with precipitation usually being defined as a fast process that results in rapid formation of (extremely) small crystals. However, a more scientific definition of precipitation is the fact that the product is formed by a chemical reaction. Thus, precipitation is often referred to as "reactive crystallization."

Another important distinction is that the solubility of precipitates is low, typically in the range 10^{-3} to 1 kg m^{-3}, in comparison to products formed by crystallization, where solubilities are in the range 10 to 300 kg m^{-3}. A direct consequence of this low solubility that requires the mixing of reactants to achieve a sufficiently high yield is that the precipitation process is often mixing dominated. This has profound implications for both control and product quality in precipitation processes.

This is also the reason why anti-solvent crystallization is covered in the same chapter, since anti-solvent crystallization is the process of crystallizing out a solute by adding a solvent in which it is relatively insoluble. Thus, the anti-solvent process also forms products that can have a very low final solubility and is also usually mixing dominated.

Chapter 12: Melt crystallization

From a practical point of view, melt crystallization is an important method of crystallization that has a number of specialized applications. In essence, it is a method of producing

ultra-pure chemicals on a large scale with low energy consumption and without using solvents.

Although the distinction between solution crystallization and melt crystallization has no theoretical basis, the very different industrial techniques used for melt crystallization have historically justified the categorization. This chapter discusses both the theoretical and the practical aspects of melt crystallization. It also discusses eutectic freeze crystallization, which is a combination of melt and cooling crystallization.

Chapter 13: Additives and impurities

Although additives and impurities are often present in relatively small concentrations, even trace amounts can have a significant effect on the crystallization process as a whole. Thus, when working in "real" crystallization processes, understanding the influence of additives and impurities is very important. This chapter discusses the mechanisms by which additives and impurities act on crystals in solution.

Chapter 14: Polymorphism

Polymorphism is the ability of a compound to form more than one crystal structure. The reason that this is important is that the physical properties of a crystal (such as solubility and dissolution rate), melting temperature, density, morphology, stability, optical properties, conductivity and color are all dependent on the polymorph.

References

Beckmann, W. 2013. *Crystallization: Basic Concepts and Industrial Applications*, Wiley.

Davey, R. and Garside, J. 2000. *From Molecules to Crystallizers*, Oxford University Press.

Hurle, D. T. J. 1993. *Handbook of Crystal Growth*, North-Holland.

Jones, A. G. 2002. *Crystallization Process Systems*, Butterworth-Heinemann.

Mersmann, A. 2001. *Crystallization Technology Handbook*, Marcel Dekker.

Mullin, J. W. 2001. *Crystallization*, Butterworth-Heinemann.

Mullin, J. W. 2003. Crystallization and precipitation. In Ullmann, F. and Gerhartz, W. (eds.) *Ullmann's Encyclopedia of Industrial Chemistry.* VCH.

Myerson, A. S. 2001. *Handbook of Industrial Crystallization*, Butterworth-Heinemann.

Nývlt, J. 1992. *Design of Crystallizers*, CRC Press.

Richardson, J. F., Coulson, J. M., Harker, J. H. and Backhurst, J. R. 2002. *Coulson and Richardson's Chemical Engineering: Particle Technology and Separation Processes*, Butterworth-Heinemann.

Ruthven, D. M. 1997. *Encyclopaedia of Separation Technology*, Wiley.

Söhnel, O. and Garside, J. 1992. *Precipitation: Basic Principles and Industrial Application*, Butterworth-Heinemann.

Ulrich, J. and Glade, H. 2003. *Melt Crystallization: Fundamentals, Equipment and Applications*, Shaker.

1 Thermodynamics, crystallization methods and supersaturation

1.1 Why this chapter is important

As crystallization is concerned with the phase change in solid–liquid systems, analysis of crystallization processes starts with consideration of *phase diagrams*. In this chapter we will show how phase diagrams help to select a crystallization method, and to determine the yield and the temperature of a crystallization process. The industrially relevant features of the main *crystallization methods* are also presented.

We next consider the state of the liquid phase during crystallization processes. The solution is said to be supersaturated with respect to the crystallizing compound, meaning the solute concentration is higher than the solid–liquid equilibrium value. The *degree of supersaturation* is important because it is the driving force for the elementary rate processes of crystallization, such as nucleation and crystal growth. Therefore, expressions to determine the degree of supersaturation are presented, both rigorous expressions based on thermodynamics and less rigorous expressions commonly found in practice.

In order to calculate the degree of supersaturation, *thermodynamic models* that provide the activity coefficients of the solute are required. The main models available are compared, so that the most suitable model may be chosen, depending on the accuracy, the ease of obtaining model experimental parameters and the types of building units (simple organic molecules, biomolecules, electrolytes, etc.).

1.2 Phase diagrams

Phase diagrams display all the possible thermodynamic states of a system: the proportion and the composition of each coexisting phase. The thermodynamic states are described by a set of independently fixed variables, such as the pressure, the temperature and the mass fractions of all components but one (since the sum of the mass fractions of all components must be unity). For a binary system at constant pressure, the phase diagram may be represented by a two-dimensional T–x plot, where T is the system temperature and x is the mass fraction of one of the components, as exemplified for the silver nitrate–water system at atmospheric pressure in Figure 1.1.

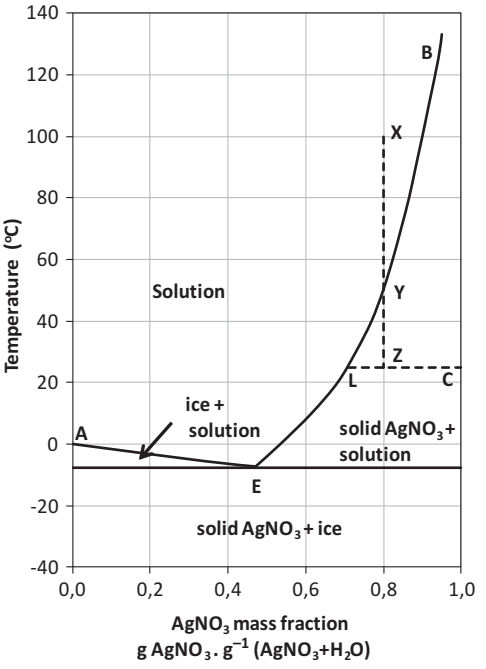

Figure 1.1 Phase diagram of the silver nitrate–water eutectic system at atmospheric pressure (Börnstein and Meyerhoffer, 1905). Reproduced with permission.

Worked example 1

Describe the composition of an $AgNO_3$–H_2O mixture containing 0.8 g $AgNO_3$/g mixture at the following temperatures: (a) 100 °C, (b) 25 °C, (c) −20 °C.

Worked example 1 solution

(a) The thermodynamic state of the system is represented by the point X in the phase diagram, Figure 1.1. The system is a homogeneous solution with a composition equal to the overall composition of the 0.8 g $AgNO_3$/g mixture.

(b) At 25 °C, point Z in the diagram, a solid is in equilibrium with a solution. The left end of the tie line (point L) gives a solution composition of 0.71 g $AgNO_3$/g and the right end (point C) gives as the solid phase pure $AgNO_3$ (there is no water within the solid). The mass fraction of solid phase in the mixture is given by the ratio LZ/LC, (0.8–0.7)/(1.0–0.7) = 0.33 g solid/g mixture. This is the so-called lever rule.

(c) For temperatures below the eutectic temperature E, the system is a heterogeneous mixture of pure water (ice) and pure salt (solid silver nitrate).

At the eutectic (point E), the two pure components as solids and a solution of eutectic composition are all in equilibrium. The curve AEB is called the *liquidus* line and gives all the possible concentrations of solutions in equilibrium with a solid.

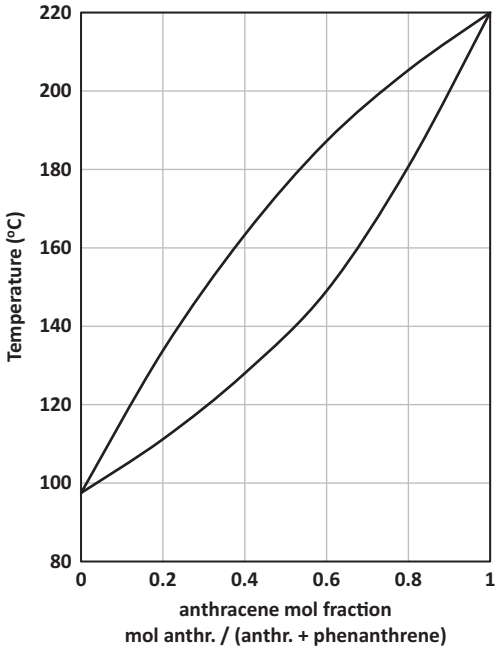

Figure 1.2 Phase diagram of the anthracene–phenanthrene solid–solution system (Schweizer, 1988).

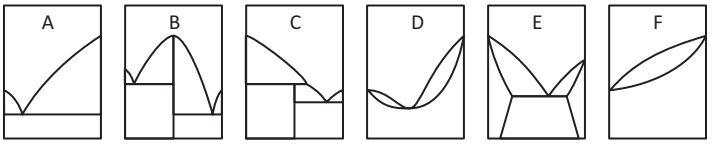

Figure 1.3 Phase diagrams for binary systems. The abscissas give the mass fraction of solute in the mixture, the ordinates represent the temperature.

Systems such as the one just presented, where the only solid phases are the pure components, are called eutectic systems. This behavior is encountered for most inorganic and many organic compounds. However, if the components in the mixture fit into each other's crystalline lattice, solid solutions may form, giving rise to a phase diagram such as the one shown in Figure 1.2. Figure 1.3 shows other common types of phase diagram for binary systems: systems exhibiting a mixed solid phase, i.e. a solid of a fixed composition A_xB_y (diagrams B, C in the figure), a solid solution with a "solid azeotrope" (D) and a combination of eutectic and solid-solution behavior (E). Phase diagrams are also available for multi-component systems and for cases where several solid phases are formed, such as polymorphs, hydrates and double salts.

For crystallization from solution, it is customary to represent the phase equilibrium information in terms of solubility curves, as shown in Figure 1.4. The use of solubility

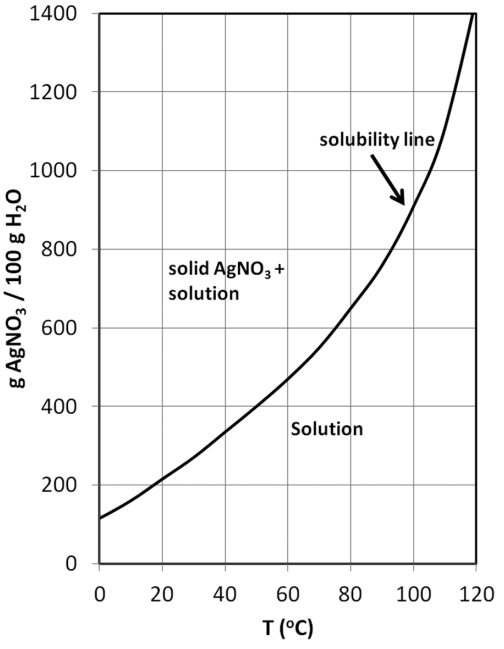

Figure 1.4 Solubility curve for the silver nitrate–water system (Börnstein and Meyerhoffer, 1905) Reproduced with permission.

lines or phase diagrams is equivalent. In a few applications, pressure is used to promote crystallization. In these cases, it is convenient to use a *P–x* phase diagram, such as the one shown in Figure 1.5.

An extensive treatment of thermodynamics for crystallization processes may be found in Nyvlt (1977). A number of excellent textbooks bring useful complimentary information, for instance Beckmann (2013), Mullin (2001) and Myerson (2001).

1.3 Crystallization methods

1.3.1 Modes of operation

Crystallization can be conducted continuously or batchwise. In the first mode, a homogeneous solution or a melt containing the solute to be crystallized is continuously fed to the crystallizer. Here some convenient interaction with the environment is applied (for instance, heat exchange) to promote crystallization. The solid is formed as a dispersed phase, which is kept in suspension by some mixing device. The suspension containing the dispersed solids and a solution leaves the reactor continuously, as exemplified in Figure 1.6. The slurry produced in the crystallizer is generally transported to a centrifuge or filter, where the crystals are separated from the mother liquor (solution or melt) and washed.

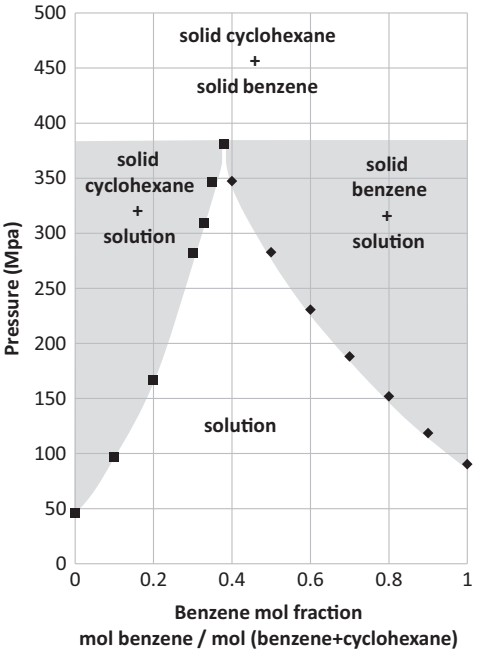

Figure 1.5 *P–x* diagram of a binary eutectic benzene–cyclohexane system (Nagaoka and Makita, 1987).

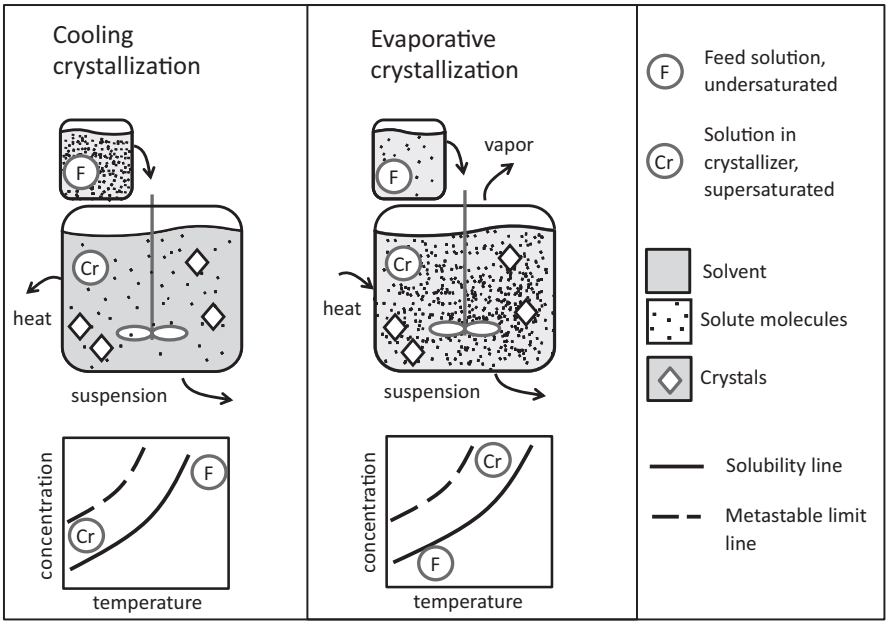

Figure 1.6 Schematic representation of continuous cooling and evaporative crystallization.

In batch crystallization, the crystallizer is initially filled with a homogeneous solution and subsequently subjected to an interaction with the environment to promote crystallization. After a pre-established batch time, the crystallizer contents are discharged. The slurry leaving the crystallizer proceeds to batchwise solid–liquid separation in a centrifuge or filter. Batch crystallization is, in a few cases, applied without agitation.

Continuous crystallization is generally applied when only one product has to be processed in a given unit and for large capacities. For multi-purpose plants, small production rates or products with severe scaling tendency, batch processes are often used. The properties of products delivered from continuous and batch processes are often very different, so the product specs may also guide the choice of operating mode. A more detailed comparison of modes of operation is found in Chapter 3.

1.3.2 Crystallization from the melt

A melt generally refers to a multi-component homogeneous liquid mixture that solidifies upon cooling. Melt crystallization is the common term applied to the crystallization of such systems to achieve ultrapurification of an (often organic) compound to purities of 99.9% to 99.999%. Phase diagrams such as those shown in Figure 1.3 D, E and F are used to determine the minimum number of crystallization steps needed for a given target. In practice, more steps are needed as high crystallization rates favor incorporation of impurities (or solvent) to a higher degree than predicted for single step processes. Since melt crystallization is merely used as a purification technique, the crystals are mostly remelted. Melt crystallization is also applied for the separation of molten compounds, such as oils and fats, into fractions, justifying the name fractional crystallization. A detailed description of melt crystallization is found in Chapter 14.

1.3.3 Crystallization from solution

Crystallization is often applied as a technique for separation of components from a solution, in which one of the components is the compound to be produced. Crystallization is also applied to obtain a product in a particular dispersed solid form (e.g. very fine or coarse particles), in which case a suitable solvent is added to a (usually impure) raw material. Compared to crystallization from a melt, it is a more easily applicable technique. Nicely faceted crystals with flat surfaces are readily obtained, while high purifications can be reached in a single crystallization stage owing to the rigidity of the crystal lattices, which prevent easy uptake of the solvent and of impurities that do not fit properly in the crystal lattice.

For crystallization from solution, the solute solubility is in general lower than 300 kg m^{-3}. For extremely soluble substances like sugars and highly hydrated sodium salts (e.g. $Na_2CO_3.10\ H_2O$), the difference between cooling crystallization from solution or from the melt becomes negligible.

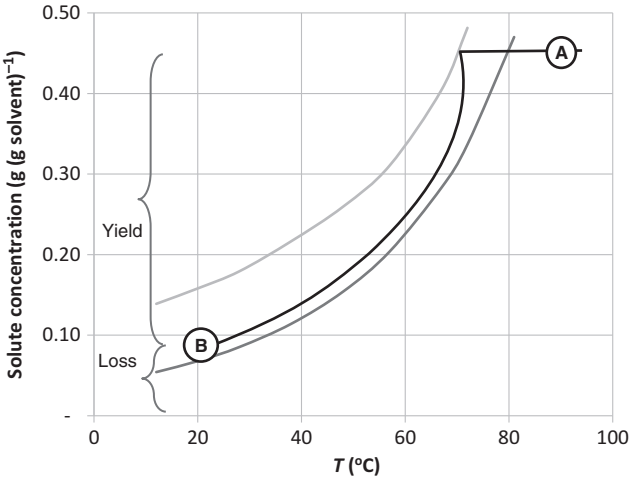

Figure 1.7 Solution trajectory during batch cooling crystallization of pentaerythritol in aqueous solution (Chianese and Mazzarotta, 1995), solubility (dark gray line) and metastable limit (light gray line). Reproduced with permission.

Four different methods of crystallization from solution can be distinguished: cooling of the solution, evaporation of the solvent, precipitation and addition of an anti-solvent.

1.3.3.1 Cooling crystallization

Cooling crystallization is generally applied for moderately or highly soluble substances (solubility in the range of 100–300 kg m^{-3}) when the slope of the solubility–temperature curve is positive and sufficiently steep. This is illustrated for a batch cooling process from state A to state B in Figure 1.7. Usually a temperature range is preferred where the slope of the solubility curve is the steepest, as a relatively large amount of solid is formed for a given degree of cooling. Besides, the final crystallizer temperature should be as low as possible in order to minimize the loss of product with the spent mother liquor. If the final crystallizer temperature is 30 °C or higher, cooling can be inexpensively achieved with water at ambient temperature. Care must be taken to avoid undesirable scaling in cold parts of the crystallization system. Mostly scaling occurs at the cold walls of the heat exchanger, hampering heat transfer. Finally, the solids content in the crystallizer should not exceed 30–35 vol% to allow further processing of the solids suspension. This requirement sets the highest possible temperature difference across a batch cycle. Too high a liquid viscosity, which could be encountered at low temperatures, should be avoided, because it leads to low crystal growth rates, low heat transfer rates and inefficient solid–liquid separation.

A similar analysis of the crystallization processes can be applied for continuous operation. The feed and the crystallizer temperatures (points A and B in Figure 1.7) are preferably located in the steepest region of the solubility curve. Low crystallizer

temperatures are chosen to reduce product loss, but temperatures below 30 °C are generally avoided.

Although during crystallization the system is not in thermodynamic equilibrium, mostly the actual concentrations do not differ much from those prescribed by equilibrium. This is why the yield can be derived from the solubility curve.

In agitated crystallizers, heat can be removed from the crystallizer via the scraped or non-scraped cooling surface of a heat exchanger. This is called indirect cooling. If incrustation (scaling) on the cooled surfaces is severe, direct cooling can be applied by introducing a refrigerant into the solution. The refrigerant is generally a gas or a liquid that is immiscible with the mother liquor.

Vacuum cooling, also called vacuum crystallization or flash cooling crystallization, is another heat removal alternative for systems exhibiting scaling tendency. A hot saturated solution is fed to a vessel maintained at a pressure that is lower than the vapor pressure of the solution. In this way, part of the solvent flashes off upon entering the vessel, and the liquid is adiabatically cooled to the boiling temperature corresponding to the vessel pressure. Crystallization is thus promoted due to loss of solvent and by cooling. As no heat-transfer surfaces are needed, scaling is restricted to the lateral walls near the liquid surface. It is often applied in multi-stage operation or with vapor recompression in order to reduce the energy consumption. Continuous vacuum crystallization is often preferred over continuous cooling because it is less sensitive to variations in process inputs and operator error. It cannot be applied, however, for salts having high boiling-point elevations or solutions containing large quantities of non-condensable gases.

The main limitation of the cooling method is that the yield is limited by the solubility of the compound at the lowest temperature. Such a limitation can sometimes be circumvented if the solution that leaves the crystallizer can be recycled to an upstream unit operation. For products with a high value, product losses are reduced by post-treatment of the mother liquor with anti-solvent crystallization.

1.3.3.2 Evaporative crystallization

In this crystallization method, the solid phase is formed by evaporation of the solvent. As crystallization proceeds from a boiling solution at a chosen temperature, the pressure and the mother-liquor concentration are fixed. The latter can be estimated from the solubility curve at atmospheric pressure, since solubility is almost pressure independent. The boiling temperature may be higher than for the pure solution if substantial amounts of impurities accumulate in solution due to solvent evaporation.

Solvent removal causes build-up of non-volatile impurities in the solution. Therefore, a bleed stream of dissolved impurities is needed. Consequently the yield is limited by the maximum acceptable amount of impurities in the mother liquor, as will be illustrated in Chapter 3. If no large bleed stream is needed, the yield approaches 100%. Such high yields are not feasible in cooling crystallization.

If the impurity content is low, the solute concentration in the mother liquor is approximately invariant during evaporation, so the yield may be calculated from a mass balance in the solution, and is directly related to the amount of solvent removed.

Evaporative crystallization is applied for moderately to highly soluble compounds (solubility in the range 100–300 kg m^{-3}), because a relatively large amount of solid is formed for a given amount of evaporated solvent. It is generally applied for compounds with a near-flat solubility–temperature curve, since under these circumstances cooling crystallization provides too small a yield to be applicable. Most evaporation units use low-pressure steam (4 bar) or by-product steam (1 to 2 bar) generated in chemical processes. Vacuum evaporation is sometimes applied to take advantage of cooling and evaporation simultaneously (flash cooling). Vacuum evaporation is also used for products that are not stable at the atmospheric boiling temperature.

In continuous processes measures are usually taken to minimize the energy consumption. The most common option is multiple-effect evaporation, wherein the solvent vaporized in one effect provides the heat needed to vaporize the solvent in a following effect, which is operated at a lower temperature and thus at a lower pressure. Sequences of three to six crystallizers can be applied. The evaporation temperature in the last stage should in general be higher than 20–30 °C and more commonly 50 °C, otherwise the vacuum system becomes too expensive. Another way of reducing energy consumption is by means of single-effect evaporators with either mechanical or thermal vapor recompression. Incrustations of compounds with a retrograde solubility, such as anhydrous sodium sulfate or calcium sulfate, are often a problem. These evaporators are said to be reduced-pressure evaporative crystallizers, to distinguish them from "true" vacuum crystallizers (see Section 1.3.3.1 on "Cooling crystallization"), for which no external heat source is provided.

1.3.3.3 Precipitation

Precipitation is applied for sparingly soluble substances (solubility in the range 0.001–1 kg m^{-3}), because cooling or evaporation would result in negligible yield. In precipitation, two highly soluble reactants are mixed to form a sparingly soluble product (see Figure 1.8). Concentrated reactant streams provide a reaction product at a concentration that largely exceeds its solubility, so that its conversion into solid particles is a fast process. The residual solute concentration compared to the initial concentration is so low that the yield can be determined from the initial concentrations only. Because of the locally very high supersaturations, solid phases other than those expected could be encountered, such as polymorphs and amorphous materials, so care must be taken to use a phase diagram that takes into account the phase of interest. The stoichiometry varies greatly near the feed inlet(s), and large concentration differences can exist over the vessel.

1.3.3.4 Anti-solvent crystallization

An anti-solvent is mixed with a concentrated solution (see Figure 1.8). Crystallization occurs because the solute has a lower solubility in the resulting mixed solvent (how much lower depends on the final mixing ratio). Since the addition of the anti-solvent also dilutes the mixture, the decrease in solubility should largely exceed the dilution effect in order to be effective (see Figure 1.9).

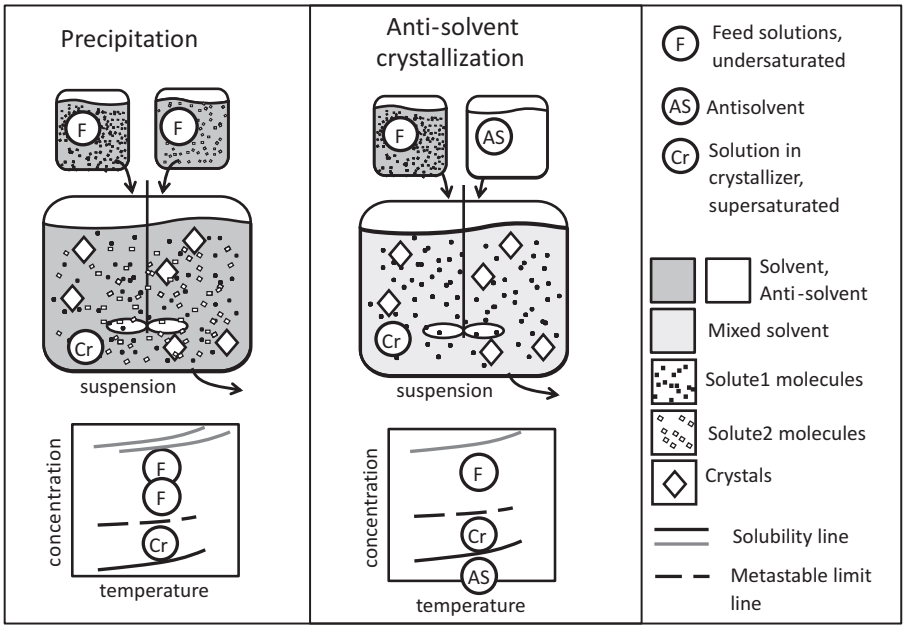

Figure 1.8 Schematic representation of precipitation and anti-solvent crystallization.

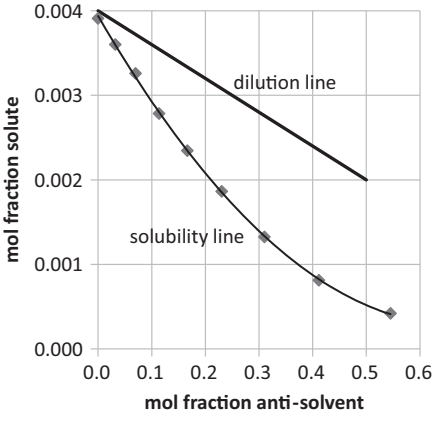

Solute: D-(p-Hydroxy)phenylglycine

Solvent: water

Anti-solvent: 2-propanol

Mol fraction anti-solvent: $x_{anti\text{-}solvent} = \dfrac{\text{mol anti-solvent}}{\text{mol (solvent + anti-solvent)}}$

Mol fraction solute: $x_{solute} = \dfrac{\text{mol solute}}{\text{mol (solute + solvent + anti-solvent)}}$

Figure 1.9 Solubility and dilution in anti-solvent crystallization (Zhou *et al.*, 2008).

Due to the low solubility of the crystallizing compound in the mixed solvent, solute concentrations much above the solubility are created near the anti-solvent inlet point, so the process is fast. Unlike precipitation, the stoichiometry is constant throughout the crystallizer.

Organic liquids are common anti-solvents for aqueous systems, so the water activity in the mixed solvent is lower than in the original aqueous solution. For compounds containing water molecules in the crystalline lattice, this lower water activity leads to the formation of a less hydrated compound for a given crystallization temperature.

Salting out is a crystallization method characterized by the addition of an easily soluble salt to an aqueous solution containing the compound to be crystallized. Crystallization occurs because the water activity decreases in the presence of the salt, and so does the solubility of the compound. It is also possible to provoke crystallization by adding a salt that contains a common ion with the crystallizing compound, i.e. an AC salt is added to an AB aqueous solution to decrease the solubility of the AB salt.

1.4 Selection of crystallization methods

Selection of the most suitable crystallization method for a given crystallization task is primarily based on thermodynamic considerations, as shown below. However, the final selection sometimes depends on operational features of the crystallizing system as well, such as the tendency to scaling and the thermal stability, among others.

Using the phase diagram as the starting point, the selection tree in Figure 1.10 can be built. Melt crystallization is mostly applied for solutions with high concentrations ($>$ 90 wt%) when ultra-purification (target purities of 99.9 to 99.9999%) is desired or when the melt and the solvent (or impurities) form solid solutions. If the target purity is not too high, other less expensive separation methods can be applied after adding a suitable solvent. Other requirements for the application of melt crystallization are a melting temperature in the range 0 to 100 °C, not too high a liquid viscosity and the absence of a solid azeotrope. For suspension melt crystallization the product comes out of the crystallizer as a solid and as a liquid after the washing step, and only for layer growth does it come out as a liquid from the crystallizer. The applicability of melt crystallization is described in detail in Chapter 12.

Cooling crystallization is recommended for solutes with moderate solubility in the range 100–300 kg m^{-3} and a steep positive slope in the temperature–solubility curve (slope >0.005 $°C^{-1}$). If the crystallizing compound has a strong tendency to scaling, vacuum cooling (flash cooling) crystallization is used, as no heat transfer surfaces are needed. If the solubility–temperature curve is near-flat, cooling crystallization results in an unacceptably low yield, so evaporative crystallization is chosen. Evaporation, vacuum evaporation and multi-stage evaporation can in fact be applied irrespective of the slope of the solubility curve. Other requirements for the application of cooling and evaporative crystallization are operational temperatures in the range 0 to 100 °C, no product degradation at operating temperatures, no solid solutions.

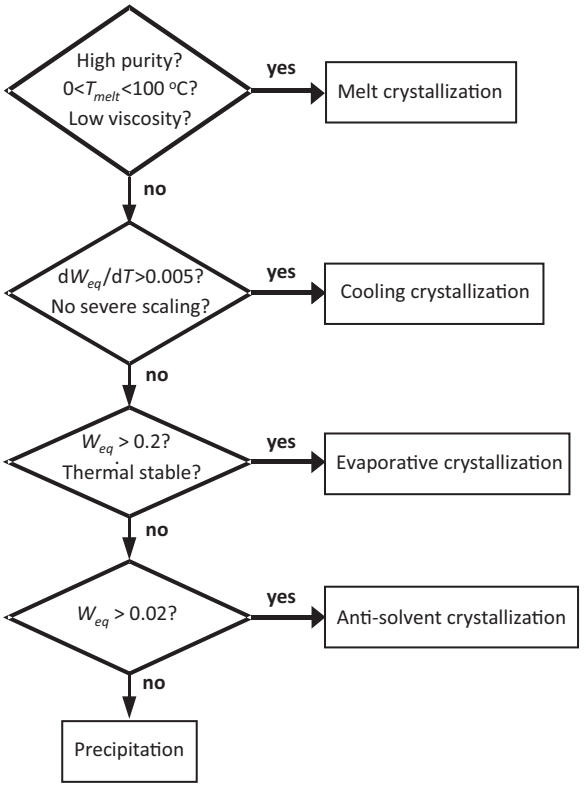

Figure 1.10 Diagram for selection of crystallization methods.

Anti-solvent crystallization is an alternative to evaporative crystallization for heat-sensitive compounds. It is also suitable for high-value products after a cooling crystallization step to recover the residual solute.

For slightly soluble compounds (0.001–1 kg m^{-3}), precipitation is employed.

The selection of the method may to a certain extent be guided by the desired product specification, as indicated in Table 1.1. Melt crystallization is chosen if the target is ultrapurification. If large, pure crystals are required, crystallization from a concentrated solution is preferred, such as in cooling or evaporative methods. For fine particulate material or aggregated particles, crystallization from diluted solutions, such as in the precipitation and anti-solvent methods, is selected. Typical products obtained by cooling crystallization and by precipitation are compared in Figure 1.11.

Worked example 2

1 metric ton/day of pentaerythritol (PE) for use in the formulation of paints is to be produced by crystallization from an aqueous solution containing 0.45 g g^{-1} solvent. Choose a crystallization method and a mode of operation, and determine the operation conditions, the yield, the PE loss, and the solids content in the final slurry.

Table 1.1 Quality of the products obtained from various crystallization methods

	Features of the process		Product quality	
Crystallization method	Solubility (wt%)	Relative supersaturation σ (-)	Particle size	Purity
Melt	90	0.001 to 0.01	Product is a liquid	Very good*
Cooling, Evaporative	10 to 30	0.001 to 0.01	100–1000 µm	Good
Precipitation, Anti-solvent	<0.01	1 to 100	0.5–100 µm (agglomerates)	Poor

* For melt crystallization, purity in one crystallization stage is poor, but final purity after many stages is very good.

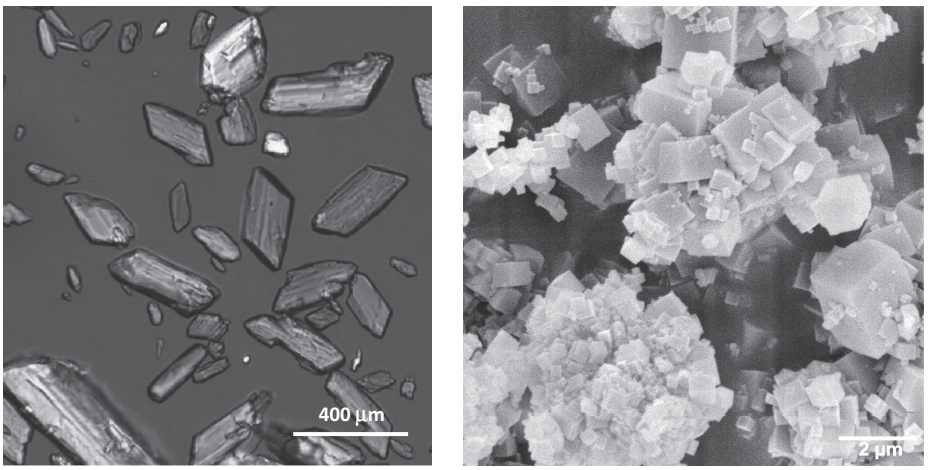

Figure 1.11 Large crystals obtained by cooling crystallization of a herbicide (left) and small calcium fluoride crystals formed by precipitation (right).

Solution to worked example 2

Inspection of the phase diagram (Figure 1.7) shows that the PE solubility varies considerably with temperature $(0.45–0.09)/(80–20) = 0.006\ °C^{-1}$. Therefore, cooling crystallization is chosen. Batch operation is chosen because the capacity is small. PE is known to have a manageable tendency to scaling, so indirect cooling may be applied. The initial temperature is the PE saturation temperature of 80 °C. To maximize the yield, a low final temperature of 25 °C may be assured with low-cost cooling-tower water. Calculations with 1 g of solvent give a yield of $(0.45–0.09)/0.45 = 0.8$ g solid PE per gram initial PE and a product loss of $(1–0.8) = 0.2$ g of PE in solution per g initial PE. The solids content at the end of the batch is $0.36/(0.45 + 1) = 0.248$ g PE per g slurry, which is easily suspended and pumped.

Crystallization methods are also described in a number of excellent texts (Beckmann, 2013, Jones, 2002, Mullin, 2001, Myerson, 2001, Randolph and Larson, 1988).

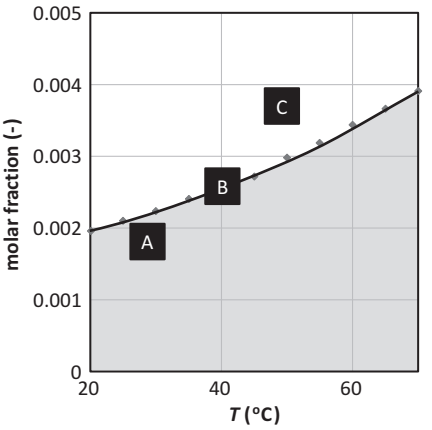

Figure 1.12 Solubility of D-(*p*-hydroxy)phenylglycine in water (Zhou *et al.*, 2008).

Thermodynamics, methods and design or crystallization systems have been nicely addressed (Jones, 2002). One can also find textbooks with an extended treatment of precipitation (Söhnel and Garside, 1992) and melt crystallization (van 't Land, 2004). Chapters of books are available on the crystallization of biomolecules (Myerson, 2002, Pessôa Filho *et al*., 2011).

1.5 Supersaturation

Consider a homogeneous solution that is not necessarily in an equilibrium state, for example the pharmaceutical intermediate D-(*p*-hydroxy)phenylglycine in water, the solubility of which is shown in Figure 1.12. If the thermodynamic state of the solution is situated below the solubility line (region A in the figure), the solution is said to be *undersaturated.* If the solution is at the solubility line (line B), the solution is said to be *saturated* and if it is above the solubility line (region C), the solution is said to be *supersaturated.*

The elementary processes related to crystallization, such as nucleation and molecular crystal growth, take place in supersaturated solutions. The degree of supersaturation often determines their mechanism and rate. Therefore, in order to properly characterize these rate processes, variables that quantitatively express the degree of supersaturation are needed. A rational basis found in thermodynamics is presented next. Thereafter, other practical quantities that describe the degree of supersaturation are introduced, based on easily measurable variables such as concentrations or temperatures.

1.5.1 General thermodynamic expression for the supersaturation

Consider a multi-phase system with allowed mass transfer of components between the phases. A requirement for thermodynamic equilibrium in such a system is equal

chemical potentials of each component through all phases. Let μ_{liquid} and μ_{solid} [J mol^{-1}] represent the chemical potential of the crystallizing compound in a solution and as a solid, respectively. If the system is in equilibrium then:

$$\mu_{liquid,eq} = \mu_{solid} \tag{1.1}$$

Suppose the system leaves its equilibrium state due to some external action, e.g. cooling or evaporation of part of the solvent, so that the solution becomes supersaturated. The chemical potential of the solute in solution μ_{liquid} is now higher than the corresponding equilibrium value $\mu_{liquid,eq}$. The difference between the chemical potential of the solute in the supersaturated and the saturated states is called "the supersaturation" $\Delta\mu$[J mol^{-1}], and represents the thermodynamic driving force for crystallization:

$$\Delta\mu = \mu_{liquid} - \mu_{liquid,eq} = \mu_{liquid} - \mu_{solid} \tag{1.2}$$

Depending on the crystallization method, the supersaturation is allowed to vary with respect to some variables, others being held constant, so that specific expressions for $\Delta\mu$ result.

1.5.2 Supersaturation for processes at constant temperature and pressure

1.5.2.1 General expression for solids constituted by a single species

Crystallization occurs at constant temperature (T) and pressure (P) for evaporative, precipitation and anti-solvent crystallization. If the solute is a single species, such as a neutral molecule, the driving force $\Delta\mu$ is given by:

$$\Delta\mu = RT\ln(a/a_{eq}) = RT\ln(\gamma c/\gamma_{eq}c_{eq}) = RT\ln S_a \tag{1.3}$$

$$S_a = \gamma c/\gamma_{eq}c_{eq} \tag{1.4}$$

where a is the activity of the solute [M], γ its activity coefficient [dimensionless], c its molar concentration in solution and the "eq" subscript indicates equilibrium at the (invariant) system temperature and pressure. R[J mol^{-1} K^{-1}] is the ideal gas constant and T[K] is the temperature. S_a is called the activity-based supersaturation ratio. For anti-solvent crystallization, the equations above are applied by making the concentrations c and c_{eq} refer to the solute in the solvent (in kg solute per kg or m^3 solvent or in kg solute per m^3 mixed solvent).

1.5.2.2 General expression for solids constituted by multiple species

Now suppose the solid is composed of more than one solute species, such as in crystallization of an electrolyte. For a solid of chemical formula $A_{\nu A}B_{\nu B}\ldots I_{\nu i}$, i.e. formed by ν_i units of species i, one writes:

$$\Delta\mu = RT\ln\left(\frac{\prod a_i^{\nu_i}}{K_{sp}}\right) = \frac{RT\prod(\gamma_i c_i)^{\nu_i}}{K_{sp}} = RT\ln S_{am} \tag{1.5}$$

$$K_{sp} = \prod(\gamma_{i,eq}c_{i,eq})^{\nu_i} \tag{1.6}$$

$$S_{am} = \frac{\prod(\gamma_i c_i)^{\nu_i}}{K_{sp}} \tag{1.7}$$

K_{sp} (with units M^{ν}, see equation 1.6) is the solubility product of the solid and S_{am}[-] is the activity-based supersaturation ratio for multiple solute species. For stoichiometric addition of the reactants, equation 1.5 simplifies to:

$$\Delta\mu = \mathrm{RT}\,\nu\,\ln\,S_a \tag{1.8}$$

$$\nu = \sum \nu_i \tag{1.9}$$

The supersaturation $\Delta\mu$ is obtained with equations 1.5 or 1.8 provided that the solubility of the solid phase (a_{eq} or K_{sp}) and the activity coefficients of the solutes in solution (γ_i) are known. These activity coefficients may in some cases be obtained by a suitable thermodynamic model (see Section 1.6). These equations are valid for both low and high supersaturation.

1.5.2.3 Expressions for low supersaturation

For low supersaturation, the thermodynamic state of the supersaturated solution during crystallization is not very far from equilibrium, so $\gamma \approx \gamma_{eq}$ and equation 1.3 simplifies to:

$$\Delta\mu = RT\ln(c/c_{eq}) == RT\ln S_c \tag{1.10}$$

$$S_c = c/c_{eq} \tag{1.11}$$

Similarly, for multiple solute species, $\gamma_i \approx \gamma_{i,eq}$, so equation 1.5 simplifies to:

$$\Delta\mu = RT\ln S_{cm} \tag{1.12}$$

$$S_{cm} = \frac{\prod (c_i)^{\nu_i}}{\prod (c_{i,eq})^{\nu_i}} \tag{1.13}$$

S_c is called the concentration-based supersaturation ratio and S_{cm} the concentration-based supersaturation ratio for multiple solute species.

Therefore, for processes conducted at constant temperature and pressure at low supersaturation, the supersaturation $\Delta\mu$ relates directly to easily measurable quantities, such as S_c and S_{cm}. The requirement of low supersaturation is fulfilled for easily or moderately soluble compounds, which crystallize slowly by evaporation. However, this simplification does not apply to slightly soluble compounds, because these compounds crystallize rapidly by precipitation and anti-solvent crystallization. In these cases, $\gamma_i \neq \gamma_{i,eq}$ and equations 1.3 or 1.5, based on activities, have to be used.

It is customary to use the so-called relative supersaturation σ as an alternative expression for the degree of supersaturation:

$$\sigma = \Delta c/c_{eq} \tag{1.14}$$

with $\Delta c = c - c_{eq}$. For a single solute at low supersaturation σ relates to the thermodynamic expression $\Delta\mu$. Under these circumstances $\sigma = \Delta c/c_{eq} \ll 1$, so equation 1.10

can be rearranged to:

$$\Delta\mu = RT \ln\left(\frac{c}{c_{eq}}\right) = RT \ln\left(1 + \frac{\Delta c}{c_{eq}}\right) = RT\frac{\Delta c}{c_{eq}} \tag{1.15}$$

$$\Delta\mu = RT\,\sigma \tag{1.16}$$

For multiple solute species in stoichiometric proportion, such as when a salt is dissolved in a solution, equation 1.8 becomes:

$$\Delta\mu = RT\,v\,\ln\sigma \tag{1.17}$$

1.5.3 Driving force for processes at constant pressure (varying temperature)

For cooling crystallization from solutions and melts at constant pressure, we apply the definition $G = H - TS$ [J mol^{-1}] for both phases:

$$-\Delta\mu = \Delta G = \Delta H - T\Delta S \tag{1.18}$$

where Δdenotes the difference in μ, G, H or S between the two phases at temperature T. For the equilibrium temperature T_{eq}[K] this becomes:

$$0 = \Delta H - T_{eq}\Delta S \tag{1.19}$$

We further assume that the temperature T of the supersaturated solution and T_{eq} of the saturated solution are not very far apart, so ΔH and ΔS have approximately the same values at temperatures T and T_{eq}. By eliminating ΔS in the expression for $\Delta\mu$, we obtain:

$$\Delta\mu = (\Delta H/T_{eq})(T - T_{eq}) \tag{1.20}$$

where $T - T_{eq}$ is known as the undercooling.

1.5.4 Driving force for processes at constant temperature (varying pressure)

For melt crystallization based on a pressure gradient, we use

$$-\Delta\mu = \Delta G = \Delta F - P\Delta V \tag{1.21}$$

with F in J/mol and P in bar. Applying the same procedure as above we obtain

$$\Delta\mu = \Delta F(P - P_{eq})/P_{eq} = \Delta V(P - P_{eq}) \tag{1.22}$$

This expression is valid for a negligible variation of ΔF and ΔV within the P to P_{eq} range.

1.5.5 Practical expressions for the supersaturation

Besides the thermodynamically derived expressions for the degree of supersaturation as presented, other practical expressions are frequently used, based on easily measurable

Table 1.2 Summary of expressions for supersaturation, as well as expressions used in practice. Note that practical expressions are usually not consistent with the thermodynamic ones.

c is the actual concentration in the solution and c_{eq} the equilibrium concentration [(kg solute) (kg solution)$^{-1}$ or (kg solute) (kg solvent)$^{-1}$ or (kg solute) (kg mixed solvent)$^{-1}$ in the case of anti-solvent crystallization]; similarly, T and T_{eq}[K] are the actual and equilibrium temperatures, respectively.

Thermodynamic expressions	Practical expressions	Crystallization method	Restriction
$\Delta H/T_{\text{eq}}$, $T - T_{eq}$	$T - T_{eq}$	Cooling, Melt	P constant, low supersaturation
[J mol^{-1}]	[K]		
$RT \ln S_{cm}$, $RT \ln S_c$	$\Delta c = c - c_{eq}$	Evaporative	T, P constant, low supersaturation
[J mol^{-1}]	[(g solute) (g solution)$^{-1}$ or (g solute) (g solvent)$^{-1}$]		T, P constant, low supersaturation, single solute
$RT \ln S_{am}$, $RT \ln S_a$	$S_c = c/c_{eq}$	Precipitation,	T, P, constant
[J mol^{-1}]	[-]	Anti-solvent	T, P constant, single solute
$\Delta\mu = RT\nu\sigma$, $\Delta\mu = RT\sigma$	$\sigma = \Delta c/c_{eq} = S - 1$	Evaporative,	T, P constant, low supersaturation
[J mol^{-1}]	[-]	Anti-solvent	T, P constant, low supersaturation, single solute

quantities, as shown in Table 1.2. The concentration c can be expressed in (kg solute) (kg solvent)$^{-1}$, (kg solute) (m^3 solvent)$^{-1}$, (kg solute) (kg solution)$^{-1}$ or (kg solute) (m^3 solution)$^{-1}$. The first expression is the least confusing, because the density of the solvent or the solution does not have to be known, and these units are therefore recommended, but the others are used as well in practice. All these expressions and units lead to different, arbitrary, representations of the degree of supersaturation. Table 1.2 shows that these practical expressions do not correspond to their thermodynamic equivalents, even when restrictive conditions and approximations are considered.

Worked example 3

Particulate acetyl salicylic acid is to be recovered from a 600 g L^{-1} solution by crystallization. Undesirable agglomeration is thought to be caused by excessive supersaturation, so crystallization under ultrasound has been proposed, because it reduces the metastable limit, as shown Figure 1.13. Do you think the proposed measure may be helpful for batchwise unseeded cooling to 40 °C? And for continuous evaporative crystallization at 40 °C?

Solution to worked example 3

For unseeded batch mode, the highest supersaturation takes place at the beginning, when primary nuclei are formed at the metastable limit. For continuous crystallization, the

Table 1.3 Comparison of modes of operation with and without unltrasound for worked example 3

Mode of operation	Without ultrasound	With ultrasound
Batchwise 90 to 40 °C	$T - T_{eq} = (79 - 90) = -11$ °C	$T - T^* = (84 - 90) = -6$ °C
Continuous at 40 °C	$S_c = 170/110 = 1.54$ or $\sigma = S_c - 1 = 0.54$	$S_c = 130/110 = 1.18$ or $\sigma = S_c - 1 = 0.18$

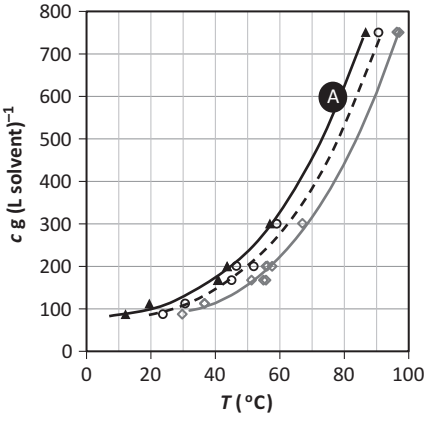

Figure 1.13 Solubility of acetyl salicylic acid in acetic acid (gray line), metastable limit (continuous black line), metastable limit with ultrasound (dashed line) (Prado, 2007).

solution state does not change with time. The supersaturation for cooling crystallization may be expressed by the undercooling ($T - T_{eq}$), whereas for evaporative crystallization the supersaturation ratio (S_c) or the relative supersaturation (σ) may be used as a first approximation, as shown in Table 1.3 above. The measured supersaturation values show that ultrasound is effective to reduce the supersaturation for both batch and continuous cases.

1.6 Thermodynamic models and speciation

As already emphasized in Section 1.2, certain features of the thermodynamic behavior of multi-phase systems may be described with phase diagrams. However, mathematical models are often more convenient, because they can handle larger numbers of components, as well as higher concentration, temperature and pressure ranges. Besides, under special circumstances some models are predictive, and they conveniently supply the solubility and the activity coefficients needed to calculate the supersaturation. In some cases they take into account chemical reactions in solution to give the nature and concentrations of chemical species in solution.

1.6.1 Activity models for organics

The relatively simple models of van Laar, Margules and Wilson, which are restricted to the description of short-range interactions, adequately describe the mixing behavior of similar, non-polar compounds like alkanes in binary mixtures.

The semi-empirical NRTL and UNIQUAC models belong to the class of so-called local composition models, which are based on the idea that the distribution of molecules around a particular molecule in the mixture is not statistically random, rather the molecular interactions drive non-random local compositions. The average interaction of one central molecule with its solution environment is calculated from binary interactions corresponding to these local compositions. A straightforward source of parameters for these models is found in Poling *et al*. (2001). These models are quite accurate and require a limited number of parameters, but their predictive capacity is limited.

In UNIFAC, a group contribution method is used, which considers molecules to be built from a limited number of functional groups. Model parameters are needed only for binary interactions of these functional groups, no parameters being required for each individual molecule. Therefore, the UNIFAC method is predictive for any new molecule that is formed by a combination of existing functional groups. The disadvantage is that it is less accurate than the NRTL and UNIQUAC models.

The Flory–Huggins theory is particularly well suited, for example, to solutions of high molecular weight macromolecules in solvents of regular molecular size. The Flory–Huggins theory has also been employed in combination with UNIFAC and other models to improve the range of applicability.

While the above-mentioned classical models require experimental data to obtain the interaction parameters, the COSMO-RS model obtains the interactions via quantum mechanical calculation of the surface charge density of the molecule. The interaction parameters are therefore derived almost entirely from first principles. COSMO is therefore useful for newly synthesized molecules. The COSMO-RS approach is limited to non-electrolytes and for estimations of weak electrolytes with known speciation.

The PC-SAFT – Perturbed Chain–Statistical Associating Fluid Theory approach is based on the SAFT equation of state. The novelty of this approach is that molecules are considered to be chains of hard spheres, which are linked by (infinitely) strong localized associations (= bonds). Each type of attractive interaction (van-der-Waals, Lennard–Jones, dipole–dipole and even ionic electrostatic) is described by a potential function. This allows the thermodynamic description of molecules based on the interactions of their constituting hard sphere atoms. Even macromolecules can be described by first-principle fundamental models of statistical thermodynamics with a minimum of empirical fit parameters. In the ideal case only one fit parameter, the hard sphere diameter, is required. This theory has been applied for polymer solutions, organic mixtures, but also for electrolyte solutions and even ionic liquids, often with the aid of empirical models for the potential functions.

1.6.2 Activity models for electrolytes

The interactions in electrolyte solutions are usually dominated by long-range electrostatic forces. The theoretically derived Debye–Hückel model assumes that the ion interactions depend only on their charge, not on the nature of the ion. The model is valid for dilute solutions up to 0.01 mol kg^{-1} (and for some salts even up to 0.1 kg mol^{-1}).

Pitzer and coworkers developed a model based on virial coefficients for binary and ternary interactions between ions as well as for interactions with neutral species. In most instances only the binary parameters suffice for accurate prediction of activity and osmotic coefficients. This is the most accurate model for multi-component electrolyte systems; however, a large number of empirical parameters are needed.

The Electro-NRTL model successfully combines an improved Debye–Hückel term for long-range interactions with the NRTL model for short-range interactions to describe electrolyte activities. It is also known as the "Chen model." The strength of this model is its ability to cope with mixed solvents (systems containing both organics and electrolytes), while only a limited number of empirical interaction parameters are required. It is also said to be more easily applicable to extremely high electrolyte concentrations ($>$ 6 molal) than the Pitzer model. Still, there are currently more electrolyte systems described with interaction parameters for the Pitzer model than for the Electro-NRTL model.

The Helgeson–Kirkham–Flowers (HKF) model describes and predicts speciation in solution by providing virial expansion expressions for the Gibbs free energy of the species in solution, from which the solubility and complexation equilibrium constants are derived. The model predicts solubility and speciation over a very large temperature and pressure range – up to 5000 bar and 1000 °C. This model was originally developed to model geological systems, i.e. to allow extrapolation to high temperature, pressure and concentration ranges. For high concentrations, Electro-NRTL or (heavily parameterized) Pitzer models produce higher accuracy in the reproduction of data, but the description of the speciation behavior gives the HKF model almost unique predictive capabilities. The speciation is usually not included in Electro-NRTL and Pitzer models – which commonly assume complete dissociation. A limitation in the actual use of the HKF model is that speciation needs to be known, quantified and fitted to the model, conditions that often are not met.

1.6.3 Selection of a thermodynamic model

Based on the mutual interactions between the species and their packing in solution, a range of suitable models and tools can be identified for the calculation of the activity coefficient(s) from the preceding sections. They may be further ranked in terms of complexity and ease of use, as indicated in Figure 1.14. On the left part of the figure, models are listed to be developed by the user. On the right part commercial software is listed. Minteqa, Visual Minteq, Cheaqs and PHREEQC are variations on the Debye–Hückel model and include models for redox reactions, equilibria with a vapor phase and adsorption, among

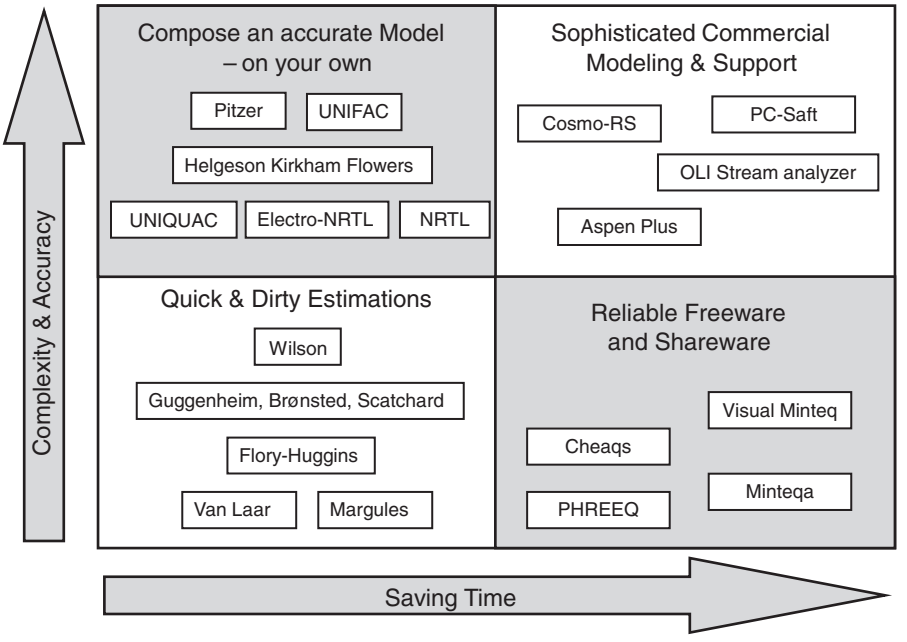

Figure 1.14 Simplified chart for selection of thermodynamic models and tools.

others. Aspen plus is a flowsheeting program that contains a number of thermodynamic models, for instance, NRTL and electrolyte-NRTL. OLI has a suite of thermodynamic models (for instance, Pitzer and HKF) and some flowsheeting capability. PC-Saft and Cosmo-RS are mathematically complex single models.

Thermodynamic models are described in a number of textbooks (Chen *et al*., 1986, Kontogeorgis and Folas, 2009, Prausnitz *et al*., 1998, Sandler, 1994, Zemaitis and Engineers, 1986).

1.7 A brief summary of the chapter

Thermodynamics supply, either in the form of phase diagrams or mathematical models, the information required to select a crystallization method. In cooling crystallization, heat is removed from the solution; in evaporative crystallization heat is added to a boiling solution; in chemical reaction crystallization (precipitation) reagents are added to form a slightly soluble compound and in anti-solvent crystallization a mass agent is added in order to reduce the solute solubility in the resulting mixed solvent. Thermodynamics also define the possible yield and energy consumption associated with crystallization.

During crystallization, the solution (or melt) is supersaturated with respect to the crystallizing compound. The supersaturation $\Delta\mu$ is defined as the difference between the chemical potential of the solute in solution or melt and in the solid. $\Delta\mu$ is important because it drives the elementary rate processes that constitute crystallization. Simplified

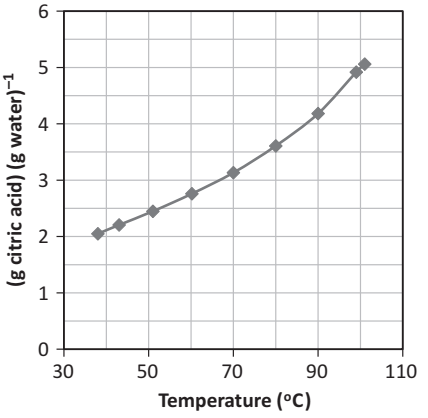

Figure 1.15 Solubility of anhydrous citric acid in water (Lafontaine *et al*., 2013).

expressions based on directly measurable quantities such as the supersaturation ratio $S = c/c_{eq}$ and the undercooling $T - T_{eq}$ may be applied respectively for evaporative and for cooling crystallization. For precipitation and anti-solvent crystallization, rigorous definitions based on activities are preferred. The activities may be calculated from thermodynamic models that are selected according to the characteristics of the system of interest (e.g. non-polar compounds, electrolytes, mixed solvents, etc.) and to the desired predictive capacity and complexity of the model.

1.8 End of chapter problems

Problem 1

The phase diagram given in Figure 1.1 describes the system $AgNO_3$-H_2O. Use the diagram to determine the phases present and their composition for the following conditions: (a) solute mass fraction of 10 wt% at −5 °C; (b) a solute mass fraction of 10 wt% at 0 °C; (c) a solute mass fraction of 80 wt% at 20 °C.

Problem 2

A citric acid–water mixture containing 4.35 g of citric acid per gram of solvent is to be purified by batch cooling crystallization, with recovery of half of the original citric acid mass as a solid. Given the phase diagram of Figure 1.15, indicate: (a) the temperature needed to completely dissolve the citric acid; (b) the temperature to which the solution must be cooled in order to recover the desired amount of solid.

Problem 3

A citric acid–water mixture containing 4.35 g of citric acid per gram of solvent is to be purified by batch evaporative crystallization, with recovery of half of the original citric acid mass as a solid. Given the phase diagram of Figure 1.15, indicate: (a) the solute concentration during crystallization, considering that boiling occurs at 100 °C; (b) the amount of water to be evaporated.

Problem 4

Consider a 400 gL^{-1} solution of acetyl salicylic acid dissolved in acetic acid at 90 °C. Considering the solubility behavior given in Figure 1.13, would you say this is an undersaturated, saturated or supersaturated solution? What if the solution is at 70 °C? What is the saturation temperature of the solution?

Problem 5

A continuous cooling crystallizer produces solid acetyl salicylic acid from an acetic acid solution. The solution thermodynamic state during crystallization is characterized by a solute concentration of 300 g L^{-1} solvent, a temperature of 60 °C and atmospheric pressure. (a) Determine the supersaturation using a thermodynamically derived expression. Indicate also a practical expression for the degree of supersaturation considering that the solution is not too far apart from equilibrium. (b) Repeat the exercise considering continuous evaporative crystallization. The solubility curve is given in Figure 1.13.

Problem 6

Suppose you want to estimate the solubility of the following solute–solvent mixtures at room temperature: (1) magnesium sulfate in water; (2) adipic acid in ethanol; (3) adipic acid in a new solvent of known chemical composition; (4) calcium carbonate in water. You have access to the following thermodynamic models: NRTL, UNIFAC, Debye–Hückel, Pitzer. Choose the most suitable model for each system, indicating in each case which system-dependent model parameters are required.

1.9 References

Beckmann, W. 2013. *Crystallization: Basic Concepts and Industrial Applications*, Wiley.

Börnstein, R. and Meyerhoffer, W. 1905. *Landolt-Börnstein Physikalisch-Chemische Tabellen*, Springer.

Chen, C. C., Evans, L. B. and Mock, B. 1986. Thermodynamic representation of phase equilibria of mixed solvent electrolyte systems. *AIChE Journal*, **32**(10), 1655–1664.

Chianese, A. K. M. and Mazzarotta, B. 1995. Nucleation kinetics of pentaerythritol. *The Chemical Engineering Journal*, **58**, 209–214.

Jones, A. G. 2002. *Crystallization Process Systems*, Butterworth-Heinemann.

Kontogeorgis, G. M. and Folas, G. K. 2009. *Thermodynamic Models for Industrial Applications: From Classical and Advanced Mixing Rules to Association Theories*, Wiley.

Lafontaine, A., Sanselme, M., Cartigny, Y., Cardinael, P. and Coquerel, G. 2013. Characterization of the transition between the monohydrate and the anhydrous citric acid. *Journal of Thermal Analysis and Calorimetry*, **112**, 307–315.

Mullin, J. W. 2001. *Crystallization*, Butterworth-Heinemann.

Myerson, A. S. 2001. *Handbook of Industrial Crystallization*, Butterworth-Heinemann.

Nagaoka, N. and Makita, T. 1987. Solid–liquid phase equilibria of benzene + cyclohexane system under high pressures. *International Journal of Thermophysics*, **8**(4), 415–424.

Nývlt, J. 1977. *Solid–Liquid Phase Equilibria*, Czechoslovak Academy of Science.

Pessôa Filho, P. A., Hirata, G. A. M. and Miranda, E. A. 2011. Precipitation and crystallization. In Moo-Young, M. (ed.) *Engineering Fundamentals of Biotechnology*, 2nd edn., Elsevier.

Poling, B. E., Prausnitz, J. M. and O'Connel, J. P. 2001. *The Properties of Gases and Liquids*, McGraw-Hill.

Prado, J. A. P. 2007. *Crystallization of acetyl salicylic acid dissolved in acetic acid by batch cooling crystallization with application of ultrasound*. MSc, Institute of Technological Research of the State of São Paulo.

Prausnitz, J. M., Lichtenthaler, R. N. and De Azevedo, E. G. 1998. *Molecular Thermodynamics of Fluid-Phase Equilibria*, Pearson Education.

Randolph, A. D. and Larson, M. A. 1988. *Theory of Particulate Processes: Analysis and Techniques of Continuous Crystallization*, Academic Press.

Sandler, S. I. 1994. *Models for Thermodynamic and Phase Equilibria Calculations*, Dekker.

Schweizer, P. A. 1988. *Handbook of Separation Techniques for Chemical Engineers*, MacGraw-Hill.

Söhnel, O. and Garside, J. 1992. *Precipitation:Basic Principles and Industrial Applications*, Butterworth-Heinemann.

Van 't Land, C. M. 2004. *Industrial Crystallization of Melts*, Marcel Dekker.

Zemaitis, J. F. and Engineers, A. I. O. C. 1986. *Handbook of Aqueous Electrolyte Thermodynamics: Theory and Application*, Design Institute for Physical Property Data.

Zhou, Z., Qu, Y., Wei, H. and Chen, L. 2008. Solubility of D-(p-hydroxy)phenylglycine in water + 2-propanol from (293 to 343) K. *Journal of Chemical Engineering Data*, **53**, 2900–2901.

2 Characterization of a crystalline product

2.1 Why this chapter is important

In a competitive market a product has to meet increasingly stringent quality demands, so a number of particle characteristics must be carefully controlled, such as:

- crystal size distribution of the product
- shape of the crystals
- occurrence of polymorphism
- mother liquor inclusions in the crystals
- uptake of impurities in the crystal lattice
- degree of agglomeration.

These characteristics determine most functional features of particulate materials during their use as products. In the food industry, for example, both the size distribution and the shape of ice crystals in ice cream are important (Myerson, 2001). The mean size of the ice crystals should be between 35 and 40 μm in order to give the required smooth texture and melt properties, whilst the crystals themselves must be round and smooth in order to give the correct mouthfeel. Obviously the impurity concentrations in food products must be very carefully controlled.

In the pharmaceutical industry, because of the final use of the compounds, strict specifications as regards size, morphology, dissolution properties and polymorphic form are enforced.

In the bulk chemical and extractive metallurgy industries, the "particle design" is crucial (Söhnel and Garside, 1992). The crystal size distribution and corresponding particle surface area are of particular importance, since these, together with the particle morphology, have a major impact on the particle processing characteristics. For example, solid–liquid separation by centrifugation or filtration, drying rates, particle flow properties, bulk density and thus packing characteristics, as well as propensity to cake are all critically dependent on these particle properties (Söhnel and Garside, 1992).

2.2 Crystal size distribution (CSD) or particle size distribution (PSD)

One of the main characteristics of a product is its crystal size distribution or, in the case of agglomerated or non-crystalline particles, its particle size distribution.

Table 2.1 Various definitions of crystal size

Name	Definition
Length	Maximal visible length
Sieve diameter	Width of the minimum square aperture through which the particle will pass
Volume diameter	Diameter of a sphere having the same volume as the crystal
Surface diameter	Diameter of a sphere having the same surface area as the crystal
Projected area diameter	Diameter of a sphere having the same projected area as the crystal viewed from a fixed direction

The CSD is important for the product quality, but also influences the performance of the process, the separation of the crystals from the mother liquor, and the subsequent drying of the crystals. It is also essential for storage and handling of the final product. For instance, small crystals, because of their relatively large surface area to mass ratio, contain more adhering mother liquor after filtration than a similar mass comprising larger crystals. This results in a less pure product after drying and a higher tendency towards caking.

Although large crystals are preferred for many applications, there are also cases where the crystals are dissolved or digested for their final use. For those purposes, small crystals are required to reduce the dissolution time.

As a final example, it is worth noting that the color of many inorganic pigments obtained by precipitation is dependent on the CSD (Hund, 1981).

Although the dominant properties of the product will usually be the average crystal size and the width of the distribution, the zeroth to third moments of the CSD are also important parameters, since they are related to the total number, total length, total surface area and total mass of the crystals. The moments of the CSD are defined in this chapter in Section 2.2.2.4.

Before defining the ways by which the CSD can be represented, it first has to be noticed that, since crystals are seldom spheres, the size of a crystal cannot be uniquely defined by a single measure, such as the diameter of a sphere.

2.2.1 Definitions of crystal size *L*

How big is a matchbox? This may seem like a fairly stupid question to ask (Rawle, 2003), but the answer to this question is critical to understanding crystal and particle size analysis. There is no single answer to "How big is a matchbox?" since the size of a matchbox may be described by its volume, its surface area or even the length of its longest or shortest sides. The similar challenges involved in characterizing the size of crystals and particles have been approached in a number of different ways and some of the many definitions of crystal size are summarized in Table 2.1.

Directly correlated with the definition of the crystal size are the surface and volumetric shape factors k_a and k_v:

$$\text{crystal surface area } A = k_a L^2 \tag{2.1}$$

$$\text{crystal volume } V = k_v L^3 \tag{2.2}$$

where:

L = length defined by the measuring technique [m]
k_a, k_v = shape factors that convert L^2 or L^3 to the crystal area or volume
The shape factors k_a and k_v are often indicated by β and α.

Worked example 1

What are the area and volume shape factors of a cube? Use as the characteristic length: (a) the cube side L; (b) the cube face diagonal L_d.

Worked example 1 solution

(a) The area shape factor:

$$A = k_a L^2$$
$$6L^2 = k_a L^2$$
$$k_a = 6$$

The volume shape factor:

$$V = L^3 = k_v L^3$$
$$k_v = 1$$

(b) The area shape factor:

$$2L^2 = L_d^2 \text{ (Pythagoras)}$$
$$A = 6L^2 = 3L_d^2$$
$$k_a = 3$$

The volume shape factor:

$$V = L^3 = 2^{-3/2} L_d$$
$$k_v = 2^{-3/2}$$

It can be concluded that the shape factors vary according to the choice of the characteristic length.

2.2.2 Representations of the CSD

Two types of CSD representations are normally considered, the cumulative oversize number distribution $N(L)$ and the mass distribution $M(L)$, representing the total number or mass of crystals between 0 and L, respectively. CSD measurement devices deliver this type of distribution. However, for a better representation of the CSD and for process calculations these cumulative distributions are often converted into the number $n(L)$ or

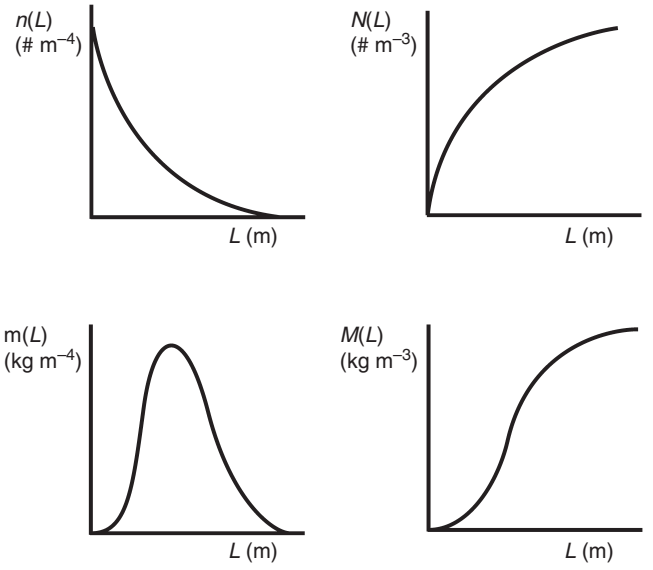

Figure 2.1 Density and cumulative distributions of a crystal population.

mass density $m(L)$ distributions, see Section 2.2.2.1. In principle, distributions such as $n(L)$ and $m(L)$ are continuous, which implies an assumption of an infinite number of particles and of infinitely small size intervals. Size measuring instruments, however, classify particles in discrete size intervals ΔL_i ranging from L_i to $L_i + \Delta L_i$.

2.2.2.1 The number $n(L)$ and the mass $m(L)$ density distribution

The number density distribution $n(L)$ gives the number of particles per unit of particle size and is obtained by taking the derivative of the cumulative number distribution with respect to the size L:

$$n(L) = \left.\frac{\mathrm{d}N(L)}{\mathrm{d}L}\right|_L$$

where $n(L) =$ the number (or population) density distribution [# m^{-1} m^{-3}].

The mass density distribution $m(L)$ gives the mass of particles within the size range L to $L + \mathrm{d}L$, divided by the width of the size range $\mathrm{d}L$:

$$m(L) = \left.\frac{\mathrm{d}M(L)}{\mathrm{d}L}\right|_L \tag{2.3}$$

where $m(L) =$ the mass density distribution [kg m^{-1} m^{-3}]

These density distributions and the cumulative distributions given in Section 2.2.2.2 are presented in Figure 2.1.

2.2.2.2 Cumulative oversize number $N(L)$ and mass $M(L)$ distributions

The cumulative oversize number function $N(L)$ gives the total number of particles with sizes between 0 and L in a given reference volume (slurry volume or total particle volume):

$$N(L) = \int_0^L n(L)\,\mathrm{d}L \tag{2.4}$$

where $N(L)$ = cumulative oversize number distribution per m^3 slurry [$\# \, m^{-3}$]

$$N_T = \int_0^\infty n(L)\,\mathrm{d}L \tag{2.5}$$

where N_T = the total number of crystals per m^3 slurry [$\# \, m^{-3}$].

The cumulative oversize mass function $M(L)$ gives the total mass of particles with sizes between 0 and L in a given reference volume:

$$M(L) = \int_0^L m(L)\,\mathrm{d}L = \rho_s k_v \int_0^L L^3 n(L)\,\mathrm{d}L \quad [\mathrm{kg\ m^{-3}}] \tag{2.6}$$

where $M(L)$ = cumulative mass distribution per m^3 slurry [$\# \, m^{-3}$].

$$M_T = \int_0^\infty m(L)\,\mathrm{d}L = \rho_s k_v \int_0^\infty L^3 n(L)\,\mathrm{d}L \tag{2.7}$$

where M_T = the total mass of crystals per m^3 slurry [$kg \, m^{-3}$].

In its normalized form:

$$\frac{1}{N_T} \int_0^\infty n(L)\,\mathrm{d}L = 1 \tag{2.8}$$

and

$$\frac{1}{M_T} \int_0^\infty m(L)\,\mathrm{d}L = 1 \tag{2.9}$$

Worked example 2

A slurry has a density of 2000 kg m^{-3}, with the crystal density being 4000 kg m^{-3} and the volume shape factor $k_v = 0.8$. Calculate the population density of a sample that has 40% in the size range between 50 and 80 μm. Calculate the population density at the midpoint of the size range.

Since $n(L) = \Delta N_i / \Delta L_i$, the number of crystals in the size range can be calculated using the mass and the shape factor, as follows:

$$\Delta N_i = \frac{\Delta M_i}{\rho k_v L_i^3} = \frac{\Delta W_i M_T}{\rho k_v L_i^3}$$

$$\Delta N_i = \frac{\left(\frac{40}{100}\right) 2000}{4000(0.8)(65 \times 10^{-6})^3} = 9.1 \times 10^{11}$$

$$n(L) = \frac{\Delta N_i}{\Delta L_i} = \frac{9.1 \times 10^{11}}{30 \times 10^{-6}} = 3.03 \times 10^{16} \, \# \, m^{-4}$$

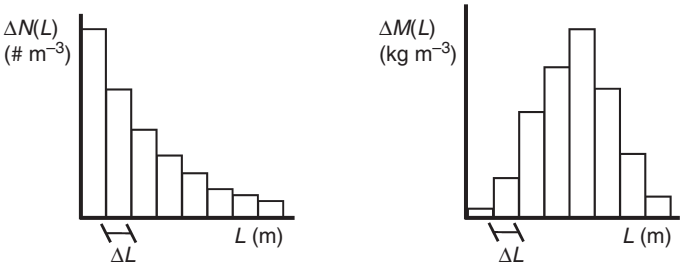

Figure 2.2 Histogram of the crystal population.

2.2.2.3 The histogram

As stated previously, size-measuring instruments classify particles in discrete size intervals ΔL. In addition, these instruments often use histograms to represent the CSD, plotting the normalized amount of measured quantity $\Delta N(L)$ or $\Delta M(L)$ over each increment ΔL of the measured particle size; see Figure 2.2. Note that as non-equidistant size grids are often used for these plots, the shape of these histograms becomes dependent on the number of size intervals and the type of size grid, so normalization is mandatory.

2.2.2.4 Derived properties of the CSD

In many systems of engineering interest, working with the complete crystal size distribution can be too complex and too detailed (Randolph and Larson, 1988). Rather, some property that "summarizes" the information contained in the distribution is often sufficient. In this case, there are a number of average or representative properties that are available. Most of the important properties that can be derived from the CSD can be calculated from the density distributions. These are:

The moments of the CSD

The moments of the CSD are defined as:

$$m_j = \int_0^\infty L^i n(L) \, \mathrm{d}L \quad [m^i / m^3] \tag{2.10}$$

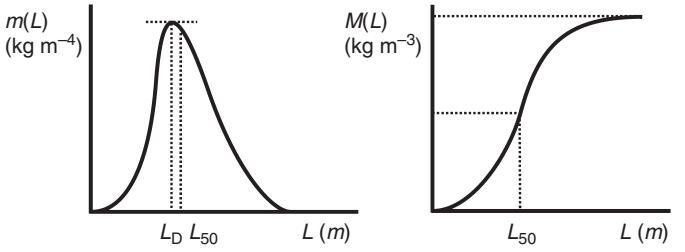

Figure 2.3 Mode (L_D) and median size (L_{50}) of a mass distribution.

Total number	$N_T = m_0$
Total length	$L_T = m_1$
Total surface area	$A_T = k_a\, m_2$
Total volume	$V_T = k_v\, m_3$
Total mass	$M_T = \rho_{crystal}\, k_v\, m_3$

The average crystal size of the CSD

There are a number of definitions of average crystal size.

The *mode*, L_D, corresponds to the maximum density value of the mass density distribution. See Figure 2.3. The *median* size of the distribution $L_m = L_{50}$ is the size that splits the mass distribution into two equal parts. In other words, for the mass density, half the mass of the particles is smaller than the median size and half the mass of the material is larger. In minerals processing, similarly, the median size is that size at which half of the material mass consists of finer crystals and half of coarser crystals (Fuerstenau and Han, 2003).

Thus, the median size for the number density is defined as follows:

$$L_m = L_{50} \text{ such that } \int_0^{L_{50}} \frac{n(L)L^3\, \mathrm{d}L}{m_3} = 0.5 \tag{2.11}$$

The number-based mean size:

$$L_{1,0} = \frac{m_1}{m_0} \tag{2.12}$$

The mass-based mean size:

$$L_{4,3} = \frac{m_4}{m_3} \tag{2.13}$$

The $L_{2,1}$ value is the ratio between the second and the first moment of the distribution, which are measures for the total surface area and the total length of crystals, respectively.

$$L_{2,1} = \frac{m_2}{m_1} \tag{2.14}$$

The $L_{2,1}$ value thus represents a kind of average crystal size.

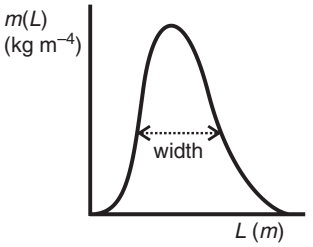

Figure 2.4 Width of one CSD.

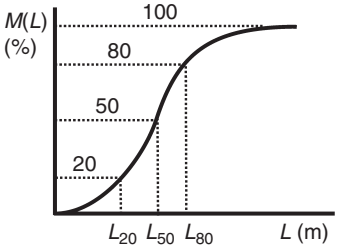

Figure 2.5 Width of the CSD given by quintiles.

The width of the CSD

The standard deviation and the variance of a distribution are measures of absolute variation, that is, they measure the actual amount of variation present in a set of data, and they depend on the scale of measurement (Johnson *et al.*, 2011). To compare the variation in several sets of data, it is generally desirable to use a measure of relative variation. One such measure for the width of the mass distribution is the coefficient of variation (see Figure 2.4), which gives the standard deviation as a percentage of the mean.

The coefficient of variation:

$$CV = \frac{\text{standard deviation } \sigma}{L_{4,3}} = \sqrt{\frac{m_3 m_5}{{m_4}^2} - 1} \tag{2.15}$$

Besides the median, which divides the data into halves, there are other possible division points. When an ordered data set is divided into quarters, the division points are called quartiles (see Figure 2.5; Johnson *et al.*, 2011). The quartile ratio is defined as:

$$CV = \ln \frac{L_{75}}{L_{25}} \tag{2.16}$$

Another definition of the width uses quintiles, which are the division points when the data is divided into fifths. The upper quintile is equivalent to the 80th percentile, whilst

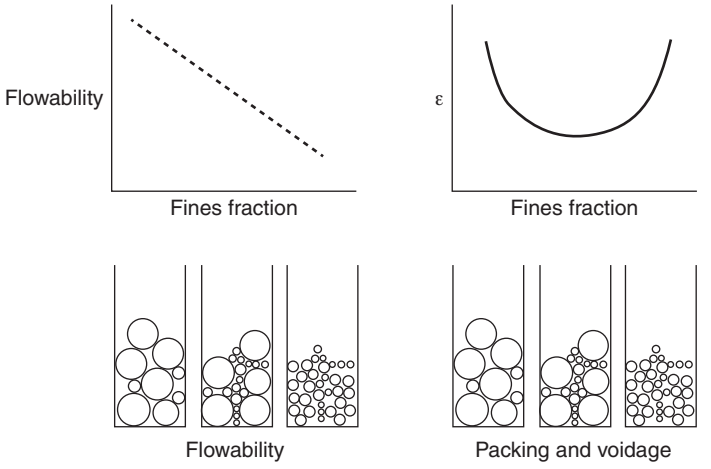

Figure 2.6 Effect of CSD on flowability and voidage (ε).

the lower quintile is equivalent to the 20th percentile. The coefficient of variation defined using quintiles is as follows:

$$CV = \frac{L_{80} - L_{20}}{2L_{50}} \tag{2.17}$$

Because of the numerous different definitions of the coefficient of variance, it is important to realise which one is being used.

The width of the CSD is particularly important in determining the permeability of the crystal cake (and therefore the filterability) during a solid–liquid separation process. It is even more important than the average crystal size, and is therefore an important product parameter to be controlled. For very narrow distributions, the permeability is proportional to the square of the median size L_m, but, for broader distributions, which are more frequently generated in practice, the permeability depends on both the $L_{2,1}$ and the porosity of the crystal bed.

Since small crystals can easily be captured in the voids between the larger crystals, the porosity of a cake is largely influenced by the left side of the distribution. It is therefore a good measure for the number of small crystals, which can often not be accurately measured.

Figure 2.6 shows schematically the effect of the CSD on flowability, packing and voidage. Perhaps unexpectedly, as the fines fraction of a CSD increases, the flowability decreases, due to the increased points of contact between particles and thus increased frictional resistance. However, the response of the voidage to an increase in the fines fraction is not monotonic. As the fines fraction increases, the voidage passes through a minimum because the smaller particles fill in the spaces between the larger ones. However, if the fines fraction increases still further, the voidage decreases because the potential for dense packing is reduced if the particles are all of a similar size.

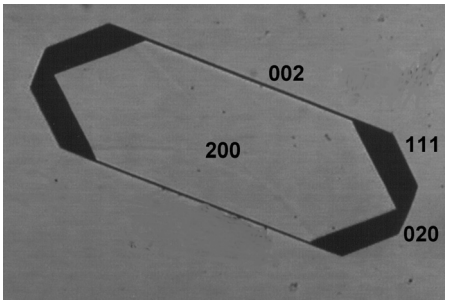

Figure 2.7 RDX crystal grown from cyclohexanon.

2.3 Crystal shape

Shape/habit and morphology are not equivalent. The morphology is given by the type of crystal faces (determined by the internal structure of the crystal) indicated by, for example, {100} faces, while the shape or habit is the external form that is also influenced by the growth conditions. So a crystal with a cubic structure can have morphology {100} of six cubic faces or can be bounded by eight octahedral {111} faces. A cubic crystal could, by uneven feeding of the faces, for example, grow out into a matchbox form, but the angles between these {100} faces remain 90° – as dictated by the internal structure (so cubic and matchbox have the same morphology, but a different shape).

The external appearance of a single crystal, called the shape or habit, is determined by two factors:

a. the periodic structure of the crystal lattice, which is imposed by the bond energies between the atoms, ions or molecules in the crystal lattice (i.e. thermodynamic factors) and
b. the conditions under which the crystal is grown, i.e. kinetic factors (Davey and Garside, 2000).

Another way of understanding these two factors is that the morphology of single crystals is determined by the relationship of the internal factors (crystal structure). Their shape or habit is also determined by external factors (crystal growth conditions and the process of crystal growth). In principle, if the crystal structure of a material is known, then its crystal morphology can be predicted (Sunagawa, 2005). However, this morphological shape is only practically valid when the influence of the external factors does not outweigh the internal ones, i.e. the growth kinetics are relatively slow, and the solvent does not differently affect the growth rate of the various types of crystal faces. See Figure 2.7 for an example of a well-defined RDX crystal (an explosive nitroamine compound) grown slowly in cyclohexane.

Often the shape of a crystal is affected by breakage or abrasion due to collisions with neighboring crystals or mechanical devices within a crystallizer. Sometimes polycrystalline particles occur as a result of agglomeration of single crystals or of other agglomerates.

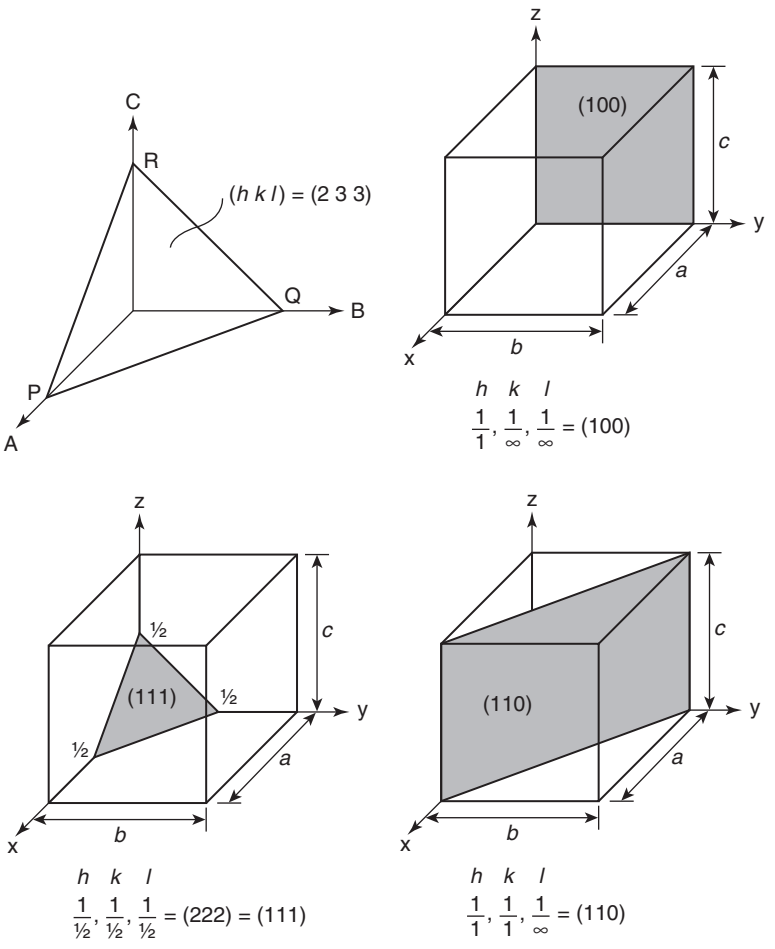

Figure 2.8 Miller indices.

2.3.1 Quantifying crystal shape

As a starting point, crystals are divided into seven symmetry classes. Cubic crystals are often block-like (NaCl), while tetragonal (KDP), hexagonal (aspartame) or monoclinic (gypsum) crystals can form needles. The classes can easily be determined by X-ray diffraction.

Crystal shapes can be quantified numerically by means of Miller indices, which numerically define the morphology of crystals in terms of their faces. It is beyond the scope of this text to describe Miller indices in detail, and thus only a summary is given here (see Figure 2.8).

The so-called Miller indices (*hkl*) uniquely describe different crystal planes in a lattice and are defined as the ratio of the reciprocals of the intercepts of the face with the three crystal axes, expressed in the corresponding unit lengths *a*, *b* and *c* and converted to

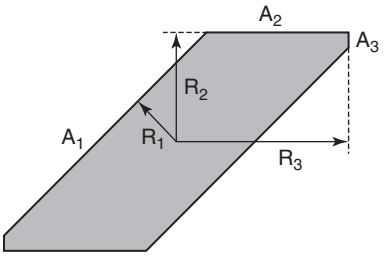

Figure 2.9 The crystal shape is determined by the slowest growing faces.

simple integers. For the face in Figure 2.8 with OP = 3, OQ = 2 and OR = 2, the Miller indices become:

$$hkl = \frac{a}{OP} : \frac{b}{OQ} : \frac{c}{OR} = \frac{1}{3} : \frac{1}{2} : \frac{1}{2} = 233 \tag{2.18}$$

where $(hkl) = (233)$ is pronounced as two three three.

If a face is parallel to a given axis, its Miller index is zero (see Figure 2.8). Negative indices are written as follows, with bars over them as $(h\bar{k}\bar{l})$. The angles between different crystal faces are thus determined by the internal stucture of the crystal.

2.3.2 Predicting crystal morphology and shape

The shape of crystals (which depends primarily on the morphology of the crystals) has a profound influence on their handling and downstream processing characteristics. For example, anisotropic crystals, such as needles, have a tendency to break easily, and thus cause poor filterability. It is not surprising, therefore, that morphology and shape prediction has been the subject of active study for many decades (Rohl, 2003) and significant progress has been made in recent years (Li *et al.*, 2006).

There are several methods to predict the morphology of crystals in vacuum or in a gas, since the influence of the solvent is not taken into account.

a. The Bravais–Friedel–Donnay–Harker (BFDH) method uses the crystal lattice and symmetry to generate a list of possible growth faces and their relative growth rates. This was the basis of many early techniques for modeling of morphology (Li *et al.*, 2006). The BFDH law states that the most important crystallographic faces have the greatest interplanar spacing and thus the morphologically most important (hkl) faces are those with the slowest growth rates (see Figure 2.9). In this figure, the growth rate of face R_1 is the slowest, followed by R_2, followed by R_3. At the same time, because of its slow growth rate, the area of face A_1 will be the largest, followed by A_2, followed by A_3. The slowest-growing faces, which have the largest interplanar distances (d_{hkl} values), will also have the lowest attachment energies (E_{att} values) since they have their strongest bonds between atoms or ions within the growth layer, and fewer or weaker bonds between the layers. Thus, the interplanar distances follow the order $d_{hkl,1} > d_{hkl,2} > d_{hkl,3}$ and the attachment energies follow the order $E_{att,1} < E_{att,2} < E_{att,3}$. As a consequence, the faces with the slowest growth rates and largest d_{hkl} values appear

on the crystal. The interplanar distances can easily be calculated from data derived from simple X-ray powder diffraction, which is stored in the Cambridge Structural Database (CSD) (Cambridge Crystallographic Data Centre (CDCC), 2013). In spite of its simplicity, the BDFH law is still useful for quickly identifying the likely growth faces.

b. Hartman–Perdok's periodic bond chain (PBC) theory or the attachment energy method assumes that the growth rate of a crystal face is proportional to its attachment energy (the energy released on attachment of a growth unit to a growing crystal surface) and thus this method is based on a comparison of attachment energy values. Since a flat face grows by the attachment of subsequent growth layers or slices, the attachment energy E_{att} is the energy released per growth unit when one slice of thickness d_{hkl} crystallizes onto the (hkl) face. These E_{att} values are calculated just the same as the d_{hkl} values, only from unit cell parameters (unit cell dimensions and atom positions in the unit cells), and are thus in fact a morphology prediction from vacuum.

Both methods a and b calculate the growth morphology of the crystals.

c. The equilibrium morphology method determines the minimum of the surface energies for all relevant crystal faces at zero Kelvin. The essence of this method is that a crystal will assume a configuration such that its Gibbs free energy is minimized. In other words:

$$\Delta G_j = \sum_j \gamma_j A_j \tag{2.19}$$

where ΔG_j = Gibbs free energy of the jth crystal face, γ_j = surface energy per unit area of the jth crystal face, A_j = surface area of the jth crystal face.

In order to calculate the Gibbs free energy of the crystal face, the surface energy term must be estimated. This presents a problem. At the moment, the methods available for calculating the term are either force fields or density functional theory, neither of which can currently take the effects of solvents into account.

The methods implementing these theories and resulting developments are now incorporated into software tools, from early versions, such as the simple Fortran programmes MORANG (Docherty *et al.*, 1988) and HABIT (Clydesdale *et al.*, 1996) to the commercially available Morphology module in the Materials Studio molecular modeling simulation package from Accelrys (2013).

These methods give a good first estimate of morphology, but their major limitation is that they have only taken into consideration the internal structural information of the crystal, such as unit cell parameters, fractional coordinates and symmetry information, but have largely ignored the effects of process operating conditions, such as supersaturation, cooling rates, solvents, impurities or additives (Li *et al.*, 2006). In practice, most crystals are grown from solution, which means that the effect of the interaction between the solvent molecules and the different crystal surfaces must be taken into account.

Some of the newer approaches have attempted to take these effects into account, by incorporating supersaturation, solvents, additives and cooling rates into the crystal

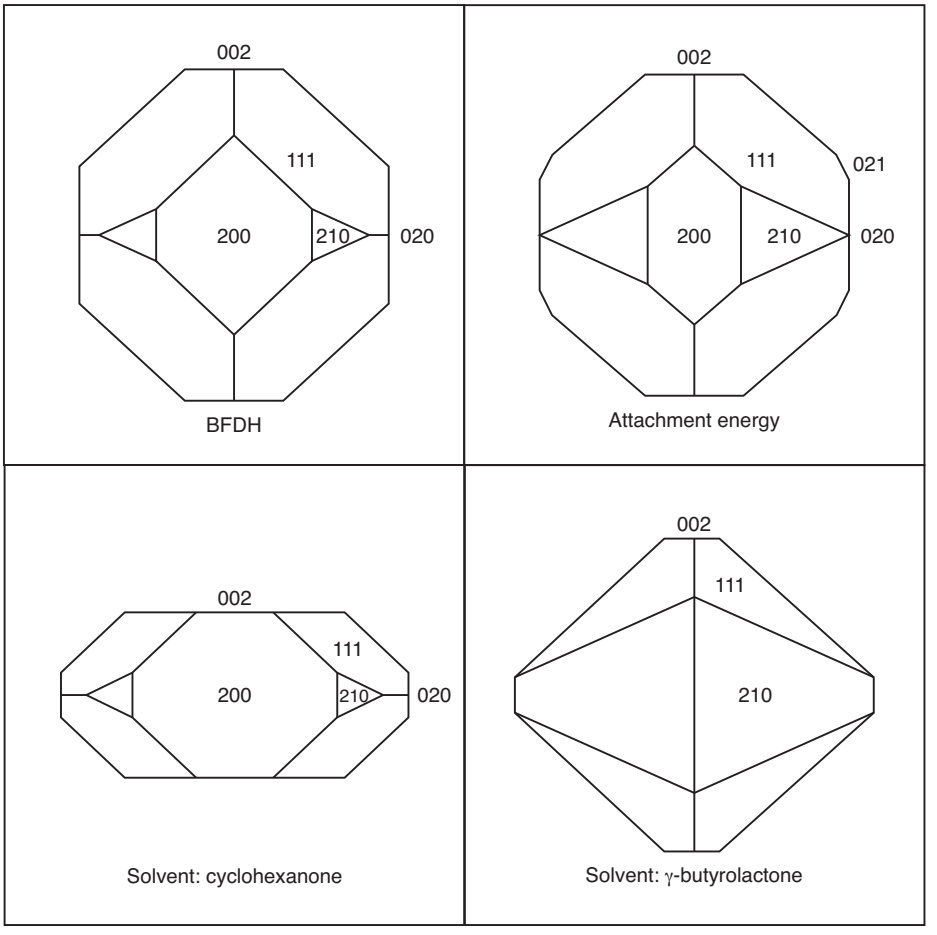

Figure 2.10 Calculated and experimental RDX crystal morphologies. The calculated morphologies are determined by calculating the interplanar distances (BFDH) and the attachment energies of the growth units and the solvent molecules with the crystal faces. The experimental morphologies are from the solvents cyclohexanone and butyrolactone.

morphology prediction models. For example, Doherty and coworkers have developed a number of models to predict crystal growth morphologies from first principles, including the most recent models (Lovette and Doherty, 2012), which can predict supersaturation-dependent growth shapes of several molecular organic crystals. For inorganic systems, Rohl and coworkers, using solvation energies, were able to demonstrate how water altered the morphology of sphalerite (Rohl *et al.*, 2003).

Figure 2.10 shows the results of a simple method that takes into account the different interactions that a solvent has with the various (*hkl*) faces of a crystal. This method estimates the influence of a solvent by calculating the attachment energy of a solvent molecule and then subtracting this value from the E_{att} value of the growth unit. This method recognizes that, the stronger the interaction of a solvent molecule with the growth

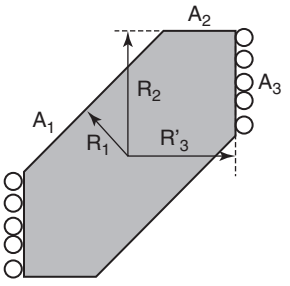

Figure 2.11 The effect of an additive on the crystal shape.

layer, the slower the growth can proceed. This explains the differing morphologies of the RDX crystals grown from two solvents, as presented in Figure 2.10 (ter Horst, 2000).

Molecular modeling thus has the potential to provide a tool for calculating the interaction of a solvent with a crystal surface, and may be useful in the future for selection of an appropriate solvent to adjust the shape of the crystals (in cases where it is possible to select the solvent). However, this is still in development and commercially available tools are still rudimentary in this aspect.

For a fixed solvent, the effect of additives can theoretically be predicted by calculating their interactions with the crystal surface. If an additive has a strong interaction with a particular crystal surface, it will slow down the growth rate. If there is no interaction with the other surfaces, in other words, if the interaction is preferential with one surface over another, the shape of the crystal will be altered, as illustrated in Figure 2.11. For example, to shorten the length of needle-shaped crystals, additives can be designed that preferentially interact with the top faces of the needles. In this way the crystal shape can be corrected.

Similarly, the effect of impurities present in the solution on the shape of the crystals can also be predicted (see also Chapter 13 on Additives and impurities). It also has to be kept in mind that the dependence of the growth rate on the supersaturation is not the same for all crystal faces (*hkl*) of a crystal, owing to differences in their growth mechanism. Therefore changing the supersaturation can also be a method of changing the shape of a crystal, since lower supersaturations mostly reduce the anisotropy of the crystal.

2.3.3 Effect of operating conditions on crystal shape

Figure 2.12 illustrates how the operating conditions can affect the crystal shape. The first three illustrations show the effect of the type of crystallizer on the product. Illustration (a) shows the product from a forced circulation (FC) crystallizer, which exhibits regular, cubic morphology and shape and hardly any attrition. These crystals are 400 to 600 μm in size. Illustration (b) shows the product from a draft tube baffled (DTB) crystallizer exhibiting a large range of sizes due to the heterogeneous environment of the crystallizer, as well as a pronounced roundedness due to the significant attrition of the larger crystals. Illustration (c) shows crystals grown rotating in a flow, which also exhibit pronounced

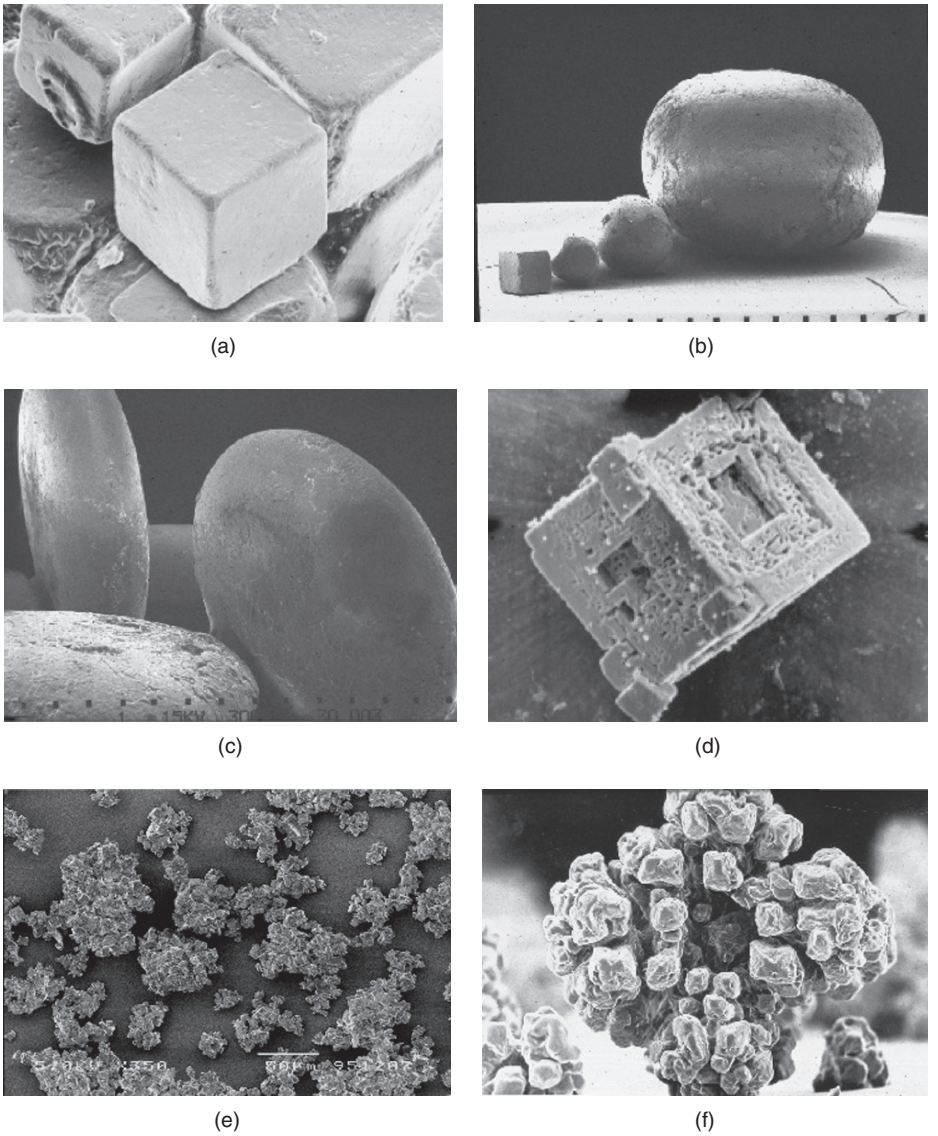

Figure 2.12 Various types of NaCl crystals: (a) from a forced circulation (FC) crystallizer, (b) from a draft tube baffled (DTB) crystallizer, (c) grown rotating in a flow, (d) grown from a highly supersaturated solution, (e) agglomerate from anti-solvent crystallization, (f) grown in the presence of $Fe(CN)_6^{4-}$ (with permission from Akzo-Nobel).

roundedness due to extensive attrition and asymmetrical feed conditions. Illustration (d) shows how the high supersaturation causes the edges of the crystal (which experience higher levels of supersaturation) to grow out faster than the middle of the faces (which experience lower levels of supersaturation due to diffusion limitations). Illustration (e) shows the significance of the type of crystallization process on the product shape. The agglomerates were produced from an anti-solvent crystallization process, and thus

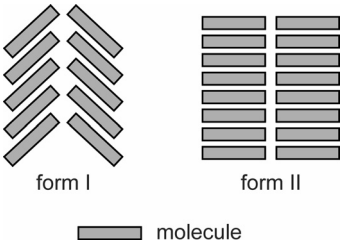

Figure 2.13 Two polymorphic forms.

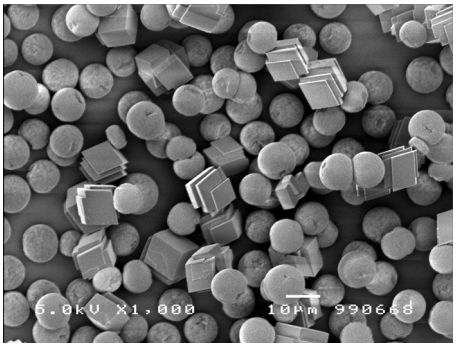

Figure 2.14 Concomitant formation of calcite (round) and vaterite (diamond-shaped) crystals.

under conditions of very high supersaturation. The primary particles in this illustration are cubic and of the order of 10 µm. Illustration (f), a NaCl crystal grown in the presence of $Fe(CN)_6^{4-}$, shows the potentially profound effect of an additive on crystal shape. The large dendritically shaped crystal is crystallographically a single crystal.

In summary, the final shape of a crystal population depends on its internal structure as well as on a large number of process variables.

2.4 Polymorphism

The occurrence of several different crystal forms for the same compound is known as polymorphism. Polymorphism arises because the molecules that make up the compound can be packed as different lattice structures in their solid state. Figure 2.13 shows two different polymorphic forms of the same compound – form I and form II. Polymorphism is more common in complex molecules, such as amino acids, because, the more complex the molecules are, the greater are the chances of a number of different lattices with comparable lattice energies.

However, even simple mineral salts such as calcium carbonate can exhibit different lattice arrangements. In Figure 2.14, rounded calcite and diamond-shaped vaterite crystals are shown. These were formed simultaneously in the same reaction vessel. Vaterite is a metastable phase of calcium carbonate, and will eventually transform into calcite in

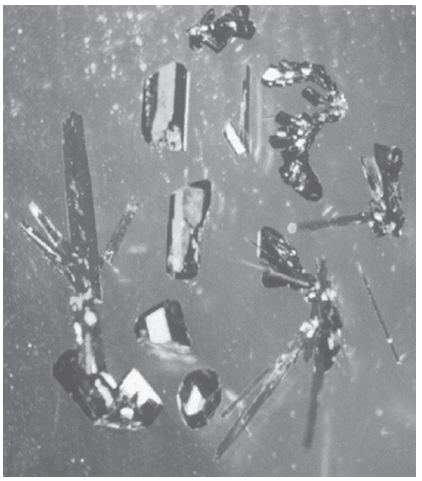

(a)

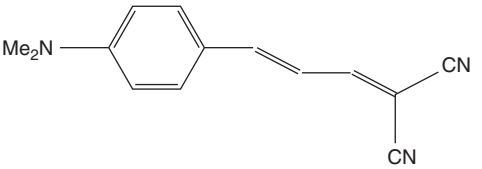

1,1-dicyano-4-(4-dimethylaminophenyl)-1,3-butadiene

A: needles/dark gray
T_{melt} = 151 °C ρ = 1.191
B: tabular/light gray
T_{melt} = 149 °C ρ = 1.206

(b)

Figure 2.15 Polymorphs of a dye.

aqueous solution at ambient temperature. The nature of the formed polymorph depends on thermodynamic factors, as well as kinetic ones such as the temperature, the supersaturation, the solvent and the type of seed crystals (see also Chapter 14 on Polymorphism). It is also possible that recrystallization from one polymorph into the other may occur, such as in the vaterite–calcite example.

Polymorphs of a given compound have different physicochemical and mechanical properties. Therefore, the processing and the end use features of a given compound strongly depend on the polymorph. Polymorphism sometimes inadvertently occurs in the production of dyes and pigments. In Figure 2.15, the concomitant formation of two types of crystals is shown that not only have a different shape, but also a different color (dark red and green, shown as different shades of gray in the black and white figure).

It is quite common that polymorphism is not recognized until the scale-up stage of a process. This arises because a particular polymorph is formed at laboratory scale, but, due to changes in local temperature and supersaturation conditions, a different one is generated on scale-up. The example in Figure 2.16 illustrates a number of different forms of cyanine and oxonol dyes with totally different colors (shown as different grays in the figure).

The phenomenon of polymorphism is extremely important in the pharmaceutical industry, not only because of the potential infringement of patents (since regulatory approval is only granted for specific polymorphic forms), but because the solubility of the more metastable phase is higher. Therefore, the bioavailability of the different polymorphs can be very different.

The very high-profile ritonavir case is an example of how seriously polymorphism can affect drug production (Bauer *et al.*, 2001). The active pharmaceutical ingredient in the drug exists as two polymorphs, Form I and Form II. Regulatory approval had been

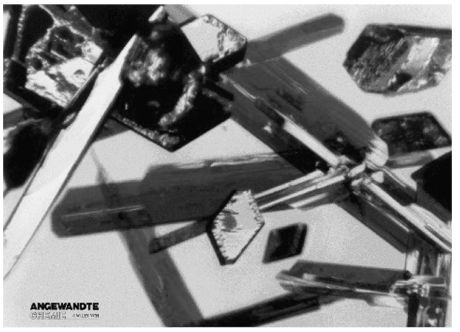

Figure 2.16 Polymorphs of cyanine/oxonol dyes.

granted for Form I, which was found to be the metastable one. It converted into Form II, the inactive one, over time, rendering the drug useless. The only way to solve the problem was to change the product from a solid formulation into a gel capsule suspension, thus preventing the polymorphic transformation (Braga and Grepioni, 2007).

2.5 Mother liquor inclusions

The presence of mother liquor inclusions is an important aspect of the characterization of a crystal product, since liquid inclusions not only negatively affect the purity of the product, but also give rise to breakage of the crystals during downstream processing.

Liquid inclusions can also be released during transport and storage of the crystals, since temperature gradients between the one side of the crystal and the other can cause the inclusion to slowly migrate from the inside to the outside of the crystal. Temperature variations can also cause the crystals to break due to the different densities of the liquid inclusion and the solid. In either case, the inclusion, thus released, slowly evaporates. As it does so, crystalline bridges are formed between adjacent crystals and severe caking of the product can result (Mullin, 2001).

The uptake of mother liquor inclusions by the crystal lattice is strongly dependent on the supersaturation, with higher supersaturations causing growth instabilities to occur, and making mother liquor inclusions almost unavoidable.

In melt crystallization, the interfacial tension between the crystal surface and the melt is usually lower than between a crystal and a solution. Large ΔT values therefore provoke surface instabilities more easily and dendrites are more likely to be formed. The process is as follows: when, for a suspension of crystals, a large heat of crystallization is released, the area immediately surrounding the crystal heats up, reducing the supersaturation in the region closest to the crystal. The areas further away from the crystal surface are at higher supersaturation and the crystal growth therefore occurs in the direction away from the crystal surface. In addition, since a protuberance, such as the tip of a dendrite, is more efficient in dissipating heat, dendrites are favored over the more compact forms when heat dissipation becomes rate controlling (Flory, 1985). These dendrites are the

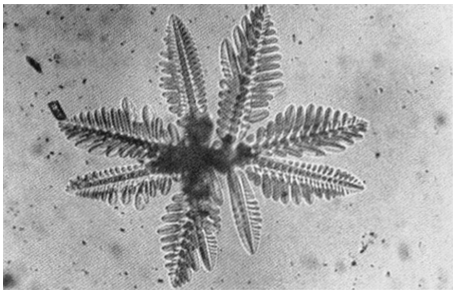

Figure 2.17 Dendrite of NH_4NO_3 (van Driel, 1994).

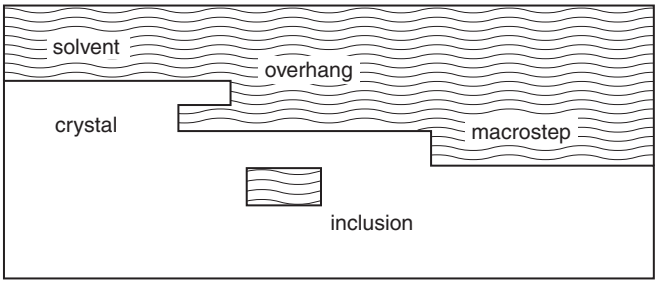

Figure 2.18 Macrosteps with overhangs.

causes of the fractal shapes that are found in melt crystallization. Figure 2.17 shows a dendritic ammonium nitrate crystal grown from a very concentrated solution.

From a purity point of view, dendrites are undesirable, as the branches of the dendrites provide spaces for the impure melt or highly concentrated solution to be captured.

In crystallization from solution, the release of heat of crystallization from the crystal surface to the solution hardly ever poses a problem. However, at high supersaturations in solution, crystallization conditions can cause the formation of macrosteps on the crystal surface (see also the section on growth kinetics in Chapter 6). These macrosteps stimulate the formation of overhangs, and these can lead to mother liquor inclusions (see Figure 2.18).

Because of their formation mechanism, these inclusions are always aligned along the outer crystal faces.

The phenomenon of solvent inclusions can be easily visualized under a microscope by suspending the crystals in a non-dissolving liquid with the same refractive index as the crystalline material. In Figure 2.19, the black areas are shadows caused by the macrosteps, which stand like cliff faces above the crystal surface.

Macrostep formation can also come about when crystals are formed from some solvents with a very strong adherence to particular crystal faces. This can promote macrostep formation and lead to more inclusions than other solvents.

When the supersaturation is high, diffusion can limit the transport of depleted solution away from the growing crystal face, and thus the edges and corners of the crystals "see"

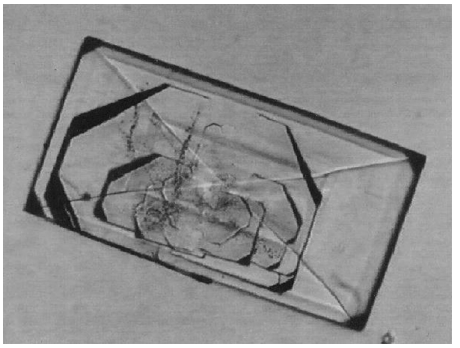

Figure 2.19 RDX crystal with large macrosteps grown from cyclohexanone without water (ter Horst, 2000). Reproduced with permission.

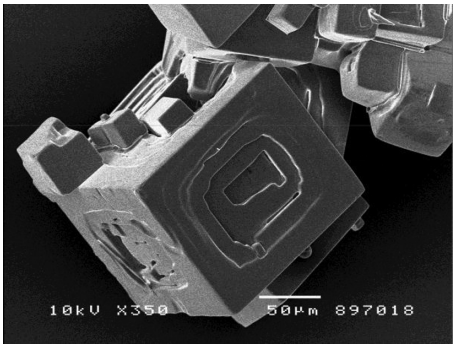

Figure 2.20 Hopper crystals of NaCl.

more supersaturation in the bulk of the solution. Thus the edges and corners benefit more from the volume diffusion of growth units towards the crystal surface than the centers of the faces. This can cause the formation of so-called "hopper crystals," crystals that have the shape of a grain hopper (Wolfram, 2002). This hopper shape tends to result in more inclusions than crystals with flat faces (see Figure 2.20).

Another cause for the formation of liquid inclusions is attrition of crystals due to crystal–crystal collisions or collisions with the impeller or pump blades. High stirrer or pump speeds and a high crystal content in the slurry lead to more attrition. If the crystals are greater than a certain size (the specific size being dependent on the material strength and the impact of the collision), the edges and specifically the corners of the crystals become attrited (worn by attrition). During the healing of the attrited surfaces due to growth (this happens especially under conditions of higher supersaturation), mother liquor can become included, because the growth layers propagating along adjacent faces no longer fit perfectly at the edges and corners (see Figure 2.21). In this figure, the black areas are solvent inclusions. It is interesting to note that the inclusions only appear once the crystal has reached a critical size such that the corners become subject to attrition. From the figure, it is apparent that the majority of the inclusions are located along the healing corners of the crystal.

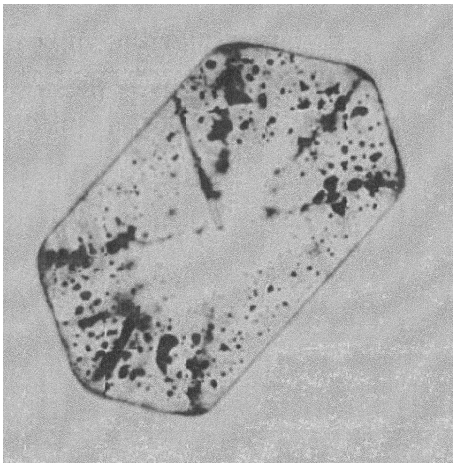

Figure 2.21 Liquid inclusions in an $(NH_4)_2SO_4$ crystal embedded in a liquid of similar refractive index.

Thus, from a product quality point of view, it is important to not only examine the external morphology, but also to inspect the crystal product for liquid inclusions.

2.6 Uptake of impurities in the crystal lattice

An important advantage of crystallization compared to other separation techniques is that the solid phase has a very rigid structure, and the incorporation of an impurity by occupation of the crystal lattice positions that are normally occupied by the growth units only occurs if the impurity fits reasonably well into the lattice.

The degree of uptake of the impurity in the lattice is reflected by a so-called effective distribution coefficient (sometimes also called a partition coefficient or a distribution coefficient; see Figure 2.22)

$$k_{distr} = \frac{c_c}{c_b} \tag{2.20}$$

where k_{distr} = effective distribution coefficient [-]

c_c = impurity concentration in the crystal [mol L^{-1}]
c_b = impurity concentration in the bulk [mol L^{-1}].

The value of the effective distribution coefficient depends on the thermodynamic distribution coefficient of the impurity in the crystal lattice at zero growth rate, k_0, on the surface distribution coefficient, k_s, and on the mass transfer coefficient of the impurity in the liquid, k_d.

The values of k_0 and k_s can be calculated by molecular mechanics, so, in principle, the potential uptake (i.e. at zero growth rate) of an impurity in a lattice can be estimated (see Figure 2.22).

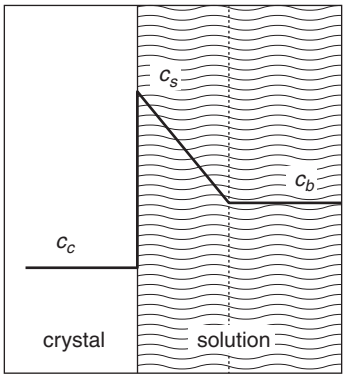

Figure 2.22 Uptake of impurity in the crystal where c_c, c_s and c_b are the impurity concentrations in the crystal, at the surface and in the bulk of the liquid.

Reliable k_{distr} values have mainly been calculated for organic crystals and organic impurities, so, in these cases, molecular modeling can be used to predict whether it is feasible to purify an organic compound by melt crystallization.

2.7 Degree of agglomeration

At high supersaturations and for relatively small crystals (e.g. with sizes up to 20 μm) agglomeration is a frequently encountered phenomenon. In both precipitation and anti-solvent crystallization, agglomeration is almost unavoidable due to the large numbers of crystals (see Chapter 11). However, sometimes, for separation purposes, agglomeration can be desirable because agglomerates filter faster than single crystals.

However, agglomeration can also occur if, during the start-up of an evaporation process, the heat input is very high. This creates a high level of supersaturation in the boiling zone, while the crystals of the very soluble compound are still small, and thus agglomeration occurs.

The reason that agglomerates are a problem is that they contain mother liquor between the primary crystals that comprise the agglomerate. This solvent is hard to remove during drying, and promotes caking of the product during storage.

In general, agglomerates also break more easily than solid crystals, and release solvent during their breakage. A crystal product therefore must always be inspected under a microscope to ascertain the occurrence of agglomerates (see Figure 2.23).

2.8 A brief summary of the chapter

Characterization of a crystalline product is an important subject because it explains the product performance during processing, such as the filtration rate or the stability during storage, as well as product end-use features, such as the color of a pigment or the bioavailability of a pharmaceutical compound. Product characterization is accomplished

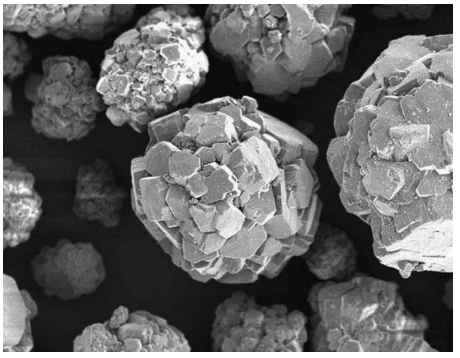

Figure 2.23 Agglomerates of the explosive compound pentaerythritol tetranitrate (PETN), which were formed in an anti-solvent crystallization process.

by considering a number of characteristics of a population of crystals, such as the crystal size or particle size distribution, including various measures of size and distribution width. Other characteristics of crystalline products were described and defined, including, crystal morphology and shape, polymorphism, mother liquor inclusions (which affect purity and caking), uptake of impurities in the lattice and finally, the degree of agglomeration.

2.9 End of chapter problems

Problem 1

i. What is a crystal?
ii. What is the difference between a polycrystalline particle and a monocrystalline particle (single crystal)?

Problem 2

i. What are the area and volume shape factors of a sphere?
ii. What are the area and volume shape factors of a rectangular prism ($L_1 = 10$, $L_2 = 6$ and $L_3 = 4$), where L_3 is the characteristic length?
iii. Show that any equi-dimensional regular object for which $L = D$ will have $k_a = 6k_v$.

Problem 3

i. What are the advantages and disadvantages of the different quantities used to express crystal size distribution?
ii. Discuss what might be the problems with using vol% as the ordinate for a crystal size distribution?
iii. Give two quantities that can be used to express size distribution in a simple way.

Problem 4

i. Why does particle size distribution affect filtration rate?
ii. Why does the width of the distribution affect filtration rate?

2.10 References

Accelrys. 2013. *Morphology*, http://accelrys.com/products/datasheets/morphology.pdf, Datasheet, Accessed 11 April 2013 [Online].

Bauer, J., Spanton, S., Henry, R. *et al.* 2001. Ritonavir: an extraordinary example of conformational polymorphism. *Pharmaceutical Research*, **18**, 859–866.

Braga, D. and Grepioni, F. 2007. *Making Crystals by Design*, Wiley.

Cambridge Crystallographic Data Centre (CDCC). 2013. http://www.ccdc.cam.ac.uk/pages/Home.aspx, Accessed 12 April 2013 [Online].

Clydesdale, G., Roberts, K. J. and Docherty, R. 1996. HABIT95 – a program for predicting the morphology of molecular crystals as a function of the growth environment. *Journal of Crystal Growth*, **166**, 78–83.

Davey, R. and Garside, J. 2000. *From Molecules to Crystallizers*, Oxford University Press.

Docherty, R., Roberts, K. J. and Dowty, E. 1988. Morang – a computer program designed to aid in the determinations of crystal morphology. *Computer Physics Communications*, **51**, 423–430.

Flory, P. J. 1985. *Selected Works of Paul J. Flory, Volume III*, Stanford University Press.

Fuerstenau, M. C. and Han, K. N. 2003. *Principles of Mineral Processing*, Society for Mining, Metallurgy & Exploration, Incorporated.

ter Horst, J. H. 2000. *Molecular Modelling and Crystallization: Morphology, Solvent Effect and Adsorption*, Universal Press Science Publishers.

Hund, F. 1981. Inorganic pigments: bases for colored, uncolored, and transparent products. *Angewandte Chemie International Edition in English*, **20**, 723–730.

Johnson, R. A., Miller, I. and Freund, J. E. 2011. *Miller & Freund's Probability and Statistics for Engineers*, Prentice Hall PTR.

Li, R. F., Thomson, G. B., White, G. *et al.* 2006. Integration of crystal morphology modeling and on-line shape measurement. *AIChE Journal*, **52**, 2297–2305.

Lovette, M. A. and Doherty, M. F. 2012. Predictive modeling of supersaturation-dependent crystal shapes. *Crystal Growth & Design*, **12**, 656–669.

Mullin, J. W. 2001. *Crystallization*, Butterworth-Heinemann.

Myerson, A. S. 2001. *Handbook of Industrial Crystallization*, Butterworth-Heinemann.

Randolph, A. D. and Larson, M. A. 1988. *Theory of Particulate Processes: Analysis and Techniques of Continuous Crystallization*, Academic Press.

Rawle, A. 2003. Basic of principles of particle-size analysis. *Surface Coatings International. Part A, Coatings Journal*, **86**, 58–65.

Rohl, A., Wright, K. and Gale, J. 2003. Realistic Modeling of Complex Surface Processes. Nano Tech 2003, San Francisco.

Rohl, A. L. 2003. Computer prediction of crystal morphology. *Current Opinion in Solid State and Materials Science*, **7**, 21–26.

Söhnel, O. and Garside, J. 1992. *Precipitation: Basic Principles and Industrial Application*, Butterworth Heinemann Ltd.

Sunagawa, I. 2005. *Crystals: Growth, Morphology and Perfection*, Cambridge University Press.

Van Driel, C. A. 1994. *Influence of additives on structure and thermal stability of ammonium nitrate*. PhD Thesis, Technical University of Delft.

Wolfram, S. 2002. *A New Kind of Science*, Wolfram Media.

3 Basic process design for crystallization

3.1 Why this chapter is important

This chapter discusses the basic design of industrial crystallizers. The major design tasks are the selection of the crystallization method, the crystallizer equipment and the mode of operation, the calculation of the flow sheet of the process and of the dimensions of the equipment, the area for heat transfer and evaporation, and the power requirement for the circulation devices. With the help of a costing model, the basic design also yields a first cost estimate of the process in terms of both capital and operational costs.

The method described in this chapter has been developed and tested for evaporative and cooling crystallization processes, but can be adapted relatively easily for melt crystallization processes from suspensions. Examples are given for evaporative and cooling processes, for a DTB evaporative crystallizer including mother liquid recycling and for an Oslo evaporative crystallizer.

The proposed procedure does not include a detailed design, in which not only the average particle size and purity have to be assured, but also the size distribution, the particle shape and degree of agglomeration, among other features that are specific to each application. In those circumstances, a detailed design procedure has to be followed that is based on a model for the industrial crystallizer that takes into account a number of compartments and the crystallization kinetics for the system of interest, followed by model validation in a pilot unit.

3.2 The basic design procedure

A hierarchical detailed design procedure has been proposed (Bermingham *et al.*, 2000, Kramer *et al.*, 1999) based on the pioneering work of Douglas (1985) with focus on a precise prediction of the final product quality through detailed mathematical modeling of the crystallization phenomena. Although this approach is suitable for consistent and reproducible design, it requires detailed knowledge of the kinetics and the hydrodynamics of the process, as well as substantial computing and experimental facilities. In Chapter 7 the detailed modeling needed to describe the product quality is discussed. In this chapter on the basic or conceptual design, a simplified procedure is presented (Seckler *et al.*, 2013) that just requires fragmentary experimental information, heuristics and theoretical considerations. The design is composed of the four hierarchical levels

Table 3.1 Design levels belonging to the hierarchical design procedure for solution crystallization processes

Design Level	Description
0	Initial design specifications
I	Crystalline product design
II	Physicochemical design of the crystallization task
III	Flow-sheet design of the crystallization process
IV	Crystallizer design

shown in Table 3.1. At each level, a limited number of aspects are considered, thereby simplifying the processes of formulating hypotheses and making decisions. This procedure also favors the development of a traceable, reproducible design, although the crystallizer design is limited to the selection of the type of crystallizer and the determination of the basic dimensions needed for economic evaluation of the process.

A number of issues related to specific systems are not covered by the present method, such as systems involving solid solutions (Lin *et al.*, 2008), fractional crystallization (Cisternas *et al.*, 2006) and systems exhibiting polymorphism (Lin *et al.*, 2007). Wibowo *et al.* (2001) developed procedures for the integrated design of crystallization and downstream processing operations, whereas Grosch *et al.* (2008) developed a procedure that integrates design and process control.

3.2.1 Design Level 0: initial design specifications

Product performance is specified in terms of its downstream handling features in the industrial unit, such as filterability and explosion hazard, as well as in terms of its features during application as a particulate product, such as color, taste and appearance. *Process specifications* are typically the *production rate* (in kg s^{-1} solids), the raw material characteristics, the utilities available, the specific energy consumption, the controllability, the availability, and the safety, health and environmental considerations. *Design specifications* include the available budget, the time-to-market, the experience of the designers and the development of in-house technology or technology transfer.

3.2.2 Design Level I: crystalline product design

At this level, the characteristics of the particulate solid are identified that provide the product performance specified in the previous level. The main characteristics are: particle size distribution (sometimes only the mean size, the width of PSD or the fines content are specified), shape, purity, degree of aggregation, polymorphic form. For instance, an easily filterable product should comprise non-tabular shaped particles of large size and narrow size distribution. If the color or the taste is important, product purity and crystal shape are important features. In the basic design procedure, however, only the *average particle size* and the *product purity* are specified.

3.2.3 Design Level II: physicochemical design of the crystallization task

At this level the crystallization method is selected that delivers the product specified in the previous level. The analysis is mainly based on thermodynamic equilibrium in multi-phase systems and on concepts of crystallization theory.

3.2.3.1 Solvent selection

A solvent in which the crystallizing compound is highly soluble is preferred, because highly soluble compounds usually display high growth rates and crystallize as large particles (in the size range 10^{-4} to 10^{-3} m). Besides, crystallization proceeds under low supersaturation, so that a relatively pure product results. Conversely, slightly soluble compounds form relatively small and impure particles (in the size range 10^{-6} to 10^{-5} m). A slight solubility may be desirable for a valuable compound, as it promotes its recovery. A more complex process results if a mixed solvent is selected, because solvent purification and recovery steps are needed. Health, safety and environmental considerations are also important when selecting a solvent.

3.2.3.2 Crystallization method

The crystallization method is primarily selected according to the crystallizing compound solubility diagram (Kramer *et al.*, 1999). A detailed description of the various methods is presented in Chapters 1 and 11. Here only a few important aspects are highlighted.

Melt crystallization is applied if the solute concentration is very high (>90 wt%) and when the product purity must be extremely high (99.9 to 99.9999 wt%). Melt crystallization processes are in general more expensive than cooling crystallization processes, as large heat exchanger areas are needed to minimize scaling. Besides, washing of the product particles to obtain a pure product is expensive.

Cooling crystallization is the preferred crystallization method when the slope in the solubility curve is larger than 0.005 $°C^{-1}$. Energetically, cooling crystallization is the most favorable (see below) option and is operationally simple. Indirect cooling requires a low heat flux through the heat exchanger to minimize scaling. Wipers or scrapers allow higher fluxes, but add complexity to the system. Indirect cooling should be disregarded for systems that severely incrustate. In such instances flash cooling or direct cooling (a refrigerant gas is blown through the crystallizer) are good alternatives. Cooling crystallization may be disregarded if the spent solution cannot be recycled upstream in the process, since it cannot be reused in the crystallization process itself. To reduce this loss, sometimes an anti-solvent crystallization process is placed after a cooling crystallization step.

Evaporative crystallization is applied for solutions with moderate to high solubility (~10 to 90 wt%) and a flat solubility curve. Technically, evaporative crystallization can be applied irrespective of the slope of the solubility curve. On the other hand, the energy demand for evaporative crystallization is higher than for cooling crystallization. As evaporative crystallizers normally operate at higher temperatures (>50 °C), they are not suitable for thermally labile compounds. Anti-solvent crystallization is an alternative in these cases.

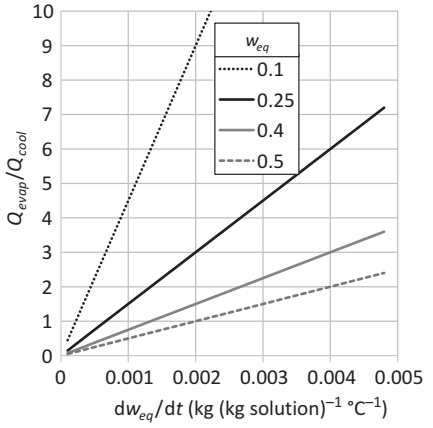

Figure 3.1 Ratio of energy consumption for evaporative to cooling crystallization as a function of the slope of the solubility curve for different values of the solubility $w_{eq}.\Delta H_{evap}/c_p = 500$.

The relative energy consumption of evaporative in relation to cooling crystallization can be estimated using the following expression, in which the heat of crystallization is neglected. This assumption is valid in most cases when water is the solvent. For other solvents, corrections for the heat of crystallization must be made.

$$\frac{Q_{evap}}{Q_{cool}} = \frac{\Delta H_{evap}}{c_p}\left(\frac{1}{w_{eq}} - 1\right)\frac{\mathrm{d}w_{eq}}{\mathrm{d}T} \tag{3.1}$$

where Q is the heat load for the evaporative or cooling crystallization, w_{eq} the solubility in mass fraction [(kg solute) (kg solution)$^{-1}$] at the equilibrium temperature, c_p the specific heat of the saturated solution and ΔH_{evap} the latent heat of evaporation. In Figure 3.1 this ratio is plotted as a function of the slope of the solubility curve for different values of the equilibrium concentration, assuming a value of 500 for the ratio between ΔH_{evap} and c_p. It is clear that energetically, cooling crystallization is often more favorable than evaporative crystallization, except for highly soluble substances and very flat solubility curves.

Precipitation is applied for slightly soluble compounds. It takes place upon mixing highly soluble reactants, which rapidly react to yield the desired particulate solid. The supersaturation values at the inlet points are generally extremely large, leading to undesirable high nucleation and agglomeration rates. Improvement of the particulate product quality can be obtained with a proper design of the inlets in order to reduce the mixing time or with application of a clear liquor advance to increase the crystal concentration in the crystallizer.

Anti-solvent crystallization is often used for high added-value products because it provides high yields (mass of compound as a particulate product per unit mass of the compound in the feed). As the solubility in an anti-solvent crystallization process is in most cases very low, the crystallization is characterized by high supersaturation and a low product quality. In this respect, anti-solvent crystallization is similar to precipitation. Note that the heat of mixing for the anti-solvent can be considerable and must be

compensated by cooling. A disadvantage of this method is that the anti-solvent must be recovered from its mixture with the solvent.

3.2.3.3 Number of crystallization steps

The number of crystallization steps, defined as the number of times that a compound crystallizes following successive dissolutions, depends on the specified product purity. In most industrially relevant applications, a single crystallization step is sufficient, but there are exceptions. Three mechanisms exist for impurities uptake into the solid phase (see also Chapter 13). Firstly, if the impurity and host molecules are similar in size and charge, the impurity isomorphically substitutes the host compound in the crystalline lattice. Secondly, if the supersaturation is high, mother-liquor inclusions occur in the crystals. The third route for impurity incorporation is associated with drying of the wet crystals after they leave the crystallizer. During drying the non-volatile mother-liquor impurities adhere to the particle surfaces. These surface-adhered impurities may be reduced if the crystals are large and if sufficient crystal washing is applied after filtration or centrifugation. Another reason for application of multiple crystallization steps is to induce the formation of larger crystals, taking advantage of the higher solution purity in successive crystallization steps.

3.2.3.4 Temperature and pressure

Higher temperatures are preferred because they usually lead to larger and purer crystals. However, high operation temperatures make the equipment more complicated. Other reasons to avoid high temperatures are possible chemical instability of the compound and high temperature differences with the feed stream. However, the highest temperature within the crystallizer is often limited by the temperature of the heat source available.

3.2.4 Design Level III: flow-sheet design of the crystallization process

At this design level, the crystallization method selected in the previous level guides the development of the flow-sheet.

3.2.4.1 Operation mode

In continuous operation, raw materials and equipment are used in an efficient way compared to batch processing, so the costs per unit mass of product are lower. Therefore this type of operation is often used for low-value products. In continuous operation, the product quality is more uniform than in batch operation, as low reproducibility between batches is a major drawback. Continuous operation has less downtime than batch operation, as it has to be interrupted every 200 to 2000 h to remove undesirable crystal deposits. However, for systems with a severe tendency to scaling, continuous operation may not be feasible. This mode of operation is also unsuitable for capacities below 50 metric tons of product per day (Bennett, 1993), otherwise very small pipes would be needed for pumping of suspensions at a velocity that prevents solids deposition.

Batch operation is suitable for multi-purpose units, as continuous mode would result in contamination of products and excessive off-spec products during transient operation. Important advantages of batch operation are the simplicity of equipment and the possibility of thorough cleaning of the vessel every cycle, thereby avoiding product contamination and the slow formation of undesirable polymorphs. It is also applied for high flexibility towards product specification and when a narrow particle size distribution is desired (an important example is the crystallization of sugar). Batch processes almost never use evaporative crystallization, most likely due to the large investment costs related to the large vapor head needed, especially at low temperatures. On the other hand, flash cooling processes often operate in batch mode.

3.2.4.2 Method for energy conservation

In continuous evaporative crystallization, energy may be conserved with multiple-effect evaporation, in which the vapor generated in one effect is used to supply energy for solvent evaporation in the following effect. As a first estimate, the energy consumption is the energy needed to evaporate the solvent divided by the number of stages. Boiling point elevation, however, decreases the benefits of staging because successive stages have to operate under decreasing pressure. In mechanical vapor recompression only one evaporator is needed, and electrical energy is used to recompress the vapor generated, which is recycled. Thermal vapor recompression is similar, but vapor recompression is achieved with high pressure steam. The preferred method of energy conservation depends on local availability and costs of steam and electric energy.

3.2.4.3 Feed configuration

For multiple-effect crystallizers, the feed is usually in parallel to each crystallizer. Operation in series with respect to the feed is applied to attain a narrow size distribution. Operation of crystallizers in series generates a narrower CSD than the same volume of crystallizers in parallel.

3.2.4.4 Recycle structure and purge

Recycling the saturated solution leaving each crystallizer is desirable in order to recover its heat and valuable solute content. Full recycle is, however, not possible, due to impurity buildup. Consequently, a purge is provided, preferably from a stream with a high impurity level (for a small purge flow) and with a low temperature (for energy conservation).

3.2.4.5 Residence time

The mean residence time τ in a continuous, mixed suspension, mixed product removal crystallizer relates to the volume-weighted mean size $L_{4,3}$ and the crystal growth rate $G[\mathrm{m\ s^{-1}}]$ by:

$$\tau = \frac{L_{4,3}}{4G} \tag{3.2}$$

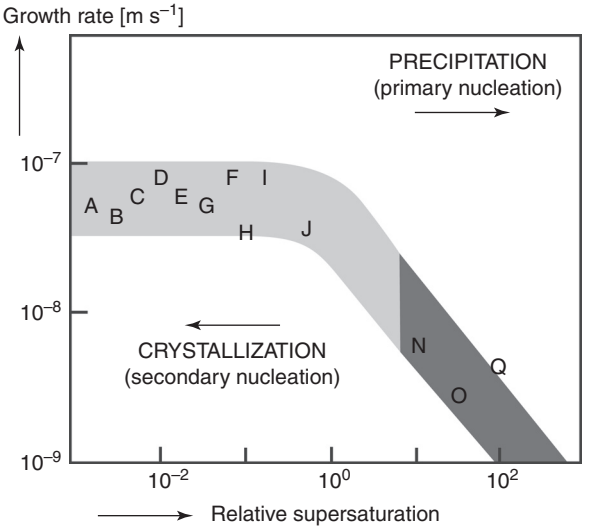

Figure 3.2 Growth rate of a number of inorganic salts versus relative supersaturation (Mersmann and Kind, 1988) A: KCl, B: NaCl, C: $(NH_2)_2CS$, D: $(NH_4)_2SO_4$, E: KNO_3 F: Na_2SO_4, G: K_2SO_4, H: $(NH_4)Al(SO_4)_2$, I: $K_2Cr_2O_7$, J: $KAl(SO_4)_2$, N: $CaCO_3$, O: TiO_2, Q: $BaSO_4$. Reproduced with permission.

whereas for a batch crystallizer the following expression holds:

$$\tau = \frac{L_{4,3}}{G} \tag{3.3}$$

The crystal growth rate can be estimated from Figure 3.2 or experimentally determined. In the figure the relative supersaturation σ is defined as:

$$\sigma = \frac{w_{liquid,1} - w_{eq}}{w_{eq}} \tag{3.4}$$

3.2.4.6 Flow-sheet calculations

A schematic flow-sheet for continuous crystallizers is shown in Figure 3.3. The suspension is recirculated between the crystallizer and the heat exchanger. The feed is added and the product suspension is removed from this recirculation stream. The product suspension is separated into a clear solution, which is recycled, and the solid product. Depending on the crystallization method, heat and an isobaric condenser may be applied. For evaporative crystallization heat is added and the condensation rate is controlled to maintain the desired boiling temperature. For cooling crystallization only heat is removed. For flash cooling no heat is removed via the heat exchanger, but by controlled evaporation of the solvent, cooling it down simultaneously.

The mass and enthalpy balances are applied around the control volume indicated by dashed lines in Figure 3.3. The balance equations and a few ancillary relations are shown in Table 3.2. The mass and enthalpy balances form the physical constraints posed by mass and enthalpy conservation, while the distribution coefficient allows for the description of

Table 3.2 Mass and energy balances for continuous crystallizers

Description	Equation
Solvent balance	$\frac{\mathrm{d}V\varepsilon\rho_{liquid}w_{liquid,solvent}}{\mathrm{d}t} = \varphi_{v,feed}(\varepsilon_{feed}\rho_{feed,liquid}w_{feed,solvent}) - \varphi_{v,prod}(1-\kappa)(\varepsilon_{prod}\rho_{liquid}w_{liquid,solvent}) - \varphi_{v,vapor}\rho_{vapor}$
Solutes balances $i = 1, \ldots, N_{comp}-1$	$\frac{\mathrm{d}M_i}{\mathrm{d}t} = \varphi_{v,feed}(\varepsilon_{feed}\rho_{feed,l}w_{feed,liquid,i} + (1-\varepsilon_{feed})\rho_{crystal}w_{feed,crystal,i}) - \varphi_{v,prod}((1-\kappa)\varepsilon_{prod}\rho_{liquid}w_{liquid,i} + (1-\varepsilon_{prod})\rho_{crystal}w_{crystal,i})$
Enthalpy balance	$\frac{\mathrm{d}H}{\mathrm{d}t} = \varphi_{H,feed} - \varphi_{H,prod} - \varphi_{H,vapor} + Q_{heat} + P\Delta H_{cr}$
Distribution coefficient $i = 2, \ldots, N_{comp}-1$	$k_{distr,i} = \frac{w_{crystal,i}}{w_{liquid,i}}$
Total liquid mass	$w_{liquid,solvent} + \sum_{i=1}^{N_{comp}-1} w_{liquid,i} = 1$
Total crystal mass	$\sum_i w_{crystal,i} = 1$

Symbols: V = suspension volume [m^3 suspension], ε = liquid volume fraction [(m^3 liquid) (m^3 suspension)$^{-1}$], ρ_{phase} [(kg phase) (m^3 phase)$^{-1}$], $w_{stream,phase,component}$ [(kg component) (kg phase in stream)$^{-1}$], $\varphi_{v,stream}$ [(m^3 phase) s^{-1}], κ [(kg recycle) (kg prod)$^{-1}$], M_i = mass of component i [kg], H = enthalpy of the supension [J], $\varphi_{H,stream}$ = enthalpy flow [J s^{-1}], Q_{heat} = heat flow supplied or removed from the crystallizer [W], P = production rate [(kg crystals) s^{-1}], ΔH_{cr} = heat of crystallization [J (kg crystal)$^{-1}$]

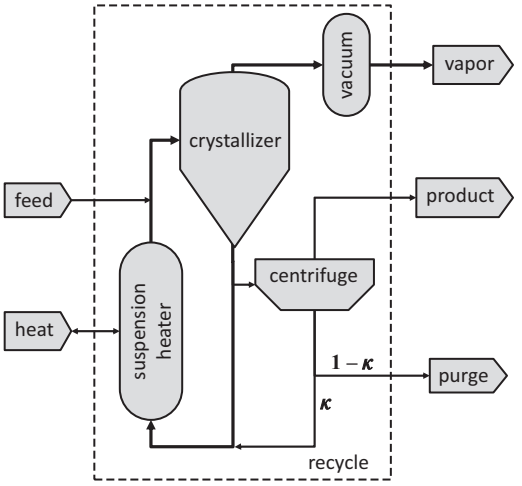

Figure 3.3 Flow-sheet of a continuous crystallizer. For evaporative crystallization heat addition and (often) vacuum apply; for cooling crystallization heat is removed and for flash cooling only vacuum applies (no heat exchange).

deposition of impurities in the crystals. Finally, for the sum of the mass fractions for the liquid and the crystal phase equal to unity, the equations in Table 3.2 can be used to calculate the yield (flow of particulate product per unit solute in the feed), the specific energy consumption (energy spent per unit mass of product) and the purity of the solid product. In addition, they supply the stream properties needed to size the crystallizer, the heat exchanger and the pumps.

For steady-state operation the terms in the left-hand side of the mass and enthalpy balances of Table 3.2 are neglected. The right-hand side of the mass balances accounts for the inlet and outlet flows of the solvent and the $N_{comp} - 1$ components. The recycle ratio κ in the balances accounts for the splitting of the liquid fraction of the product slurry into a recycle and a purge (see Figure 3.3); κ is the liquid recycle flow per unit liquid flow out of the crystallizer (upstream of the centrifuge in Figure 3.3). The purge is a small part of the recycle stream that controls the level of impurities in the system. The required purge flow is determined from the impurity mass balance and the allowable crystal purity, which is a Design Level I product specification.

In order to solve the balances the designer must specify three variables.

(a) The volumetric fraction of solids $1 - \varepsilon$ within the crystallizer. A high value is desirable because it leads to a small crystallizer volume and a low supersaturation. However, it also negatively affects the product quality, because of high attrition and secondary nucleation rates, poor mixing in the crystallizer and problems while pumping the slurry. In most industrial crystallization processes $(1-\varepsilon)$ is in the range 20–30 vol%.

(b) The solute concentration in the liquid phase $w_{liquid,1}$. For moderately and highly soluble compounds (solubility $>$ 10 wt%), $w_{liquid,1}$ generally approaches the saturation value at the crystallizer temperature. A better estimate of $w_{liquid,1}$ may be derived from the supersaturation calculated from a kinetic model, if available, otherwise a practical value of the relative supersaturation, as given Figure 3.2, may be used.

(c) The volumetric production rate $\varphi_{v,prod}$ ((m^3 suspension) s^{-1}) as derived from the production rate P ((kg solids) s^{-1}), which is a Design Level 0 specification, and $(1-\varepsilon)$:

$$\varphi_{v,prod} = \frac{P}{(1-\varepsilon)\rho_{crystal}} = \frac{P}{M_T} \tag{3.5}$$

Here M_T is the often-used concentration of crystals in suspension (kg m^{-3}).

For batch cooling crystallization, the balance equations already presented for the continuous process are applied, disregarding the terms for the feed, the product and the bleed streams, while the transient terms are adapted to provide the differences between the start and the end of the batch, as shown in Table 3.3. The final temperature is determined by the specified production of solids and the initial liquid composition. The final volume is calculated from equations 3.5 and 3.6, with the production rate P meaning the total production in a batch (kg).

Table 3.3 Mass and energy balances for batch cooling crystallizers. enthalpy [J]

Description	Equation/information/action
Solvent balance	$V_{init}(\varepsilon_{feed}\rho_{feed,liquid}w_{feed,liquid,solvent}) - V_{final}(\varepsilon\rho_{liquid}w_{liquid,solvent}) = 0$
Solutes balances $i = 1$: $N_{comp}-1$	$V_{init}(\varepsilon_{feed}\rho_{feed,liquid}w_{feed,liquid,i} + (1-\varepsilon_{feed})\rho_{crystal}w_{feed,crystal,i}) - V_{final}(\varepsilon\rho_{liquid}w_{liquid,i} + (1-\varepsilon)\rho_{crystal}w_{crystal,i}) = 0$
Enthalpy balance	$H_{init} - H_{final} = Q_{heat} + P\Delta H_{cr}$
Distribution equation $i = 2 \ldots N_{comp} - 1$	$k_{distr.,i} = \dfrac{w_{crystal,i}}{w_{liquid,i}}$
Total liquid mass	$w_{liquid,solvent} + \sum_{i=1}^{N_{comp}-1} w_{liquid,i} = 1$
Total crystal mass	$\sum_{i} w_{crystal,i} = 1$
Saturation concentration	$w_{liquid,1} = w_{eq} = f(T)$

Symbols (see also Table 3.2):
V_{init}, V_{final} = initial and final crystallizer volume [m^3]
H_{init}, H_{final} = initial and final crystallizer enthalpy [J]

The solution to the mass and enthalpy balances is conveniently found with an equation solver, although they can also be rewritten in explicit form.

3.2.5 Design Level IV: crystallizer design

3.2.5.1 Crystallizer type

For melt cooling crystallization the choices are layer crystallization and suspension crystallization. The former process is more robust, whereas the latter is much cheaper, both in equipment costs and energy consumption, and can deliver a purer product in one crystallization step when operated in combination with a wash column. For precipitation processes, generally a mixed tank reactor is used. The mixing of the two feed streams is in general of key importance for the resulting product quality, but requires a detailed analysis of the hydrodynamics combined with the crystallization kinetics (see Chapter 11). For cooling and evaporative crystallization, a number of types of crystallizers are commercially available: stirred tank reactor (ST), the draft tube crystallizer (DT), the forced circulation crystallizer (FC), the draft tube baffled crystallizer (DTB), the fluidized bed or "Oslo" crystallizer (FB), the growth crystallizer (GC), the Svensen cooling crystallizer (SCC) and the cooling disk crystallizer (CDC). For selection of the type of crystallizer see Chapter 10.

3.2.5.2 Crystallizer dimensions

The suspension volume V derives from the residence time τ specified at Design Level III:

$$V = \varphi_{v,prod} \cdot \tau \tag{3.6}$$

Assuming a cylindrical crystallizer vessel with a fixed height-to-diameter ratio R_{HD}, the diameter of the crystallizer becomes:

$$D_\tau = \sqrt[3]{\frac{4V}{\pi R_{HD}}} \tag{3.7}$$

Here the height refers to the suspension. The total vessel height is higher especially for evaporative crystallizers, which require separation between vapor and entrained droplets. For mechanically agitated cylindrical crystallizers a value of 0.6 for R_{HD} may be chosen to favor a uniform distribution of solids throughout the vessel.

For evaporative crystallizers the cross sectional area for evaporation has to be sufficiently large to avoid liquid droplet entrainment in the solvent vapor stream. To this end, the linear velocity of the vapor flow must not exceed certain limits. A conservative relation is given by Souders and Brown (1934) for distillation columns:

$$v_{max} = C_v \left(\frac{\rho_{liquid} - \rho_{vapor}}{\rho_{vapor}} \right)^{\frac{1}{2}} \tag{3.8}$$

For vapor heads, a value of 0.0244 m s^{-1} is recommended for C_v. This leads to a minimum diameter of the evaporation zone given by:

$$D_{vapor\ head} = \sqrt{\frac{4\varphi_{v,vapor}}{\pi v_{max}}} \tag{3.9}$$

where the volumetric flow of vapor $\varphi_{v,vapor}$ [m^3 s^{-1}] is derived from the process mass balances and the vapor density. The crystallizer diameter should therefore be equal to the higher of the two values determined by equations 3.7 and 3.9:

$$D_{crystallizer} = \max(D_\tau, D_{vapor\ head}) \tag{3.10}$$

If the crystallizer diameter is determined by the vapor head requirement, the resulting residence time is larger than needed. The desired residence time can sometimes be established by adjusting R_{HD} to a lower value.

For DTB crystallizers an additional cross sectional area A_{AZ} is needed to accommodate a skirt baffle or annular zone, in which the fine particles are separated from the large ones, calculated as explained in Section 3.2.5.4. The DTB crystallizer diameter becomes:

$$D_{DTB\_crystallizer} = \sqrt[2]{\frac{4}{\pi} A_{AZ} + D^2_{crystallizer}} \tag{3.11}$$

3.2.5.3 The recirculation rate and the heat exchanger area

In evaporative crystallizers the energy for evaporation is supplied by heating the suspension in a heat exchanger, which is located either within the crystallizer body or more commonly as an independent unit connected to the crystallizer by a recirculation stream. In either case, the heat exchanger must be placed far below the boiling zone of the crystallizer. In this way, the column of liquid above the heat exchanger prevents boiling which would otherwise promote scaling. In FC and fluid-bed crystallizers, however, the

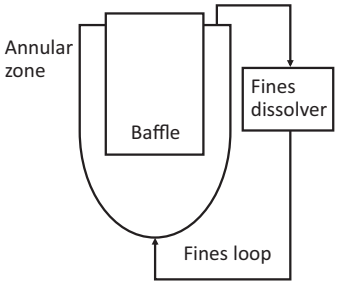

Figure 3.4 Annular zone and fines recirculation loop.

inlet of the circulation flow is situated just below the boiling zone. This poses a constraint on the temperature increase of the suspension in the heat exchanger $\Delta T_{hex,max}$. For a given heat duty Q_{heat} a minimum circulation flow through the heat exchanger $\varphi_{v,circ,min}$ is thus needed:

$$\varphi_{v,circ,min} = \frac{Q_{heat}}{\Delta T_{hex,max}(\varepsilon \rho_{liquid} c_{p,liquid} + (1-\varepsilon)\rho_{crystal} c_{p,crystal})} \tag{3.12}$$

The maximum value specified for $\Delta T_{hex,max}$ between the inlet and outlet of a heat exchanger serving a crystallizer is generally 1 to 2 °C.

In cooling crystallizers, including melt cooling, heat is most commonly removed in a heat exchanger. Because the exchanger walls are colder than the suspension, scaling occurs upon the exchanger surfaces. The simplest way to reduce scaling is to limit the heat flux to values below 100–200 W m^{-2}. When wipers or scrapers are used, heat fluxes of up to 1000 W m^{-2} are allowed, but mechanically complex equipment results. The heat exchanger area is calculated from:

$$A_{hex} = \frac{Q_{heat}}{\varphi''_{hex,max}} \tag{3.13}$$

where A_{hex} is the heat exchanger area (m^2), and $\varphi''_{hex,max}$ is the maximal allowable heat flux [W m^{-2}]. For the detailed design see Sinnott (1998).

3.2.5.4 Controlling the particle sizes

The theory of ideal continuous crystallizers reveals that the most efficient ways of controlling the particle size are by means of fines removal and product classification. Fines removal reduces the net nucleation rate within the crystallizer, yielding a larger product size. With product classification, the largest particles are selectively removed from the crystallizer, leaving smaller particles and yielding as the net effect a reduction in the mean particle size. Both fines removal and product classification deliver a narrower size distribution.

Fines removal in DTB crystallizers is applied by recirculating the suspension through a fines dissolver, as shown schematically in Figure 3.4. The cross sectional area of the annular zone around the skirt baffle A_{AZ} is selected to give a particular upward suspension velocity, which is equal to the settling velocity of particles v_{ss} of a desired cut-size L.

Table 3.4 Parameters for the settling velocity equation of Barnea and Mizrahi

$A = \sqrt{\alpha_1}$	$\alpha_1 = g\dfrac{\rho_{crystal} - \rho_{liquid}}{\rho_{crystal} + \rho_{liquid}}$
$B(L) = 0.5\alpha_4\sqrt{\alpha_2}$	$\alpha_2 = \dfrac{3}{4}\dfrac{1 + (1-\varepsilon)^{1/3}}{(\rho_{crystal} + \rho_{liquid})L^2\varepsilon}$
$C(L) = \alpha_3\sqrt{\alpha_2}$	$\alpha_3 = 0.63\sqrt{L\rho_{liquid}}$
	$\alpha_4 = 4.80\sqrt{\mu_l}\exp\left(\dfrac{5}{6}\dfrac{(1-\varepsilon)}{\varepsilon}\right)$

Particles smaller than the cut-size flow upward into the fines loop cycle, otherwise they remain in the crystallizer. To calculate the settling velocity v_{ss} of particles with size x, several approaches are available. A suitable correlation is given by the equation below (Barnea and Mizrahi, 1973) with parameters given in Table 3.4. For the volume fraction $(1 - \varepsilon)$ in the circulation loop a value around 0.01 may be used.

$$v_{ss} = \left(\frac{-B(L) + \sqrt{B(L)^2 + AC(L)}}{C(L)}\right)^2 \tag{3.14}$$

$$A_{AZ} = \frac{\varphi_{v,circ}}{v_{ss}} \tag{3.15}$$

Crystal size control by fines removal cannot be applied for FC crystallizers, since the suspension within the crystallizer is heavily mixed.

Product classification is often applied with an elutriation leg placed at the bottom of the crystallizer body, which not only removes the largest particles selectively from the crystallizer, but also washes them with fresh feed just before their removal, thereby contributing to a purer product. An elutriation leg can be applied in both FC and DTB crystallizers (see Chapter 10).

3.2.5.5 Suspension criterion

Settling of particles should be avoided everywhere within the crystallization system. In pipes, the superficial flow velocity of the solution v_{sup} must exceed the settling velocity v_{ss} of a swarm of particles. Settling velocities of suspensions of particles can be estimated using the model of Barnea and Mizrahi (1973) given in the previous secion. Mersmann (1995) recommends $v_{sup} > 5v_{ss}$ for flow in vertical pipes, $v_{sup} > 10v_{ss}$ for horizontal pipes and $v_{sup} \approx v_{ss}$ for fluidized beds. For large stirred vessels ($D_{crystallizer}/L_{mean} > 10^3$) the stirrer power input should be at least given by P_{susp}:

$$P_{susp} = 5(1-\varepsilon)v_{ss}g\frac{\rho_{crystal} - \rho_{liquid}}{\rho_{susp}} \tag{3.16}$$

where P_{susp} (W kg^{-1}) is the minimal specific power input to keep the particles in suspension, $(1 - \varepsilon)$ is the particle volumetric fraction, g is the gravitational constant,

$\rho_{crystal}$, ρ_{liquid} and ρ_{susp} are the crystal, liquid and slurry densities, respectively, the latter defined as:

$$\rho_{susp} = \varepsilon \rho_{liquid} + (1 - \varepsilon)\rho_{crystal} \tag{3.17}$$

A criterion for scaling-up to large stirred vessels is a constant stirrer tip speed, i.e.:

$$v_{tip} = \pi N D_{imp} = \text{constant} \tag{3.18}$$

where D_{imp} is the impeller diameter. For small stirred vessels ($D_{crystallizer}/L_{mean} < 500$) it is recommended to keep the same specific power input P_{susp} in each scale (Mersmann, 1995), as in narrow geometries particle settling is enhanced.

3.2.6 Economic evaluation of the design

An optimal design procedure is often based in economic objective functions, typically capital investment and operation costs on the one hand and the economic balance of the input and output streams of the process on the other hand.

Preliminary capital investment costs are primarily based on equipment costs, mainly the crystallizer, the heat exchanger, the fines dissolving system and the vacuum system. Here a simplified method described by Bermingham (2003) is used, in which only the crystallizer is considered. For DTB crystallizers with diameter $D_{crystallizer}$ for the main body, total diameter including the annular zone $D_{DTB\_crystallizer}$ and aspect ratio R_{HD}, the capital costs function ψ_{cap} (k€ year^{-1}) is:

$$\psi_{capital} = \frac{1}{t_{dep}} 20.875 D_{DTB\_crystallizer}^2 - 7.776 D_{DTB\_crystallizer} + 38.25 \tag{3.19}$$

where t_{dep} is the depreciation period for the investment.

The important operational costs are the stirring duty (W_{stir}), the pumping duty related to the recirculation stream (W_{circ}) and the heat or cooling duty. The former two are estimated from:

$$W_{stir} = \frac{P_{susp}\rho_{susp}(\pi R_{HD} D_{crystallizer}^3)}{\eta_{stir}} \tag{3.20}$$

$$W_{circ} = \frac{\varphi_{v,circ}\rho_{suspension}\Delta p}{\eta_{pump}} \tag{3.21}$$

where P_{susp} is the specific power input [W (kg suspension)$^{-1}$], Δp is the pressure drop around the crystallizer circulation pump, η_{stir} and η_{pump} are the efficiencies of the stirrer and circulation pump in converting electrical energy into fluid motion. The heat or cooling duty (Q_{heat}) is calculated from the energy balance within the process and utility costs.

The operational costs and the economic material balance are now written:

$$\psi_{oper} = ((W_{stirrer} + W_{circ}) * C_{elec} + |Q_{heat}|\, C_{HEX})\, H_{an} \tag{3.22}$$

$$\psi_{mb} = \left(P \cdot C_{prod} + \alpha\varphi_{v,prod}\varepsilon\rho_{liquid}C_{ml} - \varphi_{v,feed}\rho_{feed}C_{feed}\right) H_{an} \tag{3.23}$$

Table 3.5 Design specifications and material properties for the design of a continuous evaporative crystallizer

Design Level	Specifications
Design Level 0	$\varepsilon_{feed} = 1$, $T_{feed} = 50$ °C, $\rho_{feed,liquid} = \rho_{liquid}$ $w_{feed,1} = 0.425$ kg (kg solution)$^{-1}$ (saturated solution at T_{feed}) $P = 1$ (kg solid) s^{-1}, good filterability
Design Level 1	$L_{43} = 900$ μm
Design Level 2	Evaporative crystallization, $T = 50$ °C, $P = 0.102$ bar
Design Level 3	$1 - \varepsilon = 20\%$ $\Delta T_{circ} = 5$ °C $\varphi_{v,\,feed} = 0.0042$, $\varphi_{v,prod} = 0.008$, $\varphi_{v,vapor} = 14.8$ m^3 s^{-1} Yield = 0.45 (kg component 1 in product) (kg component 1 in feed)$^{-1}$ $Q = 2686$ kW, $Q/P = 2686$ kJ (kg particulate product)$^{-1}$ $D_{diameter} = 1.9$, $D_{crystallizer} = 2.5$ m, $V_{crystallizer} = 18.7$ m^3 $\varphi_{v,min\ circ\ flow}/\varphi_{v,\,feed} = 35$ Profit = 1106, Material balance = 1360, Capital costs = 60, Operational costs = 195 k€ year^{-1} Profit per kg product = 2.3 € kg^{-1}
Material properties	$\rho_{liquid} = 1248$, $\rho_{crystal} = 1767$, $\rho_{vapor} = 0.102$ kg m^{-3} $c_{p,liquid} = 2.79$, $c_{p,crystal} = 2.4$, $c_{p,vapor} = 4.2$ kJ kg^{-1} °C^{-1} $\Delta H_{cr} = 0$ kJ kg^{-1} $w_{liquid,1,eq}$ vs. T, see eq. 4.26 [kg kg^{-1} solution]

where H_{an} is the number of operation hours per year and C_{elec} and C_{HEX} are electricity cost and the energy cost for cooling or the heating duty [€ J^{-1}], respectively. In addition, C_{prod}, C_{ml} and C_{feed} are the economic value of the dry product, the mother liquor and the feed stream, respectively [€ kg^{-1}]. The economic evaluation of the design is completed by calculating the profit ψ_{profit} [€ year^{-1}]:

$$\psi_{profit} = \psi_{mb} - \psi_{capital} - \psi_{oper} \tag{3.24}$$

The variable ψ_{profit} is the overall objective function that is to be maximized.

3.3 Worked examples

3.3.1 A continuous evaporative crystallizer

Consider a Design Level 0 specification consisting of a production rate of 1 kg s^{-1} of an easily filterable particulate solid from a pure saturated aqueous solution. Starting with these original specifications, the design team defines new specifications hierarchically following Design Levels I through IV, as summarized in Table 3.5. The table also gives the physical properties of interest either collected from literature or determined experimentally in the early stages of the procedure.

At Design Level I a mean particle size of 900 μm is specified to deliver the desired filterability. Since the feed is a pure solution, it is not necessary to specify the crystal

purity. At Design Level II the solubility of the crystallizing compound $w_{liquid,1,eq}$ as a function of temperature is considered:

$$w_{liquid,1,eq} = k_0 + k_1 T + k_2 T^2 \tag{3.25}$$

with k_0, k_1 and k_2 equal to 0.3, 0.002439 and 10^{-5}, respectively. The compound is highly soluble (solubility $> \sim 10$ wt%), but the slope of the solubility curve is somewhat lower than 0.005 $°C^{-1}$, so evaporative crystallization is specified. A single crystallization step is chosen, as impurity is not an issue.

A high temperature is usually desirable. For evaporative crystallization, a high temperature is also advantageous because it maximizes the solubility and consequently minimizes the energy consumption (assuming the feed may be supplied close to saturation). However, in the present case the energy source for evaporation is a low-temperature waste stream, so a crystallization temperature of 50 °C is chosen. Because evaporation usually takes place in a boiling solution, low crystallization temperatures imply low pressures. The boiling pressure of the solution at 50 °C is 0.102 bar. A disadvantage of this low pressure is that the volumetric flow rate of the vapor is high, resulting in a large crystallizer diameter.

At Design Level III, continuous operation is chosen, as it is the only option for evaporative crystallization. For simplicity, a single effect crystallizer without a bleed stream ($\kappa = 0$) is considered. The residence time τ of the suspension in the crystallizer is determined from an estimated crystal growth rate G and the specified mean particle size according to equation 3.2.

The mass and energy balances (Section 3.2.4.6) are solved with $N_{comp} = 2$. The volume fraction of particles $(1 - \varepsilon)$ in the crystallizer is specified as 20% and the solution concentration $w_{liquid,1}$ within the crystallizer is chosen to be equal to the solubility at the crystallizer temperature. The resulting yield (in kg of the main compound in the product per kg in the feed) is 45 wt%. In practice, higher yields are possible by recirculating the spent solution to the crystallizer. As expected, the heat duty per unit of evaporated water is 1985 kW kg^{-1}, a value close to the latent heat of the water. Since the heat duty is directly related to the amount of water in the feed, a low heat duty results for highly soluble compounds. In practice the heat duty is further reduced by a factor of five with multiple stage crystallizers and other energy-saving measures.

The designer may now proceed to Design Level IV. A DT crystallizer is chosen because of its wide applicability (see Chapter 10). Given the residence time, the crystallizer is found to be 1.9 m in diameter and 18.7 m^3 in volume. The minimal diameter to prevent entrainment of solvent droplets in the vapor flow is, however, 2.5 m, which would result in a residence time longer than needed. One solution to this problem is to build a crystallizer with a smaller height to diameter ratio. Another possibility is to increase the process temperature to get a higher density of vapor flow.

From an estimated value of 5 °C for the temperature elevation of the circulating suspension across the heater (ΔT_{circ}), the circulation flow is determined from the energy balance in the heater. The value found is 35 times the inlet flow. An even higher circulation flow would be required if more conservative (smaller) ΔT_{circ} values were chosen. A profit of 2.3 € kg^{-1} of product is found. It is interesting to see how profit,

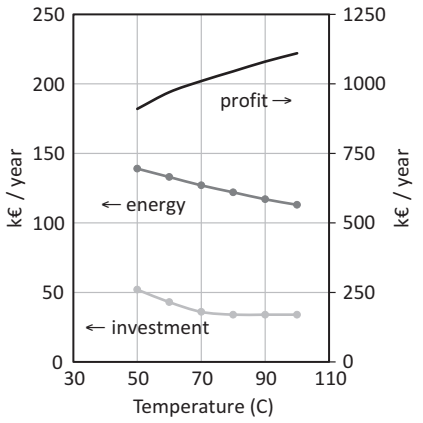

Figure 3.5 Profit (right axis), investment and energy costs (left axis) as functions of the operation temperature.

investment and operation costs vary with the design choices, as exemplified in Figure 3.5 for varying crystallization temperature.

The procedure just presented can also be applied to design a cooling crystallizer and a flash cooling crystallizer.

3.3.2 A continuous cooling crystallizer

The Level 0 specifications are as in the previous example, but the impurity level in the crystals should not exceed 5×10^{-4} kg kg^{-1}. In addition, the feed is available as a saturated solution at 90 °C and an impurity content of 0.025 kg (kg solution)$^{-1}$. The process variables and the product and process design specifications established in Design Levels 0 to IV are summarized in Table 3.6.

Although the slope of the solubility line is not very steep, spent mother liquor recovery is known to be possible elsewhere within the process, so cooling crystallization is considered. The process temperature range is set by the feed temperature. The operating pressure for cooling processes is atmospheric.

A continuous process is chosen because of the high capacity. In the continuous cooling method, a warm feed stream with a relatively high solute concentration is added to a crystallizer at a lower temperature. The difference in solubility at the feed and the process temperature drives the crystallization process. The residence time is determined from the particle size and growth rate as in the previous example.

For cooling crystallization, the mass and energy balances given in Table 3.2 are applied, neglecting the transient and the vapor terms. The mother liquor cannot be recycled into the crystallizer, so the bleed stream is also omitted ($\kappa = 0$). A relative supersaturation of 0.01 is assumed, which means that $w_{liquid,1} = 1.01 * w_{eq}$. A volume fraction of particles (ε) of 0.12 is chosen, resulting in a process temperature of 53 °C and a yield (in kg of the main compound in the product per kg in the feed) of 31%. Better

Table 3.6 Design specifications and material properties for the crystallizer design of a continuous cooling crystallizer

Design Level	Specifications
Design Level 0	$\varepsilon_{feed} = 1$, $T_{feed} = 90$ °C, $\rho_{feed,liquid} = \rho_{liquid}$ $w_{feed,1} = 0.528$ kg (kg solution)$^{-1}$ (saturated solution at T_{feed}) $w_{feed,2} = 0.025$ (kg impurity) (kg solution)$^{-1}$ $P = 1$ (kg solid) s^{-1}, good filterability
Design Level 1	$L_{43} = 900$ µm, $w_{liquid,2} = 0.0005$ (kg impurity) (kg solution)$^{-1}$
Design Level 2	Cooling crystallization, $P = 1$ bar
Design Level 3	$1 - \varepsilon = 12\%$, $\varphi''_{hex,max} = 0.5$ kW m^{-2} $\varphi_{v,\,feed} = 0.0049$, $\varphi_{v,prod} = 0.0047$ m^3 s^{-1}, $T = 53$ °C Yield = 0.31 (kg component 1 in product) (kg component 1 in feed)$^{-1}$ $w_{crystal,2} = 0.000059$ (kg impurity) (kg crystal product)$^{-1}$ $Q = 235$ kW, $Q/P = 2686$ kJ kg^{-1} $D_{diameter} = 2.4$, $V_{crystallizer} = 21.3$ m^3, $A_{hex} = 471$ m^2
Material properties	see Table 3.5; $k_{distr,i} = 0.001$

yields can be obtained if larger feed temperatures or lower crystallizer temperatures are acceptable. Note that the designer is not free to choose the crystallizer temperature, as it is connected to the yield and solids content. A heat duty of 235 kW is calculated, about one-tenth of the value needed in the evaporative process. The heat exchanger area is, however, quite large due to the low permitted heat flux. The crystallizer volume is 21.3 m^3.

A crystal impurity content of 2.9×10^{-5} kg (kg crystal)$^{-1}$ is estimated from an experimental value for the distribution coefficient $k_{distr,i}$ and the mass balance for the impurity. The product specification is easily met because of the large liquid flow leaving the crystallizer.

3.4 A brief summary of the chapter

A procedure for the basic design of industrial crystallization systems has been presented. It may be used for cooling and evaporative crystallization processes, both in continuous and batch modes. It can also be adapted for melt crystallization from suspensions. The procedure may be applied even for systems for which little experimental information is available. The hierarchical architecture of the procedure limits the number of aspects considered in each design stage, greatly simplifying the design task and leading to good quality, reproducible designs.

The design procedure yields the production capacity, the average particle size and the purity of the particulate product. If additional product specifications are to be met, such as particle size distribution and shape, a more detailed design procedure is needed, based on mathematical modeling of crystallizer compartments. Such a detailed procedure is beyond the scope of this book.

3.5 End of chapter problems

Problem 1

A new industrial unit is to be built for the production of the ammonium nitrate fertilizer for use in small communities. The fertilizer is to be applied manually. Absorption by the plants has to occur slowly upon leaching due to rain. What product characteristics should be included in this product specification (Design Level I)?

Problem 2

Potassium chloride is recovered by solution mining as a solution containing 50 g salt per 100 g water. In order to recover this salt in solid form, you are asked to select: (a) the solvent; (b) the crystallization method; (c) the crystallization temperature and pressure. Repeat the problem for recovery of anhydrous sodium sulfate from a 40 g per 100 g water solution.

Problem 3

In the example above, a capacity of 50000 (kg salt) day^{-1} of the KCl commodity is desired. Would you apply continuous or batch operation? Is it necessary to apply some method of energy conservation? Estimate the yield and the specific energy consumption. Specify the crystallizer residence time. Find the crystallizer diameter and the heat exchanger area.

Problem 4

The NaCl feed stream to a continuous crystallizer (consider the flow-sheet in Figure 3.3) contains 10 mg L^{-1} Mg as an impurity. In order to obtain a solid product impurity of 0.0002 g Mg per g crystal, what is the allowable purge flow in kg purge per kg feed solution? Assume a Mg distribution coefficient of $k_{distr,Mg} = 0.005$ (see definition in Table 3.2).

3.6 References

Barnea, E. and Mizrahi, J. 1973. A generalized approach to the fluid dynamics of particulate systems: Part 1. General correlation for fluidization and sedimentation in solid multiparticle systems. *Chemical Engineering Journal*, **5**(2), 171.

Bennett, R. C. 1993. Crystallizer selection and design. In *Handbook of Industrial Crystallization*, Myerson, A. S. (ed.) Butterworth Heinemann, 103–130.

Bermingham, S. K., Neumann, A. M., Kramer, H. J. M. *et al.* 2000. A design procedure and predictive models for solution crystallization processes. *AIChE Symposium Series*, **96**(323), 250.

Bermingham, S. K. 2003. *A Design Procedure and Predictive Models for Solution Crystallization Processes*, PhD thesis, Delft University of Technology.

Bird, R. B., Steward, W. E. and Lightfoot, E. N. 1960. *Transport Phenomena*, J. Wiley & Son.

Cisternas, L. A., Vasquez, C. M. and Swaney, R. E. 2006. On the design of crystallization-based separation processes: review and extension. *AlChE Journal*, **52**, 1754.

Douglas, J. M. 1985. A hierarchical decision procedure for process synthesis. *AlChE Journal*, **31**, 9.

Grosch, R., Monnigmann, M. and Marquardt, W. 2008. Integrated design and control for robust performance: application to an MSMPR crystallizer. *Journal of Process Control*, **18**, 173.

Kramer, H. J. M., Bermingham, S. K. and Van Rosmalen, G. M. 1999. Design of industrial crystallizers for a required product quality. *Journal of Crystal Growth*, **198**/199, 729.

Lin, S. W., Ng, K. M. and Wibowo, C. 2007. Integrative approach for polymorphic crystallization process synthesis. *Industrial and Engineering Chemistry Research*, **46**, 518.

Lin, S. W., Ng, K. M. and Wibowo, C. 2008. Synthesis of crystallization processes for systems involving solid solutions. *Computers and Chemical Engineering*, **32**, 956.

Mullin, J. W. 1993. *Crystallization*, Butterworth Heinemann.

Mersmann, A. 1995. *Crystallization Technology Handbook*, Marcel Dekker, Inc.

Mersmann, A. and Kind, M. 1988. Chemical engineering aspects of precipitation from solution. *Chemical Engineering Technology*, **11**, 264.

Nyvlt, J. 1992. *Design of crystallizers*, CRC Press.

Seckler, M. M., Giulietti, M., Bernardo, A. *et al.* 2013. Salt crystallization on a 1 m^3 scale: from hierarchical design to pilot plant operation. *Industrial and Engineering Chemistry Research*, **52**(1), 4161–4167.

Sinnott, R. K. 1998. An introduction to chemical engineering design. In *Chemical Engineering, Volume 6*, J. M. Coulson and J. F Richardson (Eds.), Pergamon Press.

Souders, M. and Brown, G. G. 1934. Design of fractionating columns. I. Entrainment and capacity. *Industrial and Engineering Chemistry*, **26**(1), 98–103.

Wibowo, C., Chang, W. C. and Ng, K. M. 2001. Design of integrated crystallization systems. *AlChE Journal*, **47**, 2474.

4 Nucleation

4.1 Why this chapter is important

To create a population of crystals from a liquid, either a solution or a melt, supersaturation has to be induced by increasing the concentration of the solute, by decreasing of the temperature or increasing of the pressure of the liquid with respect to the equilibrium value. In a continuous crystallization process the supersaturation is sustained, while in batch crystallization the supersaturation is consumed in time. If the initial fluid is a clear liquid the formation of crystals begins with a nucleation process called "primary nucleation." The type of nuclei and their rate of formation affect the size distribution of the crystal population, its polymorphic form and other properties of the crystals, so control of the nucleation process is crucial in obtaining the required product specifications. If new phase formation takes place by statistical fluctuations of solute entities clustering together in the solution or of molecules in the melt, it is called "homogeneous primary nucleation." If, however, new phase formation is facilitated by the presence of tiny, mostly invisible particles such as dust or dirt particles, on which nucleation preferentially starts, it is called "heterogeneous primary nucleation."

If, conversely, the supersaturated liquid already contains one or more crystals of the material being crystallized, these so-called parent crystals are able to breed nuclei sometimes after further outgrowth to sufficiently large sizes. This type of nucleation is called "secondary nucleation" because of the prior presence of crystals. It is the only nucleation mechanism in cooling or evaporative crystallization once crystals are present. The crystals present generally consume the supersaturation to values that are too low to induce primary nucleation, but still allow secondary nuclei to grow in the crystal population.

In batch crystallization from a clear liquid the process can either be started by primary nucleation or by the addition of seed crystals to the supersaturated liquid. The role and impact of the addition of seed crystals will be further addressed in Chapter 8.

4.2 Primary nucleation

4.2.1 Homogeneous primary nucleation

We first discuss the thermodynamic and kinetic aspects of classical nucleation theory, which still forms the framework for the understanding of the majority of nucleation

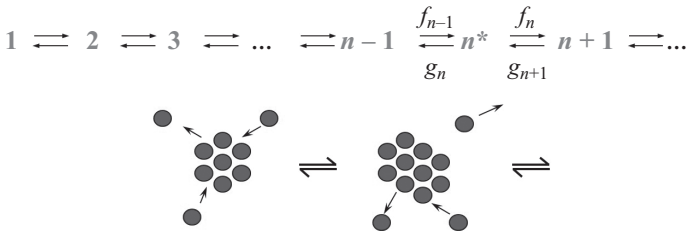

Figure 4.1 Change in cluster size by the attachment or detachment of single entities.

phenomena (Gibbs, 1875–1876, 1877–1878, Volmer, 1939). Crystallization is a first-order phase transition along two order parameters, concentration and structure. When a crystal nucleates from the melt, mainly structure fluctuations are needed, while nucleation from dilute solutions requires both density and structure fluctuations. In the classical approach these changes are assumed to proceed simultaneously. We will focus here on nucleation from solution, and leave details of nucleation from the melt to Chapter 12.

Although in a non-crystallizing solution the mean concentration of the solute remains constant, local fluctuations in concentration give rise to the formation of numerous clusters, which can fall apart as well – it is a reversible process. In the classical theory of nucleation these clusters are formed by the attachment and detachment of single solute entities (growth units or molecules) as is schematically presented in Figure 4.1. In principle, clusters can grow by the collision of clusters that contain more than one entity, but the concentration of such clusters is always much lower than that of a single entity.

In undersaturated or just saturated solutions the system of cluster formation and cluster decay is in equilibrium and the solution is stable against new phase formation. In supersaturated solutions, however, clusters of a critical size are formed that either fall apart or become nuclei that grow further.

Below, the nucleus size, the nucleation work W^* (or free energy barrier to nucleation) and the nucleation rate will be derived.

4.2.1.1 Nucleus size

There will be competition between two opposing terms constituting the Gibbs free energy of a nucleus: each solute entity that is added to a cluster will on the one hand reduce its free energy by an amount $\Delta\mu$ (which is taken here as the chemical potential difference per solute molecule instead of per mole solute in the fluid and in the solid), while on the other hand the surface increment of the cluster surface leads to a positive contribution of free energy. Both terms obviously depend on the number of solute entities n building up the cluster, and thus also on the size of the cluster:

$$\begin{aligned} \Delta G &= \Delta G_{volume} + \Delta G_{surface} \\ \Delta G &= -\frac{k_v L^3}{V_m}\Delta\mu + k_a L^2 \gamma \end{aligned} \tag{4.1}$$

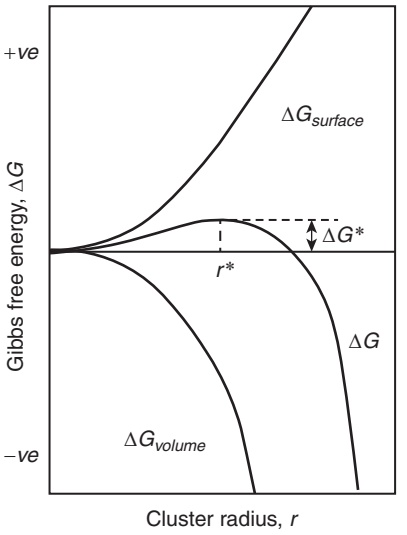

Figure 4.2 The Gibbs free energy ΔG as a function of the radius r of the cluster.

where L = size of the cluster and k_a and k_v are surface and volume shape factors

γ = interfacial free energy [J m^{-2}]
V_m = molecular volume = $M/(\rho_c N_A)$ [m^3 molecule^{-1}]
and N_A = Avogadro's number

Since such small clusters are often approximated by spheres, equation 4.1 becomes:

$$\Delta G = -\frac{4\pi r^3}{3V_m}\Delta\mu + 4\pi r^2\gamma \tag{4.2}$$

with r = radius of the cluster [m].

The Gibbs free energy shows a maximum at a certain critical cluster size, the size of the nucleus (see Figure 4.2). Each cluster below this nucleus size will eventually decay, and beyond this size all nuclei will grow out since ΔG only decreases upon attachment of new entities.

This critical cluster radius r^* can be found by minimizing the free energy (equation 4.2).

$$\frac{\mathrm{d}(\Delta G)}{\mathrm{d}r} = -\frac{4\pi r^2}{V_m}\Delta\mu + 8\pi r\gamma = 0 \tag{4.3}$$

This gives

$$r^* = \frac{2\gamma V_m}{\Delta\mu} \tag{4.4}$$

and the number of solute entities in one cluster n^* given by:

$$n^* = \frac{4}{3}\frac{\pi r^{*3}}{V_m} \tag{4.5}$$

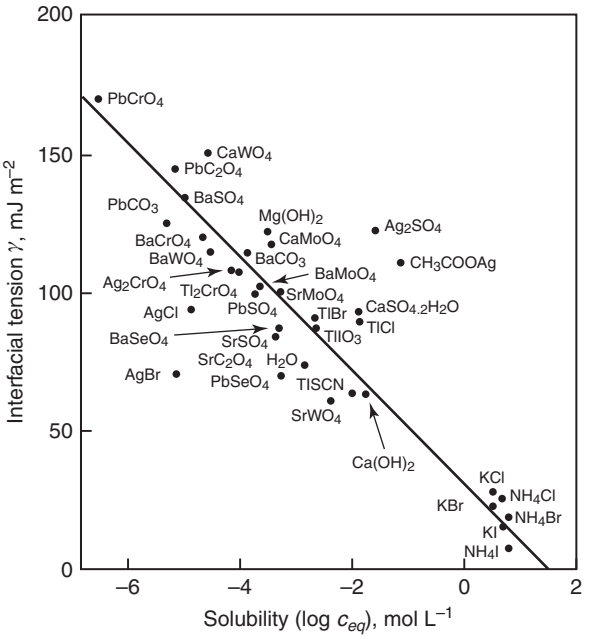

Figure 4.3 Interfacial tension as a function of solubility (Nielsen and Söhnel, 1971).

This gives:

$$n^* = \left(\frac{2a\gamma}{3\Delta\mu}\right)^3 \tag{4.6}$$

where $a =$ surface area of a solute entity in the cluster surface [m^2]. The corresponding critical Gibbs free energy is then:

$$\Delta G^* = \frac{1}{3} 4\pi r^{*2}\gamma \tag{4.7}$$

$$\Delta G^* = \frac{16\pi\gamma^3 V_m^2}{3\Delta\mu^2} \tag{4.8}$$

or for $\Delta\mu = kT\ln S$ (where S is the supersaturation ratio; see Chapter 1):

$$\Delta G^* = \frac{16\pi\gamma^3 V_m^2}{3k^2T^2(\ln S)^2} \tag{4.9}$$

Note the kT, because $\Delta\mu$ is related to one solute entity or molecule.

If the supersaturation is known, then it is recommended that n^* is calculated, in order to estimate whether primary nucleation could take place ($n^* < 10$) or if its occurrence is unrealistic ($n^* > 200$). To do so, γ has to be known. If the γ value of a cluster is assumed to be about the same as that of a crystal, which is quite unlikely, its value can be estimated from an interfacial tension, γ, versus solubility, c_{eq}, plot after Nielsen and Söhnel (1971) and shown in Figure 4.3, but it can equally well be calculated from the

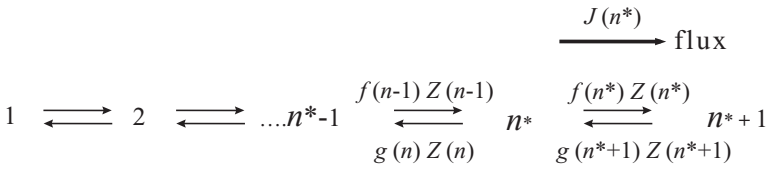

Figure 4.4 The net flux $J(n^*)$ is the net change in number concentration resulting from the attachment and detachment of entities.

solubility using an expression derived by Mersmann (2001):

$$\gamma = \beta \frac{kT}{V_m^{2/3}} \ln\left(\frac{\rho_c}{M c_{eq}}\right) \tag{4.10}$$

where c_{eq} = equilibrium concentration, and $\beta = 0.414$ for cubic clusters is used.

So it can be concluded that both the nucleus size n^* and the nucleation work ΔG^* are supersaturation dependent and their values can be calculated by using an estimated interfacial energy of the nucleus. Since the nucleation rate is determined by the number of nuclei that come across the nucleation barrier, an Arrhenius-type expression can be expected with ΔG^* in the exponential term.

4.2.1.2 Nucleation rate

The nucleation rate $J(t)$ is defined as the change in number of supercritical clusters, N, within a certain time lapse in a certain volume V [# m^{-3} s^{-1}]:

$$J(t) = \frac{1}{V}\frac{dN}{dt} \tag{4.11}$$

Supercritical clusters have sizes between n^* and the maximal size M, and N is thus given by:

$$N = V \int_{n^*}^{M} Z(n, t)\, dn \tag{4.12}$$

where $Z(n, t)$ = number concentration of clusters with n solute entities.

Under stationary conditions, when the driving force $\Delta\mu$ is constant, J equals the net flux through the nucleus size, as indicated in Figure 4.4.

In this figure, $Z(n)$ is the stationary number concentration of clusters containing n solute entities, and $f(n)$ and $g(n)$ are the frequencies of attachment and detachment of entities to a cluster of size n. These frequencies (= number fluxes or number of impingements per time unit on a cluster surface [# s^{-1}]) can also be seen as flux densities times the surface of the cluster. By correlating the $Z(n)$ values to the equilibrium $C(n)$ values the nucleation rate J can be derived from equations 4.11 and 4.12 after some simplifications (see Kashchiev, 2000):

$$J = z f(n^*) C(n^*) \tag{4.13}$$

with the Zel'dovich factor:

$$z = \left(\frac{\Delta G^*}{3\pi kTn^{*2}} \right)^{1/2} \tag{4.14}$$

The Zel'dovich factor is the probability of a cluster at the critical nucleus size becoming a stable cluster. The factor z is virtually a constant with a value between 0.01 and 1.

The attachment frequency (incoming flux times cluster surface) can either be controlled by volume diffusion of the entities towards the cluster surface or by interface transfer, where in both cases a sticking factor of 1 is assumed. Further

$$f(n^*) = f_o(n^*)S \tag{4.15}$$

and

$$C(n^*) = C_o \exp\left[-\frac{\Delta G^*}{kT} \right] \tag{4.16}$$

where $f_o(n^*)$ is the equilibrium frequency, and C_o is the concentration of nucleation sites in solution, so $C_o = 1/V_m$.

Combining these equations leads to:

$$J = AS \exp\left[-\frac{\Delta G^*}{kT} \right] \quad \text{or} \quad J = AS \exp\left[-\frac{16\pi\gamma^3 V_m^2}{3k^3T^3(\ln S)^2} \right] \tag{4.17}$$

with

$$A = C_o f_o(n^*)z \tag{4.18}$$

Here the approximately or strictly S-independent kinetic factor A is given by:

$$A = \sqrt{\frac{kT}{\gamma}} \frac{Dc_{eq}N_A}{V_m} \ln S \tag{4.19}$$

for volume diffusion control and

$$A = 2\sqrt{\frac{\gamma}{kT}} \frac{Dc_{eq}N_A}{2r} \tag{4.20}$$

for surface integration control, where D [$m^2\ s^{-1}$] is the diffusion coefficient of the single entity, and r the radius [m].

From equation 4.17 the classical nucleation rate can be calculated and compared with measured values. It is an Arrhenius type of expression, where changes in S in the pre-exponential factor AS are expected to be of minor influence compared to changes in S in the exponential factor. For this reason S in the pre-exponential factor is often put equal to 1. A value for A of 10^{30} nuclei per $m^3\ s^{-1}$ is often attained, plus or minus a few orders of magnitude.

For cooling crystallization of some melts and of viscous solutions, as in the case of citric acid, abnormal nucleation characteristics have been observed. At higher undercooling the liquid becomes more viscous and the nucleation rate decreases after reaching a maximum value.

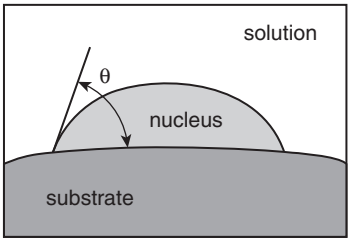

Figure 4.5 Nucleation on a foreign substrate (Kashchiev, 2000).

4.2.2 Heterogeneous primary nucleation

The occurrence of homogeneous nucleation in practice is rare because very clean solutions are required to avoid the presence of any dust particles. So in practice mostly heterogeneous nucleation takes place, i.e. nucleation facilitated by the presence of an interface different from that of the solute, unless very high supersaturations are reached, as will be shown below. The "wetting" of the foreign substrate by the nucleus is reflected by the wetting angle θ (see Figure 4.5). This angle indicates whether the presence of the substrate will substantially lower the nucleation barrier.

$$\Delta G^*_{hetero} = \varphi \Delta G^*_{homo} \tag{4.21}$$

with $0 \leq \varphi \leq 1$.

For complete wetting ($\theta = 0°$) $\varphi = 0$ and for $\theta = 90°$ the value of $\varphi = 0.5$. The value $\varphi = 0$ happens in the case of nucleation on a substrate identical to the nucleus. Mostly a two-dimensional nucleus is formed and the increase in interfacial energy is caused by the creation of the side area of the 2-D nucleus, as will be treated in Chapter 6 for the 2-D crystal growth model.

By replacing $\varphi\gamma^3$ in equation 4.17 by γ_{eff}^3 the following expression is obtained:

$$J_{hetero} = A_{hetero} S \exp\left[-\frac{16\pi \gamma_{eff}^3 V_m^2}{3k^3 T^3 (\ln S)^2}\right] \tag{4.22}$$

with

$$A_{hetero} = C_{o,het} f_o(n^*) z \tag{4.23}$$

The constant A_{hetero} is theoretically much lower than A, since the concentration of active sites C_o is much lower (e.g. values of 10^{19} have been fitted), and also $f_o(n^*)$ is lower for a nucleus on a substrate. For z, similar values are assumed as for homogeneous nucleation.

Hence two opposite effects play a role in heterogeneous nucleation. The overall effect depends on the supersaturation. At lower supersaturations, the effect of the exponential term dominates, $J_{hetero} > J_{homo}$ and A_{hetero} values of 10^{10} to 10^{20} have been found.

At much higher supersaturations that are seldom met in practice (only in the case of precipitation) the kinetic pre-exponential term takes over and $J_{hetero} < J_{homo}$ (see Figure 4.6).

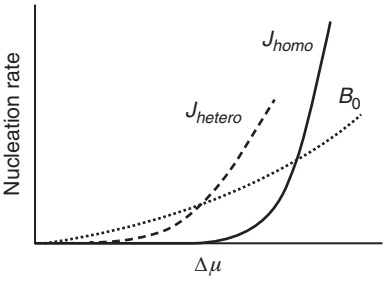

Figure 4.6 Nucleation rate as a function of the supersaturation ($\Delta\mu$). J_{homo} and J_{hetero} = homogeneous and heterogeneous nucleation rates respectively, B_o = secondary nucleation rate.

Since the value for γ_{eff} is mostly lacking, calculation of J_{hetero} is rarely feasible. Only rough estimates can be made by assuming γ_{eff} values that are half or one third of the γ_{homo} value.

4.3 Nucleation theorem

Below a few methods will be given to actually measure the nucleation rate at various supersaturations. From these functions the nucleation work W^* can be calculated. The nucleus is generally too small to be directly measured, but can be calculated from the nucleation work by applying the nucleation theorem. The power of the nucleation theorem is that it relates the nucleation work, the nucleus size and the supersaturation without any *a priori* knowledge about the nucleation model (Kaschiev, 2000). The theorem is equally valid for the classical homogeneous and heterogeneous nucleation model as for the non-classical two-step nucleation model that will be elucidated below.

As follows from equations 4.5 to 4.8:

$$\frac{dW^*}{d\Delta\mu} = -n^* \quad \text{or} \quad \frac{dW^*}{d\ln S} = -n^* kT \tag{4.24}$$

4.3.1 Induction time and metastable zone

The potential to realize thermodynamically metastable states is a characteristic feature of first-order phase transitions. Upon supersaturating a solution of a given temperature, a certain induction time t_i may elapse before a detectable amount of the new solid phase is formed. This time is a measure of the "ability" of the system to remain in metastable equilibrium and can therefore be used to determine the metastability limit.

This limit represents the critical or maximum supersaturation below which the solution of the specific compound can stay long enough (the preset induction period) without losing its metastability. The zone between the solubility line and the metastable limits at the corresponding temperatures is called the metastable zone. This zone is in fact only an effective metastable zone, where the induction time and the detection

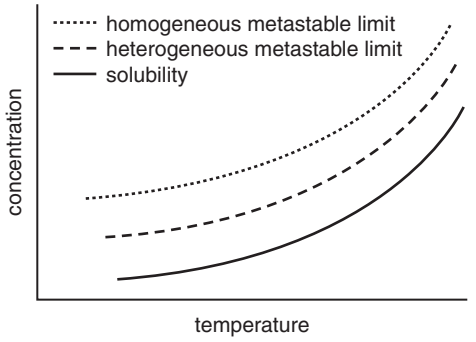

Figure 4.7 Metastable limits for homogeneous and heterogeneous nucleation as a function of temperature.

limit are respectively a freely chosen value and a value determined by the selected detection technique. The here-defined effective metastable zone is therefore not related to a thermodynamic property.

A precise thermodynamic definition of the metastability limits is the locus of points, referred to as the spinodal, where:

$$\left.\frac{\partial G}{\partial c^2}\right|_{T,P} = 0 \tag{4.25}$$

Beyond these points, spinodal decomposition occurs, and there is a spontaneous phase transformation without the need for nucleation. The effective metastable zone for most solutions does not even come close to the spinodal. Sometimes the term kinetic spinodal is also used for the supersaturation where the nucleus size becomes one entity and spontaneous nucleation occurs.

The effective metastable zone is often used as a criterion in the design of a crystallization process. The supersaturation in the crystallizer should not exceed the value dictated by the metastable zone for either homogeneous or heterogeneous nucleation. The zone for heterogeneous nucleation is of course smaller than that for homogeneous nucleation; see Figure 4.7. The preset induction time used for the measurement of the metastable zone should by far exceed the residence time of the solution in the crystallizer. Unfortunately this reasoning only holds for well-mixed crystallizers, whereas for many industrial crystallizers much higher supersaturation values occur locally.

A more important reason to measure induction times is, however, to calculate or at least estimate nucleation rates. For systems that lose their meta-stability just at the moment when the first nucleus is formed, the induction time t_i is given by:

$$t_i = \frac{1}{JV} \tag{4.26}$$

This is only the case for extremely high growth rates of the nucleus once it is born and grows to a detectable size, or for extremely small liquid volumes V, where only one nucleus is formed and detected.

A more generally applicable approach allows more nuclei to develop while the first nuclei grow to macroscopic sizes, and to a detectable macroscopic volume V_{macr}.

The induction time t_i then equals:

$$t_i = \left[\frac{\alpha}{k_v J G^3}\right]^{1/4} \tag{4.27}$$

where

$$\alpha = \frac{V_{macr}}{V} \tag{4.28}$$

and k_v = shape factor, which is $\pi/3$ for spheres, and G is the growth rate at the prevailing supersaturation. The nucleation rate J can then be calculated from the induction time t_i at the prevailing supersaturation if G is known or can be estimated from separate growth experiments and if V_{macr} can be estimated for the detection technique.

Subsequently $\ln J/S$ can be plotted versus $\ln^{-2} S$, according to equations 4.17 or 4.22, and fitted by a straight line. The intercept of the fitted line gives the value of A in the equations and the slope gives the value of $16\pi\gamma^3 V_m^2/3k^2T^2$ for either homogeneous or heterogeneous nucleation. So from the slope the interfacial energy and the nucleation work W^* can also be derived, as well as the number of entities in the nucleus n^*. Direct measurement of J by a counting technique is, however, in most cases more accurate than its indirect calculation via measurement of the induction time.

4.3.2 Measurement of nucleation rate

The most applied methods to measure the nucleation rate happen at constant supersaturation: (i) by measuring the number of nuclei N as a function of time, (ii) by measuring the induction time t_i or (iii) by measuring the nucleation probability. Determination of the nucleation rate by *measuring of the induction time* has been treated above. The two other techniques are given below.

4.3.2.1 Measuring of the number of nuclei *N* as a function of time

The number of crystals developed over time by the generation of new nuclei that grow out at constant supersaturation in a vessel of volume V is given by:

$$N(t) = JVt \tag{4.29}$$

$N(t)$ can be measured by a particle counting technique and the slope of the plot of $N(t)$ versus t gives the value of $J(S)$ for a known V value.

In the case of precipitation by mixing of two feed streams, A and B, in a T-mixer, the length of the outlet pipe of the T-mixer determines the reaction time t before the mixture enters a vessel where the supersaturation is kept low enough to prevent further nucleation. The outgrown particles are counted, and if vigorous stirring prevents agglomeration again, $N(t)$ can be measured and J can be calculated (Roelands *et al.*, 2006).

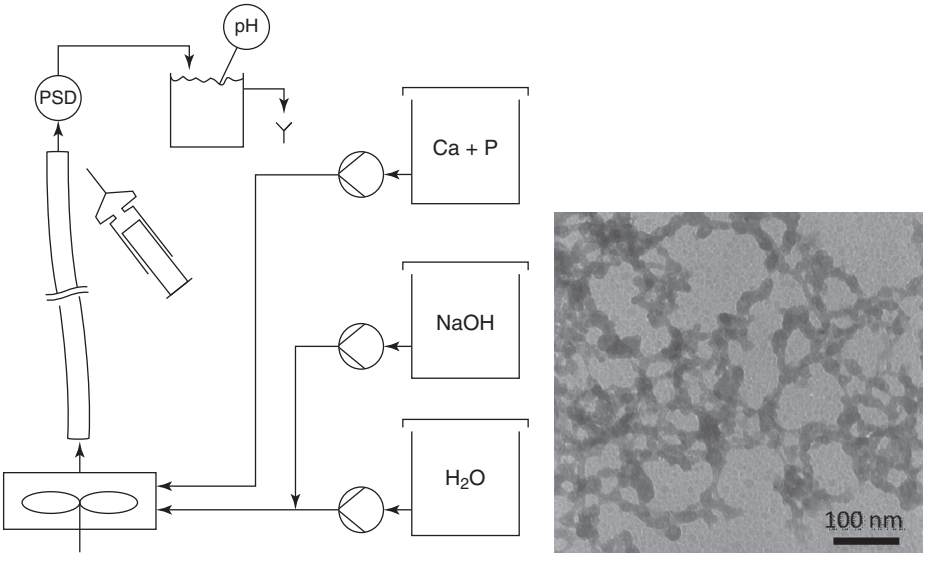

Figure 4.8 Experimental setup for measuring the nucleation rate of amorphous calcium phosphate (left). TEM views of the nanoparticles formed (right). The particles are the dark areas.

4.3.2.2 Measuring the nucleation probability

Two types of measurements are done to determine the probability of nucleation as a fraction of samples with nucleation. In the first type of experiment a large number of small volumes is exposed simultaneously to a constant supersaturation for increasing periods of time t ($t = t_{pulse}$). These small volumes are, for example, wells in a plate that can be examined together under a microscope and the fraction of wells with nucleation counted (Galkin and Vekilov, 1999). Another option is to use microfluidic volumes instead of wells (Selimović *et al*., 2009).

In the second type of experiment a solution of a few ml is exposed to a constant supersaturation for increasing periods of time t, and each experiment for a given time period is repeated many times. The fraction of experiments with nucleation occurring is then registered (Jang and ter Horst, 2008).

Subsequently the probability $P(t)$ is plotted as a function of time for a specific constant supersaturation and fitted with the probability function:

$$P(t) = 1 - \mathrm{e}^{-JV(t-t_o)} \tag{4.30}$$

From this fit J can be derived and through J, other parameters.

Worked example 1

Amorphous calcium phosphate ($Ca_3(PO_4)_2$) continuously precipitates in a tubular reactor after mixing calcium- and phosphate-containing solutions in stoichiometric ratio at alkaline pH. The suspension collected at the reactor outlet is immediately filtered; the solute concentration is determined and the particles are photographed (see Figure 4.8).

(1) Estimate the nucleation rate. (2) Was the nucleation homogeneous or heterogeneous? (3) What is the supersaturation ratio (S) at the reactor inlet? (4) Estimate the interfacial tension γ for the calcium phosphate in solution from the following simplified expression $J = 10^{30} \exp(-101610\gamma^3/S^2)$ # m^{-3} s^{-1}; does γ fit the Nielsen and Söhnel correlation? (5) Suggest three ways of increasing the nucleation rate. Given: residence time $\tau = 0.5$ s; solution concentration at the tube inlet and outlet: $c_i = 0.0016$ and $c_o = 0.0008$ kmol m^{-3}; solid density $\rho = 3140$ kg m^{-3}; solid molecular weight $M_w = 310$ kg $kmol^{-1}$.

Solution to worked example 1

1. From a mass balance for soluble calcium phosphate within the reactor, we derive the mass flow of particles and convert it to a volumetric flow (v) using the particle density: $v = (c_i - c_o)Mw/\tau/\rho = 0.00021$ (m^3 crystals) (m^3 solution)$^{-1}$ s^{-1}. From the particle micrograph we may consider them as uniformly sized spheres with a diameter d of about 50 nm. We thus derive the nucleation rate $J = v/(\pi d^3/6) = 2.4 \times 10^{18}$ m^{-3} s^{-1}.
2. Assuming a concentration of heterogeneous particles in the range 10^{12} to 10^{14} m^{-3}, the highest possible heterogeneous nucleation rate occurs when each heterogeneous particle becomes a calcium phosphate nucleus, thus $J_{het} = 10^{14}/\tau = 2.10^{14}$ m^{-3} s^{-1}. As $J \gg J_{het}$, the experimentally determined nucleation rate is for a homogeneous mechanism.
3. Assuming that at the reactor outlet the solution is saturated, then $c_{eq} = c_o$. For an induction time longer than the mixing time, the initial concentration simply equals the inlet concentration c_i. Therefore the supersaturation ratio $S = c/c_{eq}$ becomes $S = c_i/c_o = 2$.
4. Using the values of J and S just calculated we find $\gamma = 100$ mJ m^{-2}, which, considering the solubility $c_{eq} = 0.0016$ mol L^{-1}, fits well the Nielsen and Söhnel correlation in Figure 4.3.
5. Inspection of equation 4.17 for the nucleation rate indicates that it can be increased by increasing the supersaturation, increasing the temperature, or by changing the solvent to attain a lower γ.

4.4 Non-classical nucleation

Non-classical nucleation is a rather uninformative term that is used for several nucleation phenomena that do not obey classical nucleation characteristics. In this chapter it refers to a nucleation phenomenon that proceeds in two steps with a phase that is metastable with respect to the crystalline phase as an intermediate step. When the nucleation of a stable crystalline phase from a supersaturated phase is greatly retarded, the crystal nuclei might nucleate within faster-forming liquid or solid particles of an intermediate phase.

Classical nucleation theory was originally developed for the formation of dense fluid phases from dilute and disordered phases. In the case of nucleation of crystals from

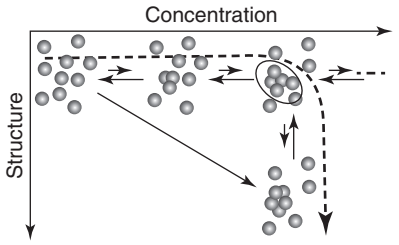

Figure 4.9 Schematic illustration of a one-step and a two-step nucleation mechanism (Vekilov, 2010a).

solution at least two order parameters, density and structure, are necessary to distinguish between the old and the new phase. By applying the classical nucleation approach it is implicitly assumed that the transitions along the two order parameters proceed simultaneously. Single entities such as molecules, atoms or ions, depending on the crystals, are directly attached to the dense final structural arrangement that is assumed to be equivalent to that of the final or intermediate crystal.

In many cases, however, nucleation rates in solutions were found to be many orders of magnitude lower than was predicted by the classical nucleation theory. The nucleation process then proceeds via two sequential steps, where the first step is solely a densification step related to the formation of an intermediate liquid or solid phase. The final structural rearrangement proceeds in a subsequent step (Vekilov, 2004, 2010a, 2010b, Sear, 2012).

4.4.1 Two-step nucleation with an intermediate liquid

Many organic and in particular protein systems exhibit a liquid–liquid phase split in their phase diagram. Droplets of a stable dense liquid of sizes that for proteins are up to hundreds of nm can be formed in the solution upon cooling, followed by the formation of structured nuclei inside or at the interface of the droplets. Recently however, it became clear that in many solutions, supersaturated with respect to the crystals, a metastable equilibrium exists between low- and high-density regions outside the L–L region. The metastable dense phase results from density fluctuations and is contained in clusters with a higher free energy than the dilute solution. This metastable phase is separated from the dilute solution by an energy barrier that is lower than the barrier for the formation of a stable droplet. Structure fluctuation in these metastable clusters subsequently leads to the formation of crystal nuclei. A schematic picture of a two-step process is given in Figure 4.9 (Vekilov, 2010a).

The number of crystals grown from a precursor phase of dense droplets was calculated for a mononuclear mechanism where only one crystalline nucleus develops per droplet (Kaschiev, 2000).

For several cases the number of nuclei with time $N_c(t)$ were related to the nucleation rate of the droplets and to the nucleation rate of the crystals in the droplets. First a fixed number of droplets N_0 of equal volume v_0 was assumed to be created instantaneously

and the crystal nucleation rate J_c to be stationary. The number of nucleated crystals $N(t)$ is then given by:

$$N_c(t) = N_0[1 - \exp(-J_c v_0 t)] \tag{4.31}$$

and for short observation times simplifies to $N_c(t) = N_0 J_c v_0 t$.

In another special case both nucleation rates were taken to be stationary, and the number of crystals $N_c(t)$ becomes a linear function of time. It also depends on the delay time of the two-step process Φ, which is merely the mean time for the appearance of a crystal nucleus in a droplet:

$$N_c(t) = J_c V(1 - \Phi) \tag{4.32}$$

In protein crystallization one- and two-step nucleation events can even occur simultaneously (Auer *et al.*, 2012). For amyloid, for example, not only is the stable solid fibrillar phase thermodynamically allowed, but also a metastable oligomeric phase. In the one-step nucleation mechanism, monomers of the protein polymerize directly into fibrils, while in the two-step nucleation mechanism monomers first aggregate into oligomers, in which the fibrils are born.

A recent study of Lee *et al*. (2011) provided evidence that the amyloid-$\beta_{1–40}$ protein forms fibrils by a nucleated conformational conversion of oligomers. The one- and two-step nucleation mechanisms are, however, extremes and the intermediate aggregation step is condition-dependent. To further explore these conditions Auer *et al.* (2012) calculated the solubilities of the oligomers and the fibrils by computer simulations and then the nucleation rates J_1, J_0 and J_2 of A-$\beta_{1–40}$ one-step fibrils, oligomers and two-step fibrils, respectively, at $T = 310$ K. The stationary J_1 dependence on the protein monomer concentration was calculated from a corrected classical nucleation rate equation, and J_0 from the classical homogeneous nucleation rate equation. Under the assumption that only one fibril could nucleate per oligomer droplet, J_2 could be expressed as a time-dependent fraction of J_0. These results did not conflict with the findings of Lee *et al.*, (2011). It can be seen from Figure 4.10 that the nucleation mechanism is monomer concentration-dependent and slightly shifts with time.

It is well known that in dense droplets nucleation is hampered by the higher viscosity of the liquid. Predensification, on the other hand, fastens the nucleation process of the solid. It is therefore not surprising that crystal nucleation by structural changes frequently proceeds faster in metastable (with respect to the solution) clusters of varying size and density than in dense droplets.

The first step in this cluster-type two-step mechanism, the formation of transient dense clusters, is fast. Their formation rate is often ten orders of magnitude faster than the total crystal nucleation rate. The formation of crystal nuclei from the pre-existing clusters can thus be considered as the rate-determining step (Vekilov, 2010b).

The nucleation rate for a two-step mechanism with an intermediate metastable state is then given by:

$$J = AC_1 \exp(-\Delta G_2^*/kT) \tag{4.33}$$

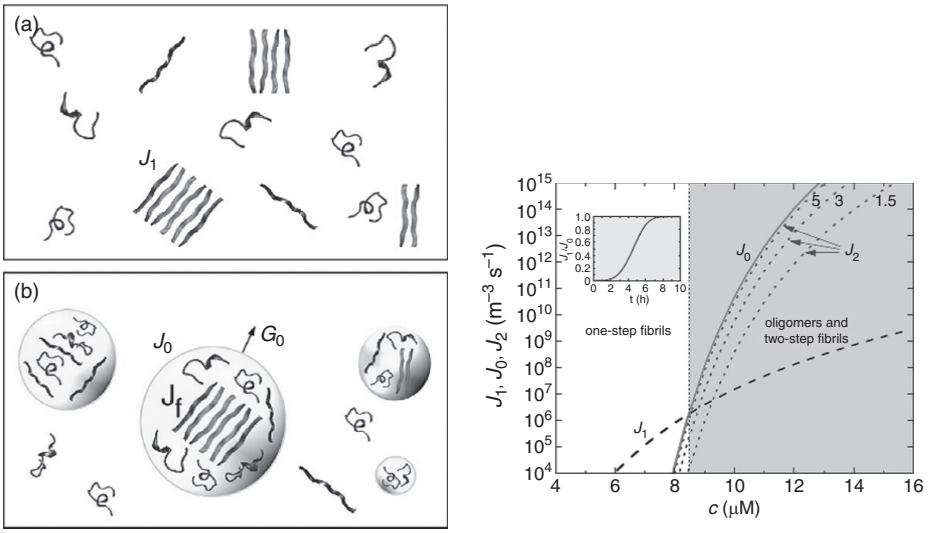

Figure 4.10 (a) Direct polymerization of β-strands into fibrils with a β-sheet structure and (b) fibril nucleation preceded by nucleation of metastable oligomers. (c) Plots of the three nucleation rates of the one-step (J_1), and two-step (J_0 and J_2) fibril formation versus the monomer protein concentration (numbers indicate time in hours).

ΔG_2^* represents the energy barrier for nucleation inside the cluster and can be experimentally obtained from the slope of the $J(c)$ dependency. AC_1 replaces the pre-exponential term AS in equation 4.17, and C_1 is the concentration of the solute in the clusters, for example of lysozyme that is often studied as a model protein.

$$A = \varphi_2 k_2 T/\eta \tag{4.34}$$

where φ_2 = cluster volume fraction, k_2 = rate constant, T = temperature and $\eta(C_1, T)$ is the viscosity inside the clusters. For lysozyme the volume fraction of clusters is estimated to be 10^{-7}–10^{-6}.

With this equation for the nucleation rate, the two-step mechanism predicts values that are up to nine orders of magnitude smaller than those predicted by classical nucleation theory. This comes from the significantly lower value of the pre-exponential factor due to the low volume fraction of clusters and the higher viscosity of the denser clusters. In addition the interfacial energy between a crystalline nucleus and a dense cluster is lower than in a dilute solution.

The nucleation rate J increases steeply as the temperature decreases, because of increasing supersaturation. This continues until T equals T_{sp}, the kinetic solution-crystal spinodal, where the critical nucleus reaches the size of a single molecule, and a maximum value for J is reached (see Figure 4.11). Below this temperature the volume of the dense liquid clusters becomes smaller and the concentration inside the clusters becomes higher.

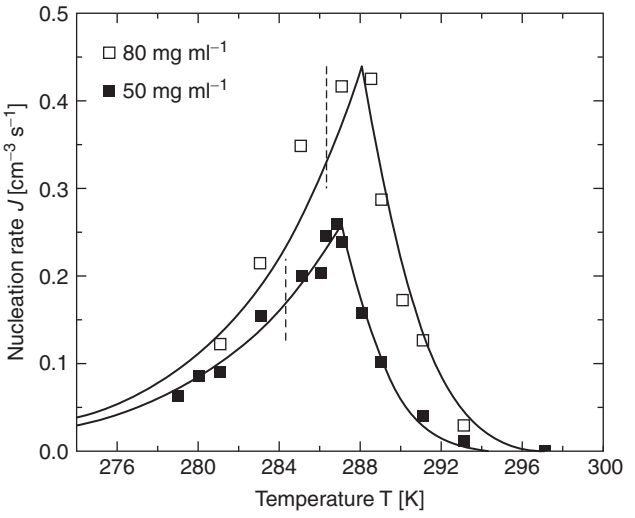

Figure 4.11 $J(T)$ dependence at two different lysozyme concentrations (Vekilov, 2010a).

This leads to a higher viscosity and the nucleation rate J decreases at a slightly gentler slope when the temperature is further decreased. This unusual pathway of J can be explained by a two-step instead of a one-step mechanism.

Another explanation for the observed nucleation rate dependence on the temperature of lysozyme was given by Sear (2006). The pre-exponential factor and the nucleation barrier as measured by Galkin and Vekilov (1999) are much smaller than calculated for homogeneous nucleation of lysozyme according to classical nucleation theory. By introducing different types of impurities into the solution as heterogeneous nucleation sites with a distribution of energy barriers, Sear could equally well describe the experimental results.

Several researchers, like those from Myerson's group, have demonstrated in experimental and simulation studies the applicability of the two-step mechanism to both macromolecules and small organic molecules without and L–L phase split, suggesting that this mechanism underlies many crystallization processes from solution. In some of their studies they used laser light for aligning of molecules in the metastable clusters. The second nucleation step of structuring of the molecules in the clusters started once the laser light encountered sufficiently large clusters in the solution (Erdemir *et al.*, 2009).

4.4.2 Two-step nucleation with an intermediate solid

In the case of nucleation of (bio)minerals, evidence was also found for a stepwise nucleation mechanism. There are, however, crucial differences from the above-described two-step mechanism where as a first step liquid metastable clusters of varying sizes are formed in solution. In this second model small stable solid prenucleation clusters are formed without the crossing of a significant activation barrier, because the prenucleation

clusters with their hydrated shell hardly have a phase interface. These clusters can be considered as amorphous solutes that are in equilibrium with the solution. The size of these clusters has been reliably determined by analytical ultracentrifugation and for calcium carbonate their size is approximately 2–3 nm (Gebauer and Cölfen, 2011). Their size measured with cryo-TEM is about 0.6–1 nm, because the water shell is not seen by this technique. At supersaturation these tiny clusters have to agglomerate before structural changes occur.

4.4.2.1 Nucleation of calcium carbonate

Because calcium carbonate has been the most investigated mineralization system, the two-step mechanism will first be discussed for this compound. The amorphous calcium carbonate (ACC) in the prenucleation clusters can become more stable (ACCI) when obtained from a solution of lower pH upon quenching or less stable (ACCII) at higher pH values. TEM pictures of these nanoparticles revealed the onset of short-range structural order of proto-calcite or proto-vaterite structures.

The initial stages of the $CaCO_3$ nucleation process was studied by Sommerdijk's group using Cryo-TEM (Pouget *et al.*, 2010). When the solution containing the prenucleation clusters becomes supersaturated with respect to ACC, an aggregation process of these clusters sets in and within a few minutes small nanoparticles with a size distribution that is centered around a size of about 30 times the size of the prenucleation clusters are observed. After longer reaction times larger particles of ACC are observed in solution in coexistence with the prenucleation clusters. Tomograms showed that in the presence of a template such as a stearic acid monolayer floating at the solution surface, the larger clusters collected preferentially at the surface of the organic template. In these adhering clusters oriented vaterite or calcite crystals grow out (see Figure 4.12). Tiny prenucleation clusters from solution attached to the larger particles contribute to their growth by dissolution and recrystallization.

The development of the final crystalline polymorph from the ACC is, however, also dependent on subsequent kinetic processes in which impurities, additives or templates play an important role (Gebauer and Cölfen, 2011).

4.4.2.2 Nucleation of calcium phosphate

Another thoroughly investigated (bio)mineralization process is that of calcium phosphate. The initial stages of the nucleation process from simulated body fluid studied by the group of Sommerdijk using cryo-TEM showed many similarities to calcium carbonate nucleation (Dey, 2010). Here also stable prenucleation clusters are present in solution before nucleation with sizes of 1–2 nm if measured with TEM. Upon supersaturation in the absence of a template only very loosely associated networks of prenucleation clusters are formed that do not lead to the formation of solid crystalline structures. In the presence of a Langmuir monolayer of arachidic acid, however, nucleation starts with the generation of about 50 nm aggregates of prenucleation clusters that densify at the monolayer as an amorphous precursor of amorphous calcium phosphate (ACP). After 12 hours, carbonated hydroxyapatite crystals (c-HA) of about 120 nm grow epitaxially at the interface (see Figures 4.13 and 4.14).

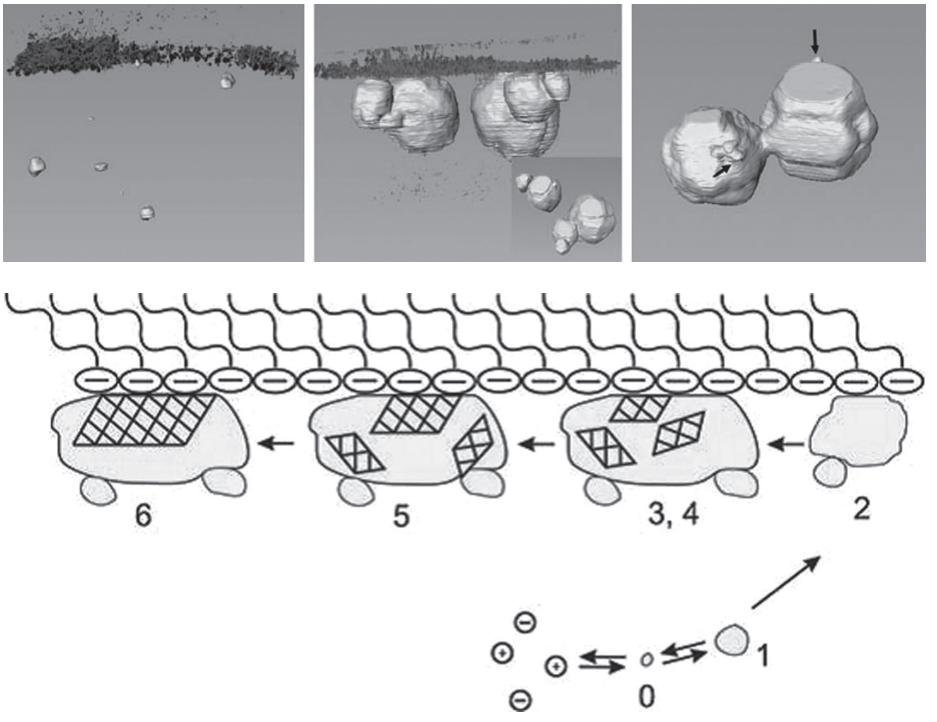

Figure 4.12 Bottom: Schematic pathway of the nucleation process of $CaCO_3$: aggregation and growth of ACC clusters at the surface of the template (steps 1, 2), formation of small crystalline domains in the amorphous ACC (steps 3, 4), prevalent growth of the domain stabilized by the template (step 5), growth of oriented single crystal (step 6). Top: Tomograms during these steps. The black arrows point at prenucleation clusters attached to the more outgrown calcite crystals (Pouget *et al.*, 2010).

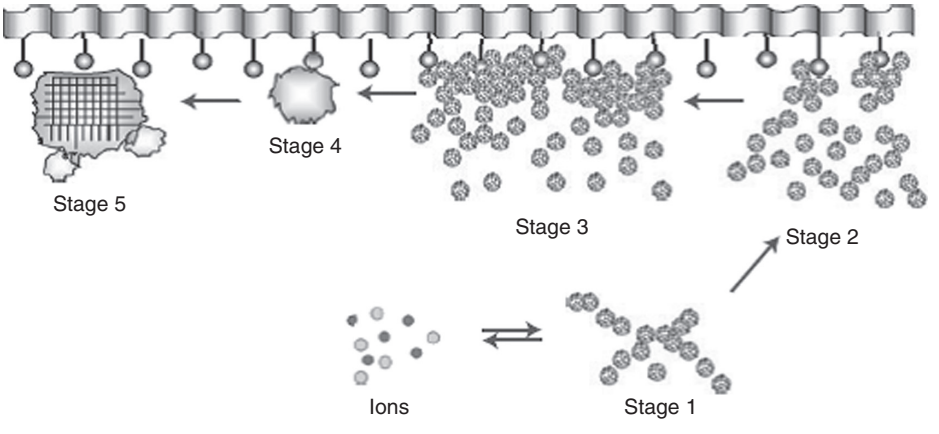

Figure 4.13 Schematic pathway of the nucleation of calcium phosphate: loose networks (stage 1), ACP (stage 4) and c-HA (Stage 5) (Pouget *et al.*, 2010).

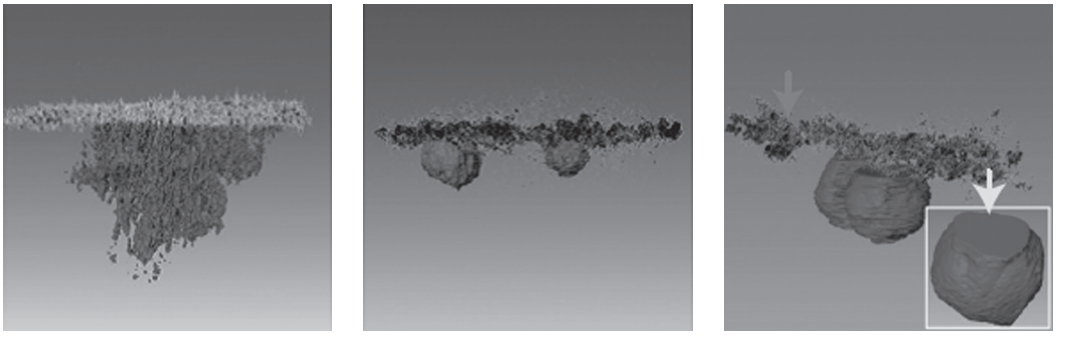

Figure 4.14 Tomograms of stage 3, 4 and 5. Arrow points to the (110) face of c-HA (Pouget *et al.*, 2010).

Closing remarks about the two-step nucleation rate

In the case of nucleation from a liquid cluster as an intermediate step, the nucleation rate can be measured by one of the methods described in Section 4.3.2.2 (Galkin and Vekilov, 1999). If for homogeneous nucleation the rate is several orders of magnitude below the value predicted by classical nucleation theory, a two-step mechanism can be operational. From the exponential function, the ΔG_2 value can be calculated that represents the activation energy for nucleation inside the cluster. Also a lower pre-exponential value is obtained.

If nucleation occurs via an amorphous precursor phase, first stable nm-sized clusters are formed that are in equilibrium with the solution. These prenucleation clusters can thus be considered as macro building blocks for nucleation. The subsequent step upon supersaturation of the solution is the aggregation of these prenucleation clusters. In a number of cases, as for $CaCO_3$, the amorphous phase or one or more of the slightly less soluble polymorphs can be crystallized from these aggregates. In these cases the nucleation rate can be measured as described above and the obtained parameters can be evaluated against a model for the mechanism.

A template can assist in the process of densification of the prenucleation clusters and by the formation of oriented nuclei of the crystallized phase. It could be treated as a type of heterogeneous nucleation event, where template matching lowers the energy barrier for the densification of the amorphous precursor phase as for the oriented nucleation in this phase.

4.5 Secondary nucleation

4.5.1 Secondary nucleation mechanisms

Secondary nucleation refers to the birth of nuclei at the interface of the parent crystals. So the prior presence of at least one primary crystal is needed. Contrary to the relatively high supersaturations required for primary nucleation, secondary nucleation occurs at low to moderate values of supersaturation. For moderately to highly soluble salts it is

considered to be the main source of nuclei. The different types of secondary nucleation are named after their origin.

- *Initial breeding* or dust breeding usually occurs if dry seed crystals are introduced into a solution. Dry handling of the seed crystals causes small fragments by attrition that adhere to the dry seeds. These fragments are liberated from the surface in the solution, and become new nuclei. It is therefore recommended to suspend fresh seeds in an undersaturated solution to dissolve the fragments before feeding the seeds as a slurry to the (generally batch) crystallizer.
- *Dendritic breeding* only happens at such high supersaturations that facet instabilities occur during outgrowth of the crystals.This implies that the corners and edges of the crystals experience a higher supersaturation than the middle of the faces (facets) and hopper-like crystals or even dendrites are formed (see Chapter 6). These protruding crystal parts easily break off and become secondary nuclei.

  At high supersaturations surface roughening of a particular crystal face may also occur followed by further growth of the crystal as a bundle of needles. These needles break off more easily and this phenomenon is referred to as *needle breeding.*

  At very high supersaturations irregular polycrystalline aggregates can be formed that are prone to fragmentation. These fragments serve as secondary nuclei and this process is called *polycrystalline breeding*. All these breeding mechanisms only occur at high supersaturations that should be avoided because of their detrimental effect on the crystal quality.
- *Contact nucleation* or *attrition breeding* is the most important source of secondary nuclei in a crystallizer, and results from collisions between crystals and impeller blades, between crystals and vessel walls and from mutual collisions between the crystals. The secondary nuclei are formed by attrition of the crystal corners, edges and macro-steps on the surfaces.
- *Fluid shear breeding* is the formation of secondary nuclei due to turbulent fluid shear forces exerted on a crystal surface. Very high shear forces are, however, needed to exceed the yield stress of a parent crystal leading to the formation of an attrition fragment. This breeding mechanism is thus considered to be less important.

A mechanism has also been proposed where the secondary nuclei do not originate from the crystal surface itself, but from a preordered layer adjacent to the crystal surface that contains clusters or aggregates of growth units. These clusters are removed by collisions and act as nuclei. Since no solid proof has ever been given for this mechanism, referred to as *catalytic breeding*, it will not be further discussed.

Therefore, only *attrition breeding* will be further treated, because it is *the most relevant breeding mechanism of secondary nuclei.*

If we consider the breeding mechanism by attrition in more detail, three consecutive steps can be identified in the formation of new nuclei. The first step is the formation of the attrition fragments due to the impact of the mother crystal with crystallizer hardware or with other crystals. The second step involves the transport of the fragments that have been formed on the surface of the mother crystals to the bulk phase. The last step concerns the survival of the crystal fragments, which are more soluble than the parent

crystals because they have a distorted crystal lattice originating from the mechanical impact during its breaking off from the parent crystal. In the next sections a number of often-used secondary models will be discussed. In most of the models, not all the mentioned steps are identified, but are lumped together (Daudey *et al.*, 1990, Gahn and Mersmann, 1997).

4.5.2 Secondary nucleation: the power law

The most classical expression for the secondary nucleation rate in a suspension of growing crystals, B_0, is the empirical power law that contains three *experimentally accessible* parameters. These parameters are the growth rate G, the stirrer rotational rate N and the solid content or crystal mass M_T of the slurry:

$$B_0 = k_N G^i N^h {M_T}^j \tag{4.35}$$

where B_0 = secondary nucleation rate [# m^{-3} s^{-1}]. Since the growth rate G is directly related to the relative supersaturation σ via $G = k_g \sigma^g$, and the rotational speed N to the specific power input P_0, the power law is also given by:

$$B_0 = k^1_N \sigma^b P_0^k {M_T}^j \tag{4.36}$$

where $i = b/g$ and $h = 3k$. Often encountered values for b, k and j are $1 < b < 3$, $0.6 < k < 0.7$ and $j = 1$ or 2. For secondary nucleation dominated by crystal–impeller collisions, $j = 1$, while for nucleation dominated by crystal–crystal collisions, $j = 2$. The three variables G (σ), N and M_T were recognized early on as being important. The crystallizer geometry, such as type of impeller, number of blades and scale of operation also have an important effect on B_0. These effects are included in k_N or ${k^1}_N$. The rate B_0 is in fact an effective nucleation rate, since it represents the number of nuclei bred at zero size per m^3 crystallizer volume per second [# m^{-3} s^{-1}], that grow into the population. Thus:

$$n_o = \left[\frac{\mathrm{d}N}{\mathrm{d}L}\right]_{L=0} = \left[\frac{\mathrm{d}N}{\mathrm{d}t}\right]\left[\frac{\mathrm{d}t}{\mathrm{d}L}\right]_{L=0} = \frac{B_o}{G} \tag{4.37}$$

As the three steps in the attrition process are lumped together in one equation, it is extremely difficult to correlate the numerical values of the powers in the power law with the mechanisms of these steps. As a result the predictive power in this equation is quite low, especially during scale-up.

Visual observation clearly shows that in particular the corners and edges of the larger crystals are prone to attrition and contribute most to the formation of secondary nuclei. For smaller crystals the impact energy of a collision does not suffice to cause attrition. In large crystallizers, when the attrition is caused by crystal impeller collisions, the crystal edges and corners mostly have time to heal by growth before another collision happens at the same corner or edge. In small crystallizers with a much shorter recycling time less healing occurs. This explains why the crystals from a small crystallizer are often more rounded off than those from a large crystallizer.

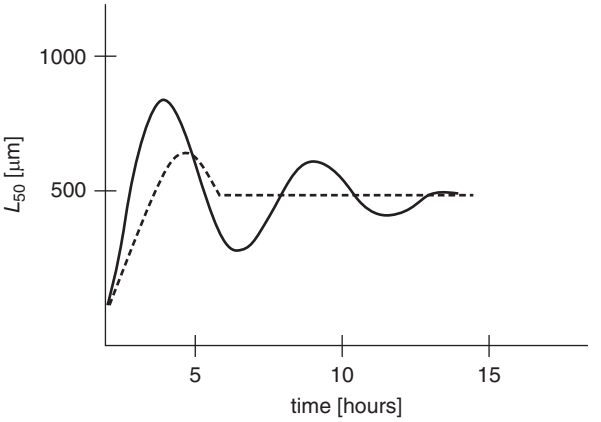

Figure 4.15 Dynamic behavior of the CSD: measured (solid line) and modeled with the power law (dashed line).

The inadequacy of the power law where the total mass of the crystals is included in the equation becomes obvious when this law is used to describe the dynamic behavior of a continuously operated crystallizer.

4.5.2.1 Dynamic behavior in continuous crystallization

The power law with its four parameters k_N^1, b, k and j (see equation 4.35) describes the steady state CSD in continuous crystallization processes. However, it fails to describe the dynamics of a crystallization process. If, for example, the median crystal size, L_{50}, is plotted versus time, an oscillating behavior is measured before a steady state is reached (see Figure 4.15). This steady state is often first reached after L_{50} has reached a maximal value, more of the larger crystals are withdrawn with the product than are grown into the larger crystal size classes, and L_{50} drops. This process continues until it dampens out. Modeling with the power law only gives one peak and does not explain the observed oscillation in L_{50} and in the width of the developing CSD.

Ottens *et al.* (1972), Ploß *et al.* (1985) and Van der Heijden *et al.* (1994) have tried to account for the phenomenon that larger crystals are more prone to attrition, by adding a target efficiency to the power law that is a function of the crystal size. Ottens introduced a step function, Van der Heijden a linear function and Ploß a more gradually increasing function. These functions gave a better description of secondary nucleation, although none was fully successful.

4.5.3 Secondary nucleation: taking into account collision mechanisms

Based on a large number of attrition experiments and a theoretical evaluation of the collision frequencies and collision energy in a stirred tank reactor, a secondary nucleation model has been proposed (Evans *et al.*, 1974), in which the nucleation rate is considered to be the result of two steps, the generation of fragments on the surface of the crystal

and the subsequent removal of these fragments from the surface of the mother crystal into the bulk of the suspension.

In this model secondary nucleation is determined by crystal collisions. The number of nuclei produced upon the impact of a crystal is assumed to be proportional to the impact energy. The rate of nucleation is then equal to the product of the collision energy $E(x)$ and the frequency of collisions $\omega(x)$ in the size range x.

Three different types of particle collisions can in principle lead to attrition: crystal–crystal, crystal–impeller and crystal–crystallizer collisions. Two types of crystal–crystal collisions were considered based on velocity differences due to gravitation forces and eddy turbulence. For the crystal–crystallizer collisions, two contributions were also taken into account, those induced by the bulk motion in the crystallizer and by the turbulence of the liquid.

The derivation of the Evans model is mathematically complex and will not be given in detail here. An adapted version of the original model is discussed with only crystal–impeller collisions due to bulk motion, no crystal–crystallizer collisions and only one type of crystal–crystal collision. In addition a lower boundary is introduced for the calculation of the integral properties of the crystal size distribution, after the concept used by Ottens *et al.* (1972). This lower boundary in the integral calculation accounts for the fact that very small crystals have a negligible influence on the nucleation rate, since they are exposed to insignificant hydrodynamic and mechanical forces compared to the larger crystals. The model can be summarized with the following equation for the nucleation rate B:

$$B = K_E(S)\left[K_{c-i}\frac{N_P}{P_0}k_v\rho_c P_{susp}m_3 + K_{c-c}\rho_{sl}\varphi_c\varepsilon^{5/4}L_{50}^4 m_0\right] \tag{4.38}$$

with $m_3 = \int_{L_{c-i}}^{\infty} L^3 n(L)\mathrm{d}L$ and $m_0 = \int_{L_{c-c}}^{\infty} n(L)\mathrm{d}L$ and where N_P = power (also called) = Newton number of the impeller, P_0 = power input of stirrer, ρ = density, P_{susp} = minimum power required to suspend the particles in the vessel, φ_c = volume fraction of crystals, m = moment of distribution, K_E = number of nuclei per collision, K_{c-i} = constant crystal–impeller collisions, K_{c-c} = constant crystal–crystal collisions and L_{c-i} and L_{c-c} are the lower integration boundaries of the moments.

The overall parameter K_E is related to the surface structure of the crystals and is assumed to be weakly dependent on the supersaturation ratio (S). The numerical values in the equations above need to be estimated by fitting from experimental data.

The model has been analyzed, estimating the parameters on experiments done on a laboratory scale DT crystallizer of 20 liters and on an 1100 liter DTB crystallizer for an aqueous ammonium sulfate solution. The model was capable of describing the dynamic behavior in both crystallizers extremely well, as shown in Figure 4.14. The model has, however, no predictive value.

4.5.4 Secondary nucleation: the attrition behavior of parent crystals

Another approach to the simulation of the dynamics of the crystallization process was introduced by O'Meadhra (1995), who determined an attrition function for the parent crystals under growing conditions.

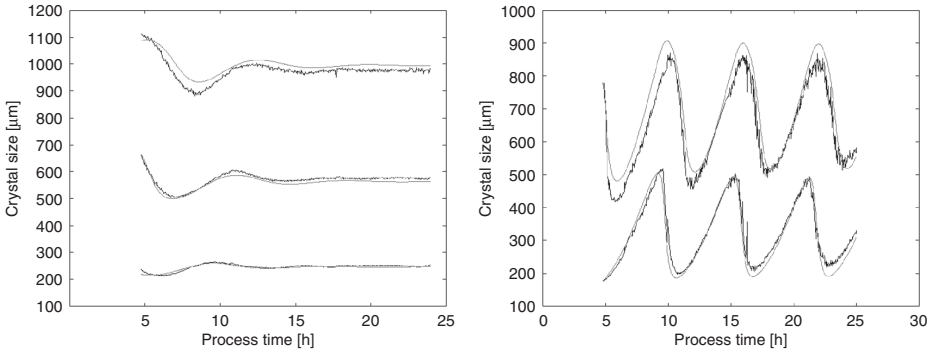

Figure 4.16 Fit of the quantiles of the crystal size distribution for an experiment in a 20 liter DT and a 1100 liter DTB crystallizer using the model of Evans.

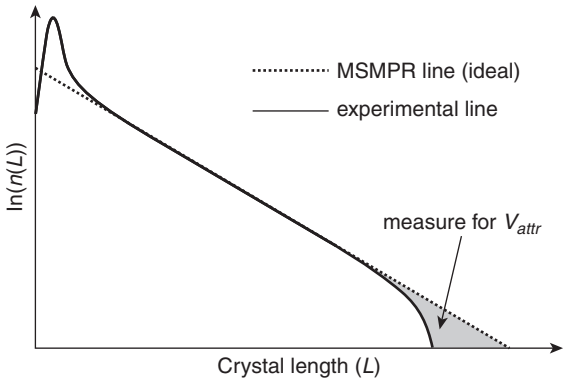

Figure 4.17 Logarithm of the number density distribution as a function of crystal size.

The larger crystals in the CSD suffer more from attrition than the smaller crystals, and beyond a certain size their growth could even be compensated by their attrition.

In the plot of the population density versus crystal length of an MSMPR (mixed suspension, mixed product removal) crystallizer (see Chapter 7) this is reflected by the downward curvature of the plot for the coarser crystals (see Figure 4.17).

The size reduction of the crystals can be taken into account by introducing an attrition rate, G_{att}, which counteracts the kinetic growth rate G_{kin}. The overall growth rate of the crystals then equals:

$$G_{eff} = G_{kin} - G_{att}(L) \tag{4.39}$$

where G_{eff} = effective growth rate [m s^{-1}] and

$$G_{kin} = G(L, \sigma) \tag{4.40}$$

with σ the relative supersaturation. It has to be kept in mind that this approach is only valid for a really well-mixed crystallizer so mostly only for relatively small crystallizer volumes (up to about 20 liters). Otherwise the downward curvature could also to some

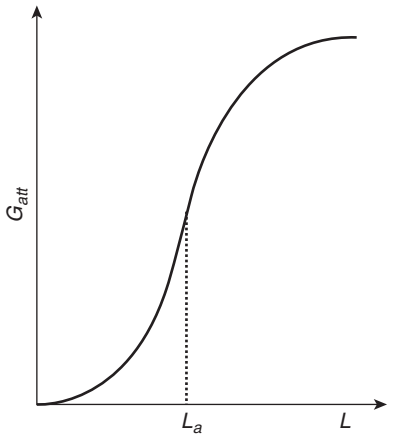

Figure 4.18 Attrition rate versus crystal size.

extent result from internal classification in the crystallizer. This causes larger crystals to settle more easily and to spend less time in the boiling zone (in case of evaporative crystallization) where the supersaturation is the highest.

The attrition rate G_{att} is obtained by fitting the measured CSD with a CSD calculated from the MSMPR population density equation with all the appropriate kinetic equations. This experimentally determined G_{att} increases with L. It can be represented by an expression such as:

$$G_{att} = K_{att}\left(1 - \frac{1}{1 + (L/L_a)^m}\right) \tag{4.41}$$

where m represents the slope of the curve in Figure 4.18 and L_a the inflection point.

Other expressions for G_{att} can be found in literature, as well as other expressions for G_{eff}, such as $G_{eff} = G_{kin} f_{att}$, where f_{att} is a crystal-length-dependent factor.

By inspecting the crystals submerged in a liquid with the same refractive index it can be checked beyond what size the crystals suffer from attrition (see Chapter 2 on Characterization), and whether this is consistent with the attrition function.

From G_{att} the volumetric attrition rate can be calculated:

$$\dot{V}_{att} = 3k_v \int_0^{L_{\max}} G_{att}(L) n(L) L^2 \, \mathrm{d}L \tag{4.42}$$

where $\dot{V}_{att}$ = volumetric attrition rate [$m^3\ m^{-3}\ s^{-1}$].

A number of fragments with a volume equal to $\dot{V}_{att}$ can now be assumed to enter the CSD per second at its smaller size range as a birth function $B(L)$. This birth function is represented by:

$$B(L) = \dot{V}_{att} H(L) \tag{4.43}$$

where $B(L)$ = birth function [# m^{-4} s^{-1}] and $H(L)$ is, for example, a normalized log-normal distribution function with arbitrarily chosen values for the mean size and width (e.g. 10 μm and 5 μm, respectively) of the fragment distribution. A survival efficiency term $\eta_{survival}$ can be added to achieve the nucleation rate of actually growing nuclei. This term is a function of the supersaturation since a high supersaturation will encourage the nuclei to grow out:

$$\eta_{survival} = k_{survival}\sigma \tag{4.44}$$

The removal efficiency is already included in $\dot{V}_{att}$.

The advantage of this modeling scheme is that the sources of the secondary nuclei are irrelevant. A large disadvantage is that, like the power law, it does not have any predictive value.

4.5.5 Secondary nucleation: a physical attrition model

Although collisions may occur with crystal faces, edges or corners, in a suspension of crystals, the corners are the most likely candidates to produce attrition fragments because higher local stresses can build up due to the smaller area of contact. Inspection of the crystals submerged in a liquid with the same refractive index also show that the crystal corners are most easily damaged. It has also been demonstrated by O'Meadhra (1995) and by the work of Chianese *et al.* (1993) that the attrition function G_{att} reduces to almost zero under non-growing conditions when the crystals become rounded off.

Gahn and Mersmann (1997) based their physical attrition model on the assumption that in particular the crystal corners contribute to the generation of attrition fragments. This model linked with that of Ploß and Sangl (Mersmann *et al.*, 1988, Ploß and Mersmann, 1989) brings us a large step forward in the direction of a more fundamental approach of the generation of secondary nuclei based on material properties and physical concepts, which should also have more predictive value.

The approach consists of three steps:

1. A procedure to determine the number of crystals colliding per second with the impeller blades and the impeller edge, and the corresponding impact energy per collision (model framework of Ploß, Sangl and Mersmann (Mersmann *et al.*, 1988, Ploß and Mersmann, 1989).
2. A relation between the impact energy of a single collision and the resulting number of attrition fragments and their total volume, as well as their normalized number density distribution.
3. A procedure to let these fragments grow into the CSD, and to link this modeling approach to the secondary nucleation function $B(L)$ or to the total volumetric attrition rate $\dot{V}_{att}$.

The model of Ploß, Sangl and Mersmann (Mersmann *et al.*, 1988, Ploß and Mersmann, 1989) can be used to determine the velocity profile of the crystals that approach the impeller, and their chance of colliding with the impeller.

The impact velocity and the chance of a crystal colliding with the impeller depend on the local two-phase flow pattern in the vicinity of the impeller. Due to the complexity of this flow pattern, a simplified model, based on geometric considerations, is used in the model framework of Gahn. The impact velocities and the chance of a collision are calculated independently for the impeller edge and the impeller blade. For this purpose the impeller is divided into segments j along its radius. This segmentation is done because the relative velocity between the fluid phase and the impeller and therefore also the impact velocity of the particles is a function of distance from the axis. Furthermore the assumption is made that the crystals will follow the fluid phase, i.e. there is no slip.

Note that more crystals collide with the blade than with the edge, but the impact energy with the edge is larger. The total number of crystals of size class i that actually collide with either the blade or the edge of the impeller segment j, Z_{ij} is given by:

$$Z_{ij} = N_i \frac{\varphi_{circ}}{V_{cryst}} \cdot \eta_{target,ij} \cdot \eta_{geo,j} \quad [\#\ \mathrm{m}^{-3}\ \mathrm{s}^{-1}] \tag{4.45}$$

where N_i = number of crystals of size class i, φ_{circ} = circulating flow rate in the crystallizer, V_{cryst} = crystallizer volume, $\eta_{target,ij}$ = target efficiency and $\eta_{geo,j}$ = geometric efficiency. The target efficiency, $\eta_{target,ij}$, is a measure of the chance of a crystal in size class i colliding with impeller segment j. The geometric efficiency, $\eta_{geometric,j}$, is a measure for the chance of a crystal being in segment j. These efficiencies can be calculated from the impeller geometry, the velocity profile around the impeller (assuming that the crystals follow the fluid phase), the axial velocity of the crystals towards the impeller plane, the tangential velocity of the impeller segment, the size L_i of the crystals and the viscosity of the fluid.

The collision velocity of a crystal $w_{coll,ij}$ can also be calculated from the velocity of the crystal normal to the impeller blade or edge, and from a dampening factor that is assumed to equal $\eta_{target,ij}$. From this collision velocity and the mass of a crystal of size L_i the impact energy is calculated to be (see also Figure 4.19):

$$W_{p,ij} = \frac{1}{2} \rho\, k_v {L_i}^3 {w_{coll,ij}}^2 \tag{4.46}$$

Gahn and Mersmann developed a model to calculate the volume of attrition fragments produced during a single collision between a hard flat surface, and a crystal corner, represented by a cone.

The model relates the attrited volume $V_{a,ij}$ to the impact energy $W_{p,ij}$ of the crystal via its relevant mechanical properties (Vickers hardness H, fracture resistance Γ / K_r, and shear modulus μ):

$$V_{a,ij} \approx \frac{2}{3} \frac{H^{2/3} K_r}{\mu \Gamma} {W_{p,ij}}^{4/3} \tag{4.47}$$

The mechanical properties in equation 4.47 can also be combined in an attrition constant C leading to the following equation:

$$V_{a,i,j} \approx C \cdot {W_{p,ij}}^{4/3} \tag{4.48}$$

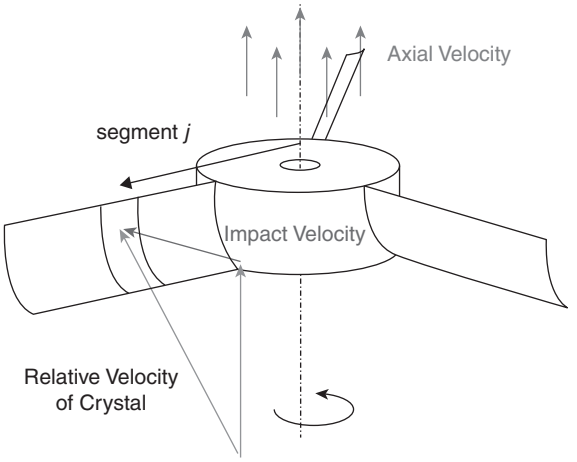

Figure 4.19 Collision of crystals with impeller blades.

The model assumes that a damaged crystal corner will have sufficient time to heal before a subsequent collision of the same corner takes place. If this healing process is not completed in time, the corners of the crystal will be more and more rounded-off. For rounded-off crystals the attrition resistance will increase, resulting in a higher value for the effective fracture resistance.

A minimum impact energy is required to cause a fracture and to remove material from the crystal:

$$W_{p,min} \approx 64 \frac{\mu^3 \Gamma}{{K_r}^3 H^5} \tag{4.49}$$

This value can be calculated from measurable material properties and is thus a constant for each given substance. It also means that for each crystal length L_i a minimal collision velocity $w_{coll,ij}$ is needed for attrition. For $(NH_4)_2SO_4$ such a plot is presented in Figure 4.20, and for a collision velocity of 6 m s^{-1} only crystals with a size larger than 80 μm suffer from attrition.

So only collisions with impact energy larger than $W_{p,min}$ are taken into account.

The model also provides a normalized number density function of the fragments, with $L_{\min}$ as the minimum and $L_{\max}$ as the maximum size of the fragments formed:

$$q(L)_{ij} = \frac{2.25}{L_{\min}^{-2.25} - L_{\max}^{-2.25}} L^{-3.25} \tag{4.50}$$

$$\int_{L_{\min}}^{L_{\max}} q(L)\,\mathrm{d}L = 1 \tag{4.51}$$

$$L_{\min} = \frac{32}{3} \frac{\mu \Gamma}{K_r H^2} \tag{4.52}$$

$$L_{\max} = \frac{1}{2} \left(\frac{K_r}{\mu \Gamma} \right)^{1/3} H^{2/9} {W_{p,ij}}^{4/9} \tag{4.53}$$

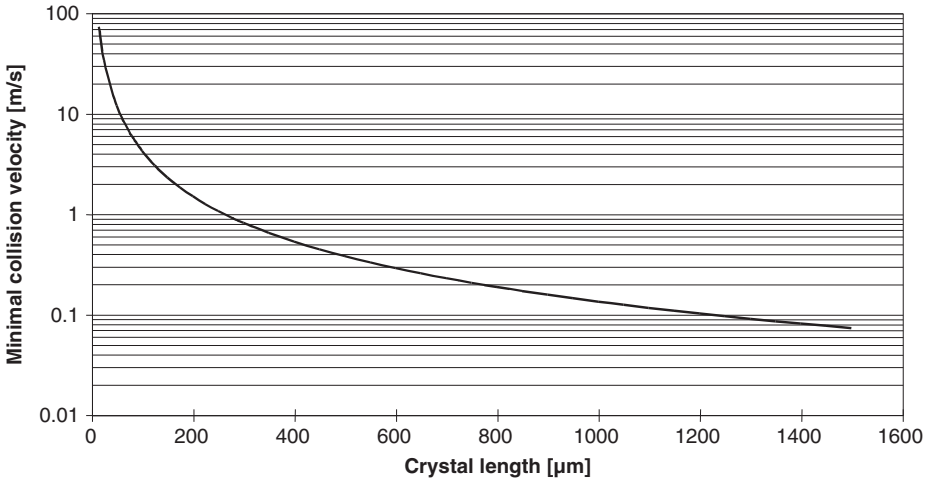

Figure 4.20 Minimal collision velocity to cause attrition of $(NH_4)_2\ SO_4$ crystals as a function of the crystal length.

The minimum size of the fragments is only a function of material properties, and therefore independent of the impact energy, and a constant for each given material.

The total number of fragments then becomes:

$$N_{fragments,ij} \approx \frac{\pi}{21} \frac{H^{1/2} K_r^{3/4}}{k_v (\mu\Gamma)^{3/4}} \left(\frac{1}{L_{\min}^{2.25}} - \frac{1}{L_{\max}^{2.25}} \right) W_{p,ij} \tag{4.54}$$

$$\approx 7 \cdot 10^{-4} \frac{H^5 K_r^3}{k_v \mu^3 \Gamma^3} W_{p,ij} \tag{4.55}$$

In general the size distribution of fragments lies in the range 2 to 100 µm.

In this successive step the rate of attrition is linked to the rate of secondary nucleation. Assuming that a certain amount of stress remains in the attrition fragments formed during a single collision, the chemical potential $\Delta\mu$ will be increased compared to an unstressed crystal. The formed fragments with sizes $L_{fragment}$ can now be tabulated with their respective length and their stress content W^*, that in Gahn's model has been put equal to $\Gamma / kT L_{fragment}$.

Their saturation concentration $c_{eq,real}$ equals:

$$c_{eq,real} = c_{eq} \exp \left[\frac{\Gamma_K}{kT L_{fragment}} \right] \tag{4.56}$$

As a result the actual driving forces for the fragments to grow decrease. With this equation the fragments that will dissolve can be eliminated. The other fragments are allowed to grow into the CSD with a growth rate that includes growth rate dispersion of the small crystals. The value of Γ_K has to be determined experimentally.

The W^* term that is used by Gahn to describe the plastic deformation stress that is introduced in the fragments during the collision and attrition process of the parent crystals has two major disadvantages. This plastic deformation energy is related to

Rittinger's law that is only meant to describe the energy needed for the formation of the additional surface area during breakage, and does not include plastic deformation. Secondly, crystals born at a length L are given the same strain energy as crystals that are grown to a size L. This is contradictory to the healing of crystals that is supposed to take place during their outgrowth.

This approach does not deliver a secondary nucleation rate B_0 with nuclei born at zero size or a birth function $B(L)$ for a distribution of secondary nuclei, but calculates from the surviving fragments per collision and the number of collisions, the developing nuclei that grow into the CSD. Since for this calculation an initial CSD is needed, it always means that iteration loops are required if this nucleation model is used as a predictive tool.

The model adapted from the model of Evans, the model of O'Meadhra and the model of Gahn are all suitable to describe the dynamic behavior of a crystallization process.

Worked example 2

Particulate copper sulfate is obtained by batchwise cooling an initially saturated solution. At the end, the solids content is 20 vol% and the crystal mean size is 300 µm. (1) What are the nucleation mechanisms at the early stage of the batch; (2) just after the first nucleation event; (3) at late stages of the batch? (4) How could larger particles be obtained by adjusting the nucleation rate?

Solution to worked example 2

(1) As the process starts in the absence of solids, the initial nucleation mechanism has to be primary nucleation. Unless extreme precautions are taken, heterogeneous primary nucleation is likely. (2) Soon after the first outburst of primary nuclei, the solution concentration drops below the metastable limit, so primary nucleation stops. The solids content is still low and the crystals are very small, so secondary nucleation is also negligible, see power law model (equation 4.35) and Evans model (equation 4.38). (3) At late stages the crystals are large and the solids content is high so secondary nucleation is likely. However, for some systems secondary nucleation is negligible at low supersaturation. (4) In order to obtain larger particles the nucleation rate must be reduced. Inspection of the power law indicates promising measures: add seeds to avoid primary nucleation, reduce the agitation rate, increase batch time to reduce the supersaturation.

4.6 A brief summary of the chapter

Primary nuclei are formed at locations of high supersaturation in the solution. To start either an unseeded batch or a continuous crystallization process a sufficiently high supersaturation is required. These nuclei grow out and in the case of moderate to good solublity substances the crystals consume the supersaturation, and primary nucleation no longer occurs. Attrition of the outgrown crystals now provides fragments that either

dissolve or grow into the crystal population. In evaporative and cooling crystallization, secondary nucleation is thus the source of new crystals.

In the case of slightly soluble salts, the growth rate of the nuclei is low and the prevailing supersaturation is only slowly consumed. As explained in the chapters on crystallization methods and precipitation, a sufficiently high yield is generally obtained by mixing of concentrated reagents. At the inlet points of these reagents the supersaturation is high, with primary nucleation as a consequence. In precipitation processes therefore, primary nucleation is the main source of new crystals. This also applies to anti-solvent crystallization if the solubility of the solute in the anti-solvent is low.

The primary nucleation rate has long been calculated by the classical nucleation theory, where the nucleation rate is an exponential function of the supersaturation. Recently the frequent occurrence of a two-step mechanism was shown. For a two-step mechanism with the formation of liquid droplets as an intermediate phase an exponential function is also expected. In addition, for a two-step mechanism based on transient density fluctuations in the liquid an exponential dependence on the supersaturation occurs, although the nucleation rate is orders of magnitude smaller than predicted by classical nucleation theory. For a two-step mechanism resulting from a solid-phase transformation the dependence on the supersaturation is a first- or second-order process.

For secondary nucleation the nucleation rate dependence on the supersaturation is also first or second order, because the rate depends on the outgrowth of attrited fragments.

In all cases nucleation rates are hard to predict from calculations, and separate measurements for their determination are recommended.

4.7 End of chapter problems

Problem 1

Derive equation 4.8, which expresses the Gibbs free energy of formation ΔG^* of a nucleus of radius r^*. Start from the expression for the Gibbs free energy of formation of a cluster of size r (equation 4.2).

Problem 2

Batch unseeded evaporative crystallization of pentaerythritol is conducted at 67 °C (solubility $c_{eq} = 1.54$ kmol m^{-3}). Crystals are formed from the aqueous solution at the metastable limit, in this case at a solute concentration $c = 2.12$ kmol m^{-3}. (a) Assume nucleation is by a homogeneous primary mechanism to estimate the interfacial tension; compare the Mersmann correlation with the Nielsen and Söhnel plot. (b) Determine the number of molecules in the critical nucleus n^*. (c) If $n^* > 200$ reject the hypothesis of homogeneous primary nucleation in favor of a heterogeneous mechanism. Assume $n^* = 200$ to estimate an effective interfacial tension. (d) Calculate the heterogeneous primary nucleation rate at c, T, assuming as pre-exponential factor the value $A \times \ln S = 1 \times 10^{27}$. A value larger than 10^{12} # s^{-1} m^{-3} is thought to be unrealistic because particles that are too small would result. (c) Determine the most likely mechanism of nucleation and justify your conclusion.

You are given the Bolzmann constant $k = 1.38065 \times 10^{-23}$, the Avogadro number $N_A = 6.023 \times 10^{-26}$ # kmol^{-1}, the crystal density $\rho_{crystal} = 1511$ kg m^{-3} and the pentaerythritol molar mass $M = 136.15$ kg kmol^{-1}.

Problem 3

Potassium sulfate is produced by seeded batch cooling crystallization. Seed particles of 300 μm in size and 4×10^5 in number were added. A linear cooling rate was applied from 80 to 18 °C such that the batch time was 1 h. Online measurements of the solution concentration throughout the batch are shown in Figure 8.9. Both the polydisperse nature of the particles and the abraded nature of crystals sampled at several time intervals suggest that secondary nucleation occurred throughout the batch. The nucleation rate has been determined for this system to follow the power law equation $B_o = k_N^1 \sigma^b \varepsilon^k M_T^j$, with $k_N^1 = 10^{10}$, $b = 1$, $k = 0.6$ and $j = 2$, with ε in W/kg, M_T in kg/kg suspension and B_0 in # (kg susp)$^{-1}$ s^{-1}. (a) Determine the nucleation rate at 80, 70, 50, 30 and 20 °C. Compare the values found and explain why the nucleation increases with time. (b) Determine the total number of particles produced by secondary nucleation and compare your answer with the number of particles added with the seed size. What measures would you propose to reduce secondary nucleation? (c) Estimate the particle mean size and compare your answer with the mean seed size. How does secondary nucleation affect the particle size?

The particles' volume shape factor was $\pi/6$, the solid density was 2660 kg m^{-3}, and the stirrer power input was $\varepsilon = 1$.

4.8 References

Auer, S., Ricchiuto, P. and Kashchiev, D. 2012. Two-step nucleation of amyloid fibrils: omnipresent or not? *Journal of Molecular Biology*, **422**, 723–730.

Becker, R. and Döring, W. 1935. Kinetische Behandlung der Keimbildung in übersättigten Dämpfen. *Annalen der Physik*, **416**, 719–752.

Chianese, A., Di Berardino, F. and Jones, A. 1993. On the effect of secondary nucleation on the crystal size distribution from a seeded batch crystallizer. *Chemical Engineering Science*, **48**, 551–560.

Daudey, P. J., van Rosmalen, G. M. and De Jong, E. J. 1990. Secondary nucleation kinetics of ammonium-sulfate in a CMSMPR crystallizer. *Journal of Crystal Growth*, **99**, 1076–1081.

Dey, A., Bomans, P. H. H., Müller, F. A. *et al.* 2010. The role of prenucleation clusters in surface-induced calcium phosphate crystallization. *Nature Materials*, **9**, 1010–1014.

Erdemir, D., Lee, A. Y. and Myerson, A. S. 2009. Nucleation of crystals from solution: classical and two-step models. *Accounts of Chemical Research*, **42**(5), 621–629.

Evans, T., Margolis, G. and Sarofim, A. 1974. Mechanisms of secondary nucleation in agitated crystallizers. *AIChE Journal*, **20**, 950–958.

Gahn, C. and Mersmann, A. 1997. Theoretical prediction and experimental determination of attrition rates. *Chemical Engineering Research and Design*, **75**, 125–131.

Galkin, O. and Vekilov, P. G. 1999. Direct determination of the nucleation rate of protein crystals. *Journal of Physical Chemistry*, **103**, 10965–10971.

Gebauer, D. and Cölfen, H. 2011. Prenucleation clusters and non/classical nucleation. *Nano Today* **6**(6), 564–584.

Gibbs, J. W. 1875–1876. On the equilibrium of heterogeneous substances, Part 1. *Transations of the Connecticut Academy of Arts and Sciences*, **3**, 108–248.

Gibbs, J. W. 1877–1878. On the equilibrium of heterogeneous substances, Part 2. *Transations of the Connecticut Academy of Arts and Sciences*, **3**, 343–524.

Jiang, S. and ter Horst, J. H. 2011. Crystal growth rates from probability distributions of induction times. *Crystal Growth Design*, **11**, 256–261.

Kashchiev, D., 2000. *Nucleation*, Elsevier Science.

Lee, J., Culyba, E. K., Powers, E. T. and Kelly, J. W. 2011. Amyloid-β forms fibrils by nucleated conformational conversion of oligomers. *Nature Chemical Biology*, **7**, 602–609.

Mersmann, A. 2001. *Crystallization Technology Handbook*, 2nd edn. Marcel Dekker.

Mersmann, A., Sangl, R., Kind, M. and Pohlisch, J. 1988. Attrition and secondary nucleation in crystallizers. *Chemical Engineering and Technology*, **11**, 80–88.

Nielsen, A. E. and Söhnel, O. 1971. Interfacial tensions electrolyte crystal-aqueous solution, from nucleation data. *Journal of Crystal Growth*, **11**, 233–242.

O'Meadhra, R. 1995. *Modelling of the Kinetics of Suspension Crystallizers*, PhD Thesis, Technische Universiteit Delft.

Ottens, E., Janse, A. and De Jong, E. 1972. Secondary nucleation in a stirred vessel cooling crystallizer. *Journal of Crystal Growth*, **13**, 500–505.

Ploß, R. and Mersmann, A. 1989. A new model of the effect of stirring intensity on the rate of secondary nucleation. *Chemical Engineering and Technology*, **12**, 137–146.

Ploß, R., Tengler, T. and Mersmann, A. 1985. Maßstabsvergrößerung von MSMPR-Kristallisatoren. *Chemie Ingenieur Technik*, **57**, 536–537.

Pouget, E. M., Bomans, P. H. H., Dey, A. *et al.* 2010. The development of morphology and structure in hexagonal vaterite. *Journal of the American Chemical Society*, **132**(33), 11560–11565.

Roelands, C. M., ter Horst, J. H., Kramer, H. J. and Jansens, P. J. 2006. Analysis of nucleation rate measurements in precipitation processes. *Crystal Growth and Design*, **6**(6), 1380–1392.

Sear, R. P. 2006. On the interpretation of quantitative experimental data on nucleation rates using classical nucleation theory, *Journal of Physical Chemistry B*, **110**, 21944–21949.

Sear, R. P. 2012. The non-classical nucleation of crystals: microscopic mechanisms and applications to molecular crystals, ice and calcium carbonate. *International Materials Review*, **57**(6), 328–356.

Selimović, S., Jia, Y. and Fraden, S. 2009. Measuring the nucleation rate of lysozyme using microfluidics. *Crystal Growth and Design*, **9**, 1806–1810.

Van der Heijden, A., Van der Eerden, J. and Van Rosmalen, G. 1994. The secondary nucleation rate: a physical model. *Chemical Engineering Science*, **49**, 3103–3113.

Volmer, M. 1939. *Kinetik der Phasenbildung*. J. W. Edwards.

Vekilov, P. G. 2004. Dense liquid precursor for the nucleation of ordered solid phases from solution. *Crystal Growth and Design*, **4**, 671–685.

Vekilov, P. G. 2010a. Nucleation. *Crystal Growth and Design*, **10**, 5007–5019.

Vekilov, P. G. 2010b. The two-step mechanism of nucleation of crystals in solution. *Nanoscale*, **2**, 2346–2357.

5 Crystal growth

5.1 Why this chapter is important

Investigations into crystal morphology were of great interest in the nineteenth and early twentieth centuries, and a large amount of descriptive data was collected during this time. However, this descriptive approach was limited because it was unable to provide insight into the reasons why crystals can be produced in a variety of forms. On the other hand, it became clear that the conditions and rate of crystal growth have a significant effect on the purity and the shape of the crystals. The need to understand and predict these phenomena was the drive behind trying to unravel the mechanisms of crystal growth (Sunagawa, 2005).

According to Dhanaraj *et al.* (2010), the most important factors affecting the growth rate, and thus the "habitus" and "tracht" of crystals are:

a. the driving force, or supersaturation;
b. the ambient phase, i.e. whether the crystal is grown from a melt or a solution;
c. the solute–solvent interaction energy, i.e. the nature of the solvent in which the crystals are grown;
d. impurities, which modify the edge free energy by adsorbing onto growth steps.

5.2 Basic concepts

The growth rate of a particular crystal face (*hkl*) is mostly described by its *linear growth rate,* R_{lin} [m s^{-1}], which refers to the rate of growth of that face in the direction normal to the face.

Since a crystal is mostly terminated by more than one crystallographically different crystal face (*hkl*), the overall linear growth rate can be defined in several ways. A commonly used definition relates the overall linear growth rate to the increase in mass of the crystal per unit surface area per unit time (R_A):

$$R_A = \frac{1}{A_{crystal}} \frac{\mathrm{d}m_{crystal}}{\mathrm{d}t} = \frac{\rho_{crystal} k_v}{k_a L^2} \frac{\mathrm{d}L^3}{\mathrm{dt}} = 3\frac{k_v}{k_a} \rho_{crystal} G = 6\frac{k_v}{k_a} \rho_{crystal} R_{lin} \quad (5.1)$$

where

$A_{crystal}$ = surface area [m^2]
$m_{crystal}$ = mass [kg]

t = time [s]
$\rho_{crystal}$ = density [kg m^{-3}]
k_v = volume shape factor [-]
k_a = area shape factor [-]
L = characteristic length [m]
G = overall crystal growth rate [m s^{-1}]
R_{lin} = average linear growth rate [m s^{-1}]
R_A = increase in crystal mass per unit surface area per unit time [kg m^{-2} s^{-1}]

For spheres:

$$\frac{k_a}{k_v} = 6 \tag{5.2}$$

and

$$R_A = \frac{1}{A_{crystal}} \frac{\mathrm{d}m_{crystal}}{\mathrm{d}t} = \frac{1}{2}\rho_{crystal} G = \rho_{crystal} R_{lin} \tag{5.3}$$

Note that

$$G = \frac{\mathrm{d}L}{\mathrm{d}t} = 2R_{lin} \tag{5.4}$$

5.3 Crystal growth mechanisms

Although the description that follows refers to growth from solution, for all growth mechanisms the overall growth rate depends on:

- lateral bonds in the growing crystal faces (i.e. a material-specific property);
- the interaction with the solvent. For example, for aqueous solutions, the water coordination mantle has to be stripped and the dehydration frequency is important and
- the number of growth units impinging on the crystal surfaces (related to the solubility).

For growth from solution, the crystal growth processes can be roughly divided into two steps: (volume) diffusion of growth units towards the crystal surface and integration of these growth units into the crystal surface.

The concentration profile perpendicular to the crystal surface for such a two-step process is given in Figure 5.1, where c_b = bulk concentration, c_i = concentration at the crystal–solution interface and c_{eq} = equilibrium concentration at the growth site where the growth unit finally becomes incorporated into the crystal surface.

For highly soluble compounds such as NaCl and $(NH_4)_2SO_4$, the surface integration step is usually not rate limiting, and the growth rate is determined by diffusion through the stagnant film or diffusion layer with thickness δ at the interface. The driving force for diffusion then becomes equal to $(c_b - c_{eq})$, since $c_i = c_{eq}$.

For poorly soluble compounds, the surface integration step becomes rate limiting, and the driving force for integration is then $c_b - c_{eq}$, since $c_i = c_b$. For most compounds, however, both steps have to be taken into account in the calculation of their growth rates.

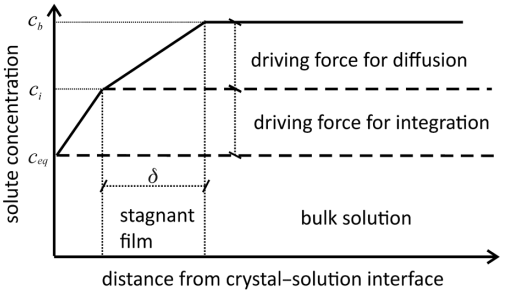

Figure 5.1 Concentration profile perpendicular to the crystal surface during growth.

Figure 5.2 Terraced fields (http://pixabay.com/en/rice-terraces-rice-fields-164410/).

For growth from the melt, transport of heat of crystallization through the bulk phases becomes a third rate-limiting step. This is also the case for very concentrated solutions, for example, in the case of crystallization of a highly hydrated salt, where the solution can almost be treated as a melt.

In the following sections, first the growth mechanisms and the related growth rate equations for surface integration controlled processes will be given. This is followed by the growth rate equation for a volume diffusion-controlled process, and finally by the growth rate equations for situations where a combination of both processes determines the eventual growth rate.

5.4 Crystal surfaces

Theories of crystal growth are based on an understanding of the structure of crystal surfaces. One of the early models was that proposed by Kossel, which, although highly schematized, does allow valuable insight into the basics of crystal nucleation and growth (Kashchiev, 2008). This model visualizes the crystal surface as made of cubic units,

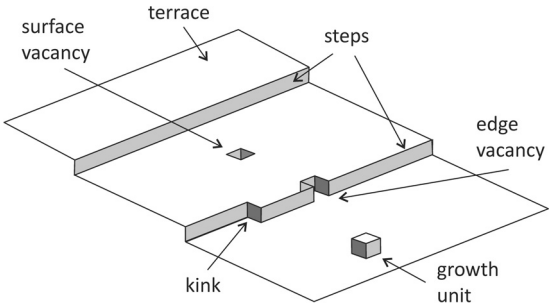

Figure 5.3 Kossel model of a crystal surface.

which form layers of monoatomic height, limited by steps (or edges). Each step contains one or more kinks along its length. The area between steps is referred to as a terrace (as in terraced fields).

The terraces may contain single adsorbed growth units, clusters, or vacancies. This is illustrated in Figure 5.3. According to this model, growth units attached to a flat surface are only required to form one bond, whereas those attached to the steps and kinks have the opportunity to form two and three bonds, respectively. Thus, kink sites are preferred, as they offer the most stable configuration. Growth therefore proceeds by the attachment of growth units to the kink sites in the steps. The kink moves along the step, causing the step to grow. Thereafter, a new step must be formed. The mechanism of new step formation is discussed below.

5.5 Surface integration-controlled growth

As suggested above, the structure of a growing surface at an atomic or molecular level is influenced by several factors: first of all by the binding energies between the atoms, ions and molecules in the surface layer, but also by the solvent, the temperature and the driving force. The powerful influence of the driving force on the morphology of the crystal surface is illustrated in Figure 5.4. At low levels of driving force, growth tends to be smooth. As the driving force increases, growth changes from smooth to rough. Each of the mechanisms will be explained below.

5.5.1 Smooth growth

For the development of smooth crystal faces, as would normally occur under moderate growth conditions, an orderly deposition of successive growth layers is needed. This can be achieved by the propagation of steps along the crystal surface, as depicted in Figure 5.3. The growth unit diffuses towards the crystal surface, where it becomes incorporated at a kink site. This can happen by integration directly from the bulk or, more likely, after diffusion of the growth unit along the surface and along a step. Because, at a kink site, the growth unit can form bonds in three directions, this position is energetically

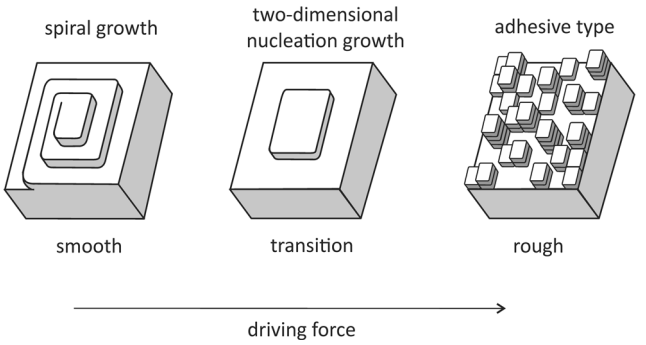

Figure 5.4 Effect of driving force on crystal growth mechanisms (Sunagawa, 2005). Reproduced with permission.

Figure 5.5 A screw dislocation that generates a growth spiral (Mullin, 2003). Copyright Wiley-VCH Verlag GmbH & Co. KGaA. Reproduced with permission.

the most favorable for integration. So in the presence of steps (that always contain kink sites) layer growth is possible.

There has, however, to be a source that generates steps. Two step sources can be identified, and the two mechanisms for layer growth have been named after the type of step source that they are based on: the "spiral growth" model and the "birth and spread" model.

5.5.1.1 Spiral growth model

In order for growth to occur at low supersaturations, there must be a permanent step source. Screw dislocations or dislocations with a screw component that emerge at the crystal surface can operate as permanent step sources.

These defects are normally developed in the crystals during their growth process. The step will curve around the defect line and thus a spiral hill is formed, because steps are preferred sites for growth units to become integrated in the surface. In this model, after a layer is completed the dislocation will still be present (see Figures 5.5 and 5.6).

These ideas were first developed by Frank (1949) and formulated into the BCF growth model by Burton *et al.* (1951). This model is also referred to as the spiral-growth step-propagation model.

The linear growth rate R_{lin} for this mechanism is proportional to the step velocity v_{step} along the surface, the step height h and the step density, which is the inverse of the step distance λ_o. This gives:

$$R_{lin} = \frac{v_{step} h}{\lambda_o} = \frac{v_{step} h}{19 r^*_{2D}} \tag{5.5}$$

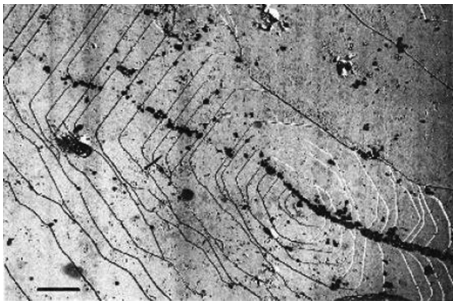

Figure 5.6 DICM photomicrograph of elemental growth spirals on (0001) face of a beryl crystal from Minas Gerais, Brazil. Bar = 500 μm. Small dots are etch pits selectively formed at dislocation outcrops (Sunagawa and Yokogi, 1999)

where v_{step} = step velocity [m s^{-1}], h = step height [m], λ_o = step distance [m] and r^*_{2D} = radius of 2D nucleus [m].

The step velocity v_{step} depends on the difference between the flux of growth units impinging on a position along the step, and the flux of growth units that leave the step. The number of growth units j that stick to the surface area h^2 of a growth unit, along the step, is thus given by:

$$j = (f - g)h^2 \tag{5.6}$$

where f, g = flux densities [# m^{-2} s^{-1}] and, in this case, g is equal to the equilibrium flux density = f^* [# m^{-2} s^{-1}] because, at equilibrium, both the fluxes g and f are equal.

When a growth unit is attached to the step, a length h (the height of a growth unit) is added to it in the direction normal to the step direction, and v_{step} becomes:

$$\begin{aligned} v_{step} &= (f - f^*)h^3 = h^3 f^* \left[e^{\frac{\Delta\mu}{kT}} - 1 \right] \\ &= h^3 f^*(S-1) = V_M f^*(S-1) = V_M f^* \sigma \end{aligned} \tag{5.7}$$

where f^* = equilibrium flux density [# m^{-2} s^{-1}] and h = height of a growth unit [m]. Since the radius of a 2D nucleus is given by:

$$r^*_{2D} = \frac{\gamma_{edge} V_M}{\Delta\mu} \tag{5.8}$$

where $\Delta\mu$ = driving force for crystallization [J mol^{-1} K^{-1}], γ_{edge} = edge free energy [J] and V_M = molecular volume [m^3 mol^{-1}], equation 5.5 becomes:

$$R_{lin} = \frac{1}{19} \frac{f^* h}{\gamma_{edge}} \sigma \cdot \Delta\mu \tag{5.9}$$

and thus:

$$R_{lin} = k_r \sigma^2 \tag{5.10}$$

where k_r = parabolic growth rate constant [m s^{-1}].

This equation is also known as the parabolic growth law (see Figure 5.8).

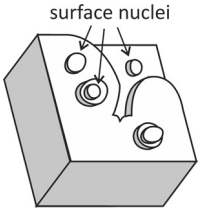

Figure 5.7 Birth and spread model (Mullin, 2003). Copyright Wiley-VCH Verlag GmbH & Co. KGaA.

At high supersaturations:

$$R_{lin} = k_r \sigma \tag{5.11}$$

where, in this case, k_r = linear growth rate constant [m s^{-1}].

In other words, the dependence of the rate of crystal growth on the solution supersaturation changes from a parabolic to a linear dependence as supersaturation increases. This is because the diffusion rate slows down as the supersaturation increases, and thus, in diffusion-limited growth, there will be a linear dependency at higher supersaturations (O'Hara and Reid, 1973). Note that k_r is directly related to the solubility of the compound in the solution via f^*.

5.5.1.2 Birth and spread (B&S) model

The birth and spread (B&S) model is a layer growth model that is also referred to as the "nuclei upon nuclei" model, the "two-dimensional nucleation" model, or the polynuclear model. Its step source comes from the formation of two-dimensional nuclei on the crystal surface, which grow into islands by spreading laterally along the crystal surface. An island can either grow and cover the whole surface area before a new island is formed on top of it (the mononuclear model) or, more realistically, islands can nucleate all over the surface and incorporate the new incomplete layers formed by laterally spreading islands, as depicted in Figure 5.7. In this model, the steps along the islands are assumed to be isotropic (uniform in all directions). In reality, this is normally not the case, and the steps are aligned along the crystallographically important directions that also border the sides of the crystal face.

Two-dimensional nucleation can occur only if the supersaturation is sufficient to overcome the 2-D nucleation barrier. The critical size of a 2-D nucleus is given by equation 5.8.

The linear growth rate for this mechanism is given by:

$$R_{lin} = \left(\frac{1}{3}\pi v_{step}^2 J_{2D}\right)^{1/3} h \tag{5.12}$$

where R_{lin} = linear growth rate [m s^{-1}], v_{step} = step velocity [m s^{-1}], J_{2D} = 2-D nucleation rate [# m^{-2} s^{-1}] and h = height of a growth unit [m].

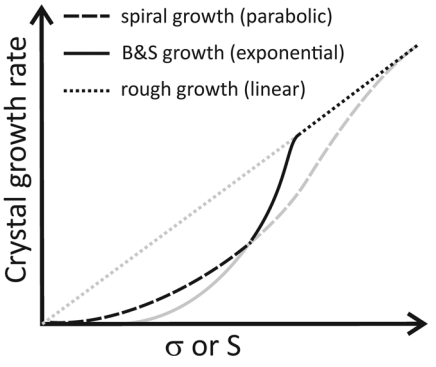

Figure 5.8 Growth curves for spiral, birth and spread and rough growth.

O'Hara and Reid (1973) employed the nucleation theory to develop an expression for the rate of formation of 2-D nuclei per unit surface area per unit time.

$$J_{2D} = A_{2D} S \, \mathrm{e}^{\left[\frac{B_{2D}}{\ln S}\right]} \tag{5.13}$$

with

$$A_{2D} = z C_o f(n^*_{2D}) \tag{5.14}$$

and

$$B_{2D} = \frac{\pi h V_m \gamma^2_{edge}}{(kT)^2} \tag{5.15}$$

where J_{2D} = 2-D nucleation rate [# m^{-2} s^{-1}], S = supersaturation ratio, z = Zel'dovich factor (explained in Chapter 4, Nucleation), C_0 = concentration of active sites [# m^{-3}] and $f(n^*_{2D})$ = frequency of attachment of growth units at the edge of a critical nucleus with a surface area of $2\pi r^*_{2D} h$ [s^{-1}]. This leads to:

$$R_{lin} = k_r (S-1)^{2/3} S^{1/3} \, \mathrm{e}^{-\frac{B_{2D}}{3 \ln S}} \tag{5.16}$$

where k_r = exponential growth rate constant.

In the original derivation by O'Hara and Reid (1973) $(\ln S)^{1/2}$ was used in the equation for J_{2D} instead of S and the expression for R_{lin} was approximated by:

$$R_{lin} = k_r \sigma^{5/6} \, \mathrm{e}^{-\frac{B_{2D}}{3\sigma}} \tag{5.17}$$

Note that, once again, since f^* is related to the solubility of the compound, the growth rate R_{lin} depends on the solubility.

Due to the exponential term in the expression for the linear growth rate R_{lin} the linear growth rate increases steeply once the critical value of the supersaturation needed for 2-D nucleation is exceeded (see Figure 5.8). Figure 5.9 shows the birth and spread of nuclei on the basal face of gibbsite.

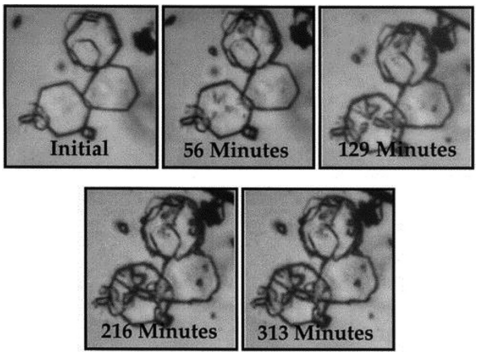

Figure 5.9 Birth and spread of nuclei on the basal face of gibbsite (Lee and Parkinson, 1999). Copyright Elsevier. Reproduced with permission.

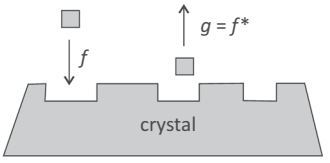

Figure 5.10 Fluxes of growth units to and from a rough crystal surface.

5.5.2 Rough growth

Rough surfaces always affect the quality of the crystals in a negative way and the occurrence of rough crystal surfaces should be prevented by a careful selection of the operating conditions to control σ and T.

Sometimes, however, rough surfaces are unavoidable. Because preferential growth sites are no longer present on the crystal surface, the growth rate of these faces simply depends on the difference between the flux of growth units from the bulk that impinges on a growth position in the crystal surface, and the flux of growth units that leaves the surface (see Figure 5.10). The number of growth units j that stick to a growth unit of surface area h^2 then equals:

$$j = (f - g)h^2 \tag{5.18}$$

The flux density g equals the equilibrium flux density f^*, and:

$$\begin{aligned} j &= f^* \left[e^{\frac{\Delta\mu}{kT}} - 1 \right] h^2 \\ &= h^2 f^* (S - 1) = h^2 f^* \sigma \end{aligned} \tag{5.19}$$

When a growth unit is attached to the crystal surface, a length h (= the height of a growth unit) is added to it in the direction normal to the crystal surface, and the linear growth rate R_{lin} becomes:

$$R_{lin} = jh = f^* V_m \sigma \tag{5.20}$$

$$R_{lin} = k_r \sigma \tag{5.21}$$

k_r is once again proportional to f^*, and thus related to the solubility of the compound. It is not surprising that R_{lin} is linearly dependent on σ for rough growth (see Figure 5.10). A rough estimate of R_{lin} can be made by calculating f^* in the same way as has been done for $f_0(n^*)$ in Chapter 4.

From comparison of the three surface integration-controlled growth curves, drawn in Figure 5.8, it follows that, at low σ values, the spiral growth mechanism dominates the process. At higher σ values, the B&S mechanism takes over and, at still higher σ values, where the surface is roughened, a linear growth mechanism dominates.

Under normal operating conditions, spiral growth is the most commonly encountered growth mechanism. Although, in this model, k_r is proportional to the solubility, Nielsen (1984) clearly demonstrated that, for electrolytes that obey the parabolic rate law, the value of k_r is not only governed by c_{eq}, but also by the integration frequency ($= 10^{-3}$ times the dehydration frequency). This is due to the activation energy of diffusion, as an ion, in order to integrate, must dehydrate and make a diffusional jump at the same time.

5.5.3 Thermal and kinetic roughening

Besides rough growth due to conditions of high supersaturation, crystal faces that are flat under moderate growth conditions (as depicted in Figure 5.3) can become roughened either by thermal or kinetic roughening. There is only a gradual difference between rough growth and kinetic roughening. At severe kinetic roughening the faces become curved. You need a roughened surface to have rough growth, and that can either happen because the supersaturation is too high or (for weak organic crystals) because the temperature is too high. Thermal roughening for a salt will never occur.

5.5.3.1 Thermal roughening

Each crystal face (hkl) has a critical temperature T_R, the roughening temperature, above which value the surface becomes rough. For salts, the roughening temperatures of the observed crystal faces are extremely high because of the strong ionic interactions, and, under normal operating temperatures, thermal roughening is not observed. For salts there is never thermal roughening below the melting temperature. The ionic bonds are too high to allow the edge free energy to become zero. It must cost no energy to remove a building unit from a position in a growth layer to a position on top of that layer. That is the meaning of zero edge free energy. The bonds of a building unit with its neighbors must thus become zero at the thermal roughening temperature.

In contrast, for organic compounds, roughening temperatures can sometimes lie quite close to room temperature, as for paraffin crystals growing from a hexane solution, where T_R equals 11 °C for the [110] faces. See Figure 5.12.

The order parameter for this smooth–rough phase transition of the surface is the edge free energy, γ_{edge}, which becomes zero at $T = T_R$. This implies that roughening of the surface, i.e. the creation of a larger surface area (see Figure 5.12) costs no additional (edge) free energy. A growth unit can then be positioned anywhere on the crystal surface.

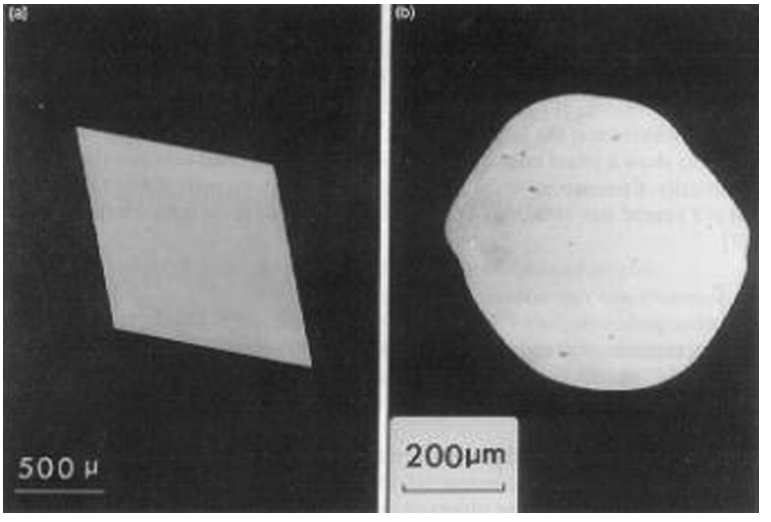

Figure 5.11 Paraffin crystal grown from hexane at (a) 6 °C and (b) 20 °C (Bennema, 1993) Copyright Elsevier. Reproduced with permission.

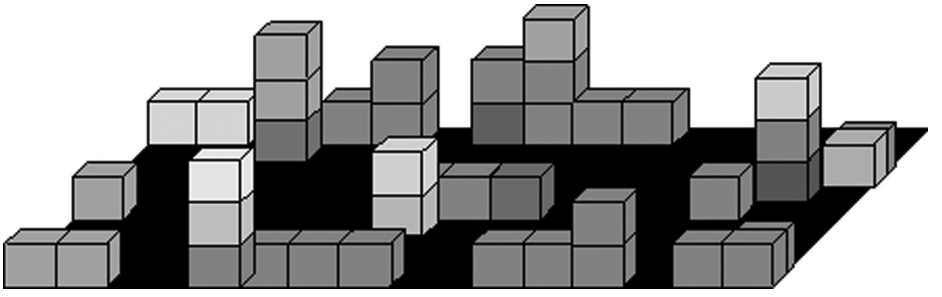

Figure 5.12 Surface roughening at $T \geq T_R$.

For rough growth, the crystal faces tend to become rounded, especially at their edges, and the crystals are no longer nicely facetted (see Figure 5.12).

5.5.3.2 Kinetic roughening

Another roughening phenomenon, called "kinetic roughening," is caused by very high supersaturation levels, and can also be observed for salts. If the driving force for crystallization, $\Delta\mu$, exceeds a value for which the corresponding two-dimensional critical nucleus (see Section 5.5.1.2, Birth and spread model) becomes of the order of a growth unit or, more precisely, for $\Delta\mu$ values where the activation energy required for the formation of a two-dimensional critical nucleus becomes of the order of kT, then the crystal surface becomes roughened. The main difference between the two roughening mechanisms is that, during kinetic roughening, the edge free energy is still non-zero. An example of kinetic roughening is presented in Figure 5.13.

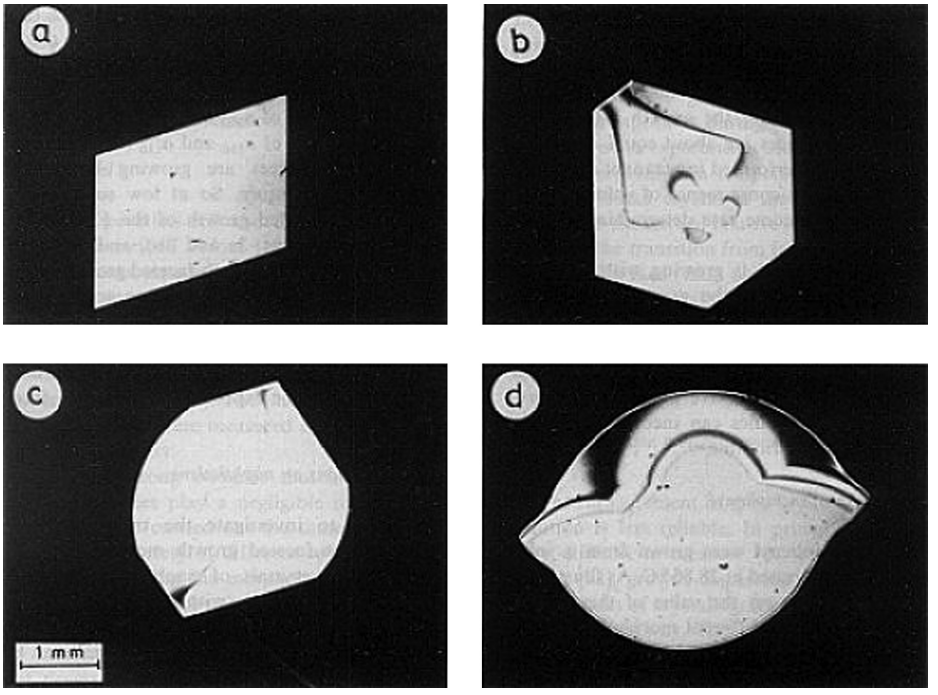

Figure 5.13 Naphthalene in toluene: (a) $\sigma = 0.1\%$, (b) $\sigma = 0.3\%$, (c) $\sigma = 1.1\%$, (d) $\sigma = 1.5\%$ (Jetten *et al.*, 1984). Copyright Elsevier. Reproduced with permission.

5.6 Volume diffusion-controlled growth

Volume diffusion-controlled growth usually dominates for very soluble compounds where surface integration is not rate limiting, but where the supply or diffusion of growth units through the stagnant boundary layer to the crystal surface is the rate-limiting step. It is therefore also called the diffusion layer model.

For this growth model, Fick's law can be used (even for rather concentrated solutions) and the mass increase of a crystal is given by:

$$\frac{\mathrm{d}m_{crystal}}{\mathrm{dt}} = \frac{D}{\delta} A_{crystal}(c_b - c_{eq}) \tag{5.22}$$

where $c_b - c_{eq}$ = the driving force for mass transport [kg m^{-3}], δ = boundary layer thickness [m] and D = diffusion coefficient [m^2 s^{-1}].

The mass transfer coefficient, k_d, is given by:

$$k_d = \frac{D}{\delta} \tag{5.23}$$

and follows from the equation for the Sherwood number:

$$Sh = \frac{k_d L}{D} \tag{5.24}$$

For the calculation of Sh, several correlations provided in the literature can be used, such as $Sh = 2 + 0.6\ Re^{1/2}\ Sc^{1/3}$(Hauke, 2008). The values for Sh generally lie between 2 and 10 (see worked example 1). A correction is only needed for highly concentrated solutions in order to account for convective transport (for counterdiffusion of the water molecules):

$$\frac{\mathrm{d}m_{crystal}}{\mathrm{d}t} = \frac{k_d}{(1-w)} A_{crystal}(c_b - c_{eq}) \tag{5.25}$$

with w = mass fraction of the solute and k_d = mass transfer coefficient [m s^{-1}].

So, for most solutions, the overall linear growth rate is given by:

$$R_{lin} = \frac{k_a}{6k_v\rho_{crystal}} \cdot \frac{1}{A_{crystal}} \cdot \frac{\mathrm{d}m_{crystal}}{\mathrm{d}t} = \frac{k_a k_d}{6k_v\rho_{crystal}}(c_b - c_{eq}) \tag{5.26}$$

or by:

$$R_{lin} = \frac{k_a k_d}{6k_v\rho_{crystal}} c_{eq}\sigma \tag{5.27}$$

The dependency of R_{lin} on σ is first order and R_{lin} is directly related to the solubility c_{eq}. If this $R_{lin}(\sigma)$ line is plotted, it always generates the maximal growth rate at which a crystal can grow at a given supersaturation.

Worked example 1

Given the following information, calculate the volume diffusion-controlled growth rate of NaCl crystals.

$\rho_{crystal} = 2164$ kg m^{-3}
$c_{NaCl,bulk} = 316$ kg m^{-3}
$c_{eq,NaCl,bulk} = 315$ kg m^{-3}
L = crystal length = 205 µm
$Re_p = 0.3$
ν = kinematic viscosity = 2.94×10^{-6} m^2 s^{-1}
D = diffusion coefficient = 10^{-9} m^2 s^{-1}

Worked example 1 solution

The volume diffusion growth rate is:

$$\frac{\mathrm{d}m_{crystal}}{\mathrm{d}t} = \rho_{crystal}\frac{\mathrm{d}V_{crystal}}{\mathrm{d}t}$$

$$\frac{\mathrm{d}m_{crystal}}{\mathrm{d}t} = \frac{D}{\delta} A_{crystal}(c_b - c_{eq})$$

$$\frac{\mathrm{d}V_{crystal}}{\mathrm{d}t} = \frac{A_{crystal} n k_d}{\rho_{crystal}}(c_b - c_{eq})$$

$$G = \frac{k_a k_d}{3k_v\rho_{crystal}}(c_b - c_{eq})$$

Since, for a cube or sphere, $k_a/k_v = 6$:

$$G = \frac{2k_d}{\rho_{crystal}}(c_b - c_{eq})$$

Therefore:

$Sc = \nu/D = 2940$
$Sh = 2 + 0.66\, Re_p{}^{1/2} Sc^{1/3} = 7.18$
$k_d = D\, Sh/L = 3.5 \times 10^{-05}$ m s^{-1}
G $= 3.24 \times 10^{-8}$ m s^{-1}

5.7 Combined volume diffusion- and surface integration-controlled growth

Apart from the solubility, both the crystal size and the supersaturation range can have an effect on which of the two growth steps dominates. For very small crystals and for very low σ values surface integration is always the dominant growth process.

In many cases, however, both volume diffusion and surface integration have an effect on the final growth rate, and a combined equation has to be derived. For this purpose the two-step process can best be described by the following equations.

For diffusion:

$$R_A = k_d(c_b - c_i) \tag{5.28}$$

For integration:

$$R_A = k_r(c_i - c_{eq})^r \tag{5.29}$$

where R_A = increase in crystal mass per unit surface area per unit time [kg m^{-2} s^{-1}], c_b = bulk solute concentration [kg m^{-3}], c_{eq} = solubility [kg m^{-3}] and c_i = interfacial solute concentration [kg m^{-3}].

Equation 5.29 serves as a simplified growth-rate equation related to spiral, B&S or rough growth. Conservation of mass requires that the surface integration mass flux equals the diffusion mass flux to the crystal surface, and elimination of c_i from equations 5.28 and 5.29 leads to:

$$R_A = k_r \left[(c_b - c_{eq}) - \frac{1}{A_{crystal} k_d} \frac{\mathrm{d}m_{crystal}}{\mathrm{d}t}\right]^r \tag{5.30}$$

For $r = 1$, equation 5.30 can be rearranged into:

$$R_A = K_G(c_b - c_{eq}) \tag{5.31}$$

where K_G = mass-based crystal growth rate coefficient [m s^{-1}], c_b = bulk solute concentration [kg m^{-3}] and c_{eq} = solubility [kg m^{-3}] with:

$$\frac{1}{K_G} = \frac{1}{k_d} + \frac{1}{k_r} \tag{5.32}$$

The situation where $r = 1$ only occurs in the case of spiral growth with $\sigma \gg \sigma_1$, and for rough growth, which should preferably be avoided.

For lower σ values, spiral growth occurs with $r = 2$. For $r = 2$ the following equation is obtained from equation 5.30:

$$R_A = k_d(c_b - c_{eq}) + \frac{k_d^2}{2k_r} - \left[\frac{k_d^4}{4k_r^2} + \frac{k_d^3(c_b - c_{eq})}{k_r}\right]^{1/2} \tag{5.33}$$

For higher values of r, it is no longer possible to derive such a simplified expression for R_A.

However, these higher r values are only found for a B&S surface integration model, which describes the growth mechanism for less soluble salts and, for those cases, volume diffusion is generally not a rate-limiting step.

So, for engineering purposes, a simplified expression of this form is often used:

$$\frac{1}{A_{crystal}}\frac{\mathrm{d}m_{crystal}}{\mathrm{d}t} = K_G(c_b - c_{eq})^g \tag{5.34}$$

with (in general) $1 \leq g \leq 2$, and $g > 2$ only for less soluble compounds.

For substitution in the population balance equation, a linear crystal growth velocity defined as $G = \mathrm{d}L/\mathrm{d}t$ is needed. G is related to equation 5.34 via equation 5.1:

$$G = \frac{k_a K_G}{3k_v\rho_{crystal}}(c_b - c_{eq})^g = \frac{k_a K_G}{3k_v\rho_{crystal}}c_{eq}\sigma^g \tag{5.35}$$

or

$$G = k_g\sigma^g \tag{5.36}$$

where k_g = linear growth rate-based crystal growth rate coefficient [m s^{-1}].

Mersmann and Kind (1988) have plotted the linear growth rate for a number of salts as a function of the corresponding supersaturations. This plot (see Figure 5.14) shows that highly soluble salts have roughly linear growth rates of 10^{-7} m s^{-1} at σ values around 0.01, while slightly soluble salts have linear growth rates of 10^{-9} to 10^{-8} m s^{-1} at σ values of 10 to 100.

Their corresponding mean crystal size varies from about 600 μm for easily soluble salts to 10 μm for slightly soluble salts (see Figure 5.15).

5.8 Effect of temperature

Both the surface integration and the volume diffusion step are temperature dependent. This dependence can be characterized by:

$$k_r = k_{ro}\mathrm{e}^{-E_r/RT} \tag{5.37}$$

and

$$k_d = k_{do}\mathrm{e}^{-E_d/RT} \tag{5.38}$$

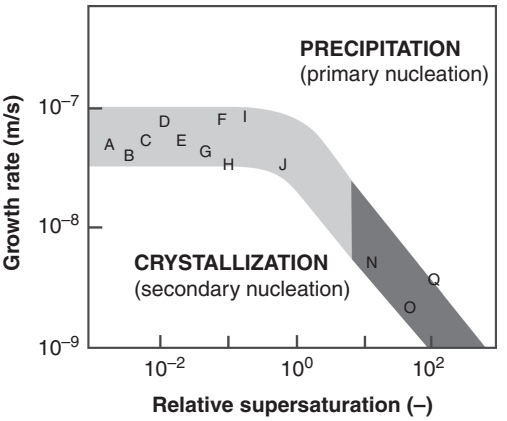

Figure 5.14 Growth rate of a number of salts versus relative supersaturation (Mersmann and Kind, 1988) A: KCl, B: NaCl, C: $(NH_2)_2CS$, D: $(NH_4)_2SO_4$, E: KNO_3 F: Na_2SO_4, G: K_2SO_4, H: $(NH_4)Al(SO_4)_2$, I: $K_2Cr_2O_7$, J: $KAl(SO_4)_2$, N: $CaCO_3$, O: T_iO_2, Q: $BaSO_4$. Copyright John Wiley & Sons. Reproduced with permission.

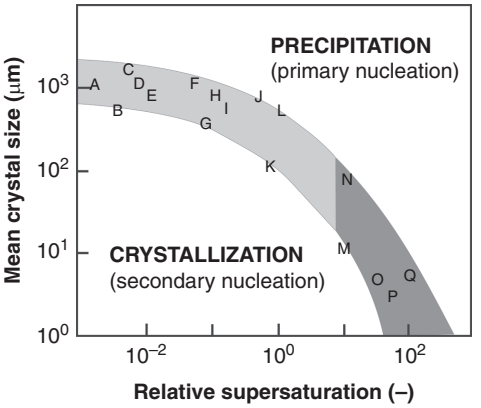

Figure 5.15 Mean crystal size versus relative supersaturation (Mersmann and Kind, 1988) A: KCl, B: NaCl, C: $(NH_2)_2CS$, D: $(NH_4)_2SO_4$, E: KNO_3 F: Na_2SO_4, G: K_2SO_4, H: $(NH_4)Al(SO_4)_2$, I: $K_2Cr_2O_7$, J: $KAl(SO_4)_2$, K: $KClO_3$, L: $NiSO_4$, M: BaF_2, N: $CaCO_3$, O: T_iO_2, P: CaF_2, Q: $BaSO_4$. Copyright John Wiley and Sons. Reproduced with permission.

where E_r and E_d are the corresponding Arrhenius activation energies. E_r is typically of the order of 40 to 60 kJ mol^{-1}, while E_d is in the order of 10 to 20 kJ mol^{-1}.

5.9 Heat transfer-controlled growth

For crystal growth from solution, the transfer of the heat of crystallization is not the rate-limiting step. Heat transfer comes into play only at very high solute concentrations or in the case of crystallization from the melt, since the latent heat of crystallization at

the crystal interface growing from its melt has to be transferred either to the melt or to a cooling surface. For heat transfer controlled growth, the mass transfer rate is given by:

$$\frac{\mathrm{d}m_{crystal}}{\mathrm{d}t} = -\alpha A_{crystal}\frac{\Delta T}{\Delta H_{cr}} \tag{5.39}$$

where α = heat transfer coefficient [W m^{-2} K^{-1}], $\Delta T = T_b - T_{eq}$, ΔH_{cr} = enthalpy of crystallization [J kg^{-1}], $\alpha = \lambda/\delta_h$, where λ = thermal conductivity [W m^{-1} K^{-1}] and δ_h = boundary layer thickness for heat transfer [m]. Here $\alpha = \lambda Nu/L$ with L = characteristic size of the crystal. Correlations for Nu are available in the literature.

5.10 Simultaneous mass and heat transfer

Situations exist where both mass and heat transfer determine the increase of mass in time $(\mathrm{d}m_{crystal}/\mathrm{d}t)_{m\&h}$. The combination of the mass transfer-based expression (equation 5.28 or 5.34 with $g = 1$) with the heat transfer expression (equation 5.39 and using the relationship between the ΔT and Δc driving forces given by Nývlt (1977) to convert the ΔT in equation 5.39 to an expression in c) leads to the following expression for crystal growth simultaneously limited by heat and mass transfer:

$$\left(\frac{\mathrm{d}m_{crystal}}{\mathrm{d}t}\right)_{m\&h} = \left[\left(\frac{\mathrm{d}m_{crystal}}{\mathrm{d}t}\right)_{mass}^{-1} + \left(\frac{\mathrm{d}m_{crystal}}{\mathrm{d}t}\right)_{heat}^{-1}\right]^{-1} = k_{m\&h}A_{crystal}(c_b - c_{eq}) \tag{5.40}$$

where $k_{m\&h}$ [m s^{-1}] is the overall mass transfer coefficient including the contributions of both mass and heat transfer. It is given by:

$$\frac{1}{k_{m\&h}} = \frac{1}{k_d c_{eq}(T_i)} + \frac{\Delta H_{cr}^2 c_{eq}(T_i)}{\alpha R T^2 M} \tag{5.41}$$

where c_{eq} = solubility (kg m^{-3}), M = molecular weight (kg mol^{-1}) of the crystallizing substance and R = ideal gas constant [(J K^{-1} mol^{-1})].

5.11 Growth rate dispersion

It has long been assumed that geometrically similar crystals of the same material have the same growth rate under identical growth conditions. However, experimental results have shown that a batch of crystals with an initially narrow size distribution could broaden their distribution considerably during further outgrowth. Also, the size distribution of a population of crystals grown continuously in an MSMPR crystallizer showed an upward curvature in the ln n versus L curve for the smaller crystals (see Figure 5.16).

This can only be explained if the smaller crystals have smaller growth rates. It is only when the newly born crystals reach a certain size L' that their growth rate reaches that of their parent crystals.

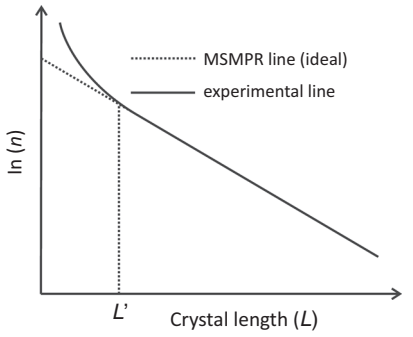

Figure 5.16 CSD from an MSMPR crystallizer.

This phenomenon was called *size-dependent growth* and size-dependent growth-rate functions were introduced to describe the observed CSD:

$$G_L(L, t) = G(L)G(t) \tag{5.42}$$

where $G(t)$ depends on the relative supersaturation $\sigma(t)$, and $G(L)$ on the size of the crystal.

The most often applied $G(L)$ functions were reviewed by Garside and Jancic (1978), by Tavare (1985) and by Berglund (1984), but also more recently the following equation was introduced by Wang and Mersmann (1992)

$$G(L) = 1 - \mathrm{e}^{-\left(\frac{L}{L_g}\right)^n} \tag{5.43}$$

where n and L_g are fit parameters.

It was also demonstrated by following the outgrowth of tiny crystals, born by either primary or secondary nucleation under a microscope, that not all small crystals of the same size had the same growth rate under identical conditions. This phenomenon was called *growth-rate dispersion*. Measurements by Ristić *et al.* (1990) showed that, for several substances, the smaller crystals, ranging in size from about 1 to 200 μm depending on the substance, contained a high degree of disorder. For crystals born by secondary contact nucleation this disorder results from the amount of stress introduced into the attrition fragments during collision of the parent crystals. Whether these nuclei survive and grow into the population depends on their stress content and on the prevailing supersaturation. If they grow out, the stress content of the initial fragments gives rise to the development of crystals consisting of smaller blocks, which are slightly misoriented with respect to one another. This misorientation is quantified by the mosaic spread η (related to the misfit angle), and can be determined from a Laue X-ray diffraction pattern (see Figure 5.17).

When the crystals grow further, the stress content of their outer shell decreases, a phenomenon called healing, and, beyond a certain size, the average growth rate of the crystals becomes the same as that of their parent crystals.

Because of the stress content of the smaller crystals, their solubility is higher, and they experience a lower supersaturation than the σ value calculated for the larger crystals.

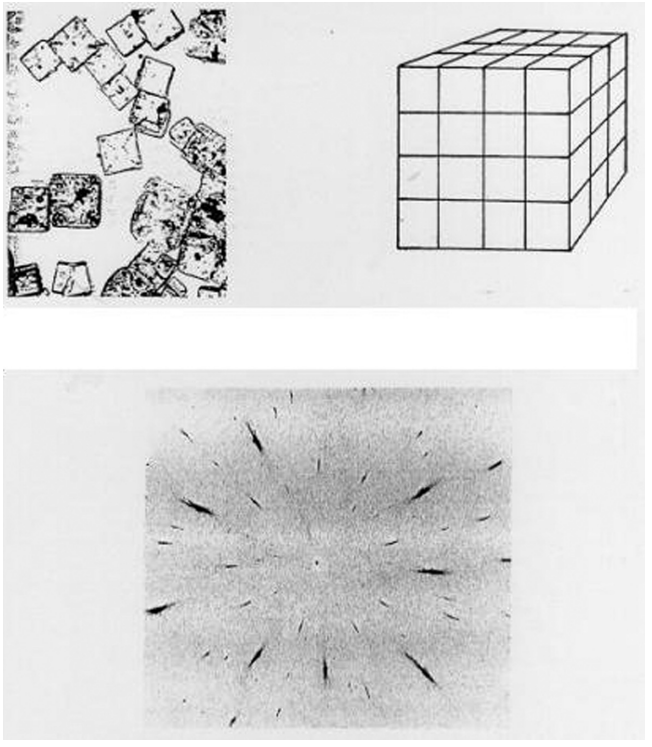

Figure 5.17 Small crystal with a mosaic structure that causes elongated instead of circular spots in a Laue diffraction pattern (Davey *et al.*, 1991). Copyright Elsevier. Reproduced with permission.

So the growth rate of the smaller crystals is represented by:

$$G_L(\eta, L, t) = k_g \left(\sigma - \frac{W_i(\eta, L)}{kT}\right)^g \tag{5.44}$$

where W_i = stress energy per crystal [J].

A simplified expression for W_i was derived by van der Heijden and van der Eerden (1992):

$$W_i = \frac{A_1 \eta}{\sqrt{L}} \ln\left(\frac{A_2\sqrt{L}}{\eta}\right) \tag{5.45}$$

with η (the mosaic spread) in rad and with:

$$\begin{aligned} A_1 &= \frac{3\mu b V_m}{8\pi(1-\upsilon)\sqrt{l}} \\ A_2 &= \frac{\alpha b}{4\pi r_c} \\ \ln\alpha &= \frac{3}{4(1-\upsilon)} \end{aligned} \tag{5.46}$$

where μ = shear modulus, b = Burgers vector [m], V_m = molecular volume [m^3 $molecule^{-1}$], υ = Poisson ratio, l = distance between point defects over the crystal [m] and r_c = length scale below which linear elasticity theory breaks down [m].

Since equations 5.44 and 5.45 clearly show the dependence of G on L, and since this equation for a constant average value of η can easily be transformed into a size-dependent function, this explains why the current size-dependent growth and growth-rate dispersion functions are not mathematically distinguishable. Both phenomena have the same physical basis. Equation 5.44 can also be used for the calculation of the growth rates of the smaller crystals. In that case, W_i in equation 5.44 is replaced by $\Gamma / L_{fragment}$, where Γ is a material property.

A surprising fact is that primary nuclei, as observed by microscopic experiments, also show growth-rate dispersion. A possible explanation for this is that stress can be built up during the outgrowth of primary clusters.

5.12 Enhanced growth rate of crystals by addition of macro-building blocks

Enhanced growth rate of crystals by addition of macro building blocks is a phenomenon that has been investigated by a number of researchers (Matsuoka and Eguchi, 1993, Matsuoka *et al.*, 1996, Takiyama *et al.*, 1998, 2002). The concept of the method is that it can be applied in order to increase the growth rate of crystals by a factor of 2 to 5. It only happens for very soluble compounds; for slightly soluble salts the mechanism reverts to agglomeration.

The method uses a suspension of crystals in a slightly supersaturated solution that is fed with tiny crystals prepared separately by nucleation (and marginal outgrowth) in a highly supersaturated solution. After feeding, these tiny crystals grow or agglomerate onto the much larger crystals of the suspension. Whether the tiny crystals align almost perfectly on the larger surfaces and grow out along their edges as macro-steps, or whether they dissolve on the larger surfaces and contribute to the growth is something that is still the subject of current research (Masaoka *et al.*, 2014).

5.13 Dissolution of crystals

During dissolution the edges of the crystals act as step sources for the dissolution process. For this reason the edges and corners of the crystals are quite easily rounded off once dissolution starts. Etch pits are also formed in the crystal surface at places, where dislocations emerge at the crystal surface, because stress is stored in the crystal lattice around these dislocations. Such etch pits are also (negative) nuclei and thus step sources for dissolution. Disintegration of the crystal surface is therefore a much faster process than surface integration-controlled growth, because more steps are available. A rough surface is also easily created, and the surface disintegration step becomes less rate limiting than the integration step for growth. So in many cases of dissolution, volume diffusion becomes the rate limiting step, and the dissolution rate can be described in

analogy with equation 5.22 by:

$$-\frac{1}{A_{crystal}}\frac{\mathrm{d}m_{crystal}}{\mathrm{d}t} = k_d(c_{eq} - c_b) \tag{5.47}$$

Also a combined volume diffusion and rough surface disintegration-controlled growth may occur, where, analogous with equations 5.31 and 5.32, the dissolution rate becomes:

$$-\frac{1}{A_{crystal}}\frac{\mathrm{d}m_{crystal}}{\mathrm{d}t} = K_D(c_{eq} - c_b) \tag{5.48}$$

with

$$\frac{1}{K_D} = \frac{1}{k_d} + \frac{1}{k_{r,D}} \tag{5.49}$$

In both cases the dissolution rate is first order in $(c_{eq} - c_b)$, and, if the crystals can be treated as spheres (see equation 5.2), the linear dissolution rate D_{lin} equals:

$$D_{lin} = \frac{2}{\rho}K_D(c_{eq} - c_b) \tag{5.50}$$

Only for very insoluble substances such as $BaSO_4$ and CaF_2 does the dissolution proceed by peeling off subsequent layers, and the dissolution rate is of higher order in $(c_{eq} - c_b)$.

Also for low supersaturations and for small crystals that remain within their Kolmogorov eddies, the dissolution process is controlled by a surface reaction process.

But, in general, it can be stated that, for a given undersaturation value Δc, the dissolution rate D is always larger than the growth rate G.

5.14 Measuring the growth rate

Measuring the crystal growth rate can be achieved by: (a) direct measurement of the linear growth rate of individual crystals or (b) indirect measurement of the growth rate of populations of crystals via mass deposition rates. Growth measurements on single crystals are preferred because the effects of collisions with the impeller and vessel sides and of fluid dynamics are avoided and because it might be necessary to study large crystals that are difficult to suspend in a solution (Garside *et al.*, 2002).

5.14.1 Direct measurement of the linear growth rate of individual crystals

The linear growth rate of single crystals can be studied by observing the individual crystal face growth rates of a crystal suspended in a glass cell. The measurement is usually conducted under conditions of precisely controlled solution temperature, supersaturation and liquid velocity. With this set-up, the lateral velocity of the moving faces can be observed using transmission light microscopy via an optical microscope (Richardson *et al.*, 2002). However, if measurement of step velocities is required, then more sophisticated techniques are necessary (Garside *et al.*, 2002).

5.14.2 Indirect measurement of the growth rate of populations of crystals via mass deposition rates

5.14.2.1 Batch measurements

Indirect measurements of the growth rate of populations of crystals in batch, multi-particle crystallizers have a number of advantages: the batch experiments are easy to conduct and the average growth rate measured is suitable for crystallizer design (Garside *et al.*, 2002). The simplest method is the fluidized bed method, which involves growing large numbers of specifically sized seeds under fluidized and carefully controlled conditions (Richardson *et al.*, 2002). An undersaturated, warm solution of known concentration is circulated in the crystallizer and then supersaturated by cooling. A known mass of seed crystals with a narrow size distribution is introduced to the crystallizer and maintained in a fluidized state with the upflow velocity in the crystallizer. The crystals are allowed to grow for a specified time, then are removed, washed, dried and weighed. The final solution concentration is measured; the mean of the initial and final supersaturations is taken as the average for the run and the overall crystal growth rate is calculated from the mass deposited per unit area per unit time at the specific supersaturation.

The "solution side" and the "solid side" mass balances are linked to one another and can be independently checked using equation 5.51:

$$-\frac{\mathrm{d}w}{\mathrm{d}t} = \frac{1}{\rho_{liquid} V_{liquid}} \frac{\mathrm{d}m_{crystal}}{\mathrm{d}t} \tag{5.51}$$

where w = solute mass fraction in the liquid phase [kg (kg solution)$^{-1}$], $m_{crystal}$ = mass of crystals in suspension [kg], ρ_{liquid} = density of the solution [kg m^{-3}] and V_{liquid} = volume of solution in the crystallizing system.

5.14.2.2 Continuous measurements

The steady state mixed-suspension mixed-product removal (MSMPR) method for measurement of kinetics (both nucleation and growth rates) has been widely adopted. Three essential assumptions are that: (i) the total crystallizer content is perfectly mixed, (ii) nucleation and growth are the only mechanisms in operation and (iii) the feed is crystal-free. These assumptions are not always true and thus this method has limited applicability for systems with fast kinetics.

Consider the well-mixed, steady-state crystallizer operating at constant slurry volume illustrated in Figure 5.18.

For size-independent growth, the following population balance applies:

$$G\frac{\mathrm{d}n(L)}{\mathrm{d}L} + \frac{n(L)}{\tau} = 0 \tag{5.52}$$

where G = size-independent overall growth rate of crystals (m s^{-1}), $n(L)$ = number density of crystals of size L (m^{-4}) and τ = residence time (s).

Integration of equation 5.51 gives the following relationship between the population density n, the crystal size L, crystal growth rate G and the residence time τ.

$$n(L) = n_0 e^{-L/(G\tau)} \tag{5.53}$$

This gives a straight line when plotted on semilogarithmic coordinates. The growth rate can thus be determined from the slope of the line, which is $(-1/G\tau)$ and the intersection

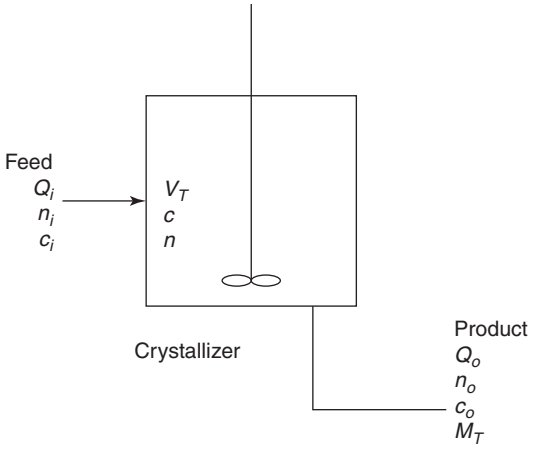

Figure 5.18 A well-mixed, steady-state crystallizer operating at constant slurry volume.

of the line with the ordinate (at $L = 0$) gives n_0, which can be used to calculate the effective nucleation rate from equation 5.54.

$$B_0 = n_0 G \tag{5.54}$$

5.15 A brief summary of the chapter

Crystal growth is the size enlargement of crystals by the deposition of growth units, preferably in layers. Crystal growth has a significant effect on the morphology of the crystal. Which growth mechanisms are dominant in a crystallization process (spiral, birth and spread or rough growth) is determined by the material to be crystallized and by the level of supersaturation. Smooth growth occurs mainly at lower supersaturations and rough growth dominates as the supersaturation level increases. Volume diffusion-controlled growth usually dominates for easily soluble compounds, when the supply or diffusion of growth units through the stagnant boundary layer to the crystal surface is the rate-limiting step. Surface integration-controlled growth usually dominates at low supersaturation levels, when the supply of growth units is plentiful, but their incorporation into the crystal surface is the rate-limiting step.

5.16 End of chapter problems

Problem 1: Growth rate measurement of hydroxy apatite: $Ca_{10}(PO_4)_6(OH)_2$

Using the graph given below, calculate the growth rate of the fastest growing face of the femur. Which is the fastest growing face? Which face determines the morphology of the bone?

Given that the growth rate of hydroxy-apatite has been modeled as follows (Dejeu *et al.*, 2010):

$$G = k_g(\sigma + 1)^g$$

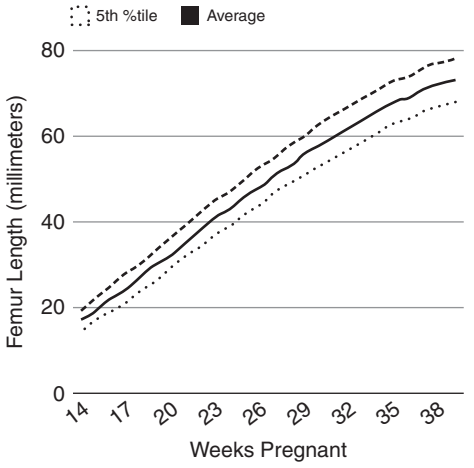

Figure 5.19 Femur length as a function of number of weeks of pregnancy (Snijders and Nicolaides, 1994).

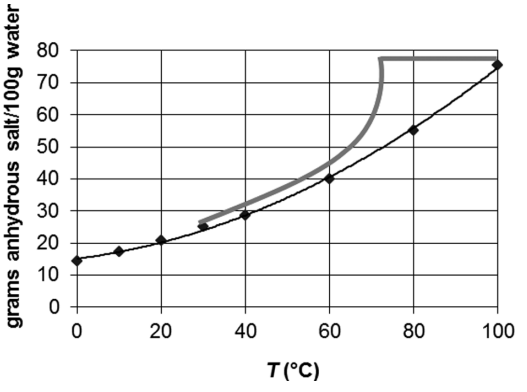

Figure 5.20 Cooling curve for copper sulfate crystallization.

with $k_g = 1 \times 10^{-13}$ m s^{-1} and $g = 2$ (parabolic, or screw-dislocation growth), what is the supersaturation experienced by the femur *in utero*, i.e. during growth?

Problem 2

A hot copper sulfate aqueous solution is obtained from the acid attack of metallic copper waste. Particulate copper sulfate is then obtained by batchwise cooling of the solution in an agitated tank. At the end, the solids content is 20 vol% and the mean crystal mean size is 300 μm.

From the cooling curve given in Figure 5.20, calculate the supersaturation: (i) at the start of the batch and (ii) at the end of the batch. Judging from the supersaturation values, what are the likely growth mechanisms: (i) at the early stage of the batch and (ii) at late stages of the batch?

You want to obtain larger particles by adjusting the growth rate. How would you achieve this in each batch stage?

Problem 3

Ammonium nitrate is obtained by continuous crystallization. The residence time is 7200 s and the mean particle size is 500 μm.

(i) Determine the experimental particle growth rate.
(ii) Calculate the growth rate assuming diffusion-controlled growth.
(iii) Compare the two values obtained above to answer the following questions.

Do the particles grow by a molecular mechanism or by aggregation?
In the case of molecular mechanism, is the growth controlled by diffusion or surface integration?

Given information:

Bulk and equilibrium concentrations: $c_b = 1023$, $c^* = 992$ kg solute m^{-3} solution.
Schmidt number $Sc = 3000$
Particle shape factors: $k_a = 6$, $k_v = 1$.
Particle velocity in relation to solution (settling velocity): $4.10 - 3$ m s^{-1}

5.17 References

Bennema, P. 1993. Growth and morphology of crystals: Integration of theories of roughening and Hartman-Perdok theory. In *Handbook of Crystal Growth: Fundamentals, Thermodynamics and Kinetics*, Hurle, D. T. J. (ed.), North-Holland.

Berglund, K. and Larson, M. 1984. Modeling of growth rate dispersion of citric acid monohydrate in continuous crystallizers. *AIChE Journal*, **30**, 280–287.

Burton, W., Cabrera, N. and Frank, F. 1951. The growth of crystals and the equilibrium structure of their surfaces. *Philosophical Transactions of the Royal Society of London. Series A, Mathematical and Physical Sciences*, **243**, 299–358.

Davey, R. J., Harding, M. M. and Rule, R. J. 1991. The microcrystalline nature of cubic, dendritic and granular salt. *Journal of Crystal Growth*, **114**, 7–12.

Dejeu, V. R., Reka, B., Cormos, A.-M., Sára, B. E. and Agachi, P.-S. 2010. *Growth Rate of Hydroxyapatite Crystals Obtained by Precipitation*. Studia Universitatis Babes-Bolyai, Chemia.

Dhanaraj, G., Byrappa, K. and Prasad, V. 2010. *Springer Handbook of Crystal Growth*, Springer.

Frank, F. C. 1949. The influence of dislocations on crystal growth. *Discussions of the Faraday Society*, **5**, 48–54.

Garside, J. and Jancic, S. J. 1978. Prediction and measurement of crystal size distributions for size-dependent growth. *Chemical Engineering Science*, **33**, 1623–1630.

Garside, J., Mersmann, A., Nývlt, J. *et al.* 2002. *Measurement of Crystal Growth and Nucleation Rates*, Institution of Chemical Engineers.

Hauke, G. 2008. *An Introduction to Fluid Mechanics and Transport Phenomena*, Springer Science+Business Media B.V.

Jetten, L. A. M. J., Human, H. J., Bennema, P. and Van Der Eerden, J. P. 1984. On the observation of the roughening transition of organic crystals, growing from solution. *Journal of Crystal Growth*, **68**, 503–516.

Judat, B. and Kind, M. 2004. Morphology and internal structure of barium sulfate–derivation of a new growth mechanism. *Journal of Colloid and Interface Science*, **269**, 341–353.

Kashchiev, D. 2008. Toward a better description of the nucleation rate of crystals and crystalline monolayers. *The Journal of Chemical Physics*, **129**, 164701.

Lee, M.-Y. and Parkinson, G. M. 1999. Growth rates of gibbsite single crystals determined using in situ optical microscopy. *Journal of Crystal Growth*, **198–199**, 270–274.

Lin, M., Fu, Z. Y., Tan, H. R. *et al.* 2012. Hydrothermal synthesis of CeO_2 nanocrystals: Ostwald ripening or oriented attachment? *Crystal Growth and Design*, **12**, 3296–3303.

Masaoka, K., Misumi, R., Nishi, K. and Kaminoyama, M. 2014. Enhancement in the crystal growth rate for a classified bed-type crystallizer using the adhesion phenomena of fine crystals. *Journal of Chemical Engineering of Japan*, **47**, 78–84.

Matsuoka, M. and Eguchi, N. 1993. Growth of m-chloronitrobenzene crystals in the presence of microcrystals. *Journal of Physics D: Applied Physics*, **26**, B162.

Matsuoka, M., Kamada, T. and Takiyama, H. 1996. Growth rate enhancement of potash alum crystals by microcrystals. *Journal of Crystal Growth*, **158**, 322–327.

Mersmann, A. and Kind, M. 1988. Chemical engineering aspects of precipitation from solution. *Chemical Engineering and Technology*, **11**, 264–276.

Mullin, J. W. 2003. Crystallization and precipitation. In *Ullmann's Encyclopedia of Industrial Chemistry*, Ullmann, F. and Gerhartz, W. (eds.) VCH.

Nielsen, A. E. 1984. Electrolyte crystal growth mechanisms. *Journal of Crystal Growth*, **67**, 289–310.

Nývlt, J. 1977. *Solid–Liquid Phase Equilibria*, Elsevier Scientific Publications.

O'Hara, M. and Reid, R. C. 1973. *Modeling Crystal Growth Rates from Solution*, Prentice-Hall.

Richardson, J. F., Coulson, J. M., Harker, J. H. and Backhurst, J. R. 2002. *Coulson and Richardson's Chemical Engineering: Particle Technology and Separation Processes*, Butterworth-Heinemann.

Ristić, R., Sherwood, J. and Shripathi, T. 1990. Strain variation in the {100} growth sectors of potash alum single crystals and its relationship to growth rate dispersion. *Journal of Crystal Growth*, **102**, 245–248.

Snijders, R. and Nicolaides, K. 1994. Fetal biometry at 14–40 weeks' gestation. *Ultrasound in Obstetrics and Gynecology*, **4**, 34–48.

Sunagawa, I. 2005. *Crystals: Growth, Morphology and Perfection*, Cambridge University Press.

Sunagawa, I. and Yokogi, A. 1999. Beryl crystals from pegmatites: Morphology and mechanism of crystal growth. *Journal of Gemmology*, **26**, 521–533.

Takiyama, H., Eto, T. and Matsuoka, M. 2002. Effects of suspension density on crystal growth rate in multiparticle agitated crystallizers. *Journal of Chemical Engineering of Japan*, **35**, 1045–1049.

Takiyama, H., Tezuka, N., Matsuoka, M., Ristic, R. I. and Sherwood, J. N. 1998. Growth rate enhancement by microcrystals and the quality of resulting potash alum crystals. *Journal of Crystal Growth*, **192**, 439–447.

Tavare, N. 1985. Crystal growth rate dispersion. *The Canadian Journal of Chemical Engineering*, **63**, 436–442.

van der Heijden, A. E. D. M. and van der Eerden, J. P. 1992. Growth rate dispersion: the role of lattice strain. *Journal of Crystal Growth*, **118**, 14–26.

Wang, S. and Mersmann, A. 1992. Initial-size-dependent growth rate dispersion of attrition fragments and secondary nuclei. *Chemical Engineering Science*, **47**, 1365–1371.

Yuwono, V. M., Burrows, N. D., Soltis, J. A. and Penn, R. L. 2010. Oriented aggregation: formation and transformation of mesocrystal intermediates revealed. *Journal of the American Chemical Society*, **132**, 2163–2165.

6 Agglomeration

6.1 Why this chapter is important

In the context of crystallization, agglomeration is the process in which two or more particles are brought in contact and stay together for a sufficiently long period such that a crystalline bridge between the particles can grow. Thus, a stable particle or agglomerate is formed. Particle agglomeration plays an important (and not always desirable) role in the formation of larger particles in precipitation and crystallization processes. Because of its significant effect on product quality, control over agglomeration is important for industrial crystallization (Hollander, 2002).

Figures 6.1 to 6.4 show examples of different types of agglomerates. It should be apparent from the pictures that the primary crystals that form agglomerates can be glued together in rather random ways. The agglomerates in the images lack the symmetry and the "esthetic beauty" of crystals formed due to growth. In fact, it is often the lack of symmetry that can be used to, at least qualitatively, identify the presence of agglomeration as a size enlargement process. The $MgSO_4 \cdot 7H_2O$ agglomerate in Figure 6.1 has a degree of symmetry that suggests that the individual "roses" are in fact a result of twinned growth, whilst the overall agglomerate is a consequence of the individual roses becoming agglomerated together. In contrast, both the agglomerates in Figure 6.2 have sufficiently disordered and random morphologies to be classified as true agglomerates.

In this chapter the physicochemical steps that lead to the formation of these agglomerates are described. In addition, the necessary mathematical models for describing the agglomeration process are discussed.

6.2 Agglomeration or aggregation?

A number of terms are used in literature to describe phenomena in which particles come together to form one entity. These include agglomeration, aggregation, conglomeration, coalescence, coagulation and flocculation. In this text, the convention adopted by Randolph and Larson (1988) is used.

- Agglomeration:the entities are formed by cementation of individual crystals together;
- Aggregation: the particles are more loosely bound and consist of mixtures of particles and agglomerates;

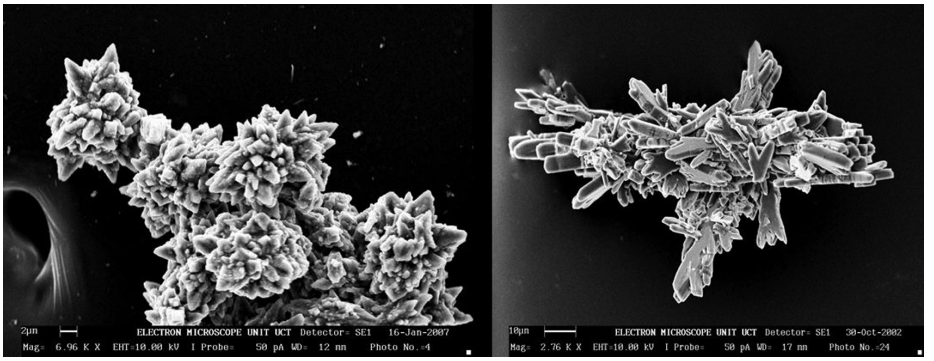

Figure 6.1 $MgSO_4 \cdot 7H_2O$ (left) and $NaHCO_3$ (right).

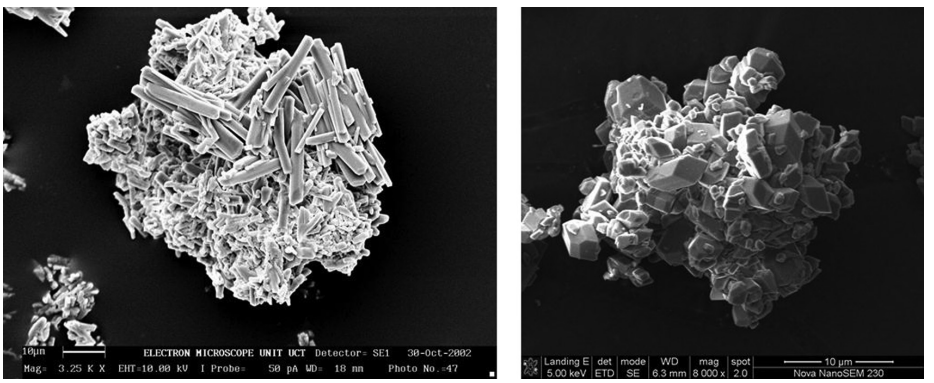

Figure 6.2 $NaHCO_3$ (left) and CaC_2O_4 (right).

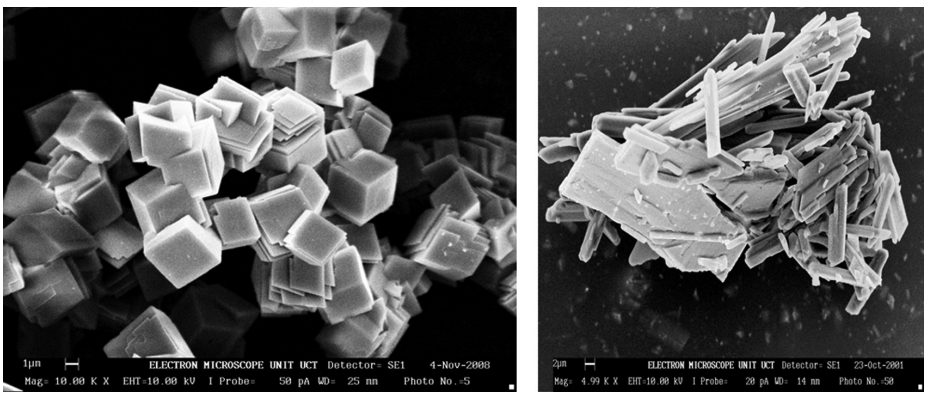

Figure 6.3 $CaCO_3$ (left) and $CaSO_4 \cdot 2H_2O$ (right).

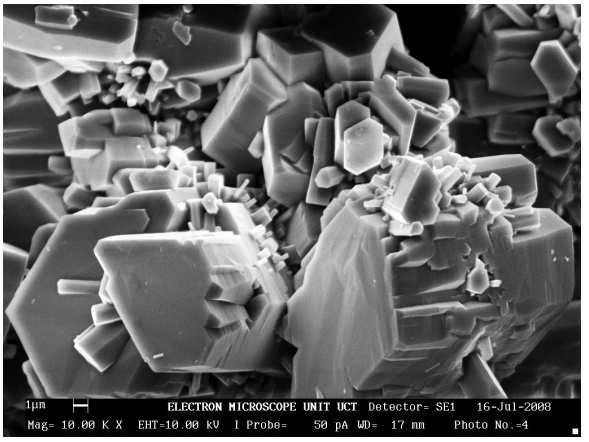

Figure 6.4 $Al(OH)_3$ (Gibbsite).

- Coalescence: droplets merge together;
- Coagulation: colloidal particles stick together due to compression of the double layer (due to the presence of salt or acid);
- Flocculation: aggregates are formed by polymers which adsorb onto the particles and form bridges between the particles.

The last three phenomena are not discussed here.

6.3 The agglomeration process

In crystallization, the formation of aggregates (in other words, the precursors to agglomerates) is a reversible process, with the rates of aggregation and break-up depending on the turbulent motion of the particles and the liquid. In addition to turbulence-induced forces, other inter-particle forces, like van der Waals forces, also act on the particles. These forces play a defining role in the attachment of the particles and thus the chance that the particles can be cemented together by the formation of bridges between the particles to form stable agglomerates. In general, agglomerates are formed by the following steps:

- Transport and collision with another particle;
- Attachment of the particles to form *aggregates*;
- *Either* rupture of the aggregates
- *Or* cementation of the particles by growth to form *agglomerates*.

Finally, the stable agglomerates can participate in the next round of the agglomeration process. The postulated steps in the formation of an agglomerate are presented in Figure 6.5.

It is also possible that all the sub-processes may occur simultaneously, so that partially cemented or loose aggregates can also trap new particles (Ilievski and White, 1994)

Each of the individual steps is briefly discussed here.

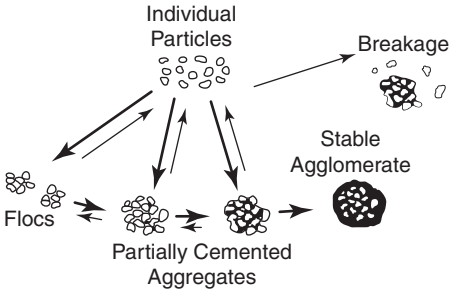

Figure 6.5 Postulated steps in the formation of an agglomerate (based on Ilievski and White, 1994).

6.3.1 Transport and collision of particles

The estimation of the relative motion of particles, and the resulting collision rate of these particles in a stirred vessel or other type of reactor has been subject of many studies (Hogg, 1992, Shamlou and Titchener-Hooker, 1993, von Smoluchowski, 1917), but are difficult to quantify. Nevertheless, for a number of simple cases, semi-empirical relations have been derived for different collision mechanisms. In this chapter these models will be discussed.

The basic equation relating the number of binary collisions per unit time between particles of size classes i and j is given by von Smoluchowski (1917):

$$r_{i,j} = \beta(L_i, L_j, T)N_i N_j \tag{6.1}$$

where $r_{i,j}$ = collision rate of particle i with particle j [$\#\,m^{-3}\,s^{-1}$], $\beta\,(L_i, L_j, T)$ = collision frequency kernel [$m^3\,\#^{-1}\,s^{-1}$] and N_i, N_j = number concentration of particles of size i or j [$\#\,m^{-3}$].

In order for particles to collide, the particles must move with respect to the fluid. The main transport mechanisms are: (i) Brownian motion, (ii) laminar or turbulent flow due to agitation and (iii) relative particle settling. The relevant agglomeration mechanism will then be determined by a combination of factors: the particle transport mechanism, the size of the particles and the Kolmogorov length scale. The Kolmogorov length scale is discussed in the section on transport and collision in stirred vessels.

There are three main mechanisms of particle transport (and thus collision).

1. *Brownian motion* is a form of particle motion induced by thermal energy and is dominant only for particles smaller than 0.5 μm. This type of particle motion leads to a so-called *perikinetic* collision mechanism, where *perikinetic* refers to a property related to the probability of cohesion during collisions with other bodies.
2. If the particles move with the fluid flow in a laminar or turbulent flow regime, the orthokinetic collision model describes the agglomeration, where *orthokinetic* refers to a property related to the kinetic energy imparted by collisions with other bodies.
3. If, on the other hand, the particles move with respect to the fluid due to *gravitational* or *inertial forces*, an inertial collision model describes the agglomeration.

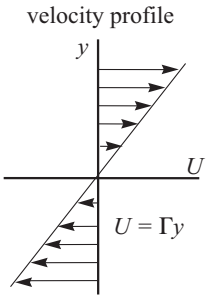

Figure 6.6 A uniform laminar shear field.

The last two mechanisms apply for particles larger than 0.5 μm, and thus either transport in *laminar* or *turbulent* flow due to agitation or *relative settling* due to gravity are the main transport mechanisms.

6.3.1.1 Perikinetic collision rate

For Brownian motion, von Smoluchowski (1917) developed an expression for the collision frequency kernel as follows:

$$\beta(L_i, L_j, T) = \frac{2kT}{3\mu}(L_i + L_j)\left(\frac{1}{L_i} + \frac{1}{L_j}\right) \tag{6.2}$$

where $\beta(L_i, L_j, T)$ = collision frequency kernel [$m^3\ s^{-1}$], k = Boltzmann constant = $1.3806503 \times 10^{-23}\ K^{-1}$, T = temperature [K], μ = dynamic viscosity [$kg\ m^{-1}\ s^{-1}$] and L_i, L_j = diameter of colliding particle i or j, respectively [m].

The latter function is only weakly size dependent since, for a monodisperse system, the collision frequency does not depend on the particle size. Then, equation 6.2 reduces to the following collision frequency constant, if $L_i = L_j$:

$$\beta(T) = \frac{8kT}{3\mu} \tag{6.3}$$

Thus, the *perikinetic collision rate* can be calculated as follows:

$$r_{i,j} = \frac{8kT}{3\mu} N_i N_j \tag{6.4}$$

It should be noted, however, that, once the system starts to agglomerate, the distribution is no longer monodisperse, and thus the constant collision frequency kernel is also no longer valid.

6.3.1.2 Orthokinetic collision rate

a. For laminar flow

The orthokinetic collision frequency for a uniform, laminar flow field has also been given by von Smoluchowski. (A uniform, laminar flow field is one in which the fluid velocity varies linearly in only one direction, perpendicular to the direction of flow; see Figure 6.6.) The velocity gradient is known as the shear rate, denoted as Γ [s^{-1}].

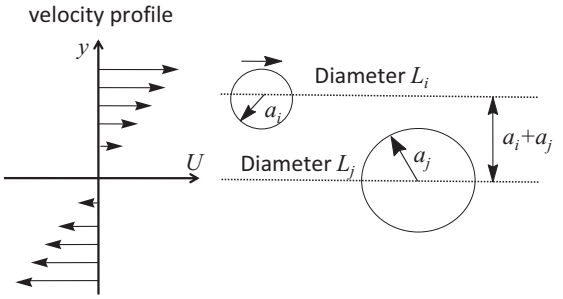

Figure 6.7 Schematic view of particles colliding in a uniform laminar shear field. The particles are on streamlines which are separated by a distance equal to the collision diameter $(L_i + L_j)/2$, and so will just collide (Elimelech *et al*., 1995).

This type of idealized flow field is unlikely to be encountered in practice, but it is useful to start with this case and to modify the result for other conditions (Elimelech *et al*., 1995). A collision is assumed to occur for a flow of particles of size (diameter) L_i streaming towards a central particle of size L_j when their centers approach each other within a distance of $(L_i + L_j)/2$, (which is the collision radius; see Figure 6.7). When the particles follow the streamlines, the collision frequency kernel (obtained by integrating the crystal flux over the collision cross section) can be shown to be:

$$\beta(L_i, L_j) = \frac{4\Gamma}{3}(L_i + L_j)^3 \tag{6.5}$$

where Γ is the shear rate [s^{-1}].

This result shows that the collision rate is proportional to the shear rate Γ, and strongly dependent (third-order) on crystal size. In fact, the most important difference between this equation and the one for perikinetic collisions is the dependence on particle size. As the orthokinetic agglomeration proceeds and the particle sizes increase, the possibility of agglomeration increases with the third power. However, this increase can only occur up to a maximum particle size, beyond which disruption of large particles due to the applied shear stresses will occur (Jones, 2002). Thus, the orthokinetic collision rate for a uniform, laminar flow field can be calculated as follows:

$$r_{i,j} = \frac{4\Gamma}{3}(L_i + L_j)^3 N_i N_j \tag{6.6}$$

b. For turbulent flow

For uniform laminar shear fields, equation 6.6 can be used to calculate the collision rate. However, since the turbulence means that a uniform shear field does not exist, one approach is to calculate a mean velocity gradient, or mean shear rate. This can be expressed for turbulent flow in a tank of volume V_{tank} as:

$$\Gamma = \sqrt{\frac{\varepsilon}{\nu}} \tag{6.7}$$

where ν = kinematic viscosity of the fluid [kg m^{-1} s^{-1}].

This mean shear rate can then be used in place of Γ in the appropriate von Smoluchowski expression (equation 6.5):

$$\beta(L_i, L_j) = \frac{4}{3}\sqrt{\frac{\varepsilon}{\nu}}(L_i + L_j)^3 \tag{6.8}$$

Thus, the orthokinetic collision rate for a turbulent shear field is given by Elimelech *et al*. (1995):

$$r_{i,j} = \frac{4}{3}\sqrt{\frac{\varepsilon}{\nu}}(L_i + L_j)^3 N_i N_j \tag{6.9}$$

These equations only apply for particles that follow the streamlines in laminar flow or that are smaller than the eddy size in turbulent flow.

6.3.1.3 Inertial collision frequency

The last mechanism to be discussed here is the important one of differential sedimentation, which causes particles to collide via the inertial collision mechanism. This occurs because particles of different sizes will settle at different rates under a gravitational field, resulting in collisions. Assuming spherical particles and Stokes law to be valid, i.e. laminar flow, the following collision frequency kernel can be derived (Gardner and Theis, 1996):

$$\beta(L_i, L_j, T) = \frac{\pi g(\rho_{crystal} - \rho_{liquid})}{72\mu}(L_i + L_j)^3 \cdot |L_i - L_j| \tag{6.10}$$

where g = gravitational acceleration [m s^{-2}], ρ_s, ρ_f = solid and fluid densities, respectively [kg m^{-3}].

This mechanism describes the collision of particles when they move relative to the fluid flow, as is the case with gravitational settling and in turbulent flow when the particles are larger than the eddies.

Thus, the inertial collision rate can be calculated as follows:

$$r_{ij} = \frac{\pi g(\rho_{crystal} - \rho_{liquid})}{72\mu}(L_i + L_j)^3 \cdot |L_i - L_j| N_i N_j \tag{6.11}$$

The equation given by Friedlander (2000) differs slightly:

$$r_{ij} = \frac{2\pi g(\rho_{crystal} - \rho_{liquid})}{9\mu}(L_i + L_j)^3 \cdot |L_i - L_j| N_i N_j \tag{6.12}$$

Another collision frequency kernel for inertial processes has been derived by Woods *et al.* (1972):

$$\beta(L_i, L_j) = 0.2\frac{\rho_{liquid}\varepsilon^{4/3}}{\rho_{crystal}\nu^{5/4}}(L_i + L_j)^2 \cdot \left|L_i^2 - L_j^2\right| \tag{6.13}$$

and by Shamlou and Tichener-Hooker (1993):

$$\beta(L_i, L_j) = \sqrt{\frac{\varepsilon}{\nu}}(L_i + L_j)^{7/3} \tag{6.14}$$

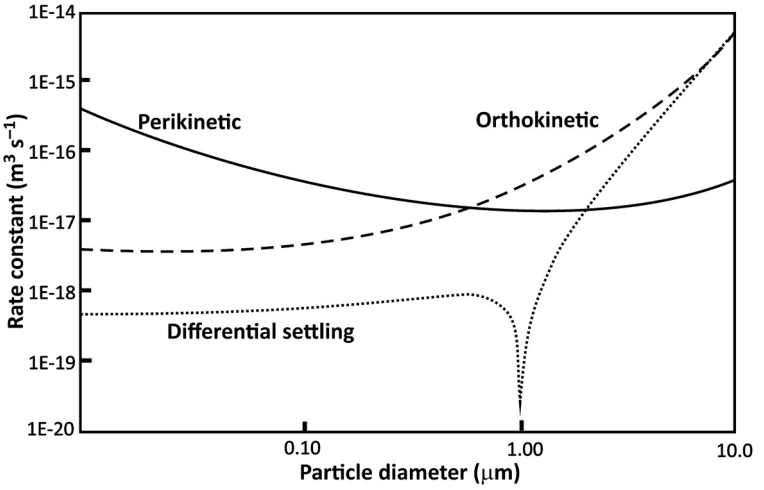

Figure 6.8 Comparison of collision rate constants for different transport mechanisms.

However, a more rigorous model should not only take the collision rate into account, but should also include the particle–particle interactions.

Figure 6.8 was developed by Elimelech and coworkers (1995) and shows a comparison of collision rate constants for different transport mechanisms. In this example, the reference particle has a diameter of 1 μm and the diameter of the other particle varies between 0.01 and 10 μm. The shear rate is assumed to be 50 s^{-1} (which is $\varepsilon = 0.0025$ W kg^{-1}). From this graph, it is apparent that, for particles with a diameter less than about 0.6 μm, the perikinetic mechanism gives the highest collision rate, but that, for larger particles, the orthokinetic and differential settling mechanisms dominate. Note that the perikinetic and differential settling mechanisms pass through a minimum at 1 μm, the size of the reference particle. As the size of the second particle becomes greater than a few millimeters, the collision rate due to differential settling increases sharply and becomes equal to the shear-induced rate.

6.3.1.4 Transport and collision in stirred vessels and the Kolmogorov length scale

In a stirred tank the transport mechanism is governed by the energy dissipation in turbulent eddies. In practice, the eddy size can range from the order of the vessel diameter to very low values (on the order of microns, i.e. the energy-dissipating eddies) depending on the mean power input to the vessel.

Richardson (1922) introduced the idea of the energy cascade, in which kinetic energy is transferred from the largest scale, through eddies of decreasing size, to smaller and smaller scales until, at the smallest scale, the energy is no longer dissipated through eddies, but instead through heat, in the viscous sub-range (Pope, 2000).

The concept of the energy cascade is summarized in the classic poem by Lewis Richardson (1922).

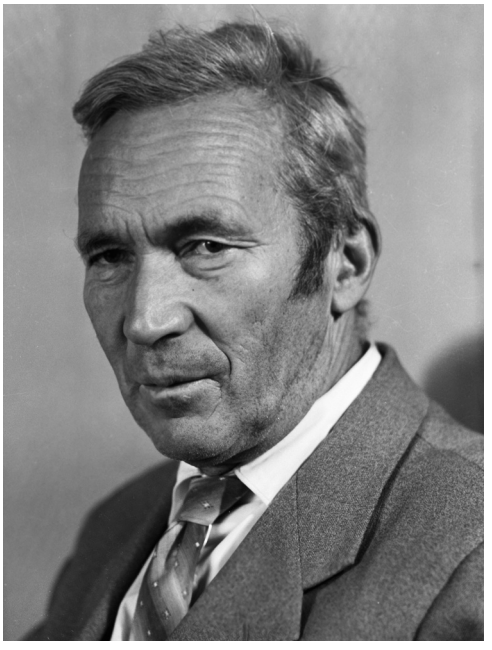

Figure 6.9 Andrei Nikolaevich Kolmogorov. Born 25 April 1903 in Tambov, Russia, died 20 October 1987 in Moscow (Vitanyi, 2007).

> Big whorls have little whorls,
> Which feed on their velocity;
> And little whorls have lesser whorls,
> And so on to viscosity.

The decreasing eddy size influences the fluid–particle interactions, since these are dependent on the size of the eddy. Particles will move with the liquid in the largest eddies, but relative to the liquid in the small eddies. Below a certain eddy size, the energy dissipation, and thus the transport mechanism, is believed to be independent of the type of impeller and the vessel configuration, but only dependent on the mean energy dissipation in the isotropic eddies (Kolmogorov, 1941 (Figure 6.9), Shamlou and Titchener-Hooker, 1993). This range of eddy sizes is generally referred to as the universal equilibrium range, which can be further sub-divided into two sub-ranges, the *inertial* sub-range, where energy is transferred with very little dissipation, and the *viscous* sub-range, where the energy is dissipated as heat. The *inertial* sub-range applies to eddies from half of the impeller diameter to about 25η, while the *viscous* sub-range applies to eddies from about 10 times the Kolmogorov microscale, 10η and smaller (see Figure 6.10, from Shamlou and Titchener-Hooker, 1993).

The Kolmogorov microscale, η, is given by:

$$\eta = \left(\frac{\nu^3}{\varepsilon}\right)^{1/4} \tag{6.15}$$

Table 6.1 Transport and collision mechanisms as a function of particle size L and the Kolmogorov length scale η

Particle size L	Particle size L	Transport mechanism	Collision mechanism
$L < 0.5$ μm		Brownian motion	Perikinetic
$L > 0.5$ μm	$L < 10\eta$	Laminar flow	Orthokinetic
		Turbulent flow	Orthokinetic
	$L > 25\eta$	Laminar flow	Inertial
		Turbulent flow	Inertial
	$L > 10\eta$	Relative particle settling	Inertial

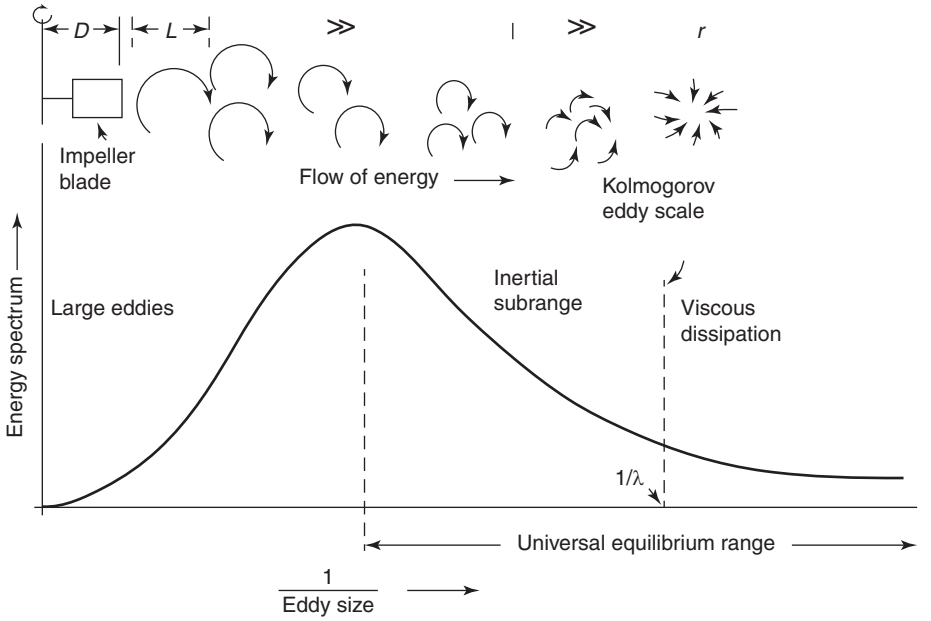

Figure 6.10 Schematic presentation of the turbulent energy spectrum Shamlou and Titchener-Hooker (1993).

where ν = kinematic viscosity [kg m^{-1} s^{-1}] and ε = the mean energy dissipation rate [m^2 s^{-3}].

In a stirred vessel, η is typically on the order of tens of microns. For example, Kusters *et al*. (1997) propose that, at a characteristic energy dissipation ε of 0.1 W kg^{-1} for a stirred tank, η will be 56 μm in water.

Using the Kolmogorov micro-scale as a guide, Table 6.1 gives an estimation of the dominant collision mechanism. According to this estimation, particles smaller than about 10η will collide according to a perikinetic or an orthokinetic collision mechanism, whilst particles larger than 25η will be predominately transported and collide according to an inertial mechanism.

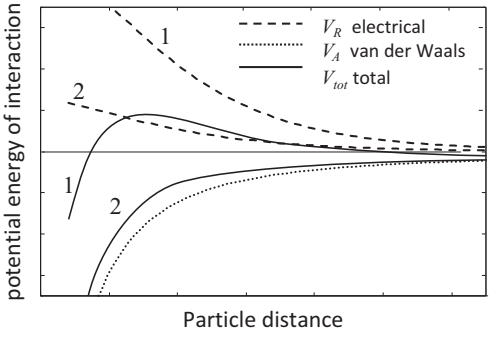

Figure 6.11 Interaction energy as a function of particle distance for two different cases of the repulsive electrical double layer forces.

This means that, for a polydisperse system, both the *orthokinetic* and the *inertial* collision mechanisms must be applied simultaneously.

6.3.2 Particle–particle interactions

6.3.2.1 Attractive forces

The main attractive forces acting on the particles are the van der Waals forces (Shamlou and Titchener-Hooker, 1993). Van der Waals forces decay rapidly with separation distance (Jones, 2002) and always lead to a weak attraction of particles composed of similar materials.

6.3.2.2 Repulsive forces

Repulsive forces are mainly due to the presence of the electrical double layer. This is because particles dispersed in aqueous solution frequently develop a surface charge due to preferential adsorption of ionic species onto their surfaces (Jones, 2002). This "layer" of ionic species is compensated for by another "layer" of opposite charge that builds up in solution; hence, the term "electrical double layer." Although the surface charge is neutral overall, the double layers will repel each other and thus cause a repulsive force between the particles.

Another important feature of inter-particle forces is that they decay at different rates as a function of the particle distances. This can lead to quite different results, depending on the combination of attractive and repulsive forces. In Figure 6.11, the potential energy of the interactions is shown for two particles as a function of distance. Case 1 exhibits a greater repulsive force between the two particles due to the electrical double layer than case 2. This could be due to the ionic strength of the solution and/or the size of the particles (Shamlou and Titchener-Hooker, 1993).

The total potential energy of the interaction, V_{tot} is the sum of the attractive van der Waals potential V_A and the repulsive double layer potential V_R, all measured in Joules. Depending on the form of the total potential energy curve, the suspension of particles will be stable due to the high energy barrier (case 1) or aggregate formation will be favored due to the absence of a potential energy barrier (case 2).

6.3.3 Collision efficiency and disruption of aggregates

Direct application of the collision equations given in equations 6.4, 6.6, 6.9 and 6.11 will result in an overestimation of the agglomeration rate because of the assumption that every collision results in a successful agglomeration event. This is not necessarily the case, and many collisions do not lead to successful agglomeration. After collision, the balance between the external flow forces and the particle–particle interactions (inter-particle attractive and repulsive forces) will determine whether or not there will be the formation of an agglomerate.

Mumtaz and coworkers (1997) modified von Smoluchowski's theory by introducing the concept of a collision efficiency, which takes into account that not all collisions are successful in forming an agglomerate. Thus, the overall agglomeration rate can be modeled as follows:

$$r_{agg} = \Psi r \tag{6.16}$$

$$\beta_{agg} = \Psi \beta \tag{6.17}$$

where r_{agg} = agglomeration rate [# m^{-3} s^{-1}], r = collision rate [# m^{-3} s^{-1}], β_{agg} = agglomeration rate constant (# m^{-3} s^{-1}), Ψ = the overall efficiency of collisions and β = collision rate constant (# m^{-3} s^{-1}).

6.3.3.1 Disruption

Instead of using the concept of collision efficiency (which is difficult to calculate directly), another approach is to directly determine a disruption function.

The disruption of aggregates in a turbulent flow field is caused by the same process variables that were responsible for the aggregation: instantaneous turbulent stresses, and therefore the disruption rate constant (or kernel) is proportional to the particle volume. In addition, disruption is affected by supersaturation, since, the higher the growth rate, the stronger the agglomerates and the lower the likelihood of disruption.

The following function has been proposed to model breakage and disruption processes (Wójcik and Jones, 1998):

$$\beta_{disr}(L_i, L_j, \varepsilon, S) = \beta_{disr}\varepsilon^r S^s (L_i + L_j)^3 \tag{6.18}$$

where β_{disr} = disruption kernel [m^2 s^{-1}], ε = the mean energy dissipation rate [m^2 s^{-3}], S = supersaturation ratio, r, s = exponents of S and ε, respectively, and L_i, L_j = size of particles i and j, respectively.

In other words, the disruption rate is proportional to the particle volume, and has a power law dependence on supersaturation and on energy dissipation.

In a stirred vessel the disruption rate can be expected to be proportional to the mean dissipation rate per unit of mass, $\bar{\varepsilon}$ in the viscous subrange and to $\bar{\varepsilon}^2$ in the inertial subrange (Shamlou and Titchener-Hooker, 1993).

Elimelech and coworkers (1995) suggest that the limiting floc size in a turbulent flow field is of the same order as the Kolmogorov micro-scale, given by equation 6.15.

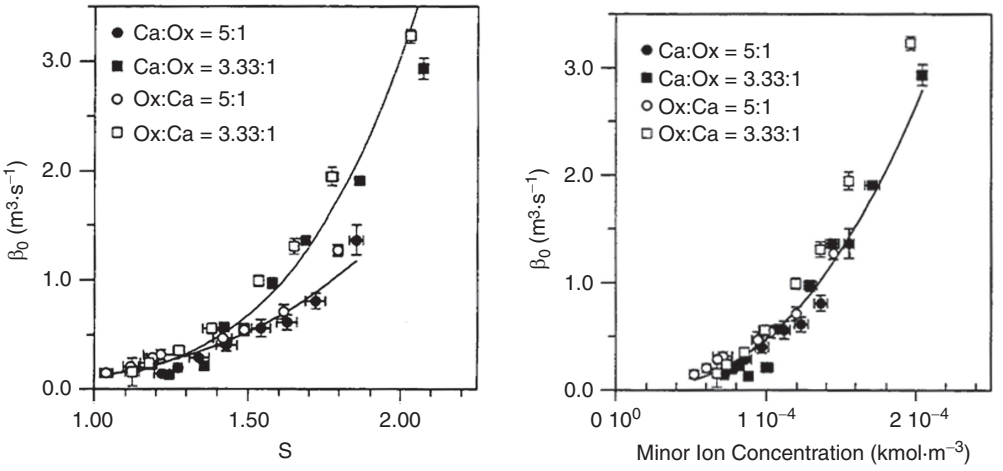

Figure 6.12 Agglomeration rate of calcium oxalate as a function of the supersaturation for different ratios of Ca and Ox ions (left). In the right figure the same data are plotted against the concentration of the ion (Ca or Ox) with the lowest concentration (Bramley *et al*., 1997).

6.3.4 Aggregate cementation

The cementation rate is directly related to the growth rate in the corners and spaces between the touching particles. This has been experimentally verified in many systems (see Figure 6.12, in which the rate of agglomeration β_0 (see Section 6.4 for a definition of β_0) is given as a function of the supersaturation for different ratios of Ca^{2+} and Ox^{2-}). These experiments strongly support the importance of the cementation step in the agglomeration kinetics. The experiments of Bramley and coworkers (1997) also showed that, in addition to the supersaturation, the ion ratio has a significant effect on the agglomeration rate. This difference can be eliminated when the agglomeration rate is plotted versus the concentration of the ion with the lowest concentration. This demonstrates that the transport of the ions to the cementing site is a rate-determining step in the agglomeration process.

6.4 Modeling agglomeration: the agglomeration kernel

In summary, agglomeration of particles is a reversible process that involves transport and collision of the particles, interaction of the particles, rupture of aggregates and cementation of aggregates into stable agglomerates. The modeling of these four steps separately is difficult, especially because they occur simultaneously. The overall agglomeration rate is therefore mostly described with one size-dependent function, the agglomeration rate constant or the so-called *agglomeration kernel*. In the literature, the symbol β is commonly used. In some publications, such as in Hartel and Randolph (1986), the rupture of the agglomerates is described with a separate breakage function. However, this will not be discussed in this chapter. Here, we present the overall agglomeration kernel, which

Table 6.2 Commonly used agglomeration kernels

Description	Agglomeration kernel β_0	Agglomeration kernel β_1	Reference
Brownian motion	$\frac{2kT}{3\mu}$	$(L_i + L_j)\left(\frac{1}{L_i} + \frac{1}{L_j}\right)$	(von Smoluchowski, 1917)
Laminar shear	$\frac{\Gamma}{6}$	$(L_i + L_j)^3$	(von Smoluchowski, 1917)
Turbulent shear	$\sqrt{\frac{\varepsilon}{\nu}}$	$(L_i + L_j)^3$	(Shamlou and Titchener-Hooker, 1993)
Turbulent inertia	$\frac{\rho_l \varepsilon^{4/3}}{\rho_c \nu^{5/4}}_0$	$(L_i + L_j)^2 \cdot \left\|L_i^2 - L_j^2\right\|$	(Woods *et al.*, 1972)
Gravitational settling	$\frac{\pi g(\rho_{crystal} - \rho_{liquid})}{72\mu}$	$(L_i + L_j)^3 \cdot \|L_i - L_j\|$	(Gardner and Theis, 1996)
Empirical kernel	C	$\frac{\left(L_i^3 + L_j^3\right)^2}{L_i^3 + L_j^3}$	(Hartel and Randolph, 1986)
Size-independent kernel	β_0	1	

is the rate constant that summarizes the *combined* effect of the individual processes (collision, interaction, rupture and cementation) outlined earlier.

The overall rate at which particles agglomerate in a crystallization or precipitation system can be modeled as a function of the following process variables:

the (local) energy dissipation
the supersaturation of the fluid phase
the number and the size distribution of the particles, as well as a number of material properties (surface charge and hardness) and process conditions (temperature and viscosity).

The agglomeration kernel, β_{agg}, is often split into a size-independent part, β_0, which is determined by the process conditions, like the energy dissipation rate and the supersaturation of the suspension, and a size-dependent part β_1 (see equation 6.19).

$$\beta_{agg}(L_i, L_j, \varepsilon, S) = \beta_0(\varepsilon, S)\beta_1(L_i, L_j) \tag{6.19}$$

A summary of commonly used agglomeration kernels is given in Table 6.2. What is striking is that all of the most commonly used kernel functions do not give a complete description of the agglomeration process.

The most significant omission in the kernels shown in Table 6.2 is the supersaturation, which strongly influences the agglomeration rate.

Adding to the problem is the fact that, in the case of precipitation processes, it is generally accepted that, on the timescale of the process, the system is far from ideally

mixed, which leads to local inhomogeneities in many parameters, such as supersaturation and energy dissipation (Shamlou and Titchener-Hooker, 1993). Thus, it is necessary to characterize the hydrodynamics of the system in order to exactly describe the local supersaturation profile and thus to determine the locally specific agglomeration kernel. This approach has been used to model precipitation processes (Lindenberg *et al*., 2008, Van Leeuwen, 1998, Vicum *et al*., 2004), but has not been extended to wider use.

In addition, the size-dependent component of the kernel function is mostly derived only from the collision mechanism. Much more research is needed in this area.

6.5 Determination of the agglomeration kernel from experimental data

Determining the agglomeration rate constant, or kernel, experimentally is not straightforward. The two major problems in determining the kernel, especially when crystal growth is present are:

1. Identification of which of the agglomeration mechanisms or mixture of mechanisms must be used for the particular system. Analogous to normal crystallization systems, the agglomeration mechanism is strongly influenced by the hydrodynamics of the system and the presence of (local) process conditions, which makes the extrapolation of the results to other configurations and scale of operation very difficult.
2. Estimation of the kinetic rate constants for systems using experimental crystal size distributions where all three of the mechanisms of growth, nucleation and agglomeration are present. As has already been outlined before, analytical solutions are only available for simplified systems that have no practical relevance. Therefore numerical methods must be used.

Willis (2014) used an oscillating multi-grid reactor to eliminate the inhomogeneity of the turbulence and thus extract agglomeration rates. The analysis was carried out using a modified method of that used by Bramley *et al*. (1996):

Given that the moments of a PSD can be calculated as follows:

$$\mathrm{m}_j = \int_0^\infty n(L) L^j \mathrm{d}L \text{ for } j = 0, 1, 2 \ldots \tag{6.20}$$

It should be apparent then that m_0, the zeroth moment, represents the total number of particles, m_1 the total length, m_2 the total surface area and m_3, the total volume of the particles, assuming the particles to be spherical.

If the total number of particles m_0 is tracked over time, then it is possible to determine an aggregation rate of the system. For size-independent growth and aggregation, it is possible to attain the following pair of equations (Bramley *et al*., 1996):

$$\frac{\mathrm{d}m_0}{\mathrm{d}t} = \frac{1}{2}\beta_0 m_0 \tag{6.21}$$

$$\frac{\mathrm{d}m_3}{\mathrm{d}t} = 3Gm_2 \tag{6.22}$$

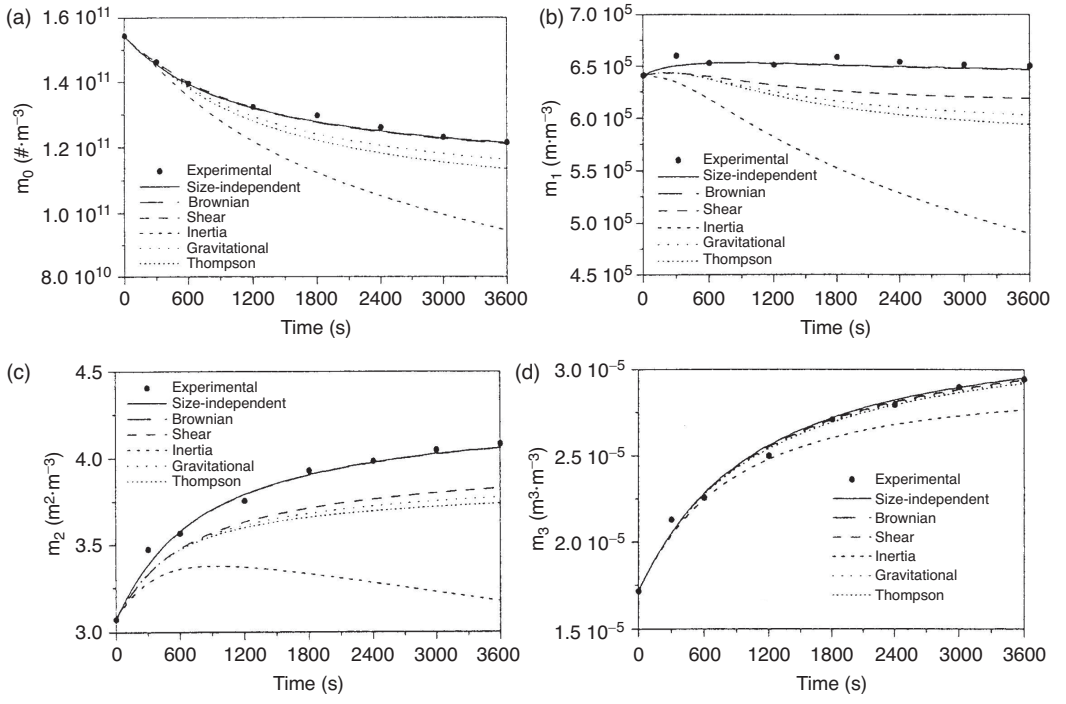

Figure 6.13 Comparison of experimental and simulated moments for various agglomeration kernels (a) m_0 (b) m_1, (c) m_2 (d) m_3.

The moments are attainable from experimental data using a discretized form of equation 6.20:

$$m_j = \sum_{0}^{k} n(\overline{L}_k)\overline{L}_k^j \Delta L_k \tag{6.23}$$

where $\overline{L}_k = (L_i + L_{i+1})/2$ is the average of the upper and lower bound of the size intervals with width $nL_k = L_{i+1} - L_i$. Via separation of variables it is possible to integrate and solve for β_0 if the zeroth moment is known at two discrete times:

$$\beta_0 = \frac{2}{\Delta t}\left[\left(m_0^{i+1}\right)^{-1} - \left(m_o^1\right)^{-1}\right] \tag{6.24}$$

6.5.1 Case study 1: calcium oxalate monohydrate (Bramley *et al.*, 1997)

Seeded batch precipitation experiments were carried out using calcium oxalate monohydrate (COM) as a model material. The authors applied a version of the technique outlined in the previous section to investigate the effect of the choice of the different kernels. The results shown in Figure 6.13 clearly show that, for all the four moments, the size-independent agglomeration kernel gives the best results. Similar results have been found by a number of authors. Only in the work of Hartel and Randolph (1986) was a size-dependent kernel found.

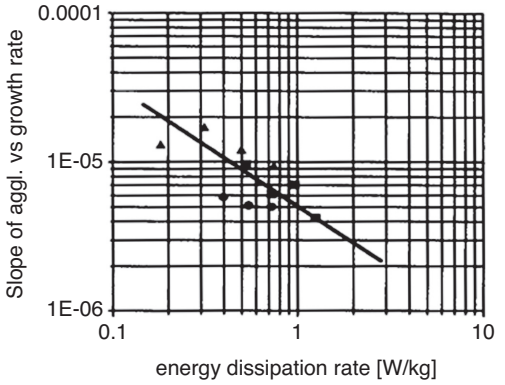

Figure 6.14 Agglomeration rate versus growth rate as function of the energy dissipation rate: (squares) Rushton, (circles), flat blade and (triangles) pitched blade impeller.

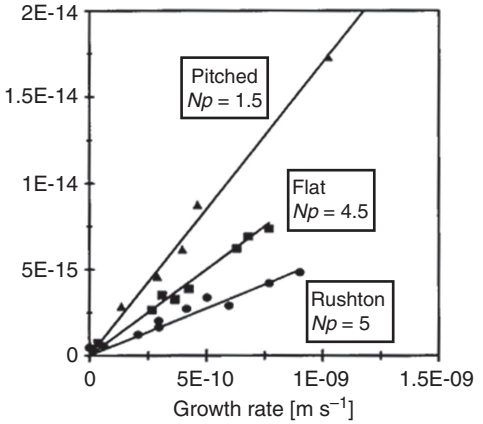

Figure 6.15 Experimental relation between the agglomeration rate constant and the growth rate for three different impellers.

6.5.2 Case study 2: $Al(OH)_3$ (Van Leeuwen, 1998)

Seeded batch experiments were performed in a 2.4 liter baffled stirred tank reactor at 27 °C. Gibbsite ($Al(OH)_3$ was precipitated. The rates of the process were determined with the method of Bramley *et al.* (1996).

In Figure 6.14, the experimental relationship is shown between the agglomeration rate divided by the growth rate and the mean energy dissipation rate. Surprisingly, a negative correlation was found. Apparently the efficiency of agglomeration decreases more rapidly with the energy dissipation than the collision frequency increases. In Figure 6.15, the experimental results, which show the effect of the growth rate and type of impeller on the agglomeration rate constant, are given.

This finding is explained to some extent by the work of Mumtaz and Hounslow (2000), who investigated the effect of the shear rate on the agglomeration kernel. They found that, at low shear rates, the agglomeration kernel varied linearly with shear rate,

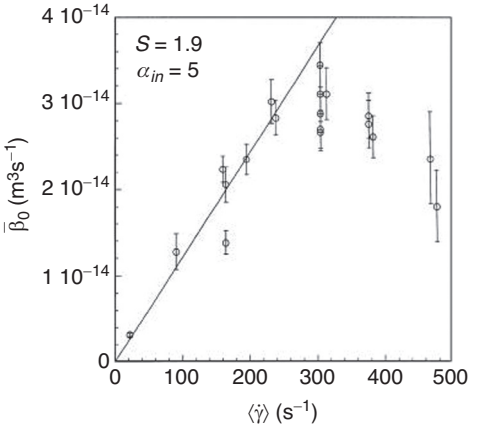

Figure 6.16 Effect of shear rate on agglomeration kernel, as measured in a Poiseuille flow reactor (Mumtaz and Hounslow, 2000).

providing good validation for von Smoluchowski's theory. However, at increasing shear rates, a maximum in the value of the agglomeration kernel was observed, confirming the disruptive role of fluid shear rate in impeding agglomeration. This is illustrated in Figure 6.16.

6.6 A brief summary of the chapter

This chapter started by outlining the four main sub-processes involved in agglomeration: transport, collision, interaction and disruption/cementation. The collision sub-process was further sub-divided into four causes of collisions as follows: those due to Brownian motion (perikinetic collisions); those due to the velocity gradient in a laminar or turbulent flow field (orthokinetic collisions); those due to the gravitational settling of particles (inertial collisions) and those due to stirring in a tank. Interaction between particles (which mainly applies to small particles) was discussed and described. For the disruption sub-process, a model that takes into account particle volume, supersaturation and energy dissipation was proposed. For the cementation sub-process, the growth rate and the transport of ions to the cementing site were identified as important variables. Finally, the chapter concluded with an overall model for agglomeration, which is presented as a function of the local energy dissipation, the supersaturation and the number and size distribution of particles in the system.

6.7 End of chapter problems

Problem 1: Kolmogorov length scale

Given three systems, a lab-scale setup, a mini plant and a pilot plant, each with fluid characteristics of water at ambient temperature, calculate the effect of the average

turbulent energy dissipation rate on the size of the Kolmogorov length scale, i.e. the size of the smallest turbulent eddy. Assume $\nu = 0.001$ and $\rho = 1000$ kg m^{-3}

Plant size	Average turbulent energy dissipation (W kg^{-1})
Lab scale	10
Mini Plant scale	0.1
Pilot Plant scale	0.001

Problem 2: Effect of different variables on agglomeration

In the following table, specify whether an *increase* in the variable identified has a positive, negative or no effect on agglomeration in the system in case of either perikinetic or orthekinetic agglomeration. These variables are particle concentration (# m^{-3}), particle size, width of particle size distribution, fluid shear rate, viscosity and temperature.

Variable	Effect on perikinetic agglomeration	Effect on orthokinetic agglomeration
Particle concentration (# m^{-3})		
Particle size		
Width of particle size distribution		
Fluid shear rate		
Viscosity		
Temperature		

Problem 3: Ammonium nitrate: agglomeration or growth?

Ammonium nitrate is obtained by continuous crystallization. The residence time is 8 min and the mean particle size increases from 50 to 1000 μm in one residence time. Determine the experimental particle "size enlargement" rate, i.e. the rate at which the particles get bigger. Using this information, as well as the growth rate information given below, determine whether the size enlargement process occurs via growth or agglomeration. Assume $G = k_g S^g$, with $k_g = 9.38 \times 10^{-9}$ m s^{-1} (Vogels *et al.*, 1990) and $g = 2$ and given bulk and equilibrium concentrations of $c_b = 1023$, $c_{eq} = 992$ kg m^{-3} solution. Assume that $S = c/c_{eq}$ and that G is the *maximum* growth rate that can occur at this supersaturation.

6.8 References

Bramley, A. S., Hounslow, M. J. and Ryall, R. L. 1996. Aggregation during precipitation from solution. A method for extracting rates from experimental data. *Journal of Colloid and Interface Science*, **183**, 155–165.

Bramley, A. S., Hounslow, M. J. and Ryall, R. L. 1997. Aggregation during precipitation from solution. Kinetics for calcium oxalate monohydrate. *Chemical Engineering Science*, **52**, 747–757.

Elimelech, M., Gregory, J., Jia, X. and Williams, R. A. 1995. *Particle Deposition and Aggregation: Measurement, Modelling and Simulation*, Elsevier Science.

Friedlander, S. K. 2000. *Smoke, Dust, and Haze: Fundamentals of Aerosol Dynamics*, Oxford University Press.

Gardner, K. H. and Theis, T. L. 1996. A unified kinetic model for particle aggregation. *Journal of Colloid and Interface Science*, **180**, 162–173.

Hartel, R. W. and Randolph, A. D. 1986. Mechanisms and kinetic modeling of calcium oxalate crystal aggregation in a urinelike liquor. Part II: Kinetic modeling. *AIChE Journal*, **32**, 1186–1195.

Hogg, R. 1992. Agglomeration models for process design and control. *Powder Technology*, **69**, 69–76.

Hollander, E. D. 2002. *Shear Induced Agglomeration and Mixing*, PhD Thesis, Delft University of Technology.

Ilievski, D. and White, E. T. 1994. Agglomeration during precipitation: agglomeration mechanism identification for Al(OH)3 crystals in stirred caustic aluminate solutions. *Chemical Engineering Science*, **49**, 3227–3239.

Jones, A. G. 2002. *Crystallization Process Systems*, Butterworth-Heinemann.

Kolmogorov, A. N. 1941. Dissipation of energy in isotropic turbulence. *Doklady Akademii Nauk SSSR*, **32**, 19–21.

Kusters, K. A., Wijers, J. G. and Thoenes, D. 1997. Aggregation kinetics of small particles in agitated vessels. *Chemical Engineering Science*, **52**, 107–121.

Lindenberg, C., Schöll, J., Vicum, L., Mazzotti, M. and Brozio, J. 2008. Experimental characterization and multi-scale modeling of mixing in static mixers. *Chemical Engineering Science*, **63**, 4135–4149.

Mumtaz, H. S. and Hounslow, M. J. 2000. Aggregation during precipitation from solution: an experimental investigation using Poiseuille flow. *Chemical Engineering Science*, **55**, 5671–5681.

Mumtaz, H. S., Hounslow, M. J., Seaton, N. A. and Paterson, W. R. 1997. Orthokinetic aggregation during precipitation: a computational model for calcium oxalate monohydrate. *Chemical Engineering Research and Design*, **75**, 152–159.

Pope, S. B. 2000. *Turbulent Flows*, Cambridge University Press.

Randolph, A. D. and Larson, M. A. 1988. *Theory of Particulate Processes: Analysis and Techniques of Continuous Crystallization*, Academic Press.

Richardson, L. F. 1922. *Weather Prediction by Numerical Process*, Cambridge University Press.

Shamlou, P. A. and Titchener-Hooker, N. 1993. Turbulent aggregation and break-up of particles in liquids in stirred vessels. In *Processing of Solid–Liquid Suspensions*, Shamlou, P. A. (ed.), Butterworth-Heinemann.

Van Leeuwen, M. L. J. 1998. *Precipitation and Mixing*. PhD Thesis, University of Delft.

Vicum, L., Ottiger, S., Mazzotti, M., Makowski, L. and Baldyga, J. 2004. Multi-scale modeling of a reactive mixing process in a semibatch stirred tank. *Chemical Engineering Science*, **59**, 1767–1781.

Vitanyi, P. M. B. 2007. Andrey Nikolaevich Kolmogorov [Online]. Available: http://www.scholarpedia.org/article/Andrey_Nikolaevich_Kolmogorov (accessed February 2015).

Vogels, L., Marsman, H., Verheijen, M., Bennema, P. and Elwenspoek, M. 1990. On the growth of ammonium nitrate (III) crystals. *Journal of Crystal Growth*, **100**, 439–446.

von Smoluchowski, M. 1917. Versuch einer mathematischen Theorie der Koagulationskinetik kolloider Lösungen. *Zeitschrift für Physikalische Chemie*, **92**, 129–168 (in German).

Willis, B. M. 2014. The Effect of Energy Input on the Aggregation Rate in an Oscillating Multi-Grid Reactor, MSc Thesis, University of Cape Town. https://open.uct.ac.za/handle/11427/9130 (accessed February 2015).

Wójcik, J. A. and Jones, A. G. 1998. Particle disruption of precipitated $CaCO_3$ crystal agglomerates in turbulently agitated suspensions. *Chemical Engineering Science*, **53**, 1097–1101.

Woods, J. D., Drake, J. C. and Goldsmith, P. 1972. Coalescence in a turbulent cloud. *Quarterly Journal of the Royal Meteorological Society*, **99**, 758–763.

7 The population balance equation

7.1 Why this chapter is important

The prediction of the product quality in industrial crystallization processes is not simple and requires detailed knowledge of the crystal size distribution (CSD). To obtain such knowledge, the population balance equation (PBE) has to be solved, describing the evolution of the CSD in the crystallizer.

In this chapter PBE-based models of the crystallization process will be discussed in detail, describing the formulation of the PBE based on either the length or the volume of the crystals, explaining the different terms of this important equation and their relation to the different kinetic processes in the crystallizer. Growth- and nucleation-dominated systems and processes that are predominantly agglomeration and breakage will be discussed separately, as they require a different formulation. The coupling of the population to the enthalpy and material balances, to obtain a realistic description of the process is discussed, as well as solution methods for a PBE-based crystallizer model. Multi-compartment models are also introduced that can be used to describe the effects of profiles in the process conditions on the performance of an industrial crystallizer, due to the large volume or complex geometry. A few examples of such multi-compartment models are given.

Having a crystallization model is extremely valuable for the development, optimization and design of a process that meets specific product requirements. To be more precise, having a PBE-based crystallization model will allow the user

- to *predict* the resulting particle size distribution even at a different scale of operation, on the basis of the known kinetic models;
- to *estimate* the parameters of a kinetic model based on an experimentally determined particle size distribution knowing the process conditions under which it was obtained;
- to *optimize* the process conditions to obtain a desired particle size distribution given a validated kinetic model.

7.2 Evolution of the crystal size distribution in a crystallizer

A crystalline product consists of a distribution of crystals (or of agglomerates of crystals that are often referred to as particles) of different sizes. This crystal size distribution

(CSD) or particle size distribution (PSD) is one of the most important product characteristics of a solid product. The CSD (or PSD, which will not further be separately mentioned) not only affects the behavior of the suspension in the crystallizer, but also determines the efficiency of the subsequent solid–liquid separation and drying steps. The CSD of the product often has to meet very strict demands. The development of the CSD during crystallization by different kinetic phenomena such as nucleation, growth and agglomeration under the prevailing process conditions in the selected crystallizer equipment is the subject of this chapter. The evolution of the CSD is mathematically described by the population balance equation (PBE), which was developed in the 1960s (Randolph, 1962). Below the mathematical formulation of the PBE is discussed and it is shown how this equation can be used to predict the influence of process conditions, operation policy and features of industrial crystallizers on the CSD of the produced crystals.

Modeling of the product quality is essential in different phases of the life cycle of an industrial crystallizer. In the conceptual design phase, relatively simple models, mostly in steady state to evaluate the viability of a process, are used while, in the detailed design phase, population balance models are needed that can predict the influence of the scale of operation and the hydrodynamics on the crystallizer performance. Finally in the operation phase these models can be used to bottleneck, optimize and control the crystallizer. In most cases the crystallizer model should be dynamic because batch processes are inherently dynamic, while continuously operated processes show dynamic behavior due to process disturbances and during the start-up and shut-down of the plant.

In Section 7.3 the mathematical formulation of the population balance is discussed for crystallization and agglomeration of a so-called well-mixed system, i.e. a system in which the process variables such as the population density, temperature, energy dissipation and supersaturation can be considered to be uniformly distributed. In reality, however, in industrial crystallizers this uniformity assumption is hardly ever met, due to the large scale and the specific crystallizer design, as will be discussed in Chapter 10. Application of a well-mixed model to such a crystallizer would lead to a geometrically lumped erroneous description of the kinetics, which are strongly dependent on the hydrodynamics and the scale of the equipment (Bennett, 1993, Bermingham *et al.*, 1998, 2003, Kramer *et al.*, 1999). In Section 7.5, the spatial distribution of the process variables is discussed in more detail using a compartmental approach, in which the crystallizer is sub-divided into a number of compartments, which are assumed to be ideally mixed and coupled via interconnecting streams (Bermingham *et al.*, 2003). In Section 7.5 it is shown how relatively simple compartmental models can take into account the gradients in the process conditions in most crystallization processes where the supersaturation gradients are relatively low, whereas complicated compartmental models consisting of many compartments are needed for precipitation and anti-solvent processes in which steep gradients in the supersaturation exist, and where agglomeration plays a dominant role.

7.3 The population balance equation

7.3.1 Formulation of the population balance

To describe the development of the CSD in the crystallizer, the concept of the population balance was introduced by Randolph and Larson in 1962 (Randolph and Larson, 1988). The population balance describes the evolution in time of the number or mass distribution of crystals as a function of the crystal or particle size. The number of crystals in a size class (i.e. between size L and $L + \Delta L$) results from crystallization kinetics like nucleation, growth and agglomeration, as well as from crystals in the size class present in the input and output flows.

From the population balance the mass of the crystals of all sizes can also be derived, and compared with the crystal mass obtained from the mass and heat balance derived in Chapter 4.

A general form of the PBE for the calculation of the number distribution of the crystals as a function of the crystal size is as follows:

$$\frac{\partial(n(L,t)V(t))}{\partial t} = -V\frac{\partial(G_L(L,t)n(L,t))}{\partial L} + B(L,t)V - D(L,t)V + \sum_{j=1}^{m}\varphi_{v,in,j}(t)n_{in,j}(L,t) - \sum_{k=1}^{n}\varphi_{v,out,k}(t)h_{out,k}(L,t)n(L,t) \quad (7.1)$$

where the amount and the size of particles are expressed in terms of number density $n(L, t)$ [# m^{-3} m^{-1}] and crystal length L [m], respectively. In other representations of the PBE, the amount of particles may also be expressed in terms of volume density $v(L, t)$ or mass density $m(L, t)$. In number density, on the other hand, crystal size may also be expressed in terms of volume, i.e. $n(v, t)$ instead of length $n(L, t)$. This type of representation is convenient in the case of the occurrence of agglomeration. V [m^3] is the crystallizer volume with m [−] streams entering and n [−] streams leaving the crystallizer with volumetric flow rates φ_v [m^3 s^{-1}]. $G_L(L, t)$ [m s^{-1}] is the linear size-dependent growth rate, and $D(L, t)$ and $B(L, t)$ [# m^{-3} m^{-1} s^{-1}] are the death and birth rates, respectively.

In Figure 7.1 an infinitesimally small size range from L to $L + \mathrm{d}L$ is shown to explain the different terms in the PBE. The effects of the kinetic processes and the inlet and outlet streams on the accumulation of crystals in this size range are visualized.

The PBE as presented in Equation 7.1 is generally valid with respect to the physical processes taking place and the operation mode. Concerning operation modes, the difference between batch, semi-batch and continuous is merely related to the in- and outflow terms in the PBE. The other terms in the PBE describe the physical processes that may occur in a crystallization process.

Nucleation is the subject of Chapter 4. It only delivers new crystals in the smallest size ranges and can be introduced in the calculation of the PBE either as a boundary condition under the assumption that all nuclei are born at zero size $B_0(t)$ or as a distribution function

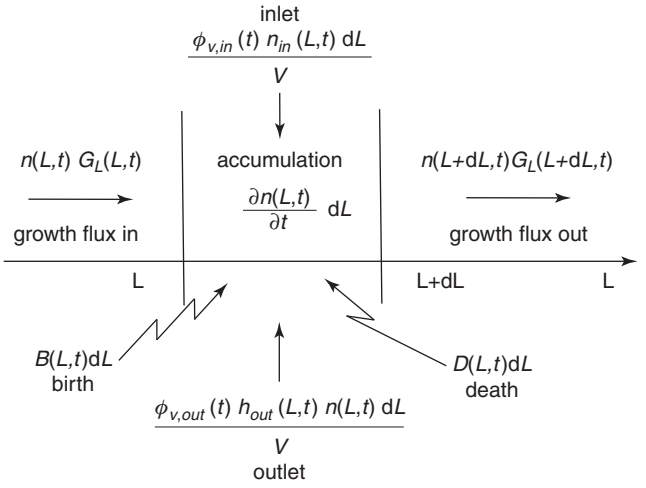

Figure 7.1 Schematic depiction of the processes affecting the CSD. In an infinitesimally small size range from L to $L + dL$, crystals may enter and leave due to growth, agglomeration, attrition, breakage and volumetric input and output flow streams.

of small crystals $B(L, t)$. A distribution function reflects the formation of fragments by attrition of larger crystals, as in secondary nucleation.

Since the PBE is a first-order partial differential equation with respect to time t [s] and crystal length L [m], one boundary condition and an initial condition are required to solve the PBE, such as:

$$n(0, t) = \frac{B_0(t)}{G_L(0, t)} \tag{7.2}$$

$$n(L, 0) = \text{initial distribution} \tag{7.3}$$

So with regard to the solution of the PBE, the nucleation rate at zero size is mostly used as a boundary condition. If the nucleation is described by the formation of new crystals $B(L, t)$ [# m^{-3} m^{-1} s^{-1}] over a certain size range of crystals ($0 \leq L \leq y$), the birth term in the boundary condition (equation 7.2) can be transformed into $B_0(t)$ [# m^{-3} s^{-1}] by the following relation:

$$B_0(t) = \int_0^y B(L, t)\, dL \tag{7.4}$$

The initial distribution can, in the case of a batch process, be physically related to a seed population. In a continuous process the initial distribution can be either a seed population or a population of outgrown nuclei.

Although secondary nucleation generally results from attrition of the larger crystals, no attrition rates are included in the PBE to account for the effect of attrition on the length of the larger crystals.

Other terms in the PBE that describe the physical processes that may occur during crystallization are:

$$\frac{\partial(G_L(L,t)n(L,t))}{\partial L} \tag{7.5}$$

which denotes the size-dependent growth of particles. If the growth rate is independent of crystal length, this term reduces to $G_L(t)\,\mathrm{d}n(L,t)/\mathrm{d}L$. Crystal growth is described in more detail in Chapter 6.

$$B(L,t)V - D(L,t)V \tag{7.6}$$

describes the birth and death of particles of a certain size as a result of agglomeration, breakage and nucleation. In the case of agglomeration, as discussed in Chapter 6, birth of new particles happens by agglomeration and thus by the disappearance of two or more crystals of smaller sizes. The disappearance of the original smaller crystals is described by the death term, which has no relation to breakage, but reflects the effective rate of disappearance of the small particles by agglomeration. See Chapter 6 for a more detailed description of agglomeration. Agglomeration is treated mathematically below in Section 7.3.2. So, nucleation or birth of new crystals happens at very small sizes ($B_0(t)$) while birth at larger sizes ($B(L,t)$) happens by agglomeration.

Breakage of crystals of size L leads to a death term $D(L,t)$. This hardly ever happens unless the shape of the crystals facilitates breakage, as for needles or dendrites, or when by severe stirring an agglomerate breaks up in smaller particles.

The term in equation 7.7

$$\sum_{j=1}^{m} \varphi_{v,in,j}(t)n_{in,j}(L,t) \tag{7.7}$$

represents an arbitrary number of inlet streams, which may or may not contain a population of crystals/particles.

$$\sum_{k=1}^{n} \varphi_{v,out,k}(t)h_{out,k}(L,t)n(L,t) \tag{7.8}$$

describes an arbitrary number of outlet streams with CSDs that may be similar or completely different to the CSD in the vessel. The relation between the CSD inside the vessel and that of an outlet stream is typically described by a so-called classification function $h(L)$. The most extreme classification functions are encountered in fines and product classification systems, whereas less severe classification functions exist if no classification is pursued. If at ideal mixing inside the crystallizer the CSD of the withdrawn product is similar to the content of the crystallizer, $h(L) = 1$. If an outlet flow contains a clear liquor $h(L) = 0$. Examples of classification functions are shown in Figure 7.2. In this figure a cumulative log normal distribution is taken for the product classification, which approaches 0 for small crystals and 1 for the largest crystals.

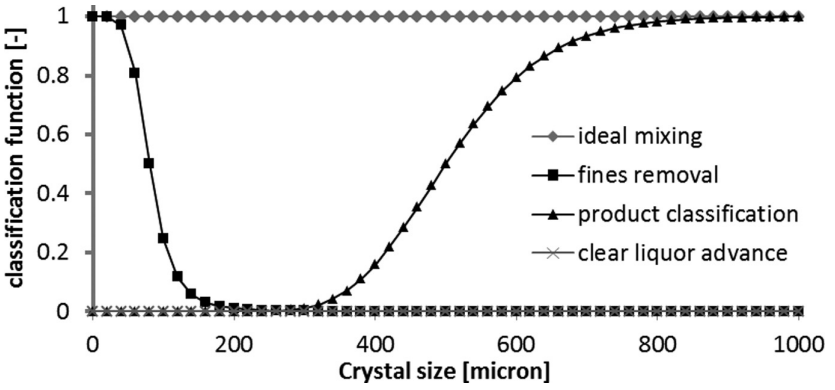

Figure 7.2 Examples of classification functions.

7.3.2 The population balance for agglomeration and breakage

Agglomeration is a volume-based mechanism that influences the number of particles in the system, but conserves the total volume of the particles. It is thus convenient to formulate the PBE in the presence of agglomeration in terms of volume coordinates. This greatly simplifies the birth ($B(v)$) and death ($D(v)$) terms.

The rate of agglomeration r_{agg}, depends on the number n of particles present, the size v of the particles involved and process conditions, such as the relative supersaturation σ and the power input P_0:

$$r_{agg}(v_1, v_2) = \beta_{agg}(v_1, v_2, \sigma, P_0)n(v_1)n(v_2) \tag{7.9}$$

The rate constant for agglomeration β_{agg}, is commonly referred to as the agglomeration kernel. In this section no further attention will be paid to the structure of this kernel, as the size, supersaturation and turbulence level dependency of the agglomeration kernel is discussed extensively in Chapter 6. Again as we consider here the model for a well-mixed compartment only, the kernel will only include dependency on size and power input, i.e. $\beta_{agg}(v_1, v_2)$ and no dependence of the spatial coordinates, because turbulence level in the compartment is assumed to be uniform.

Considering the schematic representation of agglomeration on the crystal volume axis in Figure 7.3, one can easily deduce the associated birth and death terms.

$$B(v) = \frac{1}{2}\int_0^v \beta_{agg}(\xi, v-\xi)n(\xi)n(v-\xi)\,\mathrm{d}\xi \tag{7.10}$$

$$D(v) = n(v)\int_0^\infty \beta_{agg}(\xi, v)n(\xi)\,\mathrm{d}\xi \tag{7.11}$$

The correction factor ½ in the birth equation is due to the integration of ξ from 0 to v, resulting in each particle being accounted for twice: as a particle of size ξ and as a particle of size $(v-\xi)$.

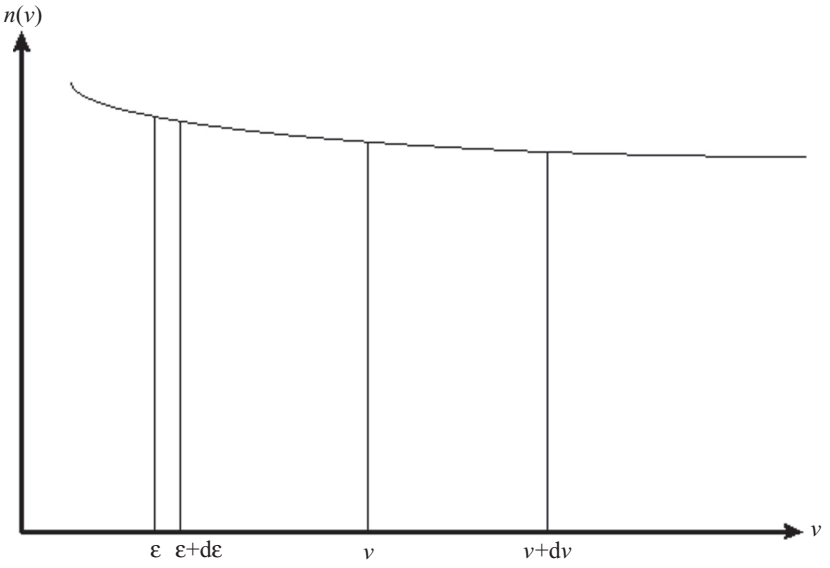

Figure 7.3 Schematic representation of the formation of agglomerates with volume v from particles with volumes ξ and $(v - \xi)$, respectively.

Substituting these expressions for the birth and death of particles of a certain size due to agglomeration into the PBE, for a system that exhibits no significant growth or breakage, leads to the following equation:

$$\frac{\partial(n(v,t)V(t))}{\partial t} = \left[\frac{1}{2}\int_0^v \beta_{agg}(\xi, v-\xi)n(\xi,t)n(v-\xi,t)\,\mathrm{d}\xi - n(v,t)\int_0^\infty \beta_{agg}(\xi,v)n(\xi,t)\,\mathrm{d}\xi\right] V + \sum_{j=1}^{m}\varphi_{v,in,j}(t)n_{in,j}(v,t) - \sum_{k=1}^{n}\varphi_{v,out,k}(t)h_{out,k}(v,t)n(v,t) \tag{7.12}$$

As mentioned above, breakage of crystals seldom occurs. Breakage is a size-reducing mechanism which, analogous to agglomeration, influences the number of particles in a system, but not their total volume. Again it is convenient to use the PBE in volume coordinates. The kinetics of breakage are described by two functions $D(v,t)$ and $B(v,t)$. These functions depend on a selection function $S(v)$ and on a breakage constant $b(\xi, v)$, which describes the sizes v into which the selected particle of size ξ breaks:

$$D(v,t) = S(v,t)\cdot n(v,t) \tag{7.13}$$

$$B(v,t) = \int_v^\infty b(\xi,v)S(\xi,t)n(\xi,t)\,\mathrm{d}\xi \tag{7.14}$$

Substitution into the PBE gives us the following equation for breakage only:

$$\frac{\partial(n(v,t)V(t))}{\partial t} = \left[\int_v^\infty b(\xi,v)S(\xi,t)n(\xi,t)\,\mathrm{d}\xi - S(v,t)n(v,t)\right]V + \sum_{j=1}^{m}\varphi_{v,in,j}(t)n_{in,j}(v,t) - \sum_{k=1}^{n}\varphi_{v,out,k}(t)h_{out,k}(v,t)n(v,t) \quad (7.15)$$

7.3.3 Relationship between the population balance and mass and heat balances

The description of the CSD evolution in a crystallizer requires that the PBE is combined with the material and enthalpy balances from Chapter 4 and with equations for kinetic phenomena as a function of process conditions. The PBE and material balances are connected through the crystal volume balance, which can be derived directly from the PBE and describes the evolution of the crystal mass in the crystallizer.

Multiplying equation 7.1 by $k_v L^3$ and integrating over the crystal domain, assuming a constant suspension volume, leads to:

$$k_v\frac{\mathrm{d}}{\mathrm{d}t}\int_0^\infty nL^3\,\mathrm{d}L = -k_v\int_0^\infty\frac{\partial(G_L n)}{\partial L}L^3\,\mathrm{d}L + k_v\int_0^\infty(B-D)L^3\,\mathrm{d}L + \frac{k_v}{V}\sum_{j=1}^{m}\varphi_{v,in,j}\int_0^\infty n_{in,j}L^3\,\mathrm{d}L - \frac{k_v}{V}\sum_{k=1}^{n}\varphi_{v,out,k}\int_0^\infty h_{out,k}nL^3\,\mathrm{d}L \quad (7.16)$$

Realizing that $\varepsilon = 1 - k_v m^3$ and that the mass in agglomeration and breakage processes is conserved, making the second term on the right-hand side of the equation equal to zero, we obtain

$$-\frac{\mathrm{d}\varepsilon}{\mathrm{d}t} = -3\int_0^\infty G_L nL^2\,\mathrm{d}L + \frac{1}{V}\sum_{j=1}^{m}\varphi_{v,in,j}(1-\varepsilon_{in,j}) - \frac{1}{V}\sum_{k=1}^{n}\varphi_{v,out,k}(1-\varepsilon_{out,j}) \quad (7.17)$$

This term is needed to solve the material and the enthalpy balances, as illustrated here for the component mass balance:

$$\frac{\mathrm{d}M_i}{\mathrm{d}t} = \sum_{j=1}^{m}M_{in,j,i} - \sum_{k=1}^{n}M_{out,k,i} \quad (7.18)$$

The first term contains a contribution from both the liquid and the crystalline phases to the mass of component i and can be written under the assumption that the suspension volume V and the crystal composition $w_{crystal,1}$ [(kg component i) (kg crystal)$^{-1}$] are

constant as:

$$\frac{\mathrm{d}(V(\varepsilon\rho_{liquid}w_{liquid,i}+(1-\varepsilon)\rho_{crystal}w_{crystal,i}))}{\mathrm{d}t} = V\varepsilon\rho_{liquid}\frac{\mathrm{d}w_{liquid,i}}{\mathrm{d}t} + V(\rho_{liquid}w_{liquid,i}-\rho_{crystal}w_{crystal,i})\frac{\mathrm{d}\varepsilon}{\mathrm{d}t} \tag{7.19}$$

By inserting the crystal volume balance from equation 7.17 in the second term on the right-hand side of equation 7.19 we obtain the component balance, which is coupled to the population balance. In the same way the enthalpy balance can be coupled to the population balance.

7.4 Solving the population balance for an ideally mixed one-compartment model

In this section we will show solutions of the PBE for stationary and non-stationary operation. For stationary operation, analytical solutions of the PBE are available for simplified idealized crystallizer configurations, as will be discussed in Section 7.4.1. The effects of different crystallizer designs on the product quality will be elucidated. For non-stationary operation and for complex crystallizer models no analytical solutions are available, so numerical solution methods have to be applied. In a number of cases it is more adequate to use the method of moments. This method uses a transformation to convert the partial differential equation of the PBE into a set of four ordinary differential equations, as will be discussed in Section 7.4.2. The most commonly used numerical solution methods will be shortly addressed in Section 7.4.4.

Commercial industrial crystallizer designs have a number of features to manipulate the CSD of the product crystals, such as a system for withdrawal and dissolution of fine crystals and for the classification (on size) of product crystals. The equipment aspects of these features are discussed in detail in Chapter 10. In the next section we will analyze the effects of the presence of these features in a crystallizer on the product CSD, which requires the solution of the population balance model. Such an analysis is required to estimate the effect of these features on the crystal quality of an existing crystallizer. The modeling of the effects of these features, however, is also required to select the most appropriate type of crystallizer in the design phase.

7.4.1 Population balance equation for stationary operation

For continuous crystallizers operating at a steady state, a simplified PBE can be obtained assuming that:

- nucleation is only reflected by a boundary condition at $L = 0$: $n(0,t) = B_0(t)/G_L(0,t)$,
- growth is not size-dependent,
- the crystallizer volume (V) is constant in time,
- there is no agglomeration or breakage,
- crystal free inlet stream.

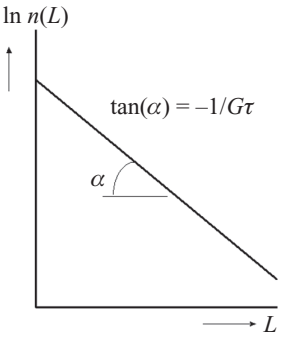

Figure 7.4 Steady-state crystal size distribution of a MSMPR crystallizer.

This results in a simplified PBE:

$$VG\frac{\partial n(L)}{\partial L} + \sum_{k=1}^{n} \varphi_{v,out,k} h_{out,k}(L) n(L) = 0 \tag{7.20}$$

In the following sub-sections, special cases of stationary continuous crystallizers will be treated. They only differ in the number of outflows, n, and the classification functions, $h(L)$, for these outflows:

1. Mixed-suspension mixed-product removal (MSMPR) crystallizer.
2. MSMPR crystallizer with clear liquor advance.
3. MSMPR crystallizer with fines removal and destruction.
4. Mixed-suspension crystallizer with classified product removal.
5. Mixed-suspension crystallizer with both classified product removal and fines removal.

7.4.1.1 Mixed-suspension mixed-product removal (MSMPR) crystallizer

The MSMPR crystallizer is the crystallization world's equivalent of the chemical engineer's CSTR. Its content is assumed to be well mixed and it has one non-classified outflow, i.e. $h(L) = 1$, which results in the following PBE:

$$VG\frac{\partial n(L)}{\partial L} + \varphi_{v,out} n(L) = 0 \tag{7.21}$$

For this simple equation an analytical solution exists. Integration of equation 7.21 results in the well-known logarithmic relation for the steady-state crystal size distribution:

$$n(L) = n(0)\mathrm{e}^{\left(-\frac{L}{G\tau}\right)} \tag{7.22}$$

where $n(0)$ [# m^{-3} m^{-1}] is the number density of negligibly small nuclei and τ is the residence time of the slurry in the crystallizer (see Figure 7.4). Such a concept of a well-mixed vessel can only be experimentally approached by using a small crystallizer that is thoroughly stirred. The steady-state crystal size distribution can be conveniently used to determine the growth rate G, as well as the nucleation rate $B(0)$.

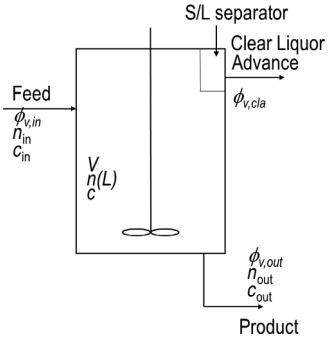

Figure 7.5 Crystallizer with clear liquor advance.

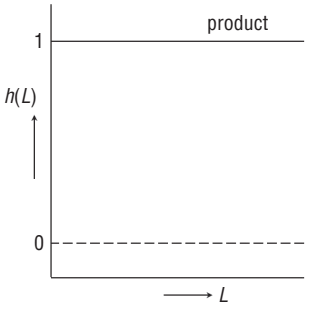

Figure 7.6 Ideal classification functions $h(L)$ for the product flow and clear liquor advance.

7.4.1.2 MSMPR crystallizer with clear liquor advance

Clear liquor advance is simply the removal of mother liquor from the crystallizer without simultaneous removal of crystals (see Figures 7.5 and 7.6). This method is often applied to reduce the quantity of liquor that must be processed by solid–liquid separation equipment. Equally important is the resulting higher solids concentration and thus an increased crystal surface area in the crystallizer, which is important for keeping the supersaturation low at relatively high production rates.

As a result of clear liquor advance, the residence time of the liquor τ_L will be smaller than the residence time of the product crystals τ_P, thus leading to an increase in the dominant crystal size L_D (as long as the increase in magma density does not lead to a significant increase in secondary nucleation). The solution of the PBE is as follows:

$$n(L) = n(0)\mathrm{e}^{-L/(G\tau_P)} \tag{7.23}$$

This steady-state crystal size distribution has the same shape as the MSMPR distribution, apart from the slope. It has been observed in practice that the increase in L_m may be greater than predicted from theory. This is because in practice the stream removed as clear liquor contains various amounts of fines. The actual classification function $h(l)$ for the fines thus deviates from zero for the tiniest crystals. This means that the stream characteristics approach those of classified-fines removal, which is discussed in the following section.

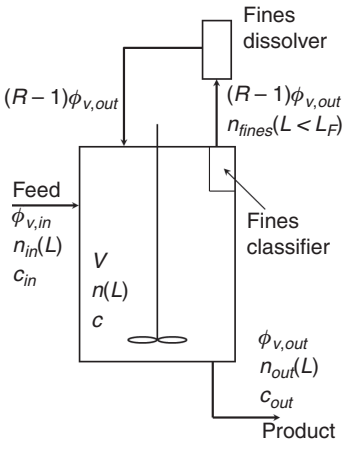

Figure 7.7 Crystallizer with fines removal and destruction.

Residence time product crystals:

$$\tau_P = \frac{V}{\varphi_{v,out}} = \tau \tag{7.24}$$

Residence time mother liquor:

$$\tau_L = \frac{V}{\varphi_{v,out} + \varphi_{v,cla}} \tag{7.25}$$

where $\varphi_{v,cla}$ represents the flow of the clear liquor advance.

7.4.1.3 MSMPR crystallizer with fines removal and destruction

Fines removal is the preferential withdrawal of crystals below some specified size L_F (= cut size) from the crystallizer. In this operation mode a crystallizer has two output streams with crystals, i.e. the fines stream and the product stream (see Figure 7.7). A typical classification function for fines removal is depicted in Figure 7.2. The product classification function $h(l) = 1$ for all sizes. The ratio between the flow rates of these streams is usually defined as $R - 1$, in order that the ratio between the residence time τ_P of crystals larger than L_F and the residence time τ_F of crystals smaller than L_F equals R. Fines removal increases the mean crystal size, but also increases the CSD spread. Analytical solutions for $n(L)$ for the product as well as the fines flow can only be derived for an idealized classification function for L with a sharp change from 1 to 0 at the cut size. Such a function is, however, unrealistic in practice.

Residence time crystals $L < L_F$:

$$\tau_F = \frac{V}{\varphi_{v,out} + (R-1)\varphi_{v,out}} = \frac{V}{R\varphi_{v,out}} = \frac{\tau}{R} \tag{7.26}$$

Residence time crystals $L > L_F$:

$$\tau_P = \frac{V}{\varphi_{v,out}} = \tau \tag{7.27}$$

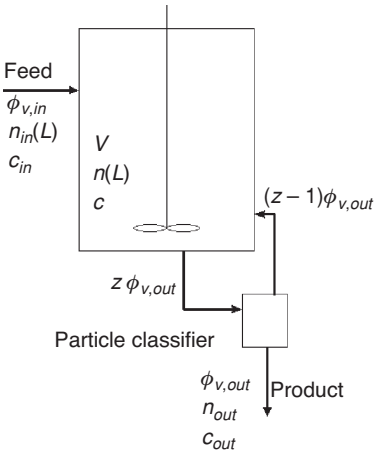

Figure 7.8 Crystallizer with classified product removal.

7.4.1.4 Mixed-suspension crystallizer with classified product removal

Classified product removal is the preferential withdrawal of crystals with sizes above a specified value L_P (= cut size). In this operation mode the crystallizer has two input streams, i.e. the feed stream of the crystallizer and the recycle stream from the classifier to the crystallizer, and one output stream, i.e. the inlet stream of the classifier (see Figure 7.8). The ratio between the volumetric flow rate of the classifier recycle flow and the volumetric flow rate of the classifier product flow is defined as $z - 1$. The classification function $h(l)$ of crystals up to the size L_P then equals $1/z$, while for crystals with sizes beyond L_P it equals 1. Crystals larger than L_P are thus removed at a rate of z times the removal rate expected for a perfectly mixed crystallizer. An analytical solution of $n(L)$ is again only available for a highly idealized classification function.

Residence time crystals $L < L_P$:

$$\tau_F = \frac{V}{\varphi_{v,out}} = \tau \tag{7.28}$$

Residence time crystals $L > L_P$:

$$\tau_P = \frac{V}{z\varphi_{v,out}} = \frac{\tau}{z} \tag{7.29}$$

The characteristics of the crystal size distribution obtained from a system with classified product removal show a narrower distribution and smaller dominant size.

7.4.1.5 Mixed-suspension crystallizer with both classified product removal and fines removal

In this process design, often referred to as the *R-z* model, classification functions for the removal of fines and of coarse particles have to be included in the PBE (see Figure 7.9). For $L_P > L > L_F$ the product classification function $h(l) = 1$, while for $L > L_P$ the classification function $h(l) = \mathrm{z}$.

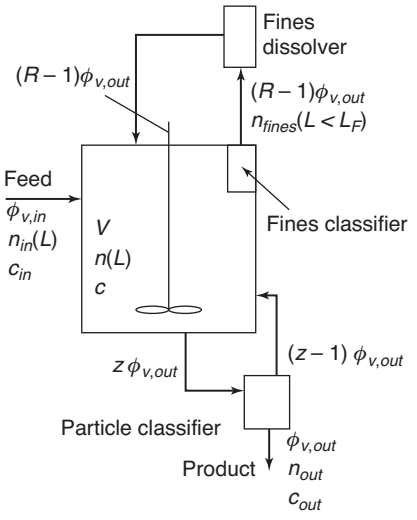

Figure 7.9 Crystallizer with both classified product removal and fines removal.

Residence time crystals $L < L_P$:

$$\tau_F = \frac{V}{j_{v,out}} + (R-1)j_{v,out} = \frac{V}{Rj_{v,out}} = \frac{\tau}{R} \tag{7.30}$$

Residence time crystals $L_F < L > L_P$:

$$\tau_{FP} = \frac{V}{\varphi_{v,out}} = \tau \tag{7.31}$$

Residence time crystals $L > L_P$:

$$\tau_P = \frac{V}{z\varphi_{v,out}} = \frac{\tau}{z} \tag{7.32}$$

The mean size of the product crystals becomes larger than for an MSMPR and the spread in the distribution of the product size is lower.

7.4.2 Moment equations for stationary and non-stationary operation

In the case of stationary or steady-state operation of a continuous crystallization process, the CSD remains constant in time. If the CSD oscillates in time, the operation is non-stationary, also named dynamic. Batch processes are, as mentioned before, inherently non-stationary. Even for ideally mixed crystallizers, analytical solutions to the population balance equation for non-stationary operation rarely exist. However, by transforming the PBE into a moment form, the PBE, being a partial differential equation, is transformed into a set of four to five ordinary differential equations that can be solved quite easily. The moment equations thus allow us to describe steady state as well as dynamic behavior of crystallizers.

Table 7.1 The meanings of the various moments of a size distribution

Moment	Meaning	Units
m_0	Total number of particles per unit crystallizer volume	[# m^{-3}]
m_1	Total length of particles per unit crystallizer volume	[m m^{-3}]
m_2	Related to total surface area of particles per unit crystallizer volume	[m^2 m^{-3}]
m_3	Related to total volume of particles per unit crystallizer volume	[m^3 m^{-3}]

The moments of a distribution are generally defined as:

$$m_j = \int_0^\infty n(L) L^j \, \mathrm{d}L \tag{7.33}$$

Moments can be related to lumped properties of the entire crystal population (Table 7.1).

For a *continuously operated crystallization system* with a constant volume, with size-independent growth, nucleation at zero size, one crystal-free inlet stream and a non-classified product stream, the PBE presented in equation 7.1 becomes:

$$\frac{\partial n(L,t)}{\partial t} = -G_L(t)\frac{\partial n(L,t)}{\partial L} + \frac{n(L,t)}{\tau} \tag{7.34}$$

with nucleation described via the birth term in the boundary condition $n(0, t)$ and an initial population $n(L, 0)$.

This partial differential equation (PDE) can be reduced to a set of ordinary differential equations (ODEs) by means of the moment transformation (Randolph and Larson, 1988):

$$\frac{\mathrm{d}m_j}{\mathrm{d}t} = jGm_{j-1} - \frac{m_j}{\tau} + B^0 L_0^j \tag{7.35}$$

where L_0 denotes the size of the nuclei, which in this case equals zero. In order to solve the transformed PBE, only four ODEs are required, namely the zeroth ($j = 0$) to the third ($j = 3$) moment to describe the crystallization process:

$$\frac{\mathrm{d}m_0}{\mathrm{d}t} = -\frac{m_0}{\tau} + B^0 \tag{7.36}$$

$$\frac{\mathrm{d}m_1}{\mathrm{d}t} = Gm_0 - \frac{m_1}{\tau} \tag{7.37}$$

$$\frac{\mathrm{d}m_2}{\mathrm{d}t} = 2Gm_1 - \frac{m_2}{\tau} \tag{7.38}$$

$$\frac{\mathrm{d}m_3}{\mathrm{d}t} = 3Gm_2 - \frac{m_3}{\tau} \tag{7.39}$$

For a *continuously operated crystallizer at steady state* the moment equations can be further simplified to obtain a set of algebraic equations describing the total number, length, surface area, volume and mass of crystals per unit crystallizer volume.

In that case the total crystal volume concentration V_T [(m^3 crystals) (m^3 suspension)$^{-1}$] that is related to the third moment via the volume shape factor, k_v, equals

$$V_T = k_v \cdot m_3 = 3 \cdot k_v \cdot G \cdot \tau \cdot m_2 = 6 \cdot k_v \cdot G^4 \cdot \tau^4 \cdot n_0 \tag{7.40}$$

Table 7.2 Moments of a particle size distribution, with size expressed in terms of both length and volume

	Length		Volume	
m_0	Total number of particles	$[m^{-3}]$	Total number of particles	$[m^{-3}]$
m_1	Total length of particles	$[m\ m^{-3}]$	Total volume of particles	$[m^3\ m^{-3}]$
m_2	Total surface area of particles	$[m^2\ m^{-3}]$	Gelation	$[m^6\ m^{-3}]$
m_3	Total volume of particles	$[m^3\ m^{-3}]$	–	–

and the total crystal concentration [kg $(m^3$ suspension$)^{-1}$] is simply obtained by multiplication with the material density of the crystals, $\rho_{crystal}$:

$$M_T = \rho_{crystal} \cdot V_T = 6 \cdot k_v \cdot n_0 \cdot G^4 \cdot \tau^4 \cdot \rho_{crystal} \tag{7.41}$$

7.4.3 Moment equations in case of agglomeration and breakage

The PBE with agglomeration and/or breakage terms can rarely be solved analytically. The subsequent steps in agglomeration of collision and adhesion are treated in Chapter 6. In case of a size-independent kernel, it is convenient to describe agglomeration using the PBE in moment equations with birth ($B(v)$) and death ($D(v)$) terms in volume coordinates.

The moment transformation is thus called for, with the moments of a distribution still defined as:

$$m_j = \int_0^\infty n(v) v^j \, \mathrm{d}v \tag{7.42}$$

Here v is the volume of the crystals $= k_v L^3$. Care must be taken to not confuse moments derived from PBEs with length and with volume as size coordinates. The third moment of a length-based size distribution equals the first moment of a volume-based size distribution, as shown in Table 7.2.

If a crystallization system with a constant volume, one inlet stream and a non-classified product stream is considered, the moment transformation of the PBE (equation 7.1) results in:

$$\frac{\mathrm{d}m_j}{\mathrm{d}t} = \frac{m_{j,in} - m_j}{\tau} + \overline{B_{agg,j}} - \overline{D_{agg,j}} \tag{7.43}$$

As mentioned above, breakage of crystals seldom occurs. Breakage is a size-reducing mechanism that influences the number of particles in a system, but not their total volume. Again it is convenient to use the PBE in volume coordinates. The kinetics of breakage are described by two functions $D(v, t)$ and $B(v, t)$. These functions depend on a selection function $S(v)$ and on a breakage constant $b(\xi, v)$, which describes the sizes v into which the selected particle of size ξ breaks:

$$D(v, t) = S(v, t) \cdot n(v, t) \tag{7.44}$$

$$B(v, t) = \int_v^\infty b(\xi, v) S(\xi, t) n(\xi, t) \, \mathrm{d}\xi \tag{7.45}$$

Substitution into the PBE gives us the following equation for breakage only:

$$\frac{\partial(n(v,t)V(t))}{\partial t} = \left[\int_v^\infty b(\xi,v)S(\xi,t)n(\xi,t)\,\mathrm{d}\xi - S(v,t)n(v,t)\right]V + \sum_{j=1}^{m}\varphi_{v,in,j}(t)n_{in,j}(v,t) - \sum_{k=1}^{n}\varphi_{v,out,k}(t)h_{out,k}(v,t)n(v,t) \quad (7.46)$$

If one again considers a crystallization system with a constant volume, one inlet stream and a non-classified product stream, moment transformation of the above PBE also results in:

$$\frac{\mathrm{d}m_j}{\mathrm{d}t} = \frac{m_{j,in} - m_j}{\tau} + \overline{B_{break,j}} - \overline{D_{break,j}} \quad (7.47)$$

7.4.4 Numerical solutions of the PBE

Since analytical solutions for the population balance equations are limited to a few simplified cases, generally numerical techniques are needed. A number of numerical techniques have been developed in recent years for different applications which roughly fall into three different categories, i.e. the method of characteristics (Kumar and Ramkrishna, 1997), the method of weighted residuals, which approximates the population density by a linear combination of basis functions (Ramkrishna, 2000), and the method of finite differences on a discretized poulation balance (Bermingham *et al.*, 2003; Kumar and Ramkrishna, 1996). The advantage of the last method is that no restrictions need to be made with respect to kinetic models or classification functions and it is therefore generally applicable. A detailed discussion of these discretization techniques falls beyond the scope of this book and the reader is referred to Qamar *et al.* (2006) and Qamar and Warnecke (2007) for a comparison between different solution methods.

In the method of finite differences/discretized PBE the population density function is approximated by a finite difference scheme. Discretization schemes with different orders of accuracy such as the finite-volume and high-resolution schemes have been discussed in detail (Qamar *et al.*, 2006). A widely used discretization method is the finite-volume method. In this method the number of crystals are considered in a size class L_i, with upper and lower boundaries $L_{i-1/2}$ and $L_{i+1/2}$ of size class i, respectively:

$$N_i = \int_{L_{i+1/2}}^{L_{i-1/2}} n\,\mathrm{d}L \approx n_i\left(L_{i+1/2} - L_{i-1/2}\right) \quad (7.48)$$

The PBE can then be written for each size class i as:

$$\frac{\partial n_i}{\partial t} = -\left|\frac{\partial Gn}{\partial L}\right|_{L=L_i} + B_i - D_i + \frac{\varphi_{v,in}}{V}n_{in,i} - \frac{\varphi_{v,out}}{V}h_{out,i}n_i \quad (7.49)$$

where the partial derivative is calculated from the values of n at the class boundaries.

$$\left[\frac{\partial Gn}{\partial L}\right]_i = G_i\frac{n_{i+1/2} - n_{i-1/2}}{L_{i+1/2} - L_{i-1/2}} \quad (7.50)$$

In a first-order upwind approximation the values at the boundary depend on whether the growth rate is positive or negative:

$$\begin{aligned} G_{L,i} \geq 0: &\quad n_{i+1/2} = n_i, \quad n_{i-1/2} = n_{i-1} \\ G_{L,i} < 0: &\quad n_{i+1/2} = n_{i+1}, \quad n_{i-1/2} = n_i \end{aligned} \tag{7.51}$$

The first-order upwind scheme gives a robust approximation that suffers from numerical diffusion, however. More accurate high-resolution schemes have been developed and are extensively discussed (Qamar *et al.*, 2006).

In addition, commercial software is available to solve the models for industrial crystallizers. The most well known are gCRYSTAL from PSEnterprse Ltd, which provides the user with an advanced modeling library to model, analyze and optimize industrial crystallization processes. The library is based on the gPROMS engine and includes advanced tools for parameter estimation and optimization. A second commercial tool is PARSIVAL, a weighted residual method on the basis of adaptive Galerkin functions (Wulkow *et al.*, 2001).

7.5 Modeling and scaling-up of crystallizers

As has been discussed before, in industrial crystallizers, which can reach more than 100 m^3 for a single unit and can have complex geometrical designs, local differences in supersaturation, turbulence and crystal concentrations are unavoidable. In industrial practice, steep supersaturation gradients have been reported in the boiling zone of evaporative crystallizers, at the heat exchanger surfaces of cooling crystallizers or at the feed points in precipitation or anti-solvent crystallization (Bermingham *et al.*, 1998, Daudey *et al.*, 1990, Fakatselis, 2002). In addition the crystal concentration in an industrial crystallizer is often far from uniform (Palosaari *et al.*, 1996). In the case of evaporation the supersaturation is highest in the boiling zone, sometimes leading to primary nucleation. Floatation of fines occurs in the boiling zone. With cooling crystallization the supersaturation is highest at the heat exchanger surface, where scaling can give heterogeneous nuclei. For precipitation by mixing of reagents or in anti-cooling crystallization the highest supersaturations are encountered in the mixing zones.

The presence of these gradients can have a strong impact on the crystallization kinetics. For instance, the differences in non-linear dependence of the growth, nucleation and agglomeration rate on the supersaturation will lead to erroneous rates for these kinetic processes and thus to a wrong CSD when the supersaturation profiles are approximated with a well-mixed crystallizer model. As a result, the parameters of a kinetic model that is fitted to describe experimental data of such a crystallizer are not the true kinetic parameters but are "contaminated" by the hydrodynamic behavior of the crystallizer. That means that the derived model will not be able to predict the crystallizer behavior, either of the same crystallizer under different process conditions or of a crystallizer with a different scale or configuration. This is particularly important for the design of a crystallizer, in which the performance of a new crystallizer is in most cases predicted using a model, but validated on a crystallizer of a different scale and design.

In order to take into account the existence of gradients in supersaturation, turbulence and particle concentration, spatially distributed models should be used, in which all the process variables are a function of the location in the crystallizer. This approach, however, turns the PBE into a four-dimensional partial differential equation, one for the internal crystal coordinate and three for the spatial location of the considered volume element. In addition, the flow field of the liquid and the crystal has to be determined for each location in the crystallizer. The complexity of such an approach is so huge that it is seldom applied. For precipitation processes, which are characterized by extreme supersaturation profiles and high nucleation rates at the inlets, modeling by either the Langrangian or the Eulerian approach is applied. These methods will be discussed in Chapter 13.

A less complex approach is to divide the crystallizer volume into a number of compartments, assuming that each compartment can be considered a well-mixed entity. Especially for crystallization processes such as cooling and evaporative crystallization, compartment modeling has been proven to describe or predict the product size distribution in a satisfactory way (Bermingham *et al.*, 2003).

For the selection of compartments in large crystallizers not only are the type of crystallization process and the crystallizer design important, but also the hydrodynamics in the crystallizer. In fact only if the rate of mixing is much faster than the rate at which the supersaturation is depleted by the kinetic processes can the crystallizer be considered a well-mixed compartment (Bermingham *et al.*, 2003). In addition, if classification of the crystals occurs in certain zones of the crystallizer, profiles in crystal concentration and supersaturation are unavoidable and a compartmental model should be considered. In such cases, classification functions must be defined for the flows between the different compartments. If information is available from measurements or CFD models on the flow rates of the suspension between the compartments, the classification functions for these flows can be estimated using a settling model. In this way the effects of impellers, boiling and settling zones, and fines dissolution can be analyzed. In compartment modeling of "large" crystallizers, the region around the agitator is mostly taken as a separate compartment, which gives more insight into the attrition rate due to collisions between the crystals and the impeller blades.

A generic approach in modeling of crystallizers is thus to select a number of compartments connected through classification functions for the crystals. Another compartment approach is the Eulerian approach where the crystallizer is divided into a large number of compartments. Each compartment has inlet and outlet flows from or towards the six attached compartments. The directions of the flows are given by the hydrodynamic pattern in the crystallizer, and each flow carries its own CSD.

So modeling of a crystallizer can only properly be achieved by the compartment approach, where the choice of the size and number of compartments depends on the size of the crystallizer, the crystallization kinetics and the hydrodynamics. It is the only way to properly scale up a crystallization process. The engineering approach to scaling up using dimensionless numbers fails in the case of crystallization.

To illustrate the impact of the effects of hydrodynamics and scale on the performance of an industrial crystallizer two examples will be given, which demonstrate how compartment models can be useful to estimate the gradients in process conditions.

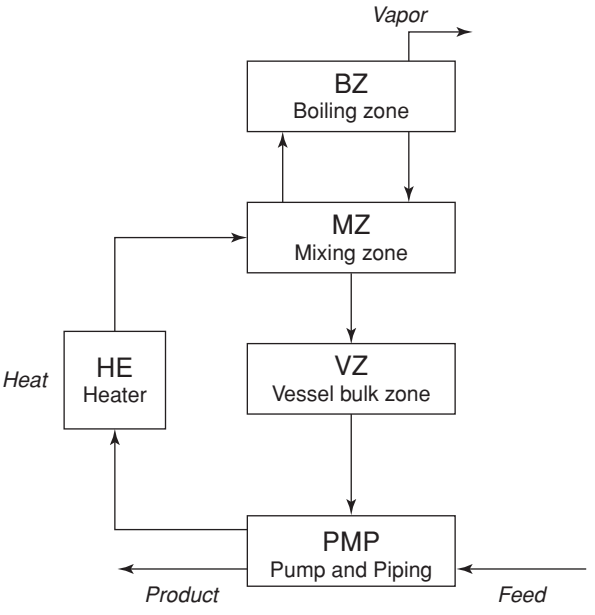

Figure 7.10 A five-compartment model for an FC crystallizer. From Bermingham *et al.*, 1998 with permission.

Case study 1: an FC crystallizer

In an FC crystallizer, which is often considered as the workhorse of industrial crystallizers (see Figure 10.9), the mixing of the crystal suspension is induced by the circulation flow over the external heat exchanger. As this crystallizer has no internal impeller, the mixing of the suspension is fully dependent on the external circulation. This type of crystallizer is mostly considered as a well-mixed vessel, although gradients in the process conditions might be expected between the boiling zone, where the solvent is flashed off, and the main body and the circulation line of the crystallizer (see Chapter 10 for details). A compartmental model has been derived to analyze the effects of the circulation flow rate on the mixing and on the supersaturation profile. A five-compartment model is used in this study (see Figure 7.10) consisting of compartments for the pump and piping, the heat exchanger, including the return line to the crystallizer, a mixing zone, a boiling zone and a bulk vessel zone. Using the kinetic model of O'Meadhra *et al.* (1996), it was shown that a large supersaturation profile exists between the different zones in the crystallizer, which is strongly dependent on the circulation flow rate. This example clearly shows that there will be a supersaturation profile in such a crystallizer, which cannot be studied by a single compartment model. Such a supersaturation profile can affect the performance of a crystallizer as high supersaturation in the boiling zone could give rise to excessive nucleation.

However, it is clear that the supersaturation profile predicted by the model might be dependent on the compartment structure chosen for the model. A model with ten compartments might show a different profile from one with five. Therefore a detailed

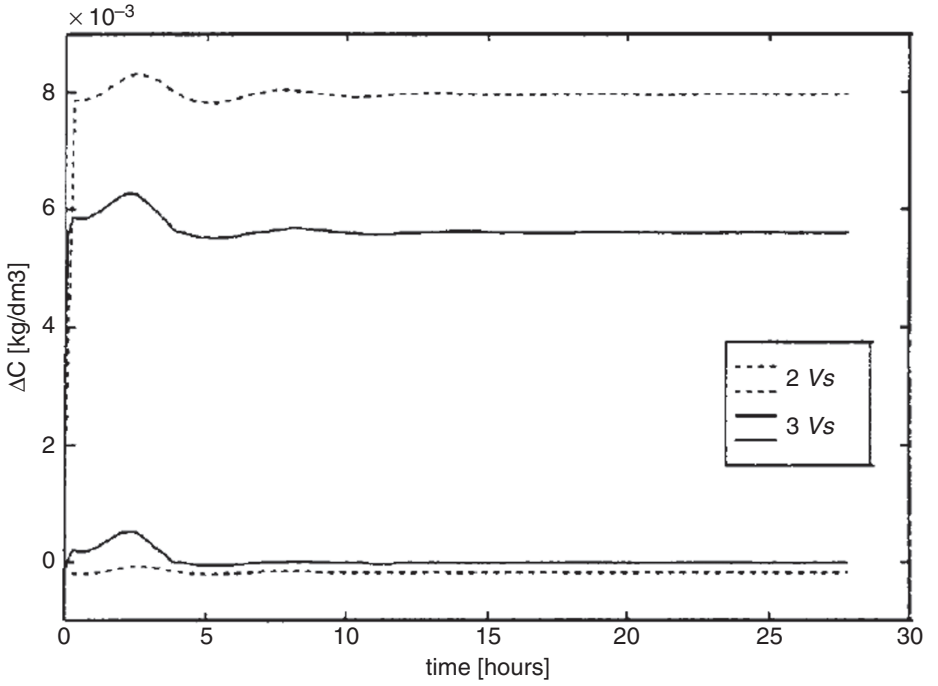

Figure 7.11 Simulated supersaturation profile in the boiling zone (upper two lines) and the heat exchanger (lower two lines) of a 200 liter FC crystallizer for two values of the circulation flow rate. From Bermingham *et al.*, 1998, with permission.

analysis of the flow pattern and the crystallization kinetics is required to design the compartment structure (see Figures 7.10 and 7.11).

Case study 2: scale up of a DTB crystallizer

Another example, which shows the subtle effect of scale and the presence of classification zones in a DTB crystallizer, is given by Bermingham *et al.* (2003). In this type of crystallizer with an external heat exchanger, the fine crystals are separated in a settling zone created by a skirt baffle around the main body. The fines are dissolved by the temperature rise in the external heat exchanger (see Figure 7.12, left and Chapter 10). In this example two different compartment models are compared, one consisting of four compartments, i.e. the stirrer compartment in the crystallizer, the crystallizer main body (part of the crystallizer enclosed by the dashed line in right part of Figure 7.12), the annular zone and the fines dissolver, while in the second the main body of the crystallizer is sub-divided into four compartments, a boiling zone, a mixing zone at the bottom of the vessel, a riser compartment inside the draft tube and a down-comer outside the draft tube. The first, four-compartment model, in which the main body was considered as a well-mixed vessel, allowed one to study the influence of settling and holdup in the annular zone. The second, seven-compartment model,

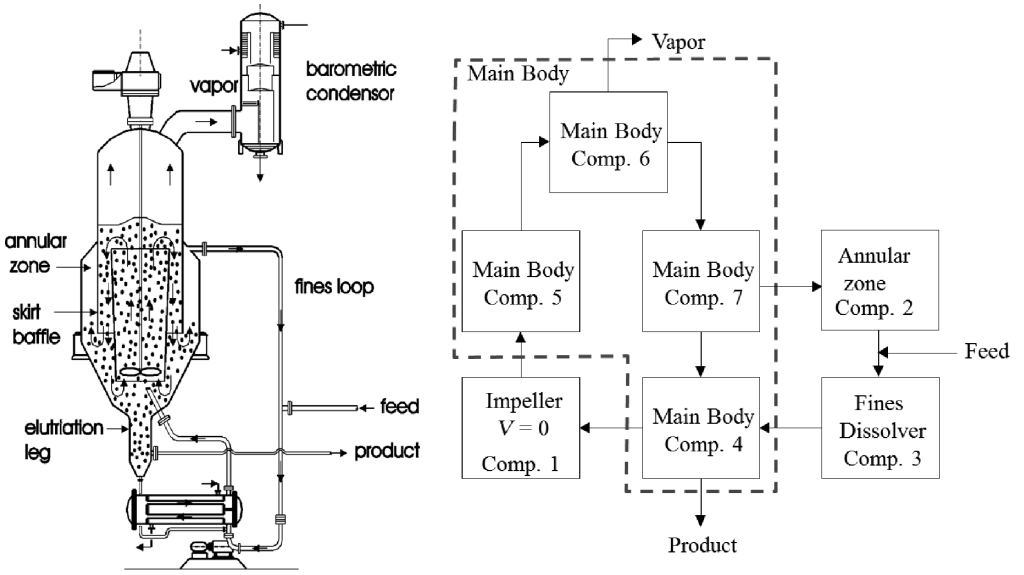

Figure 7.12 A DTB crystallizer (left) and two compartment models (right) consisting of four and seven compartments, respectively.

permitted the internal classification of the crystals in the main body to be taken into account.

The model was applied on two different crystallizer scales (1.1 versus 360 m^3).

Some of the results are shown in Figures 7.13 and 7.14 for the simulation on the 1.1 and the 360 m^3 crystallizers, respectively. The most striking difference is that for a 1.1 m^3 crystallizer the effect of compartmentation of the main body has only a minor influence on the product size, while for the 360 m^3 crystallizer a strong effect is visible. This example clearly shows the dramatic effect of the scale of operation on the efficiency of a fines removal systems in this type of crystallizer.

7.6 A brief summary of the chapter

In this chapter the population balance equation, which describes the development of the CSD in industrial crystallization processes, is introduced. An extensive discussion of the mathematical formulation, the possible solution methods and the application of this important equation is given. It is shown that the PBE allows for a mathematical description of the effect of the different kinetic phenomena that are active in industrial crystallizers on the CSD of the crystalline product. In addition the PBE can describe the effects of different features of industrial crystallizers to manipulate this CSD and is therefore a valuable tool to get insight into the kinetic processes in a crystallizer, to optimize and control the process conditions and finally for the design of such equipment.

In continuously operated crystallizers, stationary solutions can easily be determined. Application of this solution method to an idealized well-mixed crystallizer (the

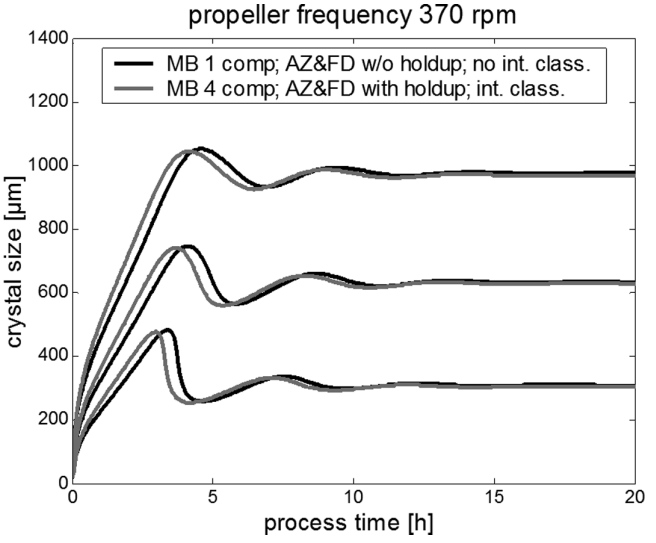

Figure 7.13 Simulations of 1100 liter DTB crystallizer illustrating the combined effect on the CSD transient of: (i) taking into account the hold-up of the annular zone and (ii) describing the main body with multiple compartments. CSD depicted here in terms of 25, 50 and 75% quantiles. From Bermingham *et al.*, 2003 with permission.

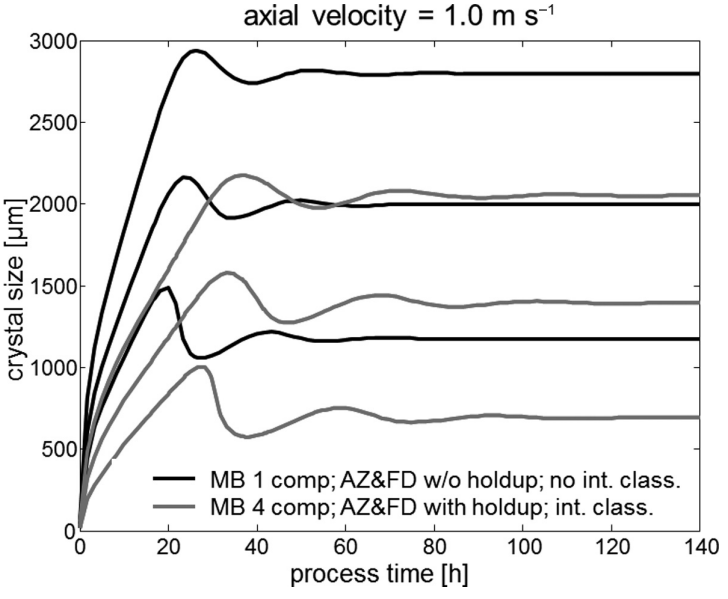

Figure 7.14 Simulations of 360 m^3 DTB crystallizer illustrating the combined effect on the CSD transient of: (i) taking into account the hold-up of the annular zone and (ii) describing the main body with multiple compartments. CSD depicted here in terms of 25, 50 and 75% quantiles. From Bermingham *et al.*, 2003 with permission.

so-called MRMPR crystallizer) and to MSMPR crystallizers with simple fines removal and product classification features allows a simple analysis of the effects of these features on the product quality. Such an analysis can be helpful in the first selection of an industrial crystallizer in the design phase.

The application of these simple solution methods, however, appears to have severe limitations and to have in general little predictive value. For a detailed analysis and design of industrial crystallizer processes, more complicated numerical methods must be used. Such numeric methods are available in commercial tools and are also discussed in this chapter.

Another aspect of the modeling of industrial crystallizers is the reported existence of steep gradients in the process variables such as the temperature, supersaturation and the particle concentration. The presence of these gradients can have a strong impact on the crystallization kinetics and will lead to erroneous prediction of the rates of these kinetic processes and thus to an incorrect CSD, when the supersaturation profiles are approximated with a well-mixed crystallizer model. In this chapter the compartmental modeling approach is discussed in which the crystallizer volume is divided into a finite number of compartments, assuming that each compartment can be considered as a well-mixed entity. Two examples are given in which a compartmental modeling approach is clearly needed to describe the physical reality in the crystallizer and to get insight into scale-up effects in particular. Especially for crystallization processes such as cooling and evaporative crystallization, compartment modeling has been proven to describe or predict the product size distribution in a satisfactory way (Bermingham *et al.*, 2003).

7.7 End of chapter problems

Problem 1

To estimate the crystallization kinetics for a compound that has to be crystallized by a company, a continuous crystallization experiment has been conducted in a small-scale MSMPR crystallizer. After reaching a steady state in the crystallizer, the CSD has been analyzed and the results are given in Table 7.3. If the residence time in the crystallizer during the experiment was 1000 seconds, calculate the growth and secondary nucleation rate, as well as the mean crystal size of the distribution.

Problem 2

Formulate the complete model for a DTB crystallizer including the total mass, the material and the enthalpy balance using the moment equations to solve the PBE. Make the following assumptions:

Table 7.3 The population density n as function of the crystal size L, determined at steady state in a MSMPR crystallizer

L [μm]	50	100	150	250	500
N [# m^4]	6.30×10^{13}	1.19×10^{13}	2.25×10^{12}	8.01×10^{10}	1.93×10^{7}

- Constant suspension volume
- Crystal-free feed
- No classification ($h_F = 0$ and $h_p = 1$ for all L)
- Only one crystal phase and no solvent in the crystal phase
- Constant crystallizer temperature
- No agglomeration or breakage
- Growth rate is size independent.
- Nucleation only takes place at L_0.

Problem 3

Implement the model in a simulation program like Matlab and calculate the profile of the moments and the mean crystal size after start-up of the crystallizer. Assume the following relation for the nucleation rate and growth rate: $G = k_g \sigma^{\delta}$.

The saturation concentration is given by the equation $W_{sat} = k_1 + k_2 * T + k_3 * T^2$ (T in °C)

Use the following information: $\alpha = 3$; $\beta = 1$; $\gamma = 1$; $\delta = 1$; $k_N = 1.06 \times 10^{14}$; $k_g = 0.00002$; $Psp = 1.5$; $\rho_1 = 1162$; $\rho_c = 2338$; $\rho_v = 1000$; $cpl = 2.9$; $cpc = 1.4$; $cpw = 4.1$; $k_1 = 0.1179$; $k_2 = 0.0031$; $k_3 = 7 \times 10^{-6}$; $\varphi_p = 0.2 \times 10^{-3}$; $W_c = 1$; $V = 1$; $T = 70$; $T_{feed} = 70$; $\mathrm{d}H_{cryst} = 0$; $\mathrm{d}H_{evap} = 2100$; $Q_{heat} = 180$ kW; $k_Y = 0.45$. What is k_v?

Initial conditions: use an initial supersaturation of 1% and 5 kg of seed crystals, assuming a normal distribution with a mean value of 120 mm and standard deviation of 20.

Us a stiff integrator with a variable time step (ODE15s in Matlab) to solve the moment model.

Problem 4

Formulate the full population balance model for the DTB crystallizer including the numerical solution of the population balance applying the finite-volume method. Use the assumptions and data from Problems 2 and 3, with the following exception:

Classification function for the product flow

- $h_p(L) = 0$ for $L < L_p$
- $= a^* (L - L_p)$ for $L_p < L < L_p + 1/a$ $a = 1/(500 \times 10^{-6})$
- $= 1$ for $L > L_p + 1/a$

Classification function for the fines flow

- $h_F(L) = 1$ for $L < L_F$

assuming that all the removed fines dissolve in the external heat exchanger.

Problem 5

Implement the model and calculate the trends in the supersaturation, moments of the distribution and the mean crystal size. Plot also the population density at steady-state conditions. Use the data from Problem 3 with the following additional information

$$\varphi_{fines} = 3^* \varphi_p; L_F = 100 \times 10^{-6}; L_p = 300 \times 10^{-6}.$$

7.8 References

Bennett, R. C. 1993. Crystallizer selection and design. In *Handbook of Industrial Crystallization*, Myerson, A. S. (ed.), Butterworth-Heinemann.

Bermingham, S. K. 2003. *A Design Procedure and Predictive Models for Solution Crystallization Processes*, PhD thesis, Delft University of Technology.

Bermingham, S. K., Neumann, A. M., Muusze, J. P., Kramer, H. J. M. and Verheijen, P. J. T. 1998. Modelling the settling, dissolution and non-uniform nucleation kinetics in a 150-litre forced circulation crystallizer. *Particle and Particle Systems Characterization*, **15**, 56–61.

Bermingham, S. K., Neumann, A. M., Kramer, H. J. M. *et al.* 2000. A design procedure and predictive models for solution crystallisation processes. *AIChE Symposium Series 323*, **96**, 250.

Bermingham, S. K., Verheijen, P. J. T. and Kramer, H. J. M. 2003. Optimal design of solution crystallization processes with rigorous models. *Chemical Engineering Research and Design*, **81**, 893–903.

Bird, R. B., Steward, W. E. and Lightfoot, E. N. 1960. *Transport Phenomena*, John Wiley & Son.

Daudey, P. J., van Rosmalen, G. M. and de Jong, E. J. 1990. Secondary nucleation kinetics of ammonium-sulfate in a CMSMPR crystallizer. *Journal of Crystal Growth*, **99**, 1076–1081.

Fakatselis, T. E. 2002. Residence time optimization in continuous crystallizers. *Crystal Growth and Design*, **2**, 375–379.

Kramer, H. J. M., Bermingham, S. K. and Van Rosmalen, G. M. 1999. Design of industrial crystallizers for a required product quality. *Journal of Crystal Growth*, **198/199**, 729.

Kumar, S. and Ramkrishna, D. 1996. On the solution of population balance equations by discretization. 1. A fixed pivot technique. *Chemical Engineering Science*, **51**, 1311–1332.

Kumar, S. and Ramkrishna, D. 1997. On the solution of population balance equations by discretization. 3. Nucleation, growth and agglomeration of particles. *Chemical Engineering Science*, **52**(24), 4659–4679.

Mesbah, A., Kramer, H. J. M., Huesman, A. E. M. and Van den Hof, P. M. J. 2009. A control oriented study on the numerical solution of the population balance equation for crystallization processes. *Chemical Engineering Science*, **64**, 4262–4277.

Mullin, J. W. 1993. *Crystallization*, Butterworth-Heinemann.

Mersmann, A. 1995. *Crystallization Technology Handbook*, Marcel Dekker, Inc.

Nývlt, J. 1992. *Design of Crystallizers*, CRC Press.

Kumar, S. and Ramkrishna, D. 1996. On the solution of population balance equations by discretization. 1. A fixed pivot technique. *Chemical Engineering Science*, **51**, 1311–1332.

O'Meadhra, R., Kramer, H. J. M. and Van Rosmalen, G. M. 1996. Model for secondary nucleation in a suspension crystallizer. *AICHE Journal*, **42**, 973–982.

Palosaari, S., Sha, Z. L. and Toyokura, K. 1996. Crystallization design chart and computer algorithm. *Acta Polytechnica Scandinavica, Civil Engineering and Building Construction Series*, **234**, 1–49.

Qamar, S., Elsner, M. P., Angelov, I. A., Warnecke, G. and Seidel-Morgenstern, A. 2006. A comparative study of high resolution schemes for solving population balances in crystallization. *Computers and Chemical Engineering*, **30**, 1119–1131.

Qamar, S. and Warnecke, G. 2007. Numerical solution of population balance equations for nucleation, growth and aggregation processes. *Computers and Chemical Engineering*, **31**, 1576–1589.

Ramkrishna, D. 2000. *Population Balances: Theory and Applications to Particulate Systems in Engineering*, Academic Press.

Randolph, A. D. and Larson, M. A. 1988. *Theory of Particulate Processes*, 2nd edn., Academic Press.

Randolph, A. D. 1962. *Size Distribution Dynamics in a Mixed Crystal Suspension*, PhD Thesis, Iowa State University of Science and Technology.

Wulkow, M., Gerstlauer, A. and Nieken, U. 2001. Modeling and simulation of crystallization processes using parsival. *Chemical Engineering Science*, **56**, 2575–2588.

8 Batch crystallization

8.1 Why this chapter is important

There are a number of situations where batch operation is chosen instead of continuous operation (see Chapter 3). Batch processing is more economical for small production capacities of approximately 1 m^3 of product per day or less, for processing of expensive materials (because product offspec losses are low) such as pharmaceuticals, as well as for processing batches of different materials in the same industrial unit. Batch crystallization is also chosen for processing of compounds that form encrustations on the crystallizer walls, because the encrustations can be washed off after each batch cycle. The major advantage of batch crystallization is the ability to produce uniformly sized particles.

Seeding is an important tool to control the product size, so the seeding technique will be treated in detail. Batch crystallization can be quantitatively described by means of population balances coupled with mass and energy balances as well as with kinetic expressions for the elementary processes. These mathematical models can be used to help understand batch processes, as well as to develop operational policies (temperature, evaporation and reactant addition trajectories throughout a batch process) aiming at improved product quality, low cost, and low raw material and energy usage.

8.2 Phenomenological description of batch crystallization processes

A batch cycle starts with a solution that is slightly undersaturated with respect to the solute to be crystallized. Crystallization is achieved by any of the methods described in Chapter 1, i.e., cooling, solvent evaporation, anti-solvent addition or chemical reaction (precipitation). Usually seeds of the crystallizing material are added early in the batch process in order to improve reproducibility and product quality. When the desired amount of solid has been formed, the slurry is transferred to a solid–liquid separation unit. The crystallizer is then washed, and fresh solution is added and brought to the desired temperature to start a new batch cycle.

The main elementary processes taking place during batch crystallization are described next. Cooling crystallization will be treated here, but the analysis can equally well be applied to evaporative crystallization. For unseeded crystallization (Figure 8.1a), a hot, slightly undersaturated solution is cooled until it becomes supersaturated (region 1 in the

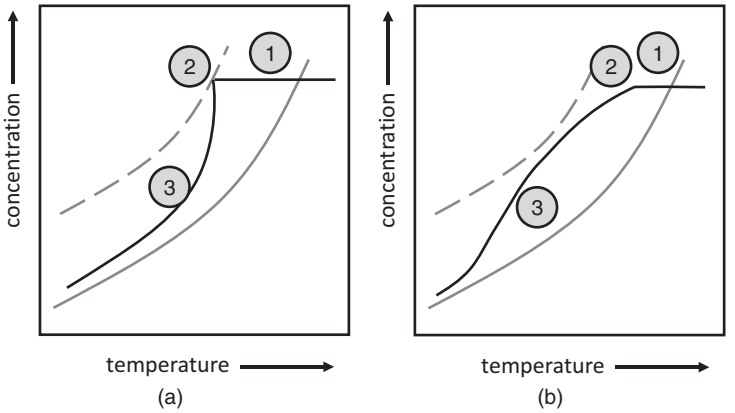

Figure 8.1 Solution concentration (black lines) throughout typical unseeded (a) and seeded (b) batch cooling crystallizations. The continuous gray line is the solubility; the dashed line is the metastable limit. See text for explanation of the numbers in the figures.

figure). Further cooling brings the solution beyond the metastable limit (beyond point 2), where primary, mostly heterogeneous, nucleation occurs, usually through an outburst of a large number of nuclei. Upon growth, these freshly formed nuclei become crystals. Since the solution is highly supersaturated, these crystals grow at a fast rate, promoting a reduction in solute concentration. This causes primary nucleation to stop. Heat released during phase transformation sometimes causes a slight increase in temperature. However, subsequent heat removal from the crystallizer results in cooling and crystal growth continues within the metastable region 3. In this region secondary nucleation may occur, provided that the crystallizer is agitated (so particles collide with each other and with the crystallizer walls), that the crystals are large enough to be prone to attrition and that the particle concentration is sufficiently large. Towards the end of the batch process the crystal surface area is large, so the solution closely approaches the solubility line.

Because the primary nucleation rate is a steep non-linear function of the supersaturation (see Chapter 5), the mentioned outburst of primary nuclei only occurs beyond the metastable limit at a high supersaturation. Due to this high supersaturation and to the stochastic nature of the nucleation process, the number and size distributions of the first crystal population have little reproduciblity between batch processes, resulting in a spread in final size distributions. Besides, tiny crystals grown at high supersaturation tend to agglomerate. In the absence of agglomeration, an excessive number of nuclei are generated, leading to a small-sized product.

In order to avoid the unwanted consequences of a primary (heterogeneous) nucleation event, seeds, i.e. small crystals of the crystallizing material, are often used. These seeds must be added at the beginning of the batch process within the metastable zone (Figure 8.1b, region 2). The seeds immediately start to grow, so the solution concentration drops (region 3). The supersaturation profile also depends on the amount and size of the seed particles, as well as on the rate of cooling. If proper seed addition and rate of cooling

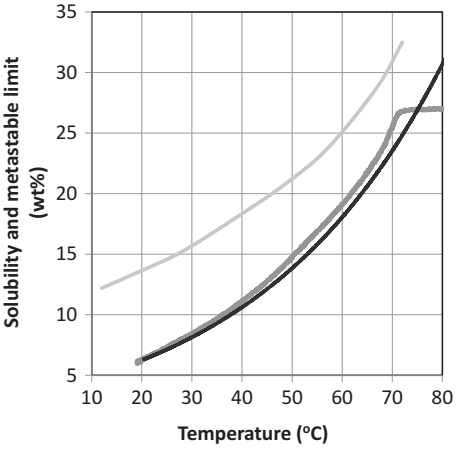

Figure 8.2 Solution mass fraction during the seeded batch cooling crystallization of pentaerythritol in aqueous solution.

are applied, the solution never reaches the metastable limit, so primary nucleation does not occur throughout the batch process.

Worked example 1

A process engineer was asked to increase the production capacity of solid pentaerythritol produced by seeded batch cooling crystallization by reducing the batch time. In order to verify whether this is a feasible solution, he determined the solute concentration trajectory in the plant, as shown in Figure 8.2. Based on these results and on the phenomenology of crystallization presented so far, did he implement the proposed change in the process?

Worked example 1 solution

The figure shows that the supersaturation is very small throughout the batch process, indicating that the crystal ability to consume the solute and approach equilibrium is high in comparison with the external action of cooling that tends to bring the solution towards the metastable limit. Therefore, the cooling rate can be increased, to make the supersaturation approach (but not reach) the metastable limit. The engineer would thus implement the recommendation.

Both unseeded and seeded batch crystallization lend themselves to the production of crystals with a narrow size distribution, which is one of the most commonly desired product specifications. Ideally, uniformly sized crystals are formed in unseeded mode or added at the start of the batch process, because all primary crystals or all seeds grow at the same rate until they reach their final uniform size. Both progressive primary nucleation or secondary nucleation throughout the batch process should be maximally

avoided; otherwise the product will be a mixture of small freshly formed crystals and large more outgrown crystals.

With seeding, the crystallization can be conducted at low supersaturation from the start. In comparison with unseeded crystallization the product is purer, the particle sizes are larger and aggregates are absent (the particles are single crystals). Therefore, in most applications of batch crystallization, a seeded process is preferred to an unseeded one. For certain compounds, seeded crystallization is the only choice. This is the case for sugar and other polyalcohols, which display very slow primary nucleation because of the high viscosity of the solution at such high solubilities, and for organic compounds that expose a liquid–liquid split at the high supersaturations required for primary heterogeneous nucleation. In some cases seeding is not allowed due to restrictions posed by authorities like the FDA.

8.3 Seeding procedure

As explained in the preceding section, seeds have a profound influence on elementary processes such as primary and secondary nucleation taking place during batch crystallization and consequently on the product quality. Proper seeding requires careful consideration of the number and size of the seed particles, the time of addition and the seed quality (which is related to the way the seeds are produced). In the following sections these aspects of the seeding procedure are further elaborated.

8.3.1 Seed load and seed size

Suppose that the design method given in Chapter 3 (see the design case on cooling crystallization in Section 3.3.2) is applied. In that case important decisions have already been taken: a product mass Δm with uniform size L_{prod} has to be crystallized in a batch process with seeding. The solvent (water) and the method of crystallization (cooling) have been chosen. The initial or final batch temperatures T_1 or T_2 may now be derived from the solubility curve of the solute–solvent system of interest (Figure 8.3):

$$\Delta m = [w_{eq}(T_1) - w_{eq}(T_2)]m_{solvent} \tag{8.1}$$

w_{eq} is the solubility in (kg solute)(kg of solvent)$^{-1}$ and $m_{solvent}$ is the mass of solvent.

The seeds mass (m_{seed}) and the seeds particle size (L_{seed}) can be calculated by assuming that: (a) no primary and secondary nucleation occurs; (b) the crystal growth rate is independent of the crystal size; (c) all crystals grow at the same rate (no growth rate dispersion); (d) the seeds are uniformly sized. The crystallization process then only consists of the growth of the seeds. For N seed crystals of size L_{seed} added at the start of the batch process, the seed mass is given by:

$$m_{seed} = Nk_v\rho L_{seed}^3 \tag{8.2}$$

where k_v and ρ are the seed volume shape factor and density, respectively. The seeds grow to a common final size, the specified product size L_{prod}. The number of particles N

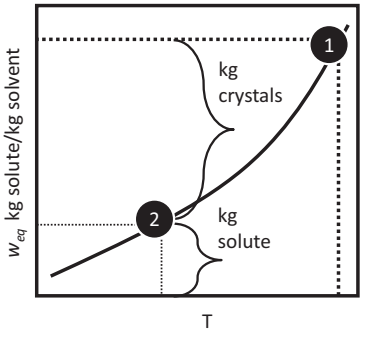

Figure 8.3 Thermodynamic state of the solution at the start (state 1) and at the end (state 2) of a batch cooling crystallization. The mass of crystals formed and the mass of solute remaining in solution (per kg of solvent) are indicated.

is constant throughout the batch process because no nucleation occurs, so the mass of solids formed in the batch process Δm is given by:

$$\Delta m = N k_v \rho (L_{prod}^3 - L_{seed}^3) \tag{8.3}$$

Combining equations 8.2 and 8.3 to eliminate N leads to:

$$\frac{m_{seed}}{\Delta m} = \frac{L_{seed}^3}{L_{prod}^3 - L_{seed}^3} \tag{8.4}$$

and defining the seed loading ratio $C_s = m_{seed}/\Delta m$ gives

$$\frac{1}{C_s} = \frac{L_{prod}^3}{L_{seed}^3} - 1 \tag{8.5}$$

Therefore, in order to obtain the specified product size, one may choose a seed loading ratio and calculate the seed size from equation 8.5. Note that larger C_s implies larger L_{seed} values. However, in practice one is not completely free to select the seed loading ratio. Too small a C_s value implies a low crystal surface area, resulting in high supersaturation, which drives either secondary or even primary nucleation during the batch process. In this situation equation 8.5 is no longer valid; the product size is smaller than predicted by this equation. Too large a value of C_s is also unacceptable, as a large proportion of the crystallizer volume is required to accommodate the seeds. The importance of the optimization of the seed loading ratio is illustrated in Figure 8.4 for the batch cooling crystallization process of ammonium paratungstate crystals. A load C_s of 25 g seeds per ml is not enough to prevent secondary nucleation, but 75 g suffices.

The best choice for the seed loading ratio (and the corresponding seed size) is the lowest value that does not promote nucleation, i.e. the so-called critical seed loading ratio (Doki *et al.*, 1999). The critical seed loading ratio C_s^* for three systems is graphically shown in Figure 8.5. The data were correlated by the following equation

$$C_s^* = 2.17 \times 10^{-6} L_{seed}^2 \tag{8.6}$$

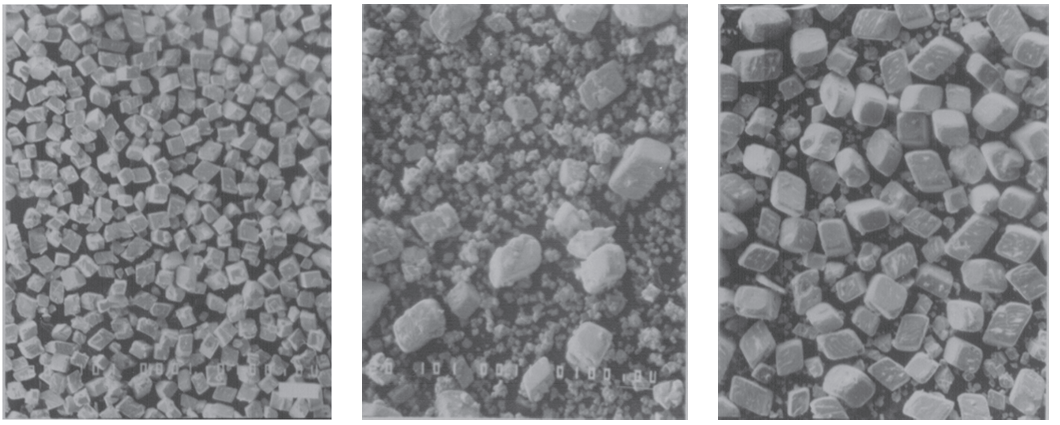

Figure 8.4 Batch crystallization of ammonium paratungstate tetrahydrate for two seed loads (Van Put, 1991). Nucleation could be avoided at a high seed load. Starting seeds (left), product from 25 g seeds (center) and product from 75 g seeds (right).

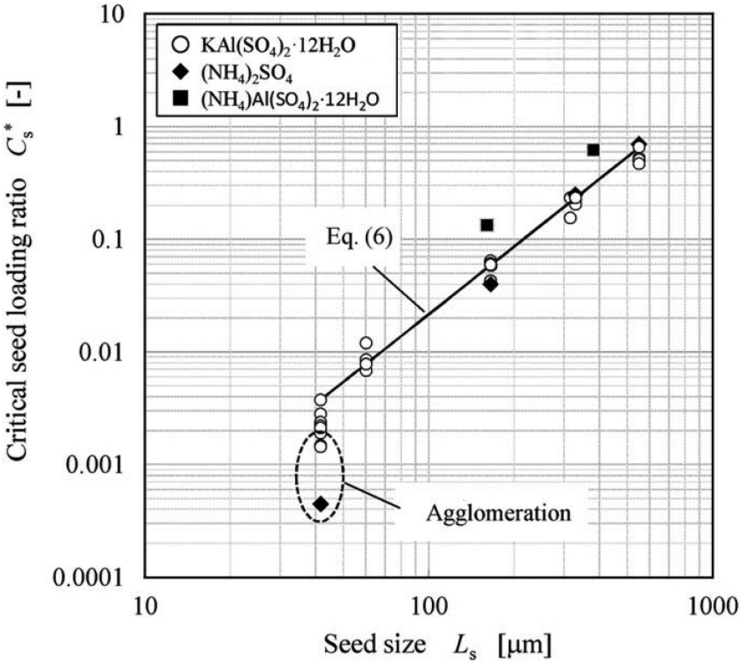

Figure 8.5 Critical seed loading ratio (Kubota and Onosawa, 2009). Copyright Elsevier. Reproduced with permission.

with L_{seed} in microns. For other systems, C_s^* has to be determined from laboratory batch crystallization experiments. Alternatively, it may be estimated from kinetic models for the primary and secondary nucleation rate of the system of interest (Tseng and Ward, 2014). If the critical seed loading ratio is used, a unimodal product size distribution is

achieved irrespective of the cooling profile, the crystal yield and the crystallizer volume, because the amount of seeds is sufficient to maintain a low supersaturation.

8.3.2 The timing of seed addition

The timing of seed addition is a decisive factor for the success of the seeding procedure.When the seeds are added too early, the seeds may partially or completely dissolve, resulting in too small a seed surface. Alternatively, when the seeds are added too late, primary heterogeneous nucleation occurs prior to seed addition and leads to the generation of an excess of nuclei.

If the crystal size distribution (CSD) is continuously monitored and the development of an unwanted population is noticed, for example by the occurrence of a bimodal distribution, the small crystals can be redissolved. This can be achieved by a short period of heat input followed by cooling. For large crystallizers one should be aware that dissolution of seed crystals or undesired primary heterogeneous nucleation can also be caused by local variations of the supersaturation in the crystallizer.

8.3.3 Generation of seeds and their quality

Seeds can be prepared by sieving of the product, by milling of larger crystals or by anti-solvent crystallization. Especially by applying the first two methods the seeds are tiny fragments of parent crystals. Milling crystals to generate small seeds should be avoided, as it may induce strain in the crystal lattice of the seeds, reducing their ability to grow or even causing their dissolution even in supersaturated solutions.

Dry seed crystals contain tiny fragments on their surface which are formed during the drying process. When suspended in a saturated solution, these fragments are released from the surface and form additional crystals of a much smaller size. Therefore, if such dry crystals are used as seeds, they often induce so-called initial breeding. To avoid this effect, the seed crystals should be suspended in a slightly undersaturated solution before use.

Seeds quality may be improved by suspending for some time in a saturated solution. Such seeds lead to better reproduciblity batch processes, larger and more uniform product sizes in comparison to strained seeds (Kalbasenka *et al.*, 2007).

Worked example 2

Consider again the previous worked example of pentaerythritol crystallization, in which the batch time has been reduced to increase the production rate. Do you expect the product quality will change in the new condition? Can you improve the seeding procedure to avoid such changes? The seeds size is 200 μm and seed loading ratio is 5%.

Worked example 2 solution

In general, a shorter batch time is accompanied by a higher supersaturation throughout the batch process. A high supersaturation potentially affects all product features: particle

size may be reduced by enhanced secondary nucleation, product purity may decrease due to liquid inclusions formed during crystal growth and the particles may aggregate.

A simple strategy to avoid high supersaturation values is to conduct the crystallization with a seeding load above the critical value. If we assume that the correlation for the critical seeding load (equation 8.6) applies to this system (otherwise laboratory experiments are needed), we have $C_s^* = 2.17 \times 10^{-6} L_{seed}^2 = 8.7\%$. Therefore, it is recommended to increase the seeding load from 5 to 8.7%.

8.4 Mathematical modeling

When one is purely interested in the yield and energy consumption of a certain crystallization process, solving the mass balances for the solvent, solutes and the solids together with the enthalpy balance, coupled with the solubility curve will be sufficient (Randolph and Larson, 1988), as explained in Chapter 3 on basic design. However, when the CSD of the solid phase has to meet further requirements, one needs to include the population balance equation (PBE). Although the PBE is discussed in detail in Chapter 7, here specific aspects of batch crystallization are emphasized.

The concept of the PBE was introduced to crystallization by Randolph (1962). A general form of the PBE for batch processes is as follows:

$$\frac{\partial(n(L,t)V(t))}{\partial t} = -V(t)\frac{\partial(G_L(L,t)n(L,t))}{\partial L} + B(L,t)V(t) - D(L,t)V(t) \qquad (8.7)$$

where the amount and the size of particles are expressed in terms of number density $n(L, t)$ [# m^{-3} m^{-1})] and particle size L [m] respectively. V [m^3] is the volume of the crystallizer content (for simplicity also called the crystallizer volume), which is not constant, $G_L(L, t)$ [m/s] is the size-dependent linear growth rate, $D(L, t)$ and $B(L, t)$ [m^{-3} m^{-1} s^{-1}] are the death and birth rates associated with particle aggregation and breakage. As the PBE is a partial differential equation with respect to time t [s] and crystal length L [m], a boundary condition and an initial condition are required:

$$n(0,t) = \frac{J(t) + B_0(t)}{G_L(0,t)} \qquad (8.8)$$

$$n(L,0) = n_{initial}(L) \qquad (8.9)$$

Here J and B_0 are the primary and secondary nucleation rates [# m^{-4} s^{-1}], respectively. Here it is assumed that nuclei sizes are negligibly small, so J and B_0 are functions of time only (secondary nucleation may also be described as the birth of new crystals over a certain size range, as explained in Chapter 7). The boundary condition gives the number of crystals of zero size at any time during the batch process.

The initial condition is physically related to the population of particles present at the start of the batch process. It may be a seed population or a population formed by rapid outgrowth of nuclei generated by primary nucleation.

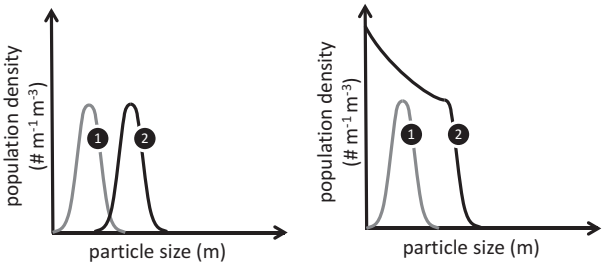

Figure 8.6 Particle size distributions in a seeded batch operation, considering (a) crystal growth alone and (b) both crystal growth and nucleation. Curve 1 represents the seeds PSD, curve 2 represents the product PSD.

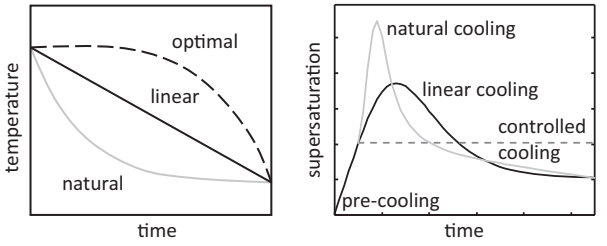

Figure 8.7 Comparison of various cooling curves (left) and the resulting supersaturation (right) for natural cooling, controlled linear cooling and controlled cooling for a seeded batch process.

The PBE can be simplified by assuming that growth is independent of particle size and by neglecting aggregation and breakage:

$$\frac{\partial n(L,t)V(t)}{\partial t} = -VG_L(t)\frac{\partial n(L,t)}{\partial L} \tag{8.10}$$

The solution of this equation is schematically shown in Figure 8.6 for a seeded operation. If the particles grow, but there is no nucleation, the seed PSD simply moves to the right in time (Figure 8.6a). If new particles nucleate throughout the batch process, then the product PSD contains particles of all sizes between zero and a maximum size (Figure 8.6b).

8.5 Cooling and evaporation trajectories

8.5.1 Natural and linear cooling

The simplest cooling trajectory for a batch crystallization process is natural cooling, i.e. a constant temperature of the cooling medium and consequently an exponentially decaying crystallizer temperature (Figure 8.7 left). However, this policy is usually not suitable. This can be easily understood when one realizes that at the early stages of a batch process, the crystal surface area is much smaller than at the end of that batch process. Consequently, at the early stages, the high heat removal rate may lead to an

extremely high supersaturation (Figure 8.7 right), which is accompanied by progressive primary nucleation and a high growth rate. At later stages, the surface area is high and the heat removal rate is low, so low supersaturation and crystal growth rate result.

The cooling trajectory may be somewhat improved in comparison to natural cooling by a constant cooling duty. This approach, however, still does not take into consideration the low crystal surface at the early stages of the batch process, so the same sequence of events described before applies, only somewhat dampened.

8.5.2 Constant supersaturation

Controlled cooling, evaporation or anti-solvent addition keeps the supersaturation constant by preventing progressive primary nucleation and by providing a constant crystal growth rate during the whole batch process. A simple expression for the required cooling trajectory can be calculated from the kinetics, mass balances, the heat balance and the moment equations, assuming: (a) constant volume of the crystallizer content; (b) a class II system, i.e. the solution concentration is negligibly higher than the saturation value; (c) constant nucleation and growth rates. The temperature–time dependence is then given by

$$\frac{T_{init} - T(t)}{T_{init} - T_{final}} = \left(\frac{t}{\tau}\right)^{a} \tag{8.11}$$

T_{init} and T_{final} are the initial and final temperatures, respectively, $T(t)$ is the temperature at crystallization time t, and τ is the batch time. For the parameter a, two limiting situations are considered: (a) $a = 3$ for seeded crystallization without nucleation during the batch process; (b) $a = 4$ for unseeded crystallization with primary nucleation over a short time interval at the beginning of the batch process. Therefore, a constant supersaturation may be obtained by following temperature profiles that are third-and fourth-order in time, respectively (Figure 8.7). Similar expressions can be derived for an evaporative batch crystallizer. Application of these curves finds some resistance in industry because of the long periods without substantial cooling during the first part of the batch process and because of the large cooling power required in its final part.

8.6 Optimal trajectories

It has been shown in the previous sections that a constant supersaturation, if compared to natural and linear cooling, leads to larger, more uniformly sized particles. However, other trajectories may be considered in order to further improve the product quality (Chianese and Kramer, 2012). This is because the trajectory determines the time-varying nucleation and growth rates, which in turn determine how the solute is distributed to the crystals.

Therefore an optimal trajectory may be found to meet a given objective. Jones (1974) was the first to demonstrate both theoretically and experimentally that an optimal

trajectory could be better than the constant supersaturation scheme. He found a temperature trajectory that maximized the terminal size of the largest crystals in cooling batch crystallization. For his system the corresponding supersaturation was low at the beginning, reached a minimum and increased towards the end of the batch process.

The optimal trajectory may be different if process restraints are considered, such as an upper limit for the solids contents and for the crystallization time. Besides, multiple objectives may be considered, such as the amount of fines in the product, the product purity or the particle shape. In the latter two cases, impure products and needle-like particles may be prevented if the supersaturation does not exceed an experimentally determined value.

Optimal trajectories (in the example above, the temperature trajectory) are derived from an optimization algorithm and a phenomenological mathematical model of the crystallization process. The optimal trajectories were implemented in a control scheme known as open-loop control, because the optimal trajectory was determined *a priori*. This approach has shortcomings related to the limitations of phenomenological models, which do not describe the effects of impurities, the quality of the seeds, spatial inhomogeneities within the crystallizer and other process variations found in industrial practice. Besides, the kinetics for nucleation and growth are difficult to obtain for the whole range of temperatures, concentrations and supersaturations of interest. Therefore, the so-called closed-loop approach (Mesbah *et al.*, 2011) is preferred, in which the optimal operating policy is continuously updated during a run, taking into account inline process measurements.

An alternative approach called "direct design" (Zhou *et al.*, 2006) usually starts with a supersaturation trajectory determined from an open-loop method. The supersaturation is experimentally determined in the course of the process, for instance from concentrations measured by a refractive index or a FTIR-ATR method. The crystallization process is then controlled in such a way as to ensure that the pre-established supersaturation trajectory is followed. The data from a given batch process can be used to improve control of the next batches.

A "direct design" approach that does not require any information on the crystallization kinetics is the so-called "direct nucleation control" method (Nagy and Braatz, 2012). The number of particles is controlled within pre-established boundaries in order to obtain large particles. In addition, a narrow size distribution is derived as small particles generated throughout the batch process are periodically dissolved. To this end, the solution is cyclically allowed to become undersaturated. As a consequence of the low supersaturation values during the batch process, agglomeration is mostly prevented. Figure 8.8a shows an example of direct nucleation control in batch cooling crystallization. The temperature (gray line) is controlled in order to keep the total number of particles (measured by an FBRM probe) close to its setpoint (black line). As shown in Figure 8.8b, the solute concentration in the liquid phase (gray line) is monitored for process analysis. The solution reaches the metastable limit (dashed lines) upon cooling, but reheating is likely to dissolve most crystals. In subsequent cooling–heating cycles, a low supersaturation is maintained. Secondary nuclei generated in each cooling cycle are dissolved upon reheating.

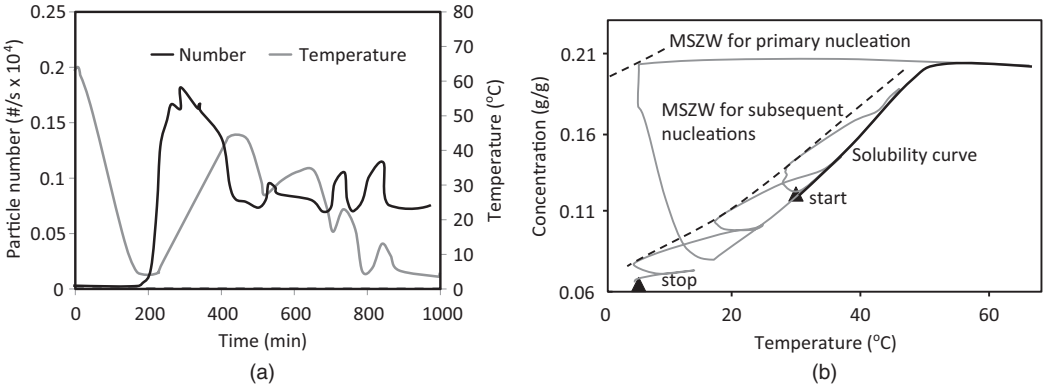

Figure 8.8 Direct nucleation control for batch cooling crystallization of paracetamol in isopropyl alcohol: (a) particle number, temperature and solute concentration; (b) trajectories of the solution thermodynamic state during the batch process. Reproduced with permission from (Saleemi *et al.*, 2012). Copyright (2012) American Chemical Society.

8.7 A brief summary of the chapter

Batch crystallization is a common operation for valuable products, for units that are used to crystallize multiple products, for low capacities and in case of severely scaling products. The elementary processes, primary heterogeneous nucleation (for unseeded operation), molecular growth and secondary nucleation, help determine product characteristics such as size, size distribution, purity and degree of aggregation. Also important is the seeding procedure. If seeds are added according to the critical loading ratio, large uniform crystals are formed. For accurate control of the product properties, mathematical models coupled to optimization routines help identify optimal cooling and evaporation trajectories. These trajectories may be implemented in open-loop or closed-loop modes, or with a direct design approach.

8.8 End of chapter problems

Problem 1

Consider the batch cooling crystallization of pentaerythritol shown in Figure 8.2, in which seeds were added at 72 °C. (a) Describe the course of the crystallization process, indicating which elementary processes are active and in which part of the cooling trajectory. Consider the following elementary processes: primary nucleation, secondary nucleation, growth, agglomeration. (b) Repeat the exercise for seeding at a temperature of 80 °C. (c) Repeat the exercise for seeding at a temperature of 55 °C.

Problem 2

For the first two batch processes described in the previous problem, the products are likely to be different in terms of mean particle size, purity and degree of aggregation. Set up a table indicating how these properties vary at each seeding temperature.

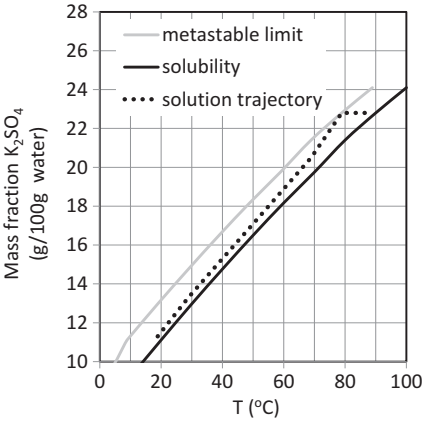

Figure 8.9 Figure for Problem 5.

Problem 3

In batch anti-solvent crystallization, specify which elementary processes you would like to happen during the initial and final parts of the batch process, considering the following situations: (a) you wish to produce very small (say 10 μm in size), uniformly sized crystals; (b) you wish to produce a polydispersed product (say from 5 to 100 μm in size). Explain how you would obtain the desired elementary processes: would you add seeds and, if so, how? How fast would you add the anti-solvent?

Problem 4

Consider a system that obeys the critical seed loading ratio correlation, equation 8.6. Determine the seeds size required to obtain a monodisperse product with 500 μm in size from batch crystallization. Determine the corresponding seed loading ratio. If a larger product is needed, how does the seed size and loading vary?

Problem 5

Particulate potassium sulfate is recovered from a 23 g/100 g solvent solution by batch cooling as shown in Figure 8.9. (a) Determine the yield and solute loss for this process; (b) calculate the highest supersaturation in the batch process, using a simplified expression suitable for cooling crystallization; (c) indicate the elementary processes for temperatures above 80 °C, between 80 °C and 70 °C, and below 70 °C; (b) considering the elementary processes you have described, what actions would you take to increase the particle size?

8.9 References

Chianese, A. and Kramer, H. J. M. 2012. *Industrial Crystallization Process Monitoring and Control*, Wiley-VCH.

Doki, N., Kubota, N., Sato, A. *et al.* 1999. Scale-up experiments on seeded batch cooling crystallization of potassium alum. *AIChE Journal*, **45**(12), 2527–2533.

Jones, A. G. 1974. Optimal operation of a batch cooling crystallizer. *Chemical Engineering Science* **29**(5): 1075–1087.

Kalbasenka, A. N., Spierings, L. C. P., Huesman, A. E. M. and Kramer, H. J. M. 2007. Application of seeding as a process actuator in a model predictive control framework for fed-batch crystallization of ammonium sulfate. *Particle and Particle Systems Characterization*, **24**(1), 40–48.

Kubota, N. and Onosawa, M. 2009. Seeded batch crystallization of ammonium aluminum sulfate from aqueous solution. *Journal of Crystal Growth*, **311**(20), 4525–4529.

Mesbah, A., Huesman, A. E. M., Kramer, H. J. M., Nagy, Z. K. and Van den Hof, P. M. J. 2011. Real-time control of a semi-industrial fed-batch evaporative crystallizer using different direct optimization strategies. *AIChE Journal*, **57**(6), 1557–1569.

Nagy, Z. K. and Braatz, R. D. 2012. Advances and new directions in crystallization control. *Annual Review of Chemical and Biomolecular Engineering*, **3**, 55–75.

Randolph, A. D. 1962. *Size Distribution Dynamics in a Mixed Crystal Suspension*, PhD Thesis, Iowa State University of Science and Technology.

Randolph, A. D. and Larson, M. A. 1988. *Theory of Particulate Processes: Analysis and Techniques of Continuous Crystallization*, Academic Press.

Saleemi, A. N., Rielly, C. D. and Nagy, Z. K. 2012. Comparative investigation of supersaturation and automated direct nucleation control of crystal size distributions using ATR-UV/vis spectroscopy and FBRM. *Crystal Growth and Design*, **12**(4), 1792–1807.

Tseng, Y.-T. and Ward, J. D. 2014. Critical seed loading from nucleation kinetics. *AIChE Journal*, **60**(5), 1645–1653.

Van Put, J. W. 1991. *Ammonium Paratungstate as a Raw Material for the Manufacturing of Lamp Filament Tungsten Wire*, PhD Thesis, Delft University of Technology.

Zhou, G. X., Fujiwara, M., Woo, X. Y. *et al.* 2006. Direct design of pharmaceutical anti-solvent crystallization through concentration control. *Crystal Growth and Design*, **6**(4), 892–898.

9 Measuring techniques

9.1 Why this chapter is important

Industrial crystallizers may be seen as devices that create a certain level of *supersaturation as the driving force for the generation of the product crystals*. Measurement of the supersaturation is therefore of paramount importance to control crystallization processes, as it determines the mechanisms and the rates of elementary crystallization processes such as nucleation, crystal growth and agglomeration. These elementary processes eventually lead to the formation of crystals of a wide spectrum of *sizes.* The so-called crystal size distribution (CSD), or more generally particle size distribution (PSD), is also a very important product characteristic that not only determines the performance of the crystalline product, but also the efficiency of the downstream processes like filtration and drying, as well as product stability during storage, as explained in Chapter 2.

In this chapter, you will learn various techniques used to measure the supersaturation and the CSD/PSD. In addition, you will have the knowledge to select the most convenient measuring technique according to a given measuring objective and crystallization system. With these tools, you will be able to understand and improve the process as well as the product quality of an industrial crystallization process.

9.2 Sampling and dilution procedures

Process measurements can be classified according to the sampling procedure: (a) inline, with a probe inserted in the process; (b) online, recirculating a side stream between the process and the instrument; (c) offline, in a laboratory. In the latter two procedures, a suspension sample must be withdrawn from the crystallizer, diluted and sometimes separated into solids and pure liquid. For the solids characterization, careful attention has to be paid to these procedures; otherwise the measurements are drastically affected (Allen, 2003, Gerla, 1995, Jager, 1990). Sampling and dilution of crystal slurries for solids characterization should obey the following recommendations:

- Take samples that represent the crystallizer contents. Therefore, avoid dead zones and particle classification zones within the crystallizer.
- Avoid particle segregation, which may occur during flow of a slurry, because the larger particles tend to settle and to accelerate less than the smaller ones. To minimize

Table 9.1 Features of offline sizing methods. Note that the size range is narrow and, spans 2 to 60% of orifice diameter; sample dilution in electrolyte is required

Variable	Sieving	Coulter counter	Dynamic light scattering
PSD type	Mass distribution	Number distribution	Volume distribution
Characteristic size	Cross section	Cross section	Diffusivity (Brownian motion)
Measuring range	20–8000 μm	0.6–800 μm	0.003–3 μm
Resolution	25 classes	16–256 classes	Low
Measuring mode	Offline	Offline	Offline
Pretreatment	Sampling, filtration, drying	Sampling and high dilution	Sampling and high dilution
Calibration required	No	Yes	No
Remarks	Laborious	Calibration required. Unsuitable for industrial environment	Clean environment

segregation, take samples isokinetically, pump slurries in turbulent flow and take into account the particles' settling tendency in any flow.
- Dilute without changing the size distribution. In general, dilution in saturated mother liquor is the best choice to avoid particle dissolution or growth.
- Avoid crystal attrition and breakage. For large, brittle and elongated crystals, avoid excessive turbulence, as well as prolonged exposure times to a circulation pump.

Sampling of slurries to obtain liquid phase information requires full separation of solids. Besides, accurate temperature control and removal of gas bubbles may be required.

9.3 PSD measuring techniques

9.3.1 Sieve analysis

Sieving is the oldest method for size analysis and, in spite of its disadvantages, is still often used in industry. In this offline technique, a filtered and dried sample is placed on a shaking stack of sieves in such a way that the mesh size decreases from the top to the bottom of the stack. The powder mass retained in each sieve is determined by weighing. In principle, the particle characteristic size corresponds to the smallest dimension that fits through the sieve aperture.

Sieving requires solids sampling, filtration, drying and commonly sample storage. Sampling brings about the difficulties explained in Section 9.2, filtration and drying may induce particle growth and agglomeration, and particle storage may promote caking due to incomplete drying and temperature oscillations. Additionally, brittle material can undergo abrasion during handling and sieving. Furthermore, the method is laborious and difficult to automate. Table 9.1 summarizes the main characteristics of the sieving method.

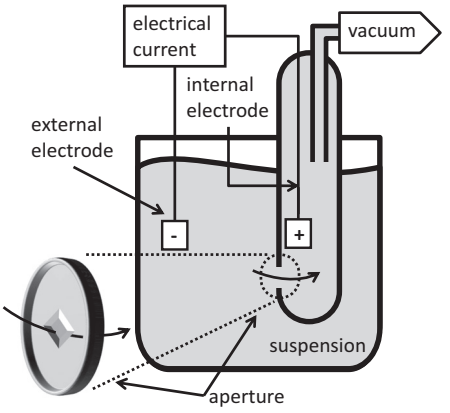

Figure 9.1 Schematic view of the Coulter counter and of the flow through an orifice (enlarged detail at the left part of the figure).

9.3.2 Coulter counter

This offline method gives accurate results, but is limited to particles with a narrow size distribution and highly diluted in an electrolyte. The method consists of pumping particles suspended in an electrolyte through a small orifice. Two electrodes, placed upstream and downstream of the orifice, detect a sudden decrease in current upon the passage of each particle. The amplitude of this pulse is proportional to the particle volume. The pulses are sized and counted, and result in a volume-based PSD. The following conditions are required: (a) very low particle concentration so a single particle passes through the orifice at a time; (b) non-conductive particles in comparison to the fluid; (c) the solvent is an electrolyte. In Figure 9.1 the operational principle of the Coulter counter is illustrated.

The change in electrical resistance due to the presence of a particle volume is nearly proportional to the volume of the particle. This leads to a low range of sizes that can be measured with one orifice. Table 9.1 summarizes the main characteristics of the Coulter counter sizing method.

9.3.3 Dynamic light scattering

Dynamic light scattering is an offline method suitable for particles in the size range between 3 nm and 3 μm. It makes use of the rapid fluctuations of the scattered light intensity caused by the particle Brownian motion. The interpretation of the signals is complicated, especially for polydisperse samples, so the method merely gives an indication of the mean particle size of a monodisperse system. Measurements require very low particle concentrations, small quantities of impurities (dust particles) and the absence of larger particles. The main features of the dynamic light scattering technique are summarized in Table 9.1.

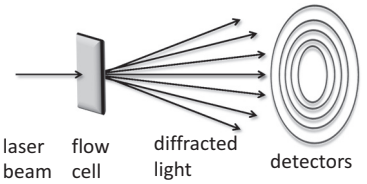

Figure 9.2 Schematic view of a FLS instrument.

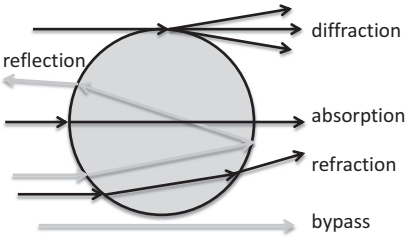

Figure 9.3 Light scatter around a particle.

9.3.4 Forward light scattering

Forward light scattering (FLS) is the most used sizing technique. The reasons for the success of these instruments is that they are easy to operate, results are reproducible and they do not require extensive calibration procedures. The major drawback of FLS is that low particle concentrations are required, so most applications are offline. Online measurement is possible, but the difficulties associated with dilution limit its widespread use.

In FLS, a parallel beam from a coherent monochromatic light source falling on an ensemble of particles creates a composite scatter pattern (Figure 9.2). The light intensity as a function of the scatter angle (with respect to the optical axis of the instrument) is detected. Multiple scattering must be avoided, which limits the particle concentration to about 1 vol%.

To deduce the size distribution from a measured scatter pattern, a mathematical deconvolution technique is used, based on a phenomenological model for the interaction of the incident light with the particles. The following phenomena can be involved (see Figure 9.3): (a) reflection on the particle surface and inside it; (b) refraction from the medium into the particle and from the particle into the medium; (c) diffraction; (d) absorption. These phenomena depend on the particle size and refractive index, as well as on the wavelength of the light beam. A number of scatter theories have been developed for specific applications. A rigorous description of light scattering is given by the generalized Lorenz–Mie theory (Bohren and Huffman, 1983, Boxman, 1992). For different particle shapes and large particles, the solution of the Lorenz–Mie theory becomes unreliable, so approximate theories are preferred, such as anomalous diffraction, ray-optics and Fraunhofer diffraction.

Table 9.2 Main features of inline and online sizing techniques

Variable	Forward light scattering	Ultrasonic attenuation	Backward light scattering	Imaging
PSD type	Volume distribution	Volume distribution	Number distribution	Number distribution
Characteristic size	Projected area	Mass	Chord length	Any two linear dimensions
Measuring range	0.1–6000 µm	0.1–3000 µm	1–800 µm	20–800 µm
Resolution	High	Medium	Medium	Medium
Measuring mode	Online	Online	Inline	Inline
Pretreatment	Sampling and dilution to 1 vol%	Sampling	None	None
Calibration required	No	Yes	No	No
Remarks	For non-spherical particles PSD is too wide. Offline mode is the most commonly used one	Calibration not needed if detailed physical properties of particles are available. Particle shape affects PSD	Conversion of chords to sizes is hardly possible. Particle shape, concentration, optical and surface properties affect PSD	Offline and online modes also possible. Needs developments for robust recovery of PSD

The shape of the crystals has a marked effect on the diffraction spectrum. Because commercial instruments do not take into account the particle shape, too broad a size distribution results. Table 9.2 summarizes the main features of the forward light scattering technique.

9.3.5 Ultrasonic attenuation

Ultrasonic attenuation allows the determination of a PSD in concentrated suspensions, either offline or online. This makes this technique useful for systems that cannot be diluted and for process monitoring and control. In this method, acoustic waves of frequencies ranging from 1 to 200 MHz travel across the suspension. Depending on the size and the physical properties of the particles, their interaction with the waves can result in entrainment, scattering or resonance. A receiver detects the sound attenuation after its passage through the sample.

To be able to determine the size distribution from a measured attenuation as a function of frequency, a model matrix must be determined. The model matrix can be calculated from theoretic models that use the laws of conservation of mass energy and momentum, thermodynamic equations of state, and stress–strain relations for isotropic elastic solids

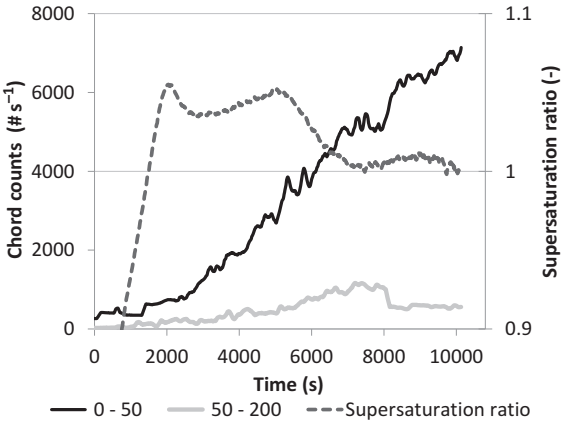

Figure 9.4 Unseeded batch crystallization of pentaerythritol. Number of particles with chord lengths < 50 μm and in the range 50–200 μm measured using an FBRM instrument. Supersaturation ratio determined by refractometry.

or viscous fluids (Allegra and Hawley, 1972). The model requires physical properties of the particles that are not easily available, so sometimes a calibration approach is used. The main features of the ultrasonic attenuation technique are summarized in Table 9.2.

9.3.6 Backward light scattering

Backward light scattering, also known as focused beam reflectance measurement (FBRM), is an inline sizing technique mainly used for process monitoring, but is also useful to detect the onset of nucleation in batch processes. The disadvantage of this method is that chord lengths are determined, which cannot be easily converted to particle sizes. In this method, a probe inserted in the process equipment emits a laser beam that hits the particles in suspension. The reflected and back-scattered light generates a light pulse, longer pulses corresponding to larger particles. As the laser focuses at a distance of a few mm from the instrument window, at this location the flow must be turbulent. Figure 9.4 exemplifies a process measurement.

The FBRM measurements are sensitive to the optical and surface properties of the particles as well as to their shape. Although measurements can be performed in concentrated suspensions of particles, at very high concentrations the measured chord size isn't very sensitive to changes in the size distribution. Table 9.2 summarizes the main features of the backward light scattering technique.

9.3.7 Imaging

Optical microscopy is a valuable technique to characterize the PSD of particles in the micrometer size range. It consists of direct observation of the particles in two dimensions (2-D). This is particularly important for recrystallization processes (Wu *et al.*, 2012) and

for systems exhibiting polymorphic transformations (Calderon de Anda *et al.*, 2005), because the particle shape changes in the course of the process. Besides the PSD, the quality of the crystals, as well as possible agglomeration and breakage, can be detected. Offline imaging is well established, but is limited to the characterization of the final product of a process. However, imaging also offers direct observation of particles online and inline. Instruments are commercially available, but for quantitative recovery of the 2-D PSD further developments are needed.

The main steps in imaging are: (a) selection of particles that are representative of the population in the crystallizer (Allen, 2003) and the number of particles in the various size classes should suffice to derive a statistically significant size distribution; (b) image acquisition of the selected particles; (c) image analysis and calculation of the PSD.

Offline configuration. In this configuration samples are taken from the process and analyzed in a laboratory optical microscope. Selection of representative particles is the most difficult step, because from the process to the microscope slide many manipulation steps are needed. The quality of the image is the highest of the three configurations, as the magnification, the particle concentration and the illumination can be optimized for each sample.

Online configuration involves leading a side stream from a crystallizer to a flow-through cell mounted on the microscope (Allen, 2003). Selection of representative particles is less problematic than in offline configuration, because many particles can be sampled. The image quality is somewhat less than in the offline configuration because the particles are moving and their distance to the lens is variable.

Inline configuration. The microscope is mounted as a probe inserted into the crystallizer. Taking representative samples is simpler than in previous configurations, as it suffices to place the probe in an appropriate position within the vessel, providing turbulent flow in its neighborhood. However, the image quality is the poorest because particle movement and distance to the lens is more free than in the flow cell configuration, particle overlapping is more extensive, especially at high suspension concentrations and also because there are more restrictions to the quality of the illumination. An image from an inline instrument is shown in Figure 9.5.

The so-called image segmentation aims at identifying the objects of interest in the image. In *edge detection segmentation*, regions of abrupt changes in pixel intensity are located. In *model-based object recognition* (Lowe, 1987), groupings and structures that are invariant over large areas, such as connectivity and parallelism, are located and matched with structures present in the expected particle shapes. Once segmentation is achieved, any geometrical feature of the individual particles may be derived, such as several characteristic sizes (see definition of particle size in Chapter 2), the length-to-width ratio, the perimeter, etc. Consequently, after measuring an appropriate number of particles (typically 400 to 10,000 per size class), properties of the whole population may be derived, the most important one being the two-dimensional (2-D) size distribution. An interesting method to measure multiple characteristics of a population of particles (nD PSD) has been proposed (Schorsch *et al.*, 2014) in which a single camera coupled with two mirrors takes images of the same crystal from different orientations, see Figure 9.6. Table 9.2 summarizes the main features of the imaging technique.

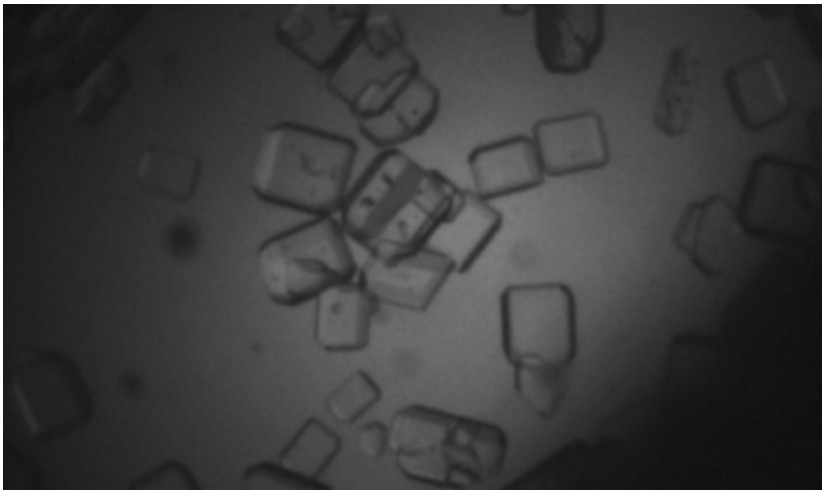

Figure 9.5 Image of ammonium sulfate crystals taken with an inline imaging probe.

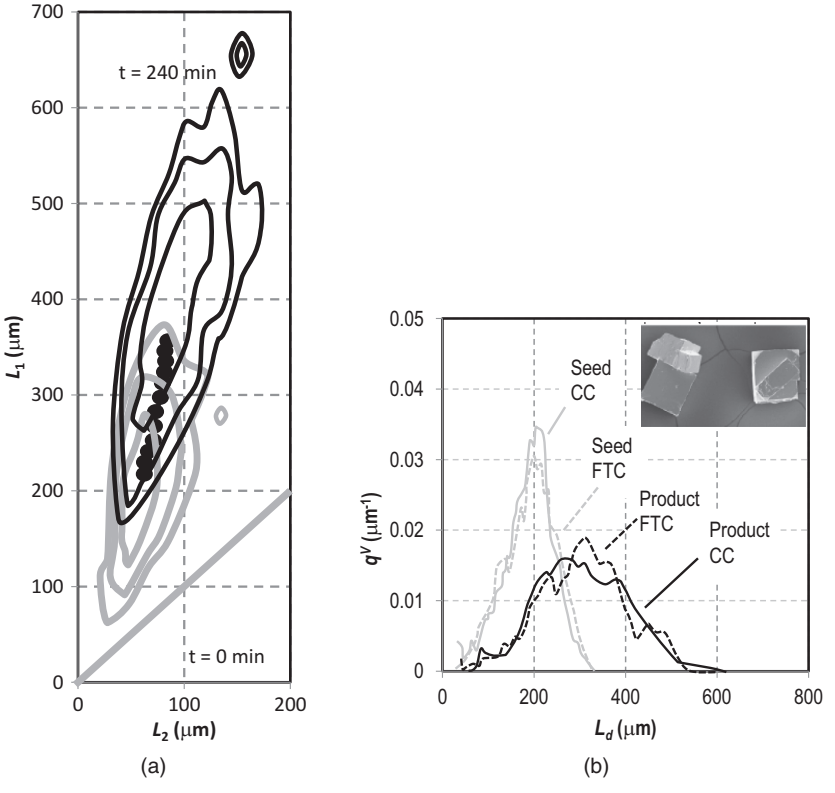

Figure 9.6 (a) Seeded cooling crystallization of β-L-glutamic acid in water. Contour line plots of the volume based 2-D PSD in the (L_1, L_2) plane at 0.35, 0.5 and 0.8 of the maximum of the PSD. (b) Volume-based PSD (q^v) of seeds and product from a batch cooling crystallization of NaCl in water, measured with a Coulter counter (continuous lines) and a flow-through-cell imaging system. Gray lines are seeds and black lines are product crystals. Particle sizes L_d in the latter system were averaged over the measured sizes in three dimensions as $L_d = \pi L_1 L_2 L_3 / 6$. Source (Schorsch *et al.*, 2014).

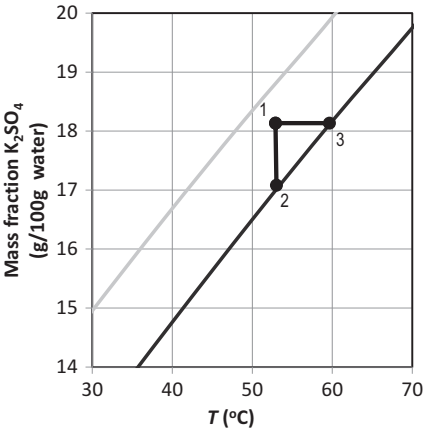

Figure 9.7 Solubility line (black) and metastable limit line (gray) for aqueous solutions of potassium sulfate. State 1 represents a supersaturated solution, and states 2 and 3 are solid–liquid equilibrium states. Metastable zone width for a cooling rate of 5 °C h^{-1} (Nývlt *et al.*, 1970).

9.4 Supersaturation measuring techniques

In order to understand, monitor or control a crystallization process, we wish to determine the degree of supersaturation with respect to the crystallizing compound. Consider the crystallization of potassium sulfate from an aqueous solution. Figure 9.7 gives the phase diagram for the region of interest (i.e. the solubility line). Suppose point 1 represents the state of the solution at a particular instant of time and location within the crystallizer. In the case of evaporative, anti-solvent or chemical reaction crystallization, the supersaturation is given by $\Delta\mu = \mu_1 - \mu_2$, whereas for cooling crystallization $\Delta\mu = \mu_1 - \mu_3$ (see Chapter 1). In order to determine μ_1, a suitable thermodynamic model can be applied, having as inputs the composition, the pressure and the temperature of the solution at the supersaturated state. For μ_2 and μ_3, the same model is applied considering saturation at the process temperature or concentration, respectively. In many instances the rigorous thermodynamic expressions just given can be substituted by simplified expressions, such as the supersaturation ratio $S = c_1/c_2$ or the undercooling $\Delta T = T_1 - T_3$. Also in these cases, the temperature, the pressure and the solute concentration in the supersaturated solution have to be determined. The next sections focus on inline methods to measure the concentration, aiming at determining the supersaturation.

9.4.1 Refractive index

The refractive index (RI) method for determining the supersaturation has a long history in the sugar industry (Myreen, 2012, Rozsa, 1998) and is accurate for many other systems, such as β-cyclodextrin (Kohl *et al.*, 2004), dextrose monohydrate (Markande *et al.*, 2013), citric acid (Mullin and Leci, 1972) and potassium nitrate (Helt and Larson,

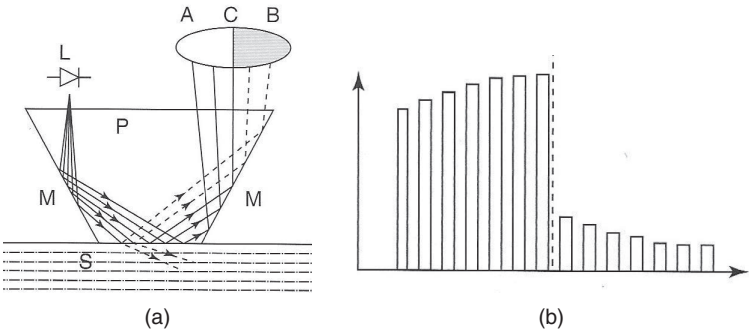

Figure 9.8 Principle of measurement of the refractometer. (a) Incident light (L) is reflected on the prism–solution interface S with a strong A or a weak B intensity. Ray C corresponds to the critical refraction angle. (b) Graph of light intensity vs. angle; the discontinuity corresponds to the critical angle. Source Myreen (2012).

1977), among others. Measurement of the RI of a solution is usually based on the critical refraction angle (Myreen, 2012), as follows. Light of known wavelength is allowed to travel through a prism towards the interface with the solution of interest at varying incident angles (Figure 9.8a). For angles with the surface smaller than the critical angle, a large part of the incident light is reflected; otherwise a large part is refracted. Therefore, by plotting the reflected light intensity against the incident angle, a sharp discontinuity is observed at the critical refraction angle (Figure 9.8b). From the critical angle just measured, the solution RI can be theoretically determined. The solution concentration is determined from calibration.

The light hardly penetrates into the solution, so solid particles do not interfere with the measurements. The measurements can be done inline and in dark liquids. The RI varies with temperature and with impurities in solution, so usually temperature and impurity compensation factors must be developed for each system. The latter is more problematic, because impurity concentrations are not available inline, so compensation factors have to be based on laboratory measurements.

The concentration range of interest lies between the solubility and the metastable limit (Figure 9.7), so the concentration measurement should be sufficiently accurate to differentiate states within this range. Given a usual accuracy of ± 0.0002 refractive index units, the more the RI varies with concentration, the more accurate is the concentration measurement. For instance, aqueous solutions of pentaerythritol display both a high sensitivity for RI with concentration and a wide metastable zone, so for this compound the method is useful, as shown in Figure 9.9. The refractive indexes of a number of inorganic salts are given elsewhere (Takubo, 1990).

9.4.2 ATR-FTIR spectroscopy

In recent years, attenuated total reflectance Fourier-transformed infrared (ATR-FTIR) spectroscopy has become the most common method for monitoring supersaturation during crystallization processes of organic molecules. In infrared spectroscopy, an infrared

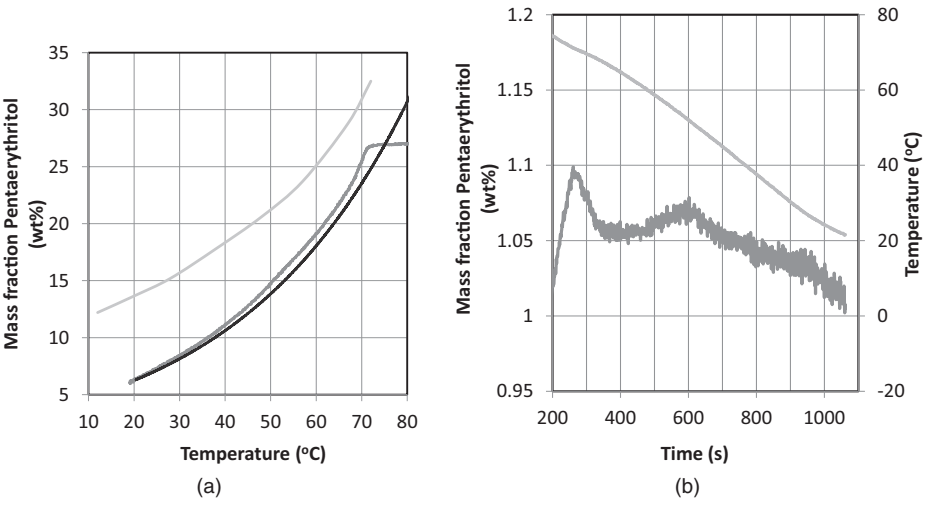

Figure 9.9 (a) Solubility line (black), metastable limit line (light gray) and pentaerythritol concentration trajectory during seeded batch cooling crystallization (dark gray line) in aqueous medium. (b) Supersaturation ratio and temperature during the batch by inline refractometry. Batch data from the authors, solubility from Chianese (1995).

photon is absorbed when its energy matches the vibrational state of a functional group within a molecule. When photons covering the mid-infrared region hit a sample, an absorbance spectrum is generated that corresponds to the absorption of the molecule's chemical groups. For example, the spectra of ammonium sulfate solutions reveal O-H, N-H and sulfate bands (Kadam *et al.*, 2011). If the molecules are in a solution, the absorbance varies with the amount of molecules, as exemplified in Figure 9.10a for maleic acid, so the method may be used to measure the molecule concentration, as shown in Figure 9.10b for a pharmaceutical compound. Calibration is usually based on more than one absorption band to improve accuracy, often with the aid of multivariate statistical analysis (Cornel *et al.*, 2008, Lindenberg *et al.*, 2012). The procedure is sometimes complicated because the bands of the solvent and of impurities overlap with those of the compound of interest. The effect of temperature has to be taken into account.

With an ATR probe, the measuring beam is reflected at the interface between the probe and the solution, with a penetration of only a few micrometers into the sample, so that solid particles do not interfere with the measurements. Since ATR-FTIR simultaneously captures features of the molecules in solution, the technique can also be used for inline monitoring of speciation in solution, impurity concentration and polymorphic transformation (Lindenberg *et al.*, 2012).

9.4.3 Density

Density is an accurate online method to determine concentration, which may be used for monitoring (Hojjati and Rohani, 2005, Redman and Rohani, 1994, Worlitschek and

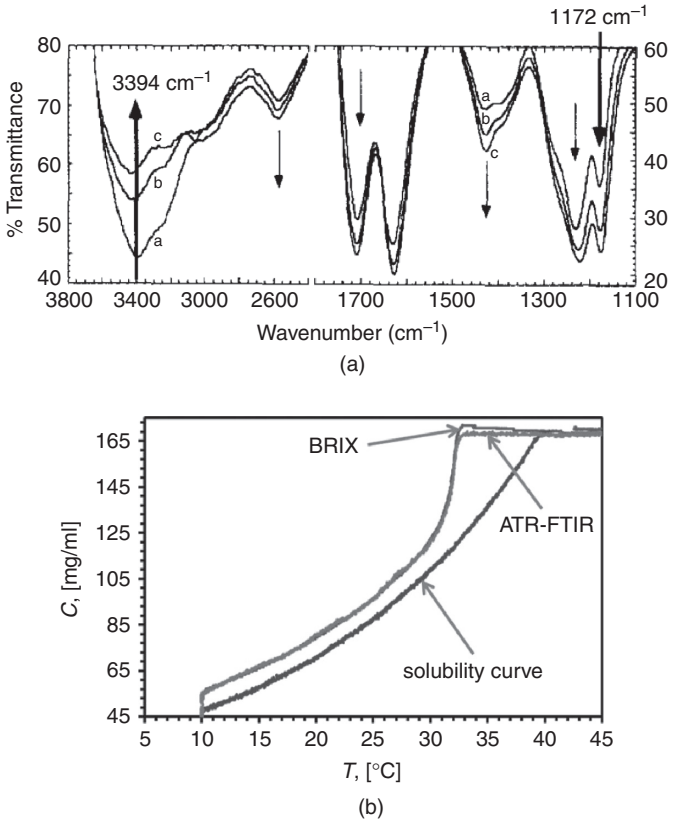

Figure 9.10 (a) ATR-FTIR spectra for aqueous maleic acid for a = 50 wt%, b = 60 wt%, c = 65 wt% maleic acid. The arrows show how the peak moves with increasing concentration. Source (Dunuwila and Berglund, 1997). (b) Supersaturation during industrial unseeded batch cooling crystallization of the pharmaceutical androsta-1,4-diene-3,17-dione, cyclic 17-(2,2-dimethyltrimethylene acetal). Reprinted with permission (Kadam *et al.*, 2012). Copyright (2012) American Chemical Society.

Mazzotti, 2004) and control applications (Matthews and Rawlings, 1998, Redman *et al.*, 1997), although its use has been limited to research purposes due to the complex sample pretreatment required. The heart of the measuring system is a flow-through density meter, usually an oscillating U-tube meter (the density is related to the vibration frequency of a U-shaped metal piece). A small slurry stream is recirculated between this device and the crystallizer. Filters are required to fully remove solids upstream of the measuring cell. The temperature must be accurately controlled because it strongly affects the density. Additionally, in order to avoid evolution of gas bubbles, the measuring temperature must be at or below the process temperature. In some cases, a gas separator has to be used. The measured density is converted to solute concentration by calibration, so the concentration of impurities must be constant. A detailed bench scale setup has been described by Worlitschek and Mazzotti (2004).

9.5 Other techniques

Because Raman spectroscopic signals are sensitive to molecules both in solution and in the solid phase, this technique is mainly applied to the inline determination of the amount of different solid compounds (polymorphs) during solvent-mediated recrystallization processes (Su *et al.*, 2010, Trifkovic *et al.*, 2012). For certain systems, they may supply an estimate of the solute concentration (Cornel *et al.*, 2008, Févotte, 2007). Often Raman and other inline techniques are applied for simultaneous determination of the supersaturation (ATR-FTIR or IR) and the particle sizes (FBRM or imaging) in order to better understand the crystallization process (Cornel *et al.*, 2008, Su *et al.*, 2010, Wu *et al.*, 2012). Such a combination of inline measurements has also been proposed as a method for fast process development of pharmaceuticals (Kadam *et al.*, 2012, Su *et al.*, 2010).

Near infrared spectroscopy (NIR) has been used inline to determine the amount of solids (Hsieh *et al.*, 2013), for example in a polymorphic transformation (Lee *et al.*, 2012). For polymerization processes, it has been shown that NIR simultaneously detects changes in solution concentration, solid concentration and even average particle size (Silva *et al.*, 2011).

The speed of sound is sensitive to both solute concentration and solids content. It is a useful inline method to detect the onset of primary nucleation and to determine the width of the metastable zone in batchwise crystallization, as well as to detect the onset of solvent-mediated recrystallization (Ulrich and Jones, 2012).

In melt crystallization and in the study of scaling issues it is often desirable to understand the close environment around a growing crystal, such as the spatial distribution of temperature and concentration at its neighborhood. To this end, several imaging techniques are available (Verma and Shlichta, 2008). For instance, color Schlieren deflectometry has been used to characterize the growth of ice in the context of eutectic freeze crystallization (Kapembwa *et al.*, 2014).

9.6 Selection of measuring methods

In order to select a measuring method, the objective of the measurement is considered first. For monitoring and control purposes, inline procedures are preferred because they offer real-time information about the process. Online procedures do too, but sampling and dilution may limit the quality of the information derived (see Section 9.3). If delayed measurement results and the interval between measurements of the order of hours is acceptable, such as in product quality assurance, an offline method is suitable.

Another consideration in selection of a measuring method is the nature and quality of the information delivered. If the measurement is intended to support modeling work, sizing with an FBRM is not adequate as chord lengths are measured instead of sizes. For example, forward light scattering may be used if the particles are not tabular or needlelike. Image analysis is an option, but lengthy calibration procedures are required. Finally, the sensitivity of the crystallization system of interest in relation to the physical principle of each measurement is of importance.

Worked example 1

Select a suitable measuring method for determining the CSD of ammonium sulfate produced by continuous evaporative crystallization for the following situations: (a) Because of product specification, we wish to know if the mass fraction of fines (<500 μm) in the product exceeds 5 wt%. (b) We suspect that variations in the product CSD are causing problems in the centrifugation step downstream of the crystallizer (smaller and less uniform particles are more difficult to separate, see Chapter 2). Therefore, we want to better control the process in order to obtain a more stable product CSD.

Worked example 1 solution

(a) Only product information is needed, so offline methods may be used. Sieving is an option, because it measures a mass distribution, so it directly supplies the information required. Because it is laborious, laser backward scattering in offline mode would be an alternative, as the particles are not needles or plates (this method loses accuracy for non-spherical particles).
(b) For process control, real-time CSD measurements are needed. Backward light scattering (an inline method) might be an option, but accuracy in the high solids content should be checked. Forward light scattering (online) is also an option, as the large particle sizes are compatible with sampling and dilution. Ultrasonic attenuation is also a possibility.

Worked example 2

Select a suitable measuring method for determining the supersaturation of ammonium sulfate produced by continuous evaporative crystallization at 60 °C for process monitoring.

Worked example 2 solution

The concentration range of interest is bounded by the saturation c_{eq} of 88 g salt/100 g solution and the metastable limit c of 88.3 g/100 g (Nývlt *et al.*, 1970). Offline methods are discarded as the objective is monitoring. Let us consider the inline refractive index (RI) method first. The RI of ammonim sulfate solutions varies with concentration at saturation as $\mathrm{d(RI)}/\mathrm{d}c = 0.00145\ (\mathrm{g}/100\ \mathrm{g})^{-1}$, so the range of RI values of interest is $0.00145\ (c - c_{eq}) = 0.00043$. This value is of the same order of magnitude as the accuracy of RI measurements of 0.0002, so RI measurements are not able to differentiate between a low and a high supersaturation. Another possibility is the online measurement of the liquid density ρ_{liquid}. At saturation $\mathrm{d}\rho_{liquid}/\mathrm{d}c = 0.0055\ (\mathrm{g/cm^3})/(\mathrm{g}/100\ \mathrm{g})^{-1}$ and the range of densities of interest is $0.0016\ \mathrm{g/cm^3}$. Since the accuracy of density measurements of about $0.0001\ \mathrm{g\ cm^{-3}}$ is much smaller than this range of densities, the density method is suitable. ATR-FTIR has been shown to be a suitable technique as well (Kadam *et al.*, 2011).

9.7 A brief summary of the chapter

In order to understand, monitor or control crystallization processes, it is necessary to measure the supersaturation and the particle size distribution (PSD). The selection of a measuring method depends: (a) on the objective of the measurement, i.e. what is the nature of the information that we consider acceptable?; (b) on how the physical properties of the system of interest behave in relation to the measuring principle of the instrument. In general, inline methods are preferred because they deliver real-time information. Online methods do also, but they require sampling and dilution. Offline methods are used when frequent and real-time process information is not required or when only the features of the final product are needed.

9.8 End of chapter problems

Problem 1
You want to develop a mathematical model of primary nucleation of $BaSO_4$ in aqueous solution, by performing lab batch precipitation runs and by counting the crystals after the process has ended. What measuring method(s) would you choose? Why? The particle sizes are ~ 10 μm.

Problem 2
You want to determine the nucleation temperature of a salicylic acid ethanolic solution upon cooling. What measuring method(s) would you choose? Why?

Problem 3
Why does the forward light scattering method deliver innacurate results for non-spherical particles?

Problem 4
You wish to determine the PSD and the particle shape in a crystallizer with a single measuring method. What method(s) would you consider? Why?

Problem 5
You wish to determine the solution supersaturation and the concentration of solid impurities in a crystallizer with a single measuring method. What method(s) would you consider? Why?

Problem 6
Suppose preliminary analysis of a case for measurement of supersaturation has led to the preselection of two methods: refractive index and density. Indicate two situations that would make you choose either of these two methods.

Problem 7
You wish to determine the polymorphic form of your crystals in a crystallizer. What method(s) would you consider? Why?

9.9 References

Allegra, J. R. and Hawley, S. A. 1972. Attenuation of sound in suspensions and emulsions: theory and experiments. *Journal of the Acoustical Society of America*, **51**, 1545–1564.

Allen, T. 2003. *Powder Sampling and Particle Size Determination*, Elsevier.

Bohren, C. F. and Huffman, D. R. 1983. *Absorption and Scattering of Light by Small Particles*, John Wiley & Sons.

Boxman, A. 1992. *Particle Size Measurement for the Control of Industrial Crystallizers.* PhD Thesis, Delft University of Technology.

Calderon de Anda, J., Wang, X. Z., Lai, X. and Roberts, K. J. 2005. Classifying organic crystals via in-process image analysis and the use of monitoring charts to follow polymorphic and morphological changes. *Journal of Process Control*, **15**, 785–797.

Chianese, A. K. M. and Mazzarotta, B. 1995. Nucleation kinetics of pentaerythritol. *The Chemical Engineering Journal*, **58**, 209–214.

Cornel, J., Lindenberg, C. and Mazzotti, M. 2008. Quantitative application of in situ ATR-FTIR and Raman spectroscopy in crystallization processes. *Industrial and Engineering Chemistry Research*, **47**, 4870–4882.

Dunuwila, D. D. and Berglund, K. A. 1997. ATR-FTIR spectroscopy for in situ measurement of supersaturation. *Journal of Crystal Growth*, **179**, 185–193.

Févotte, G. 2007. In situ Raman spectroscopy for in-line control of pharmaceutical crystallization and solids elaboration processes: a review. *Chemical Engineering Research and Design*, **85**, 906–920.

Gerla, J. H. 1995. *Modelling, Measurement and Manipulation of Crystallizers*, PhD Thesis, Delft University of Technology.

Helt, J. E. and Larson, M. A. 1977. Effects of temperature on the crystallization of potassium nitrate by direct measurement of supersaturation. *AIChE Journal*, **23**, 822–830.

Hojjati, H. and Rohani, S. 2005. Cooling and seeding effect on supersaturation and final crystal size distribution (CSD) of ammonium sulfate in a batch crystallizer. *Chemical Engineering and Processing: Process Intensification*, **44**, 949–957.

Hsieh, C. H., Billeter, J., McNally, M. E. P., Hoffman, R. M. and Gemperline, P. J. 2013. Kinetic modeling of dissolution and crystallization of slurries with attenuated total reflectance UV-visible absorbance and near-infrared reflectance measurements. *Analytical Chemistry*, **85**, 5367–5375.

Jager, J. 1990. *Control of Industrial Crystallizers: The Physical Aspects*, PhD Thesis, Delft University of Technology.

Kadam, S. S., Mesbah, A., Van Der Windt, E. and Kramer, H. J. M. 2011. Rapid online calibration for ATR-FTIR spectroscopy during batch crystallization of ammonium sulfate in a semi-industrial scale crystallizer. *Chemical Engineering Research and Design*, **89**, 995–1005.

Kadam, S. S., Vissers, J. A. W., Forgione, M. *et al.* 2012. Rapid crystallization process development strategy from lab to industrial scale with PAT tools in skid configuration. *Organic Process Research and Development*, **16**, 769–780.

Kapembwa, M., Rodríguez-Pascual, M. and Lewis, A. E. 2014. Heat and mass transfer effects on ice growth mechanisms in pure water and aqueous solutions. *Crystal Growth and Design*, **14**, 389–395.

Kohl, M., Puel, F., Klein, J. P., Hoff, C. and Monnier, O. 2004. Investigation of the growth rate of b-cyclodextrin in water during both flow-cell and batch experiments. *Journal of Crystal Growth*, **270**, 633–645.

Lee, M.-J., Seo, D.-Y., Wang *et al.* 2012. Quantitative in-line monitoring of solvent-mediated polymorphic transformation of sulfamerazine by near-infrared spectroscopy. *Journal of Pharmaceutical Science*, **101**, 1578–1586.

Lindenberg, C., Cornel, J., Scholl, J. and Mazzotti, M. 2012. ATR-FTIR Spectroscopy. In *Industrial Crystallization Process Monitoring and Control*, Chianese, A. and Kramer, H. J. M. (eds.), Wiley-VCH Verlag GmbH & Co, 81–91.

Lowe, D. 1987. Three dimensional objet recognition from single two-dimensional images. *Artificial Intelligence*, **31**, 355–395.

Markande, A., Fitzpatrick, J., Nezzal, A., Aerts, L. and Redl, A. 2013. Application of in-line monitoring for aiding interpretation and control of dextrose monohydrate crystallization. *Journal of Food Engineering*, **114**, 8–13.

Matthews, H. B. and Rawlings, J. B. 1998. Batch crystallization of a photochemical: modeling, control, and filtration. *AIChE Journal*, **44**, 1119–1127.

Mullin, J. W. and Leci, C. L. 1972. Desupersaturation of seeded citric acid solutions in a stirred vessel. *AIChE Symposium Series*, **68**, 8–20.

Myreen, K. 2012. In-line process refractometer for concentration measurement in sugar crystallizers. In *Industrial Crystallization Process Monitoring and Control*, Chianese, A. and Kramer, H. J. M. (eds.), Wiley-VCH Verlag GmbH & Co. KGaA, 71–79.

Nývlt, J., Rychlý, R., Gottfried, J. and Wurzelová, Z. 1970. Metastable zone-width of some aqueous solutions. *Journal of Crystal Growth*, **6**, 151–162.

Perry, R. H. and Chilton, C. H. 2008. *Perry's Chemical Engineers' Handbook*, McGraw-Hill.

Redman, T., Rohani, S. and Strathdee, G. 1997. Control of the crystal mean size in a pilot plant potash crystallizer. *Chemical Engineering Research and Design*, **75**, 183–192.

Redman, T. P. and Rohani, S. 1994. On-line determination of supersaturation of KCl-NaCl aqueous solution based on density measurement. *Canadian Journal of Chemical Engineering*, **72**, 64–71.

Rozsa, L. 1998. The SeedMaster device: for online supersaturation measurement and automatic crystallizer seeding. *International Sugar Journal*, **100**, 601–607.

Schorsch, S., Ochsenbein, D. R., Vetter, T., Morari, M. and Mazzotti, M. 2014. High accuracy online measurement of multidimensional particle size distributions during crystallization. *Chemical Engineering Science*, **105**, 155–168.

Silva, W. K., Chicoma, D. L. and Giudici, R. 2011. In-situ real-time monitoring of particle size, polymer, and monomer contents in emulsion polymerization of methyl methacrylate by near infrared spectroscopy. *Polymer Engineering and Science*, **51**, 2024–2034.

Su, W., Hao, H., Barrett, M. and Glennon, B. 2010. The impact of operating parameters on the polymorphic transformation of D-mannitol characterized in situ with Raman spectroscopy, FBRM, and PVM. *Organic Process Research and Development*, **14**, 1432–1437.

Takubo, H. 1990. Refractive index as a measure for saturation and supersaturation in crystal growth of water-soluble substances. *Journal of Crystal Growth*, **104**, 239–244.

Trifkovic, M., Rohani, S. and Sheikhzadeh, M. 2012. Kinetics estimation and polymorphic transformation modeling of buspirone hydrochloride. *Journal of Crystal Process Technology*, **2**, 31–43.

Ulrich, J. and Jones, M. J. 2012. Speed of sound. In *Industrial Crystallization Process Monitoring and Control*, Chianese, A. and Kramer, H. J. M. (eds.), Wiley-VCH Verlag GmbH & Co, 59–69.

Verma, S. and Shlichta, P. J. 2008. Imaging techniques for mapping solution parameters, growth rate, and surface features during the growth of crystals from solution. *Progress in Crystal Growth and Characterization of Materials*, **54**, 1–120.

Worlitschek, J. and Mazzotti, M. 2004. Model-based optimization of particle size distribution in batch-cooling crystallization of paracetamol. *Crystal Growth and Design*, **4**, 891–903.

Wu, J. X., Xia, D., Van Den Berg, F. *et al.* 2012. A novel image analysis methodology for online monitoring of nucleation and crystal growth during solid state phase transformations. *International Journal of Pharmaceutics*, **433**, 60–70.

10 Industrial crystallizers

10.1 Why this chapter is important

Once the type of crystallization process has been chosen, it is necessary to select the most suitable crystallizer. This chapter focuses on the various types of commercially available crystallizers for evaporative and cooling crystallization. The list of crystallizers makes no pretence at being complete, and only serves as a means to highlight important features of various types of crystallizers to achieve the desired product specifications. These features are related to actuators for control (fines removal, classified product removal or a combination of both) that are available in the various types of crystallizers to manipulate the CSD. There are also other features of the crystallizers that inherently affect the CSD through their impact on the hydrodynamics of the crystallizer design. In this chapter, the various designs and their effect on the final CSD of the product will be discussed.

10.2 Criteria for the choice of a crystallizer

To understand how the differences in the design between the various crystallizers affect the product quality, detailed models are needed, as discussed in Chapter 7 on population balance modeling (Bermingham *et al.*, 1998a, Kramer *et al.*, 1999). As explained in Chapter 7, the models divide the crystallizers into a number of compartments to be able to describe the effects of the hydrodynamics on the crystallization kinetics.

So, apart from giving guidance on the selection of the most appropriate crystallizer, the most appropriate compartment structures for the modeling of these crystallizers will be discussed.

In this chapter we will only discuss crystallizers for cooling and evaporative crystallization processes. Precipitation and anti-solvent crystallizers in which mixing of feed streams together or with the bulk liquor strongly affects the product properties requires a different approach in the selection of the nozzles as well as the vessel and stirrer design, and will be treated in Chapter 11. Melt crystallization, which is merely applied as an ultra-purification process, also requires a different selection procedure and will be treated in Chapter 12.

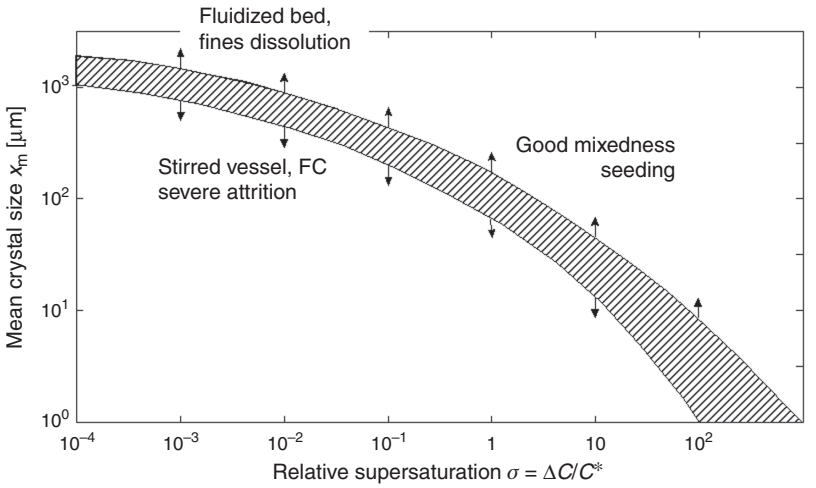

Figure 10.1 Influence of crystallizer type and hydrodynamics on mean crystal size (after Mersmann, 1995).

The choice of an evaporative or cooling crystallizer depends on:

- the material to be crystallized and the solvent;
- the method of crystallization;
- the product specifications, in particular the crystal size distribution (CSD);
- the flexibility of the design in cases where products of various coarseness (L50) must be crystallized on demand in the same equipment.

Another consideration for the choice of a crystallizer is whether the process will be carried out batchwise or continuously. For the production of small batches often less complex crystallizer designs are favored. Batchwise operation is applied for production rates up to roughly 5 kton per year. This is mostly the case when expensive materials such as fine chemicals, food additives or pharmaceuticals are being handled, and where losses must be minimized.

Batch or continuous operation is seen for production rates of 5 to 20 kton per year, while above roughly 20 kton per year continuous operation is economically more attractive.

As shown in Chapter 6, the maximum attainable mean crystal size increases with the solubility of the material, at least for solubilities up to ~10 mol per liter. Above this value the mean crystal size levels off at ~1 mm. Apart from the solubility, the type of crystallizer and the selection of its stirrer or pump also have an effect on the mean crystal size, largely through their effect on the hydrodynamics of the process and on the attrition rate of the crystals (see Figure 10.1).

Before discussing the various types of crystallizers, one generic phenomenon will be mentioned that can negatively affect the performance of a crystallizer: encrustation or scaling.

Locally, supersaturation can become quite high, e.g. at the cooling surface in a cooling crystallizer or in the boiling zone of an evaporative crystallizer. This may induce

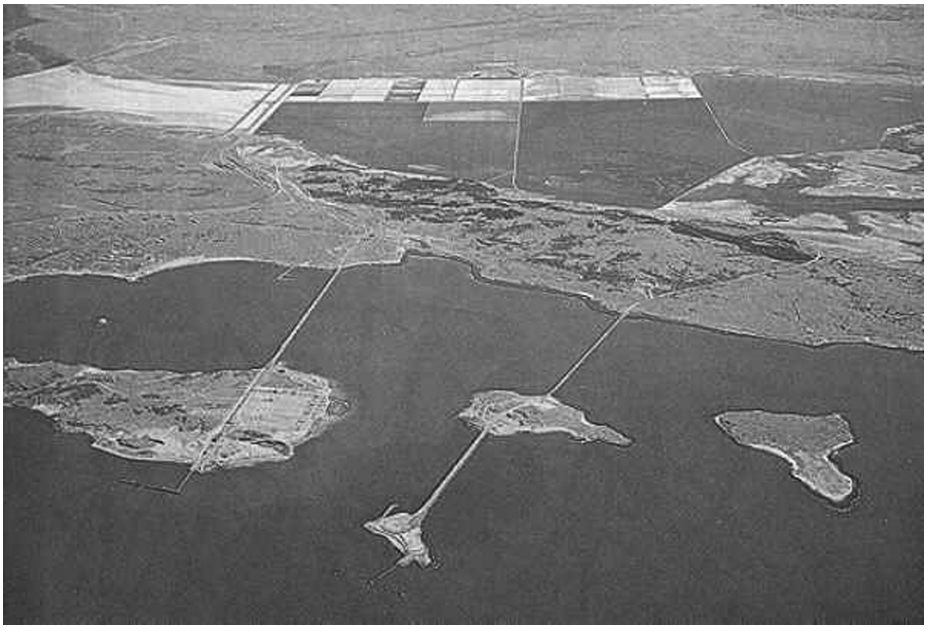

Figure 10.2 Solar pond.

encrustation or scaling. In the case of cooling this can be avoided by reducing the temperature difference over the cooling surface (normally $\Delta T = 5$ to 10 °C) and by increasing the flow rate in the heat exchanger tubes or by scraping of the cooling surface. During evaporative crystallization encrustation often occurs at the vessel walls in the boiling zone, thus reducing the effective evaporative area. The stirrer shaft may also suffer from scaling within this region, leading to unbalancing of the stirrer. Fragments of scale deposits can break away from the encrusted layers causing blocked pipelines. This emphasizes the need to avoid or at least reduce the occurrence of scaling. In some cases continuous spraying of the vessel walls and the stirrer shaft just above the boiling zone with water or an undersaturated feed is applied to reduce scaling.

10.3 Solar ponds

One of the oldest applications of evaporative crystallization is by using solar ponds (see Figure 10.2). In this way sea salt (NaCl) is still gained from sea water at relatively low costs. The number of sea salt plants is very large, and their sizes vary from small plants for local consumption up to huge plants. A large plant can consist of separate solar ponds or it can operate the ponds as a cascade. Nucleation occurs at the surface when there is not much wind, mostly at night, and the very tiny crystals are later blown to one side of the pond. The size of the crystals as well as the hardness of the product that has to be harvested therefore differ across the pond and depend on the wind and the other weather conditions. The product can be as hard as rock salt upwind and behave like quicksand downwind. If the wind that carries sand particles has to travel over large stretches of

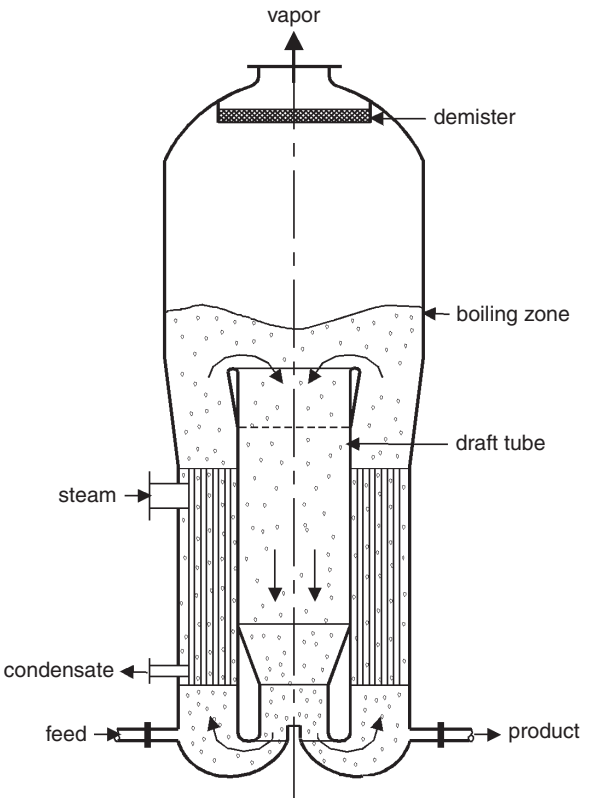

Figure 10.3 Thermo-syphon crystallizer.

sea, the sand particles, which can act as heterogeneous nuclei, are washed out and very large sea salt crystals can be formed upwind, as on Bonaire. Because of lack of control of the weather conditions the production rate is generally not predictable.

Obviously, higher yield rates can be obtained by heating the solution by means of heat exchangers. To improve heat transfer and to keep the crystals suspended, the vessel should be equipped with a stirrer or a pump. The disadvantage of a stirred open vessel is that a comparatively high energy demand for vaporization of water at atmospheric pressure is required. Therefore, industrial evaporative crystallizers are usually closed and operated at reduced pressure. The stirrer speed and, related to this, the (secondary) nucleation rate due to crystal/impeller collisions as well as the energy demand for mixing can be significantly reduced by use of a draft tube, which changes the hydrodynamic flow pattern.

10.4 Thermo-syphon crystallizer

The simplest evaporative crystallizer operating sub-atmospherically is a thermo-syphon crystallizer that comprises a heat exchanger and a draft tube, but no stirrer (see Figure 10.3).

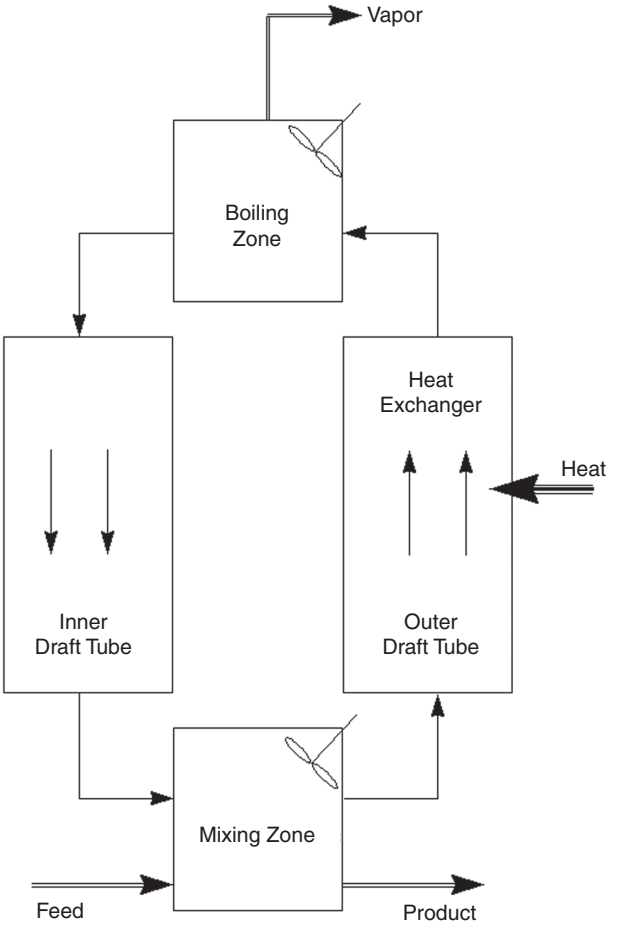

Figure 10.4 Compartment model of a thermo-syphon crystallizer.

The natural convection induced by the heat exchanger causes a circulating flow through the crystallizer.

A schematic visualization of a thermo-syphon crystallizer, divided into four compartments, is depicted in Figure 10.4. It consists of two plug flow reactors (PF) and two mixed vessels. PF I represents the inner draft tube through which the supersaturated crystal slurry flows downwards into a poorly mixed compartment where the fresh feed is added. At the bottom, large crystals settle and are removed as dense product slurry. The rest of the slurry is transported upwards by natural convection through the heat exchanger tubes in the outer draft tube, represented by PF II, where reheating takes place. Within these tubes, the supersaturation will decrease due to the usually increasing solubility with temperature. PF II may serve as an internal fines destructor since the solution concentration mostly falls slightly below its saturation level, which is beneficial both for increasing the mean crystal size and for reducing the width of the CSD. The heated solution enters the top section of the crystallizer where mixing will be rather intense due

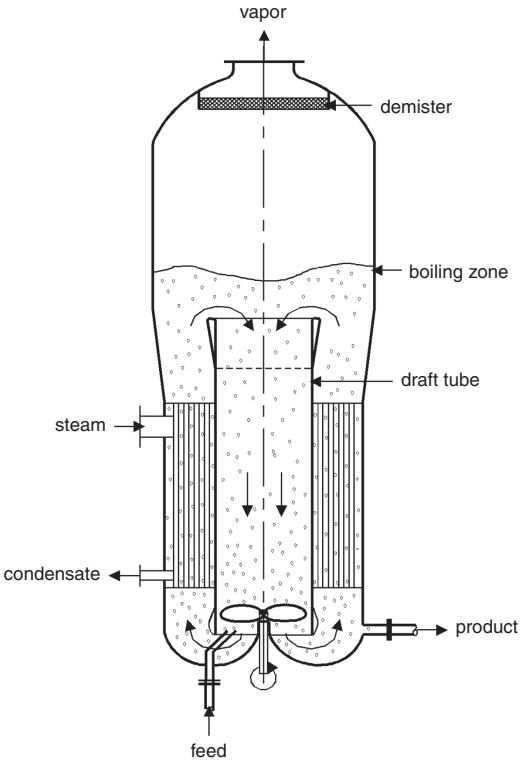

Figure 10.5 Stirred draft tube (DT) crystallizer with internal heat exchanger.

to boiling. Part of the solvent is removed as vapor and, consequently, supersaturation increases. Within this compartment where the highest supersaturation is built up, the growth rate of the crystals is the largest, and attrition fragments grow out as secondary nuclei that enter the CSD.

The cycle is completed with the entrance of the generally still supersaturated slurry into the inner draft tube (PF I). At the bottom all supersaturation should be consumed.

Although mixing through natural convection seems to be elegant, it limits the heat transfer and, related to this, the production rate per unit of crystallizer volume. Moreover, the cut size of crystals which can be transported by the natural flow up into the boiling zone, where both supersaturation and growth rate are high, may remain below the desired product size. This implies that the maximum attainable crystal size is, in a way, fixed by the process of natural convection.

10.5 Stirred draft tube crystallizer

The stirred draft tube (DT) crystallizer with an internal heat exchanger is basically similar to the previously described thermo-syphon crystallizer, but here both mixing and

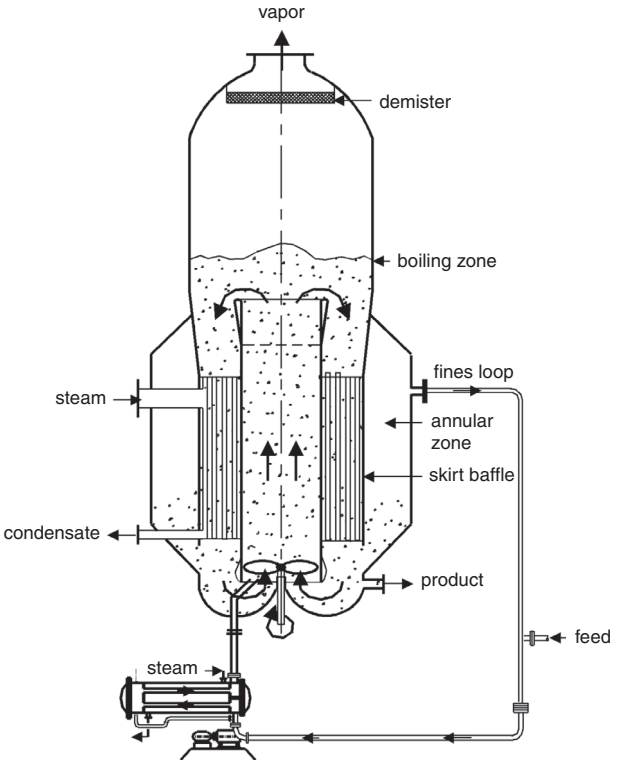

Figure 10.6 Stirred draft tube baffle (DTB) crystallizer with an internal heat exchanger and fines destruction.

heat exchange are improved by means of a slowly rotating stirrer inside the bottom part of the draft tube. First, its application as an evaporative crystallizer will be discussed. If the stirrer shaft enters the crystallizer at the top, an adequate seal is required to maintain vacuum. Since encrustation particularly occurs at the walls in the boiling zone, the stirrer shaft in this region is also a likely candidate. In spite of the rather low rotating rate, the attached encrustation may unbalance the lengthy shaft. This encrustation problem does not exist in crystallizers where the stirrer shaft enters at the bottom, and thus remains below the boiling zone. In this case sealing of the shaft is, however, even more complicated, since it is in contact with the supersaturated solution and crystals may enter or even grow into the seal.

Apart from better heat transfer in the tubes, the stirrer improves mixing of the bottom region. The forced convection induced by the stirrer, which acts as a vertical axial flow pump, is adjustable by the stirrer speed, and the flow in the inner draft tube is mostly directed downwards to match the direction of the natural flow convection. This flow direction also facilitates lifting of the larger crystals that otherwise tend to settle at the bottom of the crystallizer.

To obtain a coarser product, fines removal and destruction can be realized by adding an annular zone (see Figure 10.6). In this way a settling zone is created, which

facilitates the removal of a fines stream. Such a crystallizer with a skirt or baffle in order to obtain an annular settling zone is called a draft tube baffle (DTB) crystallizer. In this design the flow through the inner draft tube has to be directed upwards. The feed stream is mostly introduced into the draft tube just below the impeller blades.

The fines in the fines stream can be dissolved in an external loop by the addition of water, an undersaturated feed solution, or by an increase in temperature via a heat exchanger. In the last case the heat exchanger acts as an additional heat source.

The flexibility of the DT or DTB crystallizer design with an internal heating system remains, however, limited, since the size of the heater (the size of the tube plate) and the boiling surface area are coupled because both functions have to be accommodated in the same vessel. Another drawback is that the total crystal slurry is circulated through the impeller zone, which could cause considerable attrition from crystal–impeller collisions. Special attention must therefore be given to the impeller design to minimize attrition. Usually marine-type propellers with three or five blades are used, although pitched blade turbine propellers are also encountered, depending on the viscosity of the suspension and the crystal material. To avoid crushing of the larger crystals in particular, the clearance between the tips of the impeller blades and the draft tube has to be at least three times larger than the largest crystals.

The DTB crystallizer shown in Figure 10.7, separates the crystallizer from the heat exchange facilities. In this DTB crystallizer design with an external heat exchanger, the draft tube is often tapered with the wide end near the top. This reduces the fluid circulation velocity near the liquid surface (and thus reduces air entrainment), and increases the fluid velocity at the bottom of the draft tube (and thus gives a better suspension of crystals at the bottom). The diameter ratio of the draft tube and the crystallizer is in the range of 0.3 to 0.7, depending on the viscosity of the suspension, the density difference between the crystals and the solvent and for a DT also on the flow direction. Quite often a ratio of 0.7 is used for a DTB.

In a DTB with an external heat exchanger the fines are also separated in the settling zone created by a skirt baffle. The fines can be dissolved by addition of solvent, mixing with an undersaturated feed or by atemperature rise in the external heat exchanger.

For both designs a similar simplified compartment scheme is presented in Figure 10.8.

In both DTB designs the external heat exchanger serves to some extent as the fines destructor. An increase in fines flow increases the number of fines that are removed from the crystallizer, but also the cut-size of the fines. Care has thus to be taken that sufficient fines are indeed destroyed before the stream re-enters the crystallizer in order to increase the mean size of the product. As in the first design, fines dissolution only occurs in the external heat exchanger, the heat input via the external heat exchanger can be used to control the fines destruction rate as long as the total heat input and thus the production rate, can be kept constant.

The addition of an elutriation leg at the bottom of the crystallizer (see Figure 10.7) allows some classification of the product. Part of the clear liquid feed flow (mixed with the fines flow) enters the elutriation leg at the bottom and flows countercurrently to the

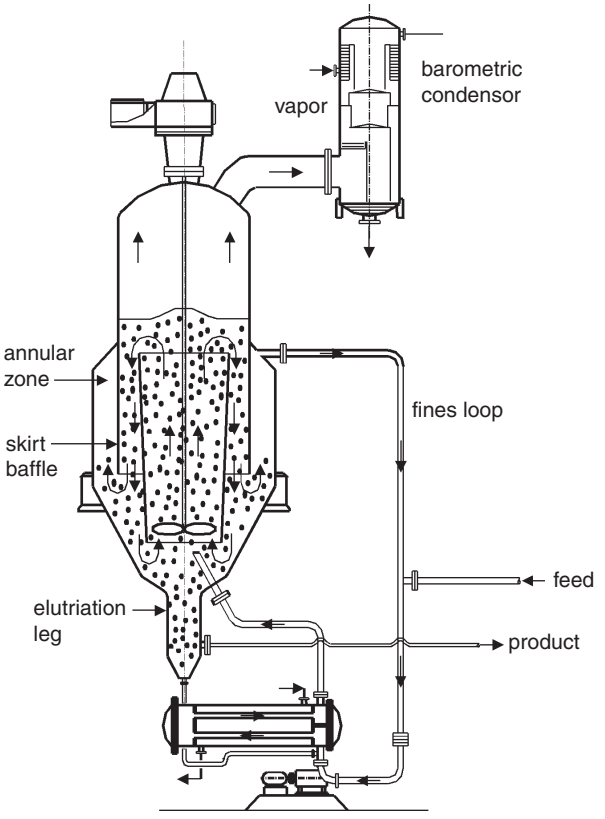

Figure 10.7 Stirred draft tube baffle (DTB) crystallizer with an external heat exchanger and fines destruction.

crystal mass. The smaller crystals are washed back into the crystallizer, and coarser product slurry leaves from the side of the leg. This classification can be added into the model as an additional compartment.

Instead of an elutriation leg, other classifiers with a sharper classification function can also be installed. Hydrocyclones, flat bottom hydrocyclones or vibrating screens can serve as such.

After the solid–liquid separation of the product, the mother liquor can be recycled into the crystallizer apart from a purge stream. A purge stream is needed to maintain an acceptable level of impurities.

DTB crystallizers of both designs can also be applied as cooling crystallizers by using the heat exchangers for cooling. In this application the fines in the stream from the annular settling zone are destroyed by heat before the stream is returned to the crystallizer separately or mixed with the feed stream; also no vapor head is needed.

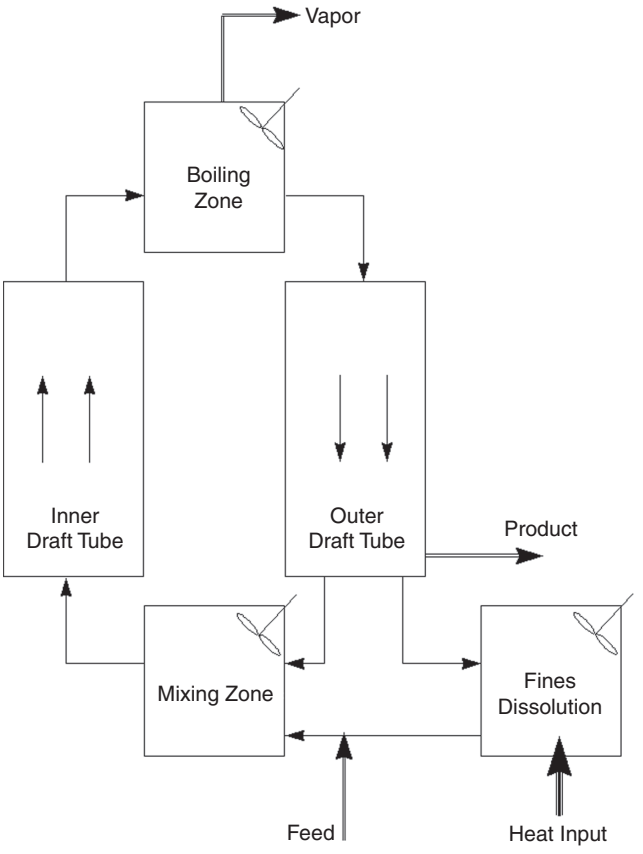

Figure 10.8 Compartment model of a DTB crystallizer.

When a crystalline product results from the reaction of two components, as in the case of ammonium sulfate obtained from gaseous NH_3 and concentrated H_2SO_4, a DTB crystallizer can also be used with two feed inlets in the draft tube just below and above the impeller blades. The heat of reaction is used to evaporate the solvent in the boiling zone.

10.5.1 Clear liquor advance

Especially for systems with a low natural solid content, the fines removal facility could be used for clear liquor advance, leaving thickened slurry in the crystallizer and a thickened underflow. By allowing the crystals to have a prolonged residence time compared to the mother liquor, and by removing fines with the "clear" liquor flow, the yield per pass, in the case of evaporation or cooling, and the mean crystal size increase. An advantage of a higher solid content is that it causes a lower supersaturation level, which improves the product size quality.

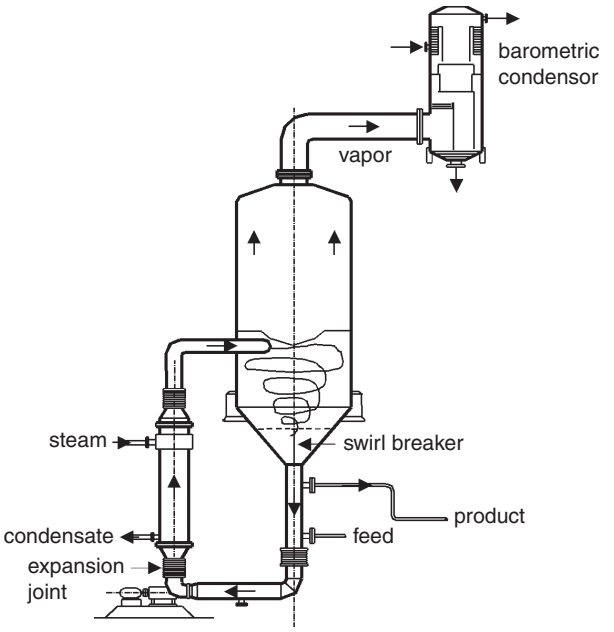

Figure 10.9 Forced circulation (FC) crystallizer with tangential inlet (Swenson type).

10.6 Forced circulation crystallizer

The forced circulation (FC) crystallizer is the most widely used crystallizer. Its most common use is in vacuum evaporative crystallization of substances with a flat solubility curve, such as NaCl, and for salts with an inverted solubility curve. It is the least expensive vacuum crystallizer, especially when substantial evaporation is required for a large production rate.

As depicted in Figure 10.9, the crystallizer comprises two separate bodies, which can be designed independently for crystallization and heat input. The crystallizer body should be large enough for vapor release, to accommodate the boiling zone and to maintain a sufficiently large liquid volume for retaining the growing crystals until the supersaturation is consumed. A slurry pump circulates the crystal slurry through the heat exchanger and back into the boiling zone via a tangential, a vertical or a radial inlet.

The heat exchanger is designed for relatively low temperature rises of the slurry per pass. This ΔT is limited to prevent boiling at the upper tube walls and subsequent scaling. Each type of inlet affects the performance of the crystallizer in several ways. A tangential inlet, for example, causes a toroidal circulation, and vortexing occurs. At the bottom of the crystallizer body a swirl breaker is installed.

The tangential inlet enters the crystallizer body where the static height of the liquid above the inlet prevents boiling of the mother liquor in the heat exchanger pipes. Its

height is thus directly coupled to the ΔT over the heat exchanger, and the liquid starts to boil directly at the outlet. The tangential stream not only causes a macroscopic swirl around the crystallizer, but superimposed on this circulation a swirl curls from the outside wall to the inside of the crystallizer (shaped like a donut), which causes the liquid to mix.

The flow pattern induced by the incoming slurry flow affects the residence time in the boiling zone for crystals of various sizes. For a tangential inlet the larger crystals almost directly leave the boiling zone. This classification effect due to the hydrodynamic characteristics results in an apparent slower growth rate of the larger crystals, and thus in a narrower CSD. On the other hand, circulation of the total slurry by a circulation pump can easily cause more attrition than that caused by the stirrer in a DTB, and special pumps must be installed to minimize the negative effect of an enhanced secondary nucleation rate on the mean crystal size. Usually an (axial-type) centrifugal pump is used.

Another often observed effect of a tangential inlet is so-called thermal short circuiting. The larger crystals with fluid entrapped between them leave the boiling zone soon after re-entering the crystallizer through the recirculation inlet nozzle, so the heat uptake by these fluid packages is not released in the boiling zone, and a temperature difference between the top and the bottom of the crystallizer body results. A new nozzle design that is meant to overcome this problem will be discussed below.

With an axial inlet, the temperature short circuiting is much lower than for a tangential inlet. An FC crystallizer with an axial inlet is therefore especially important when the FC is operated in combination with mechanical vapor recompression.

Because forced circulation causes good mixing of the crystallizer content, a FC crystallizer is supposed to come closest to an MSMPR or a one-compartment model. This is not fully the case, as has been reported in a modeling study (Bermingham *et al.*, 1998b), in which the FC crystallizer was split up in compartments, as shown in Figure 10.10.

Scaling on the walls in the boiling zone can to some extent be prevented by continuous spraying with water, and large-scale fragments that break off from the walls are collected in a conical sieve just below the heat exchanger tubes.

The mechanical construction of an FC crystallizer requires a sophisticated, and hence rather expensive, support system, because the center of gravity is located outside the equipment due to its asymmetrical design.

The construction (with its asymmetrically positioned center of gravity) has to withstand the vacuum as well as temperature changes, so it cannot be too rigidly installed. Still, very large FC crystallizers with diameters of more than 10 m are built.

The FC crystallizer can be used as a cooling crystallizer, when flash cooling suffices to produce crystals. In that case a heat exchanger is not even needed, only a circulating system. Due to the lack of an option to install a fines loop, the FC crystallizer does not have the flexibility to adapt the mean size of the CSD. Addition of a classifier in the product slurry discharge is of course always possible. Mostly an elutriation leg beneath the crystallizer body is then used.

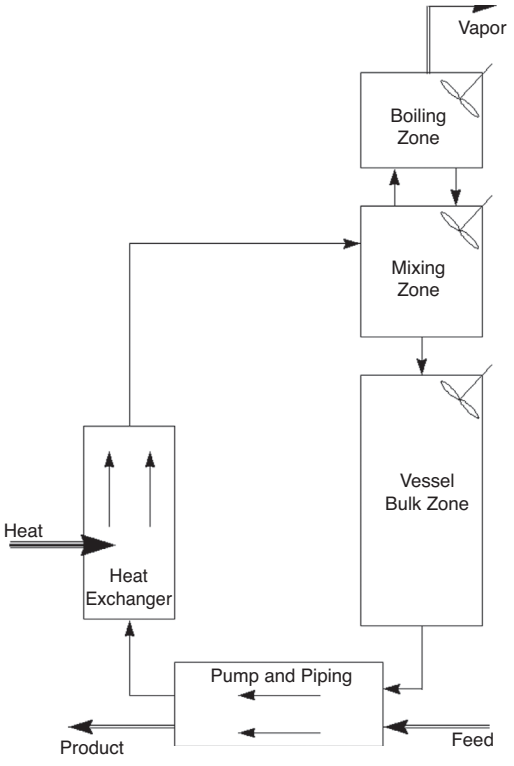

Figure 10.10 Compartment model of a FC crystallizer.

A modified design of an FC crystallizer with a novel radial inlet nozzle and a three-point feed inlet in an elutriation leg is presented in Figure 10.11. The radial horizontal inlet nozzle (Karena nozzle) contains guiding vanes (see Figure 10.12) and is designed to minimize temperature short-cuts by distributing the entering recirculating slurry across the entire vapor body cross sectional area in order to provide a uniform boiling surface (see Figure 10.13). The vanes equally distribute the inlet stream, and prevent the development of standing waves that come from collision of the inlet jet stream with the opposite wall. This allows the linear velocity in the circulation loop to be higher than 2 m s^{-1}. A gentle boiling action over the entire surface should also minimize liquid entrainment by the vapor. The position of the inlet nozzle is designed in such a way that it is at half the static height of the liquid in the vessel. Under operation the liquid level is then just at the top of or slightly above the inlet nozzle due to the presence of vapor bubbles in the liquid of the boiling zone.

The outlet of the recirculation stream at the side of the FC crystallizer with a protecting outlet baffle prevents scale parts from entering the loop. These scale crunches are collected at the bottom of the crystallizer body or when an elutriation leg is present at the bottom of this extension. The outlet baffle also forces the recirculating slurry to

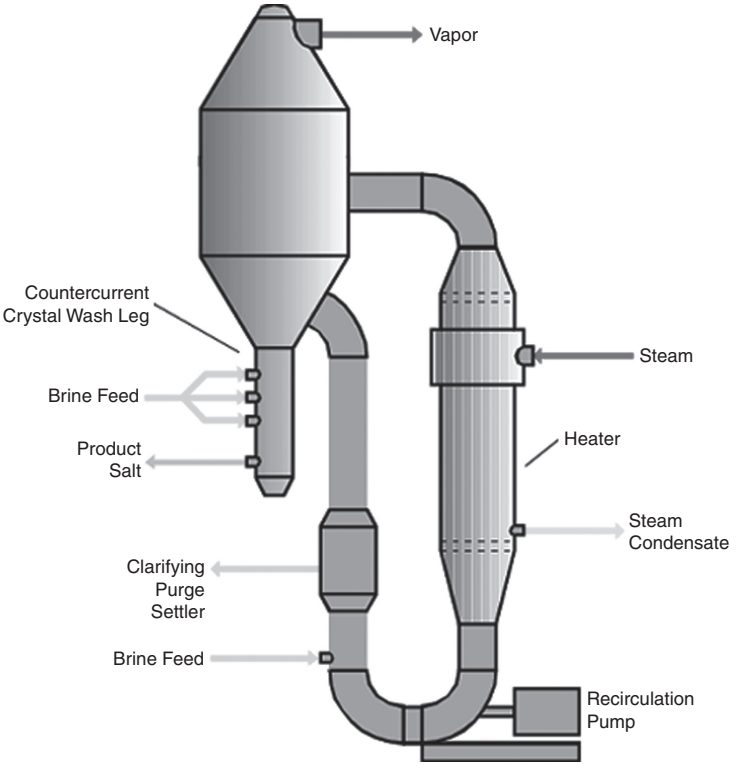

Figure 10.11 Forced circulation (FC) crystallizer with Karena nozzle and elutriation leg (US Filter type).

make a 180° turn. During this turn the larger salt crystals are supposed to be redirected to the bottom of the crystallizer body or towards the elutriation leg.

The elutriation leg consists of three zones (see Figure 10.14). The top zone is a washing zone where the downcoming crystals are washed counter currently by the upcoming stream around a hollow cylindrical body placed in the center of the elutriation leg. One of the feed inlets is therefore placed inside this cylindrical body. The top of this body contains a small hole for de-aeration. Below this body the slurry stream thickens while the volume flow decreases. The second feed inlet is in this section, where a spouting crystal bed is formed, and where the fine crystals are separated from the product crystals. The fine crystals flow upwards with the second feed flow. The product slurry removal is directly below this bed. In order to dilute this product stream, the third feed inlet is located below this product removal point. The colder feed streams cool down the crystals, which is an additional function of the elutriation leg. The feed streams also act as a washing step for the impurities in the mother liquor adhering around the crystals. It is claimed that this elutriation leg increases the average crystal size of the salt product by 50 μm while the L_{10} increases on the order of 100 μm.

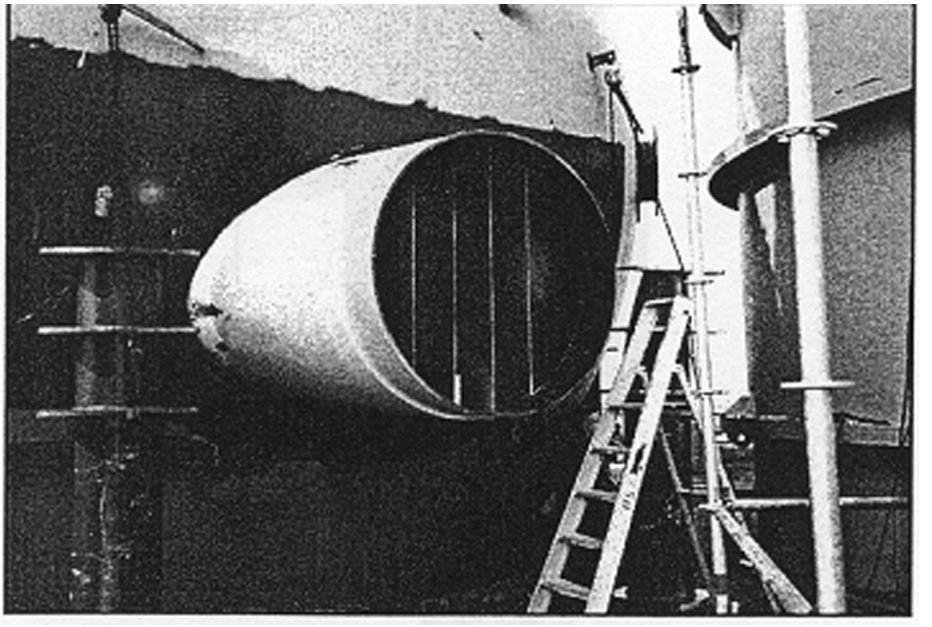

Figure 10.12 Karena nozzle with vanes.

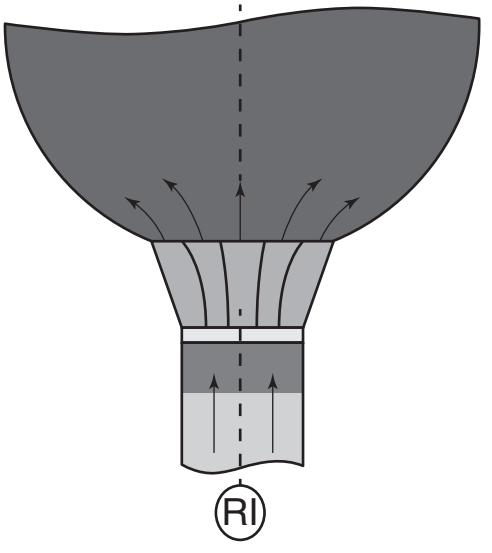

Figure 10.13 Karena nozzle from the top.

FC crystallizers are used either as single-stage large crystallizers with a large steam compressor, and with more than one recirculation loop to overcome the capacity limitations of the circulation pumps, or as multi-stage flash evaporators. Because of the large volumetric flow of low-pressure steam in the fourth and fifth stages of the Frima plant in the Netherlands for salt production, a special vapor body was constructed. For these

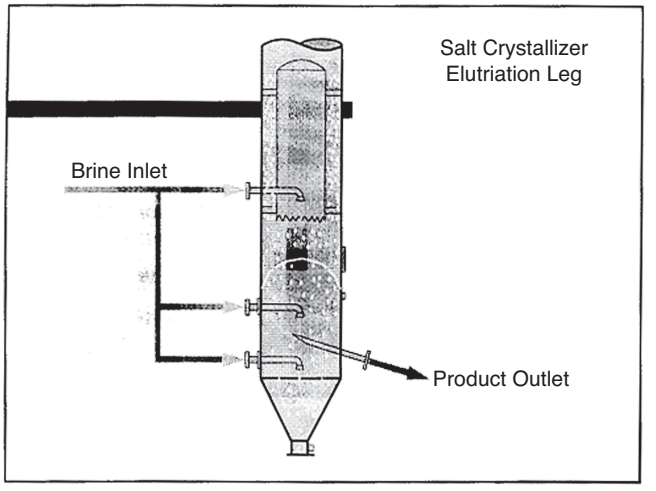

Figure 10.14 Elutriation leg (US Filter).

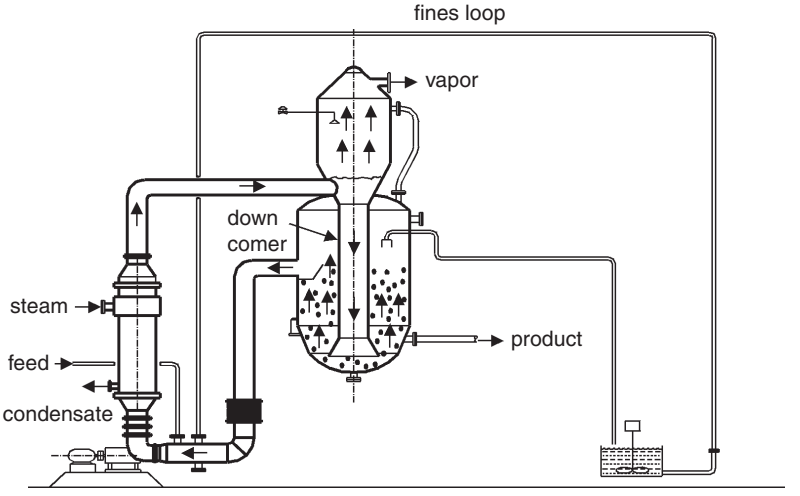

Figure 10.15 Fluidized bed crystallizer.

vapor bodies of 10 and 15 m diameter, a spherical vapor body top section was put upon a conical lower section resembling an ice cream cone. This shape resulted in considerable vessel cost savings.

10.7 Fluidized bed crystallizer

A fluidized bed or fluidized suspension crystallizer is especially designed to produce large and uniformly sized crystals. It is also called an Oslo crystallizer (see Figure 10.15).

A hot circulated stream enters the vaporizer chamber where the solvent is evaporated adiabatically. The supersaturated solution leaves the vaporizer through the downcomer and enters a densely packed fluidized bed of crystals at the bottom of the suspension chamber. The supersaturation is consumed on its way up through the bed and a coarse crystalline product is removed continuously from the bottom of the classified bed. At the top of the bed the crystals are settled, and only the fines leave the suspension chamber with the exhausted mother liquor. Since proper settling of the crystals in a bed is needed, a high settling rate due to a high specific density of the crystals is favorable.

The circulated stream is mixed with the feed stream and reheated in a heat exchanger, which is part of the recirculation line. The fines from the suspension chamber are to some extent dissolved in the heat exchanger, and also contribute to the growth of the crystals in the bed by agglomerating with these crystals, after re-entering the bed via the downcomer.

If still too many fines are recirculated, a draw-off of fines from the settling zone could be installed. These fines could be destroyed, e.g. by dissolving with water, before returning this stream to the recirculation line.

A major problem in the design of the Oslo crystallizer is the close clearance through which the supersaturated liquid enters the fluidized bed at the bottom of the reactor. Such close clearance is needed to let the incoming liquid agitate the crystals into a fluidized bed. Together with the recirculation rate, this clearance determines the superficial velocity in the bed. Partial blockage of the clearance due to local scaling (especially in the case of a slightly eccentric positioning of the downcomer pipe) or due to scaling fragments falling down from the walls will disturb the fluidization of the bed and consequently the performance of the crystallizer. To minimize occasional production stops for cleaning of the crystallizer because of such blockages, the velocity of the fluid all over the clearance has to be maintained above a certain value.

The mean residence time of the crystals can be increased considerably in the Oslo crystallizer compared to the DTB and the FC crystallizers. In addition, attrition of crystals by a stirrer or pump is avoided, since no crystals are recirculated through the pump. This pump is usually an (axial type) centrifugal pump. Crystal–crystal attrition in a fluidized bed can, however, be considerable, and in the case of, e.g., NaCl, the crystals from an Oslo crystallizer are quite rounded off. But in any case, the Oslo crystallizer yields a much coarser product; a few millimeters is not exceptional. For this reason it is sometimes also referred to as a “classifying growth”-type crystallizer.

Its production rate (kg m^{-3} s^{-1}) is in general rather low compared to that of a DTB or FC crystallizer. One of the reasons is the restriction of the circulation velocity by the requirement that a fluidized bed has to be maintained, the other that the supersaturation in the downcomer has to be low to avoid scaling. Crystal-free supersaturated mother liquor can easily cause scaling.

In a compartment model of a fluidized bed crystallizer, the feed stream enters the circulation loop from the overflow of the crystallizer body in the pump and piping compartment at the bottom, and the two mixed flows pass the heat exchanger compartment

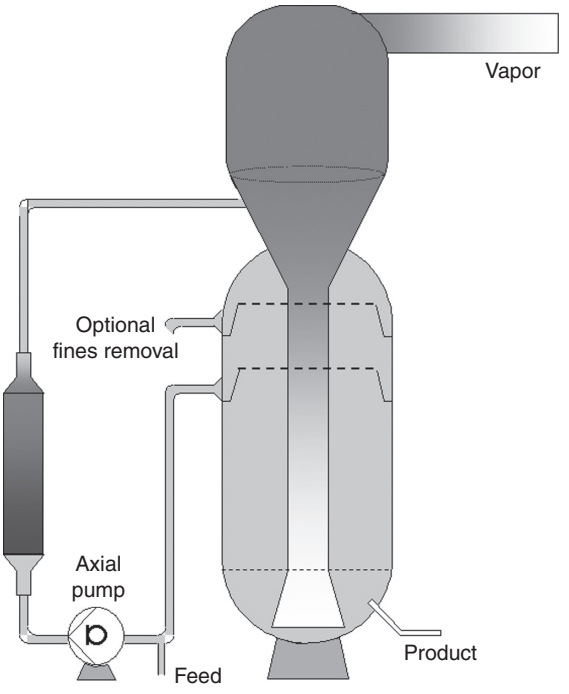

Figure 10.16 Growth-type crystallizer (US Filter, published in Kramer and Jansens (2003) with permission).

before entering the boiling zone compartment. The supersaturated solution goes via the downcomer compartment to the mixing zone compartment. The fluidized bed region can be split up into several (for example, three) suspension compartments on top of each other, before the clear liquor recirculates to the first pump and pipe compartment. The product stream leaves the lowest suspension compartment.

Clear liquid advance (CLA) to increase the height of the bed, especially for systems with a low natural solid content can be achieved by clear liquor withdrawal from the settling zone.

An Oslo-type crystallizer can be used in principle as a cooling crystallizer. The heat exchanger is used to cool the circulating stream, although the low circulation rates could cause severe scaling in the heat exchangers. Since no vapor head is needed, the recirculation pipe is directly connected to the downcomer.

10.8 Growth crystallizer

The so-called growth crystallizer has the advantage that it operates just like the fluidized bed crystallizer as a type of classifying crystallizer, but avoids the problem of a low yield (see Figure 10.16). By recycling a large fraction of the smaller crystals from the

crystallizer body, much higher supersaturations can be maintained in the downcomer without abundant scaling. The supersaturation is partly depleted in the downcomer by the circulating crystals and the production per crystallizer volume is claimed to be even higher than that of a DTB. The circulation loop contains 10 to 60% of the total crystal mass, and equals in most cases half the mass of the lower crystal bed.

High circulation flows of 1 m s^{-1} are generally applied, and the lowest part of the crystal bed acts as a spouted bed, where the velocities of the crystals decrease with the bed height. This suspended crystal bed extends to the baffle of the outlet for the circulation loop. In the section above this outlet the fines are allowed to settle. This opens the possibility of creating a clear zone at the top of the crystallizer body, where clear liquor can be withdrawn for either fines removal or as a clear liquor advance. Because of the high circulation velocities this crystallizer can easily be used as a cooling crystallizer.

10.9 Spray evaporative crystallizer

This method is often used when waste heat at a low pressure is available and when the product quality demands are not high. By cooling and evaporation of mostly an aqueous solvent from droplets obtained by spraying of the slurry into an air stream, a product is obtained.

Because nucleation at the surface of the droplets is hard to control, the primary crystals grow together as a kind of agglomerate sometimes with voids in the middle of the particle. It is a cheap method for the recovery of low-value solids from waste streams.

10.10 Direct cooling crystallizer

In direct cooling or direct contact refrigeration no heat is withdrawn from the suspension through a cooling surface of a heat exchanger, but a refrigerant is sprayed directly into the solution. It is applied in those cases where cooling crystallization has to occur at a very low temperature or when the solute has a strong tendency to form scaling on the heat exchanger tubes. The refrigerant must be insoluble in the solvent. Liquid butane, propane or liquid CO_2 are examples of refrigerants. The refrigerant absorbs heat from the suspension and evaporates. The vapor leaves the crystallizer similar to the water vapor in conventional evaporative crystallization. Therefore a slightly modified version of either a DTB (Figure 10.7) or an FC crystallizer (Figure 10.9) could be used for direct cooling crystallization (Figure 10.17).

The refrigerant vapor must be condensed by recompression and cooling, and returned to the crystallizer for reuse. Several organics with a low melting point are separated from their mother liquor or from an impure melt by this technique.

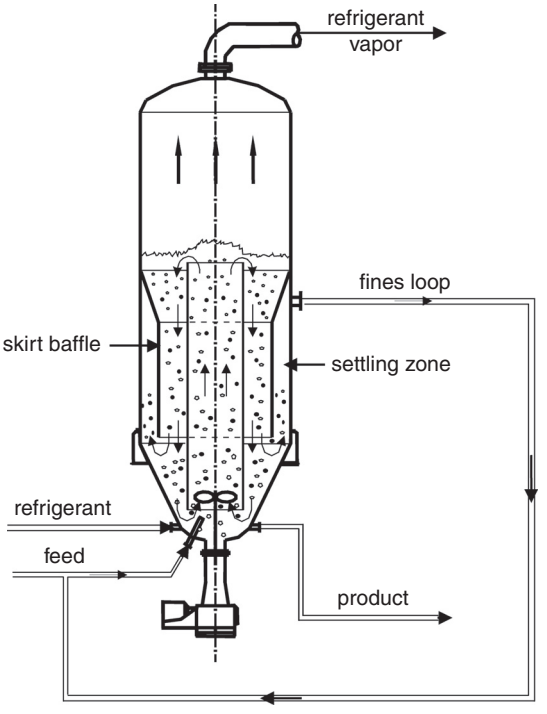

Figure 10.17 Direct cooling crystallizer.

10.11 Surface cooling crystallizer

Apart from the DTB and the Oslo crystallizer, two other types of cooling crystallizers are often encountered. In one type a crystallizer body provides the retention time for the growing crystals, and either the slurry (see Figure 10.18) or the overflow is circulated through a heat exchanger. For crystallization from solution usually the slurry is pumped through a tube and shell heat exchanger, with a ΔT range between the tube and the wall of 5–10 °C, while for melt crystallization mostly the "clear" liquor overflow is cooled down in a scraped heat exchanger to prevent scaling on the cooled surfaces.

Another often-applied cooling crystallizer for crystallization from solution in particular is the cooling disc crystallizer. A cooling disc crystallizer can be considered as a compact cascade of cooling crystallizers. The crystallizer consists of a trough that is divided by fixed hollow cooling elements into several compartments (see Figure 10.19). Each compartment acts as a separate crystallizer, and contains a disc equipped with Teflon wipers and mixing blades.

The discs are mounted on a longitudinal axis, which rotates slowly (5–45 rpm). The wipers keep the cooling surfaces clean from scaling. Internal slurry transport proceeds without the need of a pump, since both the crystals and the mother liquor flow freely from one compartment to the next via openings at the bottom of the cooling elements.

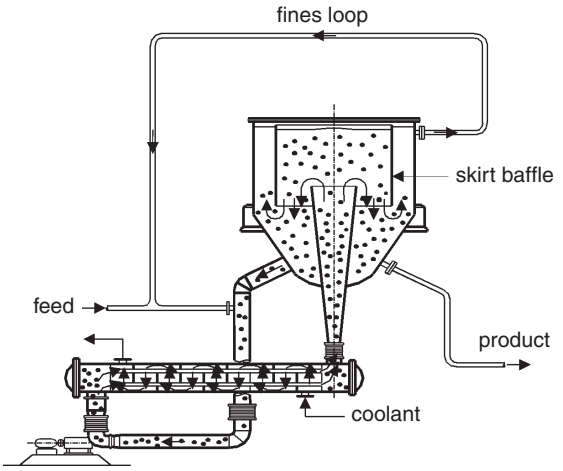

Figure 10.18 Swenson-type cooling crystallizer.

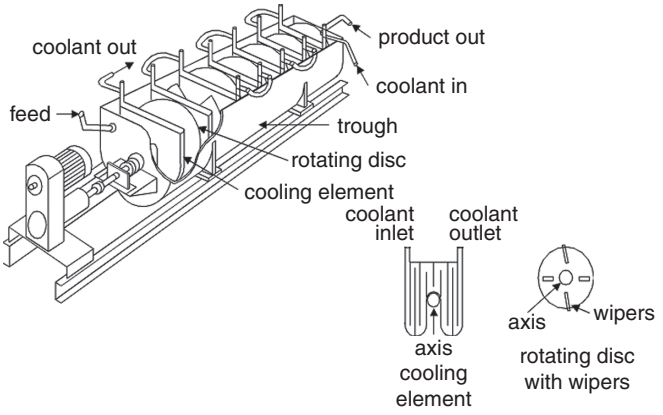

Figure 10.19 Cooling disc crystallizer with a detail of a cooling element.

The crystal content increases in the successive compartments and may reach 45 vol% in the last compartment.

The slow rotation of the discs provides a gentle agitation of the slurry in the compartments. The product leaves the last compartment via an overflow. The suspension flows counter currently to the coolant.

Another type of surface-cooled crystallizer is the Swenson cooling crystallizer with air agitation. This crystallizer consists of a shallow vessel wherein submerged heat exchanger pipes are bathed with a stream of gas bubbles that emerge from tiny holes in pipes located at the bottom of the vessel. The gas bubbles are collected at the top of the vessel and recycled to the pipes. It is important to use gas that is saturated with the water of the mother liquor to avoid scaling of the holes in the pipes. These gas bubbles are used for agitation only. They increase the local turbulence at the heat

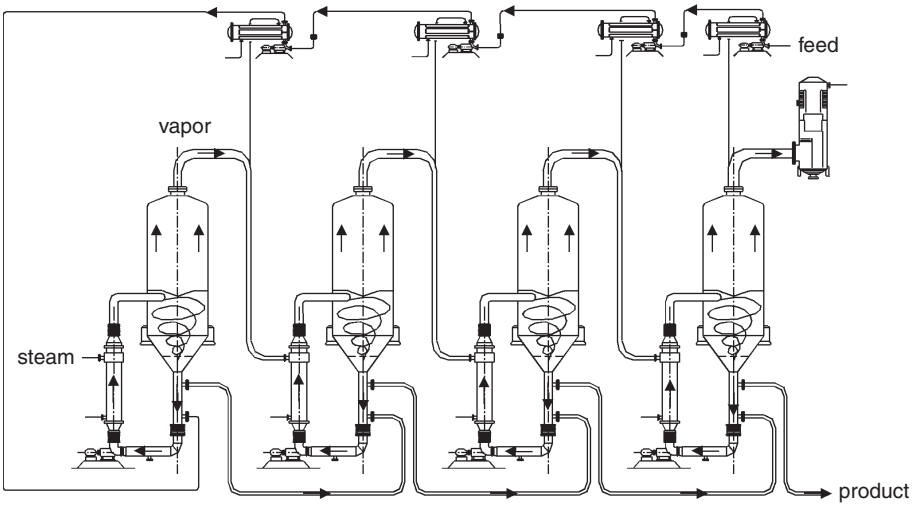

Figure 10.20 Cascade of four FC crystallizers for NaCl crystallization.

exchanger surfaces, improve heat transfer, reduce scaling on the heat exchanger surfaces and gently keep the crystals in suspension without causing much attrition and secondary nucleation.

This crystallizer is especially used for salts that are prone to attrition, like hydrates such as copper and sodium sulfate hydrates and Glauber salt.

10.12 Cascades of crystallizers

Cascades of crystallizers other than the cooling disc crystallizer are often cascades of evaporative crystallizers. Their purpose is mainly to minimize operating (mainly energy consumption) and investment costs.

Mostly DTB and FC vacuum crystallizers are operated in a cascade of three to five crystallizers, each controlled at a lower pressure and temperature. In the case of, e.g., NaCl, where the crystal production follows from flash evaporation of the aqueous solvent, the heat of condensation of the vapor is partly reused to evaporate the water in the next stage and partly for countercurrent heating of the feed (see Figure 10.20).

For KCl, often a cascade of five DTB crystallizers is used and the vapor is only used to reheat the recycled mother liquor (see Figure 10.21). Water is added for fines destruction.

For precipitation cascades of simple stirred vessels are often used. In this case a cascade is mainly applied to improve the product quality by dividing the feed stream via more than one inlet stream over the various vessels, and by recycling part of the slurry stream. In this way a higher solid content in the first vessel(s) is maintained, and the supersaturation is suppressed.

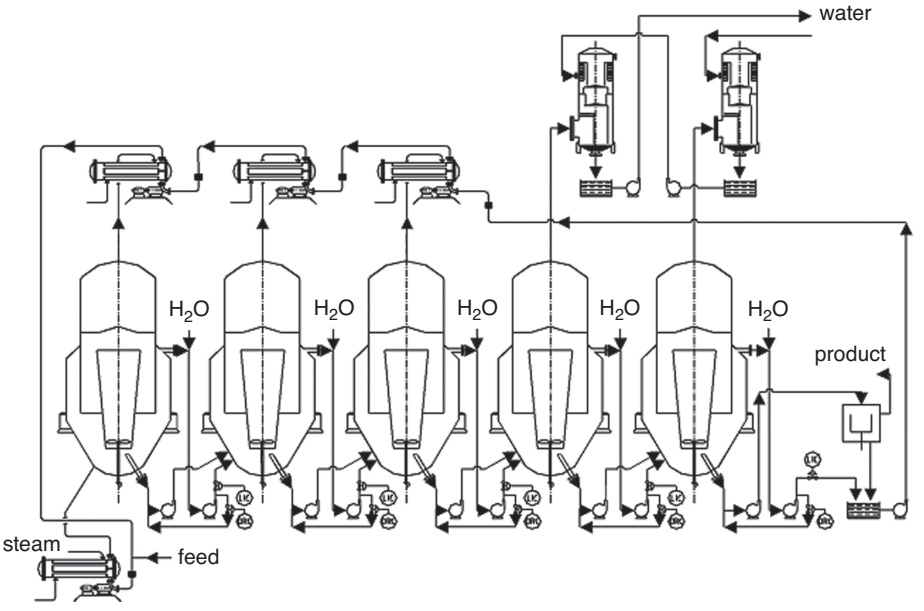

Figure 10.21 Cascade of five DTB crystallizers for KCl crystallization.

10.13 References

Bennett, R. C. 1993. Crystallizer selection and design. In *Handbook of Industrial Crystallization*, Myerson, A. S. (ed.), Butterworth-Heinemann.

Bermingham, S. K., Kramer, H. J. M. and van Rosmalen, G. M. 1998a. Towards on-scale crystallizer design using compartmental models. *Computers and Chemical Engineering*, **22**, S355–S362.

Bermingham, S. K., Neumann, A. M., Muusze, J. P., Kramer, H. J. M. and Verheijen, P. J. T. 1998b. Modelling the settling, dissolution and non-uniform nucleation kinetics in a 150-litre forced circulation crystallizer. *Particle and Particle Systems Characterization*, **15**(1), 56–61.

Bermingham, S. K., Verheijen, P. J. T. and Kramer, H. J. M. 2003. Optimal design of solution crystallization processes with rigorous models. In *Chemical Engineering Research & Design*, **81**(1), 893–903.

Kind, M. and Mersmann, A. 1989. On the width of the metastable zone of solutions. In *Proceedings of the 10th Conference on Industrial Crystallization*, Nyvlt, J. and Zacek, S. (eds.), Elsevier.

Kramer, H. J. M., Bermingham, S. K. and van Rosmalen, G. M. 1999. Design of industrial crystallizers for a given product quality. *Journal of Crystal Growth*, **198**, 729–737.

Kramer H. J. M. and van Rosmalen, G. M. Crystallization. In *Encyclopedia of Separation Science, Volume I*, Academic Press, 64–84.

Kramer, H. J. M. and Jansens, P. J. 2003. Tools for design and control of industrial crystallizers: state of the art and future needs. *Chemical Engineering and Technology*, **26**(3), 247–255.

Mersmann, A. A. 1995. *Crystallization Technology Handbook*, Marcel Dekker.

Larson, M. A. 1978. Guidelines for selecting a crystallizer. *Chemical Engineering*, **85**, 90.

Mersmann, A. and Rennie, F. W. 1995. Design of crystallizers and crystallization processes. In *Crystallization Technology Handbook*, Mersmann, A. (ed.), Marcel Dekker.

Mullin, J. W. 2001.*Crystallization*, 4th edn., Butterworth-Heinemann.

Oldshue, J. Y. 1983. *Fluid Mixing Technology*, McGraw-Hill.

Wöhlk, W., Hofmann, G. and de Jong E. J. 1991. Die Kristallisationstheorie in Praxis. *Chemie Ingenieur Technik*, **63**, 293–297.

11 Precipitation and anti-solvent crystallization

11.1 Why this chapter is important

Precipitation processes are important in a number of different fields, including extractive metallurgy, where the high recovery (i.e. recovered mass/initial mass in solution) is exploited to recover valuable metals; water treatment, where the same high recovery is exploited to cause high levels of removal of contaminants; pharmaceuticals, where a high recovery of product is important; and nano-precipitation, where the small particle size and a monodisperse crystal size distribution are important.

11.2 What is precipitation?

The distinction between crystallization and precipitation is often based on the speed of the process, with precipitation usually being defined as a fast process that results in rapid solid formation of extremely small crystals (Jarvenin, 2008). However, a more scientific definition of precipitation is the fact that the product is formed by a chemical reaction. Thus, precipitation is often referred to as "reactive crystallization."

In precipitation processes, two soluble reactants are mixed to form a sparingly soluble product. What makes it unique is that often, especially in high-recovery precipitation, the reagent streams are highly concentrated and thus very high supersaturations, especially local supersaturations, are created (Figure 11.1). Because of the high supersaturation, the conversion of the solutes into solid particles is (in contrast to crystallization) usually a very fast process.

11.3 What makes it unique?

Precipitation is used for sparingly soluble substances (solubility in the range 0.001–1 kg m^{-3}) for a number of reasons, but mostly because of:

a. the requirement for a high recovery of the product;
b. the requirement for a high degree of removal of a species;
c. other techniques not being suitable. For example, cooling crystallization is not suitable if the compound has a flat or retrograde solubility curve, whilst evaporative crystallization is too expensive due to the volume of the water to be evaporated.

Figure 11.1 A visual representation of how mixing determines the local supersaturation in a precipitation process.

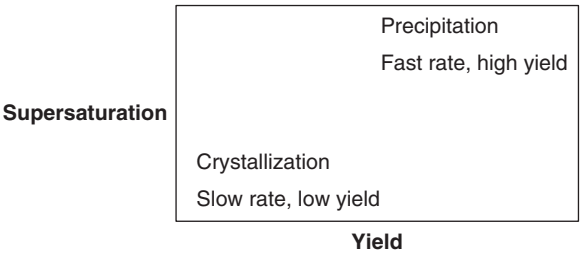

Figure 11.2 Relationship between yield, supersaturation and rate of process for precipitation and crystallization.

In contrast, cooling or evaporation, although they are often slower and more controlled processes, often result in much lower recoveries. This is illustrated schematically in Figure 11.2.

The high supersaturation levels in precipitation often lead to the formation of solid phases with a low product quality (small primary crystals and agglomerates), as well as other unexpected phases, such as polymorphs and amorphous materials. In addition, the combination of the high supersaturation and fast kinetics means that there are often

significant concentration variations in the precipitation vessel, accompanied by locally steep supersaturation gradients near the inlet point(s).

In fact, in precipitation processes, because the supersaturation is created by the feeding of a reactant solution into an agitated solution of the other reactant, as in a semi-batch operation, there is often a competition between the mixing and the reaction processes. This is because the chemical reaction is often fast – faster than the mixing of the reagents at the molecular level. Because the solubility of the product is low, the supersaturation at the feed point becomes high and the process is carried out under mixing-limited conditions (Torbacke and Rasmuson, 2001).

Thus the description of the precipitation kinetics is complicated by the fact that the mixing process can be rate limiting. This becomes a difficult problem, since, in order to develop a complete and correct description of the process, one must develop a detailed model of the local and time-dependent hydrodynamic conditions in combination with the local and time-dependent supersaturation in the reactor.

11.4 Characteristics of precipitation processes

11.4.1 Dominant phenomena in precipitation

Because precipitation processes are usually applied in cases of relatively sparingly soluble substances, and thus are operated at high supersaturations, precipitation is dominated by the following mechanisms:

a. **Primary nucleation**. Precipitation is dominated by this mechanism, largely due to the high supersaturation caused by the low solubility of the product. As a result of the high nucleation rates, mixing and thus the hydrodynamics play a dominant role.
b. **Agglomeration**. Because of the dominance of primary nucleation, large numbers of small particles are formed. The large numbers of particles, combined with low growth rates in precipitation processes, favor agglomeration. In addition, agglomeration is significantly affected by the hydrodynamics in the crystallizer, as they play an important role in influencing the particle collisions in the vessel.
c. **Growth**. In precipitation processes, the growth rate is usually slow compared to the nucleation rate, mostly because the solubility is low and thus the number of molecules in solution that have the potential to attach to a growing nucleus is very low, even when the supersaturation has a high absolute value. Growth is also an important mechanism in ensuring the success of agglomeration, as it is growth that is responsible for the formation of the crystalline bridges that form the agglomerates.
d. **Ostwald ripening**. This is an important mechanism in precipitation processes. Ostwald ripening occurs when the smaller particles in solution dissolve and recrystallize onto larger particles. The ripening occurs because solubility is a function of particle size and so the very small particles formed by primary nucleation are more soluble than larger particles. Ostwald ripening thus allows the particles to reach a more

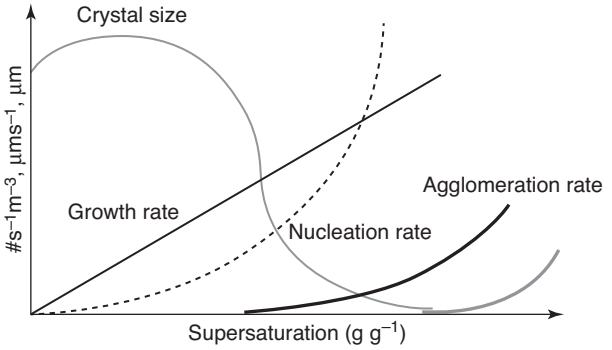

Figure 11.3 Schematic representation of the relationship between supersaturation and the rates of nucleation, growth and agglomeration in crystallization processes (O'Grady, 2011).

thermodynamically stable state by reducing the surface-area-to-volume ratio of the system. Ostwald ripening is an *extremely slow process* that does not occur during precipitation, but only afterwards, during aging.

Figure 11.3 (based on a simpler diagram by O'Grady, 2011) illustrates how the supersaturation affects the nucleation, growth and agglomeration rates, as well as the particle size for crystallization processes. The diagram also applies for *precipitation processes*: at high supersaturation levels, the nucleation rate is very high, the growth rate is low and, consequently, the particle size is relatively small. The agglomeration rate becomes significant when the nucleation rate is high and large numbers of particles are formed. Thus, at high supersaturation, the agglomeration rate begins to become significant. This results in an increase in particle size due to agglomeration. The figure is highly simplified, but sums up the dynamic relationship between nucleation, growth and agglomeration in precipitation processes as well.

11.5 Mixing in precipitation processes

Hydrodynamics and mixing have a critical role to play in reactive crystallization as they affect the mixing of reagents that generates the supersaturation, which, in turn, forms the precipitate through the mechanisms of nucleation, growth and agglomeration. In precipitation, mixing plays multiple (and often contradictory) roles, including:

a. ensuring that the reagents have maximum contact with each other;
b. reducing non-uniformities or gradients in composition;
c. keeping the slurry in suspension;
d. controlling agglomeration either by promoting contact between particles or by disrupting aggregates.

11.5.1 Macro-mixing

Macro-mixing occurs at a scale equivalent to the size of the reactor and can be described as bulk dispersion of the liquids throughout the reaction volume. Macro-mixing defines residence time distributions and determines the environment concentrations for both meso- and micro-mixing and conveys fluids that are undergoing meso-mixing and micro-mixing through environments where turbulence properties (such as the rate of energy dissipation ε and the scale of turbulence Λ) vary.

It has been experimentally found that, for a well-baffled tank and fully developed turbulence, the macro-mixing time τ_{macro} is between three and five times the circulation time τ_c (Bałdyga and Bourne, 1999):

$$\tau_{macro} = 4\tau_c \tag{11.1}$$

where τ_{macro} = macro-mixing time [s] and τ_c = circulation time [s].

For a vessel using an impeller with four pitched blades, Roelands and coworkers (2002) express the circulation time τ_c, as follows:

$$\tau_c = \frac{V}{q_c} \tag{11.2}$$

where V = vessel contents [m^3], and q_c = pumping capacity of the impeller [$m^3\ s^{-1}$].

The pumping capacity of the impeller is given as:

$$q_c = N_q N d^3 \tag{11.3}$$

where N_q = flow number (taken as 0.73 for a pitched blade turbine;Nienow, 1997), N = impeller speed [rps] and d = impeller diameter [m].

11.5.2 Meso-mixing

The term "meso-mixing" describes mixing on a scale comparable to the size of the reagent feed pipe, i.e. larger than micro-mixing (on the molecular scale), but smaller than that of macro-mixing (on the scale of the whole reactor; Bałdyga and Bourne, 1999). The meso-mixing process occurs via a combination of convective and turbulent exchange of fluids at the reactor inlets between the fresh feed and its surroundings.

Two meso-mixing mechanisms have been identified:

- Inertial-convective disintegration of large eddies in the course of dispersion;
- Turbulent dispersion, where a feed stream spreads out transverse to its local streamline.

The time constant for meso-mixing due to the inertial-convective disintegration of large eddies is determined from (Torbacke and Rasmuson, 2001):

$$\tau_{meso} = a\left(\frac{\Lambda^2}{\varepsilon}\right)^{\frac{1}{3}} \tag{11.4}$$

where $a = 1-2$ (2 for fully developed turbulence in liquids; Baldyga *et al*., 1997), Λ = macro-scale turbulence [m] and ε = local energy dissipation rate [$m^2\ s^{-3}$].

The macro-scale turbulence is estimated by (Torbacke and Rasmuson, 2001):

$$\Lambda = \sqrt{\frac{Q_f}{\pi u}} \tag{11.5}$$

where Q_f = feed flow rate [$m^3\ s^{-1}$] and u = fluid velocity [$m\ s^{-1}$].

The local energy dissipation rate is given by (Torbacke and Rasmuson, 2001):

$$\varepsilon = \frac{N_p N^3 d^5}{V} \tag{11.6}$$

where N_p = power number (taken as 1.5 for a pitched blade; Uhl and Gray, 1966), N = impeller speed [rps] and d = impeller diameter [m], with

$$N_p = \frac{Pg}{N^3 D^5} \tag{11.7}$$

where P = power [W], g = acceleration due to gravity (9.81 $m\ s^{-2}$) and ρ = liquid density [$kg\ m^{-3}$]. The time constant for meso-mixing due to turbulent dispersion is determined from:

$$t_d = \frac{Q_F}{u D_i} \tag{11.8}$$

where: τ_d = time constant for turbulent dispersion [s], Q_F = volumetric flow rate of feed solution [$m^3\ s^{-1}$], u = liquid velocity [$m\ s^{-1}$] and D_i = turbulent diffusivity [$m^2\ s^{-1}$].

11.5.3 Micro-mixing

Micro-mixing is homogenization on the molecular scale through diffusion and occurs at the Kolmogorov scale, which is the size of the smallest eddy. Since micro-mixing happens on the molecular scale, it directly influences the chemical reaction and thus nucleation and crystal growth, which are essentially molecular-level processes (Baldyga and Bourne, 1999).

The micro-mixing time can be determined from the local specific energy dissipation rate, in terms of Kolmogorov's turbulence theory (Baldyga and Bourne, 1989b):

$$\tau_{micro} = 17.24\sqrt{\frac{\nu}{\varepsilon}} \tag{11.9}$$

where ν = kinematic viscosity [$m^2\ s^{-1}$] and ε = local specific energy dissipation rate [$m^2\ s^{-3}$].

Micro-mixing takes place by:

a. molecular diffusion;
b. laminar deformation of striations below the Kolmogorov scale;
c. mutual engulfment of regions having different compositions.

Engulfment is often the limiting one of these three.

The time constant for engulfment is given by:

$$\tau_e = (\nu/\varepsilon)^{0.5} \tag{11.10}$$

where ν = kinematic viscosity [$m^2\ s^{-1}$] and ε = local turbulent energy dissipation rate [$m^2\ s^{-3}$]. In the past few years, experimental techniques like laser doppler velocimetry (LDV) and particle image velocimetry (PIV) have significantly improved, giving more reliable values of the locally specific energy dissipation rate ε from which, utilizing Kolmogorov's theory, the local micro-mixing time t_m can be calculated.

Alongside these experimental studies, much modeling work has been undertaken, especially by Baldyga and coworkers (Baldyga and Bourne, 1989b, 1989c, 1990, 1992, Bourne and Dell'Ava, 1987) and by Villermaux and coworkers (Aoun *et al*., 1999, David *et al*., 1991a, 1991b, Fournier *et al*., 1996, Houcine *et al*., 1997, Marchal *et al*., 1988). Finally, chemical reactors of special geometry have recently been proposed specifically to give enhanced micro-mixing (Atiqullah *et al*., 1993, Rivallin *et al*., 2005).

11.6 Time and length scales for mixing and precipitation

Since it is the mixing of reagents that generates the supersaturation in precipitation reactions, it is important to determine whether the precipitation process is mixing- or reaction-limited. In order to do this, the characteristic time for the various mixing processes must be compared to the characteristic time constant for the reactive precipitation process, which can be calculated for an *n*th-order chemical reaction as follows:

$$\tau_R = \frac{1}{\left(k_n(\overline{C_{A0}})^{n-1}\right)} \tag{11.11}$$

where τ_R = characteristic time constant for the chemical reaction [s], k_n = reaction rate constant [$m^3\ kg^{-1}\ s^{-1}$ for a first-order reaction], C_{A0} = initial concentration of reagent A [$kg\ m^{-3}$] and n = reaction order.

The characteristic time constants for each of the scales of mixing can then be compared with the characteristic time constant for the chemical reaction. If the characteristic time constant for the reaction is smaller than that for the mixing (i.e. the reaction is faster than any of the mixing processes), then the precipitation process is mixing limited. If the characteristic time constant for the reaction is larger than that for the mixing (i.e. the reaction is slower), then the precipitation process is reaction limited.

This is illustrated in Figure 11.4, which shows an example of identifying the rate-limiting step in the case of a fast reaction. In the figure, the nucleation time is faster than any of the mixing times and thus the precipitation process is limited by the micro-mixing time.

Worked example 1: timescales of mixing

Given the following time information about the reaction between A and B to form the product R, determine whether the precipitation process will be affected by mixing

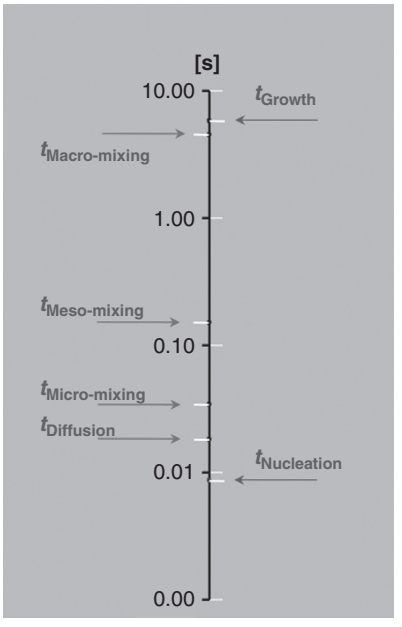

Figure 11.4 Competition between reaction and mixing: example of identification of the rate limiting step (Bałdyga and Bourne, 1999).

on scale-up if the feed point is close to the impeller. In other words, calculate the timescales of mixing (macro-, meso- and micro-), as well as the reaction time for the small reactor. Determine which scale of mixing is limiting. Do the same for the large reactor.

$$\mathrm{A} + \mathrm{B} \rightarrow \mathrm{R} \qquad k_{r1} = 2.97 \times 10^7 \, \mathrm{e}^{-4000/T} \, \mathrm{m^3 \, kmol^{-1} \, s^{-1}}$$

Semi-batch reactor:

- $C_{A0} = C_{B0} = 0.2$ kmol m^{-3}
- Small reactor volume $= 0.1$ m^3; large reactor volume $= 20$ m^3
- Small reactor diameter $= 0.13$ m; large reactor diameter $= 3.46$ m
- Energy dissipated by the impeller $= \varepsilon = 0.360$ W kg^{-1}
- $\rho = 1000$ kg m^{-3}; $\nu = 10^{-6}$ m^2 s^{-1}; $Sc = 2000$.
- Fluid velocity at the reactant addition nozzle 0.1 m s^{-1};
- Addition time $= 1$ h

Solution to worked example 1

Using equation 11.11, the reaction times for both the small and large reactors are calculated. Since the power per unit volume is provided, the following equation is used to calculate the macro-mixing time (Mersmann, 2001):

$$\tau_{macro} = 5(D^2/\varepsilon)^{\frac{1}{3}} \tag{11.12}$$

Table 11.1 Summary of macro-, meso- and micromixing times for the 100 liter and 20 000 liter reactors

Characteristic time [s]	100 liter reactor	20 000 liter reactor
Reaction time	0.14	0.14
Macro-mixing time	1.8	16.1
Meso-mixing time	0.027	0.73
Micro-mixing time	0.03	0.03

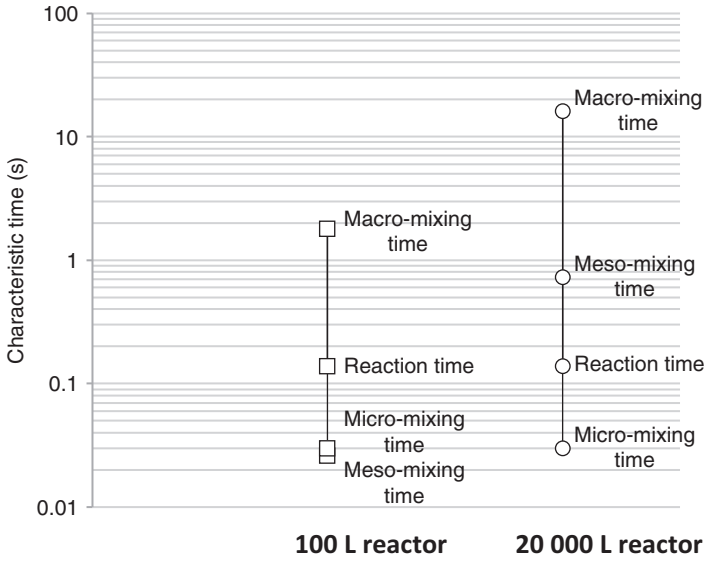

Figure 11.5 Characteristic times for the 100 liter and 20 000 liter reactors.

Equations 11.4 and 11.5 are used to calculate the meso-mixing time and equation 11.9 to calculate the micro-mixing time. As can be seen in Figure 11.5, the 100 liter reactor is limited by macro-mixing, whereas the scaled-up reactor at 20 000 liters becomes limited by meso-mixing.

11.7 Scale-up

The classical approach to scale-up precipitation processes is to use pilot-plant data and a scale-up ratio. Although this is still used very widely in industry today, it is not a scientifically based approach. Another approach that has been used is the dimensionless numbers approach, but this is also problematic, since total similarity on different scales cannot be maintained. For example, at larger scales, the maximum shear rate in the impeller zone increases, but the average shear rate in this zone decreases

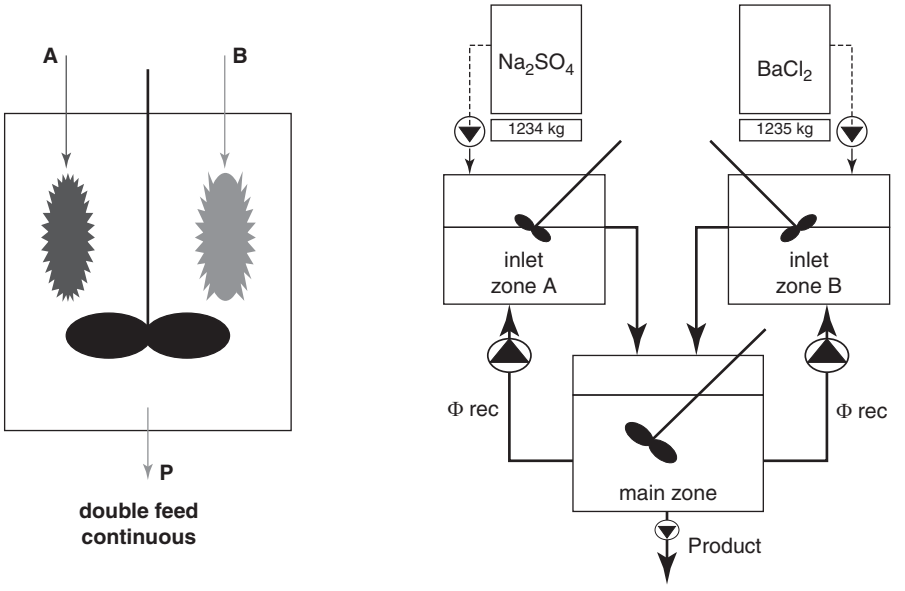

Figure 11.6 Double feed, continuous precipitator can be modeled using the three-zone model (van Leeuwen *et al*., 1996b).

(Oldshue, 1983). Thus, the shear rate distribution changes with scale-up and therefore any process that depends on the shear rate will be different when conducted on the larger scale.

A number of more modern and rigorous approaches have been adopted for scale-up. These range from a simplified compartment modeling approach, to more comprehensive numerical models developed by Vicum *et al.*, 2004a, 2004b), by Baldyga and Orciuch (2001) and by Lindenberg (2007).

11.7.1 Simplified compartmental modeling approach

The simplified compartmental modeling approach can be used to save on computational time and effort. This approach is basically a compromise between the full CFD approach (very computationally intensive) and the simplified single compartmental models (computationally cheap, but not very accurate).

Zauner and Jones (2000) successfully adopted a compartmental-mixing model to predict the effect of mixing on crystal precipitation. Van Leeuwen *et al.* (1996b) used a relatively simple three-zone model to investigate the effect of scale-up on a double feed process. They combined an experimental approach with compartmental modeling and comprehensively modeled the size distribution. However, as a consequence, the mixing effects were modeled in a relatively simple way in order to reduce computation time. This three-zone model for the precipitation of $BaSO_4$ is illustrated in Figure 11.6. In this model, only the two zones around the feed points are comprehensively modeled using a

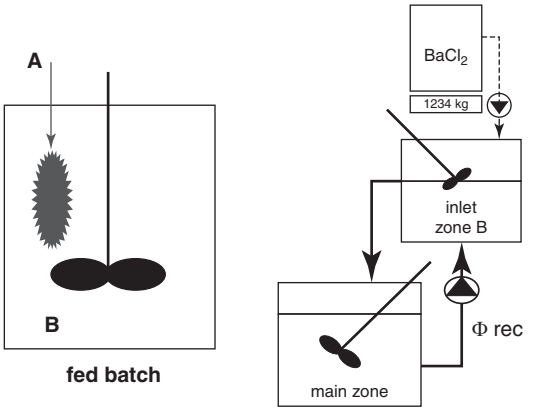

Figure 11.7 Fed batch precipitator is modeled using a two-zone model.

fine grid resolution, whilst the bulk volume of the precipitator is modeled using a much coarser grid and thus a much coarser resolution is obtained.

In contrast, for the fed-batch precipitator in Figure 11.7, a two-zone compartmental model would be the most appropriate choice.

Conditions in each zone of a single- or double-feed reactor will be primarily distinguished by different liquid compositions. This will affect:

- *The supersaturation*. Since supersaturation is the driving force for solids formation, local differences in supersaturation will have a significant influence on the precipitation mechanisms and particularly on nucleation.
- *The stoichiometry*. At the feed inlet for component A the concentration ratio A:B will be higher than that in the bulk, and lower than at feed inlet B. In many cases, this difference in stoichiometry will affect the kinetics of precipitation. However, this occurs in a manner that is difficult to predict a priori (Bramley *et al*., 1997, Gebrehiwet *et al*., 2012), although it is known that cation-rich solutions give faster growth rates than anion-rich because the dehydration frequency of the cations is often the rate-determining step. Thus, in a solution with more cations, the growth rate is faster.
- *The nucleation rate*. Nucleation, in particular, with its exponential dependence on supersaturation, must be considered as a local phenomenon. In fact the nucleation activity in large vessels is often almost completely located at the feed inlet(s).
- *Polymorphism*. The formation of different polymorphs also depends on the local composition, again predominantly by nucleation at the feed inlet(s) (Jones *et al*., 2005). Figure 11.8 shows how different operating conditions in the same vessel can result in the formation of two different polymorphs of $CaCO_3$ (calcite cubes and vaterite spheres).

Whether or not the final product consists of a mixture of polymorphs depends strongly on the composition of the bulk. Since most polymorphic transitions are solution-mediated, the bulk conditions have to be undersaturated with respect to the most soluble

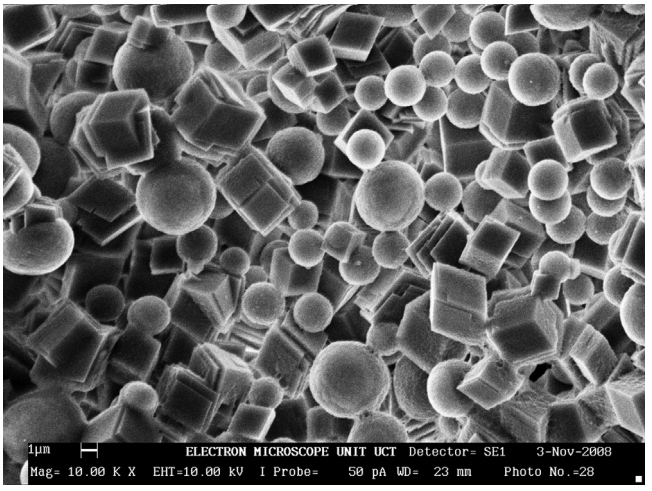

Figure 11.8 Polymorphs of $CaCO_3$ (calcite cubes and vaterite spheres) formed in different regions in the same vessel (Miller and Chuahan, 2008).

polymorph in order to dissolve this compound. This is particularly important in industrial precipitation processes, where the first solids that are formed are often the amorphous phase, and solvent-mediated transformation into a crystalline phase is an important mechanism in the control of local supersaturation levels (Hove *et al*., 2008).

As far as growth is concerned, the crystal mass and the surface area available for growth in all the zones (the feed zones, as well as in the bulk of the precipitator) can generally be considered to be the same, since this is a slow process that is not exponentially dependent on supersaturation. However, agglomeration, which is a strong function of the hydrodynamics, does not have the same rates in all zones. Particularly in a large precipitator, where the turbulent energy dissipation rate varies by orders of magnitude over the vessel, it is possible to have agglomeration that would not be possible in a small stirred tank.

11.7.2 Scale-up using an experimental approach: the three-zone model

The compartmental modeling approach can be used to examine the effects of scale-up experimentally. The essence of this approach is that:

a. it allows the micro-mixing time to be independently adjusted with respect to the macro-mixing time – something that is not possible in a single vessel;
b. it allows macro-mixing times that would occur in a process reactor to be duplicated on a laboratory scale.

The experimental setup is shown in Figure 11.9. It consists of a three-zone configuration: two feed vessels and one bulk vessel, which together determine the mean residence time, and two feed pumps and two recirculation pumps, which fix the recirculation time. The

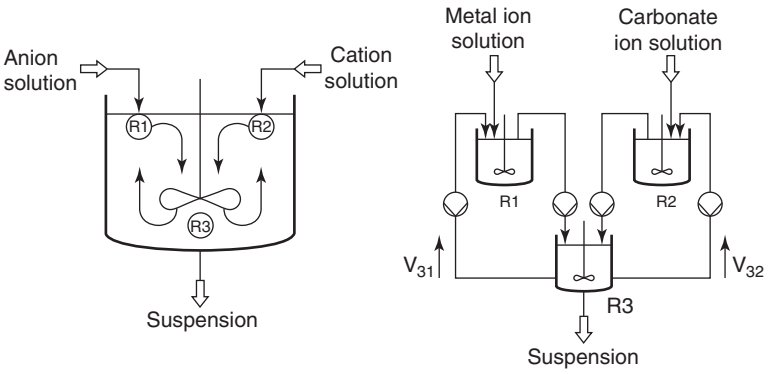

Figure 11.9 Experimental three-zone setup to study the effect of scale-up on macro-mixing. The configuration on the right simulates the precipitation reactor on the left (Gösele and Kind, 1991).

reagents A and B are fed to two well-mixed vessels. The overflow of the feed vessels is directed back into the bulk vessel.

From the bulk vessel, two streams are recirculated to the feed vessels and the product is taken off by means of an overflow of the suspension. In this way, the effect of changing the micro-mixing time can be investigated by adjusting the stirrer speeds in the vessels R1, R2 and R3. The effect of changes in the macro-mixing time can be separately investigated by changing the recirculation velocities (V_{31} and V_{32}).

The three-zone setup would typically be used to examine the relative effects of micro- vs. macro-mixing on the precipitate properties. This would show the sensitivity of the system to the different process parameters and therefore which process parameters are most important when designing the process reactor.

11.7.3 Scale-up using numerical modeling

The full numerical modeling approach that takes into account both the hydrodynamics as well as the solid phase in a large-scale vessel is a difficult problem. Current approaches are all approximations of one kind or another and include:

- the Eulerian method, which uses a fixed, three-dimensional frame of reference and monitors the movement of fluid and velocities through that fixed space;
- the Lagrangian approach, which is a way of looking at fluid motion by following an individual fluid parcel as it moves through space and time (Batchelor, 2000).

11.7.4 Eulerian modeling approach

In computational fluid dynamics (CFD) packages (such as the open source package Open FOAM and the commercial package Fluent) the Eulerian frame of reference is the most common approach used to simulate the interactions between complicated flow patterns (Versteeg and Malalasekera, 2007). These flow patterns are induced by reactor geometry,

Table 11.2 Summary of approaches and tools for modeling single- and multi-phase flows with evolving particle size distributions

Phase to be modeled →	Single-phase fluid models	Multi-phase models		Crystallization process
Approach →	Hydrodynamic models (computational fluid dynamics). The fluid is considered to be a continuum	Eulerian models. A fixed location in the flow field is considered and the flow of different materials passing through it is considered. Can be visualized as sitting on the bank of a river watching the water flow past a fixed location (Batra, 2006)	Lagrangian approach. A blob of fluid is followed around the vessel. The blob is assumed to act as a batch vessel and exchanges matter with the environment. Can be visualized as sitting in a boat and drifting down the river	Population balance models
Tools (most complex)↓	Direct numerical simulation. (Resolves the very smallest turbulence scales models in a very small volume of the flow domain)	IC (interpenetrating continua) or two-fluid model. Two fluids and the particles are modeled as two continuous phases that interpenetrate each other and exchange momentum (Green, 2002)	Direct element modeling (DEM). Predicts the trajectories of individual particles in a flow field. Computational effort depends on number of particles	Full population balance model
	Lattice Boltzmann. Instead of solving the conservation equations, Lattice Boltzmann models the fluid as composed of a collection of pseudo-particles. Particularly suitable for grossly irregular geometries (Succi, 2001)			

(*cont.*)

Table 11.2 (*cont.*)

Phase to be modeled →	Single-phase fluid models	Multi-phase models		Crystallization process
Approach →	Hydrodynamic models (computational fluid dynamics). The fluid is considered to be a continuum	Eulerian models. A fixed location in the flow field is considered and the flow of different materials passing through it is considered. Can be visualized as sitting on the bank of a river watching the water flow past a fixed location (Batra, 2006)	Lagrangian approach. A blob of fluid is followed around the vessel. The blob is assumed to act as a batch vessel and exchanges matter with the environment. Can be visualized as sitting in a boat and drifting down the river	Population balance models
Mesoscopic method falling between very intensive molecular dynamics method and simpler conventional numerical methods	Large eddy simulation. Models the large-scale turbulence realistically, i.e. non-isotropically, but assumes sub-grid turbulence to be isotropic. Can be thought of as DNS down to a relatively small size			
	Reynolds averaged Navier Stokes models, including the $k\varepsilon$ model. Simplified model. Assumes that the turbulence is isotropic		Engulfment model. Simple, non-distributed model of reactive mixing (Baldyga and Bourne, 1989a)	
↑ Tools (simplest)	Zone models. The vessel is split up into different zones, with some zones modeled at very fine resolution and others at coarse resolution (van Leeuwen *et al.*, 1996b).	Mixture (pseudo fluid) model. Considers a fluid–particle system to consist of distinct fictitious fluids. Separate hydrodynamic equations are established for both the particle and the fluid phase.	IEM (Interaction by exchange with the mean). The clump acts as a batch vessel having uniform internal concentration (David and Villermaux, 1975)	Method of moments. Loses the full PSD description to simplify the calculations

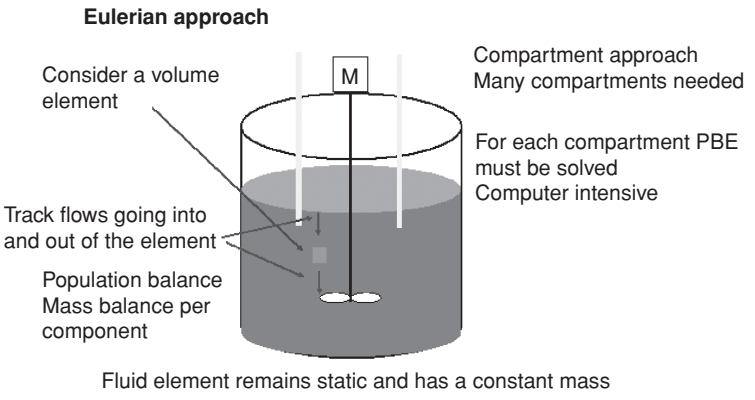

Figure 11.10 Basic features of the Eulerian approach.

stirrer characteristics, feed inlets and product outlets and sometimes-complex kinetic processes like combustion or catalytic polymerization reactions. The basic features of the Eulerian approach are illustrated in Figure 11.10.

Seckler *et al*. (1995) and Van Leeuwen *et al*. (1996a) developed a method based on a moments description of precipitation processes in a turbulent reactor environment. Both of these works had a special focus on phenomena around the inlets. The basic idea is that the moments behave as conserved species that are transferred into each other by relatively slow growth, whilst the zeroth moment is generated by heterogeneous nucleation, which is very fast in regions of high supersaturation. These moments are transported in the precipitator by convection and turbulent mixing.

A typical result of CFD modeling in precipitation is given in Figure 11.11, which shows the high supersaturation levels and the associated high nucleation rates around the inlets for barium sulfate precipitation. The precipitator is a baffled, stirred vessel with two feed points, both relatively close to the impeller.

11.7.5 Lagrangian modeling approach

In the Lagrangian approach, a fluid element is followed around the vessel, picking up the reagent by engulfment as it goes. The volume of the element increases as it travels around the vessel and the population balance is solved inside the individual volume. The basic features of the Lagrangian approach are illustrated in Figure 11.12.

The two Lagrangian type models are:

a. The IEM model (Villermaux, 1986)

In the IEM model (Interaction by Exchange with the Mean), a volume VA moves through the vessel, exchanges material with the average content (the mean) of the vessel and leaves the vessel, according to the ε-function obtained from residence time distribution (RTD) measurements. The volume VA itself is assumed to be homogeneously mixed.

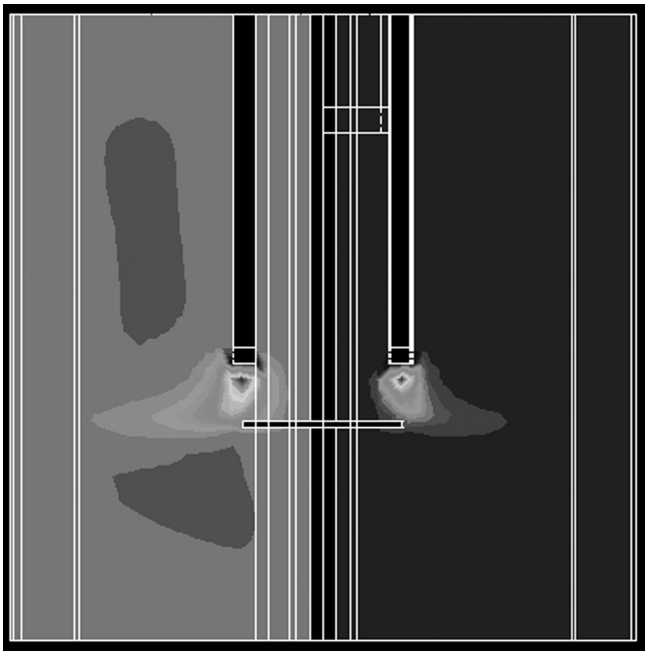

Figure 11.11 The supersaturation (left) and nucleation (right) patterns for the precipitation of barium sulfate in a stirred vessel obtained by 3-D CFD simulation (van Leeuwen, 1998).

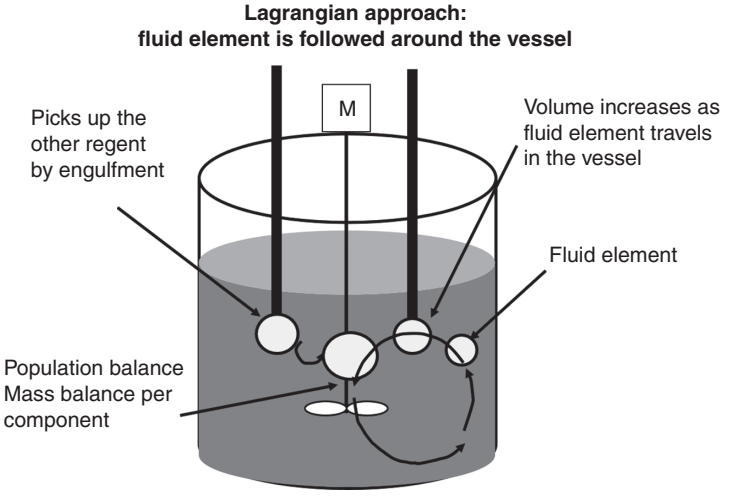

Figure 11.12 Basic features of the Lagrangian approach.

b. The engulfment model (Yu, 1993).

The engulfment theory is based on the observation that, during mixing, vortices wind up to form a lamellar structure and stretch to thin layers in the structure, as shown in Figure 11.14. The final step, molecular mixing, occurs by molecular diffusion.

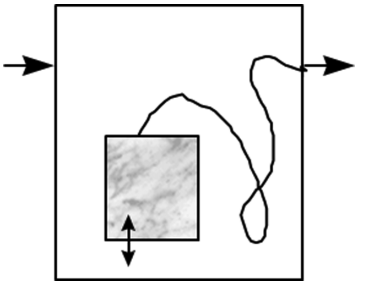

Figure 11.13 The IEM model.

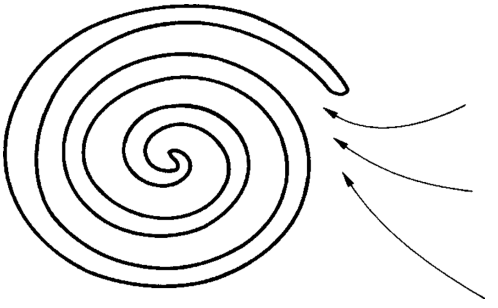

Figure 11.14 Turbulent eddy engulfing its surroundings and increasing its volume.

These Lagrangian models follow a volume on its way through the precipitator and can be used to describe the effects of micro-mixing in precipitators.

11.8 A practical approach: mixing configurations in stirred vessels

From a practical point of view, when precipitation is carried out in a stirred tank, there is not much that can be done about the high local supersaturation, since this is caused by the solubility of the precipitate as well as by the introduction of the reagents at the feed points. However, to some extent, the mixing configuration can be adjusted to minimize the effect of high local levels of supersaturation in the reaction vessel. Methods of adjusting the mixing configuration include changing the feed configuration and changing the stirring speed or type of stirrer. However, it should be borne in mind that changing the stirring speed or type of stirrer can modify the interaction between the macro-and micro-mixing in a non-linear way (David, 2001). Thus, only adjustments in feed configuration will be dealt with here.

As a rule of thumb: If the precipitate being produced is moderately soluble ($K_{sp} \geqq 1 \times 10^{-10}$), then it is possible to reduce the local supersaturation by modifying the feed configuration. However, if the precipitate being produced is very sparingly soluble ($K_{sp} < 1 \times 10^{-10}$), then modifying the feed point configuration will not have a significant

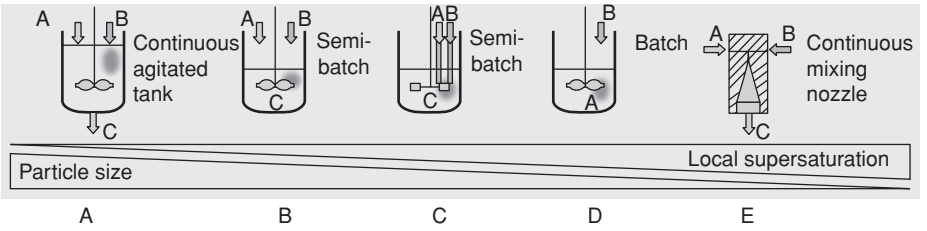

Figure 11.15 Feed point configuration modifications for moderately soluble (left-hand side) and sparingly soluble (right-hand side) substances.

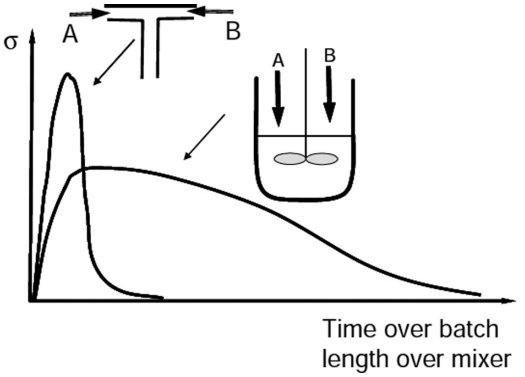

Figure 11.16 Effect of feed point configuration modifications on supersaturation and batch time.

effect on the PSD. The only practical option is to ensure that micro-mixing is as rapid as possible, in order to ensure a narrow (albeit small) PSD. See Figure 11.16.

Since a change in feed position only influences rapid phenomena like primary nucleation, any differences observed in average particle sizes will be due to changes in the primary nucleation process (Houcine *et al*., 1997). All the slow processes (growth, secondary nucleation and agglomeration) mainly occur after the mixing period and therefore these processes will remain unchanged when the feed position is varied. The following strategies can be employed to optimize the mixing conditions *for moderately soluble compounds*:

a. In a batch process, the rate of feeding of the reagent can be varied, such that the feed rate is slow at the beginning of the batch, thus minimizing excessive nucleation. At a later stage in the batch, the reagent feed rate can be increased.
b. Instead of feeding reagent A into a solution of reagent B contained in the reagent vessel, as is normally the case (see Figure 11.17, fed batch), both reagent A and reagent B can be fed into a bulk solution separately or by premixing (see Figure 11.17, double feed continuous or continuous by T-mixer).
c. The location of the feed points can be moved so that they are at the location in the vessel that experiences the highest energy dissipation rate. If the feed is introduced at

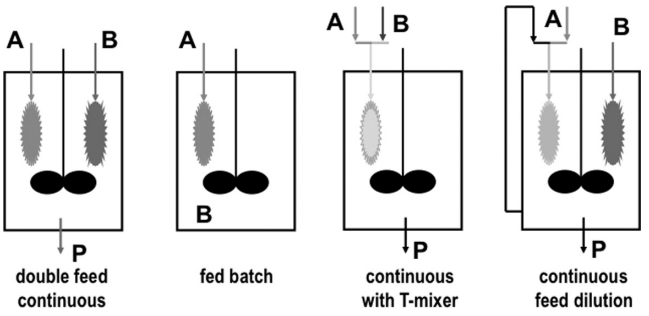

Figure 11.17 Options for feeding reagents in order to reduce local supersaturation.

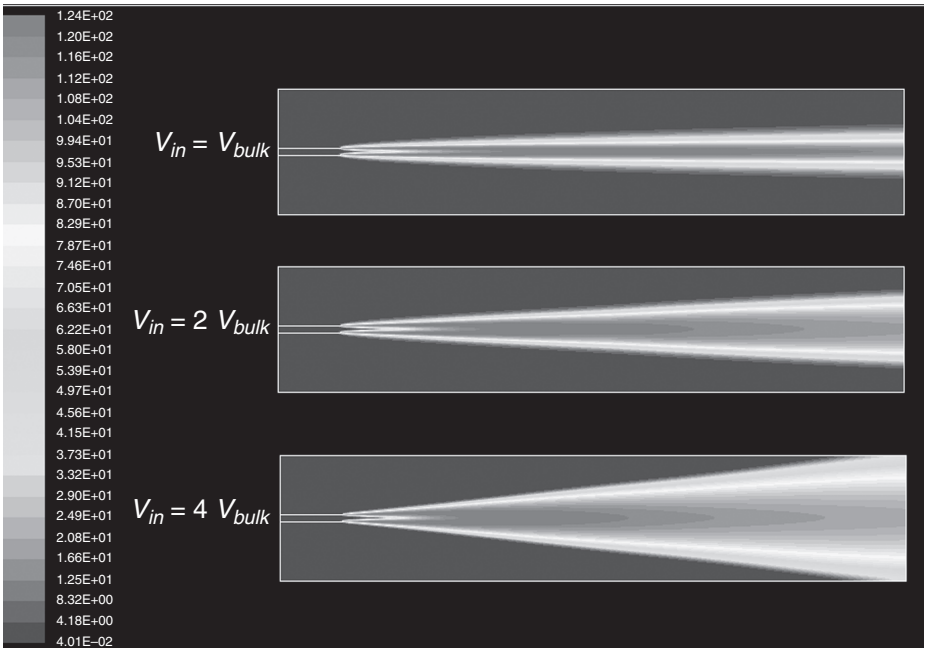

Figure 11.18 Effect of the relationship of the feed velocity to the bulk velocity on reagent mixing.

the surface of the vessel, very little turbulence is available to incorporate the reagent into the bulk, and extremely high local supersaturations develop.

d. The reagents can be diluted by mixing with the bulk concentration (as much as is economically and logistically feasible (continuous feed dilution)), so that the entering feed streams generate a reduced level of supersaturation at the feed point.
e. The number of feed points can be multiplied, using a pipeline manifold, for example, so that the reagents enter the vessel at multiple points, thus reducing the local supersaturation at the feed points.
f. The velocity of the feed can be increased to improve the mixing of the feed with the bulk of the vessel. CFD modeling has shown that introducing the feed reagent at a velocity of $V_{in} = 4V_{bulk}$ significantly improves the mixing of the reagent with the bulk (Figure 11.18).

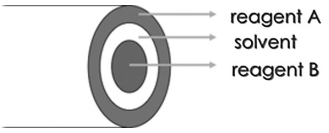

Figure 11.19 Fouling reduction strategy using layer separation.

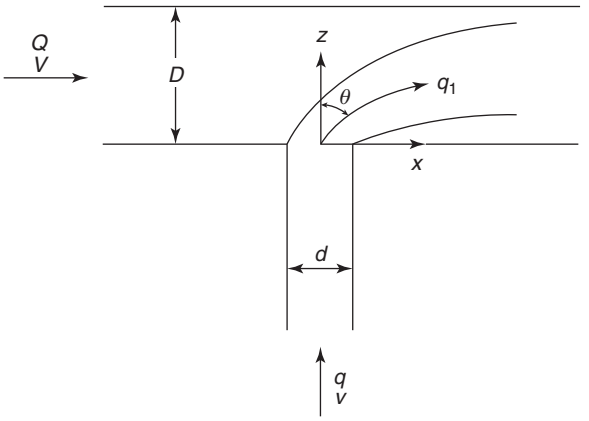

Figure 11.20 T-mixer configuration for reagent feeding in a precipitation process.

For *sparingly soluble compounds*:

a. The use of T- or Y-mixers ensures at least that the reagents are well mixed before entering the reactor. With this configuration, although the particles might be smaller, the generated particle size distribution is more predictable and reproducible.
b. The use of inline mixers, such as static or grid mixers, vortex mixers, ball mixers or multi-jet or interdigital mixers can also reduce initial segregation. Static and grid mixers improve the mixing, but suffer from high pressure drops and are sensitive to fouling. Besides static or grid mixers, ultrasound can also be used to increase mixing intensity. Fouling reduction can be achieved by the use of two impinging jets or by separating layers (Figure 11.19).
c. The feed can also be introduced into the bulk via a T-mixer in the configuration shown in Figure 11.20 (Cozewith and Busko, 1989), where each reagent is mixed with the bulk solution before feeding in the vessel.

The advantage of this model is that a highly turbulent flow regime is maintained in the injector. Optimal mixing is ensured by adjusting the relative velocities of the feed and the bulk in the T-mixer and by ensuring that the diameter of each injector is significantly smaller than the main pipe (Rice and Baud, 1990). A guideline for the range of ideal velocity ratios as a function of the diameter ratios is given in equation 11.13.

$$1.06\left(\frac{d}{D}\right)^{-0.61} \leq \frac{v}{V} \leq 1.22\left(\frac{d}{D}\right)^{-0.75} \tag{11.13}$$

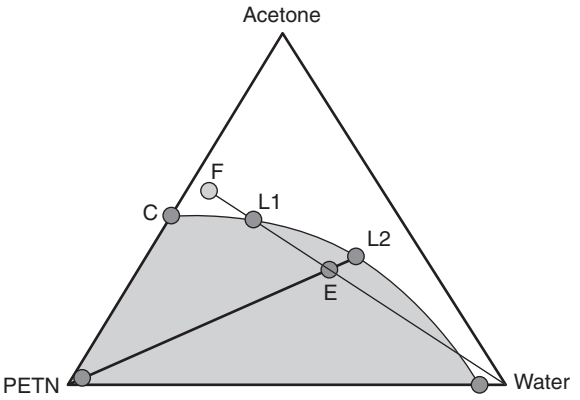

Figure 11.21 Ternary phase diagram showing the equilibrium between PETN (the product), water (the anti-solvent) and acetone (the solvent).

where d = T-branch diameter [cm], D = T-run diameter [cm], v = side-stream velocity [cm s^{-1}] and V = main stream velocity [cm s^{-1}].

Injection speeds that are too low will result in pockets of unreacted reagent, whereas speeds that are too high will result in the jet striking the far wall and causing dispersion up- and downstream.

It is also possible to use two T-mixers, one after the other, to introduce the two reagents separately into the solution. In this case, the order in which the injection is to take place, the separation distance between the mixers and the dilution ratio of the reagents would need to be determined. (The other leg of the T-mixer is filled with the bulk liquid.)

11.9 Anti-solvent crystallization

Anti-solvent crystallization is essentially a precipitation process based on mixing and is usually carried out batchwise. It is sometimes referred to as "drowning-out" crystallization. In an anti-solvent process, the solute, which is dissolved in a primary solvent, is crystallized out via the addition of an anti-solvent, i.e. another solvent in which the solute is relatively insoluble. This method is suitable for heat-sensitive compounds or to drain the solution from the residual solute. However, the product from an anti-solvent crystallization process often consists of small, impure agglomerates. Because of the fact that mixing generates the supersaturation, the formation of polymorphs due to differences in local supersaturation is also likely.

An example of an anti-solvent crystallization process is the crystallization of the explosive pentaerythritol tetranitrate (PETN). Initially, the PETN is dissolved in acetone, in which it is very soluble. In this case, the anti-solvent is water, in which the PETN is almost completely insoluble, and thus it is possible to crystallize out almost pure PETN.

The ternary phase diagram in Figure 11.21 illustrates a schematic anti-solvent process for the crystallization of PETN. The composition of the feed solution is represented by F and is 55% acetone, 39% PETN and 6% water. Water, which is the anti-solvent, is

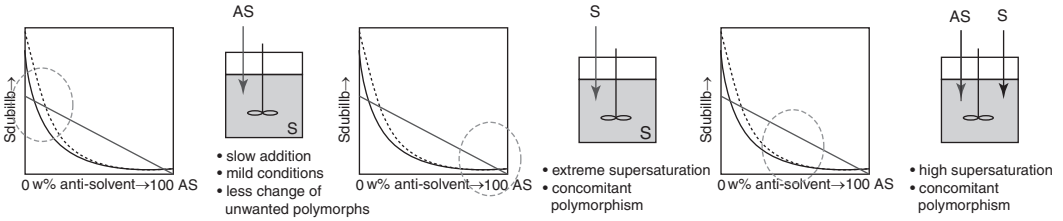

Figure 11.22 Effect of the addition configuration in anti-solvent crystallization.

added to the feed. The composition of the system moves along the line F to L1 (at which point the first molecule of PETN starts to precipitate), to the final composition, E. At point E, pure PETN is recovered, and the residual liquid composition is given by L2.

There are two main issues to be considered in anti-solvent crystallization: firstly, the method of addition of the anti-solvent has a profound effect on the supersaturation distribution in the vessel and thus on the product. Secondly, the heat generated during the mixing can sometimes be significant. Thus, heat removal must be taken into account in the design of the process.

For a compound that can form two polymorphs, the effect of the addition configuration of the anti-solvent is illustrated in Figure 11.22. In each solubility diagram, the dotted line indicates the solubility of the more soluble (and thus less stable) polymorph, and the solid line the solubility of the less soluble (and thus more stable) polymorph. In the case of adding the anti-solvent to the solvent (far left diagram), the mixing line is given by the line joining AS with the starting concentration. Since the starting point for the mixing is 100% solvent (0% anti-solvent), the operating conditions for the system will occur in the region where both solubility curves have high solubilities. Thus, a relatively low supersaturation will be generated in the system. In addition, if the anti-solvent is added slowly, mild conditions will prevail and there will be a reduced chance of the formation of the undesirable metastable polymorph. In contrast, the operating conditions when the solvent is added to the anti-solvent (center diagram) it occurs in the region where both solubility curves have very low solubilities. Thus, a high supersaturation will be generated in the system and there is a much greater chance of the formation of the unwanted polymorph. In the case where both the anti-solvent and the solvent are added to the bulk (far right diagram), the operating region is in the center of the diagram, where high supersaturations prevail, and there is the possibility of developing concomitant polymorphs.

It is possible to slightly dilute the anti-solvent with the solvent, and thus have some control over the supersaturation at the inlet (Mullin, 2001). In addition, although the operation of an anti-solvent process is, in principle, stoichiometric, the ratio of the twosolvents changes.

11.10 A brief summary of the chapter

This chapter started by defining precipitation and describing what makes it unique. The dominant phenomena in precipitation (primary nucleation, agglomeration and

growth) were then identified. Because precipitation processes are dominated by high supersaturation and thus primary nucleation, mixing plays a critical role. The various functions of mixing in precipitation (reagent mixing, bulk mixing, suspension of the slurry and agglomeration control) were described. Each scale of mixing (macro, meso and micro) was described and defined and a method of calculating the time and length scales for the precipitation reaction vs the mixing process was given. Because of the dependence of the precipitation process on both reaction and hydrodynamics, the scale-up of precipitation reactions is not straightforward. Two scale-up approaches (simple compartmental modeling and more comprehensive numerical modeling) were discussed and described. Some practical approaches to mixing configurations in stirred vessels were proposed and the chapter concluded with a brief description of anti-solvent crystallization.

11.11 End of chapter problems

Problem 1: Mixing or chemical reaction limited?

Calculate the macro-, meso- and micro-mixing times for fully developed turbulent flow in a reactor which has a 10 litre working volume and $H/D = 1.5$ with $D = 20$ cm. The reactor is fitted with a four-bladed Rushton turbine ($Np = 4.3$, $Nq = 0.33$; Post Mixing, 2013) that is operated at a stirrer speed of 120 rpm.

The feed rate of the reagent is 20 L h^{-1} and the feed pipe diameter is 2 cm. Assume that the fluid has the same kinematic viscosity as that of water: 1×10^{-6} m s^{-1}.

If the precipitation that is happening in the vessel has a characteristic time constant of 0.001 s, is the precipitation then mixing- or chemical reaction-limited?

Problem 2: Effect of feed point configurations

In Figure 11.15, describe what is happening to both the average supersaturation and the particle size distribution produced in each crystallizer as the feed point configuration is changed from configuration A through to E.

Problem 3: Effect of supersaturation on nucleation rate and particle number

Given the reaction of silver with chloride ions to form silver chloride: $Ag^{+}(aq) + Cl^{-}(aq) \rightarrow AgCl(s)$, with $K_{sp}(1.8 \times 10^{-10}$ mol^2 L$^{-2})$, calculate the maximum supersaturation that can be generated when 1 liter of solution containing 1 mol L^{-1} of sodium chloride and 1 litre of a solution containing 1 mol L^{-1} of silver nitrate are mixed together in a T-mixer.

$$S_a = \left(\frac{(a_A)^x (a_B)^y}{K_a} \right)^{1/(x+y)} \qquad A_x B_y \rightarrow x A^{z+} + y B^{z-}$$

Use your calculated supersaturation to calculate the nucleation rate and thus the number of nuclei formed.

11.12 References

Aoun, M., Plasari, E., David, R. and Villermaux, J. 1999. A simultaneous determination of nucleation and growth rates from batch spontaneous precipitation. *Chemical Engineering Science*, **54**, 1161–1180.

Atiqullah, M., Hassan, M. M. and Beg, S. A. 1993. Micromixing effects on a parallel reaction in flow reactors. *Chemical Engineering and Technology*, **16**, 243–251.

Baldyga, J. and Bourne, J. 1989a. Simplification of micromixing calculations. I. Derivation and application of new model. *The Chemical Engineering Journal*, **42**, 83–92.

Baldyga, J. and Bourne, J. R. 1989b. Simplification of micromixing calculations. I. Derivation and application of new model. *The Chemical Engineering Journal*, **42**, 83–92.

Baldyga, J. and Bourne, J. R. 1989c. Simplification of micromixing calculations. II. New applications. *The Chemical Engineering Journal*, **42**, 93–101.

Baldyga, J. and Bourne, J. R. 1990. The effect of micromixing on parallel reactions. *Chemical Engineering Science*, **45**, 907–916.

Baldyga, J. and Bourne, J. R. 1992. Interactions between mixing on various scales in stirred tank reactors. *Chemical Engineering Science*, **47**, 1839–1848.

Baldyga, J. and Bourne, J. R. 1999. *Turbulent Mixing and Chemical Reactions*, Wiley.

Baldyga, J., Bourne, J. R. and Hearn, S. J. 1997. Interaction between chemical reactions and mixing on various scales. *Chemical Engineering Science*, **52**, 457–466.

Baldyga, J. and Orciuch, W. 2001. Barium sulfate precipitation in a pipe – an experimental study and CFD modelling. *Chemical Engineering Science*, **56**, 2435–2444.

Batchelor, G. K. 2000. *An Introduction to Fluid Dynamics*, Cambridge University Press.

Batra, R. C. 2006. *Elements of Continuum Mechanics*, American Institute of Aeronautics and Astronautics.

Bourne, J. R. and Dell'Ava, P. 1987. Micro- and macro-mixing in stirred tank reactors of different sizes. *Chemical Engineering Research and Design*, **65**, 180–186.

Bramley, A., Hounslow, M., Newman, R., Paterson, W. and Pogessi, C. 1997. The role of solution composition on aggregation during precipitation. *Chemical Engineering Research and Design*, **75**, 119–124.

Cozewith, C. and Busko Jr., M. 1989. Design correlations for mixing tees. *Industrial and Engineering Chemistry Research*, **28**, 1521–1530.

David, R. 2001. General rules for prediction of the intensity of micromixing effects on precipitations. *Powder Technology*, **121**, 2–8.

David, R., Marchal, P., Klein, J.-P. and Villermaux, J. 1991a. Crystallization and precipitation engineering – III. A discrete formulation of the agglomeration rate of crystals in a crystallization process. *Chemical Engineering Science*, **46**, 205–213.

David, R. and Villermaux, J. 1975. Micromixing effects on complex reactions in a CSTR. *Chemical Engineering Science*, **30**, 1309–1313.

David, R., Villermaux, J., Marchal, P. and Klein, J.-P. 1991b. Crystallization and precipitation engineering – IV. Kinetic model of adipic acid crystallization. *Chemical Engineering Science*, **46**, 1129–1136.

Fournier, M. C., Falk, L. and Villermaux, J. 1996. A new parallel competing reaction system for assessing micromixing efficiency: experimental approach. *Chemical Engineering Science*, **51**, 5053–5064.

Gebrehiwet, T. A., Redden, G. D., Fujita, Y., Beig, M. S. and Smith, R. W. 2012. The Effect of the CO_3^{2-} to Ca^{2+} ion activity ratio on calcite precipitation kinetics and Sr^{2+} partitioning. *Geochemical Transactions*, **13**, 1.

Gösele, W. and Kind, M. 1991. Versuche zum Einfluß der Vermischung auf die Qualität eines kontinuierlich gefällten Produktes. *Chemie Ingenieur Technik*, **63**, 59–62.

Green, D. W. 2002. Understanding and modeling crystallizer mixing and suspension flow. In: *Handbook of Industrial Crystallization*, 2nd edn., Allan, S. M. (ed.), Butterworth-Heinemann.

Houcine, I., Plasari, E., David, R. and Villermaux, J. 1997. Influence of mixing characteristics on the quality and size of precipitated calcium oxalate in a pilot scale reactor. *Chemical Engineering Research and Design*, **75**, 252–256.

Hove, M., Van Hille, R. P. and Lewis, A. E. 2008. Mechanisms of formation of iron precipitates from ferrous solutions at high and low pH. *Chemical Engineering Science*, **63**, 1626–1635.

Jarvenin, G. 2008. Precipitation and Crystallization Processes. Short course: Introduction to Nuclear Chemistry and Fuel Cycle Separations, Vanderbilt University School of Engineering, Nashville, TN, December 16–18 2008, CRESP (Consortium for Risk Evaluation with Stakeholder Participation).

Jones, A., Rigopoulos, S. and Zauner, R. 2005. Crystallization and precipitation engineering. *Computers and Chemical Engineering*, **29**, 1159–1166.

Lindenberg, C., Schöll, J., Vicum, L., Mazzotti, M. and Brozio, J. 2007. L-glutamic acid precipitation: agglomeration effects. *Crystal Growth and Design*, **8**, 224–237.

Marchal, P., David, R., Klein, J. P. and Villermaux, J. 1988. Crystallization and precipitation engineering–I. An efficient method for solving population balance in crystallization with agglomeration. *Chemical Engineering Science*, **43**, 59–67.

Mersmann, A. 2001. *Crystallization Technology Handbook*, Marcel Dekker.

Miller, L. and Chuahan, M. 2008. *Spherulitic Growth*, Honours Level Project, Crystallization and Precipitation Research Unit, University of Cape Town.

Mullin, J. W. 2001. *Crystallization*, Butterworth-Heinemann.

Nienow, A. W. 1997. On impeller circulation and mixing effectiveness in the turbulent flow regime. *Chemical Engineering Science*, **52**, 2557–2565.

O'Grady, D. 2011. Supersaturation: driving force for crystal nucleation and growth [Online]. Mettler Toledo. Available: http://blog.autochem.mt.com/2011/03/supersaturation-driving-force-for-crystal-nucleation-growth/ (accessed February 2015).

Oldshue, J. Y. 1983. *Fluid Mixing Technology*, Chemical Engineering.

Post mixing. 2013. Optimisation and solutions: impellers [Online]. Available: http://www.postmixing.com/mixing forum/impellers/impellers.htm (accessed March 2014).

Rice, R. W. and Baud, R. E. 1990. The role of micromixing in the scale-up of geometrically similar batch reactors. *AIChE Journal*, **36**, 293–298.

Rivallin, M., Benmami, M., Kanaev, A. and Gaunand, A. 2005. Sol-gel reactor with rapid micromixing: modelling and measurements of titanium oxide nano-particle growth. *Chemical Engineering Research and Design*, **83**, 67–74.

Roelands, C. P. M., Derkson, J. J., Ter Horst, J. H., Kramer, H. J. M. and Jansens, P. J. 2002. Mixing time scale analysis for the measurement of nucleation rate of concomitant polymorphs. *Chemical Engineering Transactions*, **1**, 29–34.

Seckler, M., Bruinsma, O. and Van Rosmalen, G. 1995. Influence of hydrodynamics on precipitation: a computational study. *Chemical Engineering Communications*, **135**, 113–131.

Succi, S. 2001. *The Lattice Boltzmann Equation: For Fluid Dynamics and Beyond*, Clarendon Press.

Torbacke, M. and Rasmuson, Å. C. 2001. Influence of different scales of mixing in reaction crystallization. *Chemical Engineering Science*, **56**, 2459–2473.

Uhl, V. W. and Gray, J. B. 1966. *Mixing: Theory and Practice, Volume 1*, Academic Press.

Van Leeuwen, M. L. J. 1998. *Precipitation and Mixing*. PhD Thesis, University of Delft.

Van Leeuwen, M. L. J., Bruinsma, O. S. L. and Van Rosmalen, G. M. 1996a. Influence of mixing on the product quality in precipitation. *Chemical Engineering Science*, **51**, 2595–2600.

Van Leeuwen, M. L. J., Bruinsma, O. S. L. and Van Rosmalen, G. M. 1996b. Three-zone approach for precipitation of barium sulfate. *Journal of Crystal Growth*, **166**, 1004–1008.

Versteeg, H. K. and Malalasekera, W. 2007. *An Introduction to Computational Fluid Dynamics: The Finite Volume Method*, Pearson Education Limited.

Vicum, L., Mazzotti, M. and Baldyga, J. 2004a. Modeling of Stirred Tank Mixing-Precipitation Processes. Swiss Symposium on Crystallization and Precipitation, Zurich, Switzerland.

Vicum, L., Ottiger, S., Mazzotti, M., Makowski, L. and Baldyga, J. 2004b. Multi-scale modeling of a reactive mixing process in a semibatch stirred tank. *Chemical Engineering Science*, **59**, 1767–1781.

Villermaux, J. 1986. Macro and micromixing phenomena in chemical reactors. In: *Chemical Reactor Design and Technology*, Springer.

Yu, S. 1993. *Micromixing and Parallel Reactions*, Doctoral and habilitation thesis, Swiss Federal Institute of Technology Zurich. http://dx.doi.org/10.3929/ethz-a-000897454 (accessed February 2015).

Zauner, R. and Jones, A. G. 2000. Scale-up of continuous and semibatch precipitation processes. *Industrial and Engineering Chemistry Research*, **39**, 2392–2403.

12 Melt crystallization

12.1 Why this chapter is important

From a practical point of view, melt crystallization is an important "sub-class" of crystallization that has a number of specialized applications. Although the distinction between solution crystallization and melt crystallization has no theoretical basis, the very different industrial techniques used for melt crystallization have historically justified the categorization (Tähti, 2010). These techniques are known as *layer growth* and *suspension growth* melt crystallization.

There are currently three main classes of applications:

- When it is necessary to obtain an ultra-high purity product (such as in ultra-purification of organic chemicals or monomers);
- When the melting curve of a product needs to be changed (such as for fat processing in the food industry, often referred to as fractional crystallization);
- In freeze concentration of juices and waste water streams. A rapidly growing application of freeze crystallization for concentration by ice crystallization is eutectic freeze crystallization. This technique can be used to recover both pure water and pure salts from hypersaline brines, acid mine drainage, reverse osmosis retentates and oil sand brines.

Apart from the most frequent use of melt crystallization for ultra-purification, it is typically used for purification of substances such as:

- isomers with close boiling points;
- azeotropic systems;
- temperature-sensitive substances;
- components that tend to polymerize;
- explosive substances.

12.2 Definitions of melt crystallization

A melt is the common name given to a liquid or a liquid mixture at a temperature near its freezing point.

Table 12.1 Products currently produced by melt crystallization (Arkenbout, 1995)

Product	World production [million tons year^{-1}]	Year
acrylic acid	4.7	2012
phenol	10	2011
p-xylene	35	2009
caprolactam	5.7	2012

Melt crystallization is a special case for two main reasons: firstly, the crystallizing solute in melt crystallization is the melt itself (as in purification applications) or the solvent (as in freeze concentration or eutectic freeze crystallization) and secondly (and this follows from the first aspect), the operating temperature is close to the melting temperature of the main component.

Another distinction between solution and melt crystallization has been proposed by Ulrich and Glade (2003):

- When mass transfer dominates the liquid–solid phase change, it is defined as "solution crystallization"
- When heat transfer dominates the liquid–solid phase change, it is defined as "melt crystallization."

12.3 Advantages/disadvantages

The chemical industry has a special interest in melt crystallization because of its large purification potential. Table 12.1 gives a list of monomers currently produced by melt crystallization (Hengstermann, 2010) with their production capacity, as indicated in various websites.

Some of the major advantages are (Arkenbout, 1995, Mullin, 2003):

- Highly selective separations are possible, with purities of 99.99% up to 99.999% being both technically and economically feasible;
- It is possible to separate out organic substances with boiling points that are close together;
- It provides the potential for a low-energy separation because the heat of fusion is always lower than the heat of evaporation. However, this strongly depends on process efficiency. Because of limited separation efficiency, melt crystallization processes are often carried out in multi-stage crystallizers. Thus, the energy consumption per kg of product can be relatively high (Mullin, 2003);
- Melt crystallization can usually be conducted at low temperatures. This is an advantage when dealing with thermally unstable substances.

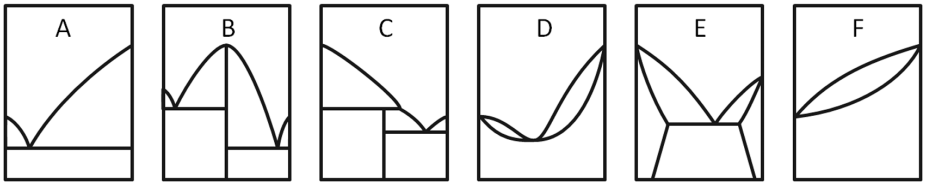

Figure 12.1 Examples of phase diagrams for eutectic systems: (A) 54.3%, (B) 24.5% and (C) 7.1% and solid solution systems (D–F) (Matsuoka, 1991).

12.4 Thermodynamics

12.4.1 Phase diagrams

A phase diagram is essential in order to provide the equilibrium information necessary to design a melt crystallization process (see Chapter 1). The complexity rapidly increases with the number of components. Multi-component phase diagrams of organic compounds are seldom available. For ultra-purification where the concentrations of impurities are already low, each impurity is mostly assumed to behave independently of the others in its relationship to the main component. Binary phase diagrams are thus used to provide insight into the purification potential.

Binary phase diagrams can be divided into eutectics, with a theoretical opportunity (at zero crystallization rate) to achieve one component with 100% purity, and solid solutions, with limited or complete solid solubility. It was already illustrated (as early as 1977, but later repeated) that close to 86% of all organic binary mixture expose eutectics, while only about 9% form solid solutions (see Figure 12.1). This can be explained by the rigidness of a crystal lattice. Isomorphous substitution of host molecules by impurity molecules often causes too much strain to happen in substantial quantities, and uptake of impurities in interstitial voids of the lattice seldom occurs in case of organic systems.

12.4.2 Impurity distribution

The binary phase diagrams thus give an indication of the purification potential of the melt crystallization process. The uptake of an impurity by a lattice is usually indicated by the ratio of the impurity concentration in the crystal phase to that in the liquid phase (the melt). This ratio is called the thermodynamic equilibrium distribution coefficient defined as:

$$K_0^* = c_{eq,0}/c_{bulk} \tag{12.1}$$

where c_{bulk} is the impurity concentration in the liquid phase and $c_{eq,0}$ is the impurity concentration in the crystalline phase.

For eutectic systems: $K_0^* = 0$
For solid solutions: $K_0^* > 0$

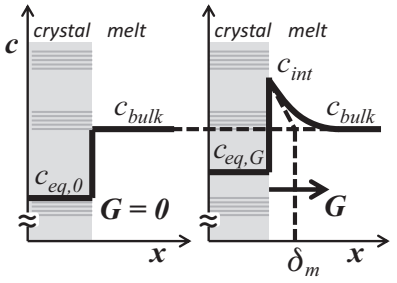

Figure 12.2 Impurity concentration profiles under non-growing (left) and growing (right) conditions.

For a crystal growing with growth rate G (m s^{-1}), the impurities will be rejected by the crystal, and the impurity concentration at the crystal interface, c_{int}, will be higher than that in the bulk: $c_{int} > c_{bulk}$. As a consequence, the incorporation in the crystal is higher and:

$$c_{eq,G} = K_0^* c_{int} \tag{12.2}$$

The rejected impurities diffuse back into the bulk liquid across the stagnant boundary layer. This results in an impurity concentration gradient in front of the crystal surface, as illustrated in Figure 12.2. For layer and suspension melt growth the thickness of the stagnant layer δ_m depends on the hydrodynamics, and often varies from about 10^{-6} to 10^{-4} m. With this boundary layer thickness δ_m and the binary diffusion coefficient in the melt (m^2 s^{-1}) the mass transfer coefficient K_m can be calculated from:

$$\delta_m = \frac{D}{K_m} \tag{12.3}$$

This leads to the following relation for the effective distribution coefficient (Burton *et al.*, 1953):

$$K_{eff} = \frac{K_0^*}{K_0^* + (1 - K_0^*) \exp\left[-\dfrac{G}{K_m}\dfrac{\rho_c}{\rho_L}\right]} \tag{12.4}$$

In this equation the term ρ_c / ρ_L compensates for the difference in specific weight ρ (kg m^{-3}) between the growing crystals and the replaced melt.

This K_{eff} value directly correlates the impurity concentration in the crystals with the impurity concentration in the bulk in dependence on the growth rate.

Apart from impurity uptake in the crystal lattice, impurities can also end up in the final product by uptake of the impure melt in the solid phase during growth or through adhering impure melt that has not been sufficiently washed off.

The uptake of impurities by the solid phase and their elimination by separation and washing before recovery of the final purified product as a melt is totally different for the two industrial crystallization techniques: solid layer melt crystallization and suspension melt crystallization.

Figure 12.3 Sulzer falling film crystallizer for dynamic melt crystallization (Sulzer Chemtech, 2014).

12.5 Melt crystallization techniques

In cooling crystallization from solution, a suspension of pure crystals is formed by direct or indirect cooling of the suspension, followed by separation of the crystals from the mother liquor and washing of the crystals. For melt crystallization, separation and washing cannot be as easily achieved for a solid and its melt, so two different techniques have been developed. Both techniques can handle large quantities of melts (Jansens and van Rosmalen, 1994).

12.5.1 Solid layer melt crystallization

12.5.1.1 Equipment

In this technique heat is withdrawn from the melt through a metal wall that is cooled by internal circulation of a heat transfer medium.

Layer crystallization processes are carried out batchwise either in static processes (stagnant melts) or dynamic processes (forced convection of the melt). The static layer processes usually use plate-type heat exchangers and suffer from low space–time yields, and are thus less suitable for large volume streams.

Dynamic layer processes are characterized by circulating melts, in which the crystallization takes place inside tubes that are cooled on the outside. An example is the Sulzer falling film process, which is illustrated in Figure 12.3. In this crystallizer, a constant

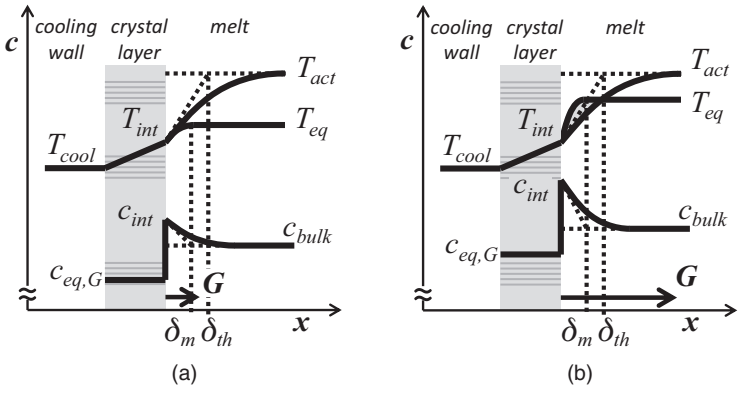

Figure 12.4 Concentration and temperature profiles in layer crystallization, without constitutional undercooling (left) and with constitutional undercooling (right).

temperature along the tube length is ensured. The temperature of the refrigerant is kept below the freezing point of the melt.

During the subsequent purification of the layer by sweating (see below) the layer can become detached from the cooling metal wall. To keep the layer in place it is supported at the bottom, by tubes with a metal ring on the inside attached to the wall.

12.5.1.2 Cooling profile

The solid crystal layer is formed at the cooled wall of the crystallizer. The actual temperature profile T_{act} for the heat transfer processes close to the wall is given in Figure 12.4. The temperature is lowest in the crystal layer closest to the wall and increases slowly through the solid layer and more rapidly through the liquid thermal conductivity layer δ_{th}, until it reaches the bulk liquid temperature. The major part of the heat of crystallization is removed from the cooled crystal surface via the crystal layer next to the wall. At the solid–liquid interface the actual temperature is at or slightly below the equilibrium value, and the bulk of the melt is undersaturated. The heat transfer layer δ_{th} is usually thicker than the mass transfer layer δ_m which is influenced by the hydrodynamics in the melt.

The ratio of the thicknesses of these layers is given by:

$$\frac{\delta_m}{\delta_{tb}} = \left(\frac{D}{a}\right)^{\frac{1}{3}} \tag{12.5}$$

where D is the diffusivity and a is the heat transfer coefficient.

12.5.1.3 Kinetics

The driving force for melt crystallization can be expressed just as for cooling crystallization from solution by (see Chapter 1):

$$\Delta\mu = (\Delta H / T^*)\Delta T \tag{12.6}$$

where ΔT [K] is known as the undercooling and ΔH is the enthalpy of crystallization. In suspension crystallization from either solution or the melt, T^* is the equilibrium temperature in the suspension, and ΔT the temperature difference between the actual temperature in the suspension and the equilibrium temperature T^*. For layer growth, the gradient of the driving force in front of the layer surface dictates the growth process. Therefore the profiles of both the actual temperature and the equilibrium close to the layer will be discussed below.

For layer growth, nucleation is induced by spraying of the pure melt against the metal wall at the top. The frozen droplets grow out laterally along the wall during the development of the crystal layer.

In melt crystallization sufficient growth units are at or close to the crystal surface, so mass transport of crystallizing material from the bulk of the melt to the crystal surface is not the rate-determining step during growth of the layer. For transfer of a growth unit from a position at the interface to the crystal lattice, an energy barrier has to be overcome. A growth unit at the interface has many bonds with the partially surrounding melt that have to be replaced by bonds with the solid. This barrier cannot be ignored and for viscous melts this energy barrier is quite high. The whole melt crystallization process is, however, generally heat transfer controlled, and higher production rates are achieved by imposing higher temperature differences across the crystal layer.

The impurities that are rejected from the crystal layer surface during growth have to diffuse back into the bulk. The larger the growth rate of the crystal layer, the steeper will be the concentration profile of the impurities in front of the layer. These impurities will not only be incorporated in the layer, they will also determine the equilibrium temperature profile T_{eq} in the melt in front of the layer (see Figure 12.4).

The equilibrium temperature profile thus shows the temperature that is in equilibrium with the impurity concentration profile from c_{int} at the interface to c_{bulk} in the bulk.

Two situations may then occur:

- The actual temperature T_{act} is always above the equilibrium temperature T_{eq}, as shown in Figure 12.4, left. This is the case when at a given impurity concentration in the bulk, the growth rate is *low* enough to allow the impurities to diffuse away from the interface. Thus, the build-up of impurities in the growth layer is less, and the impurity concentration gradient from the interface to the bulk is shallow. Thus, the equilibrium temperature close to the layer is low, which means that the actual temperature at the interface does not drop below the equilibrium temperature. The growth rate perpendicular to the interface is then about 10^{-7} m s^{-1}, as for solution growth.
- The actual temperature T_{act} drops below T_{eq} in the thermal conductivity layer (see Figure 12.4, right). This implies that the temperature ahead of the interface is colder than the freezing temperature of the melt. This happens when the growth rate at a given impurity concentration in the bulk is *high*, a steep impurity concentration gradient is built up at the interface and as a result of that, the equilibrium temperature will be not as low as in the first case. Therefore, the temperature at the interface is below the equilibrium temperature. This phenomenon is called *constitutional supercooling*. The growth rate perpendicular to the interface is then about 10^{-6}–10^{-5} m s^{-1}.

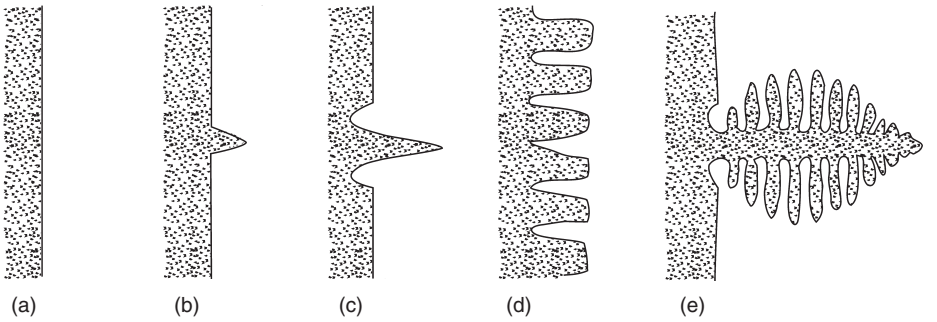

Figure 12.5 Cellular growth shapes and dendrites as growth instabilities.

The available cooling surface in industrial layer crystallizers is relatively small (<100 m^2 m^{-3}), so growth rates unfortunately have to be that high to meet the required production capacities under moderate mixing conditions.

According to the Mullin–Sekerka stability criterion the stabilizing effect of the surface tension on a flat crystal surface is weak (Mullin, 2001), and an instability wave travels along the surface. Consequently, surface instabilities occur and protrude in the case of constitutional supercooling from the crystal surface into a supercooled region where their growth rate increases. Likewise, small dips in the crystal surface become even more retarded. This leads to cellular growth at low constitutional supercooling and to dendrites at high constitutional supercooling (see Figure 12.5). For both of these growth forms a lot of impure melt is entrapped, that partly or totally solidify upon deeper cooling, and thus largely contribute to the uptake of impurities by the layer.

In solid layer crystallizers with a stagnant melt the dendrites can in particular grow out to unacceptable dimensions. This is one of the reasons for preferring falling film crystallizers.

After deposition of the layer the less pure melt is drained from the crystallizer, and the layer is further purified by sweating and washing, as explained below.

12.5.1.4 Sweating and washing

The first step in the purification of the solid layer is by a so-called *sweating* procedure. The pure product has the highest melting point, so upon gradual heating of the layer the dispersed inclusions will melt first and move towards the layer surface. Simultaneously the dendrites will recrystallize and flatten to reduce the surface area of the layer. The impure liquid forms droplets at the layer surface that drip down and are collected at the bottom (see Sulzer Chemtech, 2014). This sweating procedure seems to become even more effective when a melt is circulated as a falling film along the layer surface. This melt has the role of a wash liquid that helps in removing the sweat droplets from the surface.

After sufficient sweating and washing the residual layer is molten and drained to be either collected as final product or for a next purification step.

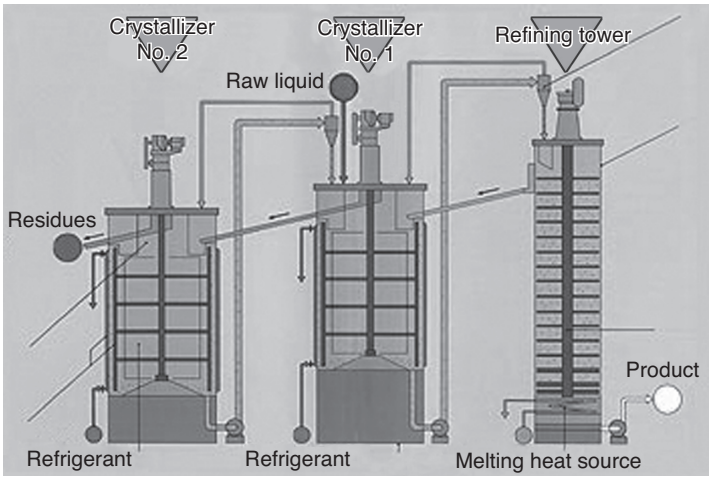

Figure 12.6 TSK-4C melt suspension crystallizers with a gravitational wash column.

12.5.1.5 Advantages and disadvantages

The advantage of solid layer melt crystallization equipment is its relatively simple operation without moving parts such as stirrers or scrapers. Also, no problems are introduced by scaling, because the layer upon the cooling plates or tubes is the final product that is melted off. No suspension handling is thus needed.

A disadvantage is the small growing surface area compared to suspension growth. The growth rate thus has to be high to meet the required production capacity. This leads to an enhanced uptake of impurities. A multi-stage operation is therefore often needed to obtain the demanded degree of purity. As a rule of thumb every stage lowers the impurity content about ten times. Sequential countercurrent staging can be performed intermittently in one crystallizer, provided that sufficient additional storage tanks are available.

12.5.2 Suspension melt crystallization

12.5.2.1 Equipment

There are several types of continuously operated suspension melt crystallizers. Tsukishima Kikai (TSK) developed the Continuous Counter Current Crystallization (4C) system. Several large crystallizers are cooled with a refrigerant in the cooling jacket and steel scrapers are mounted on a rotating draft tube. The slurry from the crystallizer is pumped to a cyclone at the top, where the concentrated slurry either enters the next crystallizer with a purer melt or finally the wash column (see Figure 12.6). The clear melt from the cyclone is returned to the crystallizer. The crystallizers are positioned at different heights, which allow the clear melt to move via an overflow to a former crystallizer with a less pure melt.

Because of the very large specific surface area of the crystals (up to 10,000 $m^2\ m^{-3}$) a large production capacity can be reached at relatively low growth rates of about

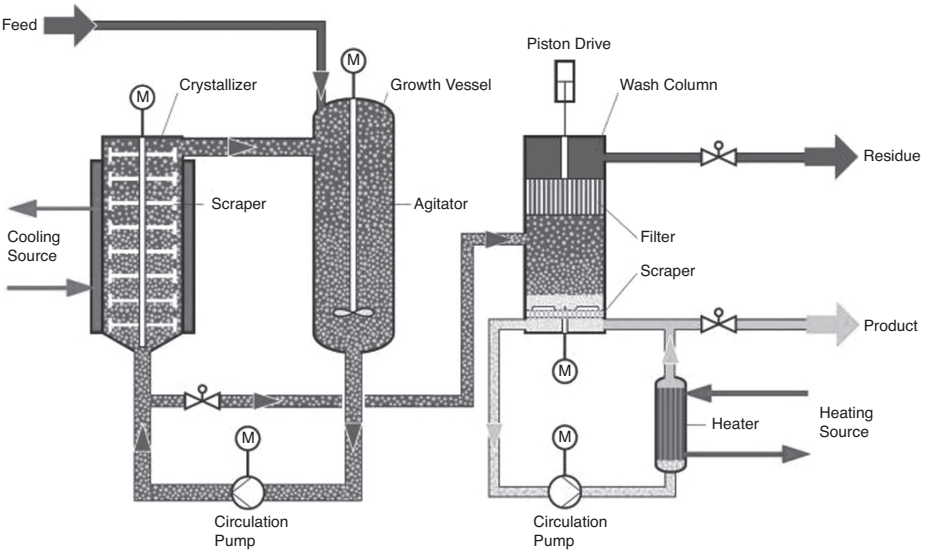

Figure 12.7 Sulzer Chemtech (2014) melt suspension crystallizer with mechanical wash column.

10^{-8} to 10^{-7} m s^{-1}, while a large temperature difference of 15 to 20 K can be maintained per stage.

The advantage of countercurrent operation is also that the purest and thus the hottest suspension is fed at the top of the wash column.

The melt suspension crystallizer design by Sulzer Chemtech (Figure 12.7) has some resemblance to that of TSK. In one or more scraped crystallizers, crystals are formed in suspension and to a minor extent on the cooling walls where they are scraped off. This suspension is fed into a growth vessel, where the crystals can further grow out, but where ripening can also happen or recrystallization of crystals that contain stress induced by the scraping action. The suspension in the growth vessel is partly recycled into the crystallizer and partly enters the wash column.

The melt suspension crystallizing system of GEA Messo is similar to that of Sulzer with one or more scraped crystallizers/heat exchangers, with often a growth vessel referred to as recrystallizer, and a hydraulic wash column (see Figure 12.8).

12.5.2.2 Cooling profile

In suspension crystallization from the melt, the suspension is cooled down and free-flowing crystals grow from a supercooled melt. The actual temperature profile T_{act} close to the crystal surface is given in Figure 12.9. Since the growth rate is low, the gradient of the impurity concentration at the crystal surface is small, so the impact of the impurity concentration on the equilibrium temperature T_{eq} is small. Nevertheless, although the supercooling is small, intrinsically unstable growth conditions exist.

Unwanted instabilities at a crystal surface can, however, only be created when an instability wave can develop upon the crystal surface. For the tiny crystals in suspension the circumference doesn't suffice to accommodate the wavelength that causes an

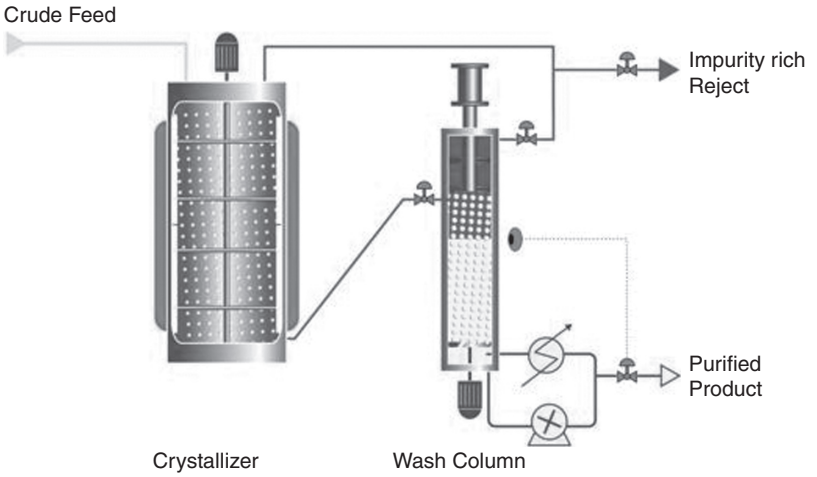

Figure 12.8 GEA Messo melt suspension crystallizer with hydraulic wash column (GEA website).

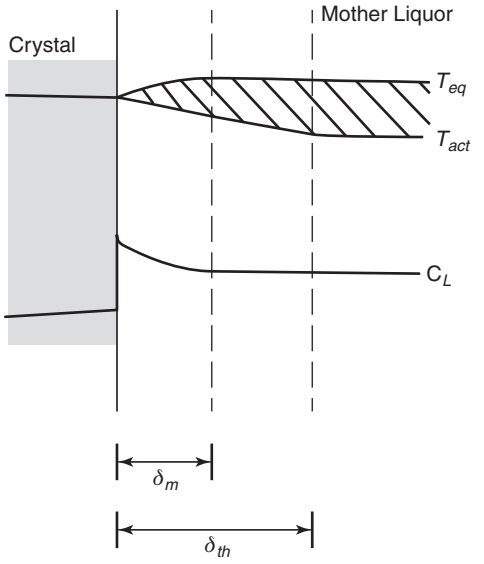

Figure 12.9 Concentration and temperature profiles in suspension crystallization with constitutional undercooling.

instability to develop. Therefore tiny crystal surfaces do not form protrusions. In other words, the stabilizing effect of the surface tension is strong because of the curvature of the crystal surface.

12.5.2.3 Kinetics

Nuclei are mainly formed by attrition of the parent crystals. In melt crystallization the crystals are generally large enough and the crystal volume density high enough

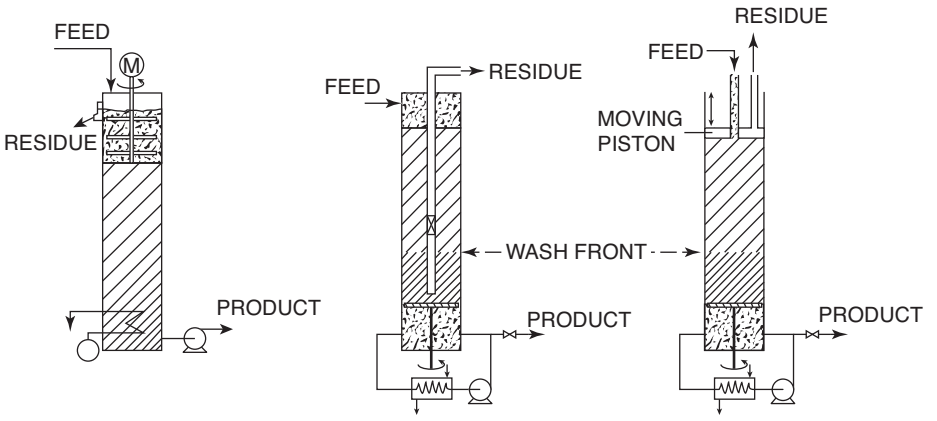

Figure 12.10 Gravity wash column (left), hydraulic wash column (middle) and mechanical wash column (right).

(about 25 vol%) for sufficient crystal–crystal and crystal–hardware collisions. Only if the viscosity of the melt is high is secondary nucleation hampered. But apart from these attrition fragments particles scraped from the walls can also act as nuclei.

As explained above, because the growth rate of the crystals is low, the uptake of impurities by the crystals is very low, in particular for eutectic systems. So actually only one crystallization step (i.e. without recrystallization) is required to yield pure crystals, and the purity of the final product mainly depends on the separation and washing step. In this step any deposition of impure melt upon the crystals must be prevented. For this purpose, three types of wash columns have been developed. Wash columns are used in particular if ultra-purifications are demanded, because a close to complete phase separation is integrated with a highly efficient washing action.

12.5.2.4 Wash columns

In countercurrent operation the suspension from the hot end of the crystallization stages is fed into the top of the wash column.

In a gravitational wash column the crystals settle by gravitational forces, and a loosely packed bed moves downwards. The thickening bed is kept homogeneously packed by slowly rotating impellers on a shaft (<1.5 rpm), and the impure melt leaves the column as a residue via an overflow at the top. Apart from the spent liquor, this residue is recycled to the crystallizer. At the bottom of the column the crystal bed that has been countercurrently washed is molten (see Figure 12.10 and 12.6). The melter is simply positioned in the bottom section inside the wash column. Because of the poor heat transfer in this unstirred section, the production capacity is low. Part of the molten pure product is pushed upwards as wash liquor, while the remainder is drawn off as pure product. The rising liquor crystallizes upon the descending crystals, thus lowering the porosity of the bed. There is no sharp wash front as in the other two designs, as will be explained below. The temperature difference over the column should not be more

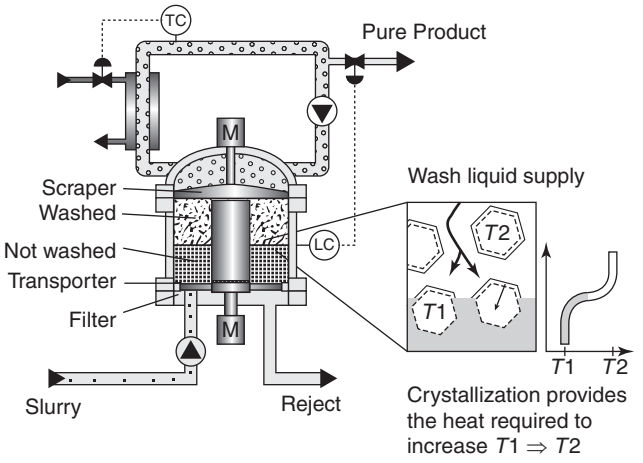

Figure 12.11 Mechanical wash column for ice (GEA Messo, 2015).

than 15 to 20 K. This column only works for large crystal sizes (about 500 μm), for a sufficient density difference between crystal and melt, and for low viscosities.

Higher production capacities can be achieved through forced transportation of a densely packed crystal bed in the wash column. If the bed is transported by a hydraulic force as in the TNO wash column, the suspension is fed into the top and after rapid thickening of the suspension, a densely packed bed slowly moves downwards. The impure melt leaves the column in the middle through filters in separate filter tubes, and this residue is recycled, apart from the spent liquor. At the bottom of the column the pure crystal bed is scraped off, and the crystals are suspended and molten in the circulating pure liquid flow. Part of the pure flow is pushed upwards back into the column by an overpressure in the external melt chamber, and the remainder of the flow is drawn off as pure product. The ascending wash liquor crystallizes upon the descending crystal bed, thus lowering the porosity. This improves the washing efficiency and facilitates upward plug flow of the impure melt that leaves the column through the filters. The overpressure should be properly tuned in order to keep the wash front sufficiently below the level of the filters. The plug flow of the wash liquor causes a stable flat wash front with a significant temperature jump across the front.

In the mechanical wash column in Figure 12.10, the dense bed is transported by a mechanical force exerted by a piston or a screw. The impure melt leaves the column through pores in the mechanical plate. Otherwise this wash column is operated similarly to the hydraulic column. Forced transport wash columns can cope with crystal sizes down to 100 μm. These kinds of wash columns are only unsuitable for organic crystals that deform under compressional stress.

In cases where melt crystallization is used as a concentration technique, as in concentration of fruit juices, ice crystals are formed. In a wash column the crystals thus float to the top, where the pure solid mass is scraped off (see Figure 12.11). At the wash front,

the color of the bed then sharply changes from the white color of ice crystals into the fruit juice colour (GEA Niro wash column).

12.5.2.5 Advantages and disadvantages of suspension melt crystallization

In suspension melt crystallization, it is impossible to avoid handling of suspensions and moving parts in the crystallizer. A high production rate is, however, feasible owing to the high specific surface of the crystals that are directly formed as pure crystals. The major challenge therefore lies in the removal of the impure melt from the suspended pure crystals. A first step can be made by counter current crystallization in a cascade of vessels, where the purity of the melt increases in the direction of the wash column. Wash columns are especially designed to further eliminate the impure melt from the pores of the packed bed of crystals and to wash off the melt adhering to the crystals. These wash columns only need careful operation to avoid unwanted blockages of the bed.

12.5.2.6 Pressure melt crystallization

Melt crystallization can also be performed by pressurizing of the crystals instead of cooling. The operating conditions and the potential separation efficiency are derived from phase diagrams with the pressure instead of the temperature as parameter. Pressure crystallization has, for example, been applied for the separation of *ortho*- and *para*-cresol. Kobe Steel has developed equipment for high-pressure crystallization. Because pressure crystallization has only specialized applications, it will not be treated further here.

12.6 Eutectic freeze crystallization

Eutectic freeze crystallization (EFC) is a combination of melt cooling and solution cooling crystallization. It is applied for the simultaneous crystallization of ice and salt from a concentrated solution close to the eutectic temperature. By cooling at a temperature slightly below the eutectic temperature, ice is formed, and salt is simultaneously crystallized because of the elimination of solvent (as ice) from the solution.

Unlike other simultaneous crystallizations of two or more salts, the density of ice crystals is lower than that of the solution. So an integrated process of cooling crystallization of ice and salt and gravity separation from the solution can be achieved. During crystallization, the ice floats to the top of the vessel, while the salt settles at the bottom. An alternative process without integration is a two-step process where ice and salt are separated in a settler after being crystallized (Gärtner *et al.*, 2005).

Ice crystallization has always been seen as expensive, because desalination of sea water by freezing has been more expensive than evaporation or reverse osmosis. However, thermodynamically, it is cheaper to freeze one kilogram of water (333 kJ) than to evaporate it (2300 kJ), but freezing is a slow process and the major costs are the high capital costs of the equipment, although this is expected to decrease as the technology matures (Nathoo *et al.*, 2009).

If, however, a pure saleable salt can be produced simultaneously with the ice, the EFC process can become profitable. It can also become an attractive solution when zero

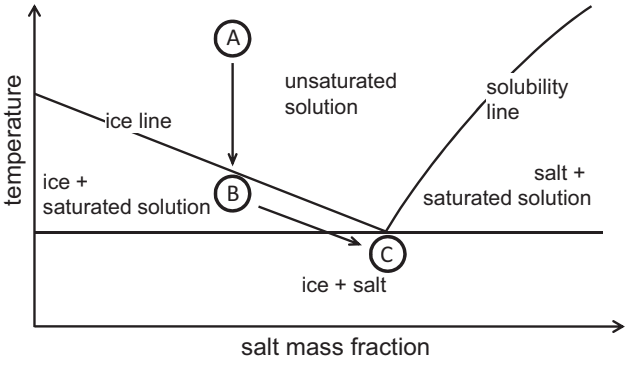

Figure 12.12 Binary phase diagram with eutectic point showing the steps in a batch crystallization by cooling an unsaturated salt solution.

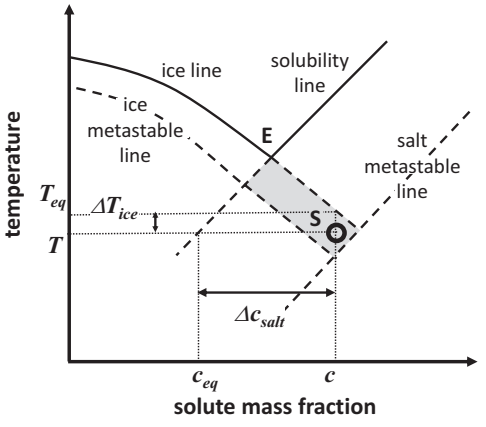

Figure 12.13 Binary phase diagram with a crystallizing solution of composition S below the eutectic temperature.

discharge of waste streams is mandatory. In those cases the often dilute solution is first preconcentrated by reverse osmosis, and can then be treated in an EFC process.

12.6.1 Binary phase diagrams

For further explanation of the features of an EFC process, a schematic binary phase diagram of a salt in water is given in Figure 12.12, where an unsaturated solution A is cooled batchwise until, at point B, the solution becomes supersaturated with respect to ice and starts to crystallize. At a temperature below the eutectic point C, both ice and salt crystallize, and this continues until cooling is stopped.

If this EFC process is performed continuously, the feed entering the crystallizer could be of composition A, while the conditions in the crystallizer are given by the temperature and concentration of point S in Figure 12.13. Point S lies within the metastable zones of both ice and salt. The metastable zone of the ice generally is

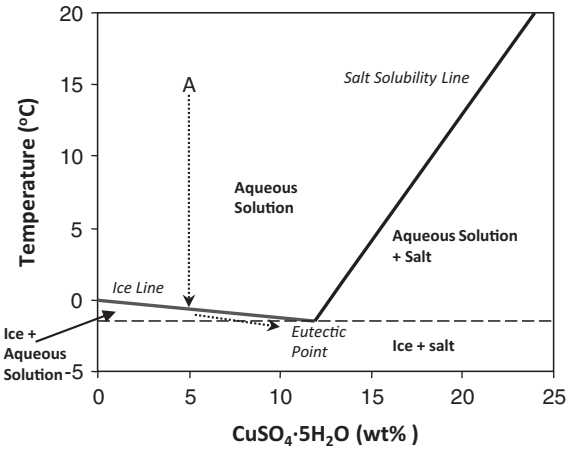

Figure 12.14 Phase diagram of the binary $CuSO_4$–water system.

rather small (depending also on the type and concentration of the salt), and in continuous operation the temperature difference between the cooling plates and the solution is kept sufficiently low to avoid excessive scaling of the ice on the scraped cooling plates.

The driving force for ice crystallization is given by (see Figure 12.13):

$$\left(\frac{\Delta\mu}{RT}\right)_{ice} \approx \left(-\frac{\Delta H_{cryst,ice}}{RT^2}\right)_{ice} \left(T - T_{ice,eq}\right) \tag{12.7}$$

and for salt crystallization by:

$$\left(\frac{\Delta\mu}{RT}\right)_{salt} = \ln\left(\frac{a}{a_{eq}}\right)_{salt} \approx \frac{C_s - C_{s,eq}}{C_{s,eq}} = \frac{\Delta C_{salt}}{C_{s,eq}} \tag{12.8}$$

Below two phase diagrams will be presented, one with a single eutectic point and one with several peri-eutectic points.

12.6.1.1 Binary phase diagram of $CuSO_4$–water

Figure 12.14 represents the eutectic phase diagram for a $CuSO_4$–water system. This simplified diagram only considers the pentahydrate form of copper sulfate with eutectic conditions at 11.9 wt% $CuSO_4 \cdot 5H_2O$ and −1.5 °C (Pronk, 2007).

Starting on the left side of the eutectic point at point A, at a temperature of 15 °C and concentration of 5 wt%, a batch eutectic freeze crystallization process would proceed by cooling of the solution until the temperature reaches the ice line. Below this point, the first crystals of ice will be seen. On further cooling, the solution will follow the ice

Table 12.2 Eutectic temperatures and compositions for three binary systems

System	Eutectic temperature (°C)	Eutectic composition (wt%)
$MgSO_4$–water	−3.9	19
NaCl–water	−21.2	23.3
$CaCl_2$–water	−49.8	30.22

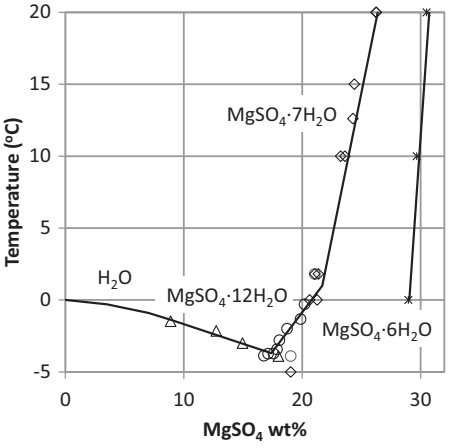

Figure 12.15 Phase diagram of the binary $MgSO_4$–water system (Pillay *et al.*, 2005).

line, with its salt concentration increasing due to ice formation, until the eutectic point is reached, where both ice and salt crystallize simultaneously.

12.6.1.2 Binary phase diagram of $MgSO_4$–water

Figure 12.15 gives the binary phase diagram for the $MgSO_4$–water system with one eutectic and several peri-eutectic points. The eutectic point for $MgSO_4 \cdot 12H_2O$ lies at −3.9 °C and 17.4 wt% $MgSO_4$.

Several other binary systems like $NiSO_4$ and $NaSO_4$ also have their eutectic point rather close to 0 °C, but the range of eutectic temperatures is considerable (see, for example, those given in Table 12.2).

12.6.2 Ternary phase diagrams: Na_2SO_4–$MgSO_4$–H_2O

EFC always involves multi-component systems because, as water is removed, the concentration of impurities increases dramatically. Figure 12.16 represents the phase diagram for the Na_2SO_4–$MgSO_4$–H_2O ternary system. As can be seen by comparing Figure 12.15 with Figure 12.16, in a ternary system the eutectic temperature for $MgSO_4$ is depressed, due to the interactions between the components. Figure 12.15 shows that an $MgSO_4$

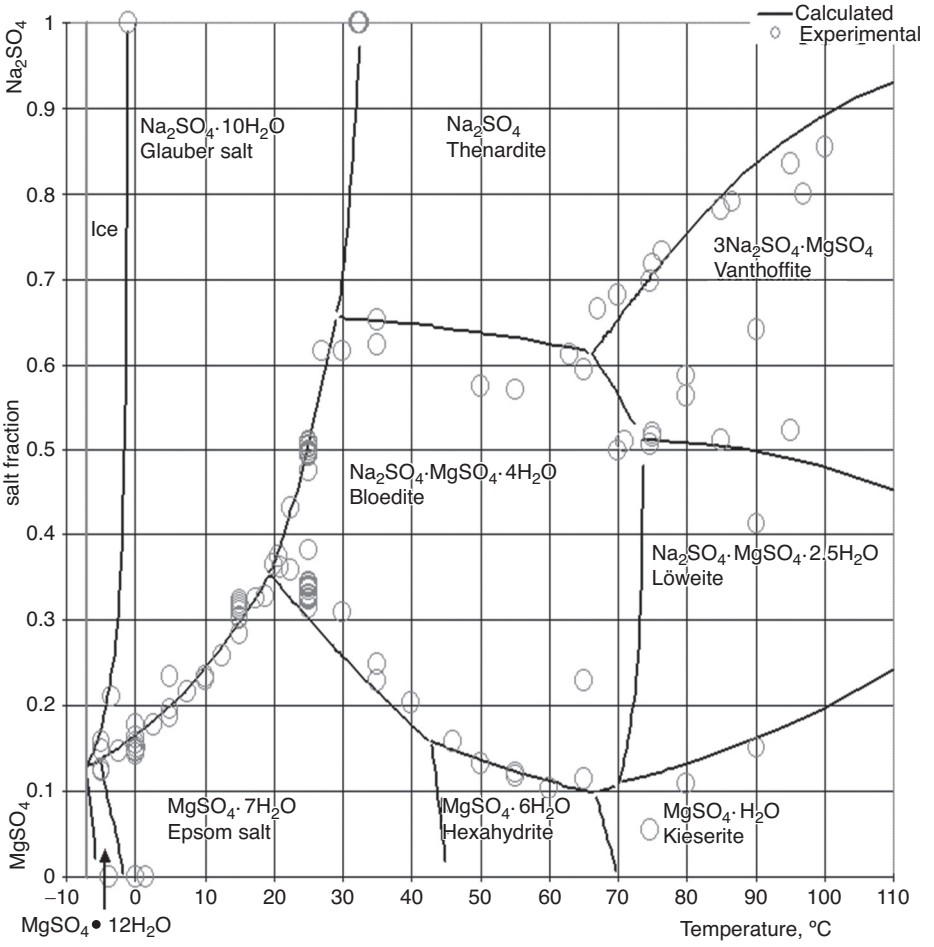

Figure 12.16 Phase diagram for the Na_2SO_4–$MgSO_4$–H_2O system from –10 to 110 °C, showing the eutectic temperature at –7 °C (Thomsen, 1997). Circles are data points.

binary system has a eutectic temperature of ~ −3.9 °C, while Figure 12.16 shows that, for the Na_2SO_4–$MgSO_4$–H_2O ternary system, the ternary eutectic temperature is −7 °C. This illustrates that it is not accurate to use a binary phase diagram to predict the eutectic temperature of a ternary system, and that a ternary or multi-component phase diagram must be employed. In Figure 12.16, the measured data are indicated by the circles.

Because of the high water activity at low temperatures, an EFC process will usually produce hydrates. When the temperature is increased from EFC operating temperatures to ambient temperatures in order to recover the hydrated salt, the increase in temperature will cause a lower hydrate to be favored. See Figure 12.15, which shows that the $MgSO_4 \cdot 12H_2O$ phase is favored at the lowest temperatures and, as the temperature is

increased, the $7H_2O$, followed by the $6H_2O$, the $1H_2O$ and finally, the anhydrous salt, will be favored. Thus, the produced hydrate will completely dissolve in the mother liquor of the holding tank, and recrystallize into the next phase. This recrystallization will occur at a low supersaturation, because the supersaturation is limited by the solubilities of the two hydrates. The advantage of this recrystallization process is that any impurity incorporation in the final salt product is reduced, and, after a washing step, a highly purified product can be obtained.

Ice crystals tend to reject impurities in their lattice (due to the small size of the water molecule). This explains why ice crystals, grown from fruit juice, are white, and why a sharp wash front is obtained in a wash column. In EFC crystallization, however, probably because of the much lower operating temperatures, there is a tendency for scale to form on the cooling plates and for agglomerates to form in solution. The lumps scraped from the cooling surface, as well as the agglomerates, can pick up the salt crystal fines in the voids between the ice crystals. Therefore it is necessary to wash the ice crystals on belt filters, where, during washing and partial melting of the ice, the tiny salt crystals are dissolved and released from the ice crystals themselves.

Up to now, the EFC process has been shown at proof-of-concept level. The current scientific understanding of the process has been developed in a series of studies that started by focusing on the EFC process as a whole (Van der Ham, 1999) and progressed via developing crystallizer designs (Pronk, 2007, Vaessen, 2003) to case studies (Jivanji *et al.*, 2011, Randall *et al.*, 2011) and recently some more fundamental studies (Apsey and Lewis, 2013, Egan *et al.*, 2014, Kapembwa *et al.*, 2014). The process has been shown at proof-of-concept level (Genceli, 2008, Lewis *et al.*, 2009, 2010, Randall *et al.*, 2011, Van der Ham, 1999), and has been run at pilot scale. At the time of writing, the process has not yet been implemented at full scale.

Worked example 1

Given the phase diagram in Figure 12.17, describe what phases are formed as the system is cooled from a point vertically above point b down to point b and eventually to the ternary eutectic point.

Solution to worked example 1

During cooling, the liquidus surface is intersected at point b and pure C begins to crystallize. This causes the remaining solution to become leaner in C and thus the system equilibrium moves along the equilibrium line (which is the extension of the tie line K) to point d. At point d, the liquid is now *also* saturated in A (and C). At this binary eutectic point, A and C crystalize simultaneously. As A and C simultaneously crystallize, the remaining mixture becomes leaner in A and C, but richer in B. Thus, as the temperature is decreased still further, the system equilibrium moves along line e1–E, the binary eutectic line, until it reaches point E, at which point all three phases (A, B and C) will simultaneously crystallize out of solution.

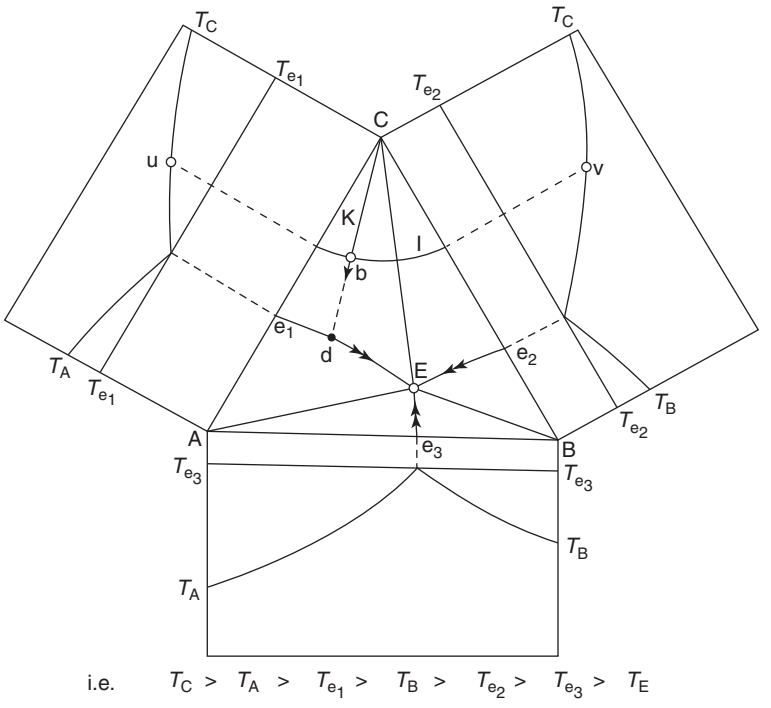

Figure 12.17 Schematic ternary phase diagram for the A-B-C system (Predel *et al.*, 2004).

12.7 A brief summary of the chapter

Melt crystallization is an important "sub-class" of crystallization that has a number of specialized applications. It can be used to produce extremely pure products, although melt crystallization is easily prone to surface instabilities. The product is generally recovered as a liquid (melt). Industrial melt crystallizers are usually either layer- or suspension-type devices. A special example of combined melt and solution cooling crystallization is eutectic freeze crystallization.

12.8 End of chapter problems

Problem 1

Given a feed stream of composition 10 wt% $CaCl_2$ at a temperature of 25 °C, use the phase diagram given in Figure 12.18 to identify what will occur when the feed is cooled down to −40 °C.

- What phase will be formed?
- What will be the purity of the solid phase?
- What will be the yield of the solid phase per 1 kg of feed?

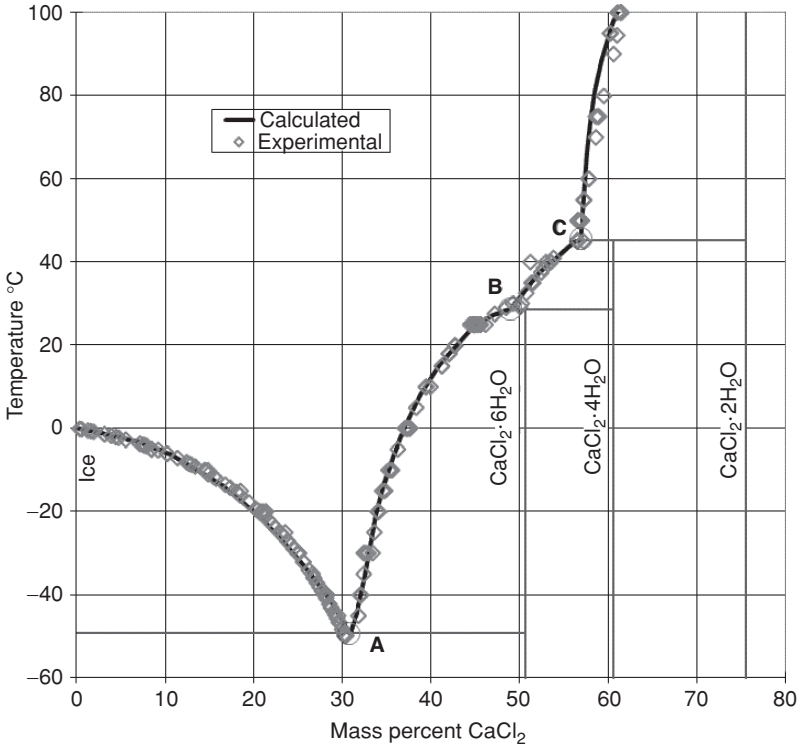

Figure 12.18 Phase diagram for the $CaCl_2$–water system C (Thomsen, 1997).

Problem 2

Given a feed stream of composition 40 wt% $CaCl_2$ at a temperature of 25 °C, use the phase diagram given in Figure 12.18 to identify what will occur when the feed is cooled down to −40 °C. Answer the same three questions given in the problem above.

Problem 3

Draw up a table that summarizes the main differences between layer and suspension crystallization, as well as the advantages and disadvantages of each.

12.9 References

Apsey, G. and Lewis, A. 2013. Selenium impurity in sodium sulfate decahydrate formed by eutectic freeze crystallization of industrial waste brine. *Journal of the Southern African Institute of Mining and Metallurgy*, **113**, 415–421.

Arkenbout, G. F. 1995. *Melt Crystallization Technology*, Technomic Publishing Company Inc.

Burton, J., Prim, R. and Slichter, W. 1953. The distribution of solute in crystals grown from the melt. Part I. Theoretical. *The Journal of Chemical Physics*, **21**(11), 1987–1991.

Egan, T., Lewis, A. E. and Rodríguez-Pascual, M. 2014. In situ growth measurements of sodium sulfate during cooling crystallization. *Chemical Engineering and Technology*, **37**, 1283–1290.

Gärtner, R. S., Genceli, F. E., Trambitas, D. O. and Witkamp, G. J. 2005. Impurity gradients in solution-grown ice and MgSO4 · 12H2O crystals measured by cryo-laser ablation and high-resolution-induced-coupled plasma mass spectrograph. *Journal of Crystal Growth*, **275**, e1773–e1778.

GEA Messo. 2015. Suspension crystallization: highly efficient product crystal separation. http://www.gea-pe.it/gpeit/cmsresources.nsf/filenames/Washcolumn_separation_Datasheet.pdf/$file/Washcolumn_separation_Datasheet.pdf (accessed Feb 2015).

Genceli, F. E. 2008. *Scaling up Eutectic Freeze Crystallization*, PhD thesis, Technical University of Delft.

Hengstermann, A. 2010. *A New Approach to Industrial Melt Crystallization of Acrylic Acid*, PhD thesis, Delft University of Technology.

Jansens, P. J. and van Rosmalen, G. M. 1994. Fractional crystallization. In *Handbook of Crystal Growth*, Hurle, D. T. J. (ed.) Elsevier Science, 289–312.

Jivanji, R., Nathoo, J., Merwe, W. V. D., Human, A. and Lewis, A. 2011. Application of eutectic freeze crystallization to the treatment of mining wastewaters. 22nd World Mining Congress, Istanbul.

Kapembwa, M., Rodríguez-Pascual, M. and Lewis, A. E. 2014. Heat and mass transfer effects on ice growth mechanisms in pure water and aqueous solutions. *Crystal Growth and Design*, **14**, 389–395.

Lewis, A. E., Nathoo, J., Thomsen, K. *et al.* 2010. Design of a eutectic freeze crystallization process for multicomponent waste water stream. *Chemical Engineering Research and Design*, **88**, 1290–1296.

Lewis, A. E., Randall, D. G., Reddy, S. T., Jivanji, R. and Nathoo, J. 2009. Worth its salt: how eutectic freeze crystallization can be used to recover water and salt from hypersaline mine waters. In: *Water in Mining, 15-17 September 2009 Perth*, Fong, O. T. (ed.), Australasian Institute of Mining and Metallurgy, 5–11.

Matsuoka, M. 1991. Developments in melt crystallization. In: *Advances in Industrial Crystallization*, Garside, J., Davey, R. and Jones, A. G. (eds.), Butterworth-Heinemann.

Mullin, J. W. 2001. *Crystallization*, Elsevier Science.

Mullin, J. W. 2003. Crystallization and precipitation. In *Ullmann's Encyclopedia of Industrial Chemistry*, Ullmann, F. and Gerhartz, W. (eds.), Wiley-VCH.

Nathoo, J., Jivanji, R. and Lewis, A. E. 2009. Freezing your brines off: eutectic freeze crystallization for brine treatment. In: *International Mine Water Conference, Pretoria*, Taylor, C. (ed.), International Mine Water Association.

Pillay, V., Gartner, R. S., Himawan, C. *et al.* 2005. $MgSO_4+H_2O$ system at eutectic conditions and thermodynamic solubility products of $MgSO_4 \cdot 12H_2O$(s) and $MgSO_4 \cdot 7H_2O$(s). *Journal of Chemical and Engineering Data*, **50**, 551–555.

Predel, B., Hoch, M. and Pool, M. J. 2004. *Phase Diagrams and Heterogeneous Equilibria: A Practical Introduction*, Springer.

Pronk, P. 2007. *Fluidised Bed Heat Exchangers to Prevent Fouling in Ice Slurry Systems and Industrial Crystallizers*, PhD thesis, Technical University of Delft.

Randall, D. G., Nathoo, J. and Lewis, A. E. 2011. A case study for treating a reverse osmosis brine using eutectic freeze crystallization: approaching a zero waste process. *Desalination*, **266**, 256–262.

Sulzer Chemtech. 2014. *Falling Film Crystallization* [Online]. (http://www.sulzer.com/en/Products-and-Services/Separation-Technology/Crystallization/Falling-Film-Crystallization, accessed Feb 2014).

Tähti, T. 2010. *Suspension Melt Crystallization in Tubular and Scraped Surface Heat Exchangers*. PhD thesis, Martin-Luther-Universität Halle–Wittenberg, Zentrum für Ingenieurwissenschaften.

Thomsen, K. 1997. *Aqueous Electrolytes: Model Parameters and Process Simulation*, PhD, Technical University of Denmark.

Ulrich, J. and Glade, H. 2003. *Melt Crystallization: Fundamentals, Equipment and Applications*, Shaker.

Vaessen, R. J. 2003. *Development of Scraped Eutectic Crystallizers*, PhD thesis, Technical University of Delft.

Van Der Ham, F. 1999. *Eutectic Freeze Crystallization*, PhD thesis, Technical University of Delft.

13 Additives and impurities

13.1 Why this chapter is important

Although additives and impurities are often present in relatively small concentrations, even trace amounts can have a significant effect on the crystallization process as a whole. Thus, when working in "real" crystallization processes, understanding the influence of additives and impurities is very important.

Although the topic of additives and impurities has been the subject of extensive study by many different researchers, it is still a difficult area, partly because the field itself is very broad and diverse, but also because there are so many different applications in which additives and impurities play an essential role (Meenan *et al.*, 2002, Sangwal, 2007).

13.2 Application and occurrence

For many centuries long chain organic additives with molecular weights of a few thousand daltons were used in particle formation processes as, for example, dispersants, flocculants and flotation agents. They were generally added, at dosages below 1 wt%, after the particles were formed.

However, in this chapter, we will discuss the role and design of additives and impurities that are present *during* crystallization at low dosages from parts per billion (ppb) to, at most, a few wt%. Highly charged metal ions can influence the crystallization process at only ppb concentrations, polymers at <1 wt% concentrations, whereas monomers must be present at the wt% level in order to have an influence.

Because of their low concentrations, additives do not influence the supersaturation (by coordination of ions in solution, for example), but only have the ability to act upon the crystal surface. Such additives are, for example, growth inhibitors, habit modifiers, anti-caking agents (applied as after-treatment) or templates for preferred nucleation.

Since impurities (i.e. additives that are unintentionally present) that can originate from the raw material, or can be formed as by-products during synthesis of the product, often have similar effects as additives on the crystallization process, they are also considered in the same chapter.

The solvent can also have similar effects on the growth kinetics and the shape of the crystals, as will be discussed.

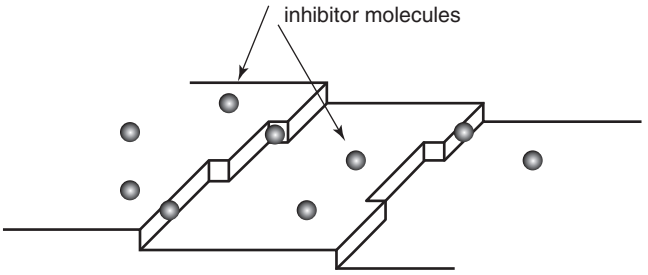

Figure 13.1 Additive adsorption at various positions upon a crystal surface.

13.3 Mechanism of organic growth inhibitors

13.3.1 Small organic molecules

The interference of additives with the growth pattern of a crystal starts with their adsorption onto and incorporation into the crystal surface in competition with the regular growth units. Their final position upon the crystal surface can be either at the terraces or along the steps or even at preferential kink positions along the steps (see Figure 13.1 and Chapter 5). Additives have the strongest impact on the growth rate when growth proceeds by the subsequent deposition of growth layers, as in spiral growth.

Rough growth caused by either a high supersaturation or by crystallizing at a temperature above the roughening temperature is much harder to inhibit. When volume diffusion is rate controlling, the impact of surface-adsorbed additives or impurities is reduced.

Because *most* dissolution processes are volume diffusion controlled, these processes are less able to be influenced by additives. It is only for slightly soluble compounds that dissolution might become a surface disintegration-controlled process, and that additives might play a role in retarding the dissolution rate.

The extent of additive interaction with a particular crystal surface determines its impact upon the growth rate of that particular face. Since this impact can be different for each crystallographic face because of the structure of the specific growth layer, this results in changes in crystal habit (see Figure 13.2).

Strongly bound additives, upon deposition of subsequent growth layers, become incorporated into the crystal lattice. This leads to strain, which hampers the growth kinetics, while the purity and mechanical strength of the crystals are altered as well. Additive adsorption along steps leads to step bunching, and macro-steps promote the formation of inclusions.

To cause sufficient growth inhibition, the concentration in solution of a small additive should in general be at the few wt% (and not at ppb) level. For many applications a few wt% is far too high, and dosages of only a few parts per million (ppm) are required.

13.3.2 Large organic molecules

One of the ways to be effective at very low dosages is if sufficient strongly adsorbing, immobile additives adsorb together on terraces of crystal surfaces and create a kind of

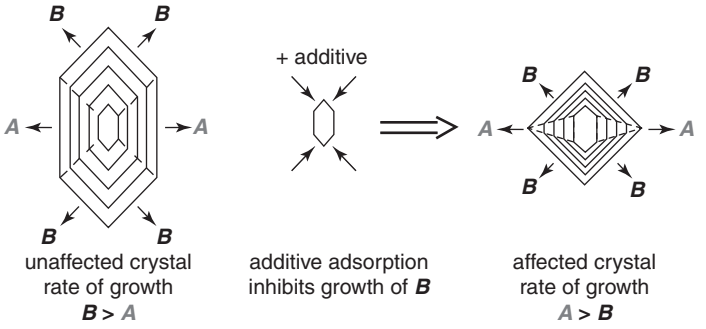

Figure 13.2 Effect of a preferentially adsorbed additive on crystal habit (Weissbuch and Lahav, 2011).

Figure 13.3 Steps squeezing through a row of impurities adsorbed on a crystal surface.

rigid fence that stops the propagation of steps along the surface. This hypothesis of a cooperative interaction was proposed in 1958 by Cabrera and Vermilyea to explain the impact of adsorbing impurities or additives on the movement of steps. They suggested that, for a distance between impurities on the crystal surface smaller than $2r^*$, where r^* is the radius of a 2-D critical nucleus, the growth of the crystal face will come to a standstill. For wider spacing between impurities the step may squeeze through the adsorbed impurities but, in doing so, will lower its characteristic growth speed (see Figure 13.3). To achieve the criterion of having a distance less than $2r^*$ between impurities or additives adsorbed at the surface, their concentration in solution has to be sufficiently high.

To lower the concentration of additives needed to stop propagation of steps along the surface, a *flexible* fence can be created by attaching strongly adsorbing groups to a polymer backbone at inter-group distances that (more or less) correlate with the distances between the intended bonding ions or groups at the crystal surface. Upon incorporation of these polymers, considerable stress is induced in the lattice, even leading to holes in the structure.

These polymers with attached functional groups must have dalton numbers between 2000 and 5000 in order to give them sufficient bonding potential, but also to give them sufficient diffusivity in order to be able to move effectively and to orientate themselves at the crystal surface.

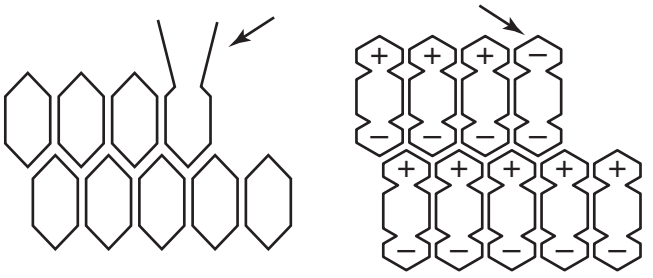

Figure 13.4 Additives for steric or electrostatic hindrance.

13.4 Tailor-made additives

The group of Lahav and Leiserowiz at the Weismann Institute were the first to formulate requirements for the design of tailor-made additives by molecular recognition at crystal interfaces (Weissbuch *et al.*, 1991). In order to retard the growth of a specific crystal face, the additive must fit into the specific growth layer, and must thus contain a part resembling the growth units. The additive must also contain a part that hinders the attachment of growth units to the subsequent growth layer. This deviating part can either form a steric hindrance or have a charge mismatch (see Figure 13.4). The steric hindrance can be a group attached to the resembling molecule that protrudes from the surface or the hindrance can be from a group that is missing something compared to the resembling molecule, thus creating a hole in the crystal surface.

13.4.1 Small organic tailor-made additives

An early illustrative example is benzamide with a (0 0 1) growth layer that consists of a ribbon of hydrogen-bonded molecules (see Figure 13.5). If a benzamide molecule is replaced by a *para*-toluamide molecule, a methyl group protrudes from the (0 0 1) face and hinders the deposition of the next (0 0 1) layer in the direction of the *c*-axis. If a benzamide molecule is replaced by a benzoic acid molecule, the ribbon formation is disrupted by repulsion between the –OH group in benzoic acid and the =O group in benzamide. This hampers deposition of the next (0 1 0) layer in the direction of the *b*-axis. *Ortho*-toluamide retards the growth of benzamide in the direction of the *a*-axis. Retardation of specific faces by adsorption of additives *always* leads to crystal habit changes.

A similar example is the adsorption of cinnamic acid molecules on the {0 1 1} faces of E-cinnamide (see Figure 13.6). This always leads to a change in crystal morphology (Weissbuch *et al.*, 1991).

Nowadays, molecular modeling is becoming an increasingly important tool to understand the influence of additives on the growth rate of the individual crystal faces, as well as to develop tailor-made additives. Hammond and coworkers (2011) used the molecular modeling package HABIT to calculate the relative influence of L-alanine on the $(0\,\bar{2}\,0)$

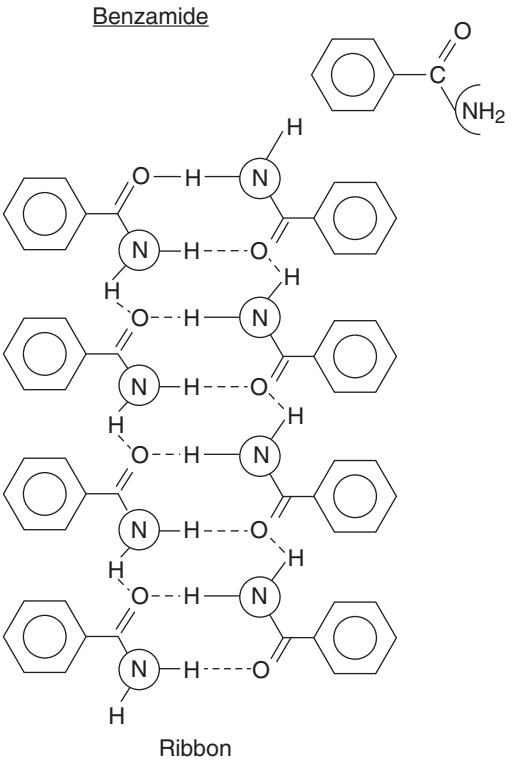

Figure 13.5 A benzamide growth layer.

and (0 2 0) growth slices of α-glycine. It was only when the intermolecular packing requirements of the total host lattice were taken into account in the energy calculations that incorporation of an L-alanine molecule was shown to retard the growth rate of the $(0\,\bar{2}\,0)$ surface slightly more than that of the (0 2 0) surface.

13.4.2 Application of tailor-made additives

Additives were designed to retard the growth rate of crystals, as well as for habit modification in order to improve the filterability of the product, as, for example, in the case of needles. Additives were also designed for the resolution of enantiomers that tended to crystallize as racemic mixtures. By adding either R- or S-oriented additives, the growth of one of the enantiomers could be inhibited.

13.4.3 Molecular modeling

The simplest method to approach the impact of an additive on the growth rate of a specific crystal face is to compare the calculated attachment energy of a growth layer

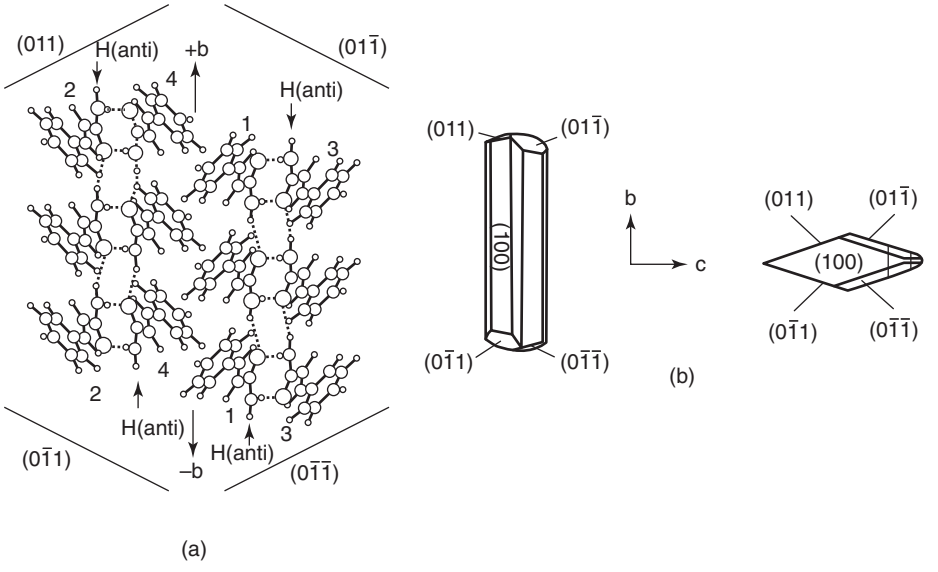

Figure 13.6 Packing arrangement of E-cinnamide (a) viewed along the *a*-axis delineated by the {0 1 1} faces, (b) morphology of pure crystals and with cinnamic acid.

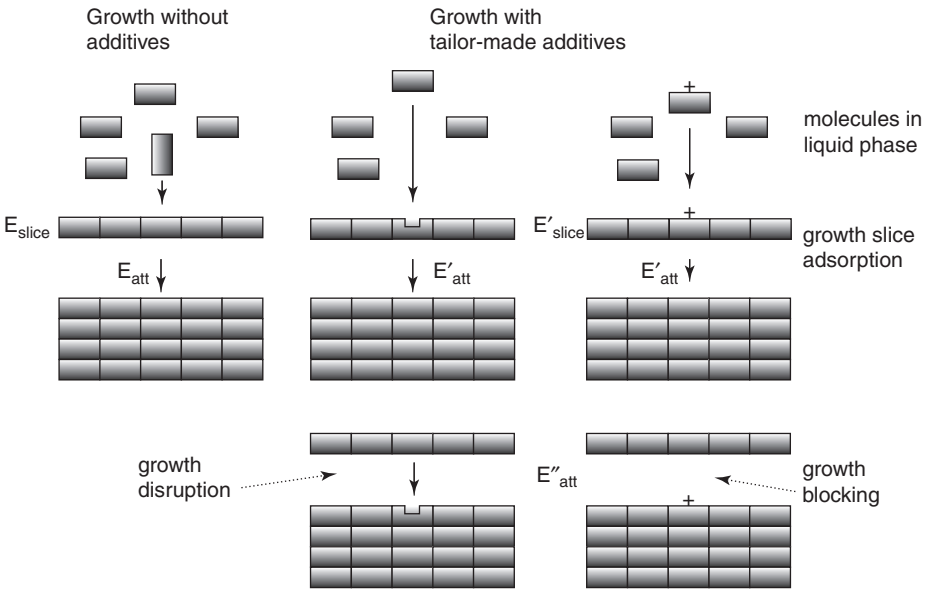

Figure 13.7 Energy released with each stage of the growth process, with and without additives.

(or growth slice) consisting of growth units upon a growth layer of the pure compound E_{att} with the attachment energy of a pure growth layer with an earlier deposited growth layer that contains a tailor-made additive E''_{att} (see Figure 13.7). To be a successful growth-retarding additive, the absolute value of E''_{att} should be far more than E'_{att}.

The attachment energy is related to the crystallization energy by:

$$E_{cr} = E_{slice} + E_{att} \tag{13.1}$$

where E_{cr} = final energy release associated with the crystallization [J g^{-1}]

E_{slice} = energy release associated with building the slice [J g^{-1}]
E_{att} = energy release associated with attaching the slice [J g^{-1}]

For the layer containing the additive, the attachment energies with the adjacent layers as well as the slice energy are affected by the additive.

In this calculation the influence of the solvent has not yet been considered, and the solvent has to be removed from the surface before the growth unit can be attached. The impact of the solvent on the crystal habit can thus be roughly estimated by comparing the various attachment energies minus the attachment energies of the solvent, $E_{att} - E_{att(solvent)}$. In most cases, this rough approach does not give accurate predictions.

With the availability of extensive computing power and molecular modeling packages like Cerius[2] and HABIT, molecular modeling has become very effective for the design of tailored additives. The choice of the appropriate force fields, however, still poses limitations.

The molecular dynamics modeling used by Salvalaglio *et al.* (2013) and the HABIT program used by Hammond *et al*. (2011) provided better results. The Cerius[2] method was successfully used by Buller *et al.* (2002) for the design of an anti-malarial drug, as described below.

13.4.4 Application of molecular modeling to the design of an anti-malarial drug

The plasmodium parasite, which causes malaria, operates by digesting hemoglobin in human red blood cells. As a by-product, the toxin hematin is produced. The parasite protects itself against this toxin by allowing it to crystallize within its body.

Previously, two main routes had been proposed to account for the primary mode of action of chloroquine, the quinoline anti-malarial agent: firstly, complexation with malaria pigment (hematin) in solution and secondly, inhibition of hematin growth by quinoline attachment to the growing crystal. In the work carried out by Buller and coworkers, it was proposed that the mechanism of quinoline is that it binds at the end face of the fastest-growing direction of the hematin, thus preventing hematin crystallization and thereby poisoning the parasite (Buller *et al.*, 2002).

In order to test this hypothesis, and thus establish the molecular mechanism of the quinoline action, it was necessary to understand the hematin crystal structure, its morphology, what surface structures are present and whether quinoline can retard the crystal growth of certain faces. Using Cerius[2] the hematin crystal structure and growth behavior was established.

Firstly it was found that the crystals are needles, due to the fast-growing {0 0 1} faces, as reflected by the highly negative attachment energy ($E_{att} = -101.5$ kcal mol^{-1}). They also found that the {0 0 1} surface was highly corrugated and that flexible propionic acid groups, vinyl and methyl groups, as well as aromatic surfaces were exposed. They

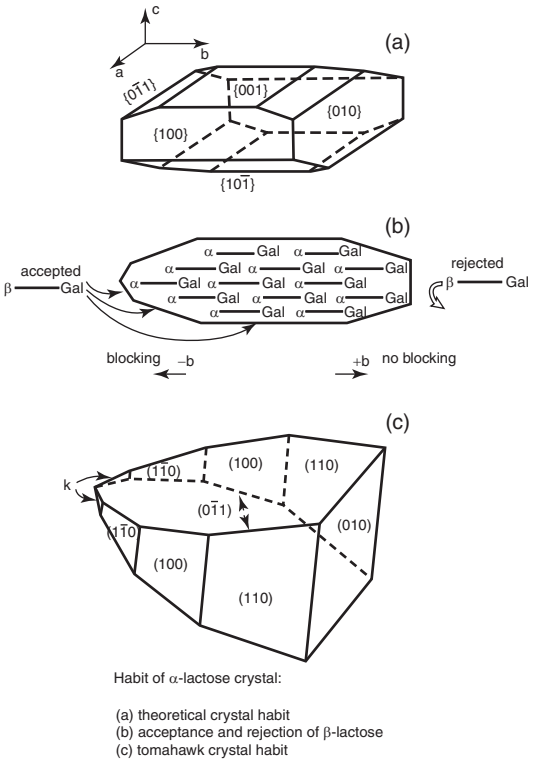

Figure 13.8 The influence of β-lactose molecules on the shape of α-lactose crystals.

then showed that a range of quinolines could each stereochemically cap onto the $\{0\,0\,1\}$ surface of the hematin crystal via an acid–amine salt bridge and still fit snugly into that surface. The existence of the quinoline on the fast-growing end of the hematin crystal then prevents further attachment of hematin molecules and thus the growth is disrupted. Because hematin can no longer be removed from solution by crystallization, the malaria parasite is poisoned due to the build-up of hematin in solution.

13.5 Small unintentionally present organic molecules and solvents

In industrial practice, impurities, solvents and reaction by-products end up in the mother liquor within the crystallizer. Such molecules may unintentionally affect crystallization.

For example, during the crystallization of lactose, two configurations are present: the desired form (α) and the undesired form (β). α-Lactose crystals are built from lactose molecules that consist of glucose and galactose moieties. In a crystallizing solution, 80% of the lactose molecules are in the β and only 20% in the α configuration. A structural analysis predicted a crystal habit as presented in Figure 13.8a that was in conflict with that observed (Visser, 1983). If, however, the preferential adsorption of lactose molecules

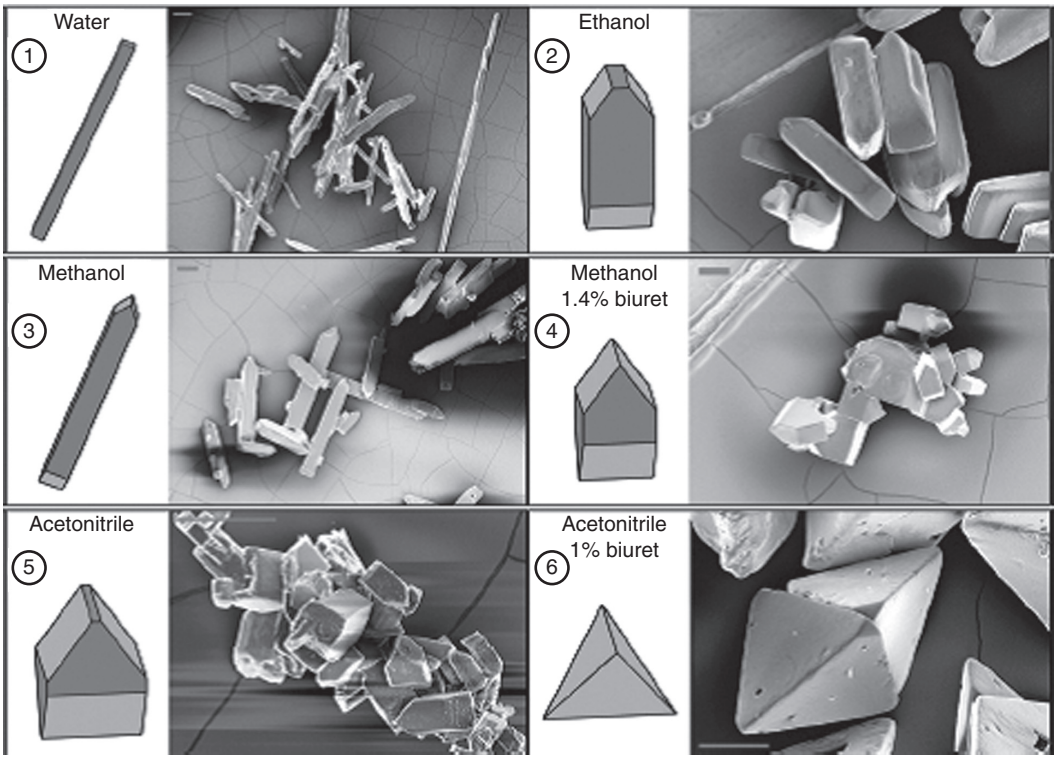

Figure 13.9 Crystal habit of urea grown from four solvents without and with biuret.

consisting of β-glucose and galactose moieties at the top end of the crystal is taken into account (Figure 13.8b), the tomahawk shape can be explained (Figure 13.8c).

Another example of an unintentional impurity that acts on the crystallization of the desired substance is during the synthesis of urea, in which up to 6 wt% biuret (Davey *et al.*, 1986), is formed. The biuret appreciably shortens the needle length. In other applications, biuret is used as a tailored additive.

Salvalaglio *et al.* (2013) studied the habit of urea crystals grown from various solutions at different biuret concentrations. They compared the habits obtained from SEM views with habits calculated using a relatively coarse-grained molecular simulation approach and found a relatively good correlation between the predicted and the measured habits (see Figure 13.9).

The large impact that solvents can have on the crystal growth and morphology has also been addressed by Lahav and Leiserowitz (2001). Solvents were thought to exert their action by preferential adsorption at specific faces and thus inhibit growth, since the removal of bound solvent poses an additional energy barrier for continued growth. They could ascribe the development of large $\{0\,1\,1\}$ and $\{1\,1\,0\}$ faces of α-glycine grown from an aqueous solution to the affinity of the exposed CO_2^- and NH_3^+ groups for water. The $\{0\,1\,0\}$ faces expose alternating layers of C-H or CO_2^- and NH_3^+ groups, and are thus, on average, less hydrophilic. Solvent–surface interaction is, however, in

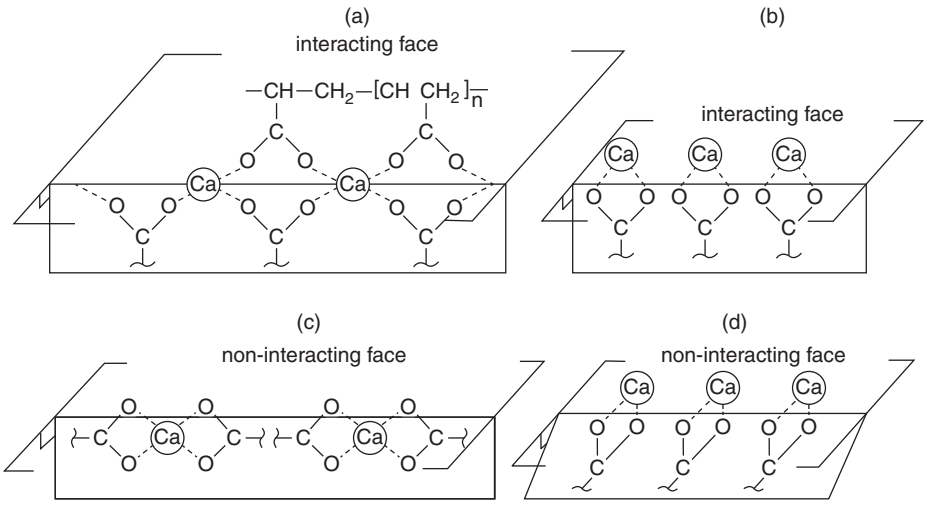

Figure 13.10 Polyaspartate attached to the calcium dicarboxylates.

many cases, less well defined than the interactions between additives that are tailored for impeding the growth of specific crystal faces.

Other ways that solvents can also change the crystal morphology is by formation of solvates or by the induction of a different polymorphic phase (Chen, 2008). Organic solvents can also have a large impact on the morphology of mineral salts, as was shown for gypsum (Trivedi *et al.*, 2013).

13.6 Tailored polyelectrolytes

13.6.1 Polyelectrolytes for organic crystals

The most important common feature of polyelectrolytes is the cooperative interaction between their binding ligands and the crystal surface, allowing them to be effective at amounts in the ppm range. A striking example of a tailored polyelectrolyte is that of aspartic acid as a growth inhibitor for various calcium salts of organic dicarboxylic acids (Addadi and Weiner, 1986). Polyaspartic acid serves as a model compound for aspartic-acid-rich proteins. Very small amounts of these proteins were known to induce clear morphological changes in malonate, fumarate and maleate crystals, for example. Polyaspartate in solution mainly adopts the β-sheet conformation, whereas the side-chain carboxylate groups are arranged in a planar array. The first step in the performance of polyaspartate as a growth retarder is its sharing of Ca^{2+} ions with the crystal surface.

The inter-distance of the Ca ions is 6.6–6.9 Å, and only the growth of those faces where at least one set of carboxylate groups in the crystal lattice is oriented perpendicular to the crystal surface is retarded (a and b in Figure 13.10). For these orientations only, the polymer backbone forms a fence upon the crystal surface that hampers the step

propagation. Upon further growth, the carboxylate groups become incorporated into the crystal without causing too much strain.

Structural matching is a predominant factor in the effectiveness of the polyelectrolyte in face-selective growth retardation, even more than the calcium density. This is particularly well demonstrated by the fact that, in calcium malonate, the {1 0 0} faces, despite having a high calcium density and being the most developed faces in pure crystals, fully disappear in the presence of polyaspartate or proteins in favor of the less calcium-dense {1 0 1} faces.

The effectiveness is not only related to structural aspects of the crystal growth layers, but also depends on the macromolecular conformation of the polyelectrolyte. In contrast to polyaspartic acid with a rigid β-sheet conformation, polyglutamate primarily adopts the random-coil formation in solution, and has only a weak, non-face-specific effect on the growth of calcium dicarboxylates. Higher amounts, although still in the ppm range, are then needed to achieve growth retardation. Also, more strain is induced by their uptake in the crystal lattice, leading to macro-steps and even holes in the crystal surface.

13.6.2 Polyelectrolytes for mineral crystals

A huge market for polyelectrolytes as growth inhibitors exists for prevention of mineral scale formation in desalination, and oil and gas recovery. The most common polyelectrolytes are polyphosphonates, polycarboxylates (polyacrylates and polymaleates) and copolymers with combined carboxylate, sulfonate and and phosphonate ligands or amide ligands attached to the backbone.

In general, a good match between the periodic spacing of the polymeric additive ligands and the array of cations at the crystal surface is sufficient for growth inhibition, but not for face-specific inhibition. For good face selectivity at ppm additive dosages, an appropriate spatial arrangement of the additive ligands, together with a special arrangement of the lattice ions with respect to the crystal surface is required, as illustrated by the example in Figure 13.10.

Rigid molecular arrangements where ligands can replace surface anions tend to be more specific for a particular mineral face in their action, while molecules with flexibility in their structures are more effective for inhibiting the growth of various minerals.

Calcite, for example, consists of alternate layers of calcium and carbonate ions along the *c*-axis. The planar carbonate ions lie in the {0 0 1} face. The best approach of a carbonate ligand would thus be parallel to this plane, which is not feasible at the exposed calcite crystal faces.

Therefore, proteins, as well as polycarboxylates, polyphosphonates and divalent cations have a non-specific inhibiting effect on the growth of calcite. For example, Sr^{2+} at 200 ppm and 600 ppm leads to the habit as illustrated in Figures 13.11(a) and (b), while in part (c) the effect of a polycarbonate that leads to fully globular crystals of size a few hundred microns is shown.

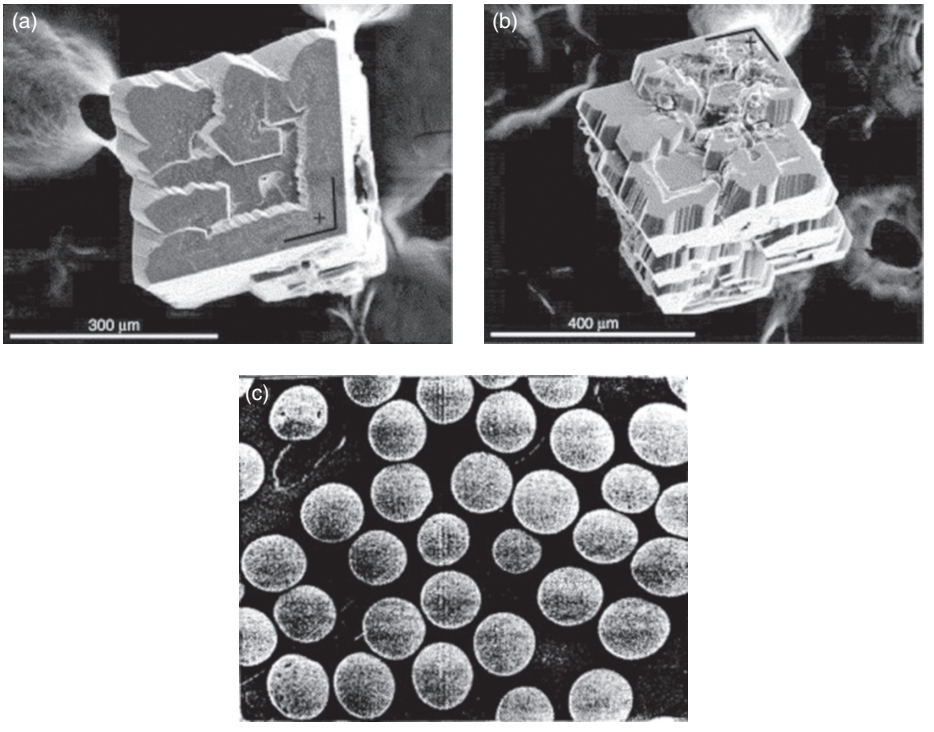

Figure 13.11 Calcite crystals grown in a gel medium doped with Sr^{2+}: the amount of Sr^{2+} in the interstitial solution was (a) 200 ppm and (b) 600 ppm. The jagged appearance of positive steps can be observed (Fernández-Díaz *et al.*, 2006). Part (c) shows globular crystals grown from an aqueous solution.

To achieve maximum growth retardation, sufficient electrostatic interactions between the row of negatively charged ligands of flexible non-specific polyelectrolytes and the cations of the crystal surfaces are needed. These attractions are followed by bonding, possibly also combined with the replacement of surface anions by the ligands. For effective electrostatic interactions over a wide range of pH values, the polyelectrolytes should contain sufficient dissociated negatively charged ligands for bonding with the surface cations. Additional functional groups attached to the polymer backbone, like hydroxyl or amino groups that form hydrogen bridges with the anions, have proved to enhance the inhibitor effectiveness, especially at low pH values. Gypsum needles with the highest charge density at the top faces of their needle shape can easily be shortened by 5 to 10 times along their needle length by the addition of 0.1 ppm polyacrylate. However, after incorporation, this flexible polymer causes holes in the gypsum crystals.

Polyelectrolytes primarily selected for their binding potential with the crystal surface have an average molecular weight between 1500 and 5000 daltons. Within this range, the adsorption time on the crystals takes a maximum of about 5 minutes to obtain the

required surface coverage of only a few percent. At higher molecular weights, their diffusivity along the crystal surface becomes too slow compared to that of the crystal growth units.

All polyelectrolytes designed for scale inhibition are relatively flexible and are intended to be effective for as many minerals as possible. In practical applications they are mostly used in the form of blends with corrosion inhibitors and dispersants.

13.6.3 Proteins for ice crystals

Anti-freeze proteins (AFPs) form a special group of polyelectrolytes generated in nature in the cells of plants and organisms to adapt to cold environments. (Ice formation in these cells is actually an example of melt crystallization.) The rate-limiting step is surface integration-controlled, so the growth rate is sensitive to surface adsorption of foreign molecules. Growth and melting of the ice crystals in the cells is often an alternating process, so the adsorption of the proteins to specific ice faces during both types of processes is important, as well as the shape of the ice crystals resulting from preferential adsorption to these faces.

AFPs can be distinguished into moderate and hyperactive AFPs for freeze tolerance and freeze resistance. Ice crystals grown in the presence of moderate AFPs develop bipyramidal shapes with elongated *c*-axes by the adsorption of the AFPs at the prismatic faces. Upon lowering of the temperature, the tips rapidly sharpen and the basal plane is eliminated. However, sharp needles pose a threat of penetrating the cell membrane.

Hyperactive AFPs also have a strong affinity for the basal planes. This is especially an issue during melting, when these planes become exposed. Then adsorption occurs, and melting of the prismatic faces proceeds faster than that of the basal faces. This eventually leads to an elongation of the crystal along the basal plane, and thus to a lemon-like shape.

Because of the importance of these proteins in nature and their potential applicability in agriculture, food preservation by freezing and in medicines, lately there has been a significant effort expended into the unravelling of their action and in measuring of their adsorption at ice specific faces (Bar-Dolev, 2012).

13.7 Metal ions

In general, metal ions are inadvertently present in crystallizing solution as impurities. It is especially the highly charged, or highly valent ions such as Fe^{3+}, Al^{3+} and Cr^{3+} that influence growth kinetics.

The adsorption of the trivalent metal ions at preferential kink sites of the specific crystal face changes the shape of the growth spirals. This can be seen from Figure 13.12. The blockage of the steps on the {0 1 0} faces of KAP (potassium hydrogen phthalate) at opposite kink sites by Ce^{3+} and Fe^{3+} ions had the effect of rounding off the polygonized growth spirals and of shortening the step distances (Hottenhuis and Lucasius, 1986). When Cr^{3+}, a strongly adsorbing impurity, was added to KAP crystals, their growth was

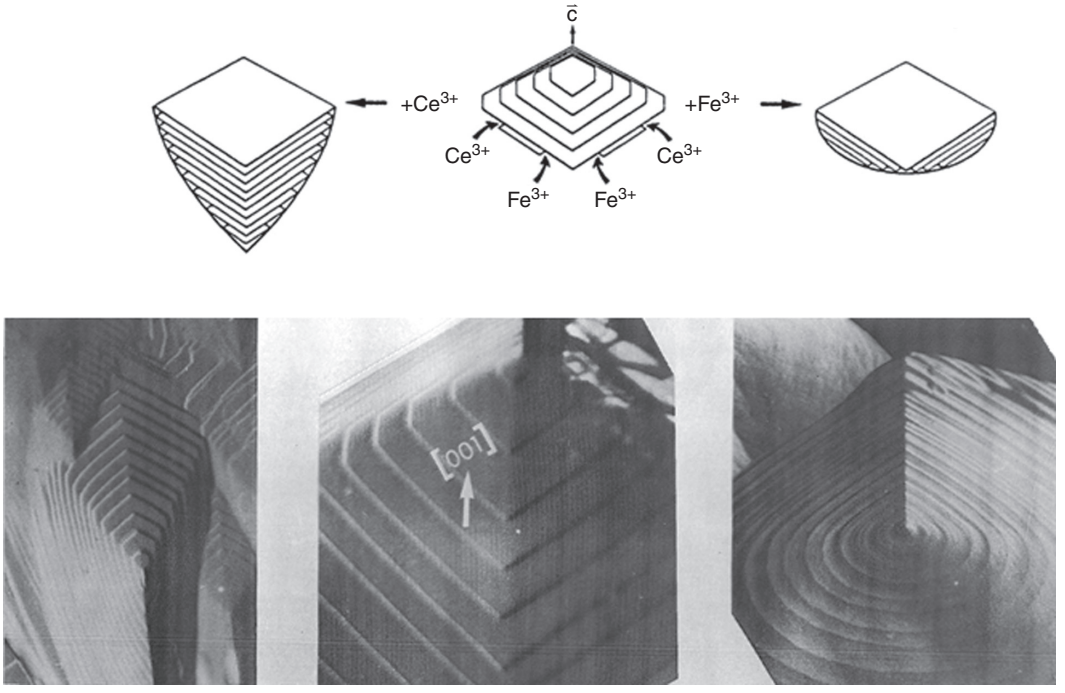

Figure 13.12 Shapes of steps on (0 1 0) face of KAP, without and with trivalent impurities (Hottenhuis and Lucasius, 1986).

completely blocked at concentrations of the order of 16 ppm. These results are in line with the prediction of the Cabrera–Vermilyea model.

Metal ions can also have significant effects on the crystallization kinetics, even at low concentrations. In the production of elemental nickel in solution via hydrogen reduction, which usually occurs in a multi-component metallurgical solution, Fe acts as a growth inhibitor via adsorption onto the surface of the seed particles (Ntuli and Lewis, 2007). Because of the growth inhibition, the supersaturation builds up in solution, and thus nucleation becomes favored.

Incorporation of strongly adsorbed metal ions appears to be unavoidable. The extent of their uptake in the crystal lattice, however, depends predominantly on the induced lattice strain. Metal ions that have hardly any affinity with a crystal surface and have no impact on the growth kinetics, could still become incorporated. This, for example, counts for the uptake of cadmium ions in a gypsum lattice because of the identical ionic radii of Cd^{2+} and Ca^{2+}.

For metal ions with a distribution coefficient smaller than one, the uptake increases at higher supersaturations. At higher growth rates, metal ions that are repelled by the crystal surface are entrapped by the propagating steps. For distribution coefficients larger than one, the capture of foreign metal ions decreases at higher supersaturations.

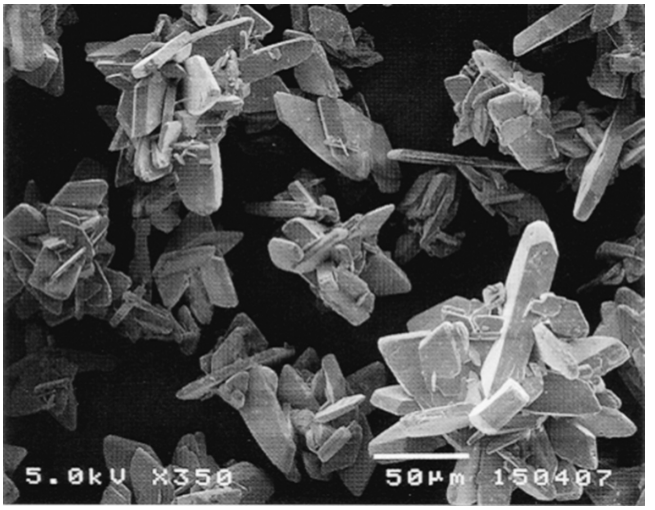

Figure 13.13 Agglomerates of gypsum crystals from phosphoric acid production (Martynowicz *et al.*, 1996).

13.8 Small anions

Many anions purposely added or unintentionally present in the solution have a considerable impact on the crystal shape. Ferrocyanide is a very effective anti-caking agent for sodium chloride and has been used since the 1950s (see Chapter 2, Figure 2.13) (Bode *et al.*, 2012). The method of action of anti-caking agents is mostly through growth inhibition, by preventing bridge formation between the crystals. An example of an anti-caking agent is iron(III) *meso*-tartrate, a metal–organic complex, which is a relatively new anti-caking agent for sodium chloride. The active complex is a binuclear iron(III) complex with two bridging *meso*–tartrate ligands (Bode *et al.*, 2012).

During the production of phosphoric acid, gypsum crystals are produced as a major by-product. Gypsum crystals normally form needles along their *c*-axis. However, during phosphoric acid production, the Al^{3+} and F^- ions from the phosphate ore form AlF_4^- complexes in solution that inhibit the growth of the faces in the needle direction by replacement of the SO_4^{2-} ions. This leads to agglomerates of shorter needles (Figure 13.13). The figure shows the gypsum agglomerates that have subsequently undergone growth, although the extent of the growth has been reduced due to the presence of the AlF_4^- complexes.

Bulutcu (Tanrikulu *et al.*, 2000) showed that NaCl, which was present as an impurity in the crystallization of ammonium perchlorate, affected the controlling mechanism for crystal growth. In pure aqueous solution, the controlling mechanism was the diffusion step. However, in the presence of sodium chloride in solution, both diffusion and integration steps affected the growth.

13.9 Additives as templates for controlled nucleation

Since homogeneous nucleation is a statistical event, additives such as growth inhibitors are, in theory, not capable of having an influence on the nucleation rate. However, as soon as the nuclei grow out as crystals, the additives will hamper their growth. This means that the available supersaturation is consumed less rapidly, and that nucleation is prolonged at about the same rate. So ultimately, the growth inhibitor does have the effect of causing the birth of more and smaller crystals.

It is also possible that foreign particles can stimulate heterogeneous nucleation by reduction of the interfacial energy, as explained in Chapter 4.

Long-chained additives such as polyelectrolytes can bind growth units, and clustering of these units can facilitate the formation of nuclei. This increases the nucleation rate, while simultaneously hampering the further outgrowth of the crystals (van der Leeden *et al.*, 1993).

Over the years there has been increasing attention paid to the design of two- or three-dimensional substrates for use as templates for controlled nucleation of compounds of a specific chirality or for the nucleation of a particular polymorph. Early experiments made use of densely packed Langmuir monolayers floating upon aqueous solutions or used solid-supported Langmuir–Blodgett films. Amphiphilic molecules such as fatty acids and lipids, have a hydrophilic and a hydrophobic part, and readily form monolayer films at the surface of an aqueous solution. The head groups of such films are charged, and their array depends on the special design of the packing density of their compressed tail groups. Therefore, such films have the ability to form templates for nucleation.

Mann *et al.* (1988) have shown that, under conditions where calcite would usually nucleate, the presence of monolayers of stearic acid promote the development of another polymorph, vaterite. These vaterite crystals only nucleate at the interface and are oriented with their $\{0\,0\,1\}$ face parallel to the interface. The positioning of the anions in vaterite provides a good match with the carboxylate positions of the stearic acid molecules. Such template-induced nucleation on organic substrates forms an essential part of the biomineralization processes in nature.

Landau *et al.* (1989) compressed amphiphilic molecules with hydrophobic tails and polar α-amino head groups at the air–water interface over supersaturated glycine solutions. The amphiphilic molecules were designed to form an interface covered either by a monolayer of resolved (R)-α-amino acids or (S)-α-amino acids. In the first case, an (S)-α- glycine crystal with its $\{0\,1\,0\}$ face underneath the interface was grown, while, in the second case, an (R)-α- glycine crystal was grown with its $\{0\,\bar{1}\,0\}$ face underneath the interface.

Mann (2000) managed to mimic many unusual shapes of biominerals by precipitating calcite and barite crystals in self-assembled 3-D organic media, such as surfactant micelles, block copolymer aggregates and micro-emulsion droplets.

More recently, nanocrystals and their composites have become more important for pharmaceutical and nanoelectronic applications. This has prompted the simulation of their nucleation step for comparison with laboratory experiments and with the formation

of biocomposites in nature (Anwar and Zahn, 2011). Apatite-collagen composites belong to the most abundant biominerals in human and animal life forms (Kawska *et al.*, 2008). From simulation studies of the self-organisation of apatite–collagen composites, Ca_3F motifs that were induced by incorporation into the triple helix (acting as protein seeds) during the embryonic stage of ion association have been identified. These motifs then act as nucleation seeds for the apatite crystal structure oriented in accordance to the alignment of the collagen fibres. So in this case, it is the collagen fibres that act as templates.

13.10 A brief summary of the chapter

This chapter discussed the role of additives and impurities that are present during crystallization at low concentrations. It was stressed that, because of their low concentrations in solution, additives and impurities only have the ability to influence the crystallization by acting upon the crystal surface, and do not have the capacity to influence the supersaturation.

The mechanisms of both small and large organic growth inhibitors, i.e. the way in which they act, were explained. Tailor-made additives, which work by molecular recognition, and their design, application and various molecular modeling approaches were also discussed.

Impurities (i.e. additives that are unintentionally present at very low concentrations) as well as the influence of the solvent were also discussed.

Tailored polyelectrolytes, which have a cooperative interaction between their binding ligands and the crystal surface, are effective at amounts in the ppm range, whilst highly charged metal anions can be effective in the ppb range.

Additives can be used as templates for controlled nucleation of specific polymorphs or chiral compounds.

13.11 References

Addadi, L. and Weiner, S. 1986. Interactions between acidic macromolecules and structured crystal surfaces: stereochemistry and biomineralisation. *Molecular Crystals and Liquid Crystals*, **134**, 305–322.

Anwar, J. and Zahn, D. 2011. Uncovering molecular processes in crystal nucleation and growth by using molecular simulation. *Angewandte Chemie International Edition*, **50**, 1996–2013.

Bar-Dolev, M., Celik, Y., Wettlaufer, J. S., Davies, P. L. and Braslavsky, I. 2012. New insights into ice growth and melting modifications by antifreeze proteins. *Journal of The Royal Society Interface*, **9**, 3249–3259.

Bode, A. A. C., Jiang, S. Meijer, J. A. M., van Enckevort, W. J. P. and Vlieg, E. 2012. Growth inhibition of sodium chloride crystals by anticacking agents: in situ observation of step pinning. *Crystal Growth and Design*, **12**(12), 5889–5896.

Buller, R., Peterson, M. L., Almarsson, Ö. and Leiserowitz, L. 2002. Quinoline binding site on malaria pigment crystal: a rational pathway for antimalaria drug design. *Crystal Growth and Design*, **2**, 553–562.

Chen, J., Wang, J., Ulrich, J., Yin, Q. and Xue, L. 2008. Effect of solvent on the crystal structure and habit of hydrocortisone. *Crystal Growth and Design*, **8**(5), 1490–1494.

Davey, R., Fila, W. and Garside, J. 1986. The influence of biuret on the growth kinetics of urea crystals from aqueous solutions. *Journal of Crystal Growth*, **79**(1), 607–613.

Fernández-Díaz, L., Astilleros, J. M. and Pina, C. M. 2006. The morphology of calcite crystals grown in a porous medium doped with divalent cations. *Chemical Geology*, **225**, 314–321.

Hammond, R. B., Ramachandran, V. and Roberts, K. J. 2011. Molecular modelling of the incorporation of habit modifying additives: α-glycine in the presence of Lalanine. *Crystal Engineering Communications*, **13**(15), 4935–4944.

Hottenhuis, M. and Lucasius, C. 1986. The influence of impurities on crystal growth; In situ observation of the $\{0\,1\,0\}$ face of potassium hydrogen phthalate. *Journal of Crystal Growth*, **78**, 379–388.

Kawska, A., Hochrein, O., Brickmann, J., Kniep, R. and Zahn, D. 2008. The nucleation mechanism of fluorapatite–collagen composites: ion association and motif control by collagen proteins. *Angewandte Chemie International Edition*, **47**, 4982–4985.

Lahav, M. and Leiserowitz, L. 2001. The effect of solvent on crystal growth and morphology. *Chemical Engineering Science*, **56**(7), 2245–2253.

Landau, E. M., Wolf, S. G., Levenon, M. *et al.* 1989. Stereochemical studies in crystal nucleation: oriented crystal growth of glycine at interfaces covered with Langmuir and Langmuir–Blodgett films of resolved alpha-amino acids. *Journal of the American Chemical Society*, **111**, 1436–1445.

Mann, S., Heywood, B. R., Rajam, S. and Birchall, J. D. 1988. Controlled crystallization of $CaCO_3$ under stearic acid. *Nature*, **334**, 692–695.

Mann, S. 2000. The chemistry of form. *Angewandte Chemie International Edition*, **39**, 3392–3406.

Martynowicz, E. T. M. J., Liao, L., Witkamp, G.-J. and Van Rosmalen, G. M. 1996. The influence of aluminium fluoride in hemi-dihydrate phosphoric acid processes. *Hydrometallurgy*, **41**, 155–170.

Meenan, P. A., Anderson, S. R. and Klug, D. L. 2002. The influence of impurities and solvents on crystallization. In *Handbook of Industrial Crystallization*, 2nd edn., Allan, S. M. (ed.), Butterworth-Heinemann.

Ntuli, F. and Lewis, A. E. 2007. The influence of iron on the precipitation behaviour of nickel powder. *Chemical Engineering Science*, **62**, 3756–3766.

Salvalaglio, M., Vetter, T., Mazzotti, M. and Parrinello, M. 2013. Controlling and predicting crystal shapes: the case of urea. *Angewandte Chemie International Edition*, **52**, 13369–13372.

Sangwal, K. 2007. *Additives and Crystallization Processes: From Fundamentals to Applications*, John Wiley & Sons.

Tanrikulu, S. Ü., Eroglu, I., Bulutcu, A. N. and Özkar, S. 2000. Crystallization kinetics of ammonium perchlorate in MSMPR crystallizer. *Journal of Crystal Growth*, **208**, 533–540.

Trivedi, T. J., Pandya, P. and Kumar, A. 2013. Effect of organic additives on the solubility behavior and morphology of calcium sulfate dihydrate (gypsum) in the aqueous sodium chloride system and physicochemical solution properties at 35 °C. *Journal of Chemical Engineering Data*, **58**, 773–779.

van der Leeden, C., Kashchiev, D. and van Rosmalen, G. M. 1993. Effect of additives on nucleation rate, crystal growth rate and induction time in precipitation. *Journal of Crystal Growth*, **130**, 221–232.

Visser, R. A. 1983. *Crystal Growth Kinetics of alpha-lactose hydrate*, PhD Thesis, University of Nijmegen.

Weissbuch, I., Addadi, L. and Leiserowitz, L. 1991. Molecular recognition at crystal interfaces. *Science*, **253**, 637–645.

Weissbuch, I. and Lahav, M. 2011. Crystalline architectures as templates of relevance to the origins of homochirality. *Chemical Reviews*, **111**, 3236–3267.

14 Polymorphism

14.1 Why this chapter is important

Polymorphism is a widely spread phenomenon in solid substances (Bernstein, 2002, Hilfiker, 2006, Brittain, 2009). A substance exhibits polymorphism when it can exist in more than one crystalline state. These various crystalline states consequently have a different thermodynamic potential, and therefore a different solubility in a given solvent. These various states also possess different physical and chemical properties. Polymorphs have, for example, different crystal shapes and can have different colors and tastes.

14.2 Occurrence and consequences

For simple substances, as in many mineral compounds, the basic entity has a fixed atomic, molecular or ionic structure and the different lattice structures result from different packing arrangements in the crystal lattice.

An example of an inorganic mineral substance is calcium carbonate, which can crystallize in three polymorphic crystalline forms, calcite (trigonal), aragonite (orthorombic) and vaterite (hexagonal), depending on the crystallization conditions (see Figure 14.1). An amorphous phase can also be directly precipitated from highly supersaturated solutions. The most stable form at ambient conditions is calcite.

Molecular structures of organic compounds are often flexible and expose rotational degrees of freedom around a single bond. They are therefore prone to polymorphism. An isolated molecule in the gas phase has one or more equilibrium structures. These equilibrium structures are at a different local or total minimum in potential energy and are called conformers. To go from one conformer to another, an energy barrier has to be crossed. A particular arrangement of atoms in a molecular crystal lattice cannot be far from an equilibrium structure in the gas phase. Its conformation in a crystal lattice is only adjusted to minimize the sum of the intra- and inter-molecular energy. A variation of any torsion angle of a molecule in a crystal lattice is a new conformation. In this way different polymorphs can be formed by only a conformational adjustment with respect to the gas-phase conformation. If, in addition to a change in torsion angle, there is a change in potential energy well in the new conformation, the new conformation is also a conformer.

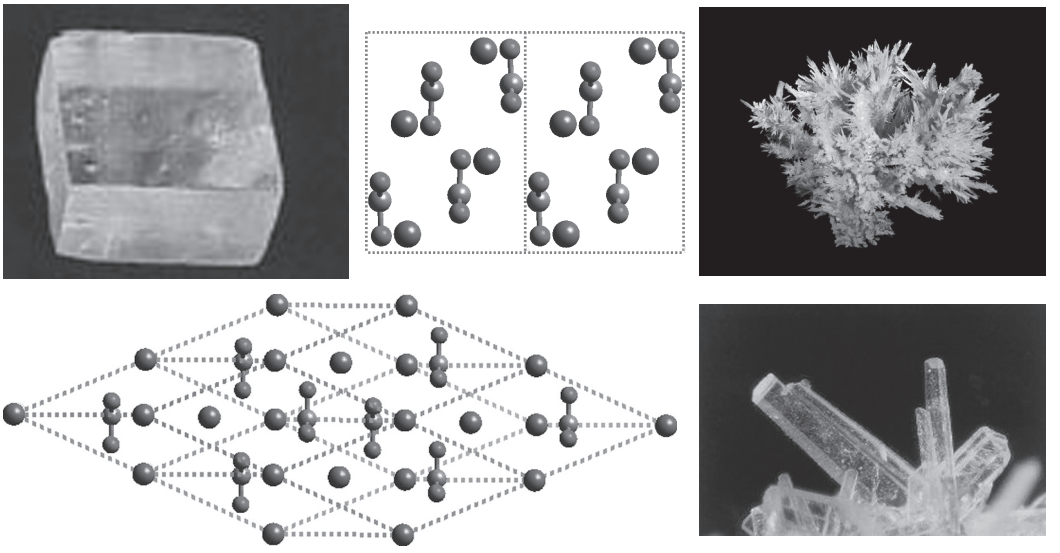

Figure 14.1 Calcite (left) and aragonite (right).

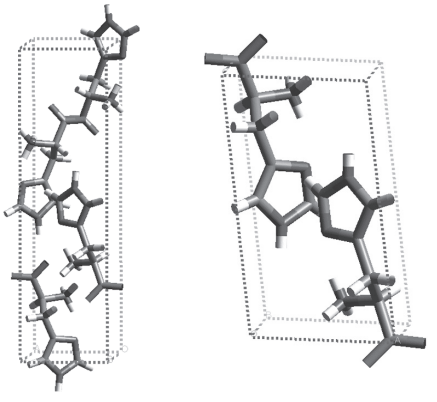

Figure 14.2 L-histidine, orthorombic α-form (left), monoclinic β-form (right).

This kind of polymorphism with different conformers is called *conformational polymorphism* (Cruz-Cabeza and Bernstein, 2014).

Because of their torsional flexibility, even simple organic compounds can be packed in different crystal lattices and thus show polymorphism. This is the case, for example, for the two polymorphs of L-histidine, with only a slight adjustment in their molecular conformation (see Figure 14.2).

An almost equally simple organic molecule such as glutamic acid has two conformational polymorphs caused by torsion along the C—C—C backbone (see Figure 14.3). Although the space groups of the two polymorphs are the same, the lattice parameters (axis lengths) are quite different, as are their torsional angles.

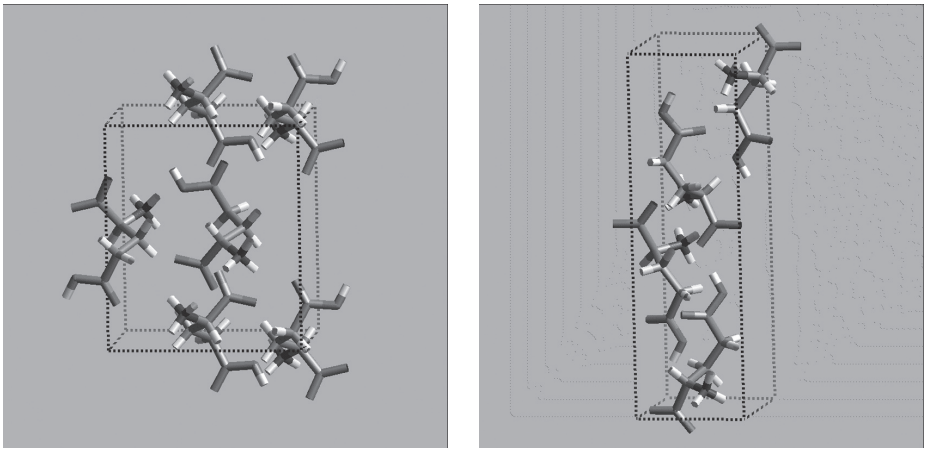

Figure 14.3 Glutamic acid, orthorhombic α-form (left), orthorhombic β-form (right).

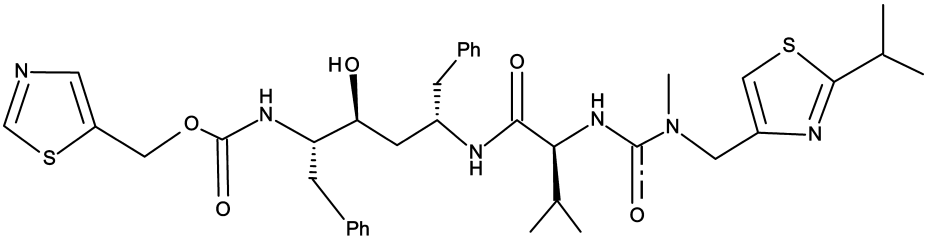

ABT-538

Figure 14.4 Ritonavir.

The difference in solubility of polymorphs of the same compound plays an important role in pharmaceutical products, because the bioavailability of the active ingredient is directly related to the solubility (Hilfiker, 2006, Brittain, 2009). An example of consequences of the development of an unwanted polymorph is Ritonavir, illustrated in Figure 14.4, which was developed in 1996 by Abbott as an HIV-1 and HIV-2 protease inhibitor.

In 1998, a new, more stable and less soluble polymorph appeared, and it was no longer possible to manufacture the original product to its specification. The lower solubility of the new form prevented the required *in vivo* concentrations of the drug from being achieved. Abbott was forced to withdraw the drug temporarily and rework it, at considerable cost (Bauer *et al.*, 2001, Chemburkar *et al.*, 2000).

The occurrence of various polymorphs in high-energy materials such as ammonium nitrate can also have a large impact. Ammonium nitrate exhibits enantiotropy, a type of polymorphism that will be addressed below. This implies that the most stable crystalline phase changes with temperature (see Table 14.1).

At the site of BASF in Ludwigshafen, ammonium nitrate had been stored in a silo at the end of a working day in 1921 for further transportation the following day. After a

Table 14.1 Polymorphs of ammonium nitrate at various temperatures

Tetragonal: <18 °C
Orthorhombic I: 18–32.3 °C
Orthorhombic II: 32.3–84.2 °C
Trigonal: 84.2–125.2 °C
Cubic: 125.2–169.6 °C
Liquid (decomp): >169.6 °C

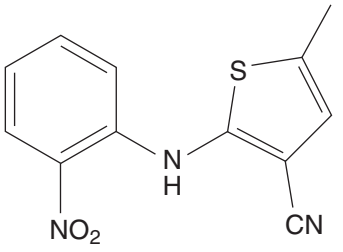

Figure 14.5 Structure of ROY (from Yu *et al*., 2000).

cold night, the contents of the silo had solidified to a solid block by caking, most likely due to polymorphic transformation. Dynamite was used to try to break up the block as was standard and established practice at the time. Upon heating the explosion of the contents was heard in Munich, 300 km away, and the position of the former silo was called Crater Lane after this event.

Another classical example in food preservation is chocolate that exists in six polymorphic forms. Form V, the one that is pleasant to eat, is not the most stable form at room temperature. Transformation to Form VI is thermodynamically favored, and a white bloom appears on chocolate that has been poorly kept, which greatly affects the quality of the product.

A property that is very important for its application and that can change significantly from one polymorph to another is its color. This is the case, for example, for many inorganic pigments, as well as for organic dyes. For example, the compound 5-methyl-2-(2-nitrophenyl)amino-3-thiophenecarbonitrile (also known as ROY) has six polymorphs that exist at room temperature, each of a different color and crystal shape, ranging from dark red, through orange to yellow (Yu *et al*., 2000). The structure of ROY is illustrated in Figure 14.5.

ROY is a good example of conformational polymorphism. The separate molecule in the gas phase has two equilibrium potential energies with a difference in rotational angle around the N bond with the 5-ring of about 100°. It crystallizes in at least nine different polymorphs, grouped into two conformational regions. The conformations of four polymorphs are only *adjustments* to one gas phase conformer by slight rotations, and the other three to the other gas phase conformer after a *change* in conformation by rotation of about 100°.

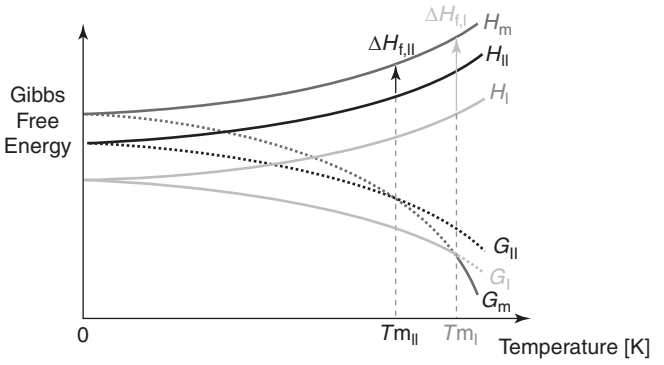

Figure 14.6 Monotropic system, where I = higher melting form, II = lower melting form, m = melt, T_m = melting temperature and ΔH_m = enthalpy of fusion.

Other properties related to different polymorphs have been highlighted in many review publications and books (Bernstein, 2002) on polymorphism.

14.3 Types of polymorphs

Because at a given temperature different polymorphs have different structures, their state functions will be different. The Gibbs free energy of formation G (invariably numerically negative) represents the relative stability of the forms, so placing them in order of their G value also places them in order of stability. G is related to the solubility, and the most stable form, the ground form, thus has the lowest solubility. The other forms are metastable and their transformation to more stable forms not only depends on the difference in G, but is also determined by kinetic factors. The kinetics can even be affected by the solvents, because transformations are often solvent mediated.

Polymorphic systems can be classified into *monotropic* and *enantiotropic* systems. This will be elucidated below for a dimorphic system with two polymorphs.

14.3.1 Monotropic system

If one polymorph is more stable than the other over the entire temperature range below the two melting points, the relationship between the two polymorphs is called *monotropic* (see Figure 14.6).

Form II may exist in a metastable state with melting point T_{mII} which will be below T_{mI}. The melting points are defined by the temperatures at the intersections of the G curves of the forms and the G curve of the melt. The G curves for forms I and II will not reach a transition point for the two phases before the forms have melted.

The enthalpy changes upon melting $\Delta H_{m,I}$ and $\Delta H_{m,II}$ can be measured by differential scanning calorimetry (DSC), along with the melting temperatures. Where the entropies

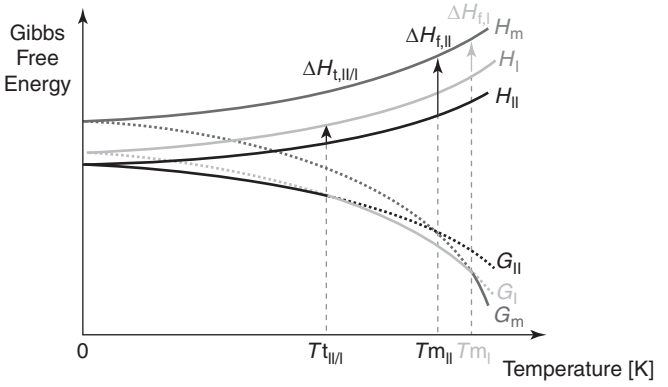

Figure 14.7 Enantiotropic system, where T_t = transition temperature, below which I is the higher melting form, and above which II is the higher melting form.

of the solid forms do not differ greatly, as in the case shown here, it can be seen that $\Delta H_{m,I} > \Delta H_{m,II}$ and also $T_{mI} > T_{mII}$. This observation is often taken to indicate that a system is monotropic, according to the Burger–Ramberger fusion rule.

14.3.2 Enantiotropic system

When the transition point of the two forms crosses below the melting point of the lower melting form the system is called *enantiomorphic* (see Figure 14.7). Below T_t, II is more stable; above T_t, I is the more stable form.

In some cases, solid-state transitions I ↔ II occur when the transition temperature is crossed, but the rates and timescales are determined by the existence of pathways and kinetic factors. In many cases, the structure is "frozen in" and can remain in its metastable condition up to its melting point. Transitions close to T_t will occur very slowly, if at all, on account of the small energy driving force.

In the case where $T_{mI} > T_{mII}$ and $\Delta H_{m,I} < \Delta H_{m,II,}$ the Burger–Ramberger Fusion rule points to an enantiotropic relationship. A further rule (the transition rule) stipulates that if a solid transition is noted, this also points to enantiotropy.

If T_t occurs outside of the temperature ranges experienced by the substance in preparation, storage and use, the distinction between monotropy and enantiotropy is largely academic. If T_t lies around room temperature, or at a temperature used in processing, then the distinction will be practically important.

The difference between monotropic and enantiotropic also has its consequences for the solubility curves, as shown by Figure 14.8. For an enantiotropic system both forms have a similar solubility at the transition temperature.

If a particular crystallization procedure yields more than one form under identical conditions, this phenomenon is termed *concomitant polymorphism.* In thermodynamic terms polymorphs are only expected to coexist in equilibrium at the transition temperature. So kinetic factors apparently play a dominant role and competing kinetic processes

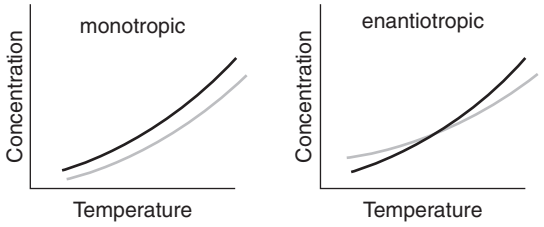

Figure 14.8 Solubility curves for monotropic and enantiontropic systems. Each curve represents a different polymorph.

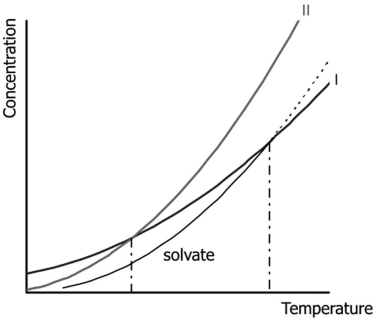

Figure 14.9 Two enantiotropic polymorphs with a solvate.

have very similar rates, because concomitant polymorphism is a widely observed phenomenon. Below, the kinetics of polymorph formation will be discussed in more detail, including the chance to crystallize forms together.

Depending on the solvent from which the polymorphs are formed, sometimes solvates are crystallized, if a solvated form is more stable than the non-solvated polymorph, as shown in Figure 14.9. This can be the case, for example, if a small solvent molecule such as water or methanol fills up an otherwise empty space in the lattice. Solvates are often referred to as pseudo-polymorphs, and hydrates are the most frequently encountered solvates.

14.4 Kinetics of polymorph formation

14.4.1 Metastable zone width

At the transition point of a dimorphic enantiotropic system both polymorphs have the same thermodynamic potential G and the same solubility (Threlfall, 2000, 2003). The transition temperature is only related to the solid lattice structures and therefore independent of the solvent from which the polymorphs are crystallized. Changing the solvent will only change the concentration axis. The solubility ratio of the two polymorphs is only a measure of the relative thermodynamic potentials G of the polymorphs at that temperature. So for ideal solutions the concentration ratio c_I/c_{II} is a constant at any temperature and the concentration axis only has to be rescaled linearly. For non-ideal

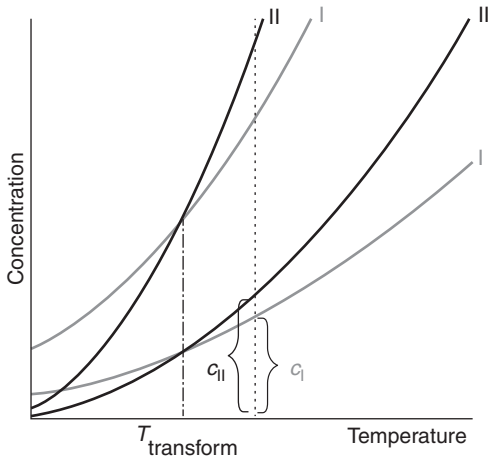

Figure 14.10 Solubilities of polymorphs in two solvents.

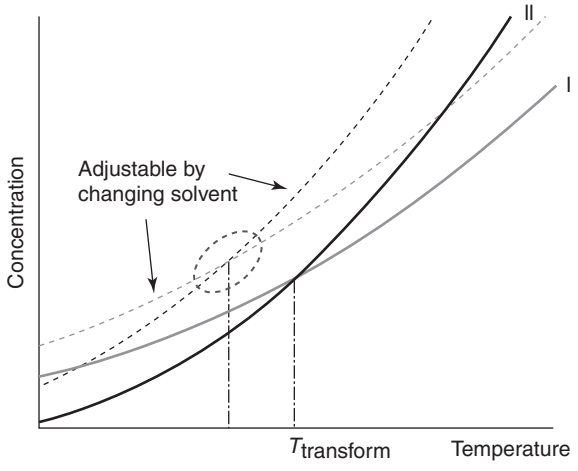

Figure 14.11 Solubilities and metastable zone widths of polymorphs in two solvents.

solutions the activity ratio a_I/a_{II} ($a = \gamma c$) remains the same for any temperature. The concentration axis has to be rescaled in a non-linear way, but the shape of the curves remains the same (see Figure 14.10).

The metastable zone width can, however, be significantly altered by changing the solvent (see Figure 14.11).

If a clear solution of a compound that exposes polymorphism is cooled down beyond the solubility of one of its polymorphs, nucleation of that particular polymorph only occurs beyond its metastable zone width. If a solution of a certain concentration is cooled beyond the metastable zones of both polymorphs the less stable polymorph is generally formed first, according to Ostwald's rule of stages. As the solubilities and zone widths depend on the solvent, different polymorphs may be formed at the same concentration

value in various solvents. Solvents may even promote or inhibit the development of a particular polymorph due to their molecular structure, as will be further elucidated below. Another consequence of metastable zones is that the temperature at their crossing point does not have to coincide with the transition temperature. This may hinder the determination of the transition point. It can be seen in Figure 14.11 that temperatures just below the transition point (within the circle drawn in Figure 14.11) can still be within the metastable zone width of polymorph II, but beyond the metastable zone of polymorph I. Cooling down of a solution with a concentration lying just above the concentration where the metastable zones are crossing to a temperature just below the transition temperature, but above the crossing point of the metastable zones can thus lead to the formation of polymorph I. Upon equilibration at the same temperature it may very slowly transform into polymorph II.

In the region close to the crossing point of the metastable zone curves, concomitant polymorphism is often observed.

At very high supersaturations an amorphous phase is generally formed as a precursor that quickly transforms into a more stable polymorph.

14.4.2 Seeding

It is common procedure to use seeding as a technique for the development of a particular polymorph. If the polymorph is stable, only a small amount of seeds of the stable phase has to be added to induce crystallization at a supersaturation lying within the metastable zone width. If the polymorph is metastable, generally a relatively large amount of seed material of the metastable polymorphic form has to be added to a solution supersaturated with respect to the metastable phase in order to ensure the further outgrowth of only this phase.

This seeding technique was used to ensure formation of the metastable form I of Ritonavir during anti-solvent crystallization. To avoid the need to add an undesired surplus of form I seeds, a reverse-addition technique was applied. A small amount of seeds was added to a stirred volume of anti-solvent heptane. Subsequently a solution of Ritonavir in ethyl acetate (the solvent) was slowly added to this heptane. As the addition progressed, the increasing amount of form I crystals acted as seeds. The initial amount of seeds was only 5% of the total end product.

When this product, after filtration, was equilibrated in a mixture of ethyl acetate (solvent)/heptane (anti-solvent) the final product remained mostly polymorph I if the solvent/anti-solvent ratio was 0:1, became 50:50 of both forms at a ratio 1:1, and transferred more than 90% into polymorph II if the ratio was 2:1. This was caused by the solubility of the forms in the mixtures that determine the driving forces for the conversion.

14.4.3 Templates

In the early stages of template-induced nucleation of organic molecules, compressed Langmuir layers at the air–water interface were frequently used. In the field of

biomineralization numerous examples were discovered where the development of mineral compounds was structured by their oriented nucleation upon an organic substrate. Such template-induced nucleation was also noticed to favor particular polymorphic forms. Nowadays self-assembled monolayers (SAMs) are designed to control polymorphism, in particular for application in the pharmaceutical industry (Singh *et al.*, 2011). One of the many examples is the crystallization of mefenamic acid (MA), a non-steroidal anti-inflammatory drug, which exposes two enantiotropic polymorphs. By using biocompatible polymer surfaces as heteronucleants concomitant polymorphism could be avoided and the metastable form II could be favored (López-Mejias *et al.*, 2013).The role of seven SAMs of different compositions in the crystallization of mefenamic acid on patterned surfaces was studied (Yang *et al.*, 2012). SAMs forming strong interactions with the carboxylic acid group of MA molecules depleted their polarity and pushed the system to form $\pi \ldots \pi$ and C—H$\ldots\pi$ interactions, which promoted form II.

14.4.4 Molecular structure of the solvent

Apart from the influence of a solvent on the growth behavior of polymorphs, and thus on their crystal shape, solvents can play an essential role in the nucleation of a polymorph through the speciation of the polymorphic compound in the specific solution. Numerous examples exist for organic compounds where potential building entities for the crystal lattice are formed in solution by mutual interaction of the molecular entities via hydrogen bonds and by their interaction with the solvent.

If a molecule has multiple conformers in the gas phase, multiple conformers can also be expected to be present in solution that can inter-convert rapidly or slowly. The solvent can promote or inhibit the formation of a conformer. Conformations prone to H-bonds can be promoted by protic solvents. Polar conformations are stabilized by polar solvents, while less polar solvents are stabilized by less polar solvents via hydrophobic interactions. The nucleation rate of a particular polymorph can thus be favored by the appropriate choice of solvent (Derdour and Skliar, 2014).

There is also strong evidence that in many cases, self-association of a conformer in solution drives systems to nucleate as specific polymorphs. In the case of crystallization of benzophenone and diphenylamine, for example, a dimer is created through aromatic ring–ring contact between the molecules in a polar solvent such as methanol, while the C=O . . . . H—N hydrogen bond creates a dimer in toluene (Davey *et al.*, 2013).

The polymorphic form of 2,6-dihydroxybenzoic acid is determined by hydrogen-bonding interactions with the solvent on crystallization from solution (see Figure 14.12). Form I nucleates from solutions in toluene, where there is little solute–solvent interaction and a preferential assembly of dimers exists. Form II was prepared from solutions in chloroform, in which the phenolic catemer motifs were strongly solvated.

The organic molecule 2-amino-4-nitrophenol is a polyfunctional molecule with many donor and acceptor sites for H-bonding (see Figure 14.13). Nitromethane solvates the amine functions, directing the lattice structure towards chains of nitro–hydroxy interactions. Similarly, methanol solvates the hydroxy groups, thus favoring nitro–amine

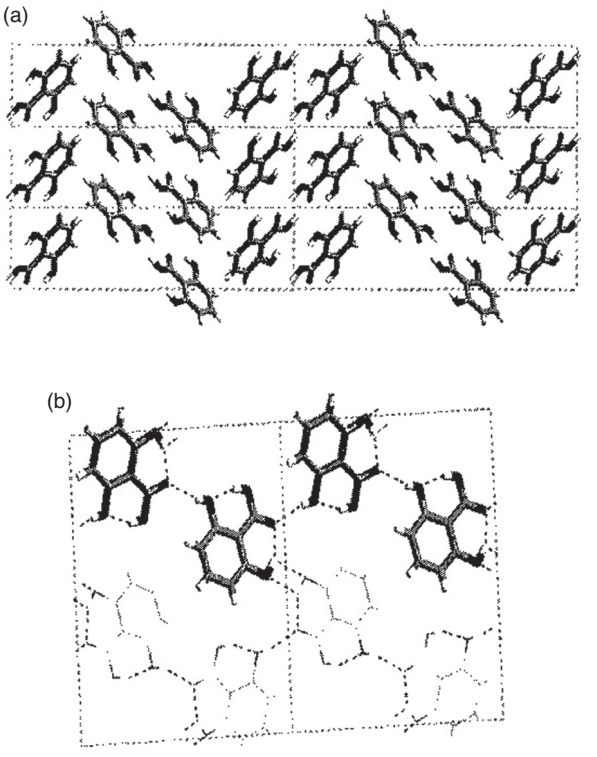

Figure 14.12 Two polymorphs of 2,6-dihydroxybenzoic acid:form I formed from centrosymmetric carboxylic acid dimers in toluene (a), and form II, catemer motifs involving carboxylic acid and *o*-hydroxy interactions (b) (Davey *et al.*, 2001).

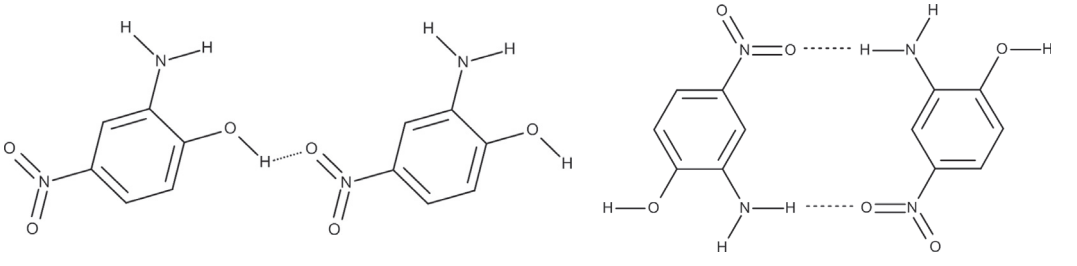

Figure 14.13 Two polymorphs of 2-amino-4-nitrophenol: form I built up by OH–NO_2 interactions, favored in nitromethane (left), and form II built from H_2N–NO_2 interactions, favored in methanol (right) (Blagden *et al.*, 2001).

dimers. Toluene promotes H-bonding interactions non-specifically, giving rise to both H_2N—NO_2 dimers and chains made up of OH—NO_2 linkages.

Similarly for *p*-aminobenzoic acid, the more stable β-form below 25 °C consists of catemers that are formed as prismatic crystals from aqueous solutions and not from hexane. Above 25 °C carboxylic dimers are the building units of needle-like crystals grown from aqueous solutions (Gracin and Rasmusson, 2004).

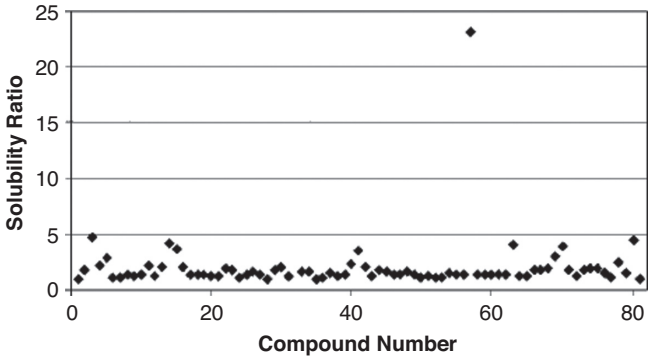

Figure 14.14 Solubility of 55 drugs compared to their ground state solubility.

14.5 Alternative solid forms

Alternative solid forms are all solid forms in which a particular compound can be isolated and consolidated. These solid forms can be divided into three groups: (I) polymorphs, including amorphous forms, and solvates (e.g. hydrates), (II) salts and (III) cocrystals. Salts and cocrystals involve the designed introduction of counterions or coformers. Especially for the pharmaceutical industry, one of the most important properties is the solubility of a compound that releases the active pharmaceutical ingredient in an aqueous solution, because the solubility is directly related to its bioavailability.

14.5.1 Polymorphic and amorphous forms

From a reliability standpoint, it seems most prudent to work with the most stable form available. But when the stable form has a very low solubility, another polymorph or even the amorphous form could be preferred. In case of an amorphous form the particles are often dispersed in a polymer matrix to avoid any transformation in a separate particle spreading immediately across the whole product. During the period before the amorphous particles transform into a more stable phase, a higher transient solubility is obtained. By choosing a metastable polymorph other than the stable ground state, the increase in solubility is, however, generally not more than 1–5 times. Figure 14.14 shows the solubility ratios in relation to the ground states for 55 drug compounds with 81 polymorphic forms (Pudipeddy and Serajuddin, 2005). The ratios should be independent of the solvent used, unless form-specific solvent interactions take place. The majority of the ratios lie between 1 and 2 with the exception of premafloxacin in ethyl acetate, where the ratio was about 23.

14.5.2 Solvates and hydrates

In many cases the solvent and particularly water molecules occupy empty spaces in the crystal lattice of the host molecules. The lattice energy is therefore lower. About 50%

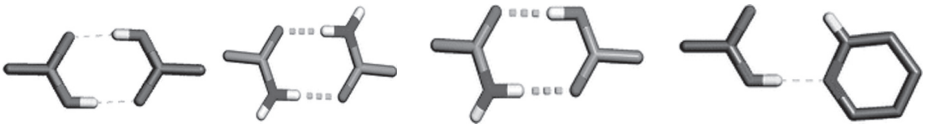

Figure 14.15 Homosynthons (carboxylic acid dimers or amide dimers) and heterosynthons (carboxylic and amide dimers or carboxylic and pyridine dimers).

of all pharmaceutical solvates are hydrates, due to the small size of the water molecule and its ability to act as both a hydrogen bond donor and an acceptor. In some cases solid phases are not even identified as hydrates because the percentage of water in the solution from which it is crystallized is minor (Rodriguez-Spong *et al.*, 2004).

14.5.3 Salts

The traditional approach to increasing the solubility of drugs is by salt formulation. The ionic nature of salts makes them more soluble in aqueous solutions. Some compounds, however, lack ionizable functional groups, are not sufficiently acidic or basic to enable salt formation or have sensitive moieties that are prone to decomposition or racemization (Babu and Nangia, 2011, Elder *et al.*, 2013). In those cases amorphous drugs or cocrystals are often used for their solubility advantage.

14.5.4 Cocrystals

Cocrystals are multi-component solids that are formed from molecules that are solids at ambient temperature. The main difference between cocrystals and solvates is that in case of solvates one of the components is a liquid at ambient temperature. It can also be difficult to separate cocrystals from salts since only the nature of the interaction between the two components will tell one how to classify such a molecular complex (Aitipamula *et al.*, 2012).

14.6 Cocrystals

Cocrystals are solids that are crystalline single-phase materials composed of two or more different molecular and/or ionic compounds, mostly in a stoichiometric ratio. The coformer is generally an easily soluble compound, and the cocrystal dissociates rapidly into amorphous or nanocrystalline clusters which transform via fast-dissolving metastable polymorphs into the poorly soluble ground phase. This creates a transient high solubility of the active drug compound in the case of a pharmaceutical product.

The crystallization of cocrystals proceeds via the formation of supramolecular synthons. These synthons are created by hydrogen bonding between two or more functional groups. These building blocks are called *homosynthons* in the case of similar functional groups or *heterosynthons* for different functional groups (see Figure 14.15 for examples of functional groups).

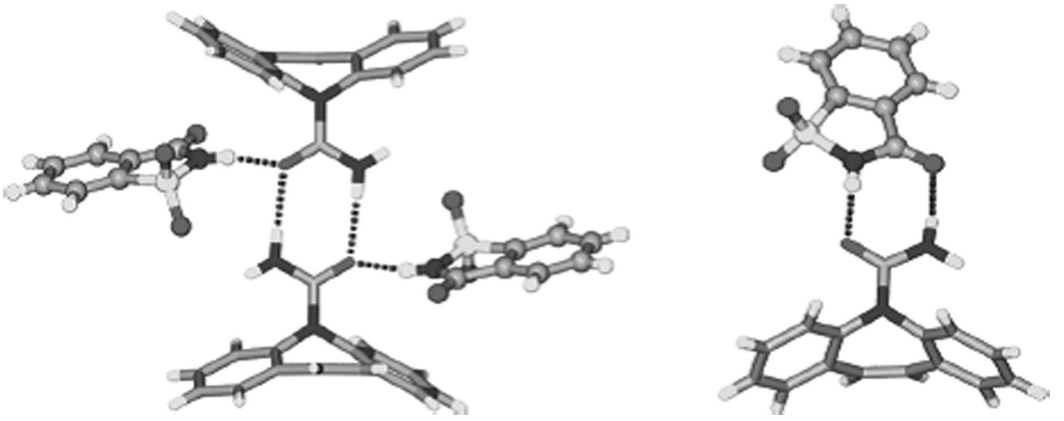

Figure 14.16 Two polymorphic forms of carbamazepine saccharin cocrystals with supramolecular synthon formation.

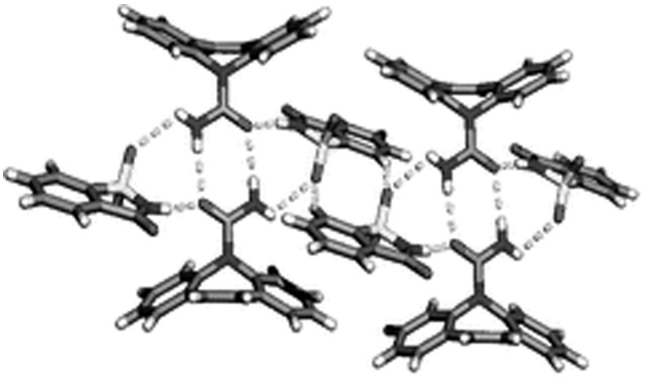

Figure 14.17 Polymorphic form of carbamazepine saccharin cocrystals with homosynthons interconnected by saccharin molecules.

Cocrystals can also show polymorphism, as illustrated in Figure 14.16 for cocrystals of carbamazepine and saccharin (Aitipamula *et al.*, 2012, Fleischman *et al.*, 2003). In the left polymorph, homosynthons between carbamazepine molecules form supramolecules by means of saccharin molecules that are stacked on top of each other in the voids (see Figure 14.17).

Cocrystals of carbamazepine and aspirin are formed through heterosynthons (Vishweshwar *et al.*, 2005), as shown in Figure 14.18.

There is an abundance of literature on polymorphs and cocrystals, because there are tens of thousands of polymorphs and cocrystals (Desiraju, 2007).

Solution crystallization is the preferred method to synthesize cocrystals. But for that purpose the ternary phase diagram of the two components in the particular solvent has to be carefully examined. The solubility curve of a 1:1 ratio cocrystal does not necessarily have to cross the 1:1 stoichiometric ratio line, resulting in incongruent dissolution.

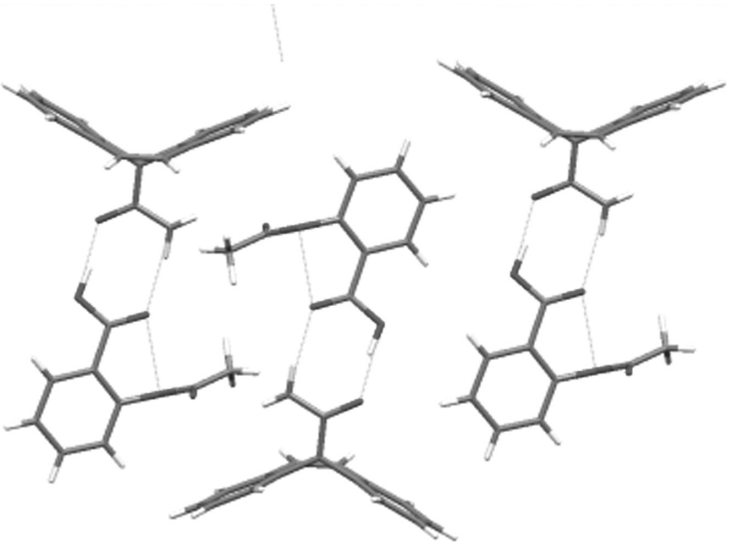

Figure 14.18 Polymorph of carbamezapine–aspirin cocrystals with heterosynthons.

This often happens because the solubilities of the two components lie far apart. To crystallize the 1:1 ratio cocrystal the correct ratio of the two components in the given solvent must be chosen (Chiarella *et al.*, 2007). If the phase diagram is unknown, often solid-state grinding, solvent drop grinding or crystallization from the melt are tried for synthesis. Solvent-mediated transformation from one type of cocrystal into another is also frequently experienced. For example, form II of carbamazepine/isonicotinamide transfers into form I when suspended in ethanol (ter Horst and Cains, 2008).

14.7 A brief summary of the chapter

Almost all inorganic and organic compounds allow packing of their building units in lattices with often only a small difference in their Gibbs free energy. If growth from solution does not inhibit kinetic pathways to form these lattices, polymorphism can be expected. The various polymorphic forms of a compound can exhibit a striking difference in their chemical and physical properties. The differences in properties are generally larger for conformational polymorphs than for polymorphs with small conformational adjustments of the same conformer of the molecule in the gas phase.

This variation in properties can have unexpected positive or detrimental effects for the use of these polymorphic compounds. Therefore a lot of effort is invested in synthesizing the right polymorph, solvate, salt or cocrystal, by applying different solvents, by designing templates and by selecting the right counterion of the salt or the right cobuilder.

In the pharmaceutical industry it has become common practice to perform an extended high-throughput polymorph screening by determining the developed polymorphs in

various solvents under different conditions, complemented by computational approaches (Abramov, 2013).

14.8 References

Abramov, Y. A. 2013. Current computational approaches to support pharmaceutical solid form selection. *Organic Process Research and Development*, **17**, 472–485.

Aitipamula, S., Desijaru, G. R., Myerson, A. S. *et al.* 2012. Polymorphs, salts and cocrystals: what's in a name? *Crystal Growth and Design*, **12**, 2147–2152.

Babu, N. J. and Nangia, A. 2011. Solubility advantage of amorphous drugs and pharmaceutical cocrystals. *Crystal Growth and Design*, **11**, 2662–2679.

Bauer, J., Spanton, S., Rodger, H. *et al.* 2001. Ritonavir: an extraordinary example of conformational polymorphism. *Pharmaceutical Research*, **18**(6), 859.

Bernstein, J. 2002. *Polymorphism in Molecular Crystals*, Clarendon Press.

Blagden, N., Cross, W. I., Davey, R. J. *et al.* 2001. Can crystal structure prediction be used as part of an integrated strategy for ensuring maximum diversity of isolated crystal forms? *Physical Chemistry and Chemical Physics*, **3**(17), 3819.

Brittain, H. G. (ed.) 2009. *Polymorphism in Pharmaceutical Solids*, CRC Press.

Chemburkar, S. R., Bauer, J., Deming, K. *et al.* 2000. Dealing with the impact of ritonavir polymorphs on the late stages of bulk drug process development. *Organic Process Research and Development*, **4**(5), 413.

Chiarella, R. A., Davey, R. J. and Peterson, M. L. 2007. Making co-crystals: the utility of ternary phase diagrams. *Crystal Growth and Design*, **7**, 1224–1225.

Cruz-Cabeza, A. J. and Bernstein, J. 2014. Conformational polymorphism. *Chemical Reviews*, **114**, 2170–2191.

Davey, R. J., Blagden, N., Righini, S. *et al.* 2001. Crystal polymorphism as a probe for molecular self assembly during nucleation from solutions: the case of 2,6-dihydroxybenzoic acid. *Crystal Growth and Design*, **1**(1), 59–65.

Davey, R, Schroeder, S. L. M. and ter Horst, J. H. 2013. Nucleation of organic crystals: a molecular perspective. *Angewandte Chemie International Edition*, **52**, 2166–2179.

Derdour, L. and Skliar, D. 2012. A review of the effect of multiple conformers on crystallization from solution and strategies for crystallizing slow inter-converting conformers. *Chemical Engineering Science*, **106**, 275–292.

Desiraju, G. R. 2007. Crystal engineering: a holistic view. *Angewandte Chemie Indernational Edition*, **46**, 2–17.

Elder, D. P., Holm, R. and Lopez de Diego, H. 2013. Use of pharmaceutical salts and cocrystals to address the issue of poor solubility. *International Journal of Pharmaceutics*, **453**, 88–100.

Fleischman, S. G., Kuduva, S. S., McMahon, J. A. *et al.* 2003. Crystal engineering of the composition of pharmaceutical phases: multiple-component crystalline solids involving carbamezepine. *Crystal Growth and Design*, **3**, 6910–6919.

Gracin, S. and Rasmusson, Å. C. 2004. Polymorphism and crystallization of *p*-aminobenzoic acid. *Crystal Growth and Design*, **4**, 1013–1023.

Hilfiker, R. (ed.) 2006. *Polymorphism in the Pharmaceutical Industry*, John Wiley & Sons.

López-Mejias, V., Myerson, A. S. and Trout, B. L. 2013. Geometric design of heterogeneous nucleation sites on biocompatible surfaces. *Crystal Growth and Design*, **13**, 3835–3841.

Pudipeddy, M. and Serajuddin, A. T. M. 2005. Trends in solubility of polymorphs. *Journal of Pharmaceutical Sciences* , **94**(5), 929–939.

Rodriguez-Spong, B., Price, C. P., Jayasankar, A., Matzger, A. J. and Rodriguez-Hornedo, N. 2004. General principles of pharmaceutical solid polymorphism: a supramolecular perspective. *Advances in Drug Delivery Reviews*, **56**, 241–274.

Singh, A. I. S., Lee, I. S., Kim, K. and Myerson, A. S. 2011. Crystal growth on self-assembled monolayers. *Crystal Engineering Communications*, **13**, 24–32.

ter Horst, J. H. and Cains, P. W. 2008. Co-crystal polymorphs from a solvent-mediated transformation. *Crystal Growth and Design*, **8**, 2537–2542.

Threlfall, T. 2000. Crystallization of polymorphs: thermodynamic insight into the role of solvent. *Organic Process Research and Development*, **4**, 384–390.

Threlfall, T. 2003. Structural and themodynamic explanations of Ostwald's rule. *Organic Process Research and Development*, **7**, 1017–1027.

Vishweshwar, P., McMahon, J. A., Oliveira, M., Peterson, M. L. and Zaworotko, M. J. 2005. The predictably elusive form II of aspirin. *Journal of the American Chemical Society*, **127**, 16802–16803.

Yang, X., Sarma, B. and Myerson, A. S. 2012. Polymorph control of micro/nano-sized mefenamic acid crystals on patterned self-assembled monolayer islands. *Crystal Growth and Design*, **12** 5521–5528.

Yu, L., Stephanson, G. A., Mitchell, C. A. *et al.* 2000. Thermochemistry and conformational polymorphism of a hexamorphic crystal system. *Journal of the American Chemical Society*, **122**(4), 585–591.

Index